

**The Electronic and Vibrational Spectroscopy of Metal
Phthalocyanines and Metal Phthalocyanine Chlorides Isolated in
Low Temperature Solids**

A Thesis submitted by

Christopher Henchy B.Sc (Hons.)

to the Maynooth University in fulfilment of the
requirements for the Degree of Doctor of Philosophy



**Maynooth
University**
National University
of Ireland Maynooth

Based on research carried out at the
Low Temperature Laboratory,
Department of Chemistry,
Maynooth University of Ireland.

Research Supervisor: Dr. John G. McCaffrey

Head of Department: Dr. John C. Stephens

Maynooth,
Co. Kildare,
Ireland.

April, 2016

Table of Contents

Table of Contents	i
Declaration.....	viii
Acknowledgements	ix
Abstract.....	xi
Chapter I: Introduction	1
I.1: Porphyrins and Phthalocyanines	1
I.1.I: Structure of Porphyrins and Phthalocyanines	2
I.1.II: Synthesis of Phthalocyanine and Tetraazaporphyrin	3
I.1.III: Applications of Phthalocyanines	6
I.1.IV: Electronic Absorption of Phthalocyanines and Tetraazaporphyrins	7
I.2: Matrix-Isolation	10
I.2.I: Matrix Hosts	11
I.2.II: Matrix Effects	12
I.2.III: Matrix Effects and Vibrational Spectra	13
I.2.IV: Matrix Effects in Electronic Spectra	15
I.3: Density Functional Theory	18
I.3.I: Density Functional Theory	18
I.3.II: Exchange-Correlation Functionals	19
I.3.III: The B3LYP Functional	21
I.3.IV: Basis Sets	21
I.3.V: Time-Dependent DFT	23
I.3.VI: Limitations of DFT	24
I.4: Research Motivations	24
I.5: Spectroscopy of Matrix-Isolated Phthalocyanines	25
I.6: Thesis Layout	27
I.7: References.....	28

Chapter II: Methods.....	38
II.1: Introduction	38
II.2: Matrix-Isolation Apparatus	38
II.3: Gas Handling System.....	41
II.4: Phthalocyanine Vapour Generation	43
II.5: Sample Deposition	45
II.6: Fourier Transform Infrared (FT-IR) Measurement	46
II.7: Luminescence Measurements.....	53
II.7.I: Steady-State Spectroscopy	53
II.7.II: Time-Resolved Spectroscopy.....	55
II.8: Raman Spectroscopy.....	66
II.9: Density Functional Theory	67
II.9.I: Geometry Optimizations	68
II.9.II: Vibrational Analysis	69
II.9.III: Isotopic Substitutions and Internal Modes	71
II.9.IV: Time Dependent DFT.....	72
II.10: The Wp Function – Lineshape Analysis	72
II.11: References	78
II.12: Appendix	82
Chapter III: Vibrational analysis of Metal Tetraazaporphyrins and Metal Phthalocyanines	83
III.1: Introduction	83
III.2: Computational details	83
III.3: Experimental Methods	84
III.4: Results.....	85
III.4.I: Geometries	85
III.4.II: Infrared Spectroscopy.....	86

III.4.III: Raman Spectroscopy	96
III.5: Discussion	101
III.5.I: Structural Analysis	101
III.5.I.a: D _{4h} Systems.....	101
III.5.I.b: C _{4v} Systems.....	104
III.5.I.c: Metal Phthalocyanine Chlorides	105
III.5.I.d: Planarity.....	107
III.5.II: Vibrational Analysis.....	110
III.5.II.a: IR Spectroscopy.....	110
III.5.II.b: Raman Spectroscopy.....	116
III.5.III: Symmetry Effects on Vibrational Spectra.....	121
III.5.III.a: Vibrational Spectra of the M-TAPs.....	121
III.5.III.b: Symmetry Influence on the Vibrational Spectra of the M-Pcs	126
III.6: Conclusions	129
III.7: References	130
III.8: Appendix	134
Chapter IV: A DFT Study of Reversed Isotope Shifts in H/D Substitution of Free-base Tetrapyrroles	146
IV.1: Introduction.....	146
IV.2: Computational Methods.....	149
IV.3: Results.....	150
IV.3.I: N-H Stretching (A _g and B _{1u}) Modes.....	153
IV.3.II: Out-of-Plane (B _{3u} & B _{2g}) Bending Modes.....	159
IV.3.IV.a: B _{3u} N-H Bending Modes	159
IV.3.IV.b: B _{2g} N-H Bending Modes.....	162
IV.3.III: In-Plane (B _{2u} & B _{3g}) Bending Modes	163
IV.3.IV.a: B _{2u} N-H Bending Modes.....	164
IV.3.IV.b: B _{3g} IP N-H Bending Modes	166

IV.4: Discussion	167
IV.4.I: Comparison with Other Calculations	167
IV.4.II: Comparison with Experiments	169
IV.5: Conclusions	173
IV.6: References	174
Chapter V: Visible Spectroscopy of GaPcCl Isolated in Inert Gas Matrices	176
V.1: Introduction	176
V.2: Experimental	176
V.3: Results	177
V.3.I: Argon	177
V.3.I.a: Sample Optimization	177
V.3.I.b: Absorption	181
V.3.I.c: Emission	183
V.3.I.d: Excitation	189
V.3.I.e: Amplified Emission	191
V.3.II: Krypton	196
V.3.II.a: Sample Optimization	196
V.3.II.b: Absorption	199
V.3.II.c: Emission	201
V.3.II.d: Excitation	207
V.3.II.e: Amplified Emission	208
V.3.III: Xenon	209
V.3.III.a: Sample Optimization	209
V.3.III.b: Absorption	212
V.3.III.c: Emission	214
V.3.III.d: Excitation	219
V.3.III.e: Amplified Emission	220
V.3.IV: Nitrogen	222
V.3.IV.a: Sample Optimization	222
V.3.IV.b: Absorption	225

V.3.IV.c: Emission	226
V.3.IV.d: Excitation.....	232
V.3.IV.e: Amplified Emission.....	234
V.3.V: Matrix Comparison	235
V.3.V.a: Absorption.....	235
V.3.V.b: Emission	240
V.3.V.c: Excitation	244
V.3.V.e: Time Dependent DFT Calculations.....	246
V.4: Discussion	247
V.4.I: TD-DFT	247
V.4.II: Comparison of the Absorption, Emission and Excitation Spectra.....	250
V.4.III: Vibronic Structure in Emission.....	252
V.4.IV: Site Structure in Emission	255
V.5: Conclusions	260
V.6: References	262
V.7: Appendix	264
Chapter VI: Amplified Emission of GaPcCl Isolated in Inert Gas Matrices.....	269
VI.1: Introduction.....	269
VI.2: Experimental	269
VI.3: Results.....	270
VI.4: Discussion	279
VI.4.I: Amplified Emission.....	279
VI.4.II: Site Splitting of Amplified Emission	281
VI.4.II.a: Argon	282
VI.4.II.b: Krypton.....	289
VI.4.II.c: Xenon.....	294
VI.4.II.d: Nitrogen	300
VI.4.II.e: Matrix Summary.....	305
VI.4.III: Temperature Effects.....	311

VI.4.IV: Matrix Influences on the Amplified Emission of GaPcCl.....	318
VI.4.IV.a: Argon.....	318
VI.4.IV.b: Krypton.....	319
VI.4.IV.c: Xenon.....	320
VI.4.IV.d: Nitrogen.....	321
VI.5.V: Phonon structure of GaPcCl/Ar.....	322
VI.5: Conclusions.....	323
VI.6: References.....	325
VI.7: Appendix.....	327
Chapter VII: Conclusions.....	333
VII.1: Symmetry of the M-Pcs and M-TAPs.....	333
VII.2: Vibrational Analysis of Matrix-Isolated MgPc, AlPcCl and GaPcCl.....	334
VII.3: Reverse ISR of Free-base Porphyrin and Related Tetrapyrroles.....	335
VII.4: Visible Spectroscopy of Matrix-Isolated GaPcCl.....	336
VII.5: Amplified Emission of Matrix-Isolated GaPcCl.....	338
VII.6: References.....	340

Declaration

This thesis has not been submitted before, in whole or in part, to this or any other University for any degree, and is, unless otherwise stated, the original work of the author.

Christopher Henchy

Acknowledgements

The first person I wish to thank is my supervisor, Dr. John (Seán) McCaffrey. His wisdom, experience and enthusiasm have been instrumental in my education and development over the past few years. I have thoroughly enjoyed many of the discussions we had on topics of both a scientific and non-scientific nature. I would also take this opportunity to show my appreciation for his encouragement and motivation during periods where my experiments were not working very well (and especially during my brief cameo as a synthetic chemist).

I would also like to thank my partner in crime from the Low Temperature Lab – Dr. Barry Davis. It has been an absolute pleasure working with you in the LTL, and living with you in Moyglare/Castlebridge/Straffan Wood. I must mention that I very much enjoyed those ~~very rare~~ occasions in which we feasted on Indian cuisine (usually enough to feed 4) and consumed a few 'light refreshments' in Brady's. A true scholar and a gentleman. I would like to thank my good friend and fellow pharmachem graduate Ross ^{Brett} Driver. I just know one of your get rich schemes will work out someday – my money is on you either going pro in CS:GO (you'll have to hit gold first, mind), or winning big in Vegas! Either way, don't forget to keep singing songs about your old pal Chig. I also wish to thank another pharmachem veteran, Dr. Adam 'Milky' Curtin. Having endured the bitter cold and a diet consisting almost entirely of aubergine in Kerry almost made our lives as PhD students seem like a life of luxury!

I would also like to say thanks to all of the postgrads who have made the chemistry department as much a place of enjoyment as a place of work. I would like to thank the synthetic folks hAndrew, the gym nut Jessica, Harlei and Matt (both of whom were no doubt inspired to pursue PhDs following my influences), Mark K, Muhib, Alba and Jack (who is alright I suppose). Thanks to Justine/Jacinta/Christine/'Special J', who sometimes gets confused about direction and temperature and once thought I would make an excellent pillow. Thanks to all of the downstairs people; Ula, Mark G, Karen, 'good' Michelle, Saidbhe and especially 'bad' Michelle, whose bed will never be fluff-free again, and Alice, who has been a wonderful landlady. I also wish to thank the old crew – Ruth, my protector Walshy, Sherro, Conor, Joey, Lynn, Roisin, Foxy, Keeley, Murph and the many more who have called this place home during my time here. Cheers for all of the amusing chats in the coffee room (and the odd scientific discussion).

I have to acknowledge the football crowd for all of the enjoyable Friday afternoons – Finno, Gamma, Ken, Niall, John, the Physics lads and the stragglers we picked up from other departments around the campus.

I would like to thank the members of the academic staff, the technicians and the office staff, all of whom have been very helpful during my time as both an undergraduate and a postgraduate student. I would like to thank the two heads of department who were in office while I was here; John Lowry and more recently John Stephens. I must say a very special thanks to Noel Williams. His knowledge of electronics and general knack for fixing/making things was a crucial part of keeping the pumps, matrix-isolation rigs and spectrometers in working order. He is one of the most unique characters in the department, and one which it can seldom cope without (as his holiday time often testified to).

Finally I would like to thank my family. To my parents Mark and Bridget for your love, support and guidance, to my sisters Claire and Rachal for the endless slagging I endure in your presence, and to my little niece Lilly-Anne who is cute and mischievous in equal measures.

Abstract

Phthalocyanines (Pcs) are an important class of dye molecules, capable of incorporating a wide range of metal atoms into their macrocyclic cavity and can be heavily substituted on their outer carbons. These highly stable molecules play an important role not only in the commercial dye industry, but have also fuelled the development of many other technologies due to their attractive physical and chemical properties. Given their potential as light harvesting molecules, dye lasers and in photodynamic therapies, it is important to have a detailed understanding of the optical properties of the phthalocyanines. The matrix-isolation technique provides an excellent opportunity to perform a detailed spectroscopic study of these molecules. Isolation of a molecule in an inert gas solid such as the rare gases or N₂ at cryogenic temperatures allows for the acquisition of highly resolved spectra with very narrow bandwidths and the absence of hot bands or rotational bands. Furthermore, the positions of the bands are only slightly shifted from gas phase values due to the weak interaction between the host and the guest species. The aim of the work presented in this thesis is to provide novel insights into the spectroscopy of matrix-isolated phthalocyanines, with particular attention given to the gallium phthalocyanine chloride (GaPcCl) molecule. The most significant findings in the current work pertain to the luminescence spectroscopy and amplified emission of matrix-isolated GaPcCl. A vibrational analysis is performed on the ground electronic state of the molecule (as well as the related molecules MgPc and AlPcCl), which is used to assign the vibronic bands observed in emission and excitation.

The infrared absorption spectra of matrix-isolated MgPc, AlPcCl and GaPcCl are recorded in the region from 400 to 4000 cm⁻¹ in solid Ar and N₂. Comparison of the spectroscopic results with predictions from large basis set *ab initio* density functional theory (DFT) calculations allow for mode assignments to be made. The most intense bands in the spectra correspond to A_{2u} (A₁) and E_u (E) modes associated with out-of-plane and in-plane motions of the macrocycle and hydrogens of MgPc (AlPcCl/GaPcCl). The high frequency modes arising from the C-H stretching modes were not observed in either matrix, but have been tentatively assigned in results from KBr discs. Two metal dependent vibrational modes were observed for AlPcCl; one at 491 (488) cm⁻¹ in Ar (N₂), and another at 519 cm⁻¹ in both Ar and N₂. A single metal dependent vibrational mode was observed in MgPc, located at 505 (504) cm⁻¹ in Ar (N₂). The remaining metal dependent modes for these two

molecules, and all of those from GaPcCl, lie in the low frequency region below 400 cm^{-1} and out of the range of the infrared detectors. The Raman scattering data recorded for MgPc, AlPcCl and GaPcCl in KBr discs are also analysed and found to be quite similar. The Raman active modes tend to correspond to in-plane distortions of the macrocycle, with the most intense bands being of B_{1g} (B_2) symmetry for MgPc (AlPcCl/GaPcCl). The Raman scattering spectra of GaPcCl are noted for being very similar to the fluorescence data.

The visible luminescence spectra of GaPcCl trapped in N_2 , Ar, Kr and Xe matrices are recorded and analysed. The visible absorption in the region of the Q band clearly show the effect of matrix shifts in different hosts, although no gas phase data exists for comparison. Resolved vibronic bands are observed to the blue of the 0-0 transition of the Q band, where there is evidence for site structure. The less resolved B bands are recorded in the UV region, and are weaker than the fully allowed Q transition. A set of very weak bands are observed to the red of the B bands in each host. The vertical excitation energies and oscillator strengths of GaPcCl (as well as a number of other M-Pc and M-TAP molecules) are calculated with TD-DFT utilizing the B3LYP hybrid functional and 6-311++G(2d,2p) basis set. The theoretical results correctly predict the trend of the strong Q band in the visible and the weaker B band in the UV region of the spectrum. The predicted bands are typically blue-shifted with respect to the experimental results. A number of very weak bands were consistently predicted in the 350 – 500 nm region for all of the M-Pcs and M-TAPs. These features are also observed in the experimental absorption spectra of matrix-isolated GaPcCl and warrant further investigation.

Emission spectra of matrix-isolated GaPcCl are recorded with pulsed dye laser excitation. Vibronic bands in emission extend up to $\sim 1600\text{ cm}^{-1}$ from the 0-0 transition. A comparison of the absorption (excitation) and emission spectra shows obvious mirror symmetry, indicating the molecule has a similar structure in its ground and excited states. A vibrational analysis of the excited electronic state is performed given the similar vibronic structure in emission (and absorption/excitation) and the ground state Raman modes. Emission lifetimes are measured and found to be in the 2.3 – 2.6 ns range which is expected for a strongly absorbing dye molecule. The lifetimes are thermally stable and not strongly host dependent but do exhibit a small wavelength dependence. The existence of multiple sites of isolation is revealed in emission, with Ar matrices showing the best examples of this due to the narrow bandwidths of its emission peaks. Sites are also

observed in Kr and Xe, but are less resolved than in Ar. The broad emission bands observed in N₂ also indicate the presence of multiple but unresolved sites. Sites are also evident in excitation, where the position of the 0-0 band (and thus the vibronic bands) shift depending on which emission wavelength is being monitored.

With a moderate increase in the laser intensity, the laser induced fluorescence spectroscopy of GaPcCl trapped in rare gas and nitrogen matrices exhibits some unusual behaviour. In all matrices, a huge increase in the intensity of one particular emission band is observed when pumping the S₁ (Q) ← S₀ transition. This band involves a vibrational mode of the ground state, located at 1540 cm⁻¹ (for GaPcCl/Ar) and from DFT calculations is assigned to the most intense Raman active mode involving an out-of-phase stretching of the bridging C_α-N_m-C_α bonds. Many of the characteristics of amplified emission (AE) are exhibited by this vibronic transition, and thus the threshold conditions and lifetime of this emission band are investigated. The narrow bandwidths of the AE bands allow for the identification and classification of phonon structures in emission and excitation, as well as the resolution of individual sites. A *Wp* function is used to analyse resolved phonon structure (the zero phonon line and phonon side bands) of GaPcCl/Ar AE spectra. 2D Excitation-emission spectra are employed to reveal the excitation and emission features in each host material. Ar matrices give the richest spectroscopy, showing a continuum of sites between two dominant species. The isolated monomer is abundant in this host, although a significant amount of aggregates are also present. Kr matrices tend to contain less of the isolated monomer and higher amounts of the aggregate, whereas Xe appears to contain only the aggregate species. Both Kr and Xe contain two dominant features, similar to what is observed in Ar. The N₂ matrix differs from the inert gas matrices in that only a single dominant feature is present, although it is evident that this feature contains several unresolved sites located very close in energy.

DFT calculations are performed on a series of M-TAPs and M-Pcs to investigate the effect the metal atom has on the structure of the porphyrin scaffold. Two situations are observed – one in which the metal fits comfortably into the macrocycle cavity and another where the metal is forced to sit above the plane of the porphyrin ring. As the metals bind to all four of the pyrrole nitrogen atoms the symmetries of these structures are found to be D_{4h} and C_{4v} for the planar and non-planar molecules respectively. Analysis of several metals with different atomic radii shows that the size of the atom is the sole property governing

whether or not the macrocycle can incorporate a given metal. The non-planar structures also show evidence of a doming of the porphyrin macrocycle, which gets progressively more pronounced as the size of the metal atom increases. Where experimental values are available, DFT calculations agree to within 3% of measured bond lengths and angles. Calculations on the M-PcCl and M-Pc⁺ molecules (M=Al/Ga) show that a counter-ion can pull the metal from the central cavity and cause a small doming effect.

DFT calculations are used to analyse the occurrence of reverse isotope shift ratios (ISR) in H/D substitution of the free-base tetrapyrroles, whereby the frequency ratio ν_H/ν_D is less than 1. The reverse ISR effect is found to be most evident in the out-of-plane bending modes (B_{2g} and B_{3u} symmetry) involving some N-H motion for the four molecules studied; porphyrin (H_2P), tetraazaporphyrin (H_2TAP), tetrabenzoporphyrin (H_2TBP), and phthalocyanine (H_2Pc). This effect was analysed by following the evolution of the normal mode frequencies with incremental variation of the H atom masses from 1 to 2 amu. This method allows direct, unambiguous mode correlations to be established between the light and the heavy isotopologues. When the NH(D) motion is predominant, the H to D frequency evolution decreases in a continuous manner for a particular normal mode. In the case of two modes of the same symmetry and whose frequencies are similar, their frequency evolutions could cross, depending on the extent of NH(D) motion involved in them. The evolution diagrams may show avoided crossings of various extents, which thereby reflects the degree of the NH(D) motion in the modes. The reverse ISR effect is directly correlated to these avoided crossings.

Chapter I: Introduction

I.1: Porphyrins and Phthalocyanines

Porphyrins are a class of important bio-molecules and are a part of what gives nature much of her colour. Often referred to as the *Colours of Life*¹, they are responsible for giving plants their bright green colour in the form of chlorophyll², and mammalian red blood cells their distinctive crimson red colour when found in the form of haemoglobin³ (Figure I.1). Both of these metallo-proteins are involved in energy transfer processes in plants and animals and have directly allowed life to populate, thrive in and shape the planet into the place we know and live in today. The word porphyrin originates from the Greek word for purple, πορφύρα, which is the colour of some of the earliest discovered porphyrins.

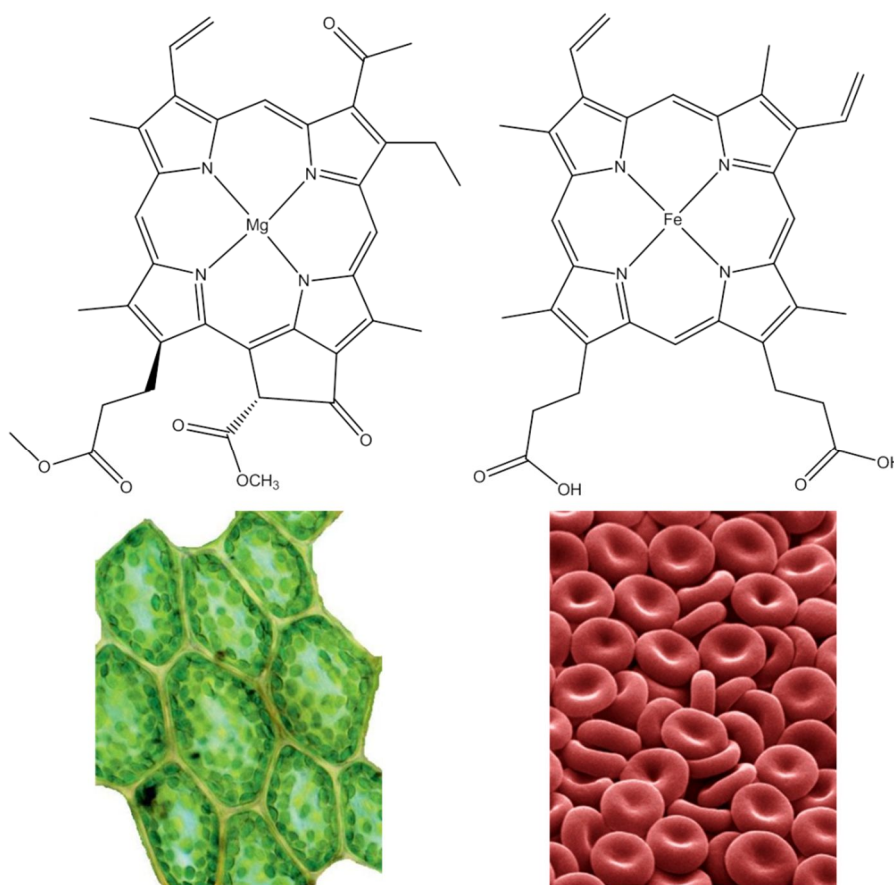


Figure I.1: Molecular structure of the chlorophyll c1 and heme molecules (top left and right respectively) and the effect these molecules have on the appearance of the cells they occupy (bottom). The images of the plant and mammalian red blood cells were taken from Reference 2 and Reference 3 respectively.

Porphyrins get their intense colours from the conjugation on the central ring of the tetrapyrroles. These chromophores are aromatic according to Hückel's definition⁴, as they are planar and have $4n+2$ conjugated π -electrons. The molecules absorb light strongly in the visible region of the spectrum, and depending on the substituents and metals occupying the macrocycle cavity, the absorption maxima can shift quite significantly, giving this class of pigments a wide range of intense colours.

The simplest porphyrin, free-base porphine (P), is a cyclic tetrapyrrole with four linking methine carbons. More complex porphyrins, such as the bio-molecules mentioned above, contain this relatively simple structure with various substituents on the β -carbons, allowing large protein scaffolds to be built around the pigment moiety. Phthalocyanines (Pcs) are synthetic counterparts of the porphyrins, where the bridging carbons have been replaced by nitrogens. An important property of porphyrins and phthalocyanines is that two protons in the central cavity of the ring can be replaced with a metal, bonded to the four pyrrole nitrogens. It is thought that approximately 70 different metals can occupy the cavity in phthalocyanine⁵. These are centres of chemical activity and play a crucial role in energy transfer processes in life. For example, the heme molecule has a central iron atom which acts as an oxygen transporter in mammalian respiration. In chlorophyll the central metal is magnesium, which acts as a binding site for water – the electron source in photosynthesis.

While colour is their most striking property, the porphyrins have other useful properties which make them ideal for use in living organisms and in man-made materials. Porphyrins and especially the phthalocyanines are very stable molecules, and do not degrade at high temperatures or when exposed to intense light. They are generally insoluble in most common solvents except in strong acids or when functionalised with sulfonate groups.

1.1.I: Structure of Porphyrins and Phthalocyanines

The structure of porphine is relatively simple, consisting of four pyrrole rings connected by bridging (methine) carbon atoms to form a 16-membered macrocycle. The tetraazaporphyrin (TAP) molecule differs from this structure only in the meso positions, where the bridging carbons have been replaced by nitrogens. Porphine and TAP are the parent molecules to the larger and more stable tetrabenzo porphyrin (TBP) and phthalocyanine (Pc) molecules, where benzo annulations to the pyrrole rings form isoindole subunits instead (Figure I.2).

The phthalocyanine anion (Pc^{2-}) can act as a tetra-dentate ligand capable of complexing with a wide variety of metal atoms via the four pyrrole nitrogens, forming metallo-phthalocyanine (M-Pc). The anion is also capable of bonding two hydrogen atoms (as shown for the free-base molecules in Figure I.2) or two small metal cations (such as Li_2 or Na_2). Similarly, TBP and the parent molecules P and TAP are also capable of these interactions, although the number of possible M-P and M-TAP systems have not been studied to the same extent as their more stable benzene annulated counterparts.

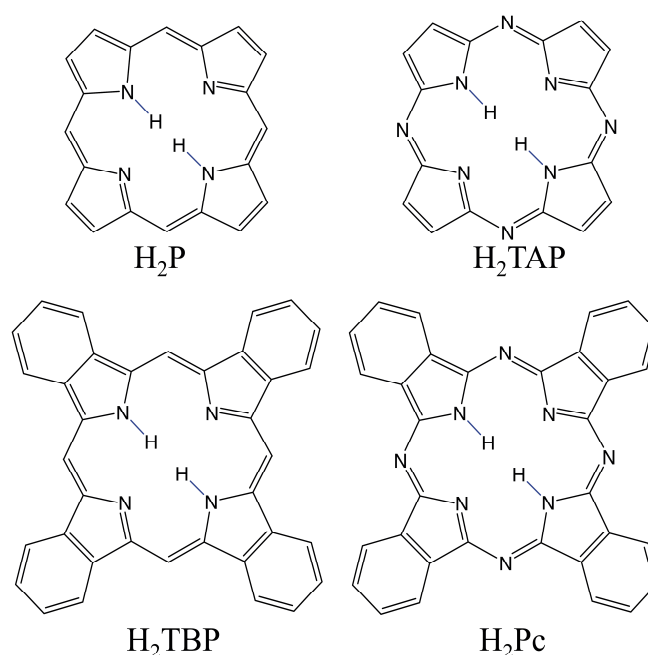


Figure I.2: Structures of the ‘free-base’ analogues of porphine (H_2P), tetraazaporphyrin (H_2TAP), tetrabenzo porphyrin (H_2TBP) and phthalocyanine (H_2Pc). The two hydrogen atoms occupying the central cavity can be replaced by a selection of different metal atoms.

I.1.II: Synthesis of Phthalocyanine and Tetraazaporphyrin

Phthalocyanine was first reported in 1907 by Braun *et al.*⁶ In 1927 Swiss researchers trying to convert *o*-dibromobenzene into phthalonitrile⁷ accidentally formed an iron containing complex as a by-product. They commented on the stability of the contaminant, but did not fully characterise it. In 1928 researchers from Scottish Dyes Ltd. (later ICI) working on the synthesis of phthalamide observed a blue contaminant and characterised it to be copper phthalocyanine^{1, 8}. Scottish Dyes went on to patent copper phthalocyanine as Monastral Blue pigment in 1928. Linstead and co-workers did much of the work in deducing the structure, reactivity and properties of free-base and metal phthalocyanines^{9,10,11,12,13,14,15}. It

was Linstead who also realised the compounds formed in 1907 by Braun *et al.* were also phthalocyanines.

Many synthetic routes exist to form free-base and metal phthalocyanine^{8,16,17}. Four of the most commonly used routes to metal phthalocyanine are shown in Figure I.3. Scheme (I) is similar to the synthesis used by Linstead and patented by Scottish Dyes Ltd. This reaction uses phthalonitrile, copper and CuCl_2 , with the Cl atom acting as the nucleophile in the reaction.

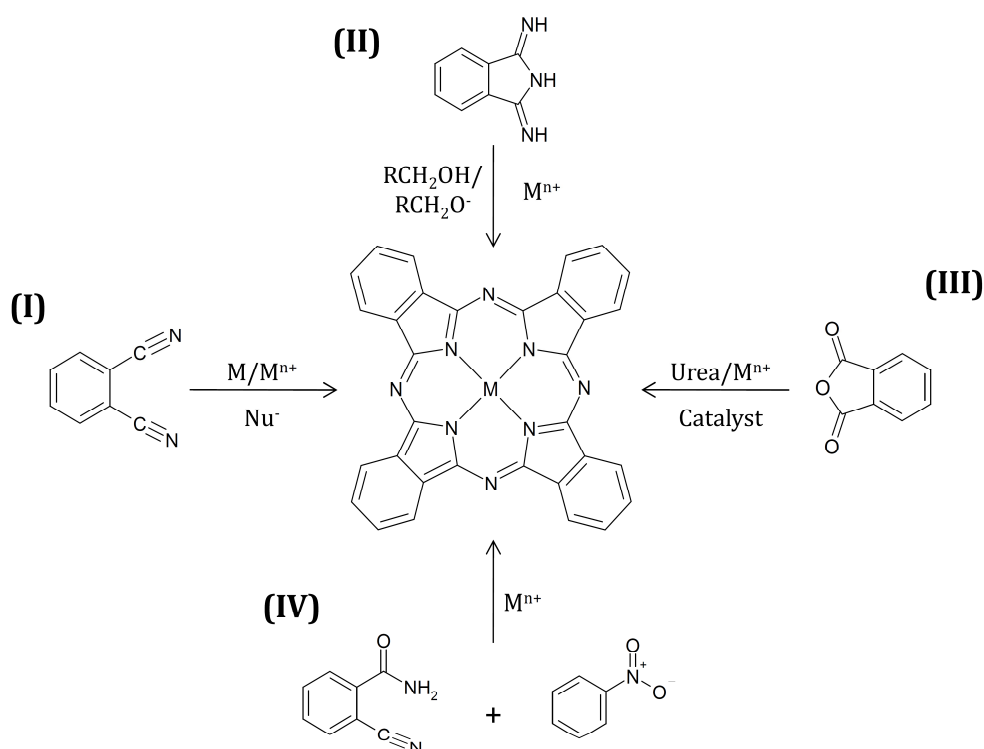


Figure I.3: Schematics showing some of the most widely used synthetic routes to metal phthalocyanine (M-Pc).

Scheme (II) uses diimidoisoindole as the precursor instead of phthalonitrile, although it is itself derived from phthalonitrile. The process shown in Scheme (III) involves using phthalic anhydride and urea with ammonium molybdate as the catalyst. This is a low cost synthesis and is commonly used in the production of pigments. Scheme (IV) uses nitrobenzene and 2-cyanobenzamide as an approach for making functionalised phthalocyanines, due to the ease of functionalization of the precursor molecules¹⁸. Free-base phthalocyanine can be easily prepared from M-Pc. This involves removal of the metal

from M-Pc by treating it with strong acids^{11,16,18}, or using the precursors used in metal phthalocyanine in conjunction with bases and reducing agents¹⁶.

By contrast, the synthesis of the tetraazaporphyrins is much more difficult than that of the phthalocyanines. This may be due to steric effects of the reagents used in the phthalocyanine synthesis or the instability of the reagents used in tetraazaporphyrin synthesis. The first reported synthesis of tetraazaporphyrin comes from Linstead¹⁹ in 1952. This work produced a number of different M-TAPs, as well as free-base TAP. Shown as Scheme (V) in Figure I.4, the synthesis involved stirring maleic dinitrile in the presence of magnesium metal to form MgTAP. Substitution of the Mg metal was straightforward and could yield a number of different M-TAP compounds. Free-base tetraazaporphyrin was formed by refluxing MgTAP in acetic acid to eliminate the magnesium. In 1999 Makarova *et al.* discovered an alternate route to H₂TAP²⁰. Scheme (VI) shows Makarova's reaction of succinonitrile with lithium dimethylaminoethylate (LiOR) in an excess of alcohol (ROH).

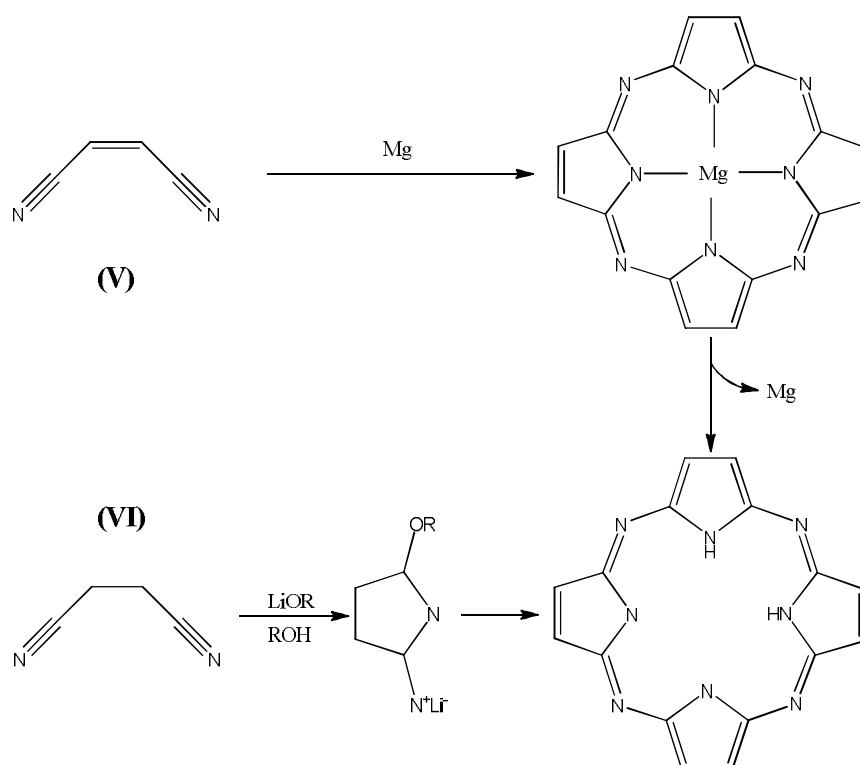


Figure I.4: Two possible synthetic routes to H₂TAP. Scheme V involves using magnesium as a scaffold to build the porphyrin followed by removal of the metal from the inner cavity. Scheme VI is a direct synthesis of the molecule, eliminating the need for the metal based intermediate.

Several different synthetic routes exist for the Group XIII metal phthalocyanine chlorides, some of which are presented in Figure I.5. Scheme VII shows the earliest reported synthesis of AlPcCl from Owen and co-workers²¹ in 1962. The synthesis involves refluxing phthalonitrile with AlCl₃ in quinoline at 175°C for 1.5 hours. A variation on this synthesis was later reported by Linsky and co-workers²² to prepare GaPcCl. It is also possible to use phthalonitrile and AlCl₃ in an assortment of different solvents and with various catalysts to improve the yield²³. An indirect synthetic route is shown in Scheme VIII²⁴, in which a metal substitution is performed on CuPc. This high yielding process involves dissolving the CuPc in a molten salt (NaCl) containing AlCl₃ as the reagent and stirring at 240°C for 6 hours. Scheme IX outlines the preparation of GaPcCl²⁵ from 1,3 diiminisoidoline and GaCl₃. Finally, Scheme X shows the synthesis performed by Wang *et al.*²⁶ to produce AlPcCl in large quantities.

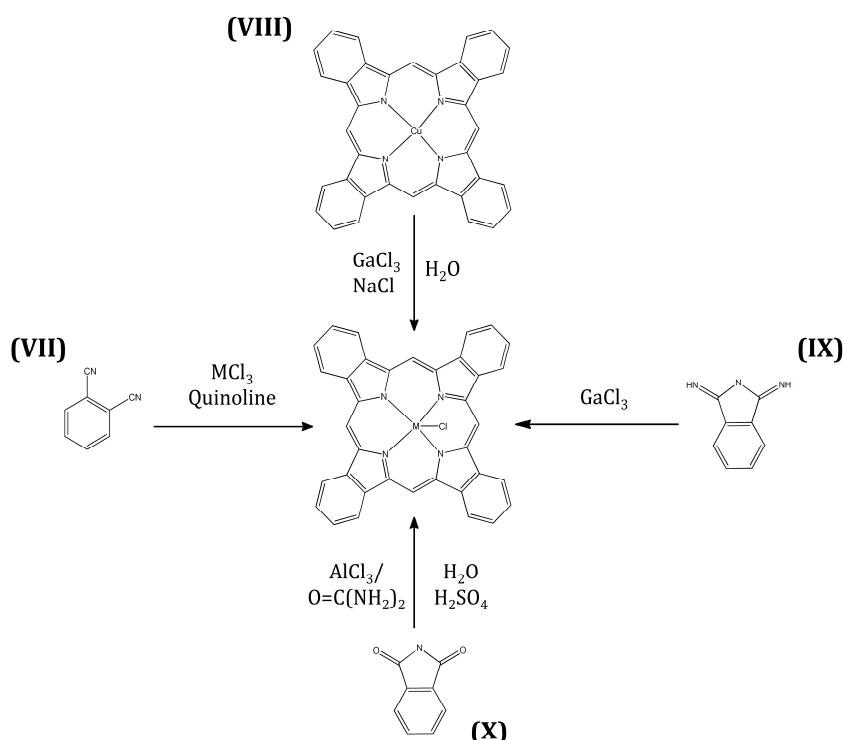


Figure I.5: Some of the synthetic routes used to produce the metal phthalocyanine chloride molecules AlPcCl and GaPcCl.

I.1.III: Applications of Phthalocyanines

Phthalocyanines have been the subject of a diverse range of studies due to their usefulness in existing technologies and their potential in novel applications. The most obvious use for

these coloured molecules is as dyes (about 25% of commercially produced dyes are synthetic porphyrins or porphyrin derivatives²⁷), but they are also found to be useful in the manufacturing of CD-R media²⁸. Aluminium phthalocyanine chloride is of considerable historical significance in the development of laser systems; it was the first molecule used as a dye laser²⁹ when a solution of AlPcCl dissolved in ethanol was pumped by a pulsed ruby laser to produce tuneable laser light.

Phthalocyanines also have useful properties which can be applied to solving chemical problems. The metal in the centre of the porphyrins can act as a very good catalyst in redox reactions, similar to its function in heme in nature. Furthermore, the choice of metal chelated to the porphyrin can alter the selectivity of the reaction it will catalyse. By choosing different substituents on the beta or meta positions, stereo selective porphyrin catalysts can also be produced^{30,31}. Due to their strong absorption in the near UV and visible regions of the electromagnetic spectrum, phthalocyanines are also useful light harvesting molecules for use in dye sensitised solar cells^{32,33,34}. They have also been incorporated into photodynamic therapy treatments^{35,36,37} and oxygen sensors³⁸. More recently they have been investigated for use as non-linear optics³⁹, qubits for quantum computing⁴⁰ and as single molecule transistors which have approached the limit of Moore's law⁴¹. Tetraazaporphyrins, while not as extensively studied as the phthalocyanines, have also been investigated with the goal of practical applications⁴².

I.1.IV: Electronic Absorption of Phthalocyanines and Tetraazaporphyrins

The colour of porphyrins comes from the electronic π to π^* transitions in the macrocyclic ring, and not from the metal centre. A good indication of this can be seen in the free-base porphyrins and free-base phthalocyanines, which have colouration as strong as their metal containing counterparts. The UV-Vis absorption spectra of porphyrins contain two main structures; an intense band in the near UV called the Soret or B band, relating to a transition into the second electronic excited state ($S_2 \leftarrow S_0$), and some weaker bands in the visible region called the Q (or quasi-allowed) bands relating to a transition into the first electronic excited state ($S_1 \leftarrow S_0$). The Q bands can show splitting depending on the symmetry of the molecule; D_{4h} symmetry metallo-porphyrins show one Q band with some intense vibronic bands, whereas lower symmetry D_{2h} free-base porphyrins show a splitting of the Q band into a lower energy Q_x and a higher energy Q_y band. Phthalocyanines show a similar electronic absorption profile to that of porphyrins, except the 'Q band' (usually in

the red region of the spectrum) carries the greater intensity, with weaker bands accruing in the UV region. The label “Q band” is perhaps misleading for phthalocyanines, in as much as the transition is fully allowed and stronger than the Soret band. It is still used partly for historic reasons to show the relationship between the absorption spectra of the porphyrins and the phthalocyanines.

The ‘Four-Orbital Model’ proposed by Martin Gouterman in the 1960s was the first successful theoretical model for describing the electronic absorption properties of porphyrins and phthalocyanines^{43,44,45}. Gouterman’s model involved predicting the orbital energies with extended LCAO-MO Hückel theory and then using configuration interaction (CI) to predict the orbital contributions to the electronic transitions in porphyrins. The theory considers the absorptions bands to be transitions between the two highest occupied molecular orbitals (HOMOs) and two lowest unoccupied molecular orbitals (LUMOs). The two LUMOs, c_1 and c_2 , are considered degenerate (as is the case with metallo porphyrins), and the two HOMOs, b_1 and b_2 , are considered ‘accidentally degenerate’. Applying the CI method to the four single electron transitions of these orbitals (b_1c_1 , b_1c_2 , b_2c_1 and b_2c_2) leads to the formation of two pairs of degenerate electronic state transitions:

$$B_y = \frac{1}{2}(b_1c_1 + b_2c_2), B_x = \frac{1}{2}(b_1c_2 + b_2c_1).$$

$$Q_y = \frac{1}{2}(b_1c_1 - b_2c_2), Q_x = \frac{1}{2}(b_1c_2 - b_2c_1). \quad \text{Eq I.1}$$

The first pair of transitions (B_y and B_x in Equation I.1), have a positive combination of the orbital contributions and the transition dipole moments of the contributions are added together to produce a strongly allowed transition at higher energies. These transitions make up the Soret or B band. The second pair (Q_x and Q_y in Equation I.1) combine negatively, causing the transition dipole moments for the individual contributions to cancel, yielding a forbidden transition. By lifting the degeneracy of the HOMO orbitals slightly (Figure I.6), the orbital coefficients do not completely cancel and the transitions become weakly allowed. The Gouterman four-orbital model correctly predicts the high energy, strongly absorbing Soret bands and the lower energy, weakly absorbing Q bands observed in the electronic absorption spectra of metallo-porphyrins. In the free-base porphyrins, the degeneracy of the LUMOs is lifted, resulting in the splitting of the B band into B_y and B_x bands and the Q band into Q_y and Q_x bands, another result observed experimentally.

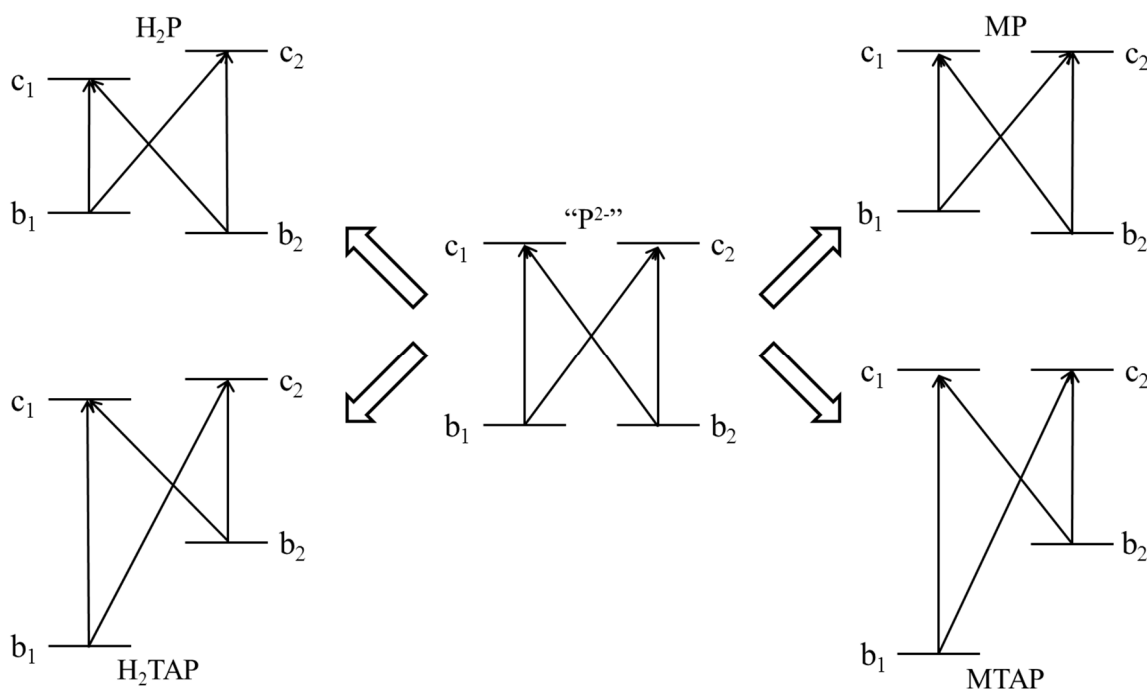


Figure I.6: Schematic of the Gouterman ‘Four-Orbital Model’ for free-base and metalloporphyrin systems. The central model is the porphyrin anion (P^{2-}), where both HOMOs and LUMOs are considered degenerate. The same rules can be applied to the benzo-annulated counterparts of the systems shown.

The four-orbital model can also be applied to the structurally related tetraazaporphyrins. Replacing the meso-carbons with nitrogens has a considerable effect on the molecular orbitals. Figure I.6 shows that the HOMO orbitals (b_1) are strongly influenced by the atoms in the meso positions. The electronegative nitrogen atoms in TAP/Pc lower the energy of b_1 relative to b_2 . The energy of both LUMOs are lowered because of the contribution of the meso atoms to the overall MO energy. The benzene rings in phthalocyanine also have the effect of lowering the energy of all orbitals, but the b_1 orbital has its energy lowered the most. The overall effect of these energy changes on the HOMOs and LUMOs is the energy of the Q transitions are lowered for the TAPs and Pcs, and the contributions from the b_1c_1 and b_1c_2 single orbital transitions in the CI equations are reduced. The Q transitions therefore become dominated by the b_2c_1 or b_2c_2 transitions, with very large transition dipole moments and are strongly allowed. A study using TD-DFT⁴⁶ shows that this model breaks down for phthalocyanine in the region of the Soret band.

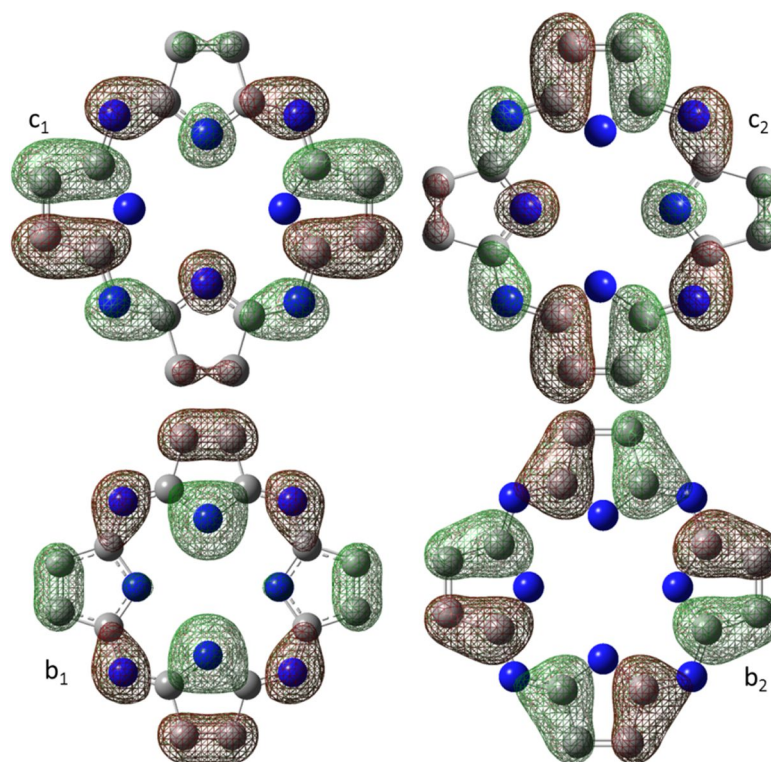


Figure I.7: The molecular orbitals described by the Gouterman four-orbital model for H₂TAP (hydrogen atoms not shown). Orbital shapes and parities have been determined by DFT calculations in the current work. It can be seen that the meso positions of the b₁, c₁ and c₂ orbitals contribute significantly to the MO and these positions are sensitive to changes.

I.2: Matrix-Isolation

The first experiments which might be considered as true matrix-isolation were conducted by Vegard^{47,48,49}, who studied the emission spectra of solid gases and their relationship with the aurora borealis. Pioneering work on ethanol glasses by Kautsky⁵⁰ was soon followed by phosphorescence studies of aromatic molecules trapped in low temperature glassy media by Lewis⁵¹. The term “matrix-isolation” was coined by two of the pioneers of the field, George Pimentel^{52,53} and George Porter⁵⁴. Matrix-isolation commonly refers to the isolation of a (usually) reactive guest species in an excess of an (usually) inert host gas. The process ideally involves having the guest species completely surrounded by host gas atoms/molecules and hence isolated from all other members of the guest species. In order to achieve complete isolation of the guest species, there are usually 10² to 10⁵ host particles for every guest particle. Preparation of matrix samples involves co-depositing the species of interest (which may be atoms, molecules, ions, free radicals or other reactive species) with the host gas onto an optical window. The sample can then be studied at the leisure of

the spectroscopist, without worrying about the reactive species degrading or reacting with other nearby species. The term has somewhat developed recently to a more general technique of trapping guest species in a rigid host material and preventing diffusion. Materials which can form effective matrices include crystals, clays, zeolites, polymers, boric acid glasses and frozen solutions, such as low temperature alkanes. From this point on, the term matrix-isolation will refer only to trapping a material in an inert gas host unless otherwise stated.

Initially matrix-isolation was seen as an effective method to study short lived species; the cryogenic temperatures used in the method are advantageous in the study of reactions, phase changes, charge transfer processes and reactive species (such as radicals). It quickly became apparent, however, that this method was also extremely useful in the study of non-reactive atoms and molecules. Spectra of matrix isolated molecules are often more simple than in the gas phase due to molecules being non-rotating (although this is not always the case⁵⁵), and more resolved than in solution due to the weak interaction between the host and guest species. Furthermore, due to the low temperatures necessary for matrices to form, transitions in molecules only occur from the very lowest energy level.

I.2.I: Matrix Hosts

When performing spectroscopic studies it is important to choose a host material that will not absorb in the spectroscopic region of interest. For this reason, the rare gases make ideal hosts for matrix-isolation experiments. These atoms are transparent over a wide spectral range, from the far infrared (IR) all the way to the vacuum UV. N₂ also makes for an excellent host material owing to its transparency and inertness. Reactive molecular gases (such as H₂, D₂, CH₄, CO) can also be used to study low temperature reactivity and photochemistry of certain species, but are not useful for IR or Raman studies due to having strong absorptions in this spectral region.

The present work utilises Ar and N₂ matrices for IR experiments and Ar, Kr, Xe and N₂ matrices for luminescence experiments. Rare gases are useful model solids due to their inertness and simple packing arrangements⁵⁶ and N₂ often gives rise to very sharp IR bands for matrix-isolated molecules. The rare gas atoms all have closed outer electron shells, and these form face centred cubic (fcc) cells upon condensation (Figure I.8). Van der Waals interactions are the predominant force holding the structure together. The lattice is made up of cubo-octahedral (O_h) sites with each atom having its 12 nearest neighbours at a distance

of R and 6 of the next nearest neighbours at a distance of a . The distance a is the lattice parameter and defines the size of the unit cell. The nearest neighbour distance R is related to a by Pythagoras's rule; $R = a/\sqrt{2}$.

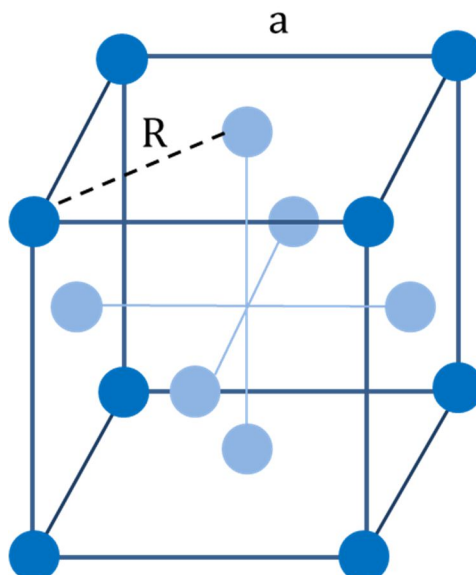


Figure I.8: Face centred cubic (*fcc*) packing of condensed rare gas atoms. The distance ' R ' shows the distance of a given atom to its 12 nearest neighbours. The distance ' a ' shows the distance to the 6 next nearest atoms.

I.2.II: Matrix Effects

It was not long after matrix-isolation was used in spectroscopic studies that subtle interactions between the host and the guest species were observed⁵⁷. The matrix can perturb the vibrational and especially the electronic bands relative to the gas phase. Three distinct, but related types of matrix effect exist; matrix shifts, matrix splitting and matrix broadening. In order to understand the origin of these effects, the interactions which allow for rare gases and inert molecules to form crystalline matrices must be discussed.

The Noble gases and homogeneous diatomic molecules such as N_2 have fully occupied outer shells and have no permanent electric dipole moment. Small changes in the electron density due to motion of the electrons around the nucleus can cause weak instantaneous dipole moments. For an isolated atom or molecule the sum of these short-lived dipole moments will average out to zero. Where more than one atom or molecule are close enough in space a dipole can be induced. If atom A has an instantaneous dipole moment of

μ_A , an electric field is generated, $E = \alpha\mu_A/r^3$. This electric field can polarize a neighbouring atom B , inducing a dipole moment $\mu_B = \alpha\mu_A/r^3$, where α is the polarizability of atom B and r is the distance between the atoms⁵⁸. The two dipoles attract each other, lowering the energy between them. The dipole moment μ_B can then polarize its neighbours, inducing more dipole moments causing more attractive forces. As the electron distribution of atom A changes with respect to time it will create new dipole moments with different direction and magnitude, and these will induce a new change in the polarity of atom B , synchronising the change in polarity throughout the entire system (e.g. the atoms in a crystalline matrix). This synchronisation means that the overall dipole moment of the system does not average zero, creating a force of attraction between the atoms. These attractions caused by induced dipoles are called London interactions and are dominant at longer distances. At shorter distances the electrostatic repulsion caused by the overlap of electron clouds of atoms dominates, abiding by the Pauli exclusion principal. The same forces are present on neutral molecules with no permanent dipole moment. Together these forces make up the van der Waals interaction, which can be expressed using the Lennard-Jones potential⁵⁸:

$$U_{L-J} = \frac{C_{12}}{r^{12}} - \frac{C_6}{r^6} \quad \text{Eq. I.2}$$

where C_{12} represents the repulsive energy and C_6 represents the dispersive energy. These van der Waals interactions have an effect on the vibrational and electronic spectra of molecules trapped in inert gas solids⁵⁹.

I.2.III: Matrix Effects and Vibrational Spectra

The absorption of IR radiation by a molecule causing a molecular vibration is often compared to two atoms joined together by a spring. Considering a diatomic molecule, which only has one vibration; it is possible to approximate this system as being a harmonic oscillator. The potential energy, (V), of the vibration of a diatomic molecule can be calculated within the harmonic approximation by,

$$V(n) = \frac{1}{2}k(r - r_{eq}) \quad \text{Eq. I.3}$$

where k is force constant, r is the distance between the two nuclei and r_{eq} is the equilibrium bond length. If such a molecule is then placed in a rigid cage of size D made up of inert atoms or molecules, then Equation I.3 must be modified to account for the

attractive and repulsive forces of the host⁶⁰. Combining the repulsive term of the Lennard-Jones potential gives a vibrational energy of,

$$V_{repulsive} = \frac{1}{2}k(r - r_{eq}) + C_{12}(D - r)^{12} \quad \text{Eq I.4}$$

and doing the same with the attractive term of the Lennard-Jones potential gives,

$$V_{attractive} = \frac{1}{2}k(r - r_{eq}) - C_6(D - r)^6 \quad \text{Eq. I.5}$$

The repulsive interaction has the effect of decreasing the length of the bond of the molecule in the matrix, thus increasing its vibrational energy relative to the gas phase vibrational energy. The attractive forces have the opposite effect, increasing the bond length of the molecule and lowering its vibrational energy relative to the gas phase⁶⁰. These differences between the vibrational energies of the matrix-isolated molecule and the molecule in the gas phase are known as matrix shifts.

Matrix shifts on the vibrational energies of a molecule are sensitive to the choice of the host material. The different polarizabilities of the host affect the magnitude of their attractive and repulsive forces, and this in turn will affect how much the vibrational energy of the guest molecule gets perturbed. The trend for the rare gases, going down the group, sees the atoms having a higher polarizability, and this leads to stronger attractive and repulsive forces, meaning the heavier atoms exhibit larger matrix shifts on their guests⁶¹. Helium and neon have polarizability volumes of 0.205 Å³ and 0.396 Å³ respectively, and generally have the smallest effect on the vibrational frequencies of matrix isolated molecules. Xenon has a much larger polarizability volume of 4.044 Å³ and has a more pronounced matrix shift than the smaller host atoms⁶¹. Other parameters which can affect the vibrational frequencies include the cage size and different sites within the matrix. The cage size is mostly dependent on the size of the guest molecule, with larger molecules requiring larger cages. The extent to which a molecule is constrained in its site affects how much the attractive and repulsive forces interact with the molecule. Molecules residing in larger host sites will have a reduced interaction compared to smaller sites. It is possible for multiple different sites to exist within the matrix, each with a different interaction with the guest and this can lead to the splitting of bands. This so called ‘site splitting’ can complicate spectra by the addition of many extra bands.

The matrix effects on the vibrational spectra of diatomic molecules are equally observed in normal modes in larger molecules. Polyatomic molecules can experience both red shifts (caused by attractive forces) and blue shifts (caused by repulsive forces) due to the different positions of the atoms relative to the matrix for a given mode. The direction of the displacement of the atoms during a vibration can affect the vibrational frequency in the same way. The polarizability of a given bond may also be considered, with highly polarizable bonds (such as C=O) experiencing a more pronounced shift than lower polarizable bonds (such as C=C). The presence of multiple sites, size of sites and the orientation of the molecule in a given site all affect the direction and the magnitude of matrix shifts and matrix splitting.

I.2.IV: Matrix Effects in Electronic Spectra

The simplest electronic transition is absorption from the ground state (E_0) to the first excited state (E_1), such as an atom or molecule in the gas phase for example. The energy of this transition can be calculated by $E(E_X) = E_1 - E_0$. The reverse process of emission whereby E_1 relaxes to E_0 is given by $E(E_{Em}) = \Delta E(E_X)$ assuming no external forces are acting on the system, as shown by the blue arrows in Figure I.9. When a molecule is placed in the crystal lattice of an inert gas, external forces need to be considered which lead to matrix shifts, matrix splitting and matrix broadening. Van der Waals interactions between the guest and host perturb the molecular orbitals, shifting the transition energies in both absorption and emission relative to the gas phase positions.

Another effect of placing the molecule in a lattice is the coupling of the lattice phonons with the vibronic energy levels of the guest species. Electron-phonon coupling has the effect of broadening the absorption bands and shifting the transition energy. Transitions can occur from $E_0(\nu_0)$ to $E_1(\nu_n)$. In this instance $\Delta E(E_X)$ in the solid phase is going to be larger than $\Delta E(E_X)$ in the gas phase. $E_1(\nu_n)$ can undergo non-radiative relaxation to $E_1(\nu_0)$, followed by emission to the phonon coupled ground state vibronic level $E_0(\nu_n)$, and finally non-radiative relaxation back to $E_0(\nu_0)$, as shown by the red arrows in Figure I.9. The sum of the radiative transfer processes will show that $\Delta E(E_X) = E_1(\nu_n) - E_0(\nu_0)$ is now greater than $\Delta E(E_{Em}) = E_1(\nu_0) - E_0(\nu_n)$. The difference between $\Delta E(E_X)$ and $\Delta E(E_{Em})$ is known as the Stokes shift and is equal to the sum of the non-radiative relaxation energies.

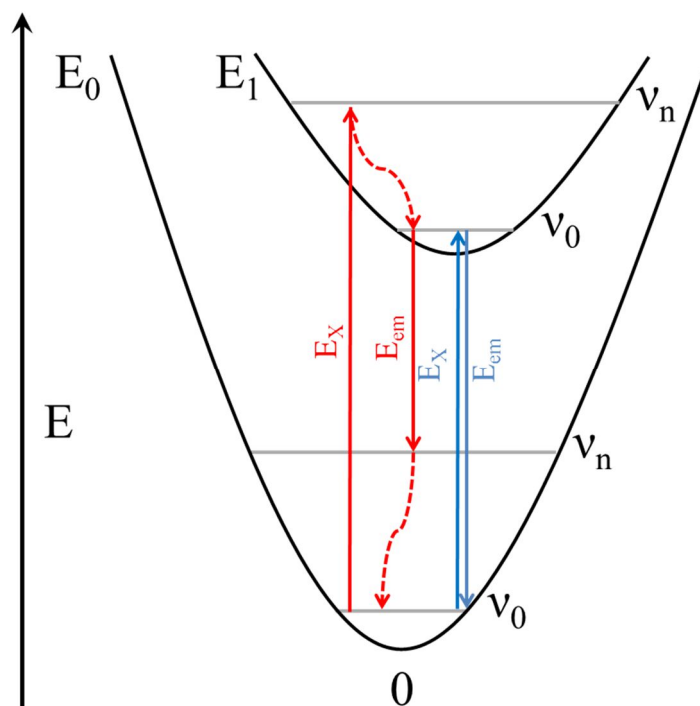


Figure I.9: Energy level diagram showing the electronic transitions between the ground and excited states, E_0 and E_1 respectively.

Coupling to multiple phonons can lead to a broadening of bands in both emission and excitation. Weak electron-phonon coupling produces an intense narrow band in excitation known as the zero phonon line (ZPL) and little or no Stokes shifts is present in the emission. Matrix bands will almost always appear broader than those recorded in the gas phase, even in cases where there is only weak electron-phonon coupling. This broadening arises from overlapping ZPLs residing in different matrix sites. Resolution of the emission and excitation spectra of these different sites may be achieved by using very narrow excitation wavelength ranges, such as laser light. Laser induced fluorescence (LIF) is often used to resolve the site selective transitions of a matrix sample⁶². Vibrational effects induced by the matrix will also have an effect on the electronic spectra by altering the zero point energy of the ground and excited electronic states relative to the gas phase, affecting the energies of the vibronic bands observed in emission and excitation.

When compared to solution phase electronic spectra, matrix-isolated molecules give very sharp bands. Solvent-solute interactions include hydrogen bonding, dipole-dipole interactions or London forces. These interactions distort the vibronic structure of the

molecule as the dipole moment of the solute aligns with the dipole moment of the solvent. This interaction changes the energy of the ground or excited state, allowing the molecule to absorb over a wider range of frequencies, almost like an averaging of the transition energies leading to the broadening of the absorption band. The weak interaction between the host and the guest species in an inert gas solid means that for a given site there will only be a single set of vibronic energy levels, culminating in narrow absorption bands. Due to the cryogenic temperatures used in the technique, no thermally excited molecules reside in the matrix, simplifying the spectra further. The degree of inhomogeneous broadening is much lower than that observed in solution, allowing for individual sites of isolation to be observed, each of which can be excited using LIF⁶³. A comparison of a solution phase and a solid state electronic spectrum of a porphyrin molecule is shown in Figure I.10.

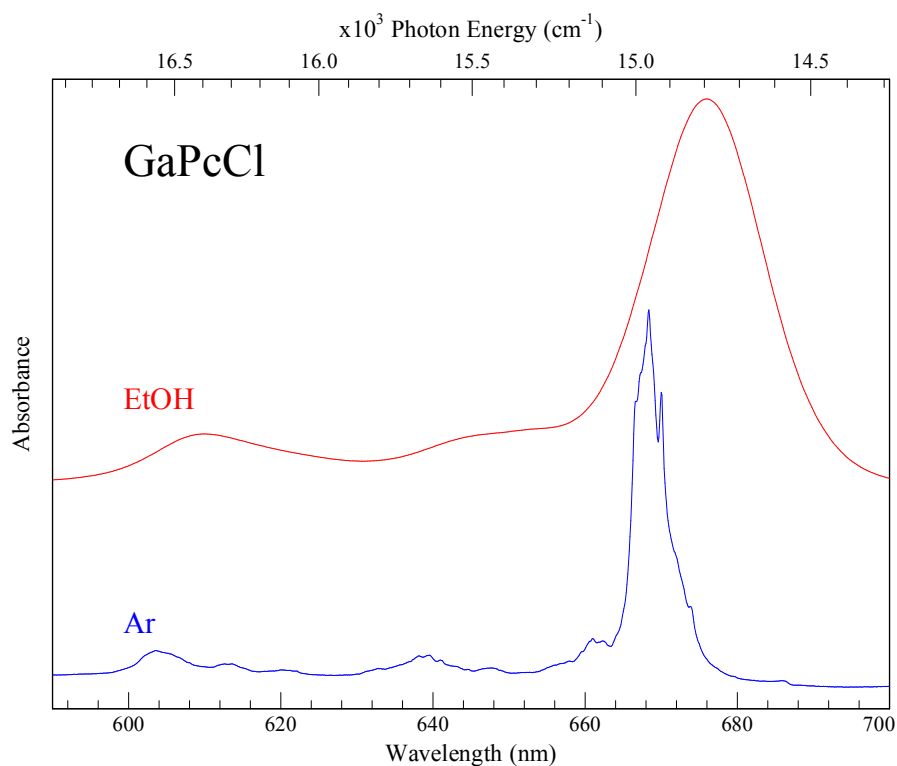


Figure I.10: Electronic absorption spectra of a porphyrin molecule in solution (red trace) and in a solid gas matrix (blue trace). The interaction between the solvent and solute is stronger than the host-guest interaction in the matrix and culminates in a red shift on the solution phase spectrum. The broad bands in solution also hide the vibronic structure which is evident in the matrix.

I.3: Density Functional Theory

The vibrational spectra of Pcs and TAPs are relatively complicated. The M-TAPs, M-Pcs and M-PcCl_s contain 93, 165 and 168 normal modes respectively. In order to perform a detailed analysis of the normal modes of these molecules, high level density functional theory (DFT) calculations have been employed. Density functional theory is one of the most widely used theoretical methods for calculating the ground state properties of molecules and has been shown to predict the vibrational energies of porphyrin and phthalocyanine systems with a high degree of accuracy⁶⁴.

I.3.I: Density Functional Theory

Density functional theory (DFT) finds its origins in Thomas-Fermi (TF) theory^{65,66}. Developed in 1927, this is DFT in its purest form, only relying on the electronic density, $\rho(\mathbf{r})$, as an input. The kinetic energy is approximated to be that of a uniform electron gas (UEG) and the interaction of the electrons was modelled using electronic Coulomb repulsion. It was not until 1964, however, when Hohenberg and Kohn developed their famous theorem⁶⁷ that DFT was truly born. Their work proved that the ground state energy of an electronic system can be completely determined by $\rho(\mathbf{r})$ and there is a one-to-one correspondence between the external potential and the density. The electron density is given by the function:

$$\rho(\mathbf{r}) = N \int |\Psi|^2 dr_1 \dots dr_n \quad \text{Eq. I.6}$$

The electron density is a property that can be observed experimentally, and the molecular properties of a system can be shown to be calculated from $\rho(\mathbf{r})$. The total electron density is dependent only on three spatial variables (x,y,z):

$$\rho(\mathbf{r}) = \rho(x, y, z) \quad \text{Eq. I.7}$$

The second of the Hohenberg-Kohn theorems proves that the minimum energy of a given state of a system is a functional of the exact electronic density:

$$E = E[\rho] = E[\rho(\mathbf{r})] \quad \text{Eq. I.8}$$

From Equation I.7 and Equation I.8 it can then be concluded that for a value of (x,y,z) there can be only a single value for the energy, E .

The implementation of orbitals into DFT methods, as proposed by Kohn and Sham led to the development of Kohn-Sham density functional theory (KS-DFT). The idea behind KS-DFT is to split the kinetic energy functional into two parts; one which can be calculated exactly, and a small correction term. Re-introducing orbitals into the DFT model increases the complexity from 3 to $3N$ variables, but the kinetic energy problem associated with orbital-free methods is fixed. In this sense KS-DFT is closely related to the Hartree-Fock (HF) method, with identical formulas for the kinetic, electron-nuclear and Coulomb electron-electron energies⁶⁸.

The key to KS theory is to calculate the kinetic energy under the assumption of non-interacting electrons, even though this is not the case. The difference between the exact kinetic energy and what is calculated is very small and the remaining kinetic energy can thus be included in the exchange-correlation term. The KS equation⁶⁹ for a system of N electrons is given by:

$$E_{DFT}[\rho] = T[\rho] + V_{Ne}[\rho] + J_{ee}[\rho] + E_{xc}[\rho] \quad \text{Eq. I.9}$$

where $T[\rho]$ is the kinetic energy of the electrons, $V_{Ne}[\rho]$ is the nucleus-electron attraction, $J_{ee}[\rho]$ is the Columbic repulsion between the electrons and $E_{xc}[\rho]$ is the exchange-correlation (xc) energy functional which includes the non-classical interactions between the electrons. One of the main challenges in developing DFT methods is finding suitable approximations for E_{xc} . Orbital-free DFT models require approximations to the kinetic, exchange and correlation functionals, whereas KS theory only requires an approximation for the exchange-correlation energy functional. The exchange-correlation energy is typically 10 times smaller than the kinetic energy term, meaning KS theory is far less sensitive to inaccuracies in the functional compared to orbital-free models. While orbital-free theory is a true density functional theory (3 variables), Kohn-Sham methods are independent particle models ($3N$ variables), analogous to Hartree Fock theory, but are still much less complicated than many-particle (correlation) wave function models.

I.3.II: Exchange-Correlation Functionals

In order to perform reliable calculations with DFT it is necessary to know the exchange-correlation energy, $E_{xc}[\rho]$. This term can be defined once the exact energy of a system is known. By tuning $E_{DFT}[\rho]$ to match the exact energy, $E_{xc}[\rho]$ can be calculated by subtracting the non-interacting kinetic energy, the E_{Ne} and J potential energy terms.

$$E_{xc}[\rho] = (T[\rho] - T_S[\rho]) + (E_{ee}[\rho] - J_{ee}[\rho]) \quad \text{Eq. I.10}$$

Where T_S is the kinetic energy calculated from a Slater determinant and E_{ee} is the total electron repulsion. The first term in Equation I.10 is the kinetic correlation energy and the second term denotes the potential correlation and exchange energy. The difference between various DFT methods then, is the choice of functional form for the exchange–correlation energy. It can be proven that the exchange–correlation potential is a unique functional, valid for all systems, but an explicit functional form of this potential has been elusive, except for special cases such as a uniform electron gas⁷⁰.

The exchange-correlation energy may be divided into the sum of its exchange energy and correlation energy functionals:

$$E_{xc}[\rho] = E_x[\rho] + E_c[\rho] \quad \text{Eq. I.11}$$

A variety of different functionals have been developed to determine the exchange and correlation energies. Most of these functionals fit into the following categories:

Local Density Approximation (LDA): In LDA it is assumed that the density locally can be treated as a uniform electron gas. These functionals depend only on $\rho(\mathbf{r})$ where ϵ_{xc} is the exchange-correlation energy of the UEG:

$$E_{xc}^{LDA}[\rho] = \int \rho(\mathbf{r}) \epsilon_{xc}(\rho(\mathbf{r})) d^3\mathbf{r} \quad \text{Eq. I.12}$$

Generalized Gradient Approximation (GGA): In GGA functionals the energy is dependent not only on the electron density, but also on derivatives of the density $\nabla\rho(\mathbf{r})$:

$$E_{xc}^{GGA}[\rho(\mathbf{r})] = \int f(\rho(\mathbf{r}) \nabla(\rho(\mathbf{r}))) d^3\mathbf{r} \quad \text{Eq. I.13}$$

Meta-GGA: The extension of GGA functionals, which are dependent on higher order derivatives of the electron density with the Laplacian ($\nabla^2\rho$) representing the second order term:

$$E_{xc}^{m-GGA}[\rho(\mathbf{r})] = \int f(\rho(\mathbf{r}) \nabla(\rho(\mathbf{r})) \nabla^2\rho(\mathbf{r})) d^3\mathbf{r} \quad \text{Eq. I.14}$$

Hybrid-GGA: Hybrid functionals contain the exact Hartree-Fock exchange in the exchange functional:

$$E_{xc}^{hybrid} = E_x^{HF} + E_c^{DFT} \quad \text{Eq. I.15}$$

I.3.III: The B3LYP Functional

LDA functionals were well known to have a large overbinding tendency. In 1993 Bekke⁷¹ noticed that GGA functionals, while not as dramatic as LDAs, still have a tendency to over bind. To overcome this problem he proposed the hybrid B3PW91 functional, which can be written as:

$$E_{xc}^{B3PW91} = E_{xc}^{LDA} + a(E_x^{HF} - E_x^{LDA}) + b\Delta E_x^{B88} + c\Delta E_c^{PW91} \quad \text{Eq. I.16}$$

Where the semi-empirical coefficients are $a = 0.20$, $b = 0.72$ and $c = 0.8$ and were fitted to experimental atomization energy data. The functional is a hybrid of the exact Hartree-Fock exchange energy, E_x^{HF} and local density approximation exchange and correlation energies, E_x^{LDA} and E_c^{LDA} . Becke's gradient corrected exchange functional⁷², ΔE_x^{B88} , and the Perdew-Wang gradient corrected exchange functional⁷³, ΔE_c^{PW91} , are also included.

Stephens *et al.*⁷⁴ modified the B3PW91 basis set by including the LYP gradient corrected correlation functional, of Lee, Yang and Parr (LYP)⁷⁵, in place of PW91 to make the B3LYP functional. It has the form:

$$E_{xc}^{B3LYP} = E_{xc}^{LDA} + a(E_x^{HF} - E_x^{LDA}) + b\Delta E_x^{B88} + c(E_c^{LYP} - E_c^{VWN}) + E_c^{VWN} \quad \text{Eq. I.17}$$

The functional also incorporated the local correlation energy functional, E_c^{VWN} , by Vosko, Wilk and Nusair (VWN)⁷⁶, which is used to determine the ratio of local and gradient corrected correlation functionals using the 'c' coefficient. The coefficients a , b and c hold the same values for B3LYP as with the B3PW91 functional.

I.3.IV: Basis Sets

A basis set is a set of mathematical formulae which represent the atomic/molecular orbitals of a system. Two types of basis functions are commonly used in electronic structure calculations: Slater Type Orbitals (STOs) and Gaussian Type Orbitals (GTOs). Slater type orbitals⁷⁷ take the general form:

$$\eta^{STO} = Nr^{n-1}\exp[-\zeta r]Y_{l,m}(\theta, \phi) \quad \text{Eq. I.18}$$

where N is a normalization factor, r is the distance from the nucleus, n is the principal quantum number, ζ is the orbital exponent (which determines how compact or diffuse the

function is) and $Y_{l,m}$ represents the angular parts of the function in terms of spherical harmonics. The exponential dependence on the distance between the nucleus and electron mirrors the exact orbitals for the hydrogen atom. STOs generally give good approximations of exact functions, but are inefficient to compute for all but the simplest of systems.

GTOs can be written in terms of Cartesian coordinates in the form:

$$\eta^{GTO} = Nx^l y^m z^n \exp[-\alpha r^2] \quad \text{Eq. I.19}$$

where N is the normalization factor and α is the orbital exponent. The exponents l, m and n represent the angular momentum of the orbitals through the relationship $L = l + m + n$, where $L = 0$ denotes an s-function, $L = 1$ denotes a p-function, $L = 2$ denotes a d-function, etc. The r^2 dependence in the exponential makes the GTOs inferior to the STOs in two ways. Firstly, GTOs have a zero slope at the nucleus (in contrast to STOs, which have a discontinuous derivative at the nucleus), which leads to them having problems representing behaviour near the nucleus. The second problem is that the GTO falls off too rapidly at further distances from the nucleus compared with an STO, which leads to a poor representation of the tail of the orbital. These disadvantages mean that approximately three times as many GTOs are required to obtain a similar level of accuracy as a given number of STOs. The large number of GTOs required to accurately describe a system is overcome by the ease at which the integrals can be computed, and because of this they are generally preferred to STOs.

After the type of function (STO/GTO) has been chosen, the next important consideration in a calculation is the size of the basis set. A minimal basis set contains the smallest number of functions possible to describe all of the electrons on the neutral atom(s) in the system. For example, hydrogen only requires a single s-function to describe its electron, whereas the first row atoms (such as carbon) require more extensive basis sets, employing a two s-functions (1s and 2s) as well as a set of p-functions ($2p_x$, $2p_y$ and $2p_z$). One of the problems with minimal basis sets is that they do not discriminate between the valence and the core electrons. Minimal basis sets can be improved upon by doubling all of the basis functions to produce a double-zeta (DZ) basis set. This will employ two s-functions for hydrogen (1s and 1s') and four s-functions (1s, 1s', 2s and 2s') and two sets of p-functions (2p and 2p') on the first row atoms. The advantage of DZ basis sets over minimal basis sets is they have

a tight and diffuse set of orbitals and this allows for description of the system more accurately, taking into account that the electron distribution is not equal in every direction. Further improvement to accuracy can be obtained by introducing split valence basis sets, which only doubles the valence orbitals. The core orbitals which are close to the nucleus are not involved in bonding and do not require as extensive a description. Building on this idea, basis sets can be improved by including triple-zeta (TZ), quadruple-zeta (QZ) and higher order zeta values with split valence orbitals. Diffuse functions can be included in the basis set, which allow for the orbitals to extend further away from the nucleus. Polarization functions can also be included, which describe orbitals with higher orbital angular momentum than is present in the ground state.

The 6-311++G(2d,2p) basis set is a triple split valence basis, where the core orbitals are a contraction of six primitive GTOs (6-). The valence orbitals are split into three functions, represented by three, one and one primitive GTOs (311) respectively. Diffuse functions (++) and polarization functions (2d,2p) have been incorporated into the basis set which allow for d-polarization of the p-functions, and p-polarization of the s-functions.

I.3.V: Time-Dependent DFT

Early work on time-dependent DFT (TD-DFT) dates back to the 1970s^{78,79} and early 1980s^{80,81}, where a group of studies culminated in the formation of the Runge and Gross (RG) theorem⁸². The RG theorem is an extension on the Hohenberg-Kohn theorem⁶⁷ to time-dependent external potentials. The work proves a one-to-one correspondence between the time-dependent electron density $\rho(\mathbf{r}, t)$ and the external potential $V_{ext}(\mathbf{r}, t)$. This allows for the construction of a time-dependent extension, $V(\mathbf{r}, t)$, of a static Slater Kohn-Sham like potential, $V(\mathbf{r})$, which generates a Slater determinant of non-interacting wave functions, $\varphi_i(\mathbf{r}, t)$, which satisfy the time-dependent Schrödinger equation, given by:

$$\left(-\frac{1}{2}\nabla^2 + v_{KS}[\rho](\mathbf{r}, t)\right)\varphi_i(\mathbf{r}, t) = i\frac{\partial}{\partial t}\varphi_i(\mathbf{r}, t) \quad \text{Eq. I.20}$$

The time-dependent electron density $\rho(\mathbf{r}, t)$ is then determined by:

$$\rho(\mathbf{r}, t) = \sum_i^N |\varphi_i(\mathbf{r}, t)|^2 \quad \text{Eq. I.21}$$

for an N electron system. The KS potential $v_{KS}[\rho](\mathbf{r}, t)$ is given by:

$$v_{KS}[\rho](\mathbf{r}, t) = v_{ext}(\mathbf{r}, t) + \int d\mathbf{r}' \frac{\rho(\mathbf{r}', t)}{|\mathbf{r}-\mathbf{r}'|} + v_{XC}(\mathbf{r}, t) \quad \text{Eq. I.22}$$

which includes the time-dependent external potential $v_{ext}(\mathbf{r}, t)$, the Coulombic electron repulsive potential and the time-dependent exchange-correlation potential, $v_{XC}(\mathbf{r}, t)$. The exchange-correlation potential can be described as:

$$v_{XC}[\rho](\mathbf{r}, t) = v_S[\rho](\mathbf{r}, t) - v(\mathbf{r}, t) - v_H[\rho](\mathbf{r}, t) \quad \text{Eq. I.23}$$

where $v(\mathbf{r}, t)$ is the external time-dependent field and $v_H[\rho](\mathbf{r}, t)$ is the time-dependent Hartree potential generated by $[\rho](\mathbf{r}, t)$;

$$v_H(\mathbf{r}, t) = \int d^3\mathbf{r}' \frac{\rho(\mathbf{r}', t)}{|\mathbf{r}-\mathbf{r}'|} \quad \text{Eq. I.24}$$

The computational simplicity of the time-dependent KS scheme makes it a more desirable system than time-dependent Hartree-Fock or time-dependent configuration interaction⁸³.

I.3.VI: Limitations of DFT

The successes of DFT are well documented, but there are some well-known problems associated with the technique. Weak interactions are not well described – van der Waals forces for example. Rare gas atoms have a purely repulsive energy curve when computed by DFT whereas in reality there should be a slight force of attraction⁸⁴. Exchange-correlation functionals which do not contain self-interaction corrections often experience problems describing systems containing loosely bound electrons, such as for anions or atoms with low electron affinities. Description of the excited states is problematic due to the absence of a wavefunction. Another method must be employed such as TD-DFT, which itself has its own host of problems. Electron-correlation is inherently localised and as such cannot describe long range charge transfer processes⁸⁵. Furthermore, the potential energy curves on charge transfer states do not comply with the expected $1/R$ dependence on the charge separation distance, R ^{86,87}.

I.4: Research Motivations

The motivation behind the research conducted in present work is to gain novel insights into the spectroscopy of matrix-isolated phthalocyanines and advance the literature for this important class of dye molecules. Over the past few years, many studies have been carried

out on the vibrational and electronic spectroscopy of matrix-isolated porphyrins and phthalocyanines, encompassing molecules such as $\text{H}_2\text{P}^{88,89}$, $\text{H}_2\text{TBP}^{90}$, $\text{H}_2\text{TAP}^{91,92}$, MgTAP^{93} , H_2Pc^{94} and $\text{ZnPc}^{64,95}$, and have been performed by numerous research groups from around the world. The infrared absorptions of MgPc^{96} and $\text{AlPcCl}^{97,98}$ have been investigated using various methods, although these two molecules have never been studied while isolated in inert gas solids. To the best of the author's knowledge, the IR absorption of GaPcCl has never been recorded.

The major experimental portion of the work conducted in this thesis focuses on the spectroscopy of matrix-isolated gallium phthalocyanine chloride (GaPcCl), which differs from the molecules mentioned above (with the exception of AlPcCl) in two key regards. Firstly, the macrocycle is slightly domed, with the Ga atom lying above the ring, and secondly, the presence of a Cl^- counter-ion. The non-planar metal phthalocyanine chlorides have not been investigated in the matrix before, so it is interesting to see how the visible spectroscopy of GaPcCl is affected by its 'domed' structure, especially since porphyrins and phthalocyanines get their intense colours from the aromaticity (conjugation) of the macrocycle ring. Amplified emission was originally observed for the structurally related molecule AlPcCl^{29} in solution, and more recently for matrix-isolated H_2Pc , ZnPc^{94} and $\text{H}_2\text{TAP}^{92}$. This leads to the obvious question as to whether or not GaPcCl can also exhibit this non-linear optical property. The narrow bandwidths of AE allow for the characterisation of the features in emission and excitation. The Cl atom also gives the molecule a permanent dipole moment, something which has not been a factor in any of the previous matrix studies on porphyrins and phthalocyanines. This produces a strong force of attraction over a range of distances and may have an effect on the number of dimers and clusters that GaPcCl form in the matrix compared to the previously studied planar porphyrins and phthalocyanines.

1.5: Spectroscopy of Matrix-Isolated Phthalocyanines

The current study concerns the vibrational and electronic spectroscopy of several phthalocyanine systems. The infrared (IR) spectra of magnesium phthalocyanine (MgPc), aluminium phthalocyanine chloride (AlPcCl) and gallium phthalocyanine chloride (GaPcCl) have been studied in the inert gas hosts Ar and N_2 . Raman scattering spectra of these three molecules have also been recorded in KBr discs as part of the ground state

vibrational analysis. These relatively large molecules contain 57, 58 and 58 atoms respectively which have in 165, 168 and 168 vibrational modes respectively. While a detailed vibrational analysis of so many modes appears difficult, the high symmetry of these molecules significantly reduces the number of bands observed experimentally. Spectral simulations generated using density functional theory (DFT) were employed to facilitate the analysis and assignment of the complex vibrational structure of the recorded spectra.

The accuracy of the DFT results presented for the vibrational analysis of several porphyrin systems allowed for a purely theoretical study to be conducted. An unusual effect was observed upon isotopic substitution of the inner hydrogen atoms on free-base porphyrins and phthalocyanines with deuterium whereby the $\nu_{\text{H}}/\nu_{\text{D}}$ ratio of certain vibrational modes was observed to be less than 1. Due to the simple mass dependence of a vibrational mode, ν , a theoretical investigation was conducted to determine the behaviour of the inner hydrogen based vibrational modes by running DFT calculations on the system with hydrogen masses between 1 and 2 amu.

Visible absorption and emission spectra were recorded of GaPcCl isolated the inert gas hosts N₂, Ar, Kr and Xe at cryogenic temperatures with steady state spectroscopy techniques. The Q and B bands are identified in each host solid. Laser induced fluorescence was used to study the emission and excitation spectra of these molecules with a tuneable dye laser capable of exciting into the region of the Q band. Emission lifetimes were measured by recording time-resolved emission spectra. Due to the similar selection rules for the vibronic bands present in fluorescence and the Raman active modes of these systems, experimental and theoretical Raman results were used to analyse and assign the vibronic bands present in emission. The non-linear optical process of stimulated emission was investigated by increasing the laser intensity and the optical densities of the sample. This phenomenon was observed in all of the matrices used in the current study. The vibrational mode associated with this process is identified with the DFT Raman calculations. Phonon structure was observed in emission and excitation spectra of the AE bands of GaPcCl/Ar and was described by performing a W_p lineshape analysis. The narrow amplified emission bands were used to study the sites and features present in samples of matrix-isolated GaPcCl.

I.6: Thesis Layout

The following section summarises the arrangement and content of the upcoming chapters of the thesis. Chapter II introduces the experimental and theoretical aspects of the work. The matrix-isolation apparatus and spectrometers are described in detail, as well as how samples were prepared. This chapter also provides details of the hardware the quantum chemical calculations were run on, the software used and the general procedure for running a set of calculations. The equations and fitting procedures used to implement the Wp lineshape analysis are also given here.

Chapter III presents a vibrational analysis for a selection of metal tetraazaporphyrin and metal phthalocyanine molecules using both experimental and theoretical techniques. A theoretical study of the effect of the metal atom size on the ground state structure of the M-TAPs and M-Pcs (M = Be, Mg, Ca, Sr, Ba, Zn, Cd, Hg, AlCl and GaCl) was conducted. Geometries were found to be either planar with D_{4h} symmetry, or non-planar with C_{4v} symmetry. Non-planar structures revealed the metal lying above the plane of the porphyrin ring, and a ‘doming’ of the rest of the structure. A detailed vibrational analysis of three phthalocyanine molecules (MgPc, AlPcCl and GaPcCl) was performed using FTIR and Raman spectroscopy. Matrix infrared (IR) spectra have been recorded on these three molecules isolated in solid Ar and N_2 at cryogenic temperatures as well as room temperature KBr pellets. Room temperature Raman spectra of these molecules have been recorded in KBr discs. DFT calculations have been conducted on these systems and showed excellent agreement with experimental spectra. DFT results were then used to conduct a detailed analysis of the experimental bands.

Chapter IV presents a theoretical study on free-base porphine (H_2P) and some closely related tetrapyrrole molecules (H_2TAP , H_2TBP and H_2Pc) using DFT. This chapter analyses the effect of H/D substitution of the inner hydrogen atoms on the vibrational spectra of the aforementioned molecules. It was observed that some vibrational modes exhibited a reverse isotope shift ratio (ISR) where the ν_H/ν_D ratio is less than 1. The effect was most pronounced in the B_{2g} and B_{3u} out-of-plane bending modes involving some N-H motion. The interesting modes were tracked by changing the mass of the inner hydrogen atoms from 1 to 2 amu in increments of 0.05 amu. This analysis showed that vibrational modes of the same symmetry and similar energy which involved N-H motion exhibited avoided crossings, yielding the reverse ISR effect.

In Chapter V the visible spectroscopy of GaPcCl trapped in various inert gas hosts is investigated using steady-state and time-resolved techniques. Absorption spectra were recorded in several inert gas hosts and compared to solution phase data and TD-DFT predictions for the Q and B bands. Emission and excitation spectra were recorded with CW lamp sources and pulsed laser excitation in the region of the Q band. The vibronic bands observed in emission are compared to the ground state Raman data. Good agreement between these spectra (as well as with the predictions made by DFT calculations in Chapter III) allows for the assignment of the vibrational modes in emission. Mirror symmetry between the emission and absorption/excitation spectra also allow for the vibronic bands of these spectra to be assigned. Emission lifetimes were measured and compared to calculated values from the extinction coefficient and TD-DFT results. Amplified emission was observed in high concentration matrix samples.

Chapter VI focusses on the process of amplified emission of GaPcCl isolated in inert gas hosts in more detail. The vibronic band associated with the process was identified. 2D-excitation-emission plots are employed to investigate the sites present in the matrices N₂, Ar, Kr and Xe. It was found that the number of sites and features capable of exhibiting AE in a matrix can vary significantly depending on the host. The main features present in each host are assigned and discussed using excitation and emission ‘slices’ from the 2D-EE plots. A Wp function is fitted to the experimental data in order to determine if any phonon structure is exhibited in a given host. A temperature dependence study on the AE bands of GaPcCl in the matrix is also performed.

Chapter VII contains the conclusions and summarises the most significant findings of the work carried out.

I.7: References

1. Smith, R. A., The Colours of Life: An Introduction to the Chemistry of Porphyrins and Related Compounds (Milgrom, Lionel R.). *Journal of Chemical Education* **1998**, 75 (4), 420.
2. <http://ichef.bbci.co.uk/images/ic/640xn/p023r74v.jpg>.

3. <http://cache3.asset-cache.net/gc/168834718-red-blood-cells-sem-gettyimages.jpg?v=1&c=IWSAsset&k=2&d=vabCLPBoh%2FVXC1ANF5Jft2vYKvskQ9hSD66HzvgICxc%3D>.
4. Hückel, E., Quantentheoretische Beiträge zum Benzolproblem. *Zeitschrift für Physik* **1931**, 70 (3-4), 204-286.
5. Claessens, C. G.; Hahn, U.; Torres, T., Phthalocyanines: from outstanding electronic properties to emerging applications. *Chemical Record* **2008**, 8 (2), 75-97.
6. Braun, A.; Tcherniac, J., Über die Produkte der Einwirkung von Acetanhydrid auf Phthalamid. *Berichte der deutschen chemischen Gesellschaft* **1907**, 40 (2), 2709-2714.
7. de Diesbach, H.; von der Weid, E., Quelques sels complexes des o-dinitriles avec le cuivre et la pyridine. *Helvetica Chimica Acta* **1927**, 10 (1), 886-888.
8. Gregory, P., Industrial applications of phthalocyanines. *Journal of Porphyrins and Phthalocyanines* **2000**, 04 (04), 432-437.
9. Linstead, R. P.; Lowe, A. R.; Heilbron, I. M.; Irving, F. Phthalocyanine dyes. GB418367, 1934.
10. Linstead, R. P., Phthalocyanines. I. A new type of synthetic coloring matters. *Journal of the Chemical Society* **1934**, 1016-17.
11. Byrne, G. T.; Linstead, R. P.; Lowe, A. R., Phthalocyanines. II. The preparation of phthalocyanine and some metallic derivatives from o-cyanobenzamide and phthalimide. *Journal of the Chemical Society* **1934**, 1017-22.
12. Linstead, R. P.; Lowe, A. R., Phthalocyanines. III. Preliminary experiments on the preparation of phthalocyanines from phthalonitrile. *Journal of the Chemical Society* **1934**, 1022-7.
13. Dent, C. E.; Linstead, R. P., Phthalocyanines. IV. Copper phthalocyanines. *Journal of the Chemical Society* **1934**, 1027-31.
14. Linstead, R. P.; Lowe, A. R., Phthalocyanines. V. The molecular weight of magnesium phthalocyanine. *Journal of the Chemical Society* **1934**, 1031-3.

15. Dent, C. E.; Linstead, R. P.; Lowe, A. R., Phthalocyanines. VI. The structure of the phthalocyanines. *Journal of the Chemical Society* **1934**, 1033-9.
16. McKeown, N. B. In *The synthesis of symmetrical phthalocyanines*, Elsevier Science: 2003; pp 61-124.
17. Sharman, W. M.; Van Lier, J. E. In *Synthesis of phthalocyanine precursors*, Elsevier Science: 2003; pp 1-60.
18. Eicher, T.; Haputmann, S.; Suschitzky, H., *The Chemistry of Heterocycles: Structure, Reactions, Syntheses and Applications*. John Wiley & Sons: 2003; p 514 pp.
19. Linstead, R. P.; Whalley, M., 944. Conjugated macrocycles. Part XXII. Tetrazaporphin and its metallic derivatives. *Journal of the Chemical Society (Resumed)* **1952**, (0), 4839-4846.
20. Makarova, E. A.; Koroleva, G. V.; Luk'yanets, E. A., Phthalocyanines and related compounds: Synthesis of tetraazachlorin and tetraazaporphine from succinonitrile. *Russian Journal of General Chemistry* **1999**, 69 (8), 1306-1311.
21. Owen, J. E.; Kenney, M. E., Phthalocyaninoaluminum compounds. *Inorganic Chemistry* **1962**, 1, 331-3.
22. Linsky, J. P.; Paul, T. R.; Nohr, R. S.; Kenney, M. E., Studies of a series of haloaluminum,-gallium, and-indium phthalocyanines. *Inorganic Chemistry* **1980**, 19 (10), 3131-3135.
23. Smith, N. W.; Merchak, P. A. Method for production of phthalocyanine pigments in the absence of heavy metal catalysts. WO2013020067A1, 2013.
24. Kimura, S.; Hikosaka, M.; Shirao, M.; Mochizuki, A.; Tsuchida, j. Preparation of aluminum phthalocyanine compositions. EP635550A1, 1995.
25. Colaitis, D. C. R., *Hebd. Seances Acad. Sei* **1956**, 242 (1026).
26. Wang, X. Method for preparation of aluminum phthalocyanine chloride. CN101717401A, 2010.
27. Löbber, G., Phthalocyanines. In *Ullmann's Encyclopedia of Industrial Chemistry*, Wiley-VCH Verlag GmbH & Co. KGaA: 2000.

28. Yokota, C.; Sasakawa, T.; Hyakutake, H., Phthalocyanine CD-R for high speed recording. *Proceeds of SPIE-International Society of Optical Engineering* **1995**, 2514, 249-57.
29. Sorokin, P. P.; Lankard, J. R., Stimulated emission observed from an organic dye, chloro-aluminum phthalocyanine. *IBM Journal of Research and Development* **1966**, 10 (2), 162-163.
30. She, Y.; Yang, J., Research progress of phthalocyanine-like catalysts. *Beijing Gongye Daxue Xuebao* **1998**, 24 (2), 115-120.
31. Bochkarev, V. V.; Feshchenko, L. I., Pyropolymer catalysts based on metallophthalocyanines and polyazamacrocyclic metal complexes. *Izvestiya Vysshikh Uchebnykh Zavedenii, Khimiya I Khimicheskaya Tekhnologiya* **2000**, 43 (3), 92-96.
32. García-Iglesias, M.; Cid, J.-J.; Yum, J.-H.; Forneli, A.; Vázquez, P.; Nazeeruddin, M. K.; Palomares, E.; Grätzel, M.; Torres, T., Increasing the efficiency of zinc-phthalocyanine based solar cells through modification of the anchoring ligand. *Energy & Environmental Science* **2011**, 4 (1), 189.
33. Liu, B.; Zhu, W.; Wang, Y.; Wu, W.; Li, X.; Chen, B.; Long, Y.-T.; Xie, Y., Modulation of energy levels by donor groups: an effective approach for optimizing the efficiency of zinc-porphyrin based solar cells. *Journal of Materials Chemistry* **2012**, 22 (15), 7434.
34. Rodriguez-Morgade, M. S.; Trukhina, O.; Bottari, G.; Echegoyen, L.; Torres, T., Dye-sensitized solar cells based on titanium phthalocyanines. *Preparations - American Chemical Society, Division of Energy Fuels* **2013**, 58 (1), 479.
35. Sternberg, E. D.; Dolphin, D.; Bruckner, C., Porphyrin-based photosensitizers for use in photodynamic therapy. *Tetrahedron* **1998**, 54 (17), 4151-4202.
36. Allen, C. M.; Sharman, W. M.; Van Lier, J. E., Current status of phthalocyanines in the photodynamic therapy of cancer. *Journal of Porphyrins and Phthalocyanines* **2001**, 05 (02), 161-169.

37. Mondal, D.; Bera, S., Porphyrins and phthalocyanines: promising molecules for light-triggered antibacterial nanoparticles. *Advances in Natural Sciences: Nanoscience Nanotechnology* **2014**, *5* (3), 33002/1-33002/14.
38. Amao, Y.; Okura, I., Optical oxygen sensor devices using metalloporphyrins. *Journal of Porphyrins and Phthalocyanines* **2009**, *13* (11), 1111-1122.
39. Chen, J.; Wang, S.-q.; Yang, G.-q., Nonlinear optical limiting properties of organic metal phthalocyanine compounds. *Wuli Huaxue Xuebao* **2015**, *31* (4), 595-611.
40. Warner, M.; Din, S.; Tupitsyn, I. S.; Morley, G. W.; Stoneham, A. M.; Gardener, J. A.; Wu, Z.; Fisher, A. J.; Heutz, S.; Kay, C. W. M.; Aepli, G., Potential for spin-based information processing in a thin-film molecular semiconductor. *Nature* **2013**, *503* (7477), 504-508.
41. Martinez-Blanco, J.; Nacci, C.; Erwin, S. C.; Kanisawa, K.; Locane, E.; Thomas, M.; von Oppen, F.; Brouwer, P. W.; Folsch, S., Gating a single-molecule transistor with individual atoms. *Nature Physics* **2015**, *advance online publication*.
42. Xu, Z.; Gao, F.; Makarova, E. A.; Heikal, A. A.; Nemykin, V. N., Energy Transfer from Colloidal Quantum Dots to Near-Infrared-Absorbing Tetraazaporphyrins for Enhanced Light Harvesting. *Journal of Physical Chemistry C* **2015**, *119* (18), 9754-9761.
43. Gouterman, M., Effects of substitution on the absorption spectra of porphin. *Journal of Chemical Physics* **1959**, *30*, 1139-61.
44. Gouterman, M., Spectra of porphyrins. *Journal of Molecular Spectroscopy* **1961**, *6*, 138-63.
45. Gouterman, M.; Wagniere, G.; Snyder, L. C., Spectra of porphyrins. II. Four-orbital model. *Journal of Molecular Spectroscopy* **1963**, *11* (2), 108-27.
46. Nguyen, K. A.; Pachter, R., Ground state electronic structures and spectra of zinc complexes of porphyrin, tetraazaporphyrin, tetrabenzoporphyrin, and phthalocyanine: A density functional theory study. *Journal of Chemical Physics*. **2001**, *114* (24), 10757-10767.
47. Vegard, L., The light emitted from solidified gases and its relation to cosmic phenomena. *Nature (London, U. K.)* **1924**, *114*, 357-9.

48. Vegard, L.; Onnes, H. K.; Keesom, W. H., Emission of light by solidified gases at the temperature of liquid helium, and the origin of the auroral spectrum. *Comptes rendues* **1925**, *180*, 1084-7.
49. Vegard, L., The spectra of solidified gases and their theoretical atomic meaning. *Annalen der Physik [5]* **1930**, *6*, 487-544.
50. Kautsky, H., *Nature* **1931**, *19* (1043).
51. Lewis, G. N.; Lipkin, D., Reversible photochemical processes in rigid media. The dissociation of organic molecules into radicals and ions. *Journal of the American Chemical Society* **1942**, *64*, 2801-8.
52. Whittle, E.; Dows, D. A.; Pimentel, G. C., Matrix isolation method for the experimental study of unstable species. *Journal of Chemical Physics*. **1954**, *22*, 1943.
53. Becker, E. D.; Pimentel, G. C., Spectroscopic studies of reactive molecules by the matrix isolation method. *Journal of Chemical Physics*. **1956**, *25*, 224-8.
54. Norman, I.; Porter, G., Trapped atoms and radicals in a glass "cage". *Nature (London, U. K.)* **1954**, *174*, 508-9.
55. Harvey, K. B.; Shurvell, H. F., Evidence for the rotation of hydrochloric acid in a solid nitrogen matrix. *Chemical Communications* **1967**, (10), 490-1.
56. Barrett, C. S.; Meyer, L., The Crystal Structures of Argon and Its Alloys. In *Low Temperature Physics LT9*, Daunt, J. G.; Edwards, D. O.; Milford, F. J.; Yaqub, M., Eds. Springer US: 1965; pp 1085-1088.
57. A. J. Barnes, W. J. O.-T., A. Müller, R. Gaufrès,, *Matrix Isolation Spectroscopy*. Springer: 1981.
58. Kittel, C., *Introduction to Solid State Physics, 7th ed.* John Wiley & Sons: New York: 1996.
59. Crepin-Gilbert, C.; Tramer, A., Photophysics of metal atoms in rare-gas complexes, clusters and matrices. *International Reviews in Physical Chemistry* **1999**, *18* (4), 485-556.
60. Cradock, S. H., A. J., *Matrix Isolation*. Cambridge University Press: Cambridge: 1975.

61. Huisken, F.; Kaloudis, M.; Vigasin, A. A., Vibrational frequency shifts caused by weak intermolecular interactions. *Chemical Physics Letters* **1997**, *269* (3–4), 235-243.
62. Hofstraat, J. W.; Gooijer, C.; Velthorst, N. H., Highly resolved molecular luminescence spectroscopy. *Chemist Analyst (N. Y.)* **1988**, *77* (Mol. Lumin. Spectrosc., Pt. 2), 283-400.
63. Wehry, E. L.; Mamantov, G. In *Low-temperature fluorometric techniques and their application to analytical chemistry*, Plenum: 1981; pp 193-250.
64. Murray, C.; Dozova, N.; McCaffrey, J. G.; FitzGerald, S.; Shafizadeh, N.; Crepin, C., Infra-red and Raman spectroscopy of free-base and zinc phthalocyanines isolated in matrices. *Physical Chemistry Chemical Physics* **2010**, *12* (35), 10406-10422.
65. Fermi, A statistical method for determining some properties of the atom. I. *Atti della Accademia Nazionale dei Lincei, Classe di Scienze Fisiche, Matematiche e Naturali, Rendiconti* **1927**, *6*, 602.
66. Fermi, A statistical method for the determination of some properties of atoms. II. Application to the periodic system of the elements. *Atti della Accademia Nazionale dei Lincei, Classe di Scienze Fisiche, Matematiche e Naturali, Rendiconti* **1928**, *7*, 342.
67. Hohenberg, P.; Kohn, W., Inhomogeneous Electron Gas. *Physical Review* **1964**, *136* (3B), B864-B871.
68. Jensen, F., *Introduction to Computational Chemistry*. 2nd ed.; Wiley: 2007.
69. Kohn, W.; Sham, L. J., Self-Consistent Equations Including Exchange and Correlation Effects. *Physical Review* **1965**, *140* (4A), A1133-A1138.
70. Perdew, J. P.; Tao, J.; Staroverov, V. N.; Scuseria, G. E., Meta-generalized gradient approximation: Explanation of a realistic nonempirical density functional. *Journal of Chemical Physics*. **2004**, *120* (15), 6898-6911.
71. Becke, A. D., Density-functional thermochemistry. III. The role of exact exchange. *Journal of Chemical Physics*. **1993**, *98* (7), 5648-52.
72. Becke, A. D., Density-functional exchange-energy approximation with correct asymptotic behavior. *Physical Reviews A: General Physics* **1988**, *38* (6), 3098-100.

73. Perdew, J. P.; Ziesche, P.; Eschrig, H., *Electronic structure of solids' 91*. Akademie Verlag, Berlin: 1991; Vol. 11.
74. Stephens, P. J.; Devlin, F. J.; Chabalowski, C. F.; Frisch, M. J., Ab Initio Calculation of Vibrational Absorption and Circular Dichroism Spectra Using Density Functional Force Fields. *Journal of Physical Chemistry* **1994**, *98* (45), 11623-7.
75. Lee, C.; Yang, W.; Parr, R. G., Development of the Colle-Salvetti correlation-energy formula into a functional of the electron density. *Physical Reviews B: Condensed Matter* **1988**, *37* (2), 785-9.
76. Vosko, S. H.; Wilk, L.; Nusair, M., Accurate spin-dependent electron liquid correlation energies for local spin density calculations: a critical analysis. *Canadian Journal of Physics* **1980**, *58* (8), 1200-11.
77. Slater, J. C., Atomic shielding constants. *Physical Reviews* **1930**, *36*, 57-64.
78. Ando, T., Inter-subband optical absorption in space-charge layers on semiconductor surfaces. *Zeitschrift fur Physik B* **1977**, *26* (3), 263-72.
79. Ando, T., Inter-subband optical transitions in a surface space-charge layer. *Solid State Communication* **1977**, *21* (1), 133-6.
80. Zangwill, A.; Soven, P., Density-functional approach to local-field effects in finite systems: photoabsorption in the rare gases. *Physical Reviews A* **1980**, *21* (5), 1561-72.
81. Zangwill, A.; Soven, P., Resonant two-electron excitation in copper. *Physical Reviews B: Condensed Matter* **1981**, *24* (8), 4121-7.
82. Runge, E.; Gross, E. K. U., Density-functional theory for time-dependent systems. *Physical Reviews Letters* **1984**, *52* (12), 997-1000.
83. Burke K.; Gross, E. K. U., A Guided Tour of Time-Dependent Density Functional Theory. In *Density Functions: Theory and Applications*, Joubert, D., Ed. Springer: 1997.
84. Meijer, E. J.; Sprik, M., A density-functional study of the intermolecular interactions of benzene. *Journal of Chemical Physics*. **1996**, *105* (19), 8684-8689.

85. Dreuw, A.; Weisman, J. L.; Head-Gordon, M., Long-range charge-transfer excited states in time-dependent density functional theory require non-local exchange. *Journal of Chemical Physics*. **2003**, *119* (6), 2943-2946.
86. Dreuw, A.; Head-Gordon, M., Single-Reference ab Initio Methods for the Calculation of Excited States of Large Molecules. *Chemical Reviews (Washington, DC, U. S.)* **2005**, *105* (11), 4009-4037.
87. Dreuw, A.; Head-Gordon, M., Failure of Time-Dependent Density Functional Theory for Long-Range Charge-Transfer Excited States: The Zincbacteriochlorin-Bacteriochlorin and Bacteriochlorophyll-Spheroidene Complexes. *Journal of the American Chemical Society* **2004**, *126* (12), 4007-4016.
88. Radziszewski, J. G.; Waluk, J.; Michl, J., Site-population conserving and site-population altering photo-orientation of matrix-isolated free-base porphine by double proton transfer: IR dichroism and vibrational symmetry assignments. *Chemical Physics* **1989**, *136* (2), 165-180.
89. Radziszewski, J. G.; Waluk, J.; Michl, J., FT visible absorption spectroscopy of porphine in noble gas matrices. *Journal of Molecular Spectroscopy* **1990**, *140* (2), 373-389.
90. Arabei, S. M.; Galaup, J. P.; McCaffrey, J. G.; Shafizadeh, N.; Crépin, C., Electronic spectroscopy, stimulated emission, and persistent spectral hole burning of cryogenic nitrogen matrices doped with tetrabenzoporphin. *Low Temperature Physics* **2012**, *38* (8), 727-731.
91. Henchy, C.; McCaffrey, J. G.; Arabei, S.; Pavich, T.; Galaup, J.-P.; Shafizadeh, N.; Crépin, C., Free base tetraazaporphine isolated in inert gas hosts: Matrix influence on its spectroscopic and photochemical properties. *The Journal of chemical physics* **2014**, *141* (12), -.
92. Arabei, S.; McCaffrey, J. G.; Galaup, J.-P.; Shafizadeh, N.; Crépin, C., Stimulated emission in cryogenic samples doped with free-base tetraazaporphine. *Physical Chemistry Chemical Physics* **2015**, Ahead of Print.

93. Starukhin, A.; Shulga, A.; Sepiol, J.; Kolos, R.; Renn, A.; Wild, U. P., Single molecule spectroscopy of Mg tetra-azaporphyrin in solid xenon. *Single Molecules* **2001**, *2* (3), 203-206.
94. Dozova, N.; Murray, C.; McCaffrey, J. G.; Shafizadeh, N.; Crepin, C., Amplified emission of phthalocyanine isolated in cryogenic matrices. *Physical Chemistry Chemical Physics* **2008**, *10* (16), 2167-2174.
95. Murray, C.; Dozova, N.; McCaffrey, J. G.; Shafizadeh, N.; Chin, W.; Broquier, M.; Crepin, C., Visible luminescence spectroscopy of free-base and zinc phthalocyanines isolated in cryogenic matrices. *Physical Chemistry Chemical Physics* **2011**, *13* (39), 17543-17554.
96. Ziminov, A. V.; Ramsh, S. M.; Terukov, E. I.; Trapeznikova, I. N.; Shamanin, V. V.; Yurre, T. A., Correlation dependences in infrared spectra of metal phthalocyanines. *Semiconductors* **2006**, *40* (10), 1131-1136.
97. Lever, A. B. P.; Minor, P. C., *Inorganic Chemistry* **1981**, *20*, 4015.
98. Napier, A.; Collins, R. A., FTIR characteristics of halogenated phthalocyanines exhibiting polymorphism. *Thin Solid Films* **1994**, *248* (2), 166-177.

Chapter II: Methods (Experimental and Theoretical)

II.1: Introduction

The experimental portion of this work involved the spectroscopy of phthalocyanines isolated in inert gas solids. This chapter will describe the apparatus used to achieve matrix-isolated samples doped with phthalocyanines as well as the conditions used in the preparation of these samples. A description of the instruments used for the recording of Fourier-transform infrared (FTIR) spectra will be given. The setup for measuring spectra in the UV/Vis region with steady-state and time-resolved techniques will also be presented. Finally, the setup used for performing high level quantum chemical calculations to complement the experimental portion of the work will be outlined, as well the general procedure for running a calculation. Experiments were carried out in the Low Temperature Laboratory in the Department of Chemistry at Maynooth University of Ireland unless otherwise stated.

II.2: Matrix-Isolation Apparatus

The matrix-isolation (MI) apparatus used in FTIR and Ultraviolet/visible (UV-Vis) experiments is shown in Figure II.1. Matrix-isolation experiments require high vacuum to prevent heat exchange and the deposition of atmospheric gases, so two similar pumping systems were incorporated into the two matrix rigs to achieve these conditions. The FTIR experimental setup used an Edwards RV5 rotary backing pump to achieve a pressure of $< 5 \times 10^{-3}$ mbar and was monitored using an Edwards Pirani PRE10K gauge head with an Edwards Pirani 501 gauge. An Edwards 100/300M *Diffstak* oil diffusion pump was used to achieve a pressure of 10^{-7} mbar at room temperature, measured with an Alcatel CF2P penning gauge capable of reading between 10^{-3} and 10^{-7} mbar. This setup was capable of reaching pressures of $< 10^{-7}$ mbar with cryo-pumping when the sample window of the apparatus was cooled down. The *Diffstak* design of the diffusion pump increases the ability of the pump to condense diffusion oil, relative to standard diffusion pump designs, and negates the need for an liquid nitrogen cold trap.

The UV-Vis experimental setup used an Edwards RV3 rotary pump to get to a base pressure of $< 5 \times 10^{-3}$ mbar, monitored using a Granville-Phillips Series 275 Convector gauge¹. It then could achieve a high vacuum using an Edwards E02 *Speedivac* oil diffusion pump capable of reaching 10^{-7} mbar at room temperature and $< 10^{-7}$ mbar at cryogenic temperature. Pressures below 10^{-3} mbar were measured with an Alcatel CF2P penning gauge. An Edwards liquid nitrogen (L-N₂) cold trap was attached to the diffusion pump to prevent contamination of the matrix apparatus with diffusion pump oil vapour when under operating conditions. An Edwards QSBR quarter swing valve allowed the isolation of the vacuum manifold from the pump system, which allowed venting the system up to atmospheric pressures without contaminating the pump oil.

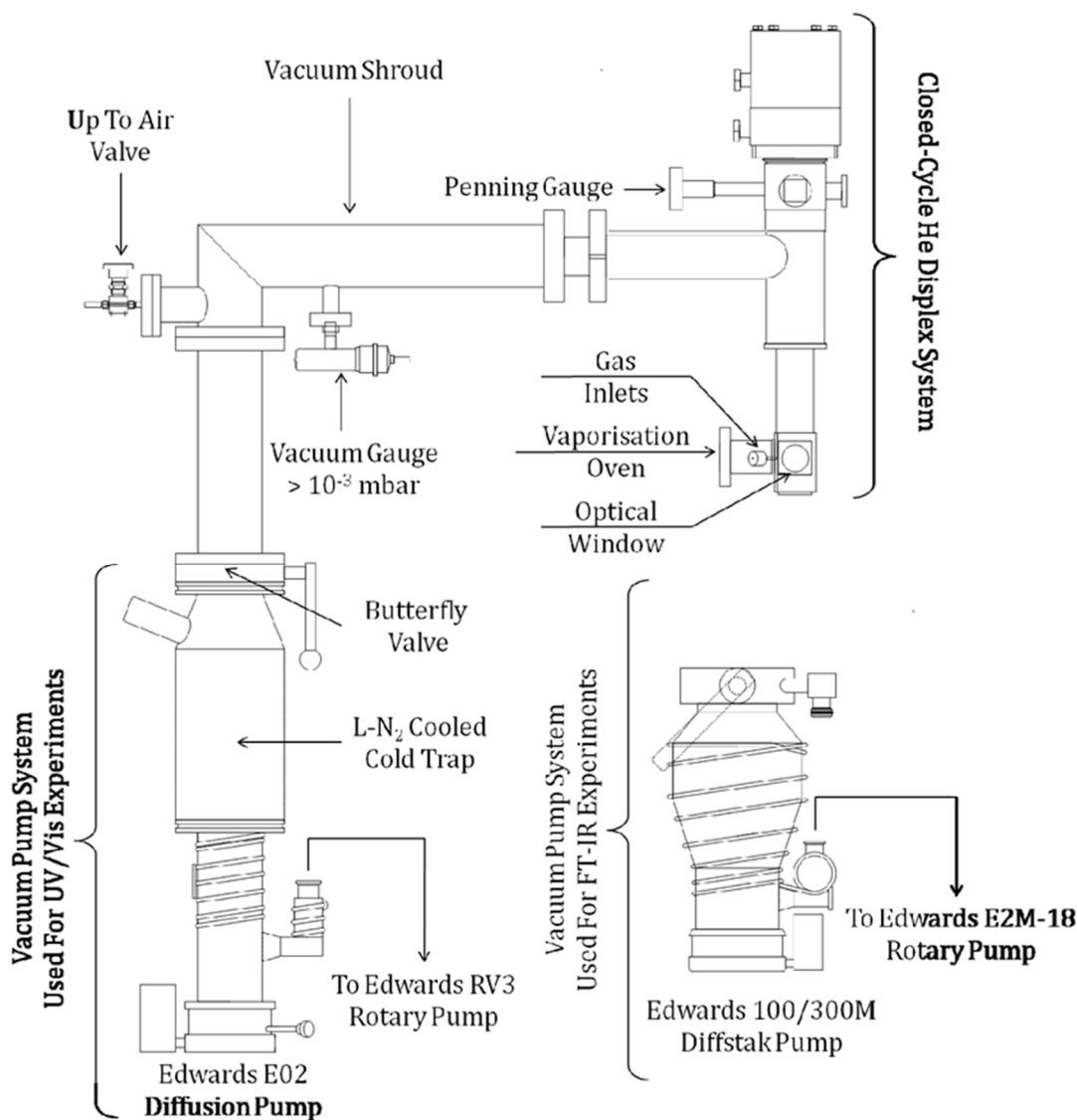


Figure II.1: Schematic for the matrix isolation apparatus showing the pumps and pressure gauges used in the system.

A schematic of the APD Cryogenics closed-cycle helium displacer system used to generate the cryogenic temperatures required to form solid matrices of inert gases, is presented in Figure II.2. Operation of the unit involves pumping helium gas at 270 psi from APD Cryogenics HC-2 compressor² into an APD Cryogenics DE-202 two-stage refrigeration unit³ through a dedicated gas line. A Gifford-Mc Mahon refrigeration cycle removes heat from the system by expanding the compressed helium within the two stages. Warm helium is recycled by returning the to the displacer compressor through another gas line. The first refrigeration stage is capable of reaching a temperature of ~ 77 K while the second stage was able to attain temperatures of 10 - 13 K, depending on whether or not a radiation shield was used. A nickel plated copper holder was mounted to the end of the second refrigeration stage, capable of holding a $\frac{3}{4}$ " sample window. An indium seal was used to hold the sample window in the copper holder and ensure a good thermal contact. The temperature at the window was monitored and controlled by a Scientific Instruments 9600-1 heater and silicon diode⁴ attached to the copper holder. Three 380 mm x 4 mm external windows were attached to the vacuum manifold with Viton O-ring seals. Potassium bromide (KBr) windows were used in the FTIR experiment due to its transmission range of approximately $43,500 - 250 \text{ cm}^{-1}$. The spectral region of interest used in FTIR experiments was typically $4,000 - 400 \text{ cm}^{-1}$. The UV/Vis experiment employed calcium fluoride (CaF_2) windows with a transmission range of $77,500 - 850 \text{ cm}^{-1}$. The spectral region of interest in these experiments was approximately $50,000 - 10,000 \text{ cm}^{-1}$.

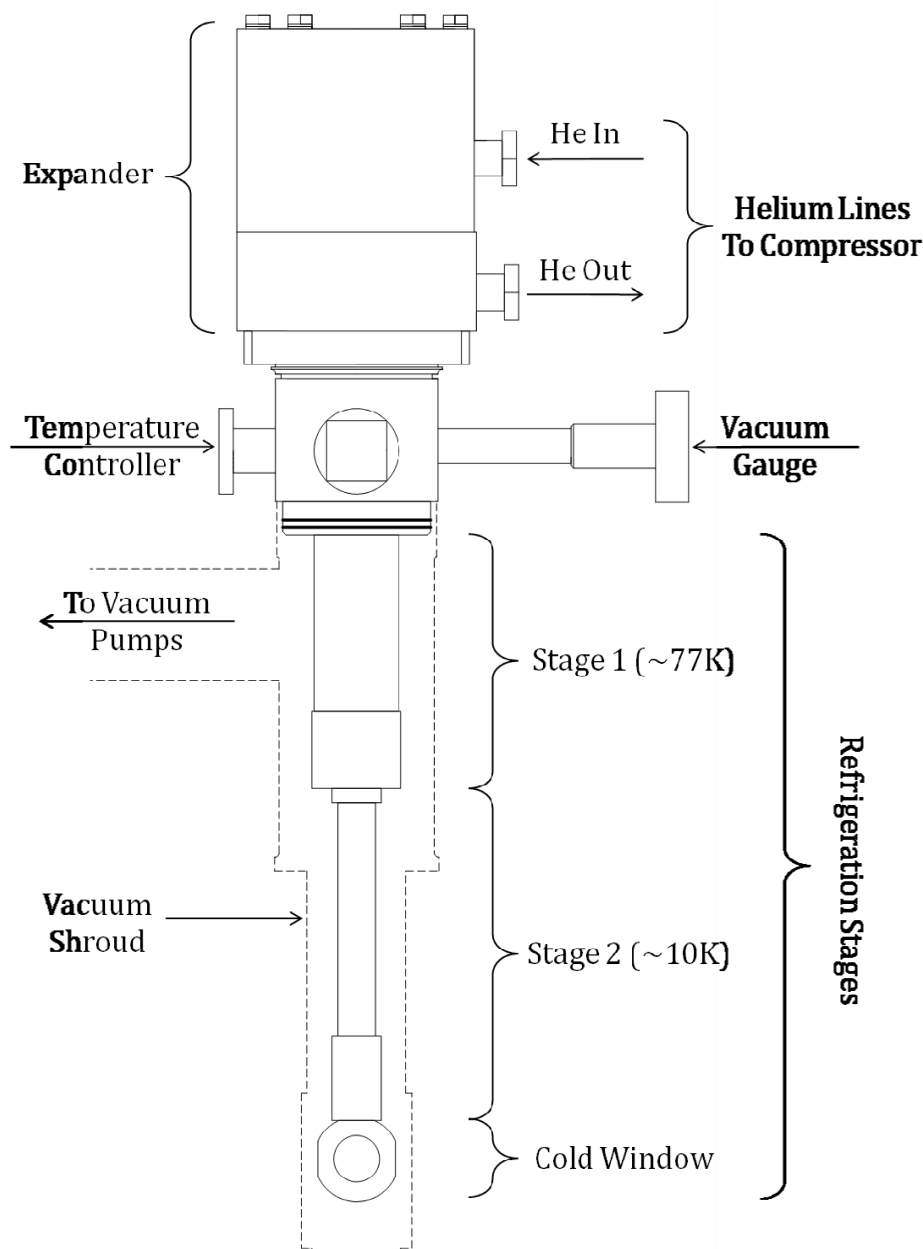


Figure II.2: APD Cryogenics closed-cycle helium displacer system. Sample temperatures of ~ 10 K were achieved on the cold windows using the two stage refrigeration system shown.

II.3: Gas Handling System

Several different host gases were used for matrix-isolation experiments and were controlled with a dedicated gas handling system (GHS) on each experimental apparatus, shown in Figure II.3. The gas handling systems on both experiments worked on the same principals but were distinct from one another. Vacuum was achieved on the FTIR system

using the same pump set-up as the rest of MI apparatus *i.e.* an Edwards 100/300M *Diffstak* oil diffusion pump backed with an Edwards E2M-18 rotary pump. The pumps were attached to the GHS with via an MKS $\frac{3}{4}$ " angle valve (AV-075M). When filled with a host gas, the pressure inside the GHS were monitored using two MKS Type 626 *Baratron*® gauges with pressure ranges of 0-10 and 0-1000 torr. A vacuum of $\sim 10^{-8}$ mbar was maintained in the UV-Vis GHS using a Pfeiffer Balzers TPU-180H turbo-molecular pump⁵ backed by an Edwards E2M-18 rotary pump. The pumping system was attached to the GHS via an AEI MV38 all-metal angle valve. Gas pressures within the GHS were monitored using two Tylan General Capacitance Diaphragm Gauges; a model CDLD-11 with a pressure range of 0-10 torr and a model CDLD-31 with a pressure range of 0-1000 torr. A Granville-Phillips type 203 variable leak valve⁶ was used to control the gas flow in both experiments and was attached to the vaporisation apparatus via a length of $\frac{1}{4}$ " VCR tubing. This valve was also used to isolate the GHS from the rest of the vacuum manifold. Gases were stored in lecture bottles and attached to the gas handling system with $\frac{1}{4}$ " VCR tubing.

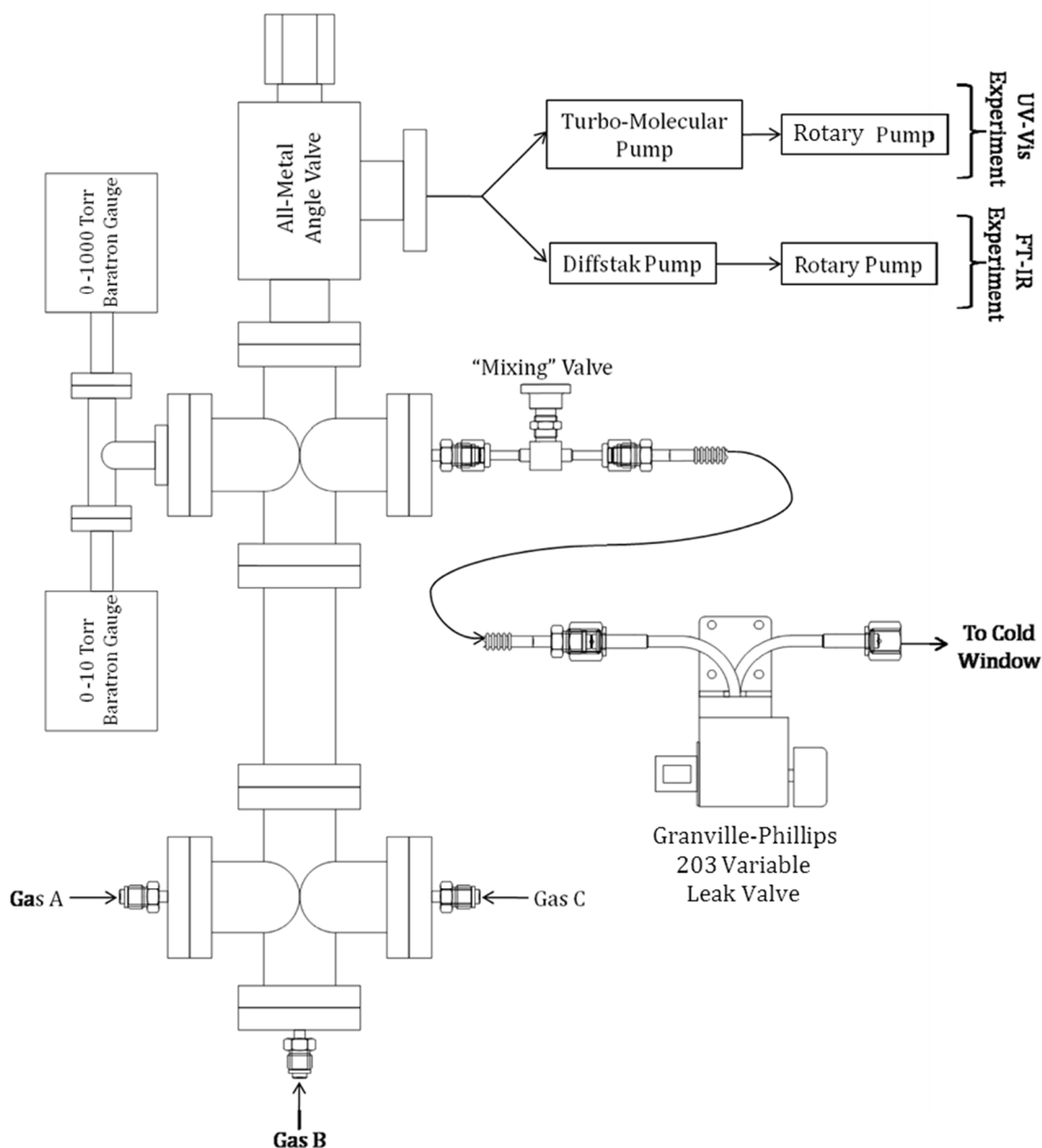


Figure II.3: Schematic of the gas handling system used in the matrix-isolation apparatus.

II.4: Phthalocyanine Vapour Generation

Aluminum phthalocyanine chloride (AlPcCl), gallium phthalocyanine chloride (GaPcCl), and magnesium phthalocyanine (MgPc) were purchased from TCI Chemicals, Santa Cruz Biotechnology Inc. and Sigma Aldrich respectively and were used without further purification. Matrix samples were prepared by resistive heating of the phthalocyanines to around 350 °C and using the flowing host gas to entrain the Pc vapour for deposition onto

a cryogenically cooled window. An oven mounted to the matrix rig was used to generate the phthalocyanine vapour and is presented in Figure II.4. Phthalocyanine powder was compacted into a hollowed out screw and fitted into a cylindrical stainless steel crucible. The crucible contained a 2 mm aperture at 90° to the screw running the entire length of the cylinder into which gas was flowed through. The crucible was connected by a Swagelok compression seal to a 1/4" gas inlet line, which in turn was connected to the GHS. The gas flow was directed towards the sample window with a stainless steel nozzle attached to the outlet of the crucible, located 5 cm from the sample window. The oven was heated by a resistive heating wire which was coiled around the crucible and temperature monitored by an n-type thermocouple. A calibration curve for this type of thermocouple is shown in Figure II.5. To prevent heat loss, the entire assembly was surrounded by a stainless steel heat shield.

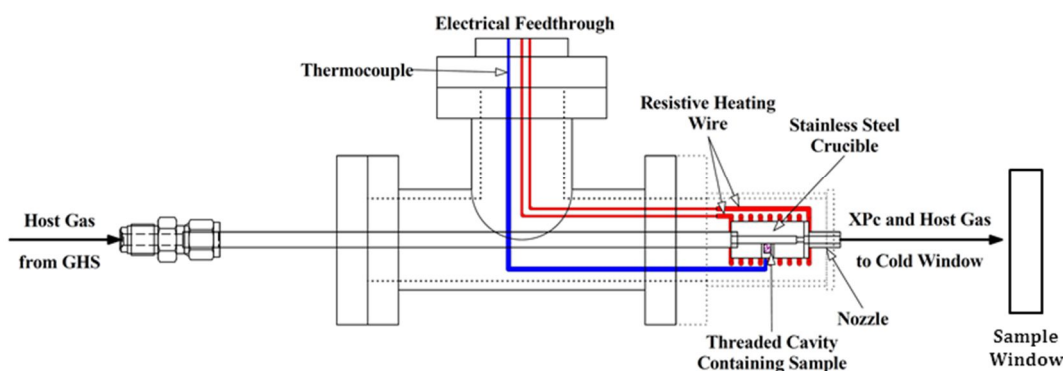


Figure II.4: Diagram of the heating apparatus used to vaporise M-Pc powder for matrix-isolation experiments.

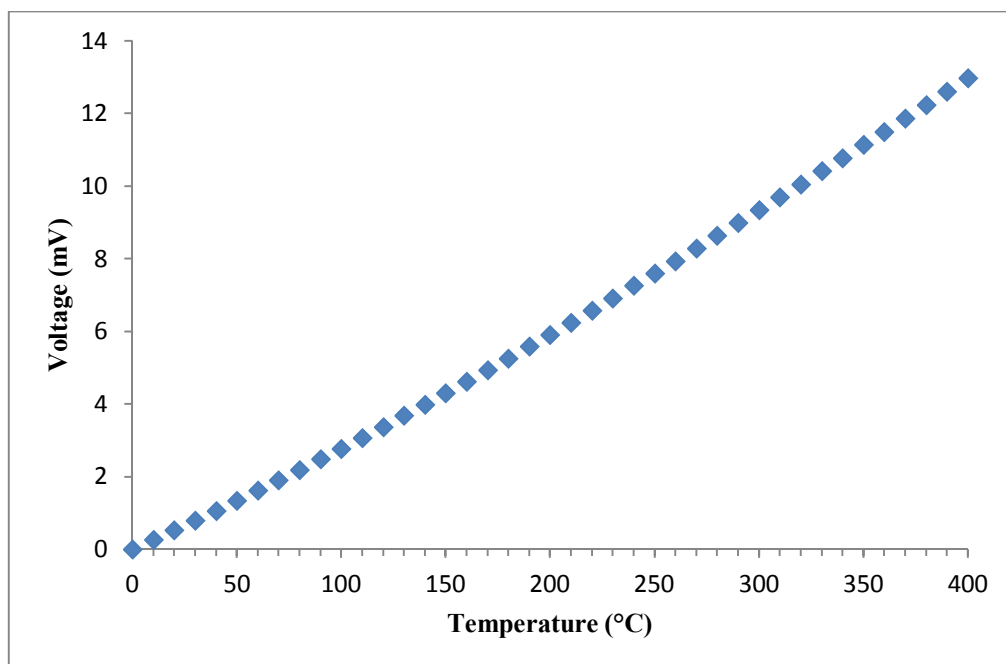


Figure II.5: Calibration curve for the n-type thermocouple used to monitor the temperature of the phthalocyanine oven during a deposition for matrix-isolation experiments.

II.5: Sample Deposition

Matrix-isolated samples of AlPcCl, GaPcCl and MgPc were prepared by co-depositing the phthalocyanine vapour with an inert gas onto a cryogenically cooled sample window. The inert gases used in the current work included the rare gases Argon, Krypton and Xenon, as well as the molecular gas Nitrogen. The gases were controlled using the GHS described above. The window temperature used during the deposition depended on the melting point, M_p , of the host gas being used, which are shown in Table II.1. In general the window temperature was not allowed to exceed $\frac{1}{4}$ of the M_p of the host gas.

Table II.1: Host gases used in the preparation of matrix-isolated phthalocyanine samples in the current work. Their melting points (M_p) and refractive indices are also reported.

Host Gas	Chemical Purity	Supplier	M_p (K) ⁷	Refractive index ⁸
Argon (Ar)	99.998%	BOC	83.8	1.29
Krypton (Kr)	99.559%	Linde Gas	115.79	1.28
Xenon (Xe)	99.999%	Linde Gas	161.4	1.49
Nitrogen (N ₂)	99.999%	Linde Gas	63.15	1.22

Prior to the co-deposition of the host gas/phthalocyanine mixture onto the sample window, a layer of pure gas was deposited onto the sample window to prevent a film of phthalocyanine forming after evaporation of the sample. To achieve isolation of the Pc as a monomer, large gas flows (4 torr/min) and window temperatures of ~ 20 K were required. Samples were deposited onto the matrix window at 10 – 22 K for Ar and N₂ matrices. Slightly higher temperatures of 10 – 35 K were used for the heavy rare gas matrices Kr and Xe, in order to avoid the formation of highly scattering samples. Deposition times for the UV-Vis experiments were typically 30 minutes. Deposition times for FTIR experiments were longer (60 – 120 minutes) owing to weaker oscillator strengths of vibrational transitions compared to those of electronic transitions. Concentrations of M-Pc in the host matrix were controlled by adjusting the oven temperature and gas flow. Spectra were typically recorded at 10 K unless a temperature specific phenomenon was being investigated.

II.6: Fourier Transform Infrared (FT-IR) Measurement

A Bruker Optics IFS 66/S FTIR spectrometer⁹ was used to record all Fourier transform infrared (FTIR) absorption spectra of matrix-isolated samples. A schematic of the spectrometer is shown in Figure II.6. A silicon carbide Global® was used as a mid IR (MIR) light source. The amount of light entering the spectrometer was controlled by a rotating aperture wheel with openings from 0.25 to 12 mm in diameter. The MIR beam was directed into a Michelson interferometer through a Ge/KBr beamsplitter¹⁰ with a range of 7,800 – 370 cm⁻¹. The beamsplitter directs half of the light onto a stationary mirror and half onto a moving mirror. Both beams are then recombined and sent towards the sample

compartment and detectors¹¹. Two detectors were used in the current work; a Deuterated L-alanine doped triglycine sulphate (DTGS) detector with a spectral range between 11,000 and 250 cm^{-1} , and a liquid nitrogen cooled mercury cadmium tellurium (MCT) detector with a spectral range between 8,000 and 800 cm^{-1} . The DTGS detector has a wider spectral range and works at room temperature, but is about 100 times less sensitive than the MCT detector. Switching between the two detectors is controlled by a hinged mirror.

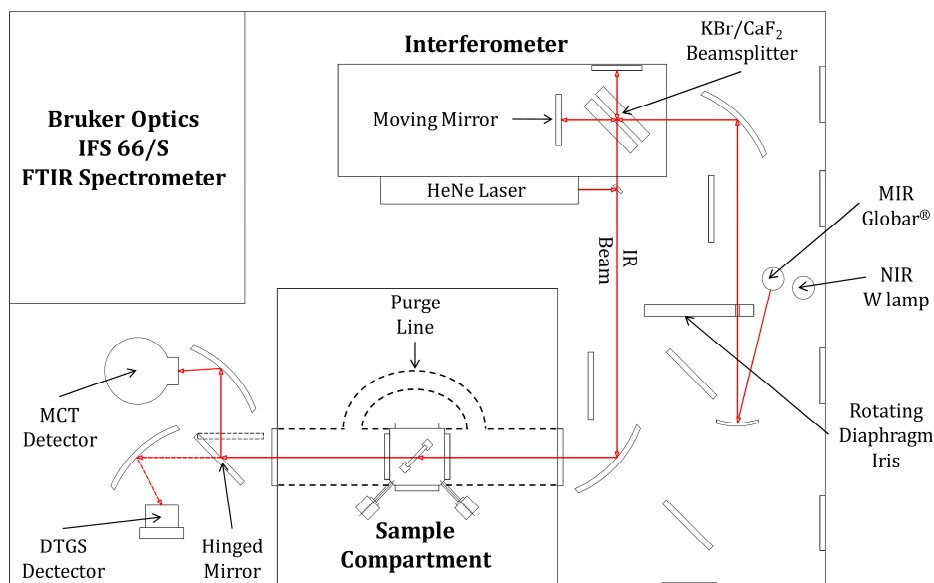


Figure II.6: Schematic of the Bruker IFS 66/S infrared spectrometer.

The mechanism on which the moving mirror operates is a cylindrical air bearing. The advantage of using an air bearing over a mechanical bearing is a massive reduction in friction between the mirror and the mirror path and hence reduces errors during scans. A constant flow of dried air was delivered to the air bearing in the IFS 66/S, supplied by a Balston 75-47 FTIR purge gas generator. The same air supply was also used to purge the sample compartment with dry air to reduce the atmospheric contaminants (H_2O and CO_2) in the IR spectra recorded and to protect the water sensitive KBr optics. The position of the moving mirror was controlled by a Helium-Neon (HeNe) laser with an output of 632.8 nm. The laser beam was directed through a beamsplitter into the interferometer below the axis of the MIR beam. The rest of the beam was split into three and sent towards the detectors parallel to the IR beam to act as a positioning guide for the sample. The sample compartment was modified to incorporate the matrix-isolation apparatus. The lid for the

sample compartment was removed completely and the MI apparatus placed inside with the sample window positioned at the focal point of the laser beams, ensuring the IR beam would pass through the sample. Because the lid was removed, the purge in the sample compartment was broken. This was remedied by constructing a purge line from rubber tubing and connecting the external windows of the MI apparatus to the spectrometer and purging with a Peak Scientific Instruments PG28L air drier. This ensured the entire optical path was free of atmospheric contaminants and the KBr windows were protected.

One of the key components in the generation of IR spectra is the interferometer. A simplified diagram of an infrared Michelson interferometer is shown Figure II.7. Light from the mid-IR light source is passed through the beamsplitter. Half of the light is transmitted onto the moving mirror and the other half is reflected onto the stationary mirror. The moving mirror travels continuously along one axis, increasing and decreasing the path length which the beam has to travel. Both beams are then passed back through the beamsplitter where they are recombined and focussed onto a detector, which records the intensity of the recombined light coming from the interferometer^{12,13}.

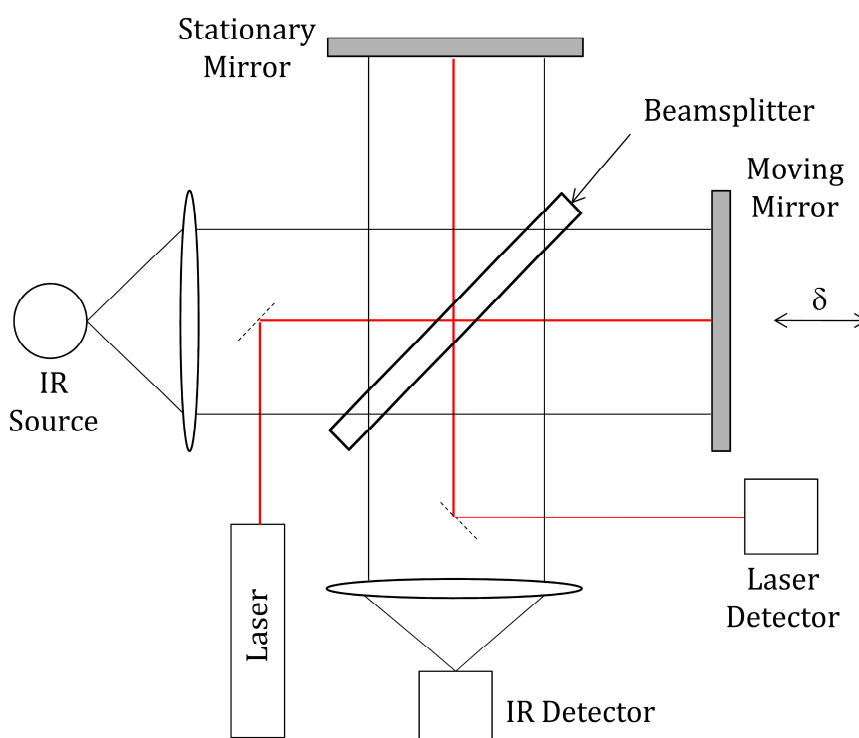


Figure II.7: Schematic of a Michelson interferometer.

An interferogram, $I(\delta)$, is produced by plotting the intensity of the recombined beams as a function of the moving mirror position. The difference in path length between the stationary and moving mirrors is known as the Optical Path Difference (OPD) or optical retardation, δ^{14} . The recombining IR beams interfere with each other either constructively or destructively which will determine the intensity of the beam for a given mirror position. When the pathlengths between the mirrors is zero, all wavelengths of the MIR beam will interfere constructively and a large intensity will be detected. This is known as the zero path difference (ZPD). As the optical path elongates wavelengths will interfere both constructively and destructively, resulting in a lower intensity signal being detected. A typical interferogram of a broadband source is presented in the left-hand panel of Figure II.8 showing the characteristic ‘centre-burst’ shape with large intensity interference at the centre and lower intensity at the wings.

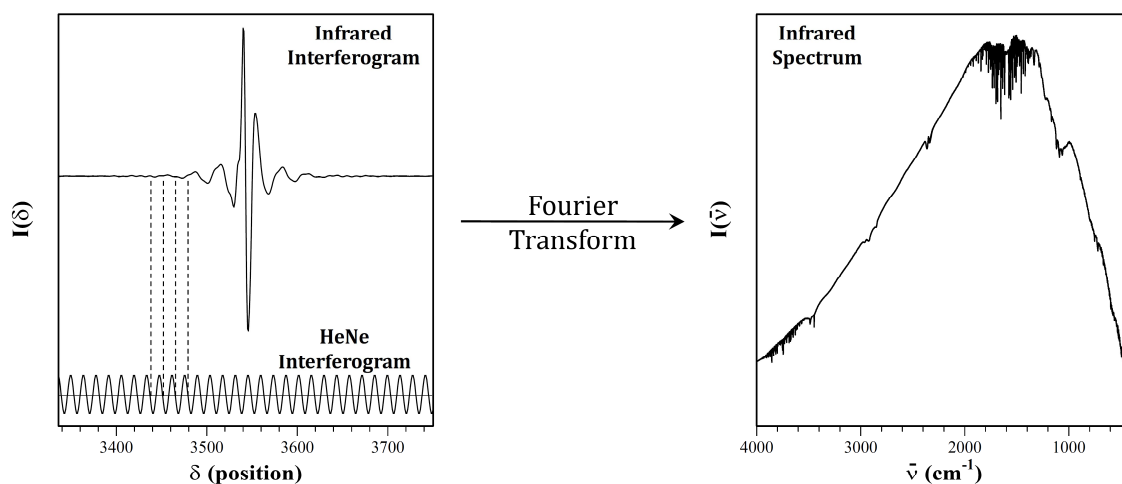


Figure II.8: Conversion of an interferogram into an infrared spectrum following the application of a Fourier transform operation.

An accurate measurement of the position of the moving mirror is necessary, and is achieved by directing a laser beam from the HeNe along the same optical path as the IR beam. The laser beam experiences the same process as the IR beam of being split in two, passed through the interferometer, recombined and sent to a separate detector. Due to the laser light being monochromatic, a perfect sine-squared pattern interferogram should be generated as the optical path changes, as shown in the lower plot of Figure II.8. The fringes of the laser interferogram are then used to calibrate the position of the moving mirror and

to indicate when the detector should record a signal, as shown by the vertical dashed lines in Figure II.8.

All of the spectral information of a scan is contained within an interferogram, but cannot be seen directly without performing a mathematical operation on the signal known as a Fourier transform. A mathematical transform to convert an interferogram, $I(\delta)$, into a wavenumber spectrum, $I(\bar{\nu})$, may be expressed by the integral:

$$I(\bar{\nu}) = \int_{-\infty}^{+\infty} I(\delta) \cos(2\pi\bar{\nu}\delta) d\delta \quad \text{Eq. II.1}$$

where $\bar{\nu}$ is the frequency in wavenumbers and δ is the optical retardation of the moving mirror. The transform works on the principle of two sine waves of the same frequency interfering either constructively or destructively. The intensity at a given frequency is dependent on the difference in the phases of the two waves which is determined by the path length each wave has travelled (i.e. $\delta = \alpha_1 - \alpha_2$ where α_1 and α_2 are the phase angles of the two waves).

Equation II.1 is not easy to use in practice because experimental interferograms are not recorded continuously, but rather are condensed into a finite number of points, N . To perform a transformation on an experimental interferogram of N points a discrete Fourier transform¹⁵ is applied and may be given by:

$$S(k\Delta\bar{\nu}) = \sum_{n=0}^{N-1} I(n\Delta\delta) \exp\left(\frac{2\pi ink}{N}\right) \quad \text{Eq. II.2}$$

where k and n are the spectral and interferogram points and the spectral resolution $\Delta\bar{\nu} = 1/N\Delta\delta$. Algorithms known as Fast Fourier Transforms (FFTs) have been developed in order to solve Equation II.2, the most common of which is the Cooley-Tukey FFT¹⁶. A well-known issue with applying a Fourier transform to a condensed interferogram is the ‘picket fence’ effect, in which some of the frequencies in the interferogram do not correspond with the sample points $k\Delta\bar{\nu}$ of the discrete Fourier transform. This will result in a spectrum with missing frequencies; almost as if it is being viewed from behind a picket fence. This is particularly troublesome for matrix infrared experiments, where vibrational bands tend to be quite narrow. A ‘zero filling’ technique can be used to overcome this effect, which involves adding zeros to the end of the interferogram, increasing the number of points per wavenumber in the final spectrum. This does not introduce errors into the spectrum as the overall instrumental lineshape has not been changed. Extensive zero filling

is required for matrix-isolated and gas phase IR spectra as the band widths are sufficiently narrow that they may be missing entirely from a spectrum. An eight order zero filling was used in the matrix IR experiments in the current work.

In order to obtain a complete spectrum from an interferogram, the optical retardation sampled must range from $-\infty$ to $+\infty$. This is clearly not feasible in reality, so experimental interferograms are recorded within the finite range ($-\delta$ to $+\delta$); a truncation of the infinite interferogram. Mathematically, a finite interferogram may be considered as a convolution of the infinite interferogram by applying a function with values of 1 from $-\delta$ to $+\delta$ and 0 outside these limits. This simplest function is called a Boxcar function and is the process of apodization¹⁵. A Fourier transform applied to a Boxcar apodized interferogram will result in broad spectral lines and the generation of oscillating side-lobes (leakage) which can be clearly seen in the top left panel of Figure II.9.

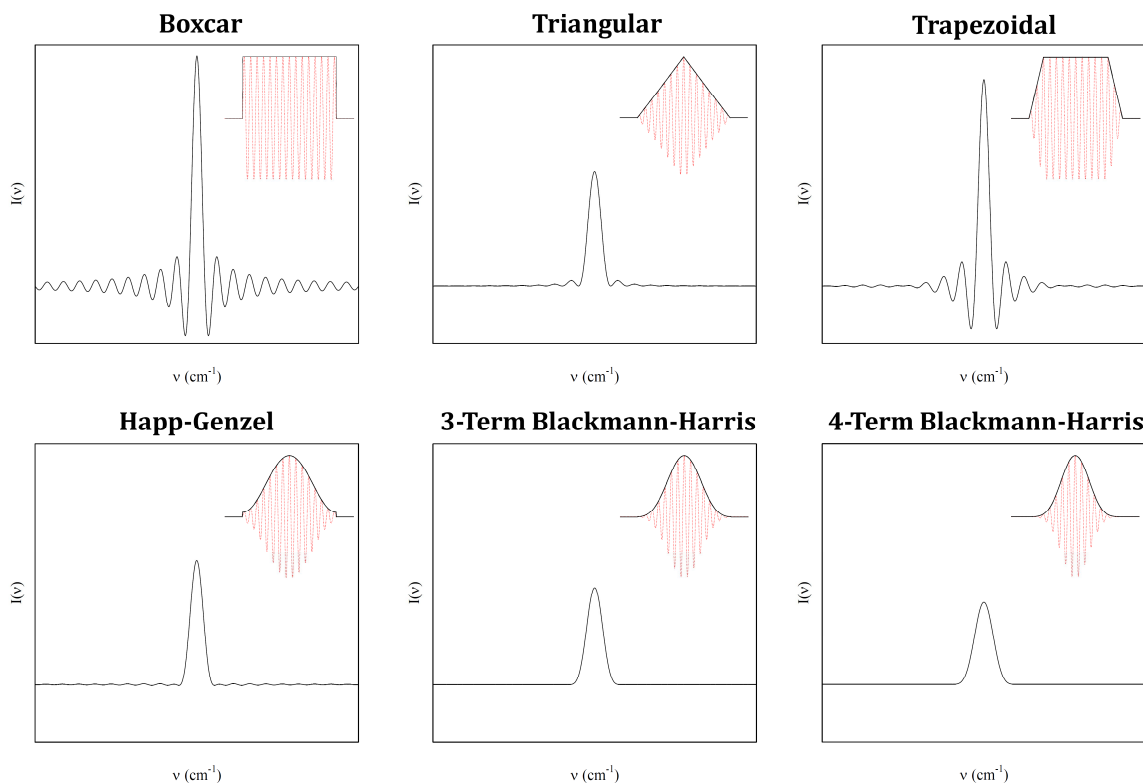


Figure II.9: The effect of various apodization functions on the DFT transformed interferogram of a monochromatic light source. Shown inset are the shapes of the apodization functions and their effect on a finite interferogram of a monochromatic light source (red-dotted trace).

The leakage problem can be improved upon by choosing a different apodization function which gradually brings the ends of the interferogram to zero. A selection of different apodization functions are shown in the remaining panels of Figure II.9, each of which has varying degrees of success at reducing leakage. A simple triangular function (top middle of Figure II.9) improves on the boxcar function by applying linear functions from 0 to 1 between the centre and the ends of the interferogram. The trapezoidal function (top right of Figure II.9) is a modified boxcar function situated between two breakpoints with linear functions applied towards the ends of the interferogram. The Happ-Genzel or Hamming function (bottom left of Figure II.9) consists of a cosine wave function fitted to a boxcar function, with the parameters optimized to diminish leakage. The three- and four-term Blackmann-Harris functions (bottom middle and right of Figure II.9 respectively) are similar to the Happ-Genzel function with multiple parameters that reduce the interferogram smoothly to zero at the ends of the interferogram. The n-Term Blackmann-Harris functions are particularly effective at reducing leakage, however, the payoff for this is that the resulting spectral lines are broadened which reduces the resolution of the spectrum¹⁷.

Recorded interferograms tend not to be perfectly symmetric. This asymmetry stems from a number of sources; phase delays due to the optics, detector or electronics, sampling positions not coinciding with the ZPD and longer sampling of one side of the interferogram than the other. A phase correction can be applied to improve the quality of the interferogram; it attempts to remove sine components introduced by asymmetry in order to determine the spectral intensities correctly. One of the most common phase corrections employed by FTIR spectroscopy is the Mertz algorithm¹⁸, which works by first calculating a low resolution phase spectrum by performing a Fourier transform on a small amount of data centred on the ZPD. Once the Fourier transform has been performed on the entire interferogram, the low resolution phase spectrum is used to correct the FT spectrum by interpolation. Another problem associated with applying a Fourier transform to a finite interferogram is known as aliasing, where a mirror image of the spectrum is produced. When Equation II.3 is applied to an interferogram containing N data points taken at optical path differences of Δx , a spectrum of N points will be generated with a resolution of $\Delta \nu$. The correct spectrum will be produced for the first $N/2$ points, and mirrored over the second $N/2$ points. The ‘folding’ or ‘aliasing’ of the spectrum occurs about the Nyquist wavenumber, ν_f , given by,

$$\nu_f = N/2\Delta\nu = 1/2\Delta x \quad \text{Eq. II.3}$$

with replication of the spectrum and its mirror image occurring over all integer multiples of N . When the range of the spectrum exceeds the Nyquist value (i.e. when the maximum wavenumber $\nu_{\max} > \nu_f$), aliasing can occur in the low energy region of the spectrum with the intensities of the signals greater than ν_f . In the Bruker IFS 66/S spectrometer, the sampling positions determined by a HeNe laser with a wavelength of $\lambda = 1/15,798.002 \text{ cm}^{-1}$ occur at the zero crossing points $\lambda/2$ leading to a minimum sampling spacing $\Delta x_{\min} = 1/31,596.004 \text{ cm}^{-1}$. Substituting this value for Δx_{\min} into Equation II.3 yields a result of $\nu_f = 15,798.002 \text{ cm}^{-1}$. The value for ν_f is the maximum bandwidth that can be measured without overlapping occurring, but is much larger than the bandwidth observed in MIR absorptions. It is useful to instead use an m -fold integer multiple of Δx , reducing the size of the interferogram (e.g. $2 \times \Delta x_{\min} = 15,798.002 \text{ cm}^{-1} \rightarrow \nu_f = 7899.001 \text{ cm}^{-1}$).

II.7: Luminescence Measurements

In the analysis of the matrix isolated GaPcCl samples, two classes of visible luminescence spectroscopy were employed: steady-state spectroscopy using continuous lamp excitation and time-resolved spectroscopy using pulsed laser excitation. The following section describes the optical set-up, detectors and excitation sources used for both types of visible spectroscopy.

II.7.I: Steady-State Spectroscopy

The spectrometer set-up used for the recording of steady-state luminescence spectra is shown in Figure II.10. A 30 W, GE DZA tungsten (W) lamp was used for continuous lamp excitation in the 300 to 900 nm range and a Hamamatsu L631016 deuterium (D_2) lamp¹⁹ with a Cathodeon C713 power supply²⁰ was used for higher energy excitations in the 180 - 500 nm region. An Acton Research Corporation (ARC) SpectraPro-300i monochromator²¹ with a focal length of 300 mm was used to produce monochromatic light from the two lamps for the recording of absorption and excitation spectra. The monochromator was installed with a high resolution 1200 grooves/mm grating blazed at 300 nm which was used extensively, and a lower resolution 300 grooves/mm grating also blazed at 300 nm, which was not used in the current work. Calibration of the monochromator was performed using the atomic lines from a mercury pen lamp²². The

ARC SpectraPro-300i monochromator had a resolution of 0.1 nm at 435.8 nm when fitted with the 1200 grooves/mm grating.

Light exiting the absorption/excitation monochromator was focused onto the CaF₂ sample window through the external windows (also made from CaF₂) using a 1” focusing lens. For the recording of absorption spectra, the monochromatic light transmitted through the sample was focused onto a Hamamatsu R928 Photo-Multiplier Tube (PMT)²³ using a 1” collecting lens. The absorption spectra, A , was determined by using the equation,

$$A = -\log(I/I_0) \quad \text{Eq. II.4}$$

where I_0 is the intensity of the light entering the sample from the monochromator and I is the intensity of the light transmitted through the sample. The apparatus outlined above is an example of a single beam experiment. In order to obtain an absorption spectrum an transmittance spectrum of the sample, (I), and another of a ‘blank’ matrix of similar thickness, (I_0) were recorded and the absorption determined using Equation II.4.

Emission spectra were recorded by monitoring the sample at right angles to the excitation axis through an ARC SpectraPro-500i monochromator²⁴ with a focal length of 500 mm. The emitted light was focussed by a 1” collecting lens. This monochromator was installed with three diffraction gratings; a 1200 grooves/mm grating blazed at 300 nm, a 600 grooves/mm grating blazed at 600 nm and a 150 grooves/mm grating blazed at 300 nm. This ‘emission’ monochromator was calibrated with the atomic lines from a mercury pen lamp and was capable of a resolution of 0.04 nm when fitted with the high resolution grating. Emission spectra were recorded using a Hamamatsu R928-P PMT cooled to -20°C in a Products for Research Photocool S600 cooled-housing²⁵. The ARC NCL control unit and SpectraSense software package were used to control both spectrometers and the data acquisition from the PMTs.

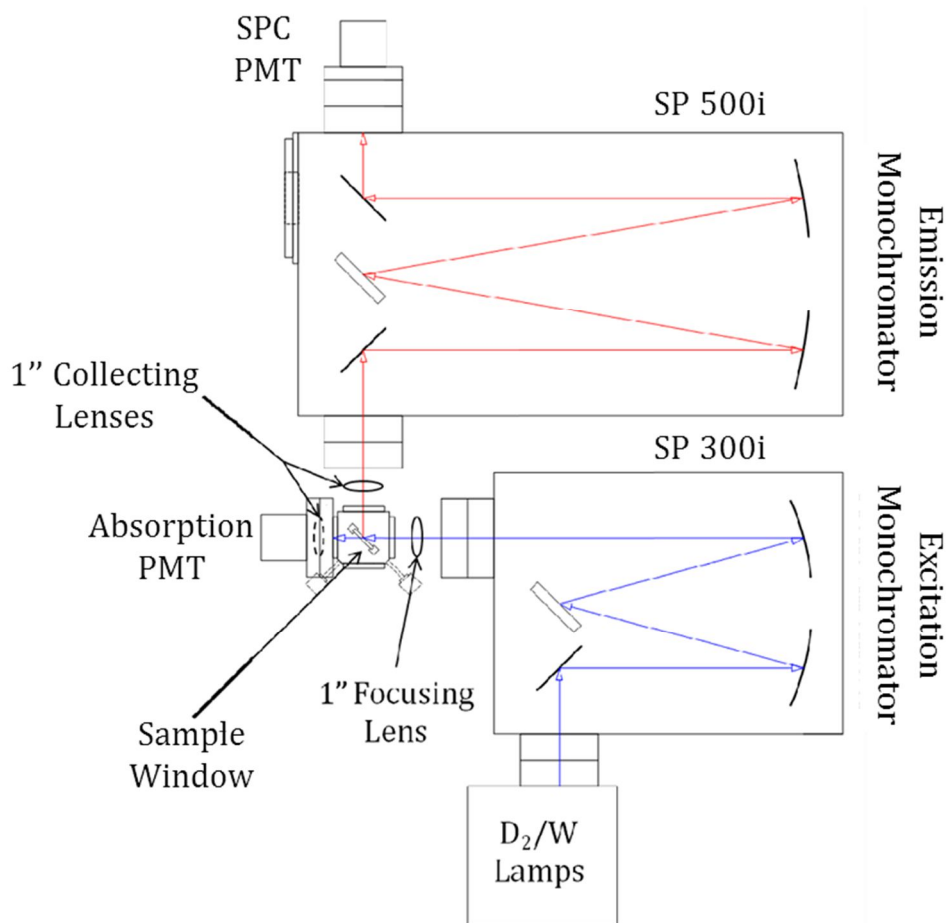


Figure II.10: Schematic of the ARC luminescence spectrometer setup used to record steady-state spectroscopy. Absorption, emission and excitation spectra were recorded with the setup shown above.

II.7.II: Time-Resolved Spectroscopy

Time-resolved emission and excitation spectra were recorded using the set-up shown in Figure II.11. A Quantel YG 980E-10 Nd:YAG laser²⁶ operating at 10 Hz was used as a pulsed excitation source. A Neodymium (Nd) doped Yttrium Aluminum Garnet (YAG) crystal acts as the gain medium excited by flash-lamps within a resonator cavity. A Q-switch is used to control the nanosecond pulsed output of the laser with the optimum laser output achieved with a flash-lamp/Q-switch delay of 242 μ s. The fundamental output of the Nd:YAG is 1064 nm with 2nd, 3rd and 4th harmonic wavelengths of 532, 355 and 266 nm respectively generated using suitable optics. The energy of the 532 nm 2nd harmonic output was measured at 110 μ J for the current experiments.

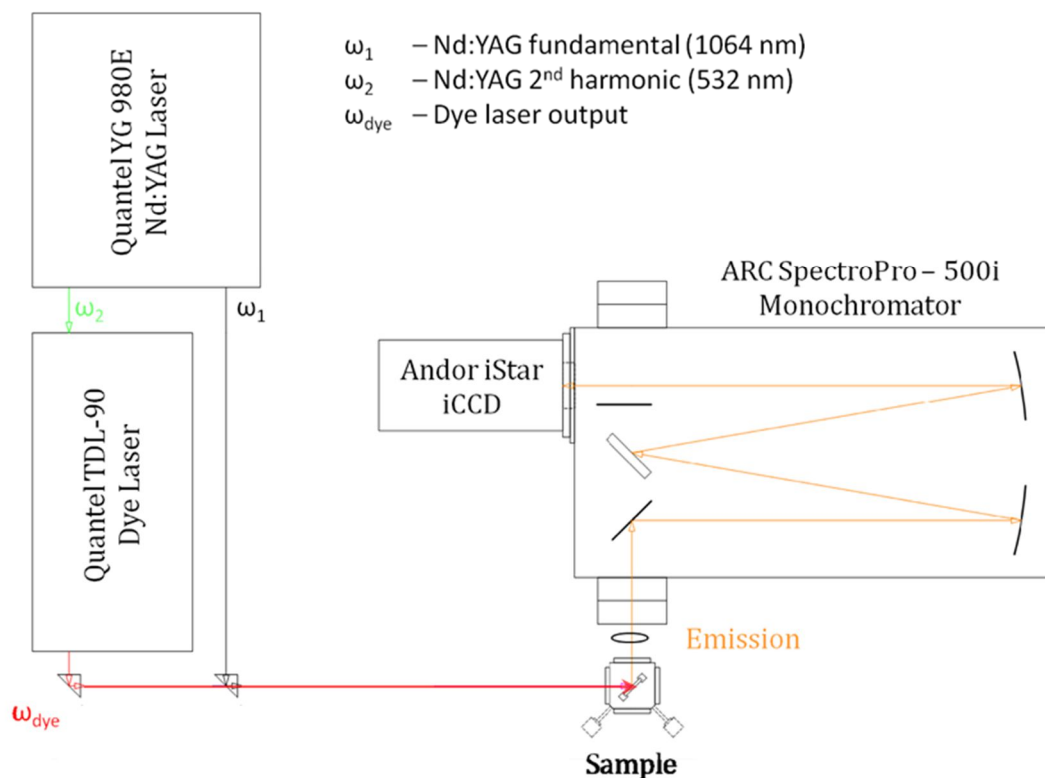


Figure II.11: Schematic of the Quantel YG 980E-10 Nd:YAG laser and the Quantel TDL-90 dye laser setup used for recording time-resolved spectra with the Andor iStar iCCD device.

Tunable visible laser light was produced using a Quantel TDL-90 dye laser²⁷ pumped by the 2nd harmonic (ω_2) of the Nd:YAG. Excitation of the dye is achieved through one of three stages with the TDL-90 dye laser; the oscillator, pre-amplifier and amplifier, with each stage yielding increasing laser intensity. Typically, the oscillator stage was used to study fluorescence spectroscopy and the pre-amplifier stage for investigating amplified emission in samples. The amplifier was only used in scenarios where amplified emission was difficult to achieve.

As laser dyes tend to have broad emission bands, the dye laser may be tuned using a diffraction grating to select a particular wavelength within the dye laser emission range. A mixture of 66% DCM²⁸ and 33% LDS 698²⁹ (both manufactured by Exciton) in ethanol was used for the visible excitation of GaPcCl, which has an absorption maximum in the 665 – 680 nm region. The output curve for this dye mixture is shown in Figure II.12 and is in the correct range for selectively exciting into the 0-0 band of GaPcCl isolated in various

matrix hosts, as well as some of the vibronic bands to the blue of the band origin. A table of the properties of this dye mixture as well as its components is shown in Table II.2.

Table II.2: Characteristics of the dye materials used for time resolved-spectroscopy experiments using the TDL Dye Laser.

Dye	Absorption Max (nm)	Fluorescence Max (nm)	Dye Laser Range (nm)
100 % DCM	472	639	615-666
100 % LDS 698	476	690	645-730
66% DCM, 33 % LDS 698	-	658	620-710

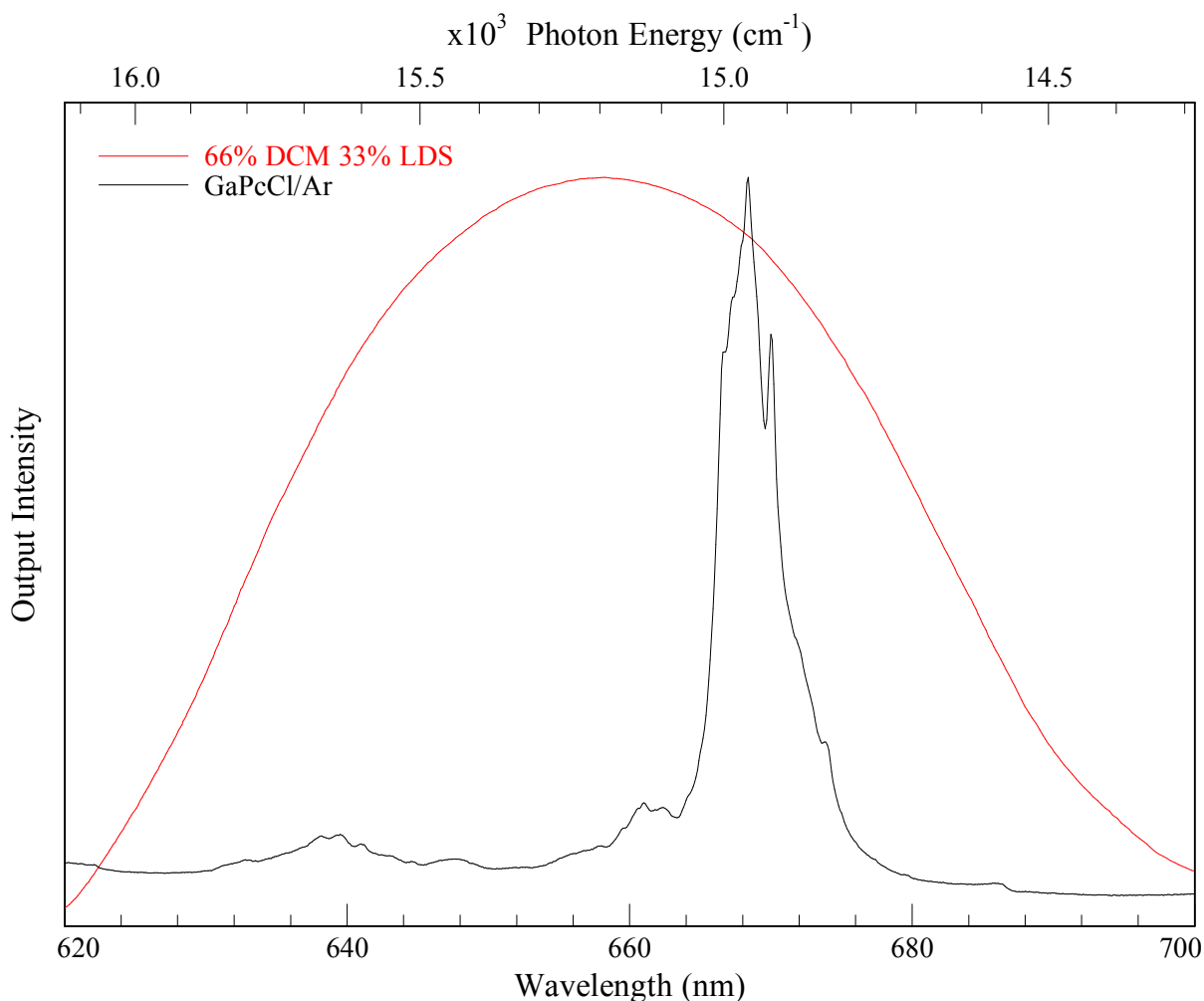


Figure II.12: Output of the 66% DCM 33% LDS 698 dye mixture in ethanol excited with the 532 nm output of the Nd:YAG laser. The broad output range allows for a wide range of experimental phenomena to be investigated without the need for changing the dye. The

absorption spectrum of GaPcCl/Ar is overlaid to demonstrate the good overlap between the dye output and the strongest matrix absorption bands of GaPcCl.

Time-resolved emission was monitored using the same ARC SpectraPro-500i monochromator used for the monitoring of steady-state emission described above. Time-resolved emission was also recorded at right angles to the incident light, with the exciting laser radiation entering through the window where the absorption PMT is located during steady-state spectroscopy (Figure II.10). The mirror directing the emitted radiation in to the emission PMT is removed, allowing the light to be directed onto an Andor Technologies iStar iCCD (Intensified Charged Coupled Device) camera³⁰. The iStar iCCD (Model DH 720-25F-03) comprises of a two-dimensional array of 256 rows x 1024 columns (262,144 pixels or 0.25 megapixels) photo-sensors on a silicon based semiconductor chip. Each pixel has an effective area of $26 \mu\text{m}^2$, giving the CCD an active area of 25 mm x 6.7 mm, made up from 960 x 256 pixels. The CCD was cooled to -12°C by a Peltier integral fan cooling system in order to reduce noise in recorded spectra. The operation of the iStar iCCD was controlled via a PC equipped with a CCI-101 control card and the Andor Solis software. This software was also used to control the ARC SpectraPro-500i monochromator via an RS232 cable.

The iCCD is a multichannel detector in which each column of pixels simultaneously detects a different wavelength of diffracted light, allowing it to act as a multiplexing detector. The resolution of the iCCD is determined by two things; the diffraction grating being used in the monochromator and the number of pixels in the device. The dispersal range and resolution obtained using the Andor iStar iCCD mounted to the SpectraPro-500i monochromator with the three different diffraction gratings are shown in Table II.3. The iCCD camera was mounted on the SpectraPro-500i and positioned so that the dispersed light and focal plane of the camera were aligned.

Table II.3: Diffraction gratings mounted on the ARC spectraPro-500i monochromator and their dispersal ranges. The resolution values quoted are the highest achievable when used in conjunction with the Andor iStar iCCD camera.

Diffraction Grating	Dispersal Range (nm)	Resolution (nm)
1200 g/mm; Blz 300 nm	40	0.04
600 g/mm; Blz 600 nm	80	0.08
300 g/mm; Blz 300 nm	320	0.32

A wavelength calibration was performed on the iCCD in order to have an accurate representation of the energy of light collected. An initial calibration was performed in two regions prior to the current work getting underway; a calibration in the UV spectral region using the Hg 1S_0 — 3P_1 emission line at 253.6521 nm, generated using a low pressure mercury arc pen lamp and in the visible region using the Na $^2S_{1/2}$ — $^2P_{3/2}$ and $^2S_{1/2}$ — $^2P_{1/2}$ emission lines at 588.995 and 589.5924 nm respectively, generated using a sodium hollow cathode lamp³¹. The monochromator was centred on one of the atomic emission lines (e.g. 588.995 nm using the Na hollow cathode lamp) and the pixels off-set so that the central wavelength displayed coincided with the spectral line. The camera was rotated so that each of the pixels along a column of the CCD detected the same wavelength and the lines observed were as narrow as the resolution of the grating and monochromator allowed. Because a ‘global’ calibration of the CCD was not possible, and the two lamps used for the initial calibration were not in the region of interest, a custom calibration was performed in the 680 – 760 nm range using the Ar I emission lines from the sodium lamp described earlier. The Ar lines on each region were identified based on their rough position and relative intensity from Table II.4 and assigned a pixel number. The exact wavelengths of the Ar lines from the NIST database^{32,33} were then assigned to each line in the spectrum and a cubic polynomial function was fitted to the data, which amended each pixel to the correct wavelength value (to within 0.1 nm) for a given wavelength centre. The procedure was performed in 5 nm intervals to ensure the entire spectroscopic region of interest was calibrated correctly. A spectrum of an ‘raw’ and a corrected spectrum of the Ar lines is shown in Figure II.13, and the positions of the uncalibrated and calibrated data are compared to the exact wavelength values in Table II.4.

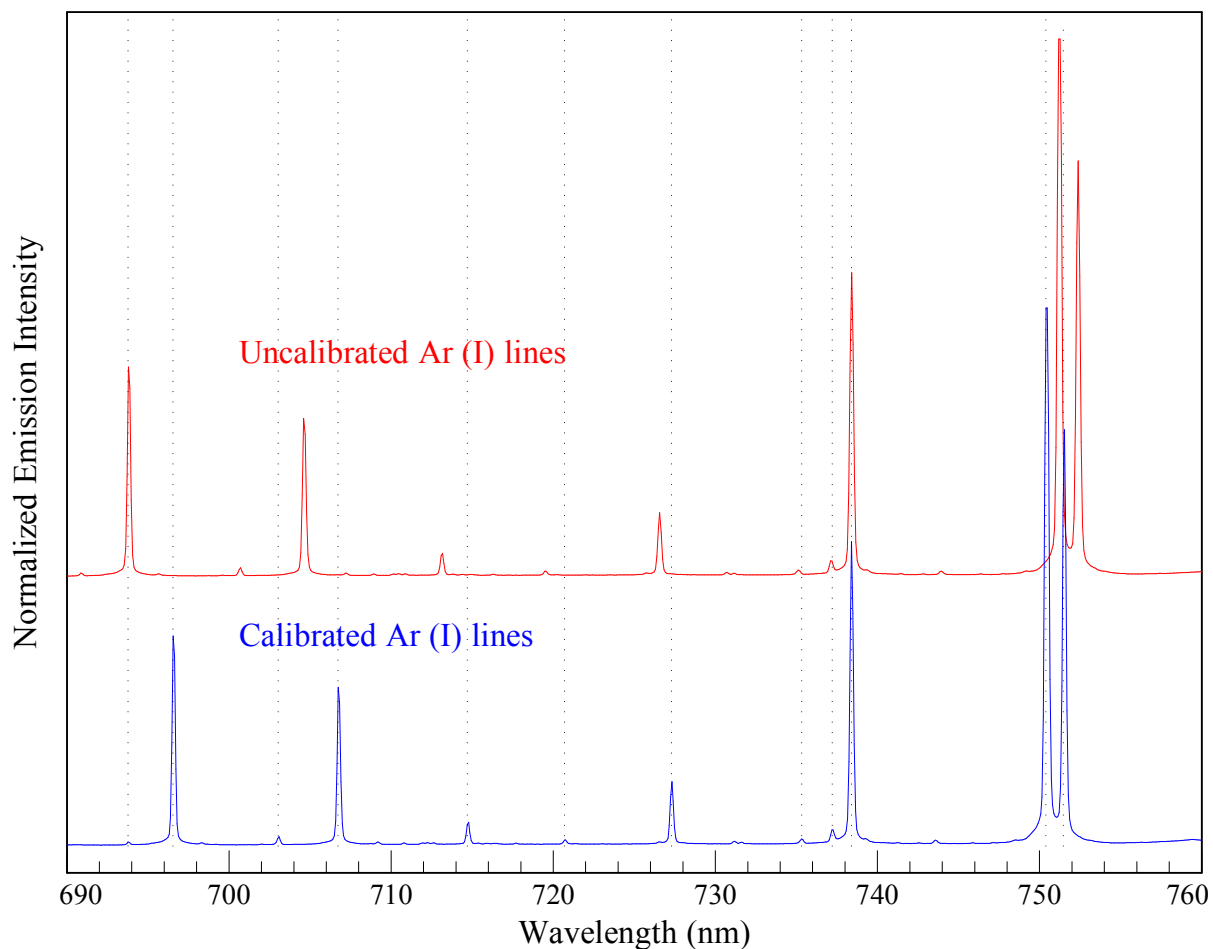


Figure II.13: A spectrum of the Ar (I) emission lines (red trace) recorded with the uncalibrated iCCD after the initial calibrations in the UV and visible regions using the Hg and Na emission lines respectively. The spectrum shown by the blue trace was recorded after measuring the Ar lines and performing a cubic calibration over the entire region shown (a wide range is shown with the 600 grooves/mm grating). The calibrated Ar (I) lines are accurate to greater than 0.1 nm of the values reported in the NIST database, shown by the dotted lines.

Table II.4: Wavelengths (in nm) and relative intensities of the persistent Ar I lines obtained from the NIST database used to calibrate the Andor iCCD camera in the 680 – 760 nm region. The measurements of the uncalibrated and calibrated iCCD device are shown for comparison. The difference between the calibrated iCCD values and the true gas phase values are also shown.

Ar emission wavelength (nm)	iCCD Uncalibrated	iCCD Calibrated	Difference
667.72821	664.42	667.73	0.00179
675.28339	672.38	675.27	-0.01339
687.12891	684.93	687.12	-0.00891
693.76642	692.02	693.8	0.03358
696.54309	694.97	696.56	0.01691
703.02509	701.8	702.98	-0.04509
706.72180	705.78	706.72	-0.00180
714.70422	714.34	714.74	0.03578
720.69800	720.65	720.66	-0.03800
727.29358	727.73	727.3	0.00642
735.32928	734.99	735.39	0.06072
737.21179	738.27	737.17	-0.04179
738.39801	739.56	738.39	-0.00801
750.38690	751.27	750.48	0.09310
751.46521	752.39	751.54	0.07479

A schematic of the image intensifier used to amplify the signal detected by the CCD is shown in Figure II.14. When a photon enters the iCCD through the input window it hits a photocathode, which produces an electron. The electron is directed towards a micro channel plate (MCP) by an electric field. When it hits the MCP it sends a flow of electrons down the honeycomb channels of the MCP which in turn produce secondary electrons. This causes 10,000 fold amplification of the electron produced by the initial photon. The shower of electrons from the MCP is accelerated by a potential difference and directed towards the P43 phosphor coating on the fibre-optic window of the intensifier. The phosphor coating emits photons which hit the photosensitive pixels on the iCCD, detecting them as a change in charge proportional to the intensity. A spectrum is then generated by adding the charge from each column of pixels together by a series of horizontal transparent electrodes and is removed from the CCD by an efficient charge transport (or charge coupling) process known as ‘vertical binning’³⁴. Finally, the electrode signal is transferred to an on-chip amplifier and then an analogue/digital (A/D) converter on a CCI-010 control card. Recorded spectra were viewed using the Andor SOLIS software.

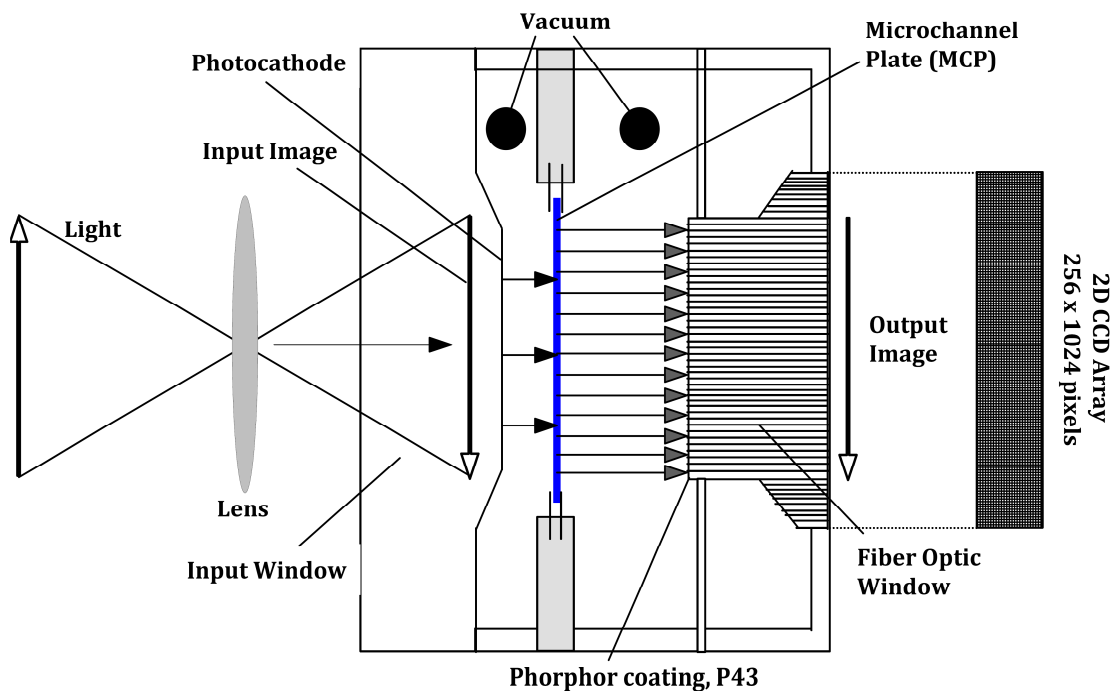


Figure II.14: Cross section of the Andor iStar iCCD camera showing the main components used in its operation.

Laser excitation combined with iCCD detection is capable of achieving much better resolution than what is possible with steady-state spectroscopy. This is because of the high sensitivity of the CCD detector, and due to the monochromatic light of the laser, it is possible to excite into a single site of isolation and observe very narrow fluorescence bands. Lamp excitations are limited by the resolution of the monochromator and tend to excite into a broader range of sites. A comparison of a CCD scan with laser excitation and a PMT scan with lamp excitation are shown in Figure II.15. While the lamp scan is adequate at observing the main fluorescence bands, the resolution is too low to observe the site structure present in emission.

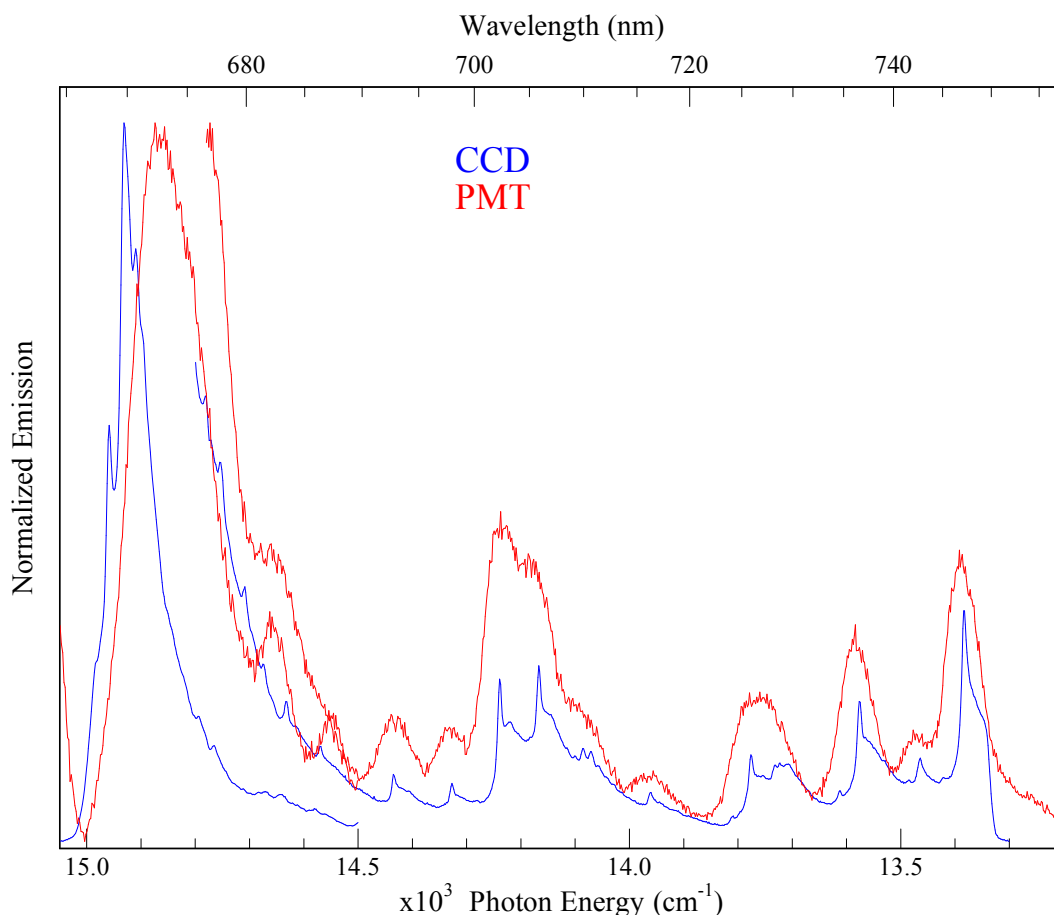


Figure II.15: Comparison of an emission spectrum of GaPcCl/Ar recorded with the iCCD (blue trace) and the PMT (red trace). The region between 15,000 – 14,500 cm^{-1} was recorded with an excitation wavelength of 659 nm and the region between 14,800 – 13,300 cm^{-1} with an excitation wavelength of 670 nm.

Time-resolved emission spectra were used to determine the emission lifetimes of excited species in the matrix. It was possible to record time-resolved and time-gated emission spectra with the iCCD by synchronising the timing of the laser pulse and controlling the temporal gate width of the iCCD camera. The iCCD and laser were synchronised by triggering the camera with the TTL output from the Q-switch pre-pulse of the YG 980 Nd:YAG laser. A digital delay generator (DDG) on the iCCD software was used to achieve the time gating on the iCCD and controlled when the photocathode was to be switched on or off. By varying the delay between the TTL pulse and activation of the photocathode and/or varying the time duration (gate width) when the photocathode is switched on, time-gated emission spectra were recorded using the iCCD. Time-resolved emission spectra were obtained by recording a series of time-gated spectra, setting a suitably short gate width (5 ns) and stepping in time. The time-resolved emission spectrum (TRES), shown in

Figure II.16, is built from individual time-gated emission spectra recorded in known temporal slices. Emission lifetimes were determined by analysis of the time-resolved emission. The temporal profile of an emission feature was found by taking a ‘kinetic slice’ through a time-resolved spectrum, extracting a plot of the emission intensities at a particular wavelength against time. Decay times were determined by fitting single exponential functions, modelling the rise and decay function of the temporal profile. The fits were convoluted with the temporal profile of the pulsed laser to extract the excited state decay times, which were typically accurate to ± 0.1 ns.

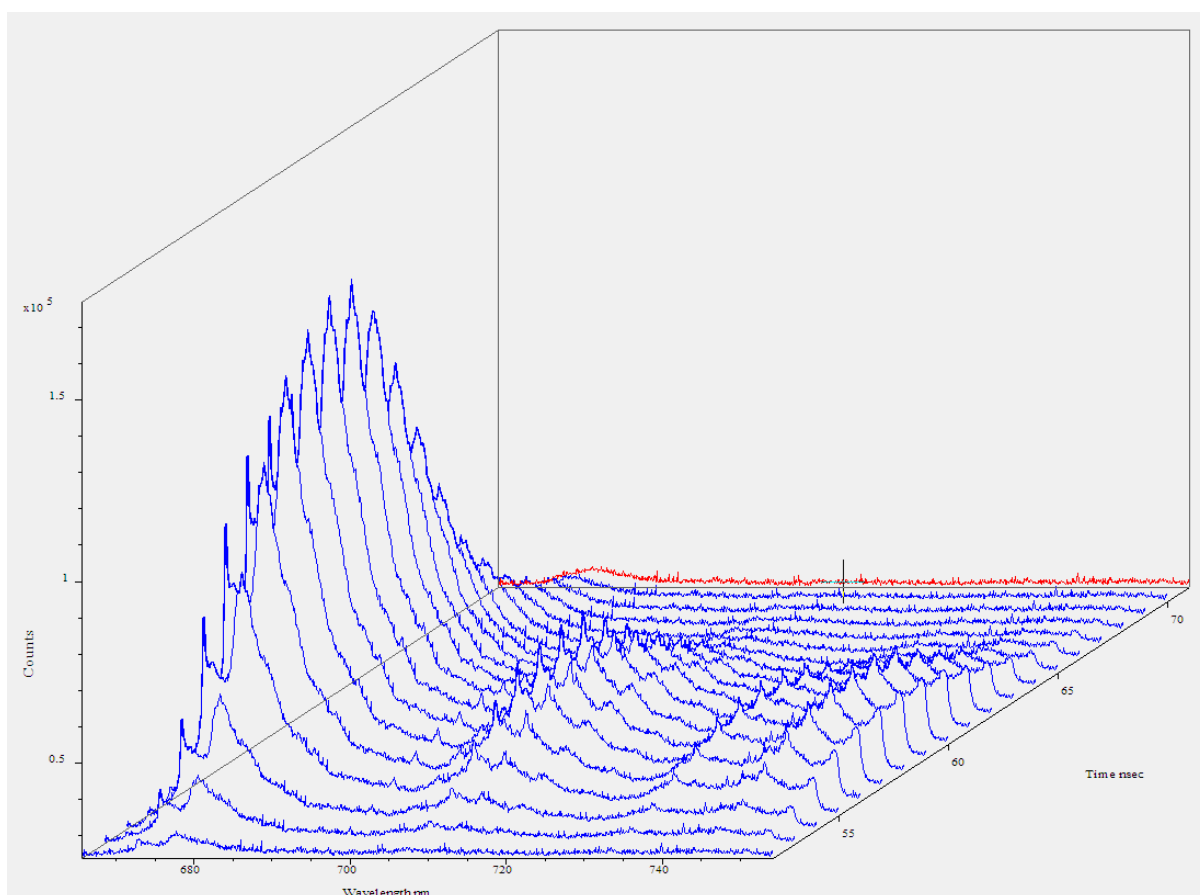


Figure II.16: Example of a time-resolved emission spectrum of GaPcCl/Ar recorded with the Andor iStar iCCD detector. A ‘kinetic slice’ taken through one of the emission bands can be used to determine the emission lifetime of the excited state species.

2D excitation-emission spectra were generated using the same method described above, without the delay between the TDL pulse and activation of the photocathode, and a longer gate width (100 ns) was used. Instead of having a constant wavelength output from the dye laser, it was scanned over a range of wavelengths at a constant rate (0.002 nm/s) using the

TDL90 software. This then allowed each scan number on from the 2D excitation-emission plot to be correlated back to its excitation wavelength. Every scan in this 2D spectrum now corresponds to an emission spectrum recorded with a unique excitation wavelength and can be extracted from the 2D plot. An example of this is shown by the red line and the top spectrum in Figure II.17. Taking a 'kinetic slice' through the spectrum will now generate an excitation spectrum instead of a temporal profile. An excitation spectrum is shown in Figure II.17 which was generated by extracting a kinetic slice through the emission band indicated by the green line.

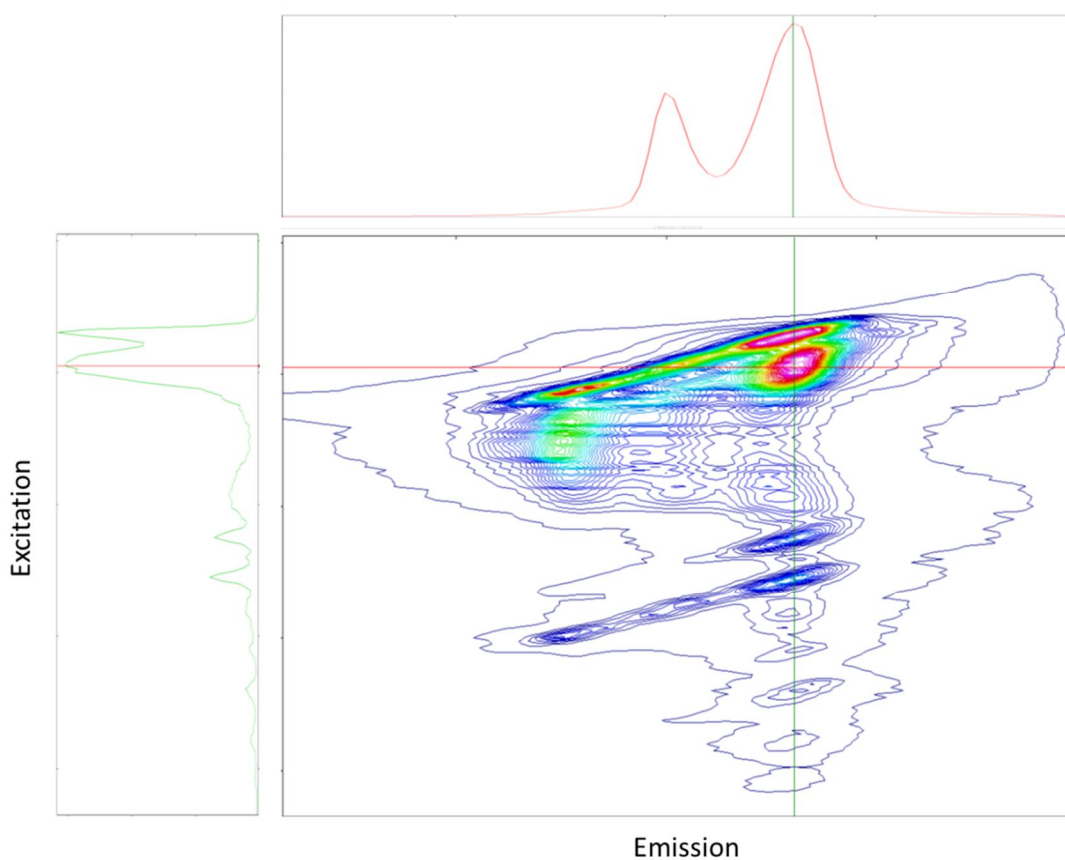


Figure II.17: Example of a 2D Excitation-Emission plot recorded with the CCD by scanning the dye laser. Emission is shown on the x-axis and excitation on the y-axis. Intensity is plotted as a contour map. The red line shows a slice through the emission direction, the spectrum corresponding to which is shown on the top panel. The green line shows a slice through the excitation direction, with the corresponding spectrum on the side panel.

II.8: Raman Spectroscopy

Raman spectroscopy was performed at the Focas institute in the Dublin Institute of Technology using a HORIBA Jobin YVON LabRAM HR 800 Dual Microscope spectrometer fitted with Andor EMCCD and Synapse CCD detectors. Excitation was achieved with continuous wave (CW) laser light with an output of 532 nm or 660 nm. The 532nm laser is an M-PC 3000 DPSS (Diode Pumped Solid State) laser and the 660nm is a SMD (Surface Mounted Diode) 6000 laser, both of which are manufactured by Laser Quantum, out of Stockport, UK. Accumulation times were set to 10-30 seconds and several accumulations were performed to reduce the noise contribution. Numerous spots were examined on the surface of the KBr disc to ensure an even dispersion of material throughout the sample. Raman bands were recorded up to energies of 1700 cm^{-1} .

Due to the strong absorption of the phthalocyanines in the red region of the visible spectrum, Raman spectra recorded with the 660 nm laser line contained a strong fluorescence background. This was 'corrected' by fitting a Gaussian curve to the fluorescence band and subtracting it from the spectrum. An example of this correction is shown in Figure II.18, where the red trace shows the Raman spectrum containing the broad fluorescence band and the blue trace shows the spectrum after subtracting the fluorescence band out. Fluorescence was not a problem with the 532 nm line, where the phthalocyanines tend to have little or no absorption.

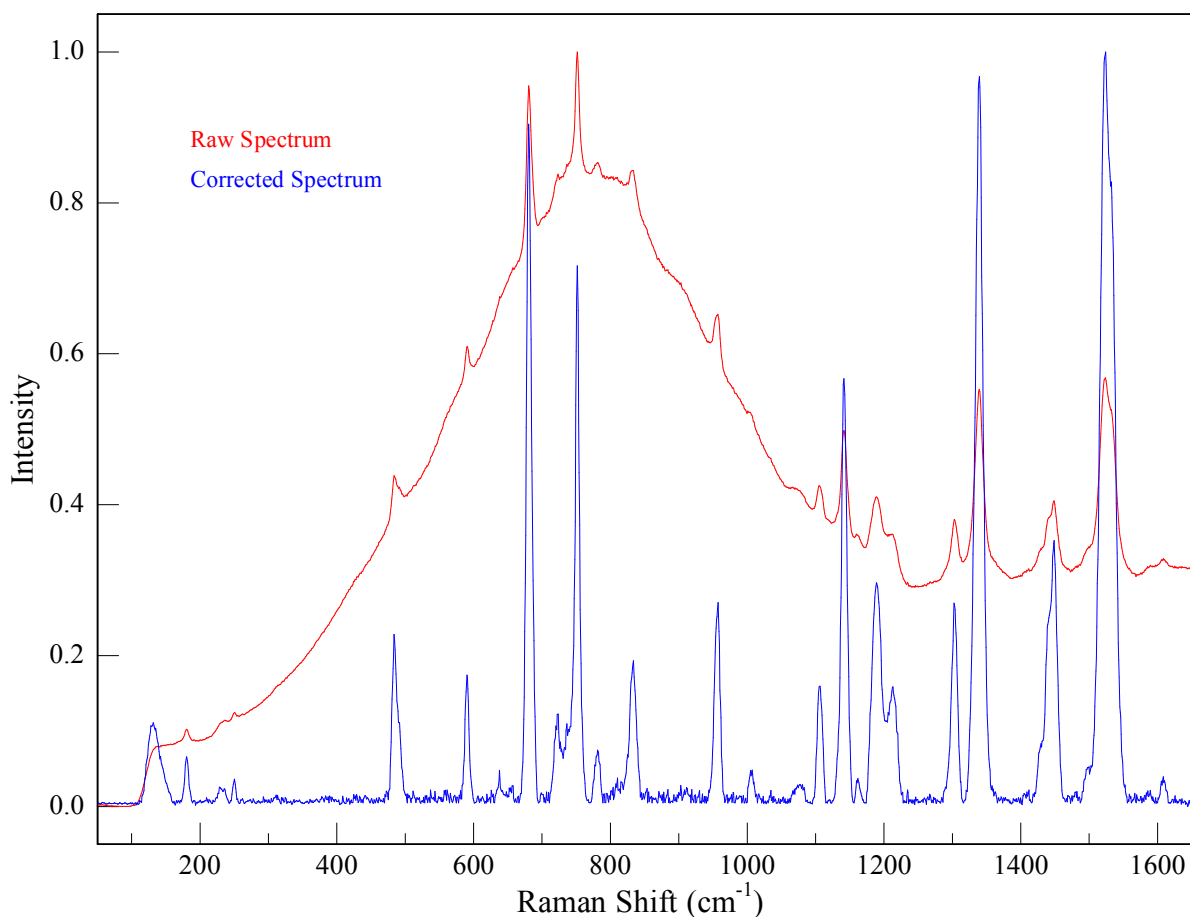


Figure II.18: A raw Raman spectrum (red trace) showing a strong fluorescence background. The excitation wavelength of the laser was 660 nm. A corrected Raman spectrum (blue trace) was generated by fitting a Gaussian curve to the fluorescence background.

A calibration issue is known to exist on the Raman spectrometer following experiments conducted 12 months apart. Because the calibration is performed with a single laser line, a degree of uncertainty is introduced if the CCD is not correctly calibrated in the first place. The calibration problem affects the high frequency modes of the Raman spectra recorded for AlPcCl and GaPcCl.

II.9: Density Functional Theory

Throughout this work quantum mechanical (QM) calculations were employed extensively both to complement experiments and as a standalone method for investigating phenomena which could not be deduced experimentally. All QM calculations were implemented using

the Gaussian-03³⁵ suite of programs running on a Linux workstation with two AMD “Barcelona” 64-bit quad core processors running at 2.0 GHz and with 16 GB RAM. Density functional theory (DFT) was the preferred method in the current work as it is well known to describe the ground state of molecules to a high degree of accuracy. The B3LYP functional and 6-311++g(2d,2p) basis set were used for most of the work, unless otherwise stated. Some of the fundamental aspects of DFT have been described in Chapter I. The following section outlines the array of different calculations performed as part of the current work, as well as some of the theory behind how they are implemented by the Gaussian-03 program.

II.9.I: Geometry Optimizations

A geometry optimization was performed as the first step in each theoretical investigation. Not only does an optimization yield accurate structural information about the molecule being studied, it acts as a precursor for all of the other steps performed thereafter. The geometry optimisation attempts to find an equilibrium structure by locating a minimum on the potential energy surface (PES) of the molecules atomic coordinates. A minimum is found by calculating the first derivative of the energy with respect to the atomic coordinates, known as the gradient. A stationary point is found when the gradient is equal to zero and the forces are also equal to zero. A stationary point may not necessarily be the global minimum but may be a local minimum or saddle point on the PES. The energy and gradient are calculated at each point and are used to determine how far and in what direction to move the atoms in order to find a minimum. An initial guess for the second derivative matrix (Hessian matrix) is computed from the connectivity derived from the atomic radii and a simple valence force field³⁶. The Hessian matrix determines the curvature of the PES at a point and is used to help determine the next step to be taken. The optimization is said to have converged when the absolute minimum on the PES has been found. Gaussian 03 incorporates the Berny algorithm³⁷ using GEDIIS³⁸ into geometry optimizations, which has four convergence criteria to be satisfied; the maximum force and root-mean-square of the forces must be close to zero and the maximum displacement and root-mean-square of the displacements for the next step must be small. The cut off threshold points for the convergence criteria are set by the user for each optimisation. Tight convergence criteria were used throughout this work with the max and RMS energy thresholds of 1.5×10^{-5} and 1.0×10^{-5} a.u. respectively while the max and RMS displacement thresholds were of 6.0×10^{-5} and 4.0×10^{-5} a.u. respectively.

Optimizations were performed by reading in the initial molecular geometry as a set of Cartesian coordinates and the connectivity to denote how the atoms are bonded to one another. In special cases such as the highly symmetric phthalocyanines the point group of the molecule can be assigned and set which radically reduces computational time as the calculation will be constrained to work within that framework. For example, MgTAP belongs to the highly symmetric D_{4h} point group. Each of the four pyrrole sub-units must all have the exact same geometric properties and all must be equidistant from the Mg moiety in order for the D_{4h} symmetry to be maintained. Therefore, instead of needing to minimize the energy for each bond length and angle (dihedrals will all be zero in a planar molecule) individually, DFT needs only to calculate the parameters for the symmetry unique atoms. This significantly reduces the computational cost and speed of performing calculations of fairly large systems like phthalocyanine.

An array of basis sets is stored internally in the Gaussian program, but these do not always suffice for the system being studied. The 6-311g basis set does not sufficiently describe the orbitals on atoms with an atomic number higher than 36 (Kr). Instead, a custom basis set must be placed onto these heavier atoms at the users' request. The custom basis sets used throughout this work were all supplied by the Basis Set Exchange³⁹. A mixture of basis sets was used on systems combining both light and heavy atoms; 6-311++g(2d,2p) on the lighter atoms, and def2-TZVPP^{40,41} on the heavier atoms. Calculations involving atoms heavier than Kr also tended to have convergence problems, so 'very tight' convergence criteria were applied to these optimizations as well as specifying an ultrafine grid.

II.9.II: Vibrational Analysis

A vibrational analysis was performed immediately after a geometry optimization to validate the result. Vibrational frequencies are computed by determining the second derivatives of the energy with respect to the Cartesian nuclear coordinates and then transforming into mass weighted coordinates. This transformation is only valid at a stationary point (i.e. the energy minimum) so it is important to use the same level of theory in both the optimization and frequency calculations. A frequency job performed on the true ground state structure will yield no imaginary frequencies upon completion. A single imaginary frequency points to a transition state structure, while more than one imaginary frequency indicates an unstable structure.

Frequency calculations are performed within the harmonic approximation and therefore tend to overestimate the energy of even the fundamental vibrational modes. The harmonic oscillator method approximates the movement of nuclei during a vibration as a simple oscillation around an equilibrium distance with equal restoring forces upon compression and stretching but in reality, their vibrations have an anharmonic motion where the restoring forces are different for compression and stretching and whose potential is better described using the Morse potential as shown in Figure II.19. As the value of a vibrational level, n , gets larger, the discrepancy between the values of the vibrational mode, ν_n , calculated within the harmonic and anharmonic approximations increases.

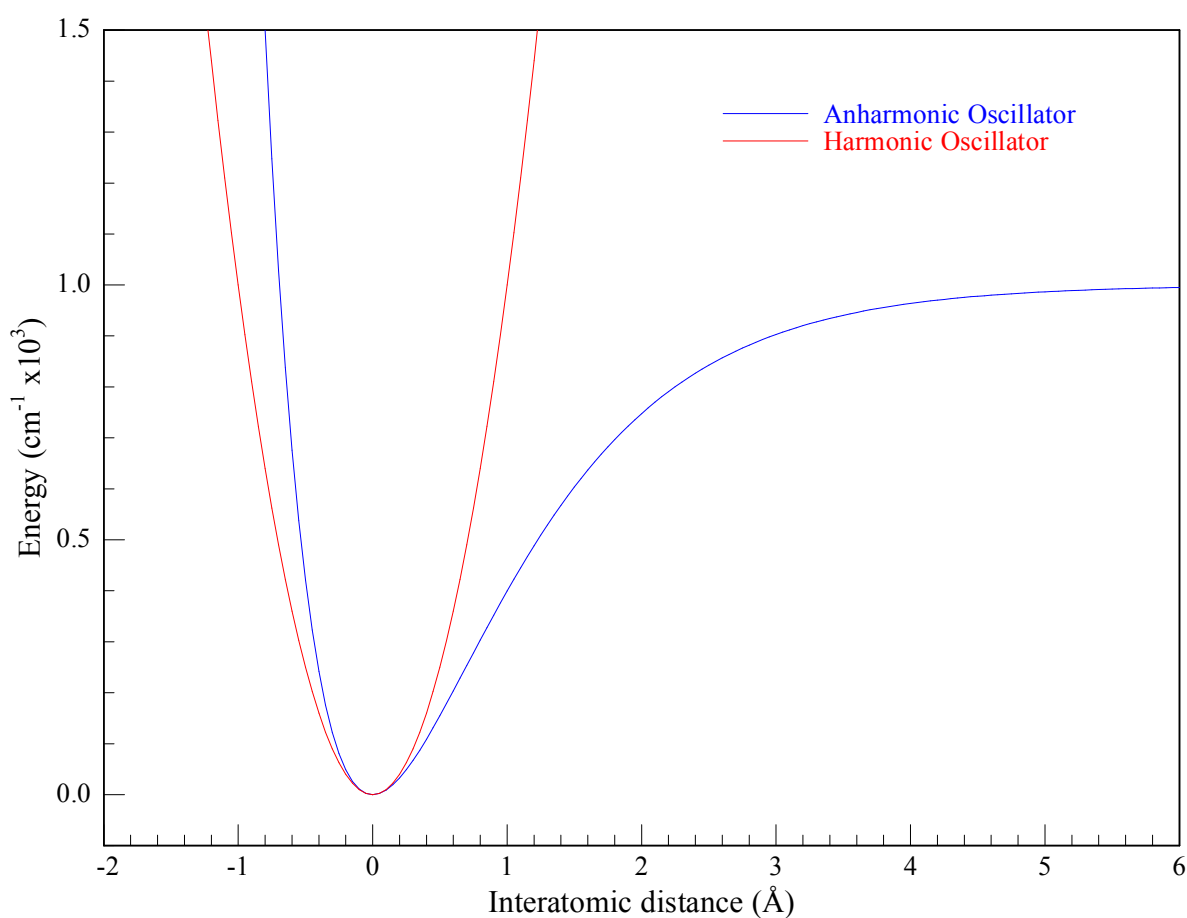


Figure II.19: Plot showing the shape of a harmonic and an anharmonic oscillator. The different shape of the curves also has an effect on the vibrational energy of the fundamental modes of a molecule.

For comparison with experimental results a scaling factor was applied to the predicted harmonic frequencies. Two such scale factors were applied; 0.98 for frequencies below 2000 cm⁻¹ and 0.95 for frequencies above 2000 cm⁻¹. While it is possible to implement an

anharmonic correction with Gaussian-03, it is a computationally expensive task and yields only a modest improvement on scaled harmonic frequencies.

The infrared intensity of an infrared mode i is determined from the integrated absorption coefficient and using the harmonic oscillator approximation, may be given by

$$I_i^{IR} = \frac{N\pi d_i}{3c^2} \left| \frac{d\mu}{dQ_i} \right|^2 \quad \text{Eq. II.5}$$

where N is the total number of molecules per unit volume expressed as Avogadro's number (mol^{-1}), d_i is the degeneracy of normal mode i and c is the speed of light. The absolute infrared intensity $|d\mu/dQ_i|^2$ is the square of the derivative of the electric dipole moment μ with respect to the mass weighted normal coordinates, Q_i . The absolute infrared intensity is the only molecular parameter used in determining the IR intensity and may be given in the non-SI units of $(\text{D}/\text{\AA})^2\text{amu}^{-1}$. However, it is usually converted to the SI derived units for absorption intensity of km mol^{-1} (where $1 (\text{D}/\text{\AA})^2\text{amu}^{-1} = 42.2561 \text{ km mol}^{-1}$), which are commonly used when comparing experimental results.

Raman activities are not calculated by default in Gaussian 03, and must be specified in the input section with the keyword 'freq=Raman'. Raman activities are produced by numerical differentiation of the dipole derivatives with respect to the electric field. Raman intensities can be calculated from the computed Raman activities by applying the following equation⁴²:

$$I_i^{Ram} = \frac{C(\nu_0 - \nu_i)^4 S_i}{B_i \nu_i} \quad \text{Eq II.6}$$

Where C is a constant, ν_0 and ν_i denotes the frequency of the incident light and a normal mode i , S_i is the Raman scattering computed from DFT and B_i is the Boltzmann distribution of the normal modes.

II.9.III: Isotopic Substitutions and Internal Modes

When a frequency job has been completed it is relatively easy to compute the frequencies of a range of different isotopes as the electronic properties of the molecule are unaffected by changing the mass of an atom. This means the same optimized geometry will hold true for any given isotope substituted into the molecule. A simple mass dependence on the vibrational frequency of a normal mode, ν , does exist however, and is given by the expression:

$$\nu = \frac{1}{2\pi} \sqrt{\frac{k}{m}} \quad \text{Eq. II.7}$$

in which k is the force constant and m is the mass of the isotope. It is evident from Equation II.7 that increasing the mass of an atom will reduce the vibrational frequency of the normal modes associated with that atom whereas decreasing its mass will have the opposite effect.

The internal modes can also be determined easily once the vibrational analysis has successfully completed. The 'freq=internal' command must be included in the input section in order for the internal modes to be printed out at the end of a job. An internal mode will show which bond lengths, angles and dihedrals move for a given normal mode. The percentage contribution of each parameter associated with the vibration is also given.

II.9.IV: Time Dependent DFT

Time dependent DFT calculations were used to study the excited molecular states. The ground state geometry is always used as the starting point for a TD-DFT calculation. By default Gaussian 03 will compute the first 10 singlet excited states, although triplet states can also be calculated. Due to the degeneracy of many of the orbitals and the presence of forbidden states it was often the case that 10 excited states was too small to obtain all of the relevant data. In general the first 50 singlet excited states were calculated in order to obtain information about the Q and the B transitions for the phthalocyanines. The significant results outputted by a TD-DFT calculation include the transition energy between the ground and excited states, the oscillator strengths and the molecular orbitals involved in each transition. The linewidths of the calculated spectra could be altered depending on the system being compared to, and was typically chosen as 80 cm^{-1} for comparison with experimental matrix spectra.

II.10: The W_p Function – Lineshape Analysis

A W_p line fitting analysis was applied to the high resolution emission and excitation bands recorded for GaPcCl at cryogenic temperatures in order to gain an insight into the true band structure of the electronic transition in inert matrices. The W_p function is an analytic expression capable of describing the line shapes of narrow optical bands, especially those exhibiting zero phonon lines (ZPL). Narrow peaks such as the ZPL are often evident in spectra recorded in inert gas solids⁴³, due to weak interactions between the host and guest

species and the low temperatures used in the matrix technique. The W_p function pertains to the so-called single configurational-coordinate (SCC) model, which predicts the Franck-Condon factors (intensity distribution) for phonons (p) with a single frequency, $\hbar\omega$, coupling to the electronic transition with a strength S .

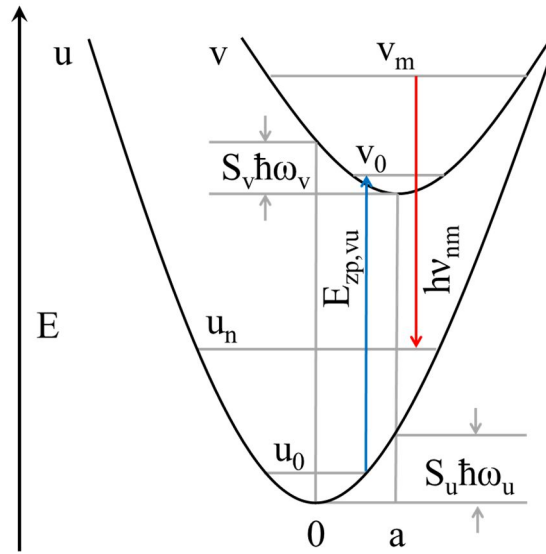


Figure II.20: A generalized schematic of the single-configurational-coordinate (SCC) model. In the current lineshape analysis a single frequency has been used, $\hbar\omega$ ($\hbar\omega_u = \hbar\omega_v$).

A schematic of the SCC model for a luminescence centre is shown in Figure II.20. The diagram presents the ground and excited electronic state potentials as two displaced parabolas, labelled u and v respectively. The ground state minimum is located at $x = 0$ and the excited state minimum is at $x = a$. The values $S_u \hbar\omega_u$ and $S_v \hbar\omega_v$ give the energy difference between the two parabolas at their minima, 0 and a respectively in units of the phonon energies. A reasonable estimate of the energy difference between the two electronic states is given by the zero-phonon energy, $h\nu_{zp,uv} \equiv E_{zp, vu}$. The broadness of the resulting optical band is determined by the displacement of the two parabolas. For a close to zero, i.e. small displacement, the optical bands will be narrow. For larger values of a , i.e. greater displacements of the two parabolas, broader optical bands will occur.

In the limiting situation of equal force constants occurring in the ground and excited states, a single coupling frequency, $\hbar\omega$, exists as well as a single coupling strength S . In this

situation an analytic expression, first derived by Huang and Rhys⁴⁴ and generally called the W_p function, provides the intensity distribution of the phonon lines. This function has been described in detail by Struck and Fonger⁴⁵, and takes the following form:

$$W_p = \exp(-S \langle 2m + 1 \rangle) \sum_{j=\max(0,-p)}^{\infty} \frac{(S \langle m \rangle)^j (S \langle 1+m \rangle)^{p+j}}{j!(p+j)!} \quad \text{Eq. II.8}$$

where p is the phonon number, S is the electron-phonon coupling strength and j is the range of the sum, determined by the coupling strength and the temperature. In this equation $\langle m \rangle$ is Planck's measure of temperature, given by:

$$\langle m \rangle = 1 / (\exp\left(-\frac{\hbar\omega}{kT}\right) - 1) \quad \text{Eq. II.9}$$

Equation II.8 can be simplified by incorporating a Bessel function, giving it the form:

$$W_p = \exp\left(-S \frac{1+r}{1-r}\right) r^{-p/2} I_p\left(2S \frac{r^{1/2}}{1-r}\right) \quad \text{Eq. II.10}$$

In this expression $I_p(x)$ is a modified Bessel function of variable order p . The summation form of the modified Bessel function⁴⁶ used in the current calculations is given by the expression:

$$I_\alpha(x) = \sum_{m=0}^{\infty} \frac{1}{m!(m+\alpha+1)} \left(\frac{x}{2}\right)^{2m+\alpha} \quad \text{Eq. II.11}$$

The variable r is the Boltzmann factor, and is given by:

$$r = \exp(-\hbar\omega/kT) \quad \text{Eq. II.12}$$

which is related to Planck's measure of temperature, $\langle m \rangle$, by:

$$\langle m \rangle = \frac{r}{1-r} \quad \text{Eq. II.13}$$

The sum rather than the Bessel form of the W_p function is used in the current work in order to maintain numerical accuracy in the weak electron-phonon characteristics of the recorded emission/excitation spectra. It is given by:

$$W_p = \exp\left(-S \frac{1+r}{1-r}\right) \left(\frac{\theta}{2}\right)^p \sum_{j=0}^{\theta_m} \left(\frac{\theta^2}{4}\right)^j / [j! \Gamma(p+j+1)] \quad \text{Eq. II.14}$$

The sum is truncated at θ_m , the next integer greater than $\theta + 1$, where at a given temperature, T , of fixed argument $\theta_m = 2Sr^{\frac{1}{2}}/(1 - r)$. The extent of the sum increases with the electron-phonon coupling strength S and the temperature. The Gamma function, $\Gamma(p + j + 1)$, is such that $\Gamma(n) = (n - 1)!$ for all positive integer values of n . Hot bands, $-p$, corresponding to phonon annihilation (instead of phonon generation) are not given by Equation II.14. They are calculated separately with the following equation:

$$W_{-p} = \exp\left(-p \frac{\hbar\omega}{kT}\right) W_p \quad \text{Eq. II.15}$$

in which p is the phonon number and W_p is of the form shown by Equation II.14. All W_p plots shown in the current work were generated with Equation II.14, with the hot bands calculated with Equation II.15. The code used to generate the W_p function in Genplot is given in the Appendix at the end of this Chapter. The results obtained with Equation II.14 are shown in Figure II.21, and when compared with those obtained from Equation II.8 were found to agree identically.

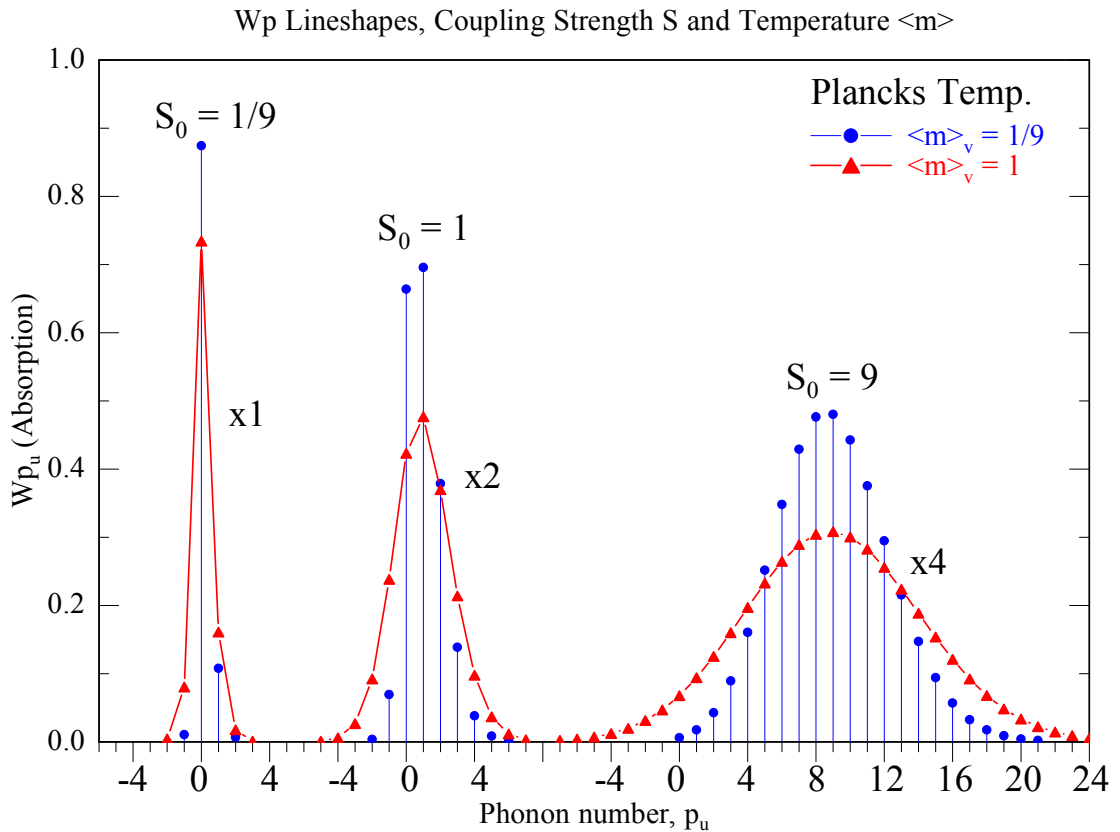


Figure II.21: Plots of the optical band shapes calculated with the W_p function incorporating different values for the coupling strength, S , and temperature, $\langle m \rangle$. Note

that the intensities of the $S_0=1$ and $S_0=9$ lines have been multiplied by 2 and 4 respectively to aid comparison.

The shapes of the optical bands predicted by the W_p function are plotted in Figure II.21 for a variety of different conditions, namely three electron-phonon (e-p) coupling strengths, S_0 , and two temperatures, $\langle m \rangle$. With weak e-p coupling, when S is small (calculated for $S_0 = 1/9$) the lineshape is extremely narrow at low temperatures as depicted by the blue stick spectrum shown in the left hand region of Figure II.21. The lineshape consists of a dominant zero phonon line (located at $p_u=0$) with only very weak phonon-side bands (PSB) present. The intensities of the PSBs decrease rapidly with increasing phonon number. At higher temperatures, shown by the red curve, it is evident that the first hot band ($p_u = -1$) gains appreciable intensity. For medium S values ($S_0 = 1$) shown in the middle section, a pronounced asymmetry is evident on the low temperature band, with the ZPL and first PSB having the greatest intensities. At higher temperatures the curves become more Gaussian like. With strong electron-phonon coupling (calculated with a value of $S_0 = 9$ in the W_p function), the lineshape shown by the right hand region of Figure II.21 closely resembles a Gaussian distribution, even at the lower temperature. By definition, the ZPL is always located at $p_u = 0$. It is evident from Figure II.21 that changing the coupling strength has a pronounced effect on the intensity of the ZPL, being dominant when $S_0 = 1/9$ and barely identifiable when $S_0 = 9$.

The W_p fit allows the position of the ZPL of a given species/site to be identified as well as the strength of the electron-phonon couplings. This is achieved by determining the phonon frequency, $\hbar\omega$, which is the energy difference between the maximum of the ZPL and that of the first phonon side band (PSB). The highly resolved excitation and emission spectra recorded for matrix-isolated GaPcCl exhibit a well-defined ZPL and PSB, allowing for an accurate value of $\hbar\omega$ to be extracted. The temperature at which the spectrum is recorded is an experimental parameter. The appropriate value for S is obtained by adjusting its value such that the W_p function correctly matches the relative intensities of the ZPL and PSB. When convoluted with a spectral bandwidth and plotted against experimental spectra, it allows for the identification of several features in the spectrum such as additional PSBs and hot bands, as shown in Figure II.22.

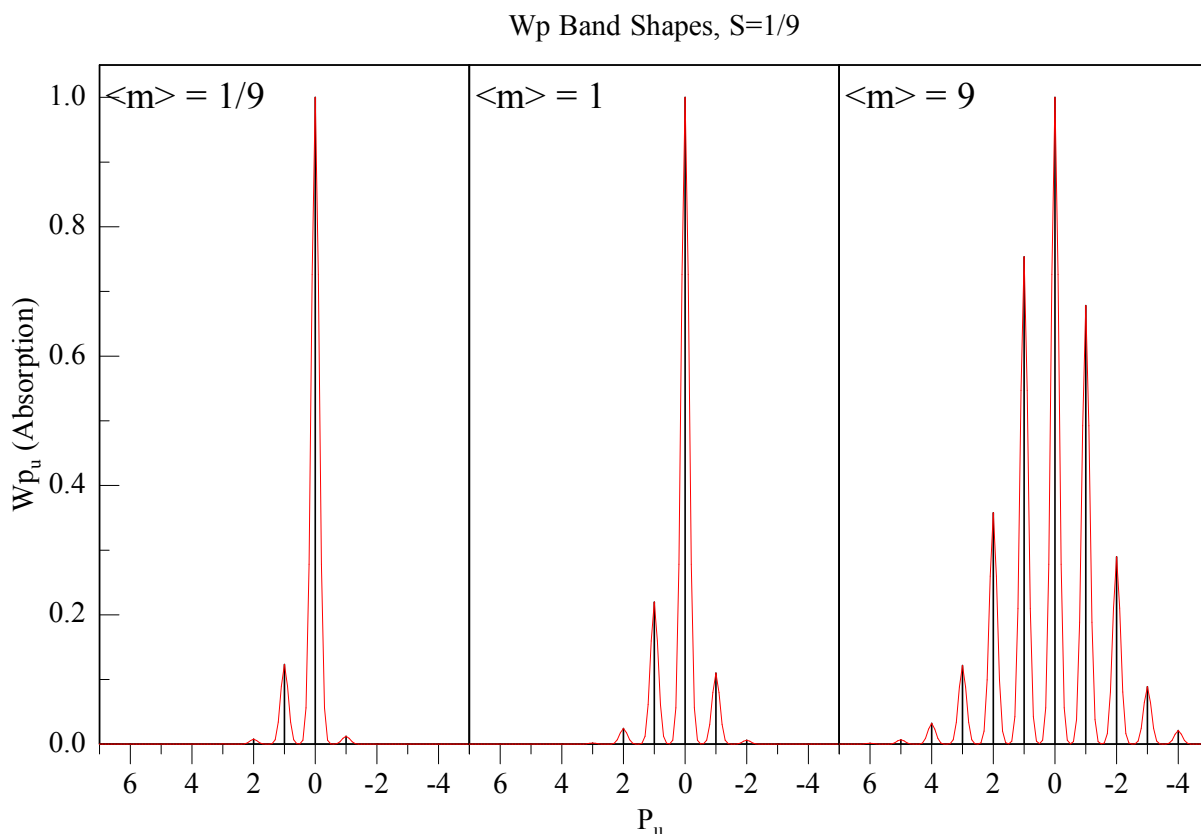


Figure II.22: Band shapes of the W_p function plotted at various temperatures with an S value of $1/9$, a $\hbar\omega$ of 1 cm^{-1} , a fwhm of 0.125 cm^{-1} . The linewidth was chosen to match the spectral resolution of the dye laser and the emission monochromator described earlier. As the temperature increases additional features are evident in the spectra, which eventually take on a Gaussian distribution.

The plot with $S_0 = 1/9$ is a good approximation for the optical transitions of matrix-isolated GaPcCl, pertaining to the weak electron-phonon coupling constant observed experimentally. For each temperature shown in Figure II.22, the ZPL is centred on $p_u = 0$, with PSBs located on positive integer values, and hot bands located on negative integer values. At low temperatures ($\langle m \rangle = 1/9$) the ZPL dominates and the first PSB has a moderate intensity. Subsequent PSBs and hot bands are barely visible at this temperature. At mid-range temperatures ($\langle m \rangle = 1$), the ZPL still dominates, but the first PSB appears stronger, and the first of the hot bands has gained considerable intensity. A second PSB is evident as well as a second (very weak) hot band. With the conditions used in the current work, it is likely that the experimental data will most closely match the line shapes in Figure II.22 obtained with a low or medium value for $\langle m \rangle$. At higher temperatures ($\langle m \rangle = 9$), the curve takes on a more Gaussian like appearance, with several PSBs and hot bands

showing up with significant intensities. This will not be an issue experimentally due to the extremely low temperatures used in the matrix-isolation technique. The actual values for each parameter used in the W_p fit on the experimental data are provided in Chapter VI, where the results of the analysis performed on the amplified emission bands of GaPcCl in both emission and excitation will be presented.

While the W_p function is a powerful tool in the analysis of experimental spectra, it does have limitations. The most significant of these is that the function is working within the SCC model, meaning the coupling phonon frequencies of the ground and excited electronic states are identical. This implies $\hbar\omega$ will be the same in absorption and emission, something which is not always the case experimentally. W_p functions can only be used in conjunction with low temperature experimental work, as the function has a tendency to lose its structure at higher temperatures (as shown in Figure II.21 and Figure II.22). The current work applies the W_p function in an analysis of amplified emission data, which, because of its non-linear optical origins, is not as straightforward to interpret as normal fluorescence. Additional effects, such as the threshold dependence of AE, may affect the intensities of particular bands, and this is not accounted for in the SCC model.

II.11: References

1. Granville-Phillips, 275 Wide-range Convectron Vacuum Gauges. 1990.
2. APD Cryogenics Inc., Helium Compressor HC-2D Technical Manual. 1992.
3. APD Cryogenics Inc., DE-202 Expander Technical Manual. **1989**.
4. Scientific Instruments Inc., Instruction Manual, Series 9600 microprocessor - based digital temperature indicators/controllers manual. 1990
5. Balzers, Operating Instructions, Turbo Molecular Pump, TPU 180H, Ed. 3.
6. Granville-Phillips, 203 Variable Leak Valve. Technical Manual. 1993.
7. Dunkin, I., *Matrix-Isolation (A Practical Approach)*. Oxford University Press: 1998.

8. Jodl, H. J., *Solid-state Aspects of Matrices in the Chemistry and Physics of Matrix-Isolated Species*. North-Holland: 1989.
9. Bruker Optik GmbH, IFS 66/S User's Manual. 2000.
10. Bruker Optics, Product Note M26-02/08 Beamsplitters. **2008**.
11. Bruker Optics, Product Note M25-01/04, Detectors for Bruker FT-IR and FT-NIR Spectrometers. **2004**.
12. Diem, M., *Introduction to modern vibrational spectroscopy*. Wiley-Interscience: New York: 1993.
13. Griffiths, P. R. d. H., J. A., *Fourier Transform Infrared Spectroscopy, 2nd ed.* Wiley-Interscience: New York: 2007.
14. Perkins, W. D., Fourier transform-infrared spectroscopy. Part I. Instrumentation. *Journal of Chemical Education* **1986**, 63 (1), A5-A10.
15. Herres, W.; Gronholz, J., Understanding FT-IR data processing. Part 1: Data acquisition and Fourier transformation. *Computational and Applied Mathematics* **1984**, 2 (4), 216-20.
16. Cooley, J. W. T. J. W., *Math Comput* **1965**, 19 (297).
17. Herres, W., FT-IR: the renaissance of infrared spectrometry. *Chimia* **1985**, 39 (2-3), 64-8.
18. Mertz, L., *Infrared Phys* **1967**, 7 (17).
19. Hamamatsu, L2D2 Series Deuterium Lamps, Specifications. 1998.
20. Cathodeon, Deuterium Lamp Power Supply C713, Operation Notes, Specifications.
21. Acton Research Corporation, Operating Instructions SpectraPro - 300i, SP - 3--i Manual, Rev 997.1.
22. ARC Mercury Pen-Rat Light Source (Model MS-416).
23. Hamamatsu, Data Sheet Title 'Photomultiplier Tubes R928, R955'.
24. Acton Research Corporation, SpectraPro - 500i, 500i Manual V1097.1.

25. Products For Research, Inc., Photocool Series Power Supply, Instruction Manual, (Model PC1177CE009 for R928).
26. Instruction Manual QUANTEL YG 980 Q-switched ND:YAG laser, Doc. 980, Version #1, anglaise PM/DT (12.05.97).
27. Quantel - TDL 90, Instruction Manual - Issue 1.
28. 4-(dicyanomethylene)-2-methyl-6-(4-dimethylaminostyryl)-4H-pyran (C₁₉H₁₇N₃O).
29. [2-[4-[4-(dimethylamino)phenyl]-1,3-butadienyl]-1-ethylpyridinium monoperchlorate (C₁₉H₂₃ClO₄).
30. Andor Technology, A User's Guide to the Andor iStar, Version 3B.
31. Cathodeou Ltd., Sodium Hollow Cathode Lamp (Type 3UNX/Na).
32. Minnhagen, L., Spectrum and the energy levels of neutral argon(Ar I). *Journal of the Optical Society of America* **1973**, 63 (10), 1185-98.
33. Velchev, I.; Hogervorst, W.; Ubachs, W., Precision VUV spectroscopy of Ar I at 105 nm. *Journal of Physics B: Atomic, Molecular and Optical Physics* **1999**, 32 (17), L511-L516.
34. Janesick, J. R., *Scientific charge-coupled devices*. SPIE Press: Bellingham WA: 2001.
35. Frisch, M. J.; Trucks, G. W.; Schlegel, H. B.; Scuseria, G. E.; Robb, M. A.; Cheeseman, J. R.; Scalmani, G.; Barone, V.; Mennucci, B.; Petersson, G. A.; Nakatsuji, H.; Caricato, M.; Li, X.; Hratchian, H. P.; Izmaylov, A. F.; Bloino, J.; Zheng, G.; Sonnenberg, J. L.; Hada, M.; Ehara, M.; Toyota, K.; Fukuda, R.; Hasegawa, J.; Ishida, M.; Nakajima, T.; Honda, Y.; Kitao, O.; Nakai, H.; Vreven, T.; Montgomery, J. A.; Peralta, J. E.; Ogliaro, F.; Bearpark, M.; Heyd, J. J.; Brothers, E.; Kudin, K. N.; Staroverov, V. N.; Kobayashi, R.; Normand, J.; Raghavachari, K.; Rendell, A.; Burant, J. C.; Iyengar, S. S.; Tomasi, J.; Cossi, M.; Rega, N.; Millam, J. M.; Klene, M.; Knox, J. E.; Cross, J. B.; Bakken, V.; Adamo, C.; Jaramillo, J.; Gomperts, R. E.; Stratmann, O.; Yazyev, A. J.; Austin, R.; Cammi, C.; Pomelli, J. W.; Ochterski, R.; Martin, R. L.; Morokuma, K.; Zakrzewski, V. G.; Voth, G. A.; Salvador, P.; Dannenberg, J. J.; Dapprich, S.; Daniels, A. D.; Farkas, O.; Foresman, J. B.; Ortiz, J. V.; Cioslowski, J.; Fox, D. J., *Gaussian 09*. 2009.

36. Schlegel, H. B., Estimating the Hessian for gradient-type geometry optimizations. *Theoretica Chimica Acta* **1984**, *66* (5), 333-40.
37. Schlegel, H. B., Optimization of equilibrium geometries and transition structures. *J. Computational Chemistry* **1982**, *3* (2), 214-18.
38. Li, X.; Frisch, M. J., Energy-Represented Direct Inversion in the Iterative Subspace within a Hybrid Geometry Optimization Method. *Journal of Chemical Theory and Computation* **2006**, *2* (3), 835-839.
39. (a) Feller, D., The role of databases in support of computational chemistry calculations. *J. Comput. Chem.* **1996**, *17* (13), 1571-1586; (b) Schuchardt, K. L.; Didier, B. T.; Elsethagen, T.; Sun, L.; Gurumoorthi, V.; Chase, J.; Li, J.; Windus, T. L., Basis Set Exchange: A Community Database for Computational Sciences. *Journal of Chemical Information and Modelling* **2007**, *47* (3), 1045-1052.
40. Andrae, D.; Haeussermann, U.; Dolg, M.; Stoll, H.; Preuss, H., Energy-adjusted ab initio pseudopotentials for the second and third row transition elements. *Theoretica Chimica Acta* **1990**, *77* (2), 123-41.
41. Kaupp, M.; Schleyer, P. v. R.; Stoll, H.; Preuss, H., Pseudopotential approaches to calcium, strontium, and barium hydrides. Why are some alkaline earth MX₂ compounds bent? *Journal of Chemical Physics*. **1991**, *94* (2), 1360-6.
42. Michalska, D.; Wysocki, R., The prediction of Raman spectra of platinum(II) anticancer drugs by density functional theory. *Chemical Physics Letters* **2005**, *403* (1-3), 211-217.
43. Collier, M. A.; McCaffrey, J. G., Luminescence spectroscopy of matrix-isolated z6P state atomic manganese. *Journal of Chemical Physics*. **2005**, *122*, 184507/1-184507/15.
44. Huang, K.; Rhys, A., Theory of light absorption and nonradiative transitions in F-centers. *Proceedings of the Royal Society of London, Series A* **1950**, *204*, 406-23.
45. Fonger, C. W. S. W. H., *Understanding Luminescence Spectra and Efficiency Using Wp and Related Functions*. Springer-Verlag Berlin Heidelberg: 1991.

46. Abramowitz, M., *Handbook of Mathematical Functions, With Formulas, Graphs, and Mathematical Tables*. Dover Publications, Incorporated: 1974.

II.12: Appendix

The following appendix shows the coding used to generate the W_p fits given by Equation II.14 and Equation II.15.

```

/* Creating a Wp lineshape with a Bessel function.
/* Set variables
setv T=9.80
setv hw=3.9
setv fw=1.20
setv k=0.6950387
setv beta=hw/(k*T)
setv mt=1/(exp(beta)-1)
setv S=0.2
setv theta=2*S*(exp(-beta/2)/(1-exp(-beta)))
eval mt
eval theta

/* Set up an ascending series sum for the Bessel function
create y=0.0 -range 0.0 30.0 -points 31
arch bes
def thetam=ceil(theta)+1
def nmax=thetam
alloc j integer let j=0
:loop
create y=(theta^2/4)^j/(j!*Gamma(x+j+1)) -range 0.0 30.0 -points 31
let y=y+bes:y
arch bes
let j=j+1
IF j<=nmax goto loop
create y=(bes:y)*(theta/2)^x -range 0.0 30.0 -points 31
arch besj

/* Wp function given by Struck and Fonger at low temperature
create y=(exp(-S*(2*mt+1))*((1+mt)/mt)^(x/2))*(besj:y) -range 0.0 30.0 -
points 31
arch Wp
arch wpx

/* W-p function used to calculate Hot bands
create y=exp(-x*beta)*(Wp:y) -range 0.0 30.0 -points 31
let x=-1*x
arch wpe

retr Wp -append
arch Wp
sort -strict
arch Wp

```

Chapter III: Vibrational analysis of Metal Tetraazaporphyrins and Metal Phthalocyanines

III.1: Introduction

This chapter focuses on the ground state structures and vibrational spectra of selected metal tetraazaporphyrins (M-TAPs), metal phthalocyanines (M-Pcs) and metal phthalocyanine chlorides (M-PcCl). Ground state geometries are calculated using high level DFT calculations. Vibrational spectra (Infrared and Raman) of MgPc, AlPcCl and GaPcCl recorded in various hosts are compared with DFT predictions. The results to be presented concern two topics; the structural dependence on the metal centre and the vibrational spectra of the molecules. Four-fold rotational symmetry is observed in all cases, giving the molecules either D_{4h} or C_{4v} symmetry. Comparisons with experimentally determined crystal structures are presented where data are available. Group theory was used to correlate the vibrational modes of the D_{4h} and C_{4v} molecules. Infrared and Raman spectra of MgPc, AlPcCl and GaPcCl are presented and analysed in detail. The Raman active modes of GaPcCl will be compared to the matrix emission spectra in Chapter V. An analysis of the IR and Raman spectra of MgTAP and CaTAP, with D_{4h} or C_{4v} symmetry respectively, is conducted in order to elucidate information about the modes which become active under reduced symmetry. This effect is also observed experimentally with MgPc and AlPcCl.

III.2: Computational details

In the present study the density functional method was utilised with the 6-311G++(2d,2p) basis set for both geometry optimisation and the calculation of the vibrational frequencies. The B3LYP functional is known to be an effective choice for calculating ground state molecular vibrational frequencies and when used with a large basis set, generates accurate infrared intensities. Moreover, as demonstrated in a previous study¹ on free-base tetraazaporphyrin (H_2TAP), the Raman intensities are also reliable. Another advantage of this method is that it runs efficiently on multi-processor computers. The present calculations were conducted with the Gaussian-03 suite of programmes running, (as described in chapter II) on a Linux workstation with two quad-core processors. All of the

calculated vibrational frequencies presented in this work are, unless stated otherwise, unscaled values obtained within the harmonic approximation.

A set of geometry optimizations was performed on the M-TAPs and M-Pcs (M = Be, Mg, Ca, Sr, Ba, Zn, Cd, Hg, AlCl or GaCl). All molecules were given an initial D_{4h} symmetry and were allowed the freedom to optimize to whichever symmetry was determined to be most energetically stable. A vibrational analysis was performed on the optimized structures to confirm that the ground state geometries had been achieved for each system. Raman activities were computed for MgPc, ZnPc, AlPcCl and GaPcCl and were transformed into Raman intensities (cf. equation II.6) for comparison with experimental results. Raman activities were also calculated for MgTAP and CaTAP to investigate how the metal centre affects the Raman active modes.

III.3: Experimental Methods

The Infrared spectroscopy of three M-Pcs/M-PcCls was examined in inert gas matrices at cryogenic temperatures. The setup for this experiment has been described in Chapter II. MgPc, AlPcCl and GaPcCl were purchased from Sigma Aldrich, TCI chemicals and Santa Cruz Biotechnologies Inc. respectively and were used without further purification. Matrix samples were prepared by heating the phthalocyanine to 330°C and flowing the host gas (Ar or N₂) over the vapour to accumulate the material on a KBr window held at 13 K. Sample deposition times were typically 2 hours to ensure acceptable absorption strengths. Infrared spectra were recorded with a Bruker IFS/66s infrared spectrometer with a DTGS detector with a resolution of 0.5 (or 1) cm⁻¹. The range examined was 4000 – 400 cm⁻¹.

Raman spectroscopy of AlPcCl, GaPcCl and MgPc in KBr pellets was performed in on a HORIBA Jobin YVON HR800 spectrometer with Andor and Synapse detectors. Excitation was achieved by a 532 nm or 660 nm CW laser. The phthalocyanines typically absorb strongly in the red, so spectra contained traces of fluorescence and resonance Raman lines. These effects were minimized by the use of the 532 nm line. Accumulation times were set to 10-30 seconds depending on the area on the disc being examined. Several accumulations were performed to reduce the noise contribution. Numerous spots were examined on the surface of the KBr disc to ensure homogeneity of the samples. Raman bands were recorded up to energies of 1700 cm⁻¹.

III.4: Results

III.4.I: Geometries

Geometry optimizations performed on the systems mentioned above show the molecules take up one of two possible arrangements; a planar geometry belonging to the D_{4h} point group, or a non-planar geometry belonging to the C_{4v} point group. The structures of a non-planar M-TAP and M-Pc molecule are shown in Figure III.1, with labels on the symmetry unique atoms. The structures of the related molecules AlPcCl and GaPcCl and their TAP counterparts are shown in Figure III.A1. A summary of the key geometric parameters of the computed metal porphyrins are given in Table III.1. AlPcCl and GaPcCl were also investigated due to the wealth of experimental results available on these molecules compared to the other C_{4v} porphyrin systems. The symmetry is not affected by the addition of the aryl rings onto the pyrrole subunits upon going from TAP to Pc. It appears that the size of the metal atom is the only factor which determines the symmetry the molecule possesses.

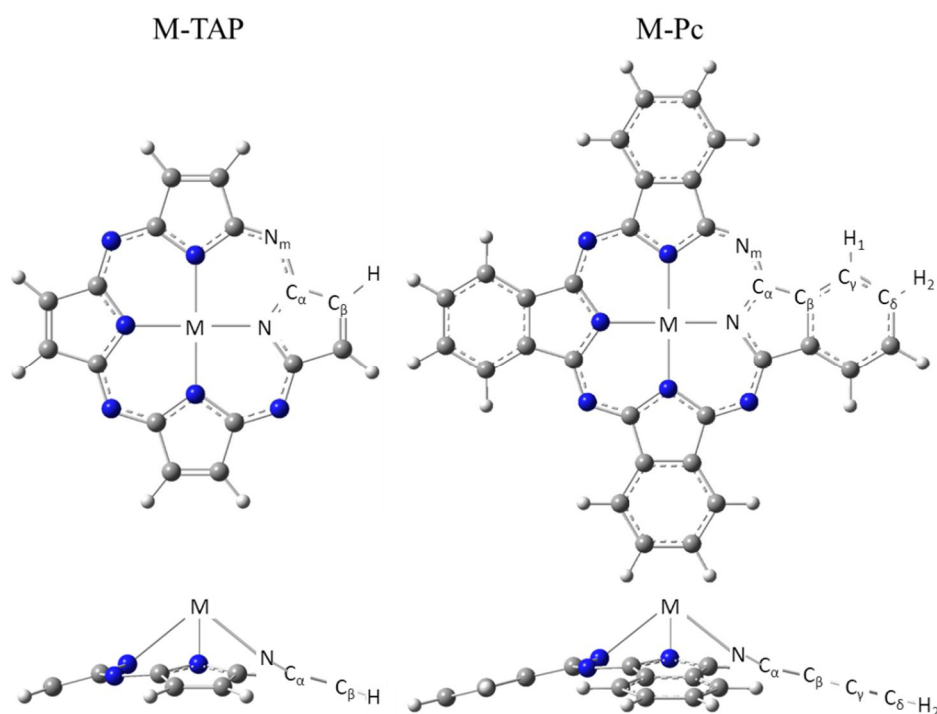


Figure III.1: The top down view in D_{4h} and C_{4v} symmetry and side view in C_{4v} symmetry of M-TAP and M-Pc. The labelling system shows the symmetry unique atoms the molecules possess. A ‘doming’ of the macrocycle is evident from the side view, which is more pronounced for M-Pc than M-TAP. The N_m atom labels have not been shown on the side views in order to see the extent of the doming on the pyrrole and isoindole atoms of TAP and Pc respectively.

A vibrational analysis was performed on the optimized geometries. In no instances were imaginary frequencies observed, indicating that the ground state geometry had been found by the optimization. Vibrational frequencies and infrared intensities were computed for all molecules. Raman activities were only calculated for comparison with experimental values (where available) and for the MgTAP and CaTAP molecules to allow for a symmetry analysis of the Raman modes.

Table III.1: The symmetries and key geometric parameters of the M-TAP and M-Pc systems studied. The M-N bond lengths and height of the metal above the N₄ plane are also shown. (The N₄ plane is the plane on which the four central N atoms lie).

		M-N Bond length (Å)	Height above N ₄ plane (Å)
BePc	D_{4h}	1.874	0
BeTAP		1.851	0
MgPc		2.002	0
MgTAP		1.986	0
ZnPc		1.999	0
ZnTAP		1.979	0
AlPc ⁺		1.915	0
GaPc ⁺		1.954	0
AlPcCl	C_{4v}	1.981	0.451
GaPcCl		2.220	0.506
CdPc		2.157	0.606
CdTAP		2.154	0.674
HgPc		2.027	0.973
HgTAP		2.211	0.836
CaPc		2.283	1.052
CaTAP		2.325	1.128
SrPc		2.431	1.334
SrTAP		2.423	1.354
BaPc		2.595	1.617
BaTAP		2.586	1.627

III.4.II: Infrared Spectroscopy

The matrix infrared absorption spectra of MgPc, AlPcCl and GaPcCl were recorded in solid Ar and N₂ at cryogenic temperatures as well as in room temperature KBr pellets. Experimental results have been compared with DFT results scaled by a factor of 0.98 in the region below 2000 cm⁻¹. The infrared spectra of MgPc in the aforementioned hosts are presented in Figure III.2. A high degree of agreement is evident between the experimental

spectra and the DFT results, indicating the theoretical model describes the experimental values well. Small shifts ($< 5 \text{ cm}^{-1}$) exist between some bands upon changing the matrix, but due to the agreement with band intensities, it is possible to correlate the peaks. Because of the relative inertness of the matrices, vibrational bands are expected to be very close to their equivalent gas phase positions. Shifts in the KBr pellet are more pronounced than in the matrix, possibly due to a stronger interaction between the guest molecules and the host. The band widths of the vibrational modes are strongly dependent on its environment. The matrix spectra show well resolved, narrow lines in comparison to the KBr spectrum. These narrow lines are the result of the low temperatures used to record spectra of highly isolated molecules and lower concentrations of aggregates; conditions that cannot be achieved in KBr samples.

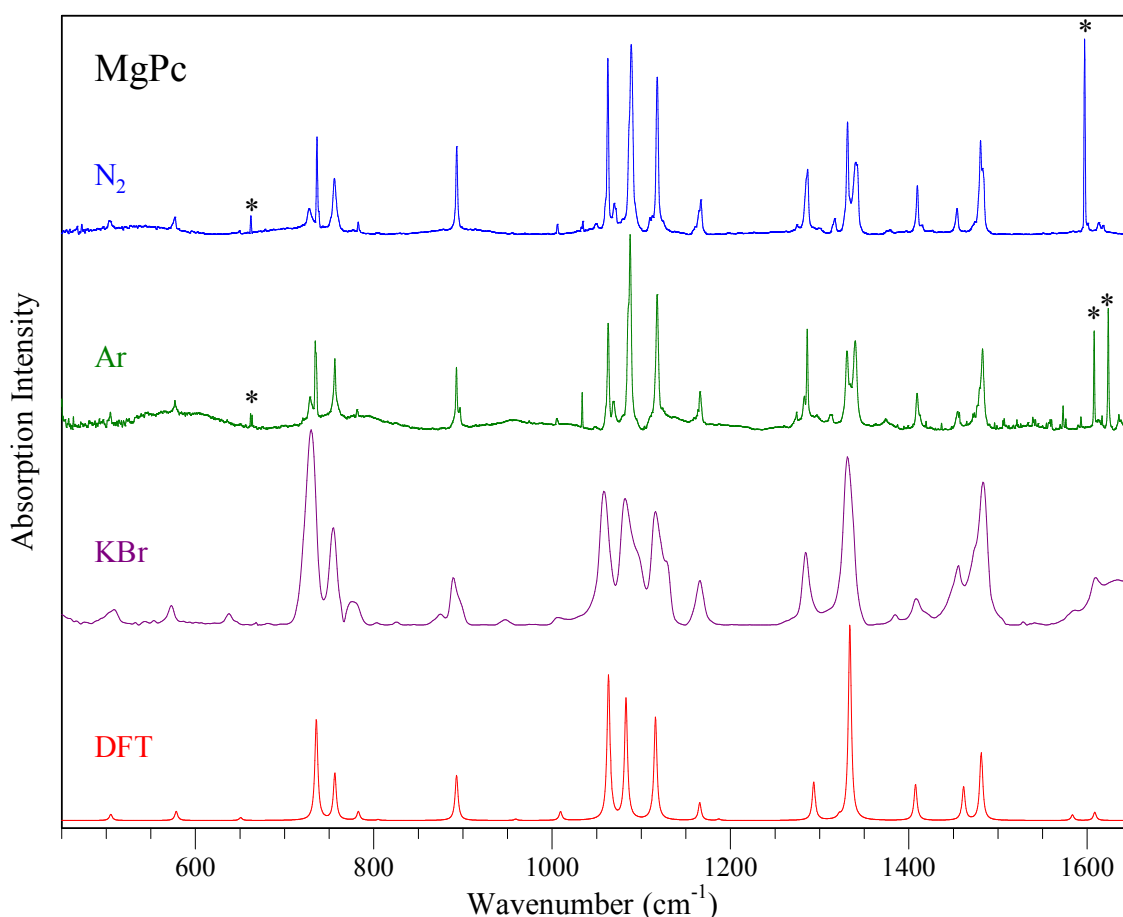


Figure III.2: Infrared absorption spectra of MgPc recorded in N₂, Ar and KBr hosts as well as results predicted using DFT calculations. DFT calculations have been scaled by a factor of 0.98 to account for anharmonicity. Experimental spectra are largely free of contaminants, combination bands and overtones. Small amounts of matrix-isolated carbon dioxide² (CO₂) and water³ (H₂O) are present 667 cm^{-1} and 1600 cm^{-1} respectively and have been highlighted with asterisks.

The DFT results presented in Figure III.2 (red trace) predict the vibrational modes observed in the experimental matrix and KBr spectra with a high level of accuracy. The vibrational frequencies of scaled DFT results match the N₂ data (blue trace) the most closely, as demonstrated by the 'Δ' column in Table III.2. While the DFT generally matches most of the vibrational modes excellently (within 2 cm⁻¹ of matrix values), rather large discrepancies from experiment are noted; as much as 10 cm⁻¹ in some cases. The high frequency modes pertaining to the C-H stretches (region not shown in Figure III.2, but will be shown later) were only observed definitively in the KBr sample. In the matrix samples broad, unresolved bands were located in the C-H stretch region, but could not be conclusively assigned as the C-H stretching modes. The broadening of peaks in this region could be due to site effects, since the C-H bonds of the aryl group are located on the outer part of the ring. As a result, these stretching modes are most sensitive to the trapping environment (as revealed by a pronounced KBr – matrix shift.) Although it is the most likely scenario, these peaks have not been definitively assigned as the C-H stretching modes due to the poor resolution in this region and the fact that they have not been observed in either matrix host. A full list of the fundamental vibrational modes of MgPc in the various hosts is given in Table III.2, along with the results from DFT calculations. From this it can be seen that there is excellent agreement between the theoretical and experimental spectra.

Table III.2: Infrared absorption energies of MgPc recorded in various hosts. All values are given in wavenumbers (cm^{-1}). DFT values have been scaled by a factor of 0.98 below 2000 cm^{-1} and 0.95 above 2000 cm^{-1} . Symmetry labels assume the molecule belongs to the D_{4h} point group with the z-axis passing through the Mg atom perpendicular to the plane of the porphyrin ring. The ‘ Δ ’ column lists the difference between the scaled DFT and N_2 results in the region below 2000 cm^{-1} , and between scaled DFT and KBr results in the region above 2000 cm^{-1} .

N_2	Ar	KBr	DFT x 0.98	Δ (cm^{-1})	DFT Raw	Sym
-	-	-	419.22	-	427.77	E_U
-	-	431.04	438.17	-	447.11	A_{2U}
503.72	505.13	508.78	504.57	-0.85	514.87	E_U
577.06	577.14	573.38	578.01	-0.95	589.81	E_U
649.55	650.60	637.92	649.76	-0.21	663.02	E_U
736.46	734.57	730.16	736.05	0.41	751.07	A_{2U}
755.96	756.59	755.20	755.31	0.65	770.73	E_U
782.67	781.56	776.94	783.10	-0.43	799.08	A_{2U}
804.83	-	803.30	803.79	1.04	820.19	E_U
893.03	892.98	889.61	891.45	1.58	909.64	E_U
955.50	947.33	947.66	959.24	-3.74	978.82	A_{2U}
1006.12	1005.55	1006.82	1009.44	-3.32	1030.04	E_U
1062.66	1063.06	1058.75	1061.03	1.63	1082.69	E_U
1088.82	1087.71	1082.41	1080.67	8.15	1102.73	E_U
1117.94	1117.95	1116.59	1115.09	2.85	1137.85	E_U
1166.89	1166.26	1165.89	1165.08	1.81	1188.86	E_U
1187.01	1186.50	-	1185.50	1.51	1209.70	E_U
1287.02	1286.18	1285.52	1292.67	-5.65	1319.05	E_U
1316.98	1312.80	-	1319.09	-2.11	1346.01	E_U
1331.33	1331.20	1331.53	1332.58	-1.25	1359.78	E_U
1410.24	1409.48	1408.43	1403.86	6.38	1432.51	E_U
1454.12	1454.84	1455.76	1456.60	-2.48	1486.33	E_U
1480.72	1482.77	1483.37	1474.43	6.29	1504.52	E_U
-	-	-	1478.72	-	1508.90	E_U
1584.30	1593.16	1586.50	1582.30	2.00	1614.59	E_U
1613.00	1612.55	1610.82	1608.25	4.75	1641.07	E_U
-	-	-	3015.06	-	3173.75	E_U
-	-	3022.14	3027.99	-5.85	3187.35	E_U
-	-	3049.00	3041.14	7.86	3201.20	E_U
-	-	3079.88	3044.32	35.56	3204.55	E_U

The infrared spectra of the C_{4v} molecule AlPcCl in various hosts, and as calculated by DFT are presented in Figure III.3. A strong similarity between the spectra recorded in different media is evident. In the same manner as MgPc, subtle shifts are observed on the vibrational modes upon changing the matrix, and these shifts are even more pronounced in KBr. The weaker intensity modes were only observed in matrix samples, most likely due to the

narrow linewidths of the bands. The scaled DFT results again show excellent agreement with experimental values. Differences from the experimental spectra are typically less than 5 cm^{-1} , but examples of shifts closer to 15 cm^{-1} have been observed, as demonstrated in the Δ column of Table III.3. Several intensity mismatches arise in the spectra (particularly obvious around 1350 cm^{-1}), but overall the intensities match up very well between experiment and theory. In a similar manner to MgPc, the C-H stretching region was less clear-cut to assign. These bands have only been observed in KBr and have been correlated with the DFT results. In the two matrix environments only broad bands were observed in this region and could not be definitively assigned. A full list of the vibrational modes in the various matrices as well as DFT results is presented in Table III.3.

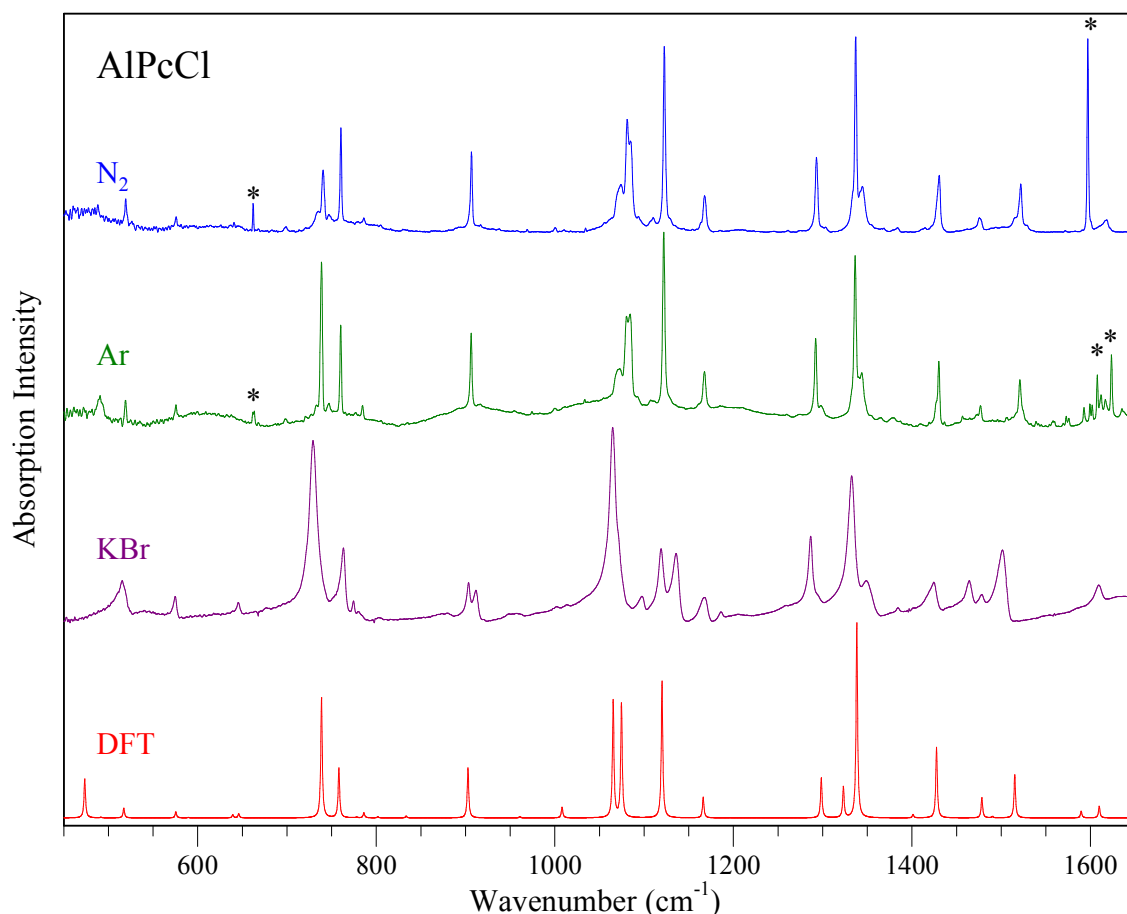


Figure III.3: Infrared absorption spectra of AlPcCl recorded in N_2 , Ar and KBr hosts as well as results predicted by with DFT calculations. DFT calculations have been scaled by a factor of 0.98 to account for anharmonicity. CO_2 and H_2O contaminants have been highlighted with asterisks.

Table III.3: Infrared absorption energies (in cm^{-1}) of AlPcCl in various hosts. DFT values have been scaled by a factor of 0.98 below 2000 cm^{-1} and 0.95 above 2000 cm^{-1} . The Δ column shows the difference between experimental and calculated results, as described in Table III.2.

N_2	Ar	KBr	DFT x 0.98	Δ (cm^{-1})	DFT Raw	Sym
432.22	433.43	-	434.29	-2.07	443.16	A ₁
488.25	490.78	-	473.50	14.75	483.16	A ₁
497.58	496.33	-	491.41	6.17	501.44	E
519.47	519.38	515.32	517.28	2.19	527.84	E
576.04	575.75	574.87	575.53	0.51	587.27	E
-	587.05	-	589.38	-	601.41	A ₁
640.71	639.15	639.42	639.33	1.38	652.38	E
646.27	646.59	645.74	645.99	0.28	659.17	E
-	727.32	-	728.22	-	743.09	E
740.75	738.62	729.48	738.69	2.06	753.76	A ₁
760.56	760.40	763.20	758.15	2.41	773.62	E
778.80	777.35	-	778.02	0.78	793.89	E
786.21	784.80	774.80	786.20	0.01	802.24	A ₁
804.76	799.96	-	801.73	3.03	818.09	E
829.22	835.32	-	833.45	-4.23	850.46	A ₁
906.76	906.43	903.43	902.76	4.00	921.18	E
969.07	955.10	-	960.62	8.45	980.23	A ₁
1000.70	999.64	1013.58	1008.12	-7.42	1028.69	E
1074.07	1072.76	1064.91	1065.42	8.65	1087.16	E
1081.37	1080.40	1071.51 ^{sh}	1074.67	6.70	1096.60	E
1122.61	1122.11	1119.45	1120.12	2.49	1142.98	E
1129.27	1133.68	-	1132.48	-3.21	1155.59	A ₁
1167.71	1167.73	1167.93	1166.24	1.47	1190.04	E
1185.27	1209.71	-	1196.27	-11.00	1220.68	E
1293.14	1292.26	1286.52	1298.48	-5.34	1324.98	E
1333.64	1343.99	1348.96	1323.26	10.38	1350.26	E
1337.03	1336.46	1332.63	1338.31	-1.28	1365.62	E
1414.75	1409.45	-	1401.27	13.48	1429.87	A ₁
1430.68	1430.14	1424.85	1427.55	3.13	1456.69	E
1475.43	1477.04	1478.41	1478.39	-2.96	1508.56	E
1493.42	1490.79	-	1489.94	3.48	1520.34	E
1521.95	1521.12	1501.60	1515.19	6.76	1546.11	E
1590.49	1592.95	-	1589.57	0.92	1622.01	E
1618.45	1611.88	1609.62	1609.84	8.61	1642.69	E
-	-	3014.24	3017.38	-3.14	3176.18	E
-	-	3029.98	3030.38	-0.40	3189.88	E
-	-	-	3030.45	-	3189.94	A ₁
-	-	3042.99	3045.06	-2.07	3205.33	E
-	-	3049.12	3047.80	1.32	3208.21	E
-	-	-	3047.96	-2.07	3208.38	A ₁

Figure III.4 presents the IR absorption spectra of GaPcCl in various hosts, as well as a DFT prediction. The matrix samples show very strong similarities in terms of both band positions and intensities, however, small shifts in the energies of the bands are apparent upon changing the host. A peculiar baseline is observed in the N₂ spectrum. This arises due to internal reflections in the matrix which are seen due to a difference in the sample thickness of the working and the blank samples. The KBr spectra agrees well with the matrix results, albeit the peaks are much broader and the resolved structure is lost as peaks blend together or form shoulders. There is good agreement between the predicted and the experimental spectra, with DFT predicting the band positions to within 5 cm⁻¹ in most instances although certain modes differ by more than 10 cm⁻¹ (which can be seen in the Δ column of Table III.4) but this may be an effect of using a constant scaling factor throughout the entire region of the spectrum. The amount of correction required to account for anharmonicity generally increases with increasing vibrational frequency, as shown by the Morse potentials in Figure II.18.

The C-H stretching modes were not observed clearly in any host, including KBr. This may again be explained by virtue of the hydrogens being on the outer part of the molecule, and the intensity of the modes is being diminished by interactions with the matrix. Based on the MgPc and AlPcCl results, it is expected that they would have been observed in the KBr spectra, but this was not the case.

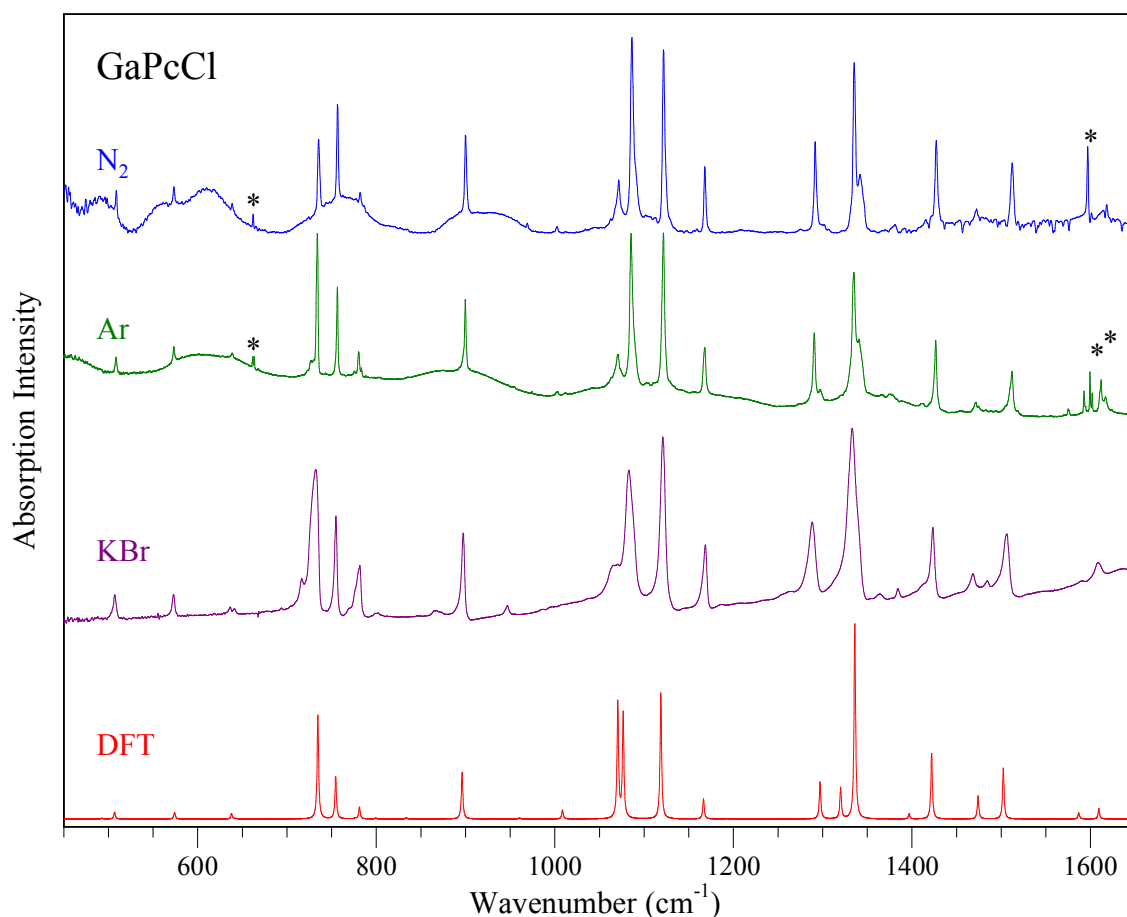


Figure III.4: Infrared absorption spectra of GaPcCl recorded in N₂, Ar and KBr hosts as well results predicted by with DFT calculations. DFT calculations have been scaled by a factor of 0.98 to account for anharmonicity. CO₂ and H₂O contaminants have been highlighted with asterisks.

An obvious similarity exists between the IR spectra of all three molecules. Group theory predicts the AlPcCl and GaPcCl molecules to have three extra vibrational degrees of freedom compared to MgPc, culminating in three extra bands in their vibrational spectra. These bands are expected to involve motion of the Cl-M bond. The extra vibrational modes of AlPcCl were found with DFT calculations to be a relatively intense A₁ mode at 473 cm⁻¹ and a pair of degenerate E modes at 92 cm⁻¹. The A₁ mode corresponding to the Al-Cl stretch is observed at 490.8 cm⁻¹ in Ar (488.3 cm⁻¹ in N₂), albeit at a significantly weaker intensity than is predicted by DFT. It was not observed at all in KBr. GaPcCl is predicted to also have an A₁ symmetry Cl-M stretch occurring at 363 cm⁻¹, and a pair of degenerate E modes occurring at 91 cm⁻¹. Both of these modes fall outside of the range of the detectors used in this experiment. No corresponding peaks arise in either the experimental or predicted IR spectra of MgPc. The most significant deviations are expected in the low

energy region of the spectrum where the metal based normal modes are located. These modes are out of the range of the spectrometer but can be identified in the DFT predictions, where shifts of up to 30 cm^{-1} are found. With the exception of these low frequency modes the appearance of the spectra is quite similar, especially above 500 cm^{-1} , owing to the similarity in the structure of the molecules.

Table III.4: Infrared absorption energies (in cm^{-1}) of GaPcCl in various hosts. The Δ column shows the difference between experimental N_2 and scaled DFT results, as described in Table III.2.

N_2	Ar	KBr	DFT x 0.98	$\Delta (\text{cm}^{-1})$	DFT Raw	Sym
-	424.18	-	424.07	-	432.73	E
-	433.83	-	434.86	-	443.74	A ₁
-	496.22	488.16	492.64	-	502.69	E
509.01	509.09	507.32	506.97	2.04	517.32	E
573.43	573.82	572.9	574.14	-0.71	585.86	E
-	-	588.74	588.69	-	600.70	A ₁
638.96	638.55	636.63	637.92	1.04	650.94	E
-	-	641.42	642.76	-	655.88	E
-	-	-	678.02	-	691.86	A ₁
-	-	-	724.39	-	739.17	E
735.87	733.99	732.04	734.60	1.27	749.59	A ₁
757.03	756.6	755.18	754.54	2.49	769.94	E
778.51	775.71	769.87	776.16	2.35	792.00	E
781.82	780.39	781.63	781.23	0.59	797.17	A ₁
-	-	789.97	788.33	-	804.42	E
-	803.4	802.56	799.30	-	815.61	E
826.98	825.62??	-	833.61	-6.63	850.63	A ₁
-	-	-	879.14	-	897.08	E
900.24	900.1	897.69	896.16	4.08	914.44	E
-	-	-	960.11	-	979.71	E
969.64	960.76	946.86	960.36	9.28	979.96	A ₁
-	-	-	988.23	-	1008.39	E
1002.69	-	-	1008.62	-5.93	1029.20	E
-	-	-	1009.04	-	1029.64	A ₁
1071.94	1070.72	1070.7	1070.57	1.37	1092.42	E
1086.56	1085.93	1082.86	1076.56	10.00	1098.53	E
1121.82	1121.8	1121.19	1118.79	3.03	1141.62	E
-	-	-	1130.08	-	1153.15	A ₁
-	-	-	1164.95	-	1188.72	A ₁
1168.19	1167.81	1168.84	1166.56	1.63	1190.36	E
-	-	-	1192.87	-	1217.21	E
1291.64	1290.83	1288.63	1297.08	-5.44	1323.56	E
-	1320.46	-	1320.15	-	1347.09	E
1335.42	1334.89	1333.22	1336.06	-0.64	1363.32	E
1342.4	-	1364.12	1339.07	3.33	1366.39	A ₁
-	1394.06	1384.38	1396.85	-	1425.35	A ₁
1415.85	-	-	1422.05	-6.20	1451.08	E
1427.41	1426.92	1423.25	1435.81	-8.40	1465.11	A ₁
1472.33	1472.48	1468.41	1474.09	-1.76	1504.18	E
-	-	1483.64	1484.03	-	1514.32	E
1512.3	1511.86	1506.38	1502.35	9.95	1533.01	E
-	-	-	1521.42	-	1552.47	A ₁
-	-	-	1586.86	-	1619.24	E
1584.94	1593.86	1590.51	1588.97	-4.03	1621.39	A ₁
1618.56	1616.76	1608.57	1609.37	9.19	1642.21	E

The C-H stretching region of all three molecules is shown in Figure III.5. Because no useful data was recorded in either the Ar or N₂ matrix, the KBr data is shown. Moderate agreement is observed between the experimental and predicted spectra of MgPc and AlPcCl. The experimental spectrum of GaPcCl exhibits several ‘extra’ bands which are not predicted by DFT. Given the good agreement between experiment and theory in the low frequency modes for GaPcCl (Figure III.4), it is unexpected that the high frequency region should show such a strong disagreement. If the extra bands are due to impurities in the sample then these impurities do not show up in the region below 1700 cm⁻¹ with any significant intensity.

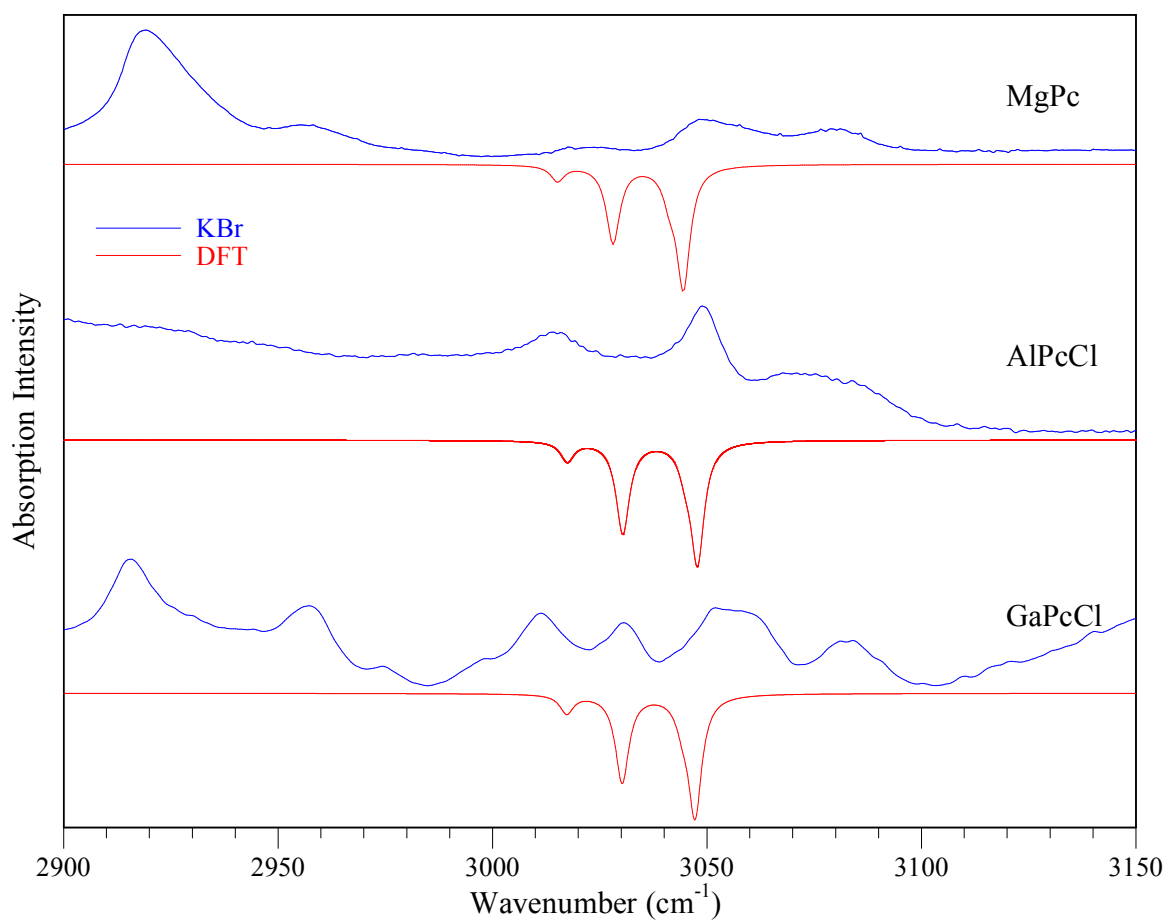


Figure III.5: The C-H stretching region of the IR absorption spectra of MgPc, AlPcCl and GaPcCl recorded in KBr discs (blue) and predicted by DFT calculations (red). DFT calculations have been scaled by a factor of 0.95 for comparison with experimental values.

III.4.III: Raman Spectroscopy

The Raman scattering spectra of MgPc, AlPcCl and GaPcCl were recorded in KBr Pellets using 532 nm and 660 nm excitation wavelengths. Raman bands were observed up to 1700 cm^{-1} using two laser lines. A strong fluorescence band was observed in all molecules with excitation using the 660 nm line. This was removed from the spectrum by fitting a Gaussian curve to the baseline and subtracting the fluorescence out. The Raman scattering of MgPc is presented in Figure III.6. Both the 532 nm and 660 nm generated spectra agree well in their band positions, although the intensities of many of the peaks are quite different. This may be due to resonance Raman⁴ effects occurring with the 660 nm excitation, as this wavelength is quite close to the $Q(S_1) \leftarrow G(S_0)$ electronic transition. This results in some of the low frequency Raman bands achieving a much higher intensity than what is observed with the 532 nm excitation (where MgPc is known to have very weak absorption⁵) and as predicted by DFT calculations.

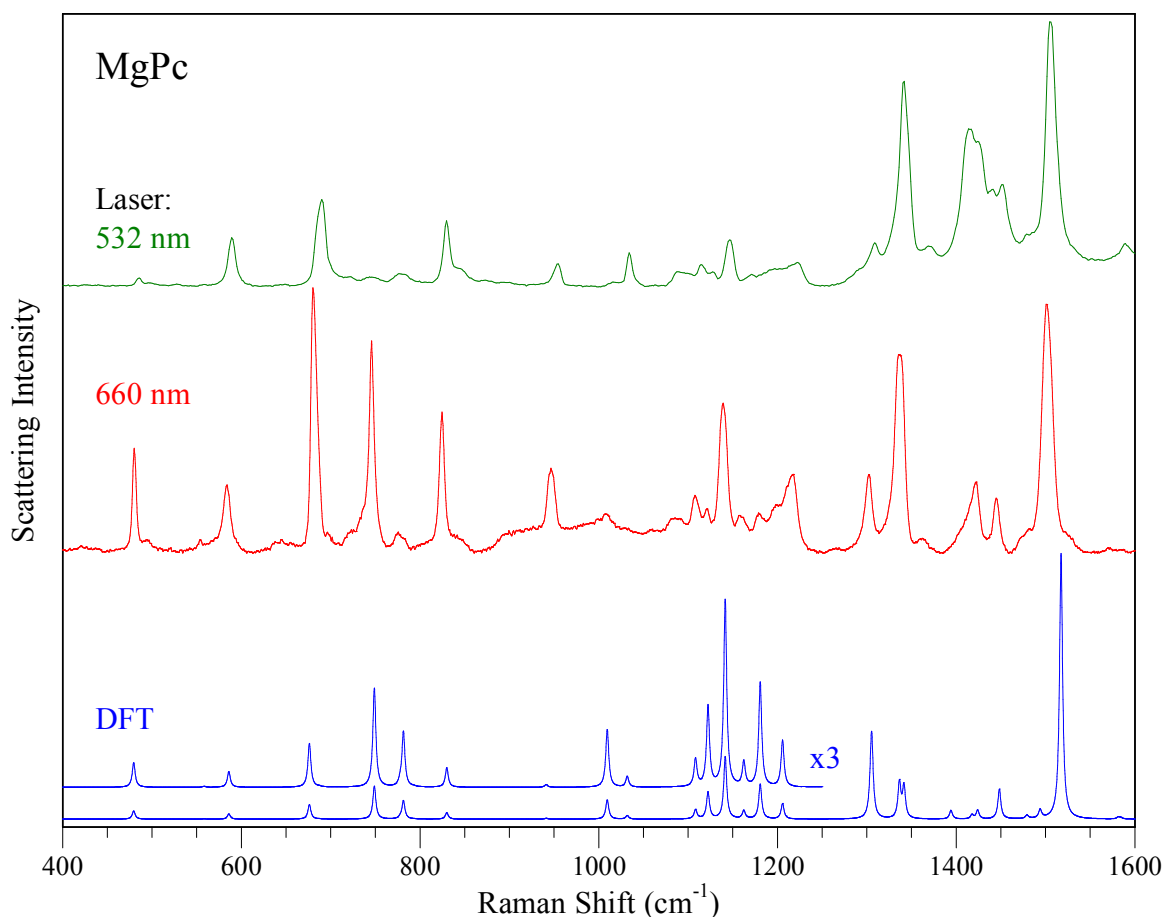


Figure III.6: Raman scattering spectra of MgPc recorded in KBr pellets compared with scaled DFT frequencies. The region below 1250 cm^{-1} has been magnified x3 on the DFT spectrum.

DFT results are also shown in Figure III.6 and have been scaled by a factor of 0.98 throughout the spectrum. Good agreement was observed between experiment and theory. While most peak positions match up, numerous intensity mismatches are evident, particularly at energies lower than 1000 cm^{-1} . DFT results in this region have been magnified three-fold to compare with the experimental bands. The largest deviation of the DFT from experiment is the prediction of the most intense Raman peak; the B_{1g} mode at 1502.1 cm^{-1} . Scaled DFT results show this peak to occur at 1517.4 cm^{-1} , a shift of almost 15 cm^{-1} . This peak has been previously identified to be the peak responsible for the stimulated emission in H_2Pc , ZnPc ⁶, and more recently in H_2TAP ⁷. This result will be investigated in more detail in the Discussion section of this chapter.

The Raman scattering spectra of AlPcCl recorded with the same two excitation wavelengths as MgPc are shown in Figure III.7. In a similar manner to MgPc the band positions match up well in the two experimental spectra, but a few intensity mismatches are present. They are not quite as pronounced in AlPcCl as they were for MgPc , indicating resonance Raman effects are not as strong in the AlPcCl molecule.

DFT results are shown scaled by a factor of 0.98 and show good agreement with experimental band positions, but not band intensities. The region below 1000 cm^{-1} has been magnified by a factor of 3 to allow for comparison with experimental results. Another significant mismatch between experiment and theory is noted on the most intense band in the spectrum. An analysis of the vector diagrams produced by DFT shows that the same motion of the molecule is associated with these peaks in AlPcCl and MgPc . No bands were observed in the C-H stretching region ($\sim 3000\text{ cm}^{-1}$) with either excitation source, and this result is consistent with the low intensities of the bands predicted by DFT in this region.

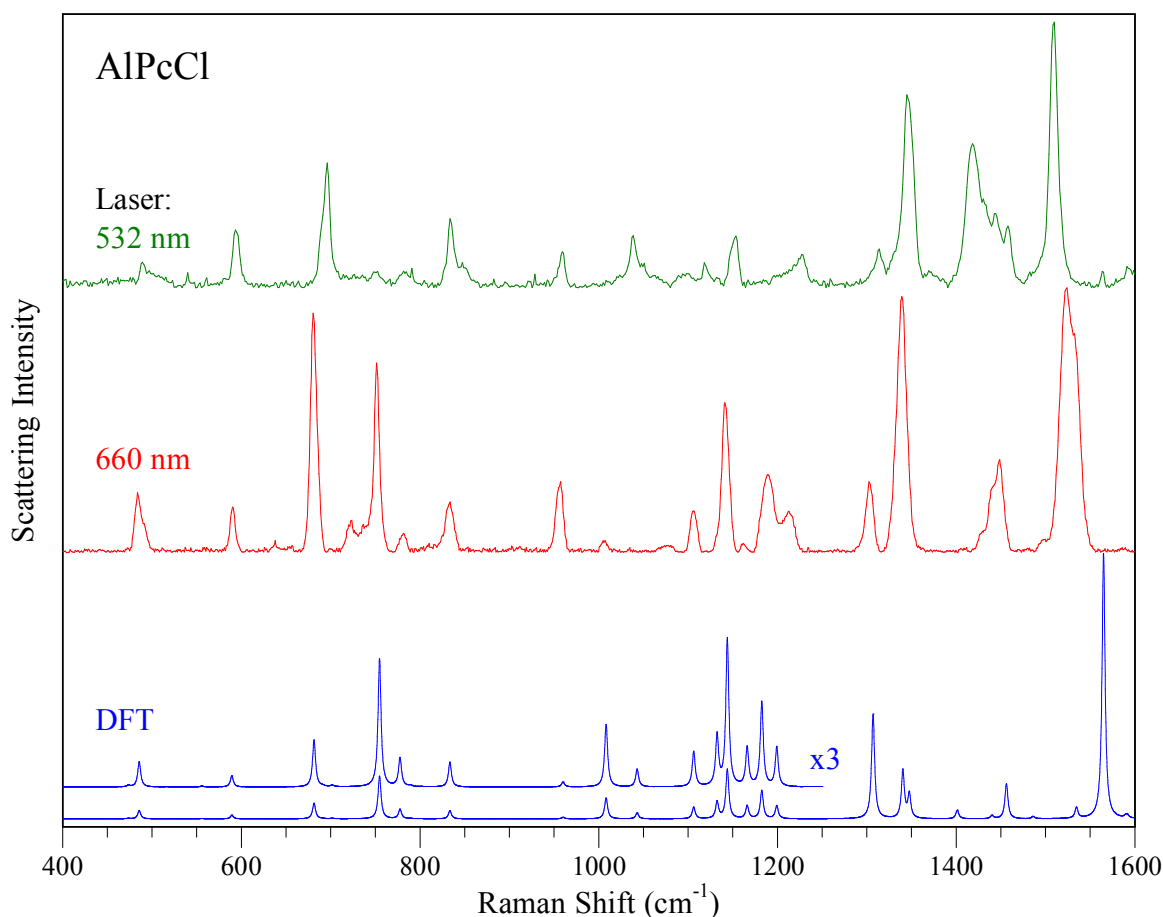


Figure III.7: Raman scattering spectra of AlPcCl recorded in KBr pellets compared with scaled DFT frequencies. The area below 1250 cm^{-1} has been magnified $\times 3$ on the DFT spectrum.

The Raman spectra of GaPcCl recorded with the 532 and 660 nm lines, as well as scaled DFT values are presented in Figure III.8. The resulting spectra appear highly dependent on the excitation wavelength. The spectrum recorded with the 532 nm excitation line shows fairly intense bands through the entire range of the spectrum up to 1650 cm^{-1} . The spectrum recorded with the 660 nm line shows fewer intense bands, but contains most of the bands observed with the 532 nm excitation. A comparison with scaled DFT results shows that the intensities of the 660 nm excitation agree much better than those of the 532 nm excitation. Intensity mismatches are particularly obvious in the regions around $650 - 800 \text{ cm}^{-1}$, $1100 - 1250 \text{ cm}^{-1}$ and $1400 - 1475 \text{ cm}^{-1}$.

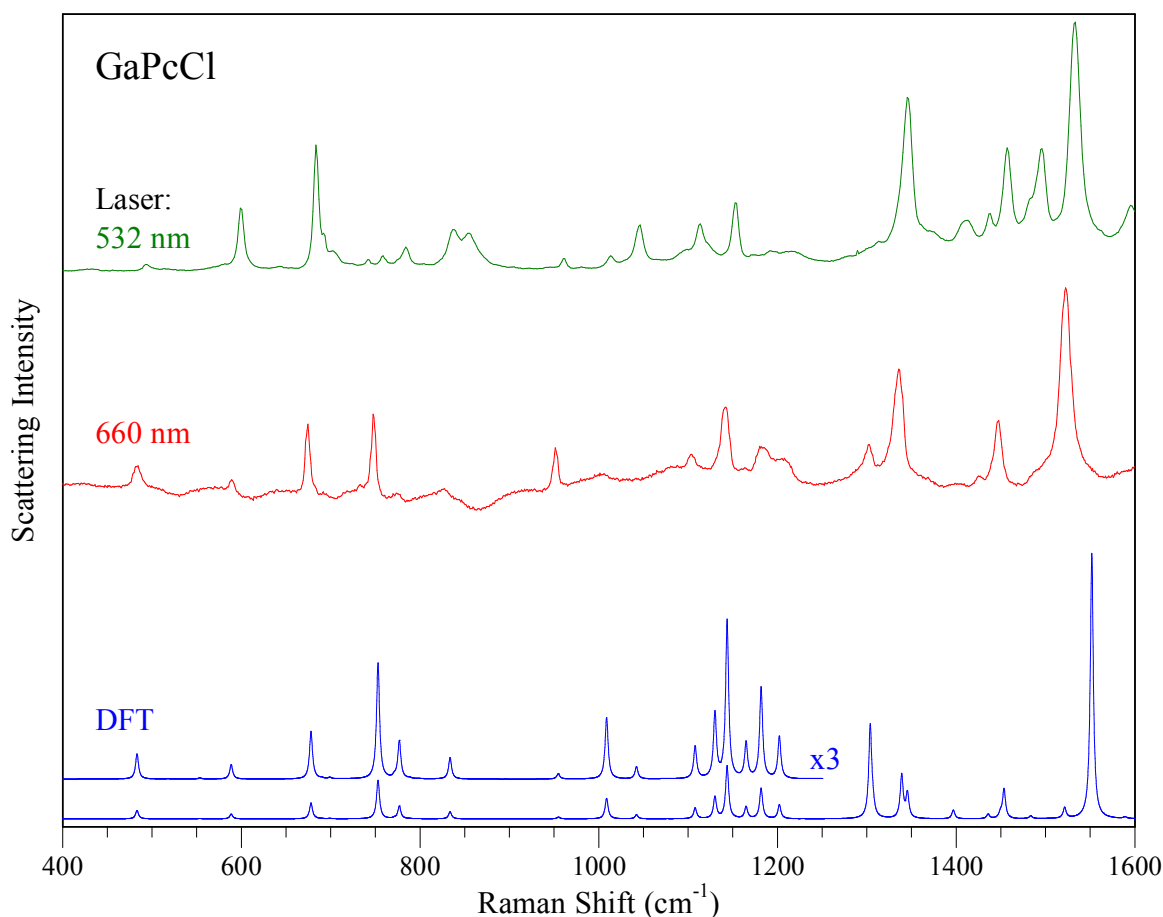


Figure III.8: Raman scattering spectra of GaPcCl recorded in room temperature KBr pellets and as predicted by scaled DFT calculations. The area below 1250 cm^{-1} has been magnified x3 on the DFT spectrum.

Intensity mismatches between the two excitation wavelengths and with DFT calculations are evident in all three molecules. Resonance Raman effects are the most likely source of these anomalies, where the intensity of certain Raman modes is enhanced significantly. MgPc shows an intense band at 480 cm^{-1} with the 660 nm line. This band is shown to be much weaker with the 532 nm excitation and with the DFT calculations. A similar, albeit not as extreme example of this is also found with the 660 nm excitations of AlPcCl and GaPcCl with the bands at 484.2 and 483.9 cm^{-1} respectively. The three intense bands between 650 and 850 cm^{-1} , the bands at 946.4 and 1336.4 cm^{-1} and the band 1416.0 cm^{-1} at all show this enhanced intensity with the 660 nm excitation of MgPc. The 532 nm excitation also leads to the enhancement of several bands, most notably the bands at 1341.9 and 1414.1 cm^{-1} . This enhancement may be due to resonance Raman effects, which are unexpected with a 532 nm excitation, because as Zawadzka demonstrated⁸, this molecule

has no strong absorptions in this region. Zawadzka's result has been consolidated by the absorption spectra of GaPcCl recorded in EtOH and several inert gas matrices in the current work, which will be presented in Chapter V.

Similarly for the 660 nm spectrum of AlPcCl two enhanced bands are located between 650 and 800 cm^{-1} , one at 957.3 and one at 1339.6 cm^{-1} . The 532 nm excitation causes an enhancement of the bands at 694.5, 956.3, and 1419.3 cm^{-1} . The source of these enhanced bands may be due to resonance Raman effects, which are dependent on the excitation laser used and the electronic absorption of the molecule being examined. Neither AlPcCl nor GaPcCl are expected to absorb at 532 nm, so it is surprising that resonance Raman effects arise in these spectra.

The Raman spectra of GaPcCl seem to be the most susceptible to resonance Raman effects, with the 532 nm excitation giving a spectrum containing several enhanced modes, as evident in Figure III.8. The low frequency modes at 599.4 and 683.5 cm^{-1} show modest enhancement, but almost all of the bands between 1346 and 1613.9 cm^{-1} show strong enhancement (with the exception of the band at 1532.9 cm^{-1}). The 660 nm spectrum of GaPcCl seems to be well represented by the DFT results, having fairly good agreement with band intensities throughout the spectrum. The low intensity modes predicted by DFT are barely, if at all visible in the experimental spectrum. The complete set of results for the MgPc, AlPcCl and GaPcCl Raman scattering experiments and DFT calculations are compiled in Table III.A1, which demonstrates the generally very good agreement between scaled DFT results and the experimental data. The correlations between the vibrational modes of the different symmetry molecules have been made based on group theory relationships. Due to the lower symmetry of the metal phthalocyanine chlorides, there will be more Raman active modes for these molecules. This is shown in Table III.A1, where many of the predicted vibrational modes of the MgPc modes have 'u' symmetry. These modes are predicted by group theory (and DFT) to be Raman inactive, and this is observed experimentally.

III.5: Discussion

III.5.I: Structural Analysis

The geometries of the M-TAPs and M-Pcs have been predicted by DFT calculations. Geometries were found to be either planar with D_{4h} symmetry or non-planar with C_{4v} symmetry. Arillo-Flores⁹ performed a DFT study on the first row d-block M-Pcs as well as CaPc and AgPc using modest basis set DFT calculations. This work predicted all of the d-block metals to give planar D_{4h} complexes, with the exception of ScPc and the s-block metal CaPc. The results reported for CaPc and ZnPc are consistent with what is observed in this work. The M-N bond lengths obtained by Arillo-Flores are given as 2.322 Å and 1.975 Å for CaPc and ZnPc respectively. The M-N bond lengths of CaPc and ZnPc are longer and shorter respectively than the calculated values in the current work (2.283 Å and 1.999 Å). Arillo-Flores predicted the Ca atom to sit 1.12 Å above the molecular plane, which is higher than the 1.05 Å predicted by the larger basis set calculations from this work, but is consistent with the longer bond lengths.

Sliznev *et al.*¹⁰ performed a theoretical study on the related alkali metal (M = Li, Na, K) complexes of porphine (M_2P), tetraazaporphyrin (M_2TAP) and phthalocyanine (M_2Pc) with DFT and MP2 calculations using modest basis sets. Sliznev predicted the M_2 porphyrins could form a number of different structures. The smaller metal ions could both lie in the plane of the macrocycle, whereas the larger metal ions either sat above and below the ring, or both above it, similar to the C_{4v} systems described in the current work.

III.5.I.a: D_{4h} Systems

The geometries of BePc, MgPc and ZnPc computed by DFT were all shown to have D_{4h} symmetry. A list of the bond lengths and angles of these three molecules is presented in Table III.5, along with existing experimental data. The corresponding M-TAP results are also shown in Table III.5 to examine how the aryl rings affect the structural parameters. In all instances the structural parameters of the porphyrin ring is similar. The largest difference arises from the M-N bond length. The BePc molecule shows the shortest M-N bond length at 1.874 Å. MgPc and ZnPc show remarkably similar M-N bond lengths, predicted to be 2.002 Å and 1.999 Å respectively. It is expected that both of these should have longer M-N bond lengths when compared to BePc as they both have a larger principal quantum number. Zn forms a shorter M-N bond than Mg due to d-block contraction,¹¹ reducing the atomic radius of the Zn atom.

The calculated geometry of BePc was compared to the crystal data provided by Kubiak¹². Experimental and theoretical results agree excellently. For both bond lengths and bond angles the deviation between experiment and theory is typically less than 1%, and in the most extreme cases is only slightly above 3% (C_β-C_β bond).

Table III.5: Structural parameters of BePc, MgPc and ZnPc predicted by DFT calculations and deduced experimentally. Experimental values of BePc have been taken directly from the crystallography database. The MgPc results are taken from the 200 K data set from reference 13. Experimental ZnPc values are taken directly from the results presented in reference 14. Also shown are the calculated M-TAP structural parameters. All bond lengths are given in Angstroms and bond angles are given in degrees, with the atom labelling system described in Figure III.1.

Bond Lengths (Å)	BePc		BeTAP	MgPc		MgTAP	ZnPc		ZnTAP
	DFT	Exp¹²	DFT	DFT	Exp¹³	DFT	DFT	Exp¹⁴	DFT
M-N	1.874	1.863	1.851	2.002	2.005	1.986	1.999	1.980	1.979
N-C _α	1.381	1.376	1.382	1.329	1.327	1.369	1.369	1.369	1.369
C _α -C _β	1.450	1.448	1.449	1.369	1.375	1.461	1.459	1.455	1.461
C _α -N _m	1.313	1.315	1.323	1.460	1.472	1.339	1.327	1.331	1.337
C _β -C _β	1.394	1.379	1.356	1.460	1.412	1.364	1.407	1.400	1.363
C _β -C _γ	1.393	1.392	-	1.391	1.378	-	1.391	1.393	-
C _γ -C _δ	1.388	1.381	-	1.389	1.384	-	1.390	1.391	-
C _δ -C _δ	1.406	1.397	-	1.403	1.385	-	1.403	1.396	-
C _β -H	-	-	1.081	-	-	1.081	-	-	1.081
C _γ -H ₁	1.080	1.062	-	1.080	1.333	-	1.080	-	-
C _δ -H ₂	1.081	1.051	-	1.081	1.351	-	1.081	-	-
Bond angles (°)									
M-N-C _α	127.3	127.1	128.1	125.1	-	125.7	125.1	125.4	125.8
C _α -N-C _α	105.3	104.7	103.8	109.8	-	108.5	109.9	109.1	108.4
N-C _α -C _β	111.3	111.8	111.7	108.5	-	108.6	108.5	108.8	108.7
N-C _α -N _m	127.3	127.7	127.1	127.4	-	127.1	127.5	127.8	127.2
C _α -N _m -C _α	120.7	119.5	119.5	125.1	-	124.3	125.0	123.5	124.0
C _α -C _β -C _β	106.1	106.1	106.4	106.6	-	107.1	106.6	106.6	107.1
C _α -C _β -C _γ	132.6	132.3	-	132.4	-	-	132.4	132.1	-
C _β -C _β -C _γ	121.4	121.6	-	120.9	-	-	121.0	121.3	-
C _β -C _γ -C _δ	117.4	117.2	-	117.9	-	-	117.8	117.3	-
C _γ -C _δ -C _δ	121.2	121.5	-	121.1	-	-	121.1	121.5	-
C _β -C _γ -H ₁	121.0	117.4	-	120.7	-	-	120.7	-	-
C _γ -C _δ -H ₂	119.6	120.3	-	119.6	-	-	119.6	-	-
C _α -C _β -H	-	-	123.5	-	-	124.2	-	-	124.1
C _β -C _β -H	-	-	130.1	-	-	128.7	-	-	128.8
H ₁ -C _γ -C _δ	121.6	125.4	-	121.5	-	-	121.5	-	-
C _δ -C _δ -H ₂	119.2	118.1	-	119.2	-	-	119.2	-	-

The calculated geometry of MgPc was compared to crystal data provided by Miziguchi¹³. DFT predicts the molecule to be planar with D_{4h} symmetry, similar to BePc. Miziguchi's work showed the molecule to be non-planar, with the Mg atom popping out of the central cavity and lying above the plane of the ring. It was also observed that the ring structure was not equivalent for each of the isoindole subunits, giving it C_1 symmetry. The discrepancy between experiment and theory may be due to the different environments both are performed in. The DFT calculation predicts the geometry of the molecule in the 'gas phase' with no external forces acting upon the molecule. The experiment is performed with the molecule trapped in a crystal lattice. A scheme showing stacking interactions in a crystal lattice is presented in the work by Kubiak¹⁵. These interactions potentially distort the molecule, disturbing the D_{4h} symmetry it is predicted to have. A comparison of the bond lengths does in fact show a very good agreement, generally less than 1% deviation. As was the case with the BePc, the C_{β} - C_{β} bond length deviates by around 3%. The C-H bond lengths differ by almost 20% between experiment and theory. Given the success of the DFT results at predicting all of the other structural parameters, it may be in fact an inaccuracy of the experiment that leads to the discrepancy between the C-H bond lengths. Bond angles were not reported for MgPc.

A set of calculations by Tackley *et al*¹⁶ on the ZnPc molecule with the 6-31g(d,p) basis set predicted a C_{4v} structure with a doming effect on the ring. The current set of calculations with the larger 6-311g++(2d,2p) basis set predict a planar D_{4h} structure, in agreement with the earlier results obtained by Murray *et al*¹⁷. A more recent study of the first row d-block M-Pcs by Arrilo-Flores *et al*⁹ also predicts D_{4h} symmetry for ZnPc. Experimental data on the structure of ZnPc has been reported by Scheidt¹⁴ by X-ray diffraction. A comparison of the results predicted by DFT and experimental data has been performed. The agreements with Scheidt's results are excellent. The bond lengths are accurate to better than 1%, and the bond angles follow the same trend except for the C_{α} - N_m - C_{α} angle (1.2%).

While the D_{4h} M-Pc systems all agree excellently with the experimental crystal data, no such comparison can be made with the M-TAPs as experimentally determined structures do not exist for these molecules. Table III.5 also shows that the addition of the aryl rings in the Pcs affects the structure of the pyrrole rings and hence the M-N bond length. The M-N bond lengths of the D_{4h} M-Pcs are all consistently longer (by 0.016 – 0.023 Å) than the corresponding M-TAPs.

III.5.1.b: C_{4v} Systems

The geometries of the M-TAPs and M-Pcs where M = Ca, Sr, Ba, Cd and Hg were predicted to be C_{4v} by DFT calculations. The bond lengths and angles of these systems are presented in Table III.6. The trend is similar to the one observed for the D_{4h} porphyrins; the M-N bond lengths increase moving down a given group. CdPc and HgPc show shorter bond lengths than the group II counterparts due to the d-block contraction of the atomic radii of the d-10 atoms. An almost linear relationship between the metal radii and the predicted M-N bond lengths holds true. The degree of ‘doming’ observed on the TAPs is very similar to that observed for the Pcs in the current work. To the best of the author’s knowledge, there has been no experimental work carried out on the crystal structures of these C_{4v} molecules. The M-N bond length is very similar between the M-TAPs and M-Pcs for a given metal. The exception to this trend is the HgPc, where the HgTAP has a significantly longer M-N bond length (2.211 Å) than the HgPc (2.027 Å). This difference is ten times larger than for most of the other metals.

Table III.6: Structural parameters of the M-Pcs and M-TAPs predicted to have C_{4v} symmetry by DFT calculations. All bond lengths are given in Angstroms and bond angles are given in degrees. The atom labelling takes the same format as that shown in Figure III.1.

Bond Lengths (Å)	Cd		Hg		Ca		Sr		Ba	
	Pc	TAP								
M-N	2.157	2.154	2.027	2.211	2.283	2.325	2.431	2.423	2.595	2.586
N-C $_{\alpha}$	1.365	1.364	1.364	1.362	1.368	1.369	1.367	1.369	1.366	1.366
C $_{\alpha}$ -C $_{\beta}$	1.465	1.465	1.465	1.462	1.462	1.464	1.463	1.464	1.464	1.464
C $_{\alpha}$ -N $_{m}$	1.333	1.339	1.332	1.335	1.331	1.340	1.331	1.340	1.332	1.337
C $_{\beta}$ -C $_{\beta}$	1.411	1.364	1.412	1.357	1.407	1.361	1.407	1.362	1.406	1.360
C $_{\beta}$ -C $_{\gamma}$	1.390	-	1.390	-	1.391	-	1.391	-	1.391	-
C $_{\gamma}$ -C $_{\delta}$	1.390	-	1.390	-	1.390	-	1.390	-	1.390	-
C $_{\delta}$ -C $_{\delta}$	1.402	-	1.401	-	1.403	-	1.403	-	1.403	-
C $_{\beta}$ -H	-	1.080	-	1.077	-	1.082	-	1.082	-	1.080
C $_{\gamma}$ -H $_1$	1.081	-	1.081	-	1.081	-	1.081	-	1.081	-
C $_{\delta}$ -H $_2$	1.081	-	1.081	-	1.081	-	1.082	-	1.082	-
Bond Angles (°)										
M-N-C $_{\alpha}$	124.3	125.3	123.8	125.0	124.3	125.7	123.6	124.9	122.6	124.0
C $_{\alpha}$ -N-C $_{\alpha}$	111.4	109.4	111.8	109.7	109.5	107.8	109.3	107.3	109.2	107.3
N-C $_{\alpha}$ -C $_{\beta}$	107.5	108.1	107.3	107.8	108.8	109.1	108.9	109.5	109.0	109.6
N-C $_{\alpha}$ -N $_{m}$	127.8	127.7	127.8	127.8	127.7	127.9	127.7	127.6	127.8	127.7
C $_{\alpha}$ -N $_{m}$ -C $_{\alpha}$	127.1	125.9	127.3	126.0	125.5	124.9	125.5	124.4	125.4	124.3
C $_{\alpha}$ -C $_{\beta}$ -C $_{\beta}$	106.8	107.1	106.8	107.3	106.4	106.9	106.3	106.7	106.3	106.7
C $_{\alpha}$ -C $_{\beta}$ -C $_{\gamma}$	132.3	-	132.3	-	132.6	-	132.6	-	132.7	-
C $_{\beta}$ -C $_{\beta}$ -C $_{\gamma}$	120.9	-	120.9	-	121.0	-	121.0	-	121.0	-
C $_{\beta}$ -C $_{\gamma}$ -C $_{\delta}$	118.0	-	118.0	-	117.9	-	117.9	-	117.9	-
C $_{\gamma}$ -C $_{\delta}$ -C $_{\delta}$	121.1	-	121.1	-	121.1	-	121.1	-	121.1	-
C $_{\beta}$ -C $_{\gamma}$ -H $_1$	120.6	-	120.6	-	120.7	-	120.7	-	120.7	-
C $_{\gamma}$ -C $_{\delta}$ -H $_2$	119.6	-	119.6	-	119.7	-	119.7	-	119.7	-
C $_{\alpha}$ -C $_{\beta}$ -H	-	124.2	-	124.2	-	124.2	-	124.2	-	124.2
C $_{\beta}$ -C $_{\beta}$ -H	-	128.6	-	128.4	-	128.8	-	129.0	-	129.0
H $_1$ -C $_{\gamma}$ -C $_{\delta}$	121.4	-	121.4	-	121.4	-	121.4	-	121.4	-
C $_{\delta}$ -C $_{\delta}$ -H $_2$	119.3	-	119.3	-	119.2	-	119.2	-	119.2	-

III.5.I.c: Metal Phthalocyanine Chlorides

The optimized structures of AlPcCl and GaPcCl are presented in Table III.7. Both molecules have C_{4v} symmetry with the metal and chlorine atoms lying above the N_4 plane and a slight doming of the phthalocyanine ring, as shown in Figure III.9. A calculation performed on the structurally related molecule AlPc $^+$ gave a planar structure with D_{4h} symmetry. In this molecule the Al $^+$ lies in the centre of the macrocycle cavity. This

indicates that the Cl⁻ ion pulls the Al out of the plane of the ring causing the doming effect on the ring. A similar result was observed with a calculation on the GaPc⁺ molecule.

The DFT result compares well with existing calculations by Strenalyuk¹⁸ and experimental crystallography results obtained by Wynne¹⁹ (Table III.7). Both sets of calculations were carried out with the B3LYP functional. This work used the 6-311++g(2d,2p) basis set, whereas Strenalyuk used cc-pVTZ. There is an insignificant difference between the results obtained with the two basis sets, with all bond lengths within 100th of an Angstrom of one another and all bond lengths within 0.1° of one another.

The DFT results for AlPcCl agree excellently with the crystal structure deduced by Wynne¹⁹. In all instances the calculations predict the bond lengths correctly to better than a tenth of an Angstrom. The largest deviation is with the C_α-C_β bond, a difference of 0.079 Å (5.7%). The other parameters are typically accurate to within 3%. All bond angles are accurate to within 3% of their experimental counterparts in most instances, with only the C_α-N-C_α and C_α-C_β-C_γ angles deviating more than this from the experimental results. The GaPcCl results generally show an even better agreement with Wynne's crystal structures. Differences between experiment and theory tend to be much less than 2%. The only exceptions are the C_γ-H₁ and C_δ-H₂ bond lengths, which have either been significantly overestimated by DFT, or determined inaccurately in the crystal structure.

While excellent agreement with Wynne's results is observed, it should be noted that the DFT calculations do not have the molecule simulated as part of a crystal lattice as is the case with the experiment. This may explain some of the larger deviations observed between the two sets of results. Different measurement techniques may be the source of the large variation in the C-H bond lengths recorded experimentally by Kubiak¹², Miziguchi¹³ and Wynne¹⁹.

Table III.7: Structural parameters of AlPcCl and GaPcCl predicted by DFT calculations and deduced experimentally. Experimental results shown are the average bond lengths and angles taken from Table XI-S and Table IV-S in reference 19. All bond lengths are given in Angstroms and bond angles are given in degrees. The atom labelling takes the same format as that shown in Figure III.A1.

Bond Lengths (Å)	AlPcCl		GaPcCl	
	DFT	Exp ¹⁹	DFT	Exp ¹⁹
Cl-M	2.175	2.179	2.220	2.217
M-N	1.981	1.977	2.025	1.983
N-C _α	1.379	1.441	1.375	1.381
C _α -C _β	1.450	1.371	1.453	1.448
C _α -N _m	1.317	1.361	1.320	1.323
C _β -C _β	1.399	1.360	1.402	1.381
C _β -C _γ	1.393	1.458	1.392	1.386
C _γ -C _δ	1.388	1.408	1.388	1.377
C _δ -C _δ	1.406	1.418	1.405	1.385
C _γ -H ₁	1.080	-	1.080	0.889
C _δ -H ₂	1.081	-	1.081	0.989
Bond Angles (°)				
Cl-M-N	103.2	101.5	104.5	102.8
M-N-C _α	125.7	127.8	125.0	125.6
C _α -N-C _α	107.4	103.0	108.6	107.4
N-C _α -C _β	109.8	108.9	109.1	108.6
N-C _α -N _m	127.4	123.6	127.6	127.4
C _α -N _m -C _α	122.6	125.5	123.6	122.6
C _α -C _β -C _β	106.5	108.8	106.6	106.8
C _α -C _β -C _γ	132.3	127.5	132.2	131.9
C _β -C _β -C _γ	121.2	122.0	121.2	121.1
C _β -C _γ -C _δ	117.5	115.5	117.6	117.3
C _γ -C _δ -C _δ	121.2	122.0	121.2	121.3
C _β -C _γ -H ₁	120.9	-	120.8	121.0
C _γ -C _δ -H ₂	119.6	-	119.6	119.1
H ₁ -C _γ -C _δ	121.6	-	121.6	121.1
C _δ -C _δ -H ₂	119.1	-	119.2	119.9

III.5.I.d: Planarity

The non-planar porphyrins have been examined by looking at the positions of the symmetry unique atoms with respect to the four pyrrole nitrogen atoms (N₄ plane). Side-on views of the M-TAP and M-Pc structures are shown in Figure III.9. Evidently there is a correlation between how high the metal sits above this plane and how much the rest of the ring is domed. Taking a closer look at the group II metal porphyrins, it is clear that the

larger the metal atomic radius, the higher it sits above the ring. This is an expected result considering that the cavity size is unable to expand enough to facilitate the larger metal atoms. The CaPc is the lowest lying s-block metal, sitting 1.052 Å above the N₄ plane. The Sr metal sits 1.337 Å above the plane and the largest metal studied, Ba, sits 1.617 Å above the N₄ plane. The d-10 metals show contraction compared to their s-block counterparts. This is reflected in how high these metals sit above the ring Cd at 0.606 Å and Hg at 0.836 Å. Zn being a smaller atom lies in the plane of the molecule.

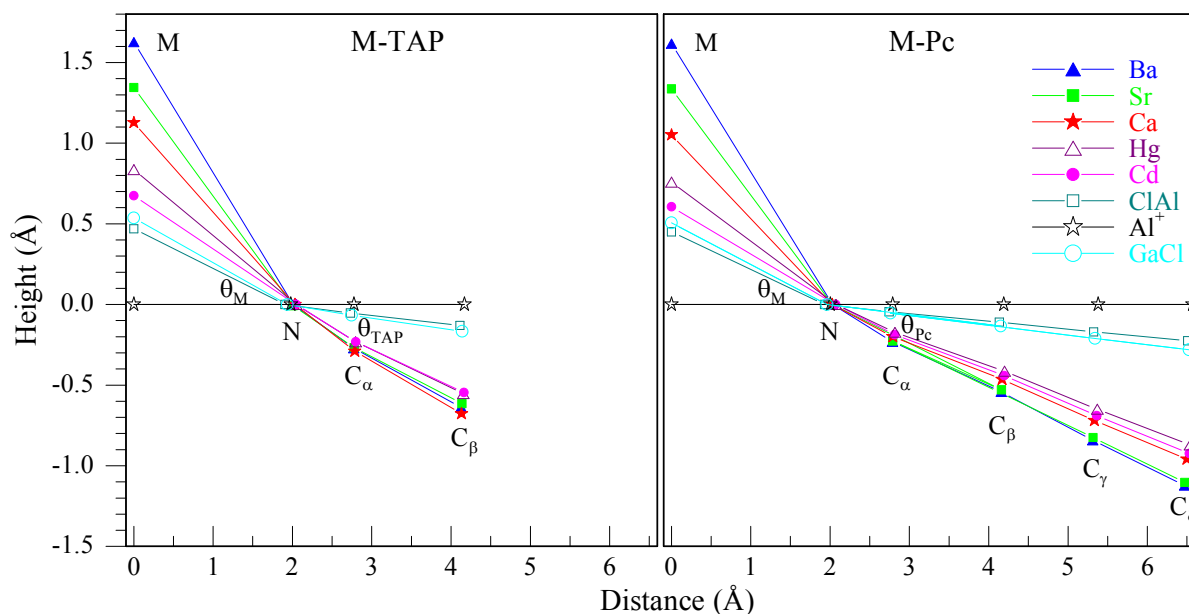


Figure III.9: Structures and doming effect in the non-planar M-TAP and M-Pc molecules. The atom labelling system is the same as that shown in Figure III.1. The plane of the 4 pyrrole nitrogens has been selected as the reference plane. For comparison, the planar AlTAP⁺ and AlPc⁺ molecules are also shown. The metal atoms are shown above this plane and the carbon atoms below it. The label θ_M , shows the angle between the M-N bond and the N₄ plane. θ_{Pc} and θ_{TAP} show the angles between the N-C bond and the N₄ plane. The values of these angles are listed in Table III.8.

AlPcCl and GaPcCl are slightly different to the other C_{4v} M-Pc systems because it is not the size of the metals which cause them to take up the non-planar structure; rather it is the presence of the Cl atom (not shown in Figure III.9). Calculations on the AlPc⁺ and GaPc⁺ molecules show them to be planar with D_{4h} symmetry. The Al and Ga ions in the PcCls are only slightly above the pyrrole nitrogen plane, and the extent of doming on the porphyrin ring is minimal. The larger metals which lie higher above the pyrrole nitrogen plane, cause a more pronounced effect on the doming of the porphyrin ring. This can be seen by virtue of the fact that the carbon atoms of the s-block M-Pcs lie lower than the d-block M-Pcs

which in turn are lower than the AlPcCl with respect to the N₄ plane. A similar trend is observed with the C_{4v} M-TAPs. As was the case with the M-Pcs, the s-block metals lie the highest above the N₄ plane when compared to their d-block counterparts. A greater doming effect is caused by the larger metals.

The angles θ_M and θ_{TAP}/θ_{Pc} are given in Table III.8. θ_M is measured for the angle between the N₄ plane and N-M, θ_{TAP} between the N₄ plane and N-C _{β} , and θ_{Pc} between the N₄ plane and N-C _{δ} . The θ_M results show the expected trend from Table III.1, where metals which lie higher above the N₄ plane show a greater angle. The θ_M angles of the M-TAPs are consistently larger than the corresponding M-Pcs. AlCl shows the smallest angle difference (0.8°) upon changing from TAP to Pc, whereas Ca shows the largest (2.8°). Hg acts differently to the other systems and shows a reversal of this trend, with the θ_M angle of HgPc being larger than that of HgTAP by 4.3°. The θ_{TAP} angles are all larger than the corresponding θ_{Pc} angles, even for Hg. The smallest angle difference is unsurprisingly AlCl (0.6°), whereas the largest is Ca again (7.4°). The fact that the θ_{TAP}/θ_{Pc} angles are more sensitive to changes of the metal atom can be explained because, being benzannulated derivatives of TAP, the Pc molecules have a more rigid structure.

Table III.8: The angles (in degrees) between the metal atom and the N₄ plane of the M-TAPs and M-Pcs are given by θ_M . The corresponding angles between the macrocycle and the N₄ plane are given by θ_{TAP} and θ_{Pc} respectively.

M	θ_M		θ_{TAP}	θ_{Pc}
	TAP	Pc	TAP	Pc
AlCl	14.4	13.6	3.5	2.8
GaCl	16.3	15.1	4.3	3.9
Ca	35.5	32.7	19.2	11.7
Sr	45.7	44.2	16.8	14.5
Ba	60.1	58.6	17.8	14.8
Cd	19.6	17.3	15.1	12.0
Hg	24.8	29.1	15.4	11.3

A very small doming of the M-PcCls is apparent from Figure III.9 and Table III.8, which may be the reason that AlPcCl and GaPcCl are still considered dye molecules. The degree of doming is not sufficient that the molecules lose their aromaticity and thus maintain strong absorption strengths in the visible region of the spectrum, similar to the planar Pcs.

III.5.II: Vibrational Analysis

III.5.II.a: IR Spectroscopy

The Infrared spectroscopy of AlPcCl was studied by sublimation of pure material onto KBr discs and by compression in KBr discs by Napier *et al.*²⁰ They also show a comparison of their data with earlier work carried out by Lever²¹. Napier's results show the transition between the α and β states of the molecule before and after annealing. No such effect was observed upon annealing in either matrix in the current work, as expected considering the molecules are so highly isolated. A comparison of the current work made with Napier's and Lever's results shows good agreement between the different hosts. The difference (compared with N₂ results) was typically less than 5 cm⁻¹, but there were a few modes which differed by up to 35 cm⁻¹ – the band reported at 864 cm⁻¹ by Napier has been correlated to the band at 829 cm⁻¹ in N₂. The weaker bands, which were only identified with the assistance of DFT calculations, were not reported by either Napier or Lever. Additionally, there were several extra bands described in Napier's spectra which were assigned as C=O modes. These were not present in either matrix or KBr due to the high vacuum apparatus used in preparing matrix samples.

Napier²⁰ performed an analysis of the fundamental modes which was mostly accurate. They assigned the modes above 1620 cm⁻¹ to being C=O stretches. These modes were not present in the present DFT calculation, so seem to be reasonable assignments. The modes between 1275 and 1620 cm⁻¹ were assigned to C-C stretches on the benzene rings (with the exception of the water mode at 1505 cm⁻¹). These modes were found to agree with the DFT results from the present work, with the exception of the modes at 1598.6 cm⁻¹, which was shown to be a C _{α} -N _{m} stretch, and the mode at 1298.5 cm⁻¹ which was a C-H IPB. The modes between 1000 and 1200 cm⁻¹ were assigned to C-H IPBs. These were all shown to being the correct assignments, although the internal modes were somewhat more complex, often involving contributions from C-C stretches and Al-N stretches. The modes between 850 and 950 cm⁻¹ were assigned as metal dependent rocking vibrations, which again were shown to be mostly correct. The only incorrect assignment was the mode at 960.6 cm⁻¹, which was a C-H OPB, with no motion of the metal atom. The modes between 700 and 800 cm⁻¹ were assigned as C-H OPBs, and all of these were correctly assigned. The internal modes predicted by DFT again showed more complexity on some of these vibrations. The modes between 500 and 650 cm⁻¹ were assigned as out-of-plane (OOP) ring deformations. The modes at 643, 637 and 519 cm⁻¹ were correctly assigned. DFT showed

that the modes at 589.4 and 575.5 cm^{-1} were in-plane vibrations of the isoindole ring. The Al-Cl stretch was assigned to the peak at 441 cm^{-1} (α) and 450 cm^{-1} (β). This shows a significant shift from the energy predicted by DFT (473.5 cm^{-1}). This mode was difficult to observe in the matrix, but has tentatively assigned to the band at 488.3 cm^{-1} in N_2 and 490.8 cm^{-1} in Ar. Linsky²² placed this vibrational mode at 440 cm^{-1} , as reported in the IR spectrum shown by Starke and Hamann²³. Linsky also describes the metal-halide stretching modes for a number of other metallo-porphyrin halides, but does not report a frequency for the Cl-Ga stretch, probably because it falls outside the range of the detector, as was observed in this work. To the best of the author's knowledge, no other work has been carried out on the IR absorption spectra of GaPcCl.

The IR absorptions of a series of substituted and un-substituted M-Pcs in KBr discs were recorded by Ziminov²⁴. The vibrational bands of MgPc were reported as low as 700 cm^{-1} . These results have been compared with the experimental results in this work and show good agreement. Values reported are typically within 5 cm^{-1} of results recorded in KBr discs from this work. A mode assignment conducted by Ziminov was shown to be accurate by examining the vector diagrams associated with the vibrational modes calculated by DFT. The modes up to 800 cm^{-1} generally involve C-H OPBs. The modes between 800 and 1300 cm^{-1} are mostly made up of either C-H IPBs or isoindole deformations. The modes between 1300 and 1500 cm^{-1} have been correctly assigned as deformations of the pyrrole and isoindole subunits, with the remaining modes up to 1800 cm^{-1} involving C=C and N=C stretches. Finally the high frequency modes have been assigned as the C-H stretches. An analysis of the vector diagrams from DFT calculations show that the only incorrect assignment from Ziminov is the mode at 1114 cm^{-1} , which was assigned as a totally symmetric isoindole deformation instead of a C-H IPB.

The fundamental vibrational modes of MgPc have also been observed in thin films²⁵. All of the modes described in this work were described as having A_{2u} symmetry. A comparison with matrix results from the current work show the frequencies shift by as much as 12 cm^{-1} in places and the modes are a mixture of A_{2u} and E_u symmetries.

The IR spectra of MgPc, AlPcCl and GaPcCl recorded in N_2 matrices and DFT calculations are shown in Figure III.10. The similarity of the IR spectra arises due to the closeness of the structures of the three molecules. The extra atom in metal phthalocyanine chlorides give them 3 extra vibrational modes which have been described as a Cl-M stretch

which has A_1 symmetry and moderate IR intensity, and a pair of degenerate E modes which are only weakly IR active. The other modes which are expected to be significantly different are the metal based modes. These modes are all observed in the region below 400 cm^{-1} , which is outside of the range of the DTGS detector used to record the experimental spectra. These modes can however be analysed with DFT calculations and shifts of up to 50 cm^{-1} can be seen. The region of the spectrum shown in Figure III.10 shows the remarkable similarity of the IR spectra of these molecules. The band positions of many of the vibrational modes are quite similar, to well within 10 cm^{-1} of one another, albeit with intensity differences.

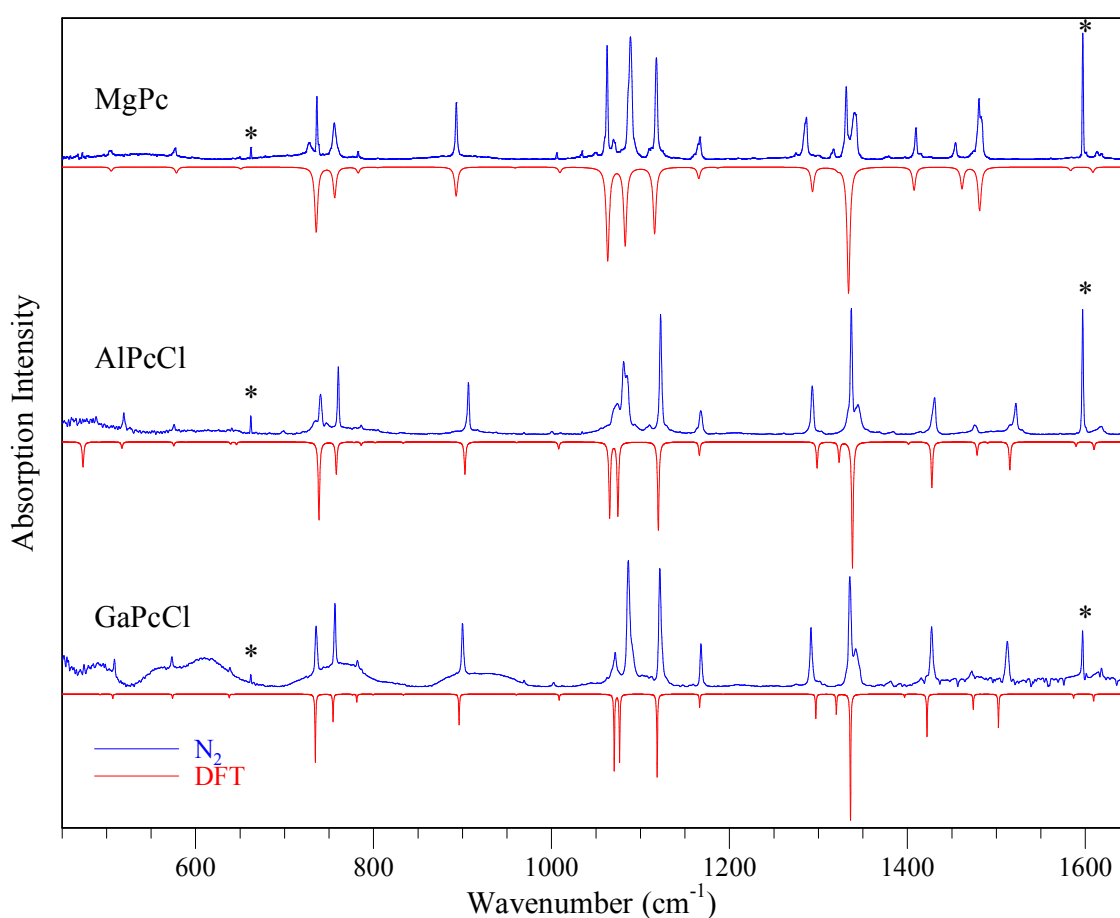


Figure III.10: Matrix infrared absorption spectra recorded in solid N_2 (blue) and as predicted by scaled DFT results (red) of MgPc, AlPcCl and GaPcCl. CO_2 and H_2O impurities are highlighted by asterisks.

DFT calculations of MgPc show that the vibrational modes are of A_{2u} and E_u symmetry to be IR active. The corresponding A_1 and E modes in AlPcCl and GaPcCl are also IR active. A_{2u} modes are primarily associated with out-of-plane bending (OPB) motions. Only 4 of

these modes were observed in the IR spectrum of MgPc. The E_u modes involved in-plane motions of the molecule, usually a C-H in-plane bend (IPB) and/or a distortion of the isoindole rings or the central ring. In general the E_u modes are much more intense than the A_{2u} modes, with the exception of the A_{2u} mode at 751 cm^{-1} , corresponding to a 'pure' C-H OPB.

In a similar manner to MgPc, the IR spectrum of AlPcCl is made up mostly of intense E modes and weaker A_1 modes. Two A_1 modes carry significant intensity; the Cl-Al stretch at 483 cm^{-1} , and the pure C-H OPB at 753 cm^{-1} . Many more A_1 and E modes are spectroscopically active in AlPcCl than the A_{2u} and E_u modes in MgPc and this will be discussed in more detail in the Section III.5.III.

The IR absorption of GaPcCl is remarkably similar to that of AlPcCl, and the same trend of intense E modes and weak A_1 dominating the spectra persists with this molecule. There is only one intense A_1 mode above 400 cm^{-1} (the pure C-H OPB at 750 cm^{-1}) in the GaPcCl spectrum shown in Figure III.10. This is due to the intense Cl-Ga stretch having a frequency of 363 cm^{-1} , just below the range of the DTGS detector. With the exception of a the metal dependent normal modes, the vibrational frequencies of AlPcCl and GaPcCl are within 5 cm^{-1} of one another and the intensities of the bands agree excellently. This similarity in the vibrational structure of the two molecules originates in them having comparable ground state structures.

While the region of the experimental IR spectra shows a high degree of agreement, the same cannot be said for the low frequency region as shown in Figure III.11, where the similarity between the structures of the spectra of the three molecules is reduced. Two main factors contribute to this; the geometry of the molecules change from planar to domed and the metal occupying the central cavity changes from molecule to molecule. The region below 500 cm^{-1} is where most of the metal dependent vibrations are found. Vibrational modes are sensitive to changes in mass, and this can be seen as the Cl-M stretching mode (highlighted with an 'x' in Figure III.11) shifts in energy from 483 cm^{-1} to 363 cm^{-1} as the mass of the metal changes from 27 amu in Al to 70 amu in Ga. Table III.9 collects all of the metal dependent vibrational modes of these molecules, which have also been highlighted with stars on Figure III.11.

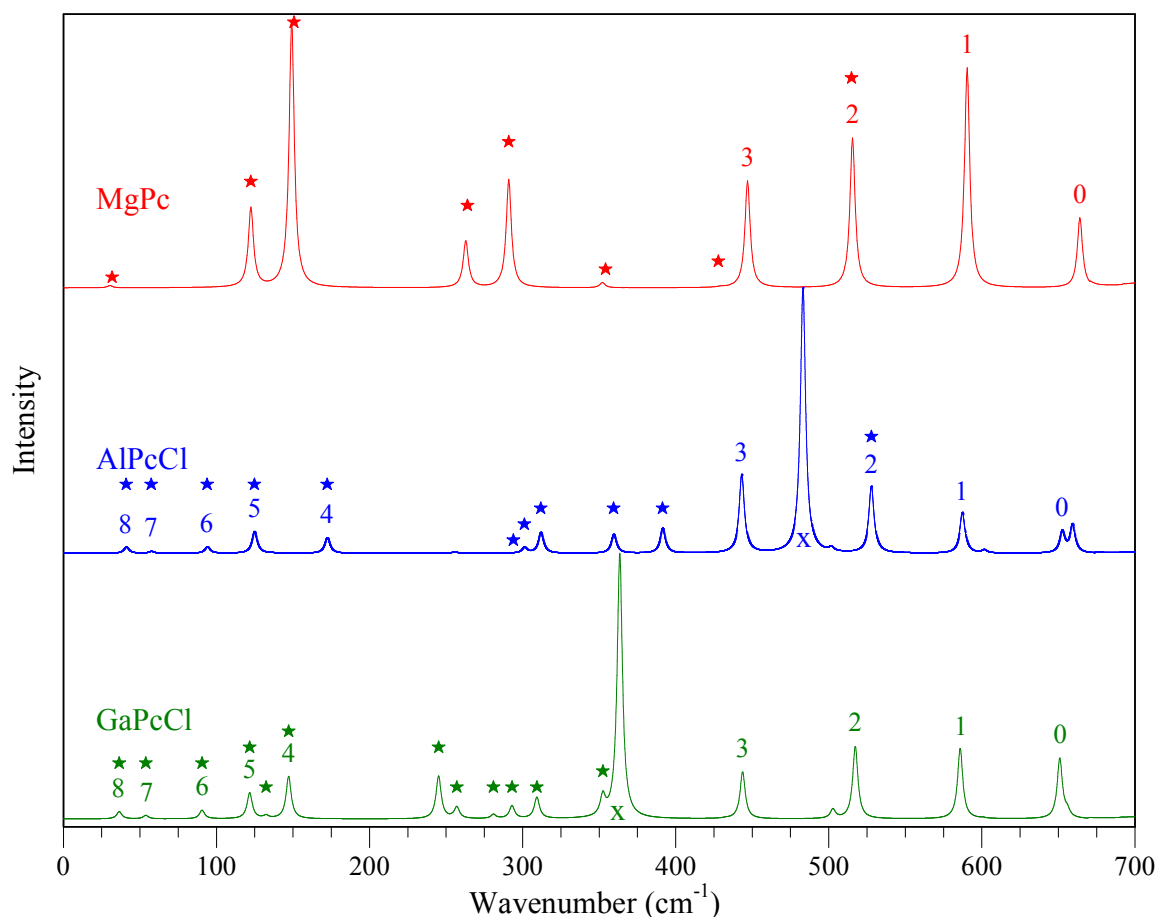


Figure III.11: Low frequency IR active modes of MgPc, AlPcCl and GaPcCl predicted by DFT calculations. Values are plotted in wavenumbers and are unscaled. The calculated frequencies for MgPc and AlPcCl are given in and those of GaPcCl are given in Table III.A4.

The other major difference between the molecules is their symmetry; MgPc is planar with D_{4h} symmetry, and both M-PcCl are domed with C_{4v} symmetry. The MgPc molecule contains a centre of inversion which means the rule of “mutual exclusion” applies to its vibrational modes. The impact this has on the IR spectrum is that totally symmetric vibrations are forbidden and thus will carry no intensity. The M-PcCl do not have an inversion centre, and hence they do not have totally symmetric vibrations. This means all of its vibrational modes will cause a change in the electric dipole moment of the molecule, giving them IR activity. It can be seen in Figure III.11 that fewer bands are present in the MgPc spectrum than in the M-PcCl spectra. The bands labelled 0 – 3 are common to all three spectra, and correspond to distortions of the macrocycle. The peaks labelled 4 – 8, however are only common to AlPcCl and GaPcCl, a direct effect of changing the symmetry of the molecule. Intensity differences are obvious throughout all three spectra,

with the most intense band in each shifting from 149 cm^{-1} to 480 cm^{-1} to 363 cm^{-1} for MgPc, AlPcCl and GaPcCl respectively. These modes correspond to the Mg OPB, the Al-Cl stretch and the Ga-Cl stretch. The corresponding OPB modes in AlPcCl and GaPcCl which match the MgPc occur at 172 cm^{-1} and 147 cm^{-1} respectively. These modes are all labelled '4' in Figure III.11.

A summary of the metal dependent modes of MgPc, AlPcCl and GaPcCl is presented in Table III.9. The chlorine dependent modes of the metal phthalocyanine chlorides have also been included. These modes have been correlated based on the vector diagrams produced by DFT calculations. The modes which show the smallest frequency differences between the molecules mostly involve motion of the phthalocyanine ring, with a minimal contribution of the metal centre. The more characteristic modes are the ones whose energies change significantly from molecule to molecule. These modes contain a significant motion of the metal and thereby show the largest energy shifts. The IPB mode of MgPc with a frequency of 428 cm^{-1} corresponds to the 'purest' Mg IPB vibration, and this is mimicked by the AlPcCl and GaPcCl modes at 391 cm^{-1} and 293 cm^{-1} respectively. The same can be said of the out-of-plane modes mentioned above. The other modes which change quite significantly contain more extensive motion of the porphyrin ring, as well as motion of the metals.

The chlorine based modes show the effect of having two metals in the same group, differing only by their size and mass. As expected, the Ga based vibrations are consistently lower in energy than the Al counterparts due to the Ga atom having a greater mass.

Table III.9: Metal related vibrational frequencies (in cm^{-1}) for MgPc, AlPcCl and GaPcCl as predicted by DFT calculations. Values are reported in wavenumbers and are unscaled. The values reported here are represented by the stars in Figure III.11.

	MgPc	AlPcCl	GaPcCl
In-plane Bend	122.43	124.72	121.70
	290.89	301.08	245.11
	-	311.82	257.05
	427.77	391.41	293.07
Out-of-plane Bend	514.87	527.84	309.30
	31.81	40.98	36.46
	150.63	172.26	147.14
	263.95	293.97	280.93
Stretch	354.20	359.43	352.41
	182.16	167.52	131.83
Chlorine	-	57.34	53.86
	-	93.88	90.58
	-	135.09	132.40
	-	483.16	363.46

III.5.II.b: Raman Spectroscopy

The Raman spectroscopy of MgPc (as well as a number of other metal phthalocyanines) on silicon substrates has been studied by Szybowicz *et al*²⁶. A 488 nm excitation source was used for the study, significantly higher in energy than the source used in the current work. The authors reported an A_{1g} mode at 592 cm^{-1} corresponding to a benzene ring deformation, a B_{1g} mode at 684 cm^{-1} coming from the macrocycle breathing, and a B_{1g} mode associated with pyrrole stretch at 1499 cm^{-1} . These bands correspond to the bands at 584, 681 and 1501 cm^{-1} in the current work. The labelling of the band at 684 cm^{-1} appears incorrect, as the DFT results show no B_{1g} modes in this region (the band at 681 cm^{-1} in the present work is A_{1g} symmetry). Szybowicz's descriptions of the modes are reasonably accurate. The two lower frequency modes both involve deformations of the benzene rings and macrocycle breathing. The high frequency mode description is in line with what DFT predicts.

Aroca and Jennings have carried out an analysis of the Raman active modes of many phthalocyanine systems grown as thin solid films on various substrates. Included in their

studies are MgPc^{25, 27}, AlPcCl^{28,29} and GaPcCl²⁸. The Raman spectrum of a thin film of MgPc²⁵ grown on a Ag coated Sn sphere surface was recorded up to 1600 cm⁻¹ with a 647.1 nm excitation wavelength. Only fundamental vibrational frequencies were observed, and all observed bands had A_{1g} symmetry. A comparison of Aroca's work with the KBr spectra recorded in the present study and the scaled DFT values show they match up very well, typically to within 3 cm⁻¹ of experimental values. The labelling of the modes by Aroca was not entirely correct, with some modes being of B_{1g} or B_{2g} symmetry. The intensity of the bands is almost exactly the same as those recorded with the 660 nm line in the current work, which is to be expected given the molecule absorbs strongly in the red region of the spectrum^{30,5}.

The Raman spectra of AlPcCl grown on quartz²⁸ and NaCl substrates²⁹ have been recorded by Jennings and Aroca respectively. In both sets of experiments an excitation wavelength of 647.1 nm was used. No broad fluorescence band was observed below 1600 cm⁻¹, as was the case with the 660 nm excitation in this work. The spectra recorded by Aroca and Jennings show a very good agreement with the most intense bands in the present work. The bands are accurate typically to within about 3 cm⁻¹, although several bands above 1000 cm⁻¹ are shifted by as much as 20 cm⁻¹. Band intensities for all three spectra are almost identical, although the resolution of the current work is slightly better, allowing weaker intensity peaks to be analysed more comprehensively. The mode assignments of the AlPcCl molecule presented in Aroca's work has been compared to the vector diagrams obtained from the present DFT calculations. In most instances the assignments are accurate, but as was the case with Napier's IR assignments²⁰, the internal modes show more complexity than can reasonably be expected to be described without the insights given by DFT calculations.

The Raman spectrum of GaPcCl has been published by Jennings²⁸. Due to the 647.1 nm excitation, this spectrum most closely resembles the 660 nm spectrum recorded in KBr. Deviations from the KBr spectra in this work are often < 5 cm⁻¹, but can be as much as 10 cm⁻¹. Band intensities are in good agreement with the KBr spectra. Only the strongest bands have been labelled, with many of the modes assigned A₁ symmetry, and a few mode descriptions have been performed. The mode assignments and the mode descriptions all appear to be correct.

Davydov splitting has previously been observed in the Raman spectra of AlPcCl²⁹. It has not been identified for AlPcCl or MgPc in the current work, but it may be present in the Raman spectra of GaPcCl. The spectrum recorded with the 660 nm excitation does show a broad fluorescence background, as described earlier, but when subtracted out the spectrum is relatively simple, with only a few strong bands. The spectrum recorded with the 532 nm laser shows a splitting of several of the high frequency bands. The extra bands may be due to Davydov splitting caused by the presence of aggregates in the KBr disc. In a crystalline system with m molecules occupying a unit cell, the number of Davydov components, N , is given by

$$N(\mu, \nu) = \frac{m}{h} \sum_R \chi_\mu(R) \chi_\nu(R) \quad \text{Eq. III.1}$$

where h is the order of the group factor, $\chi_\mu(R)$ and $\chi_\nu(R)$ are the characters of the irreducible representations μ and ν under the operation of the R class of the factor and site group respectively³¹. It is also strange that the 660 nm excitation gives simpler spectra than the 532 nm excitation. It would be expected that resonance Raman effects should occur with 660 nm excitation owing to the strong absorption of GaPcCl in this region of the spectrum. It has also been shown recently by Zawadzka⁸ that this molecule has no absorption in either the 1064 or 534 nm regions. Given that the 532 nm Raman spectrum is clearly more complicated, another effect must be causing extra bands to selectively arise with this excitation wavelength.

A comparison of the Raman scattering spectra of MgPc, AlPcCl and GaPcCl recorded in room temperature KBr discs with a 532 nm excitation wavelength and the frequencies predicted by DFT calculations is shown in Figure III.12. For the most part all three spectra appear to be quite similar. The number of intense bands present in these spectra and their frequencies and intensities match up rather well.

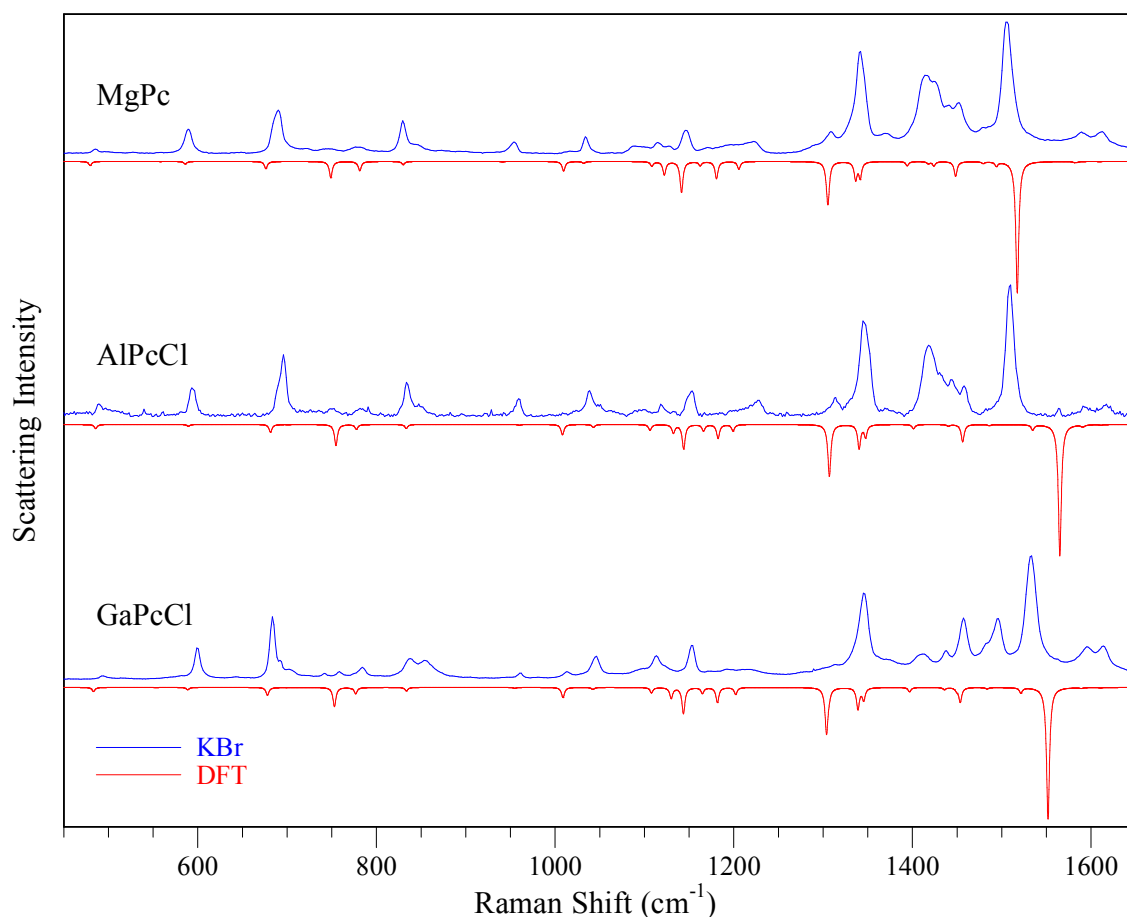


Figure III.12: Raman scattering of MgPc, AlPcCl and GaPcCl recorded in KBr discs with a 532 nm excitation line and predicted frequencies from scaled DFT results.

The most obvious mismatch between the DFT results and the experimental spectra is with the highest intensity bands in each spectrum (Table III.9). For MgPc a difference of almost 12 cm^{-1} exists between experiment and theory. This is even worse for AlPcCl and GaPcCl, where a shift of 56 cm^{-1} is observed. This mismatch has been reported before in other porphyrin systems, namely by Murray⁶ for ZnPc and H₂Pc and Crepin⁷ for H₂TAP. Both of these works noted that this particular Raman mode is strongly associated with the process of stimulated emission in these molecules. It has also been noted by Szybowicz²⁶ that this mode is very sensitive to the choice of the metal centre. The mode shifts from 1499 cm^{-1} in MgPc to 1544 cm^{-1} in CoPc. The experimentally measured frequency changes very little from MgPc to AlPcCl in the current work, shifting by less than 4 cm^{-1} . It can be seen from Table III.A1 that the choice of excitation wavelength also affects this mode strongly, with

differences of 4.5 cm^{-1} , -14.7 cm^{-1} and 10.2 cm^{-1} observed upon changing the source from 532 nm to 660 nm for MgPc, AlPcCl and GaPcCl respectively[†].

Aroca and Jennings' results also show mismatches with DFT for the intense bands responsible for stimulated emission, indicating that the shift is not dependent on the substrate used in the experiment. The agreement with KBr Raman results is shown for MgPc^{25,20}, ZnPc²⁵, AlPcCl^{28,29} and GaPcCl²⁸ in Table III.10.

Table III.10: Frequencies of the Raman modes which correspond to the stimulated emission band for various phthalocyanine systems. Experimental values taken for H₂Pc and ZnPc come from the work of Murray⁶. Experimental values for MgPc, AlPcCl and GaPcCl were obtained with the 532 nm excitation wavelength. All values are reported in wavenumbers (cm^{-1}).

	DFT	DFT x 0.98	Exp	Shift
H ₂ Pc	1582.9	1551.3	1539.5	11.8
MgPc	1548.4	1517.4	1505.7	11.7
ZnPc	1557.2	1526.1	1506.8	19.3
AlPcCl	1597.0	1565.0	1509.2	55.8
GaPcCl	1583.5	1551.9	1532.9	19.0

The most intense bands in the Raman spectra of MgPc (M-PcCl) are the B_{1g} (B₂) modes. These modes correspond mostly to in-plane motions of the molecule, usually a C-H stretch coupled with a deformation of the isoindole units or the macrocycle. The A_{1g} (A₁) and B_{2g} (B₁) modes show medium intensity in most cases and correspond to fully symmetric or partially symmetric deformations on the isoindole rings or the macrocycle respectively. The E_g (E) modes are OPBs and are very weak and difficult to identify experimentally in most cases. The M-PcCl molecules, lacking a centre of inversion, also have 'in-plane' E modes, but these are strongly IR active and only very weakly Raman active. This effect will be investigated in more detail in the upcoming section.

[†] The mismatch of the Raman spectra recorded with the two excitation wavelengths points to a calibration issue. This has been discussed in greater detail in Chapter II.

III.5.III: Symmetry Effects on Vibrational Spectra

The two geometric forms (planar/domed) of M-TAPs and M-Pcs have been examined in relation to their structures in Section III.5.I. This section was primarily concerned with how the metal centre affects the planarity of the molecule and how much of a doming effect it exhibits on the porphyrin ring. This section is concerned with how the vibrational spectra of the M-TAPs and M-Pcs are affected by their symmetry. Non-planar M-TAPs and M-Pcs fall into the C_{4v} point group, which is a subgroup of D_{4h} , the point group pertaining to the planar systems. This means that the symmetry labels of the vibrational modes can be correlated as shown in Table III.11. Each symmetry block in C_{4v} corresponds to two in D_{4h} ; a symmetric and an asymmetric set. The symmetry or asymmetry is in relation to the centre of inversion in the molecule, something the non-planar molecules are lacking. The centre of inversion in the planar porphyrins means the rule of mutual exclusion applies to the vibrational modes of the molecule i.e. IR active modes cannot be Raman active and vice versa. The C_{4v} systems do not adhere to this rule, which means the vibrational spectra of the D_{4h} and C_{4v} M-TAPs and M-Pcs should show subtle differences.

III.5.III.a: Vibrational Spectra of the M-TAPs

M-TAP has 33 atoms resulting in 93 ($3N-6$) fundamental vibrational modes. These modes can be split up into symmetry blocks by applying the reduction formula to the reducible representations of the vibrational modes. In D_{4h} symmetry the vibrational modes of M-TAP are $A_{1u}(3)$, $A_{2u}(5)$, $B_{1u}(4)$, $B_{2u}(4)$, $E_u(32)$, $A_{1g}(8)$, $A_{2g}(7)$, $B_{1g}(8)$, $B_{2g}(8)$ and $E_g(14)$. In C_{4v} symmetry these are $A_1(13)$, $A_2(10)$, $B_1(12)$, $B_2(12)$, and $E(46)$. The correlations between the two sets of symmetry labels are presented in Table III.11.

Owing to the almost identical structures of the M-TAPs, the vibrational spectra are expected to exhibit strong similarities. This is evident in Figure III.13, which shows the calculated IR spectra of five M-TAPs. The most extreme shifts are expected to originate from the metal dependent vibrational modes. A pronounced shift on the band at $\sim 1000\text{ cm}^{-1}$ in Be and Mg TAPs to $\sim 970\text{ cm}^{-1}$ is observed for the Ca, Sr and Ba TAPs. The mode responsible for this shift is an M-N stretch and is clearly affected by both the mass of the metal ion and the symmetry of the molecule. The pair of weak bands located between 725 and 775 cm^{-1} in each molecule are both weakly metal dependent, and show a small shift as the mass of the metal changes.

The remainder of the peaks in the region shown are associated with deformations of the pyrrole rings and C-H bending modes. These particular modes are not strongly dependent on the choice of metal centre or the planarity of the molecules. The weak vibrational modes labelled 0 – 3 on the C_{4v} spectra are not present in the D_{4h} spectra due to the ‘rule of mutual exclusion’. These bands arise out of the lower symmetry of the Ca, Sr and Ba TAPs compared to Be and Mg TAP, which contain a centre of inversion.

Table III.11: Correlations of the symmetry blocks of D_{4h} and C_{4v} M-TAP and M-Pc molecules. Each symmetry block in C_{4v} corresponds to two in D_{4h} symmetry.

Sym	D_{4h}		C_{4v}		Sym
	M-TAP	M-Pc	M-TAP	M-Pc	
A_{1G}	8	14	13	22	A_1
A_{2U}	5	8			
A_{2G}	7	13	10	19	A_2
A_{1U}	3	6			
B_{2G}	8	14	12	21	B_1
B_{1U}	4	7			
B_{1G}	8	14	12	21	B_2
B_{2U}	4	7			
E_G	14	26	46	82	E
E_U	32	56			
Total	93	165	93	165	Total

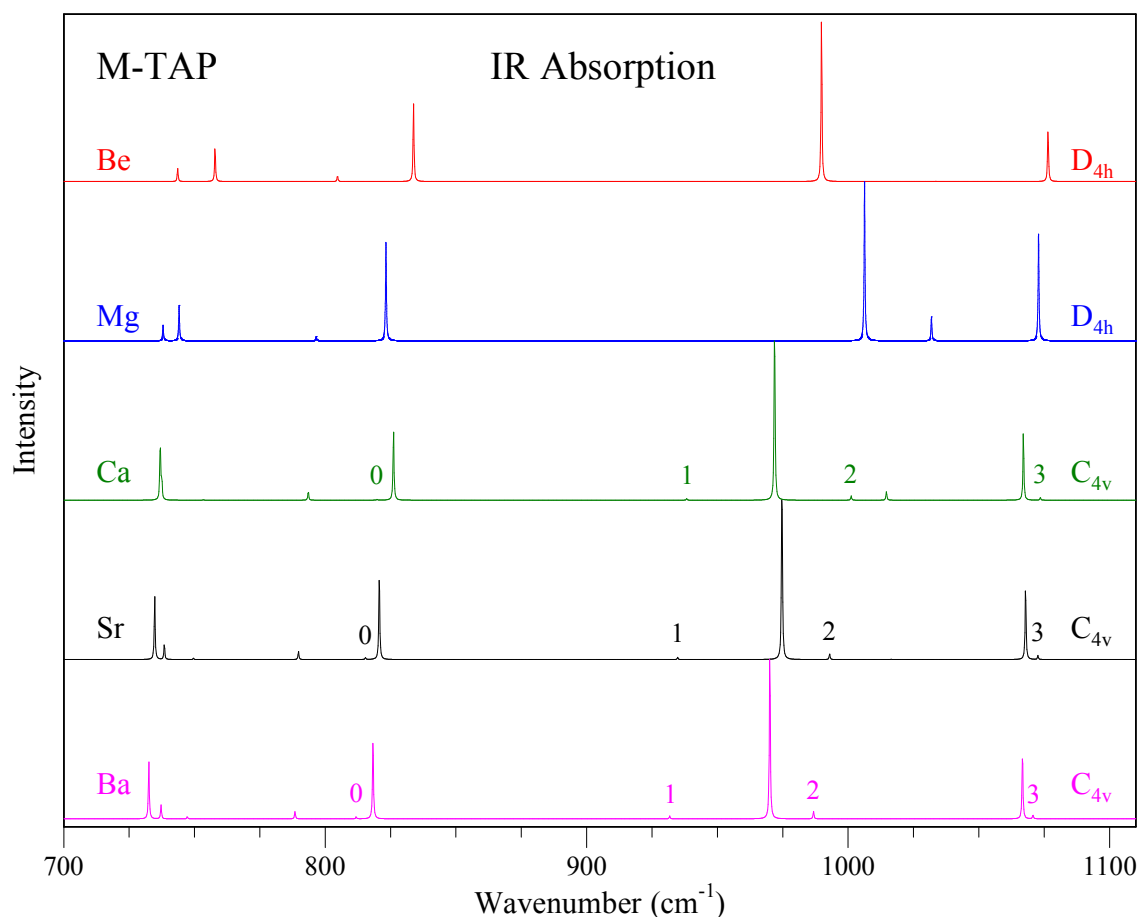


Figure III.13: Infrared absorption spectra of the s-block M-TAPs predicted by DFT calculations. The spectra shown were obtained within the harmonic approximation and frequencies are unscaled.

Figure III.14 shows a lower frequency region of the same spectra presented in Figure III.13. This is the region where most of the metal based vibrational modes are predicted to arise. It can be seen that the similarity of the spectra in Figure III.13 is lost in this region of the spectrum as the vibrational modes are highly sensitive to both the metal in the centre of the porphyrin cavity and the symmetry of the molecule. The peaks labelled 0 – 3 on the C_{4v} spectra arise due to symmetry arguments from group theory, similar to Figure III.13. The intense bands between 0 – 1 and 2 – 3 are the strongest metal dependent modes in this region and a clear trend is observed; as the mass of the metal increases, the vibrational frequency of the metal dependent modes decrease. This trend appears to continue for the D_{4h} molecules, with the bands at 387 and 404 cm^{-1} of MgTAP and BeTAP following the same pattern as the bands located in between 2 – 3 on the C_{4v} spectra. This trend breaks down, however, for MgTAP where the band at 225 cm^{-1} (highlighted with an asterisk) does

not follow the trend of the metal based modes between bands 0 and 1. Based on this trend, the band would be expected to appear around 280 cm^{-1} . The corresponding mode in BeTAP does follow the pattern, with the band arising at a frequency of 343 cm^{-1} .

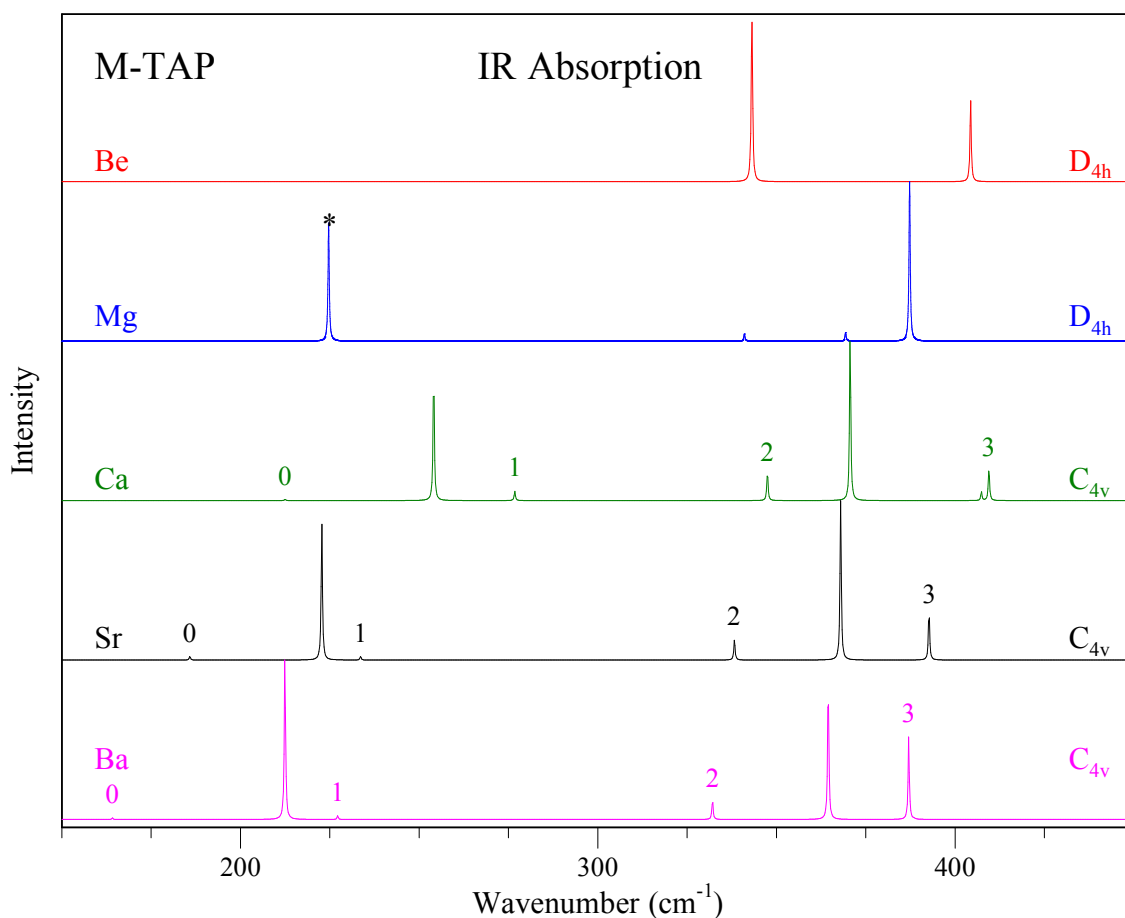


Figure III.14: Low frequency region of the IR spectra of the s-block M-TAPs calculated by DFT. The vibrational modes here shift around significantly depending on the metal at the centre of the cavity. The symmetry of the molecules also seems to have an effect on the spectra. All frequencies shown are unscaled.

An analysis of the computed vibrational spectra of MgTAP (D_{4h}) and CaTAP (C_{4v}) has been performed to investigate how the “rule of mutual exclusion” affects the vibration spectra of structurally related large molecules. These two metals were chosen as they are the most closely related which potentially show the change in molecular geometry. Experimental IR and Raman spectra exist for MgTAP³², but not for CaTAP. Good agreement between theory and experiment is observed for MgTAP, as is the case with MgPc. A region of the predicted IR and Raman spectra of MgTAP and CaTAP are presented in Figure III.15. The symmetry labels of each vibrational mode are shown to

help identify which bands correlate to one another. Overall a good agreement exists between the two spectra, but a couple of bands which shift by as much as 20 cm^{-1} , and a few intensity mismatches are observed. The result of most interest in this comparison is the medium intensity A_1 mode at 1403 cm^{-1} in the CaTAP spectrum. The Raman band correlates to the A_{1g} mode at 1426 cm^{-1} in MgTAP, but no corresponding bands occur in the infrared spectrum. Another IR and Raman active A_1 mode 1451 cm^{-1} in CaTAP corresponding to a Raman active A_{1g} peak at 1449 cm^{-1} is present, but no complementary IR peak in MgTAP is observed. The E modes of CaTAP have both IR and Raman intensity but only correlate to the IR active E_u modes in MgTAP. The high energy of these modes indicates that they are not metal dependent vibrational modes; they mostly occur at energies below 500 cm^{-1} , as shown in Figure III.14. The vector diagram and internal mode analysis confirms that this is the case. As the metal is the only other difference in their structure apart from the symmetry, this effect can be attributed to being caused purely by the symmetry of the molecule, and specifically the loss of the centre of inversion in the CaTAP molecule. This phenomenon is evident throughout the whole spectrum and the most pronounced examples of the mutual exclusion effect have been highlighted in bold in Table III.A2. This effect occurs on bands carrying significant intensity for the M-TAPs. Unfortunately, the effect is dampened for the Pcs, but has been observed both with DFT calculations and more significantly, experimentally. The upcoming section will deal with the mutual exclusion effect on the experimental spectra of AlPcCl and MgPc.

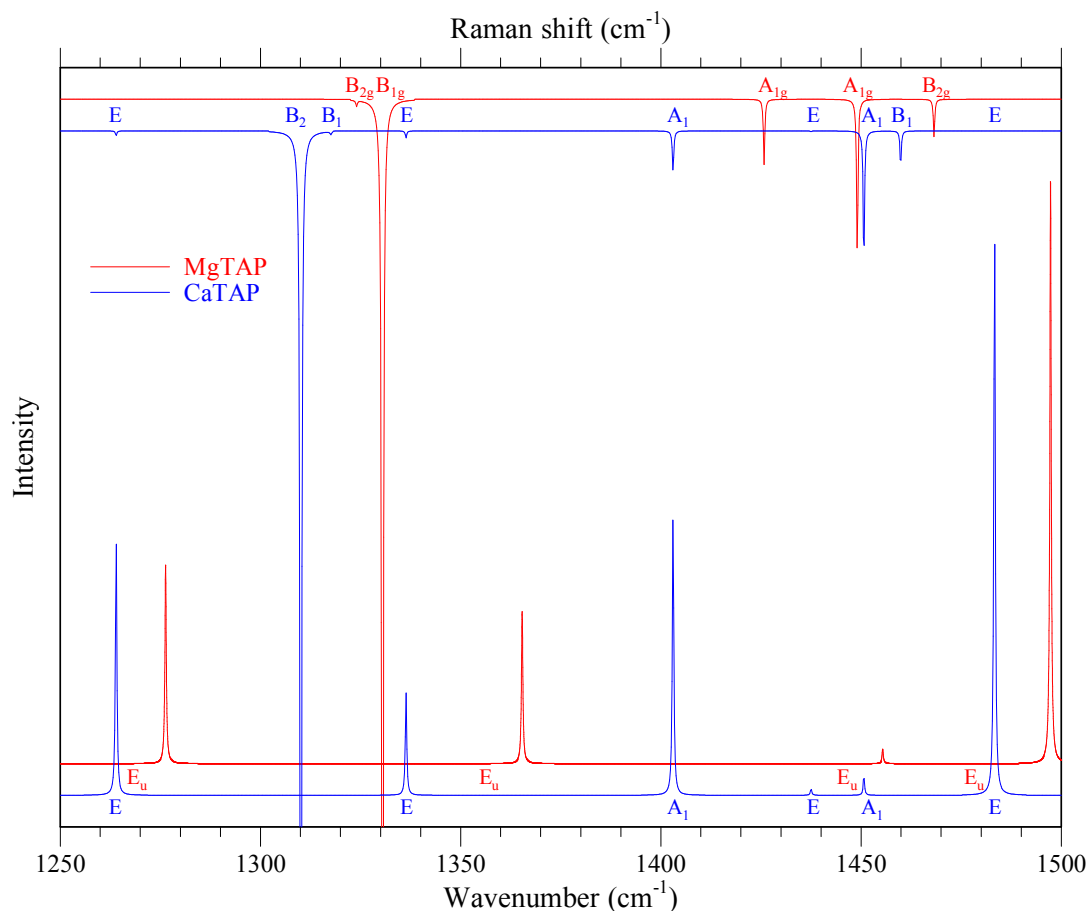


Figure III.15: IR and Raman spectra of the D_{4h} molecule MgTAP and C_{4v} molecule CaTAP. Each vibrational band has been labelled with its symmetry. This allows for easy identification of the correlations of modes between the molecules. ‘Extra’ peaks are observed in the CaTAP spectra, specifically IR active A_1 modes and Raman active E modes. The locations of the bands which gain the most intensity from the change in symmetry are highlighted in bold in Table III.A2.

III.5.III.b: Symmetry Influence on the Vibrational Spectra of the M-Pcs

M-Pcs with 57 atoms have 165 fundamental vibrational modes. The mode can be categorised as A_{1u} (6), A_{2u} (8), B_{1u} (7), B_{2u} (7), E_u (56), A_{1g} (14), A_{2g} (13), B_{1g} (14), B_{2g} (14) and E_g (26) in D_{4h} symmetry. The C_{4v} M-Pcs also have 165 vibrational modes, categorized as A_1 (22), A_2 (19), B_1 (21), B_2 (21), and E (82). The relationship between the irreducible representations of the two systems is presented in Table III.11. From this it can be clearly seen that the A_1 modes in C_{4v} symmetry split into the symmetric A_{1g} and asymmetric A_{2u} representations as a centre of inversion is introduced when the molecule becomes planar (D_{4h}). In the same manner, the A_2 modes split into A_{2g} and A_{1u} , the B_1 into B_{1u} and B_{2g} , the B_2 into B_{1g} and B_{2u} , and the E into $E_{g,u}$.

The Cl atom in the M-PcCls gives them 168 normal modes, categorised as $A_1(23)$, $A_2(19)$, $B_1(21)$, $B_2(21)$, and $E(84)$ for these C_{4v} molecules. The extra modes pertain to an Al-Cl stretch (A_1 symmetry) a degenerate pair of N-Al-Cl bends coupled with a twisting of the isoindole rings (E symmetry). A comparison of the vibrational frequencies, IR absorption intensities and Raman activities of AlPcCl and MgPc predicted by DFT is presented in Table III.A3. Frequencies are sorted by the symmetry blocks of AlPcCl and compared with the frequencies of MgPc. Upon lowering the symmetry from D_{4h} to C_{4v} the centre of inversion is lost, meaning the rule of mutual exclusion no longer applies to the vibrational modes. Modes which were exclusively IR or Raman active in D_{4h} symmetry can be both IR and Raman active in C_{4v} symmetry. It can be seen in Table III.A3 that the A_{1g} and A_{2u} modes of MgPc only show Raman and IR activity respectively, as predicted by the D_{4h} character tables. Conversely the A_1 modes of AlPcCl are both IR and Raman active. The Raman active B_1 modes of AlPcCl correspond to the Raman active B_{2g} modes and optically inactive B_{1u} modes in MgPc. A similar trend is observed with the B_2 modes of AlPcCl correlating to the Raman active B_{1g} and inactive B_{2u} modes of MgPc. The optically inactive B_{1u} and B_{2u} modes of MgPc show Raman activity in AlPcCl, but it is very weak. The same result is observed with the E_g and E_u modes of MgPc gaining weak IR and Raman activity respectively as the E modes of AlPcCl.

While many examples of bands which are only active in the AlPcCl molecule are observed, they are generally very weak, especially in comparison to the more intense bands in the spectrum. It is possible to use DFT results to identify these modes (highlighted in bold in Table III.A3), but several modes are strong enough to be observed experimentally. The spectra presented in Figure III.16 shows the mutual exclusion effect on the vibrational spectra of MgPc and AlPcCl. The Raman spectrum of MgPc between 770 and 850 cm^{-1} is shown in the left panel of Figure III.16 as the blue trace. Two bands are evident in the spectrum; a B_{1g} mode located at 780 cm^{-1} and an A_{1g} mode at 825 cm^{-1} . These peaks do not match up with any of the peaks in the IR spectrum shown as the red trace in the left panel. The corresponding regions are shown for AlPcCl in the right panel of Figure III.16. The A_1 peak at 833.5 cm^{-1} in the Raman spectrum (blue trace) clearly has a corresponding peak in the IR spectrum (red trace). A slight shift of 1 cm^{-1} (due to the different host environments) between the experimental peaks is observed, but the DFT spectra (black trace) shows that they are the same vibrational mode, having identical frequencies. Several more instances of this are observed in the region shown, with the bands at 777 and 785 cm^{-1} clearly showing

the relationship. The IR band at 802 cm^{-1} (E symmetry) does not appear to have a complementary Raman active mode, but the DFT results show a weakly Raman active mode in the correct wavenumber region.

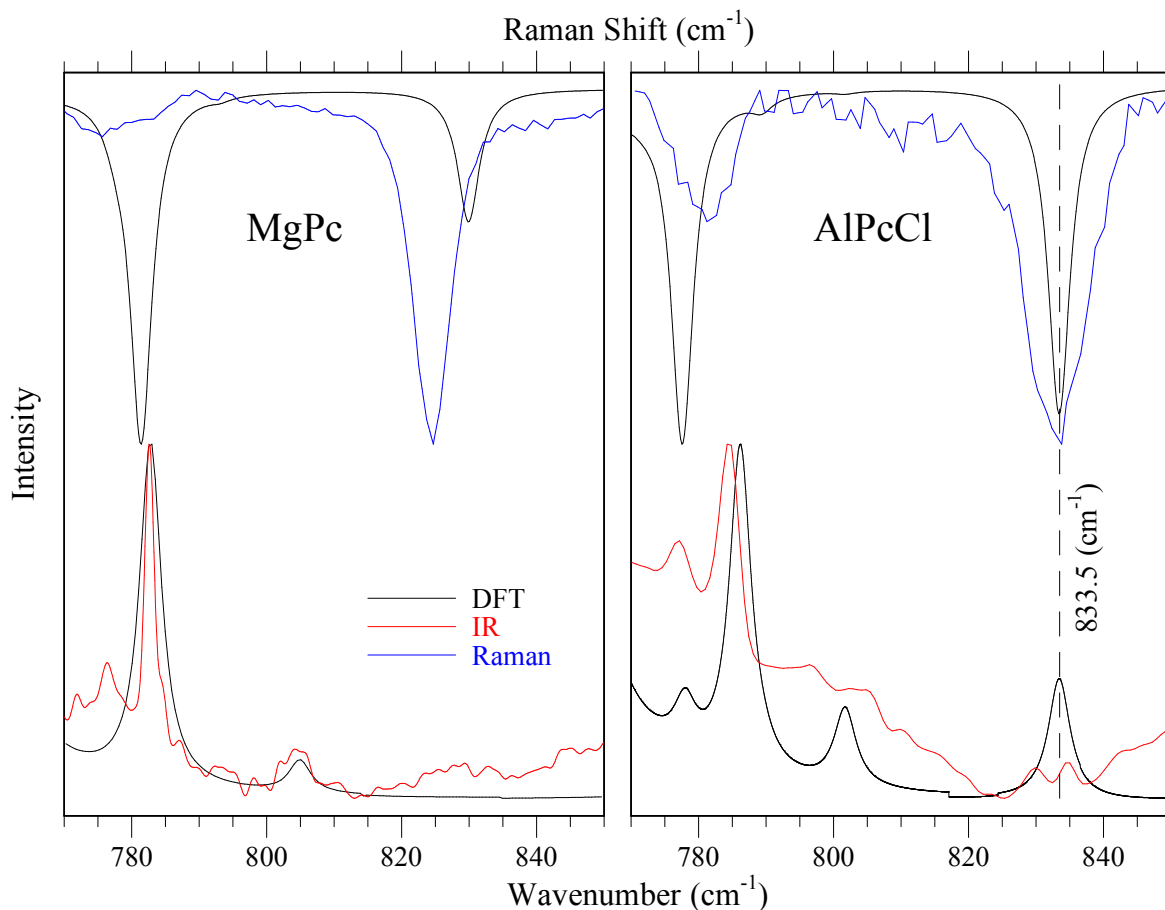


Figure III.16: The Infrared and Raman spectra of MgPc and AlPcCl in the 770 to 850 cm^{-1} region. Infrared spectra were recorded in N_2 and Ar matrices for MgPc and AlPcCl respectively. Raman spectra were recorded in KBr discs. The vibrational mode at 830 cm^{-1} in the AlPcCl spectra is both IR and Raman active. The equivalent Raman active mode of MgPc is located at 825 cm^{-1} . The corresponding MgPc mode does not have any IR intensity.

A similar trend is observed over the entire spectral region for these molecules, where several AlPcCl modes ‘gain’ IR or Raman activity under the reduced symmetry of C_{4v} . These modes have been highlighted in Table III.A3.

III.6: Conclusions

The structures of a number of M-TAPs and M-Pcs have been investigated with respect to their metal centres. A strong symmetry dependence is evident on the choice of the metal and dependent on whether or not it can fit into the macrocycle cavity. Where available, the structures predicted by DFT calculations agreed excellently with experimental data, giving confidence in the calculations on systems where no such data exists. The degree of non-planarity of the M-TAPs and M-Pcs was investigated with respect to changing the metal centre in the molecule. It was observed that the s-block metals lie the highest above the N₄ plane owing to their large atomic radii. The d-10 metals have smaller atomic radii than their same row s-block elements (the same principal quantum number), due to d-block contraction. This leads to the d-10 metals sitting lower above the N₄ plane than the s-block metals. The Al ion fits comfortably into the macrocycle cavity, as shown with the AlPc⁺ molecular cation. In contrast, the neutral AlPcCl molecule has the Al atom lying above the N₄ plane, meaning the Cl⁻ ion has the effect of ‘pulling’ the Al out of the porphyrin cavity. The large (ns)² metal atoms also cause a doming effect on the porphyrin ring. The extent on this doming is dependent on the height of the metal above the ring. Generally the higher the metal lies above the ring the more domed the rest of the molecule is.

The vibrational spectra of the M-TAPs and M-Pcs have been calculated using DFT and results have shown good agreement with both present experimental and literature results. The infrared spectroscopy of MgPc, AlPcCl and GaPcCl has been recorded in inert gas hosts at cryogenic temperatures. These spectra show highly resolved bands in the 400 cm⁻¹ to 1700 cm⁻¹ region. Spectra have also been recorded in room temperature KBr discs, which show a broadening of the peaks when compared to their matrix isolated counterparts. This has been attributed to the presence of aggregates in the KBr samples compared to the highly isolated molecules present in the matrix samples. Scaled DFT calculations were compared to experimental results and were shown to agree very well. A vibrational analysis of the IR active modes of MgPc (AlPcCl, GaPcCl) was performed and the spectra were found to consist of mostly A_{2u} (A₁) and E_u (E) symmetry, pertaining to OPBs and IPBs of the molecules respectively.

The Raman spectra of MgPc, AlPcCl and GaPcCl were recorded in room temperature KBr discs using two excitation wavelengths; a 532 nm and a 660 nm CW laser. Very slight deviations in the positions of the bands recorded with the different excitations was noted.

The intensity of certain Raman bands are enhanced due to resonance Raman effects caused by different excitation wavelengths. Scaled DFT results compared well with the experimental spectra, although the intensity of the modes below 1000 cm^{-1} was underestimated. An analysis of the Raman spectra shows that the Raman active modes which carry the most intensity are all IP vibrations, usually involving distortion of either the macrocycle or the isoindole units.

The effect of symmetry on the vibrational spectra of the M-TAPs and M-Pcs was studied. The IR spectra of the s-block M-TAPs were shown to have a somewhat different structure depending on whether the symmetry of the molecule was D_{4h} or C_{4v} . The IR and Raman spectra of MgTAP and CaTAP were investigated further and it was observed that many modes which appear in the CaTAP that do not correspond to anything in the MgTAP spectrum. This effect is associated with the rule of mutual exclusion and has to do with the loss of the centre inversion in CaTAP. This mutual exclusion effect was examined in the experimental spectra of AlPcCl and MgPc in which it was observed that certain vibrational modes which 'gain' enough intensity upon losing the centre of inversion to become active in C_{4v} symmetry where they were inactive in D_{4h} symmetry.

III.7: References

1. Henchy, C.; McCaffrey, J. G.; Arabei, S.; Pavich, T.; Galaup, J.-P.; Shafizadeh, N.; Crépin, C., Free base tetraazaporphine isolated in inert gas hosts: Matrix influence on its spectroscopic and photochemical properties. *The Journal of Chemical Physics* **2014**, *141* (12), -.
2. Jacox, M. E.; Thompson, W. E., The vibrational spectra of molecular ions isolated in solid neon. I. Carbon dioxide ion(1+) and ion(1-). *Journal of Chemical Physics*. **1989**, *91* (3), 1410-16.
3. Forney, D.; Jacox, M. E.; Thompson, W. E., The Mid- and Near-Infrared Spectra of Water and Water Dimer Isolated in Solid Neon. *Journal of Molecular Spectroscopy* **1993**, *157* (2), 479-493.
4. Raman, C. V., A change of wave length in light scattering. *Nature (London, U. K.)* **1928**, *121*, 619.

5. El-Nahass, M. M.; Atta, A. A.; El-Sayed, H. E. A.; El-Zaidia, E. F. M., Structural and optical properties of thermal evaporated magnesium phthalocyanine (MgPc) thin films. *Applied Surface Science* **2008**, *254* (8), 2458-2465.
6. Murray, C.; Dozova, N.; McCaffrey, J. G.; Shafizadeh, N.; Chin, W.; Broquier, M.; Crepin, C., Visible luminescence spectroscopy of free-base and zinc phthalocyanines isolated in cryogenic matrices. *Physical Chemistry Chemical Physics* **2011**, *13* (39), 17543-17554.
7. Arabei, S.; McCaffrey, J. G.; Galaup, J.-P.; Shafizadeh, N.; Crepin, C., Stimulated emission in cryogenic samples doped with free-base tetraazaporphine. *Physical Chemistry Chemical Physics* **2015**, Ahead of Print.
8. Zawadzka, A.; Karakas, A.; Plociennik, P.; Szatkowski, J.; Lukasiak, Z.; Kapceoglu, A.; Ceylan, Y.; Sahraoui, B., Optical and structural characterization of thin films containing metallophthalocyanine chlorides. *Dyes and Pigments* **2015**, *112*, 116-126.
9. Arillo-Flores, O. I.; Fadlallah, M. M.; Schuster, C.; Eckern, U.; Romero, A. H., Magnetic, electronic, and vibrational properties of metal and fluorinated metal phthalocyanines. *Physical Review B* **2013**, *87* (16), 165115.
10. Sliznev, V. V.; Girichev, G. V., Theoretical study of alkali metal complexes of porphyrin (M2P), porphyrazine (M2Pz) and phthalocyanine (M2Pc), M = Li, Na, K. *Makroeterotsikly* **2011**, *4* (1), 8-17.
11. Greenwood, N., *Chemistry of the Elements*. Academic Press, U.S. : 2007.
12. Kubiak, R.; Waškowska, A.; Śledź, M.; Jezierski, A., Synthesis, X-ray structures and characterization of beryllium phthalocyanine and (2-ethoxyethanol)-aqua-beryllium phthalocyanine. *Inorganica Chimica Acta* **2006**, *359* (5), 1344-1350.
13. Mizuguchi, J., *Journal of Physical Chemistry A* **2001**, *105*, 1121.
14. Scheidt, W. R.; Dow, W., Molecular stereochemistry of phthalocyanatozinc(II). *Journal of the American Chemical Society* **1977**, *99* (4), 1101-1104.
15. Kubiak, R.; Janczak, J., Coordination geometries of metal ions in metallophthalocyaninato complexes. *Crystal Research and Technology* **2001**, *36* (8-10), 1095-1104.

16. Tackley, D. R.; Dent, G.; Ewen Smith, W., Phthalocyanines: structure and vibrations. *Physical Chemistry Chemical Physics* **2001**, 3 (8), 1419-1426.
17. Murray, C.; Dozova, N.; McCaffrey, J. G.; FitzGerald, S.; Shafizadeh, N.; Crepin, C., Infra-red and Raman spectroscopy of free-base and zinc phthalocyanines isolated in matrices. *Physical Chemistry Chemical Physics* **2010**, 12 (35), 10406-10422.
18. Strenalyuk, T.; Samdal, S.; Volden, H. V., *Journal of Physical Chemistry A* **2008**, 112, 9075.
19. Wynne, K., *Journal of Inorganic Chemistry* **1984**, 23, 4658.
20. Napier, A.; Collins, R. A., FTIR characteristics of halogenated phthalocyanines exhibiting polymorphism. *Thin Solid Films* **1994**, 248 (2), 166-177.
21. Lever, A. B. P.; Minor, P. C., *Inorganic Chemistry* **1981**, 20, 4015.
22. Linsky, J. P.; Paul, T. R.; Nohr, R. S.; Kenney, M. E., Studies of a series of haloaluminum,-gallium, and-indium phthalocyanines. *Inorganic Chemistry* **1980**, 19 (10), 3131-3135.
23. Starke, M.; Hamann, C., Die elektrischen und thermoelektrischen Eigenschaften einiger polykristalliner Komplexe des Phthalocyanins mit drei- und vierwertigen Metallen. *Zeitschrift für anorganische und allgemeine Chemie* **1967**, 354 (1-2), 1-9.
24. Ziminov, A. V.; Ramsh, S. M.; Terukov, E. I.; Trapeznikova, I. N.; Shamanin, V. V.; Yurre, T. A., Correlation dependences in infrared spectra of metal phthalocyanines. *Semiconductors* **2006**, 40 (10), 1131-1136.
25. Aroca, R.; Zeng, Z. Q.; Mink, J., Vibrational assignment of totally symmetric modes in phthalocyanine molecules. *Journal of Physics and Chemistry of Solids* **1990**, 51 (2), 135-139.
26. Szybowicz, M.; Bala, W.; Fabisiak, K.; Paprocki, K.; Drozdowski, M., The molecular structure ordering and orientation of the metallophthalocyanine CoPc, ZnPc, CuPc, and MgPc thin layers deposited on silicon substrate, as studied by micro-Raman spectroscopy. *Journal of Material Science* **2011**, 46 (20), 6589-6595.

27. Jennings, C.; Aroca, R.; Hor, A.-M.; Loutfy, R. O., Raman spectra of solid films 3—Mg, Cu and Zn phthalocyanine complexes. *Journal of Raman Spectroscopy* **1984**, *15* (1), 34-37.
28. Jennings, C.; Aroca, R.; Hor, A.-M.; Loutfy, R. O., Raman spectra of solid films—V. Chloroaluminum, chlorogallium and chloroindium phthalocyanine complexes. *Spectrochimica Acta Part A: Molecular Spectroscopy* **1986**, *42* (9), 991-995.
29. Aroca, R.; Jennings, C.; Loutfy, R. O.; Hor, A.-M., Raman spectra of thin solid films—VI. Davydov splitting. *Spectrochimica Acta Part A: Molecular Spectroscopy* **1987**, *43* (6), 725-730.
30. Akimov, I. A.; Meshkov, A. M., Spectroscopy of Polymorphic Forms of Mg Phthalocyanine. *Optics & Spectroscopy* **2005**, *98* (3), 415-419.
31. Wilson, E. B., Jr.; Decius, J. C.; Cross, P. C., *Molecular Vibrations*. McGraw-Hill Book Co.: 1955; p 388 pp.
32. Gorski, A.; Gawinkowski, S.; Starukhin, A.; Gladkov, L.; Chizhova, N.; Mamardashvili, N.; Scheblykin, I.; Waluk, J., Resonance Raman and FTIR spectra of Mg-porphyrazines. *Journal of Molecular Structure* **2014**, *1058*, 197-204.

Table III.A1: Raman frequencies (in cm^{-1}) of MgPc, AlPcCl and GaPcCl recorded in room temperature KBr discs with 523 and 660 nm CW laser excitation and predicted by DFT calculations. Scaled DFT results show excellent agreement with experimental values in most instances.

MgPc					AlPcCl					GaPcCl				
532	660	DFT x	DFT	Sym	532	660	DFT x	DFT	Sym	532	660	DFT x	DFT	Sym
nm	nm	0.98	Raw		nm	nm	0.98	Raw		nm	nm	0.98	Raw	
-	-	21.2	21.6	B _{2U}	22.5	-	19.0	19.4	B ₂	-	-	20.2	20.7	B ₂
-	-	31.2	31.8	A _{2U}	41.2	-	40.2	41.0	A ₁	-	-	35.7	36.5	A ₁
-	-	62.6	63.9	B _{1U}	45.2	-	44.8	45.7	B ₁	-	-	51.0	52.0	B ₁
-	-	58.4	59.6	E _G	-	-	56.2	57.3	E	-	-	52.8	53.9	E
-	-	-	-	-	91.9	-	92.0	93.9	E	90.9	-	88.8	90.6	E
111.2	-	109.0	111.2	B _{2G}	100.9	-	114.8	117.1	B ₁	114.7	-	113.7	116.0	B ₁
-	-	135.1	137.8	B _{2U}	131.1	137.4	130.7	133.4	B ₂	124.7	-	129.2	131.8	B ₂
127.7	-	123.6	126.1	E _G	-	-	132.4	135.1	E	146.1	135.7	129.7	132.4	E
178.1	172.8	178.5	182.2	B _{1G}	166.2	180.7	164.2	167.5	B ₂	175.0	165.0	158.3	161.6	B ₂
224.2	221.8	221.0	225.5	B _{2G}	-	-	213.9	218.3	B ₁	217.0	221.0	215.3	219.6	B ₁
232.8	234.9	231.9	236.6	E _G	-	-	250.2	255.3	E	-	-	240.2	245.1	E
-	-	240.2	245.1	B _{2U}	249.2	-	250.0	255.1	B ₁	254.0	237.4	244.0	249.0	B ₁
251.3	246.2	249.7	254.8	A _{1G}	250.7	250.1	250.5	255.6	A ₁	254.0	242.2	249.1	254.2	A ₁
-	-	-	-	-	297.0	-	288.1	294.0	A ₁	290.6	284.8	275.3	280.9	A ₁
-	-	283.9	289.7	E _G	-	310.9	305.6	311.8	E	-	-	303.1	309.3	E
-	-	347.1	354.2	A _{2U}	361.5	-	352.2	359.4	A ₁	-	347.3	345.4	352.4	A ₁
485.7	480.0	479.5	489.3	B _{2G}	492.8	484.2	485.7	495.6	B ₁	494.3	483.9	483.3	493.1	B ₁
-	-	-	-	-	469.7	-	473.5	483.2	A ₁	-	-	356.2	363.5	A ₁
-	-	523.6	534.3	B _{1U}	521.9	-	516.4	526.9	B ₁	-	-	517.8	528.4	B ₁
557.5	554.9	558.3	569.7	B _{1G}	564.8	-	555.8	567.1	B ₂	-	-	553.4	564.7	B ₂
589.5	584.3	586.0	598.0	A _{1G}	594.4	590.7	589.4	601.4	A ₁	599.4	590.2	588.7	600.7	A ₁

690.3	681.3	676.2	690.0	A _{1G}	694.5	680.5	681.4	695.3	A ₁	683.5	674.4	678.0	691.9	A ₁
-	-	687.3	701.3	B _{2G}	-	-	691.1	705.3	B ₁	692.2	691.7	689.8	703.9	B ₁
-	-	700.7	715.0	B _{2U}	-	-	701.7	716.0	B ₂	702.2	701.4	698.8	713.1	B ₂
-	-	727.0	741.8	E _G	694.5	721.3	728.2	743.1	E	-	-	724.4	739.2	E
743.5	745.9	748.9	764.2	B _{1G}	750.6	751.5	754.7	770.1	B ₂	758.6	747.8	753.0	768.4	B ₂
776.6	776.1	781.4	797.4	B _{1G}	784.2	784.2	777.6	793.4	B ₂	784.5	773.7	776.9	792.7	B ₂
790.8	792.4	793.1	809.3	E _G	790.9	-	778.0	793.9	E	-	-	776.2	792.0	E
-	-	793.1	809.3	E _G	808.4	-	789.4	805.5	E	-	-	788.3	804.4	E
829.9	824.1	829.9	846.9	A _{1G}	835.5	832.8	833.5	850.5	A ₁	838.4	826.9	833.6	850.6	A ₁
872.88	-	880.4	898.3	E _G	-	-	878.7	896.6	E	-	-	879.1	897.1	E
954.5	946.4	941.1	960.3	B _{2G}	956.3	957.3	960.0	979.6	B ₁	960.8	951.2	954.8	974.2	B ₁
970.8	-	959.0	978.6	E _G	-	-	960.3	979.9	E	-	-	960.1	979.7	E
1016.1	1006.1	1009.2	1029.8	B _{1G}	-	-	1007.9	1028.4	B ₂	1013.6	1002.3	1008.4	1029.0	B ₂
1016.1	-	1009.7	1030.3	A _{1G}	-	1005.0	1008.5	1029.1	A ₁	1013.6	1002.3	1009.0	1029.6	A ₁
1034.3	1033.3	1031.9	1053.0	B _{2G}	1040.6	1034.7	1042.9	1064.2	B ₁	1046.6	1039.8	1042.2	1063.5	B ₁
1114.8	1107.8	1108.3	1130.9	B _{2G}	1096.0	1105.5	1106.3	1128.9	B ₁	1113.5	1103.8	1107.9	1130.5	B ₁
-	-	1115.1	1137.9	E _U	1120.2	1132.8	1120.1	1143.0	E	-	-	1118.8	1141.6	E
1127.6	1121.5	1122.3	1145.2	A _{1G}	-	-	1132.5	1155.6	A ₁	1125.0	1131.4	1130.1	1153.1	A ₁
1146.4	1139.4	1141.6	1164.9	B _{1G}	1151.3	1141.2	1144.0	1167.3	B ₂	1152.5	1140.4	1143.7	1167.1	B ₂
1170.9	1157.0	1162.4	1186.1	A _{1G}	1179.3	1159.6	1166.2	1190.0	A ₁	1171.6	1162.6	1164.9	1188.7	A ₁
1196.7	1179.2	1180.7	1204.8	B _{1G}	1202.6	1188.6	1182.5	1206.6	B ₂	1184.6	1181.4	1181.7	1205.9	B ₂
1122.7	1198.2	1205.7	1230.4	B _{2G}	1225.6	1212.2	1199.3	1223.7	B ₁	1211.1	1208.0	1202.2	1226.7	B ₁
1309.1	1302.6	1304.1	1330.7	B _{2G}	1314.0	1302.7	1307.0	1333.7	B ₂	-	1302.1	1303.9	1330.5	B ₂
1309.1	1302.6	1305.5	1332.1	B _{1G}	-	-	1307.8	1334.5	B ₁	-	1302.1	1306.9	1333.5	B ₁
1341.9	1336.4	1336.5	1363.8	A _{1G}	1346.4	1339.6	1340.4	1367.8	A ₁	1346.0	1335.2	1339.1	1366.4	A ₁
1341.9	1336.4	1341.6	1369.0	B _{1G}	-	-	1347.6	1375.1	B ₂	1346.0	1335.2	1345.5	1373.0	B ₂
1372.6	-	1394.2	1422.7	A _{1G}	-	-	1401.3	1429.9	A ₁	1412.0	1404.2	1396.8	1425.4	A ₁
1414.1	1416.0	1417.7	1446.7	B _{2G}	-	-	1457.0	1486.8	B ₁	1449.7	1439.4	1449.5	1479.1	B ₁
-	-	1456.6	1486.3	E _U	1419.3	1428.4	1427.6	1456.7	E	-	-	1422.1	1451.1	E

1424.3	1422.4	1424.1	1453.1	A _{1G}	1440.4	1441.7	1440.1	1469.5	A ₁	1437.8	1427.9	1435.8	1465.1	A ₁
1451.6	1445.4	1448.4	1477.9	B _{1G}	1452.8	1448.6	1456.2	1485.9	B ₂	1457.8	1446.6	1453.6	1483.3	B ₂
1478.8	1481.8	1479.3	1509.4	B _{2G}	1481.5	1499.9	1485.9	1516.3	B ₁	1482.1	1490.7	1483.5	1513.7	B ₁
1484.6	-	1494.0	1524.5	A _{1G}	1562.8	1532.7	1534.7	1566.0	A ₁	1495.4	1506.2	1521.4	1552.5	A ₁
1505.9	1501.4	1517.4	1548.4	B _{1G}	1509.2	1523.9	1565.0	1597.0	B ₂	-	-	1551.9	1583.5	B ₂
1589.5	1570.5	1581.3	1613.6	B _{1G}	1594.0	1590.4	1589.8	1622.2	B ₂	1532.9	1522.7	1586.4	1618.8	B ₂
1592.1	-	1584.2	1616.5	A _{1G}	1594.0	1593.2	1591.8	1624.3	A ₁	1596.8	1609.1	1589.0	1621.4	A ₁
1612.6	1606.3	1609.3	1642.2	B _{2G}	1615.6	1608.6	1611.0	1643.9	B ₁	1613.9	1631.1	1610.6	1643.5	B ₁

Table III.A2: DFT results of the vibrational frequencies (in cm^{-1}) of CaTAP and MgTAP. Vibrational frequencies have been correlated based on the information in Table III.10. CaTAP modes which gain significant intensity/activity when compared to their inactive counterparts in MgTAP have been highlighted in bold.

C_{4v}	CaTAP			D_{4h}	MgTAP		
Sym	Frequency (cm^{-1})	IR Intensity	Raman Activity	Sym	Frequency (cm^{-1})	IR Intensity	Raman Activity
A ₁	95.21	0.74	2.84	A _{2U}	50.51	0.07	0
A ₁	254.10	42.97	6.86	A _{2U}	203.91	46.69	0
A ₁	347.49	9.90	33.94	A _{2U}	367.16	4.05	0
A ₁	407.37	2.91	64.60	A _{1G}	391.94	0	106.26
A ₁	697.56	2.58	8.46	A _{1G}	701.53	0	11.95
A ₁	737.49	36.72	1.50	A _{2U}	736.39	41.42	0
A ₁	826.13	152.88	5.05	A _{2U}	828.27	175.44	0
A ₁	1001.18	8.81	152.04	A _{1G}	1021.71	0	152.32
A ₁	1073.53	5.84	2.23	A _{1G}	1080.78	0	0.13
A ₁	1403.05	29.69	28.57	A _{1G}	1425.81	0	43.24
A ₁	1450.71	2.06	96.33	A _{1G}	1449.06	0	106.58
A ₁	1563.97	0.21	211.14	A _{1G}	1561.32	0	200.93
A ₁	3257.48	0.10	953.32	A _{1G}	3259.78	0	1011.52
A ₂	313.85	0	0	A _{1U}	318.62	0	0
A ₂	464.25	0	0	A _{2G}	471.77	0	0
A ₂	721.24	0	0	A _{1U}	725.38	0	0
A ₂	799.31	0	0	A _{2G}	796.34	0	0
A ₂	937.81	0	0	A _{1U}	941.04	0	0
A ₂	996.69	0	0	A _{2G}	1004.30	0	0
A ₂	1207.59	0	0	A _{2G}	1219.43	0	0
A ₂	1339.75	0	0	A _{2G}	1339.95	0	0
A ₂	1467.81	0	0	A _{2G}	1468.20	0	0
A ₂	3238.65	0	0	A _{2G}	3241.73	0	0
B ₁	92.08	0	2.43	B _{1U}	99.02	0	0
B ₁	183.92	0	12.27	B _{2G}	217.85	0	13.62
B ₁	440.84	0	5.37	B _{2G}	435.05	0	6.34
B ₁	500.51	0	2.39	B _{1U}	504.08	0	0
B ₁	761.77	0	8.89	B _{1U}	764.54	0	0
B ₁	813.52	0	12.61	B _{2G}	818.39	0	12.98
B ₁	938.30	0	0.10	B _{1U}	941.51	0	0
B ₁	1036.24	0	19.15	B _{2G}	1049.96	0	19.84
B ₁	1192.23	0	12.36	B _{2G}	1200.23	0	15.36
B ₁	1317.58	0	2.02	B _{2G}	1324.00	0	3.84
B ₁	1459.90	0	25.22	B _{2G}	1468.23	0	25.44
B ₁	3238.91	0	490.41	B _{2G}	3241.96	0	508.00
B ₂	55.32	0	1.12	B _{2U}	60.55	0	0
B ₂	162.83	0	14.10	B _{2U}	174.96	0	0
B ₂	270.90	0	11.28	B _{1G}	264.58	0	24.55
B ₂	675.11	0	0.67	B _{2U}	681.00	0	0
B ₂	757.38	0	110.63	B _{1G}	761.85	0	103.77

B ₂	819.80	0	6.80	B _{2U}	822.39	0	0
B ₂	1002.84	0	115.09	B _{1G}	1021.40	0	148.57
B ₂	1075.56	0	91.62	B _{1G}	1076.87	0	124.94
B ₂	1310.10	0	935.54	B _{1G}	1330.48	0	1005.17
B ₂	1519.05	0	2379.72	B _{1G}	1517.73	0	2403.49
B ₂	1561.50	0	196.83	B _{1G}	1555.84	0	298.36
B ₂	3257.26	0	257.21	B _{1G}	3259.60	0	287.41
E	117.26	1.78	1.39	E _G	120.77	0	1.14
E	212.51	0.21	0.37	E _G	223.00	0	0.26
E	276.80	1.55	0.41	E _U	342.40	1.51	0
E	370.64	27.52	0.09	E _U	388.28	32.26	0
E	461.52	0.42	0.02	E _G	462.19	0	0.66
E	409.48	5.58	0.46	E _U	531.17	0.08	0
E	692.78	3.55	2.98	E _G	697.16	0	2.94
E	736.90	61.31	0.04	E _U	744.96	40.25	0
E	753.38	0.41	1.50	E _G	756.03	0	1.74
E	793.51	9.28	0.57	E _U	798.35	5.65	0
E	819.83	0.84	0.44	E _G	825.20	0	0.65
E	938.24	1.61	0.06	E _G	941.45	0	0.10
E	971.89	191.09	0.26	E _U	995.63	172.87	0
E	1014.65	8.90	0.53	E _U	1030.69	35.73	0
E	1067.04	69.30	0.00	E _U	1069.73	91.43	0
E	1177.28	0.09	1.34	E _U	1189.83	0.53	0
E	1263.95	13.49	1.60	E _U	1268.37	8.98	0
E	1336.38	5.26	2.38	E _U	1356.15	6.75	0
E	1437.52	0.34	0.27	E _U	1446.45	0.45	0
E	1483.34	30.85	0.02	E _U	1481.97	25.78	0
E	1551.09	97.40	5.46	E _U	1546.61	91.92	0
E	3238.79	0.61	6.42	E _U	3241.86	0.25	0
E	3257.35	7.36	32.55	E _U	3259.66	4.18	0

Table III.A3: DFT results of the vibrational frequencies (in cm^{-1}) of AlPcCl and MgPc. Vibrational frequencies have been correlated based on the information in Table III.10. AlPcCl modes which gain significant intensity/activity when compared to their inactive counterparts in MgPc have been highlighted in bold. Corresponding experimental values can be located in Table III.2, Table III.3 and Table III.A1.

C_{4v}		AlPcCl		D_{4h}		MgPc	
Sym	Freq	IR Intensity	Raman Activity	Sym	Freq	IR Intensity	Raman Activity
A ₁	40.98	2.16	0.74	A _{2U}	31.81	0.27	0
A ₁	172.26	5.44	0.21	A _{2U}	150.63	28.64	0
A ₁	255.58	0.25	70.68	A _{1G}	254.76	0	72.25
A ₁	293.97	0.01	3.13	A _{2U}	263.95	5.20	0
A ₁	359.43	6.51	5.41	A _{2U}	354.20	0.57	0
A ₁	443.16	26.91	0.27	A _{2U}	447.11	11.56	0
A ₁	483.16	91.08	7.10	-	-	-	-
A ₁	601.41	1.05	63.80	A _{1G}	598.01	0	100.50
A ₁	695.31	0.01	320.44	A _{1G}	690.02	0	337.39
A ₁	753.76	281.31	0.01	A _{2U}	751.07	263.55	0
A ₁	802.24	11.92	1.16	A _{2U}	799.08	21.80	0
A ₁	850.46	4.41	226.48	A _{1G}	846.86	0.00	197.69
A ₁	980.23	2.73	0.04	A _{2U}	978.82	3.71	0
A ₁	1029.09	0.24	505.28	A _{1G}	1030.3	0	529.33
A ₁	1155.59	0.61	727.46	A _{1G}	1145.2	0	1255.51
A ₁	1189.96	0.40	582.47	A _{1G}	1186.1	0	401.21
A ₁	1367.76	1.75	2733.99	A _{1G}	1363.7		2185.04
A ₁	1429.87	8.14	532.55	A _{1G}	1422.6	0	577.07
A ₁	1469.50	0.02	210.73	A _{1G}	1453.1	0	608.78
A ₁	1565.98	0.00	785.28	A _{1G}	1524.5	0	630.80
A ₁	1624.27	0.25	170.24	A _{1G}	1616.5	0	109.11
A ₁	3189.94	0.07	743.12	A _{1G}	3187.4	0.00	617.55
A ₁	3208.38	0.14	1327.42	A _{1G}	3204.7	0	1454.21
A ₂	117.79	0	0	A _{1U}	123.02	0	0
A ₂	217.14	0	0	A _{2G}	213.13	0	0
A ₂	434.48	0	0	A _{1U}	446.04	0	0
A ₂	590.85	0	0	A _{2G}	588.85	0	0
A ₂	630.77	0	0	A _{2G}	625.80	0	0
A ₂	638.58	0	0	A _{1U}	639.08	0	0
A ₂	802.19	0	0	A _{1U}	808.31	0	0
A ₂	873.73	0	0	A _{2G}	862.59	0	0
A ₂	896.40	0	0	A _{1U}	898.50	0	0
A ₂	1008.00	0	0	A _{1U}	1006.7	0	0
A ₂	1120.24	0	0	A _{2G}	1116.0	0	0
A ₂	1127.32	0	0	A _{2G}	1154.6	0	0
A ₂	1218.19	0	0	A _{2G}	1208.6	0	0
A ₂	1328.62	0	0	A _{2G}	1324.5	0	0
A ₂	1510.96	0	0	A _{2G}	1474.3	0	0
A ₂	1529.06	0	0	A _{2G}	1507.5	0	0

A ₂	1641.03	0	0	A _{2G}	1639.8	0	0
A ₂	3176.17	0	0	A _{2G}	3173.7	0	0
A ₂	3205.23	0	0	A _{2G}	3201.1	0	0
B ₁	45.68	0	0.27	B _{1U}	63.85	0	0
B ₁	117.14	0	12.63	B _{2G}	111.21	0	12.98
B ₁	218.27	0	0.08	B _{2G}	225.54	0	29.61
B ₁	255.09	0	36.15	B _{1U}	225.91	0	0
B ₁	495.62	0	112.13	B _{2G}	489.33	0	122.55
B ₁	526.94	0	0.97	B _{1U}	534.28	0	0
B ₁	696.59	0	3.28	B _{2G}	701.34	0	4.61
B ₁	705.25	0	5.60	B _{1U}	701.92	0	0
B ₁	804.15	0	0.40	B _{1U}	807.63	0	0
B ₁	896.62	0	0.01	B _{1U}	897.97	0	0
B ₁	979.62	0	54.35	B _{2G}	960.32	0	32.66
B ₁	1008.36	0	0.01	B _{1U}	1007.1	0	0
B ₁	1064.23	0	224.81	B _{2G}	1052.9	0	146.96
B ₁	1128.87	0	486.10	B _{2G}	1130.9	0	420.14
B ₁	1223.74	0	619.93	B _{2G}	1230.3	0	814.29
B ₁	1334.48	0	484.86	B _{2G}	1330.6	0	496.61
B ₁	1486.76	0	324.76	B _{2G}	1446.6	0	282.41
B ₁	1516.27	0	167.63	B _{2G}	1509.4	0	248.54
B ₁	1643.91	0	89.04	B _{2G}	1642.1	0	51.99
B ₁	3176.21	0	423.36	B _{2G}	3173.7	0	404.04
B ₁	3205.43	0	321.30	B _{2G}	3201.2	0	346.24
B ₂	19.42	0	0.09	B _{2U}	21.62	0	0
B ₂	133.42	0	4.22	B _{2U}	137.84	0	0
B ₂	167.52	0	15.70	B _{1G}	182.16	0	15.69
B ₂	296.83	0	1.03	B _{2U}	245.10	0	0
B ₂	434.24	0	0.48	B _{2U}	433.78	0	0
B ₂	567.12	0	5.71	B _{1G}	569.72	0	5.36
B ₂	716.00	0	11.58	B _{2U}	714.96	0	0
B ₂	770.10	0	1009.37	B _{1G}	764.20	0	870.20
B ₂	787.69	0	3.62	B _{2U}	788.10	0	0
B ₂	793.42	0	213.17	B _{1G}	797.37	0	513.23
B ₂	979.64	0	0.06	B _{2U}	978.42	0	0
B ₂	1028.44	0	263.83	B _{1G}	1029.8	0	253.24
B ₂	1167.30	0	2161.73	B _{1G}	1164.8	0	2998.36
B ₂	1206.62	0	1302.10	B _{1G}	1204.8	0	1762.44
B ₂	1333.66	0	5299.85	B _{1G}	1332.1	0	4872.34
B ₂	1375.12	0	1393.48	B _{1G}	1369.0	0	1976.24
B ₂	1485.90	0	2027.59	B _{1G}	1477.9	0	2095.32
B ₂	1596.95	0	19915.46	B _{1G}	1548.3	0	20262.4
B ₂	1622.21	0	184.91	B _{1G}	1613.5	0	145.97
B ₂	3189.85	0	697.72	B _{1G}	3187.3	0	671.89
B ₂	3208.13	0	70.36	B _{1G}	3204.4	0	101.00
E	57.34	0.33	1.92	E _G	59.59	0	0.17
E	93.88	1.12	3.80	-	-	-	-
E	124.72	3.75	0.04	E _U	122.43	4.28	0
E	135.09	0.08	2.86	E _G	126.08	0	5.16

E	255.32	0.14	0.89	E _G	236.62	0	2.08
E	301.08	0.98	0.44	E _G	289.67	0	0.03
E	311.82	3.58	0.42	E _U	290.89	5.88	0
E	391.41	4.29	0.05	E _U	427.77	0.02	0
E	434.82	0.03	0.00	E _G	434.43	0	0
E	501.44	0.67	0.01	E _G	509.75	0	0.03
E	527.84	11.42	0.00	E _U	514.87	8.07	0
E	587.27	7.01	0.05	E _U	589.81	11.88	0
E	652.38	3.62	0.19	E _G	660.50	0	0.03
E	659.17	4.84	0.06	E _U	663.02	4.25	0
E	743.09	0.34	0.21	E _G	741.83	0	0.29
E	773.62	58.12	0.72	E _U	770.73	62.06	0
E	793.89	0.89	12.20	E _G	793.59	0	17.28
E	805.50	0.12	4.55	E _G	809.29	0	2.73
E	818.09	1.42	0.85	E _U	820.19	1.08	0
E	896.60	0.01	0.33	E _G	898.32	0	0.39
E	921.18	58.48	0.09	E _U	909.64	61.04	0
E	979.92	0.02	0.40	E _G	978.62	0	0.27
E	1008.24	0.00	0.35	E _G	1006.8	0	0.25
E	1028.69	12.57	0.43	E _U	1030.0	11.02	0
E	1087.16	136.92	1.19	E _U	1082.6	204.08	0
E	1096.60	132.95	0.61	E _U	1102.7	150.99	0
E	1142.98	159.63	0.54	E _U	1137.8	127.65	0
E	1190.04	24.20	0.37	E _U	1188.8	20.59	0
E	1220.68	0.16	0.73	E _U	1209.7	1.53	0
E	1324.98	46.96	0.01	E _U	1319.0	48.87	0
E	1350.26	35.91	3.86	E _U	1346.0	6.36	0
E	1365.62	227.49	0.92	E _U	1359.7	250.50	0
E	1456.69	83.08	0.08	E _U	1432.5	37.49	0
E	1508.56	23.80	0.00	E _U	1486.3	32.44	0
E	1520.34	1.64	0.24	E _U	1504.5	104.09	0
E	1546.11	50.64	1.50	E _U	1508.9	2.29	0
E	1622.01	7.80	0.67	E _U	1614.5	6.96	0
E	1642.69	13.72	0.03	E _U	1641.0	10.48	0
E	3176.18	6.52	0.23	E _U	3173.7	6.15	0
E	3189.88	29.97	2.03	E _U	3187.3	30.21	0
E	3205.33	6.83	0.10	E _U	3201.2	9.95	0
E	3208.21	38.50	0.74	E _U	3204.5	47.40	0

Table III.A4: DFT results of the vibrational frequencies (in cm^{-1}) of GaPcCl. Values shown here are unscaled and obtained within the harmonic approximation. The corresponding experimental results are given in Table III.4 and

Table III.A1.

GaPcCl			
Sym	Frequency	IR	Raman
		Intensity	Activity
A ₁	36.46	1.65	1.03
A ₁	147.14	9.65	0.10
A ₁	254.22	0.15	62.34
A ₁	280.93	0.95	11.29
A ₁	352.41	4.41	7.40
A ₁	363.46	60.30	5.44
A ₁	443.74	10.69	0.04
A ₁	600.70	0.15	83.18
A ₁	691.86	0.00	330.52
A ₁	749.59	252.79	0.12
A ₁	797.17	29.13	0.76
A ₁	850.63	3.85	198.31
A ₁	979.96	2.88	0.05
A ₁	1029.64	0.31	511.57
A ₁	1153.15	0.59	947.57
A ₁	1188.72	0.35	541.21
A ₁	1366.39	2.85	2504.66
A ₁	1425.35	12.63	546.26
A ₁	1465.11	0.03	293.00
A ₁	1552.47	0.24	775.31
A ₁	1621.39	0.47	127.76
A ₁	3189.78	0.11	712.90
A ₁	3207.77	0.20	1359.57
A ₂	119.40	0	0
A ₂	215.81	0	0
A ₂	436.70	0	0
A ₂	589.48	0	0
A ₂	631.99	0	0
A ₂	636.60	0	0
A ₂	802.56	0	0
A ₂	871.09	0	0
A ₂	896.99	0	0
A ₂	1008.13	0	0
A ₂	1119.70	0	0
A ₂	1143.06	0	0
A ₂	1215.24	0	0
A ₂	1327.80	0	0
A ₂	1509.89	0	0
A ₂	1518.35	0	0
A ₂	1640.65	0	0
A ₂	3176.09	0	0
A ₂	3204.52	0	0
B ₁	52.01	0	0.46
B ₁	115.97	0	12.62
B ₁	219.65	0	0.53
B ₁	249.02	0	34.75

B ₁	493.13	0	112.93
B ₁	528.39	0	1.29
B ₁	696.72	0	3.75
B ₁	703.88	0	6.17
B ₁	803.47	0	0.58
B ₁	897.12	0	0.01
B ₁	974.24	0	58.73
B ₁	1008.52	0	0.01
B ₁	1063.49	0	158.16
B ₁	1130.51	0	456.64
B ₁	1226.73	0	678.73
B ₁	1333.54	0	483.08
B ₁	1479.08	0	328.55
B ₁	1513.74	0	193.03
B ₁	1643.46	0	69.04
B ₁	3176.13	0	415.95
B ₁	3204.71	0	327.77
B ₂	20.66	0	0.14
B ₂	131.83	0	7.64
B ₂	161.57	0	13.78
B ₂	285.85	0	1.29
B ₂	432.75	0	0.31
B ₂	564.69	0	6.16
B ₂	713.10	0	9.75
B ₂	768.38	0	927.43
B ₂	786.94	0	18.37
B ₂	792.74	0	291.82
B ₂	979.44	0	0.08
B ₂	1028.99	0	256.76
B ₂	1167.06	0	2355.22
B ₂	1205.85	0	1430.07
B ₂	1330.49	0	5126.95
B ₂	1372.99	0	1445.38
B ₂	1483.27	0	1986.28
B ₂	1583.52	0	20003.13
B ₂	1618.79	0	1.46
B ₂	3189.69	0	692.65
B ₂	3207.53	0	76.78
E	53.86	0.40	2.71
E	90.58	0.98	3.08
E	121.70	2.95	0.04
E	132.40	0.32	3.22
E	245.11	4.85	0.57
E	257.05	1.27	0.90
E	293.07	1.45	0.53
E	309.30	2.41	0.28
E	432.73	0.06	0.00
E	502.69	1.03	0.02
E	517.32	8.23	0.00
E	585.86	8.02	0.06
E	650.94	6.83	0.26
E	655.88	0.73	0.01
E	739.17	0.17	0.41
E	769.94	51.69	0.84
E	792.00	1.39	13.26
E	804.42	0.07	2.93
E	815.61	1.27	0.85
E	897.08	0.04	0.33
E	914.44	57.23	0.06
E	979.71	0.03	0.32
E	1008.39	0.00	0.31

E	1029.20	11.00	0.62
E	1092.42	141.39	1.12
E	1098.53	128.48	1.10
E	1141.62	153.44	0.99
E	1190.36	24.68	0.44
E	1217.21	0.43	1.36
E	1323.56	45.28	0.04
E	1347.09	38.01	4.36
E	1363.32	238.69	1.17
E	1451.08	80.51	0.29
E	1504.18	28.20	0.03
E	1514.32	0.17	0.28
E	1533.01	61.95	1.98
E	1619.24	7.51	0.80
E	1642.21	12.88	0.04
E	3176.10	6.26	0.38
E	3189.72	29.20	3.15
E	3204.62	7.08	0.15
E	3207.60	39.41	1.25

Chapter IV: A DFT Study of Reversed Isotope Shifts in H/D Substitution of Free-base Tetrapyrroles

IV.1: Introduction

This chapter presents a theoretical study on the effect of performing an isotopic substitution of the inner hydrogens on the free-base analogues of porphine (H₂P), tetraazaporphyrin (H₂TAP), tetrabenzo porphyrin (H₂TBP) and phthalocyanine (H₂Pc). The capability of the DFT method in accurately describing the ground state structures and vibrational spectra of porphyrins was established in Chapter III. The upcoming work builds on this observation by analysing molecules containing isotopes of various masses, specifically the masses of the inner hydrogen atoms of selected porphyrin molecules are changed.

The tautomerism exhibited by the free-base tetrapyrroles, in which the two inner hydrogen atoms migrate between opposite pairs of the four central nitrogens, has been studied with a wide variety of both experimental¹ and theoretical² means. Of the methods applied, vibrational spectroscopy is a direct means of probing the mechanism underlying the tautomerism since the N-H stretch and in-plane bending modes have been proposed to be involved. In spectroscopic work, isotope substitution³ is a well-known tool in achieving reliable vibrational analysis, with substitution of hydrogen (H) by deuterium (D) by far the most utilised as it produces the largest frequency shifts due to the approximate factor of two difference in the masses of the isotopes⁴. Arising from the inverse relationship between mode frequency, ν , and the reduced mass, μ , given by the expression

$$\nu = \frac{1}{2\pi} \sqrt{\frac{k}{\mu}} \quad \text{Eq. IV.1}$$

in which k is the force constant, the heavier isotope is thereby expected to occur at lower values. This behaviour assists greatly in making mode assignments in experimental spectra. Moreover, for the free-base tetrapyrroles H₂/D₂ substitution of the two inner hydrogens is particularly appealing as the D_{2h} molecular symmetry is maintained, allowing direct comparisons between the two isotopomers.

However, in a recent combined IR/Raman and high level, density functional theory (DFT) study of free-base phthalocyanine (Pc), Murray *et al.*⁵ observed quite peculiar behaviour

upon H₂/D₂ substitution whereby the frequency of one particular mode of the deuterium isotopomer was found to be higher than that of hydrogen. The mode in question is the IR-active out-of-plane bending mode observed in Ar matrices at 722.7 cm⁻¹ for H₂Pc but which shifts up to 729.9 cm⁻¹ in D₂Pc. The observed isotope shift ratio (ISR) of 0.990, determined as the $\nu_{\text{H}}/\nu_{\text{D}}$ ratio, was very well reproduced in the theoretical DFT results. To probe whether this unusual, reversed ISR (< 1) effect is a peculiarity of Pc, the theoretical work in the present study has been extended to cover the three most closely related free-base tetrapyrroles, namely porphyrin (P), tetraaza-porphyrin (TAP) and tetrabenzo-porphyrin (TBP). The structures of all four molecules are provided in Figure IV.1 revealing the strong similarities of these molecules.

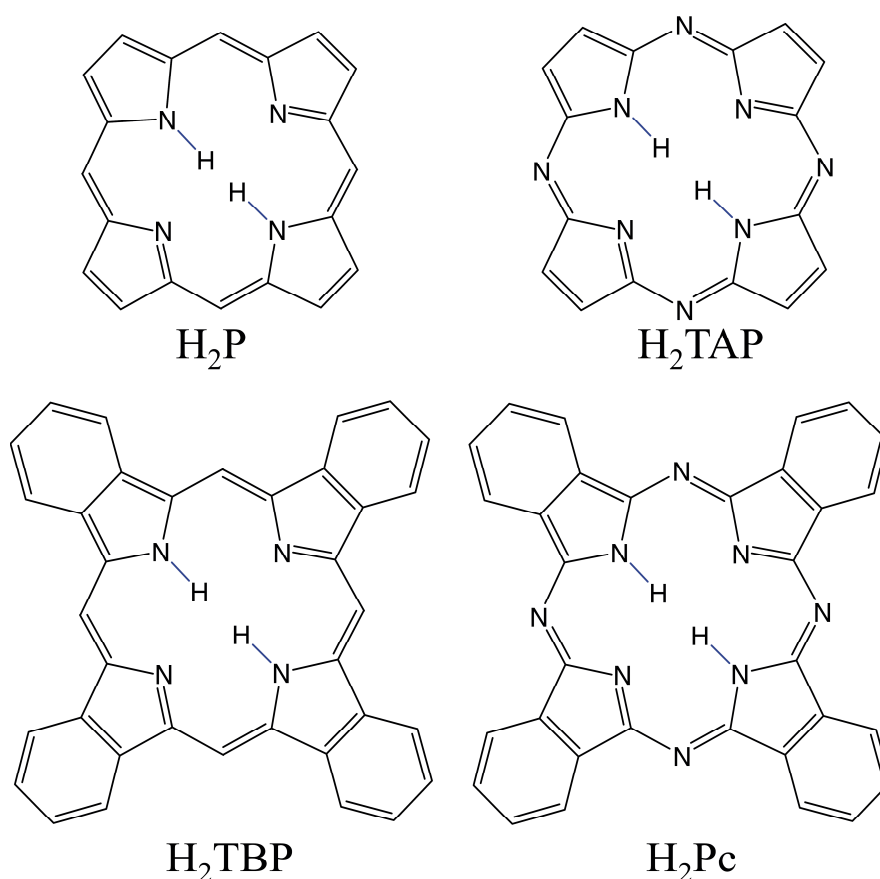


Figure IV.1: Structures of the four closely related free-base tetrapyrrole molecules, namely porphine (H₂P), tetraaza-porphyrin (H₂TAP), tetrabenzo-porphyrin (H₂TBP) and phthalocyanine (H₂Pc) whose vibrational frequency shifts upon H/D isotope substitution have been studied by the DFT method. The bond lengths and bond angles found in the DFT/B3LYP geometry optimisations are provided in Table IV.1 for the four molecules. With the present method, all are found to have high (D_{2h}) symmetry.

A theoretical prediction of such a reversed isotope shift effect ($ISR < 1$) was made several years ago by Li and Zgierski⁶ in their work on developing a local mode description of the vibrations in the porphyrins – both free-base and metallo-porphyrins. Their vibrational analysis was based on a valence force field and conducted with the Wilson-GF matrix⁷ method. However, as will be shown ahead, the upward shifts in the heavier isotope were much larger than what has been seen with the force fields generated in the present quantum chemical method. This earlier work⁶ seems only to have considered only the N-H stretches and in-plane bends. However, as Murray *et al.* found experimentally⁵, the most easily identifiable instance of the reversed ISR effect in the phthalocyanines involved an out-of-plane N-H bending motion. A more recent DFT calculation of free-base phthalocyanine by Liu *et al* also found a reverse ISR^{8,9} but the Authors presented no analysis of the origins of this effect.

Table IV.1: A summary of a group theoretical analysis the normal modes of vibration for the four tetra-pyrrole molecules examined in the present work. The values in parenthesis are the numbers of atoms in each of the molecules. On the right hand side the symmetries of the six possible N-H motions are provided for an analysis conducted with the z-axis co-linear with the two central N-H bonds. The abbreviations STR, IPB and OPB represent the N-H stretching, in-plane bending and out-of-plane bending modes respectively.

D_{2h}	Species				N-H vibration modes		
	H ₂ P	H ₂ TAP	H ₂ TBP	H ₂ Pc	STR	IPB	OPB
A_g	19	17	31	29	✓		
B_{1g}	8	7	14	13			
B_{2g}	9	8	15	14			✓
B_{3g}	18	16	30	28		✓	
A_u	8	7	14	13			
B_{1u}	18	16	30	28	✓		
B_{2u}	18	16	30	28		✓	
B_{3u}	10	9	16	15			✓
#Modes	108	96	180	168			

A group theoretical analysis of the four free-base tetrapyrroles, all belonging to the D_{2h} point group, provides the symmetry types and numbers of the normal vibrational modes of the molecules being studied. The results of such an analysis, in which the z-axis is aligned

with the two central N-H bonds, are collected in Table IV.1. As expected, the numbers of modes in the two tetra-aryl molecules (tetrabenzo-porphyrin and phthalocyanine) are much larger due to the increase in the number of atoms, N . For the purposes of illustration, the material presented herein will concentrate on the smaller parent molecules porphine and tetraazaporphyrin. However, in all four molecules the symmetry types of the 6 modes involving N-H motion are the same and can be compared with the complete normal vibrational modes in Table IV.1.

The main goal then is to establish the correlations between similar NH and ND modes and to rationalize the observed and calculated frequency shifts. Calculating normal mode frequencies with incremental (artificial) variation of the masses of H from 1 to 2 clearly show these correlations. When the NH(D) motion is predominant, the H to D evolution in the normal mode frequency will decrease in a continuous manner. In the case of two modes of the same symmetry and whose frequencies are similar, their frequency evolutions could cross, depending on the extent of NH(D) motion involved in them. The evolution diagrams will thus show avoided crossings of various extents which thereby inform on the degree of the NH(D) motion in the modes. If both normal modes involve similar atomic motions, including the NH(D) one, they will be distorted around the mass of H corresponding to the crossing, in order to avoid it. This is similar to the well-known characteristic of avoided crossing found in potential energy surfaces for electronic states with the same spatial symmetry. It allows an analysis of the underlying mode interactions and situations where $ISR < 1$ are present are especially studied in the current work¹⁰.

IV.2: Computational Methods

In the present study the density functional theory (DFT) was utilised with the 6-311g++(2d,2p) basis set for both geometry optimisations and the calculation of the vibrational frequencies. The present calculations were conducted with the Gaussian-03 suite of programmes running, as described in Chapter II, on a Linux workstation with two quad-core processors. All the calculated vibrational frequencies presented in this work are, unless stated otherwise, unscaled values obtained within the harmonic approximation.

Due to the unintuitive nature of the effect being analysed, the approach taken in calculating the vibrational frequencies, involves increasing the masses between H and D

incrementally, in steps of 0.05 amu, so that the evolution of the modes from the light to the heavy isotopomer can be followed in a near-continuous manner. This is the approach utilised in the earlier work by Murray and co-workers⁵. Recently this method has been applied successfully by Wright and co-workers¹¹ in their work on re-numbering the vibrational modes of benzene and its fluoro-derivatives. The task in the present analysis is to track the mass dependence of the normal modes to see where they cross but more importantly, it is to identify where curve-avoidance occurs and analyse the underlying mode coupling which produce ISR values less than 1. In doing this we exploit the high symmetries found in the optimised geometries of the free-base tetrapyrroles. Accordingly, this analysis is done on normal modes of the same symmetry with a particular focus on those modes involving the N-H vibrations. As mentioned earlier, and shown in Table IV.1, there are only 3 types of N-H motions but 6 distinct symmetries are involved.

In order to analyse details of the atomic motions producing the reverse isotope substitution ratios (ISR values < 1) the contributions of the internal coordinates to the normal modes of a given symmetry type have been extracted. The internal mode contributions to a specific normal mode are expressed as percentages which were generated directly in the Gaussian-03 package and implemented with the “freq=internal” command in the input file¹².

IV.3: Results

The optimised geometries obtained with the DFT B3LYP method and the 6-311g++(2d,2p) basis set for the four free-base tetrapyrrole molecules studied are shown in Figure IV.1. Complete listings of the geometric parameters for the free-base tetrapyrroles, porphine (P), tetraaza-porphyrin (TAP), tetrabenzo-porphyrin (TBP) and phthalocyanine (Pc) are provided in Table IV.2. In all cases, high (D_{2h}) symmetry was preserved in the geometry optimisations and no imaginary low frequencies were found. These results indicate that the planar geometry is the most stable in all four molecules.

Table IV.2: A summary of the geometric parameters obtained with the DFT/B3LYP optimization conducted in the present work on the four free-base tetrapyrrole molecules, porphine (H₂P), tetraaza-porphyrin (H₂TAP) and tetrabenzo-porphyrin (H₂TBP) and phthalocyanine (H₂Pc). The atom labelling for TAP and Pc follows standard notation used in Figure III.1. The labelling system for P and TBP follows that of TAP and Pc respectively, with the exception of the N_m atoms being replaced by C_m-H_m atoms.

Length(Å)	P	TAP	TBP	Pc
N-H	1.0104	1.0076	1.0112	1.009
N-C _α	1.3692	1.3701	1.3709	1.375
C _α -C _m	1.3900	N/A	1.3839	N/A
C _α -N _m	N/A	1.3195	N/A	1.313
C _α -C _β	1.4316	1.4436	1.4448	1.45
C _β -C _β	1.368	1.3616	1.413	1.409
C _β -H ₁	1.0768	1.0759	N/A	N/A
C _β -C _γ	N/A	N/A	1.3985	1.394
C _γ -C _δ	N/A	N/A	1.3828	1.386
C _δ -C _δ	N/A	N/A	1.4073	1.406
C _γ -H ₁	N/A	N/A	1.0812	1.08
C _δ -H ₂	N/A	N/A	1.0812	1.081
N'-C _{α'}	1.3600	1.3593	1.3598	1.362
C _{α'} -C _m	1.3961	N/A	1.3949	N/A
C _{α'} -N _m	N/A	1.3338	N/A	1.332
C _m -H _m	1.0812	N/A	1.0806	N/A
C _{α'} -C _{β'}	1.457	1.4657	1.4632	1.465
C _{β'} -C _{β'}	1.3521	1.3466	1.404	1.4
C _{β'} -H _{1'}	1.078	1.0766	N/A	N/A
C _{γ'} -C _{γ'}	N/A	N/A	1.3931	1.389
C _{γ'} -C _{δ'}	N/A	N/A	1.3894	1.392
C _{δ'} -C _{δ'}	N/A	N/A	1.4014	1.401
C _{γ'} -H _{1'}	N/A	N/A	1.0818	1.081
C _{δ'} -H _{2'}	N/A	N/A	1.0814	1.081
Angle (°)				
H-N-C _α	124.5724	124.5932	123.6462	123.736
N-C _α -C _m	125.652	N/A	126.1288	N/A
N-C _α -N _m	N/A	127.7457	N/A	128.100
C _α -N-C _α	110.8552	110.8136	112.7076	112.527

N-C _α -C _β	106.5301	106.5535	106.1348	106.135
C _α -C _β -C _β	108.0423	108.0397	107.5114	107.601
C _α -C _β - H ₁	124.3741	123.3376	N/A	N/A
C _β -C _β - H ₁	127.5835	128.6226	N/A	N/A
C _β -C _β -C _γ	N/A	N/A	120.5013	120.960
C _β -C _γ -C _δ	N/A	N/A	118.4767	117.829
C _γ -C _δ -C _δ	N/A	N/A	121.022	121.211
C _β -C _γ -H ₁	N/A	N/A	121.1432	120.586
C _γ -C _δ -H ₂	N/A	N/A	119.696	119.622
C _α -C _β - H	115.9102	N/A	115.3433	N/A
C _{α'} -C _β - H	116.9554	N/A	116.3284	N/A
N'-C _{α'} - C _m	125.5188	N/A	125.6994	N/A
N'-C _{α'} - N _m	N/A	127.5626	N/A	121.688
C _α -N'-C _{α'}	105.7553	105.5281	107.6054	107.226
N'-C _{α'} -C _{β'}	110.8457	111.0377	110.5212	110.697
C _{α'} -C _{β'} -C _{β'}	106.2767	106.1983	105.6761	105.690
C _α -C _{β'} - H ₁	125.4496	124.2356	N/A	N/A
C _{β'} -C _{β'} - H ₂	128.2737	129.5661	N/A	N/A
C _{β'} -C _{β'} -C _{γ'}	N/A	N/A	120.7253	121.223
C _{β'} -C _{γ'} -C _{δ'}	N/A	N/A	118.3937	117.670
C _{γ'} -C _{δ'} -C _{δ'}	N/A	N/A	120.8811	121.107
C _{β'} -C _{γ'} -H _{1'}	N/A	N/A	121.4854	120.925
C _{γ'} -C _{δ'} -H _{2'}	N/A	N/A	119.7205	119.636

In the present H/D isotope substitution study we are focussed on the vibrations involving N-H motion of which there are three types. As indicated in Table IV.1 the N-H stretching (STR) modes are the A_g and B_{1u} symmetries corresponding to the Raman-active symmetric and IR-active asymmetric vibrations respectively. The N-H In-Plane Bending (IPB) modes are of B_{3g} and B_{2u} symmetry, arising from the in-phase and out-of-phase bending motions which are Raman-active and IR-active respectively. The N-H Out-of-Plane Bending (OPB) modes are of B_{2g} and B_{3u} symmetry – the Raman-active in-phase and IR-active out-of-phase modes respectively. The behaviour of each of these three N-H modes will now be analysed on the basis of the six possible symmetries that they possess.

From the results provided in Table IV.1 one might expect that the H/D isotope dependence of the N-H Out-of-Plane Bending (OPB) mode would be the easiest to follow. For instance, in H₂TAP the OPB mode is 1 of only 8 (B_{2g}) modes while the N-H stretch should be the most difficult, being 1 of 19 (A_g) modes. In H₂TBP this stretching mode is 1 of 31 modes. However, as has been found experimentally⁵ for H₂Pc, identifying the OP bending in H/D substitution is far from obvious when the frequency of this mode in D₂Pc increases. The contrasting behaviour of these modes arises, as will be elaborated later, for two reasons. The first is that the N-H stretch modes occur at high frequencies, energetically distinct from all other modes except for the C-H stretching modes, while the In-Plane Bending (IPB) and OPB modes occur in congested regions where multiple mode crossings may occur. The second reason is that the internal N-H stretching modes are very well localised on the N-H bonds. In contrast, avoided-crossings occur in the IP and OP bending motions rendering mode attributions in the deuterium isotopomer difficult.

IV.3.I: N-H Stretching (A_g and B_{1u}) Modes

The frequencies of the N-H stretching modes are shown in Figure IV.2 and Figure IV.3 for the four molecules studied P, TAP, TBP and Pc as a function of incrementally increasing the H-atom mass from 1 to 2 amu. Taking porphyrin as an example, (upper left in Figure IV.2) the Raman-active (but weak) A_g N-H stretching mode crosses directly over three C-H stretching modes and continues to decrease monotonically from 3593.5 cm⁻¹ in H₂P to 2638.3 cm⁻¹ in D₂P. This corresponds to a shift of 955.2 cm⁻¹ and a ν_H/ν_D (ISR) ratio of 1.362. This value is close to the expected value of approximately $\sqrt{2}$ for H/D isotopic substitution of a normal mode involving nearly pure N-H motion. The solid curve in Figure IV.2 shows the theoretical mass dependence ($1/\sqrt{m_H}$) given by Equation IV.1. It is evident that the agreement between the predicted data and this theoretical dependence is good.

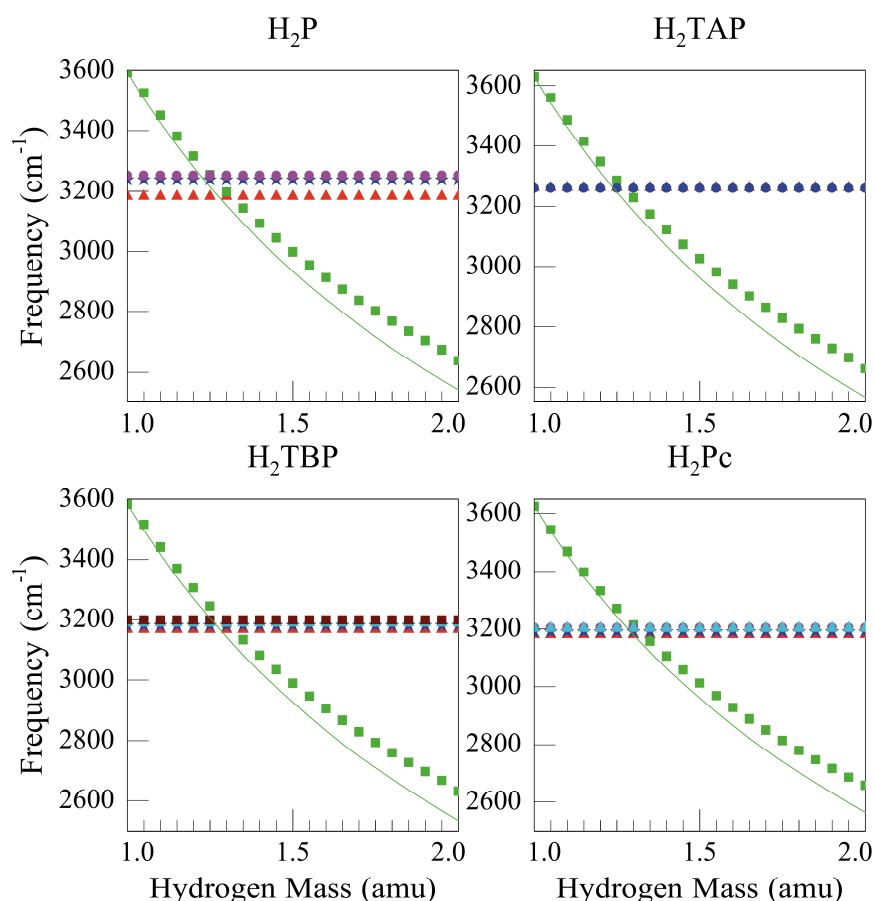


Figure IV.2: Dependence of the vibrational frequencies of the Raman-active N-H stretch (A_g symmetry) normal modes of the four (D_{2h}) free-base tetrapyrrole molecules with H/D isotope substitution of the two inner hydrogens. The values shown are harmonic results calculated by increasing the H mass from 1 to 2 in increments of 0.05 amu. The solid trace provides the predicted dependence of the frequency on the square root of the mass, indicating close agreement with the calculated values. The frequencies of the C-H stretching modes are completely unaffected by the H/D isotope substitution of the two inner hydrogens.

The mass dependence of the strong IR-active B_{1u} mode, shown in Figure IV.3 exhibits a similar pattern with the N-H stretch at 3552.3 cm^{-1} in H₂P crossing over three C-H stretches as the masses of the central hydrogens are increased. The N-D mode has a frequency of 2611.9 cm^{-1} , which gives a ν_H/ν_D ratio of 1.360. This pattern is observed for the three other molecules studied as illustrated in Figure IV.3. H₂TAP is the simplest having the least number of C-H modes, 2 in number. In contrast the tetra-aryl molecules, TBP and Pc have numerous C-H modes. However, in all cases direct crossings of the normal modes occur indicating the absence of coupling between NH(D) stretching modes and CH stretching modes.

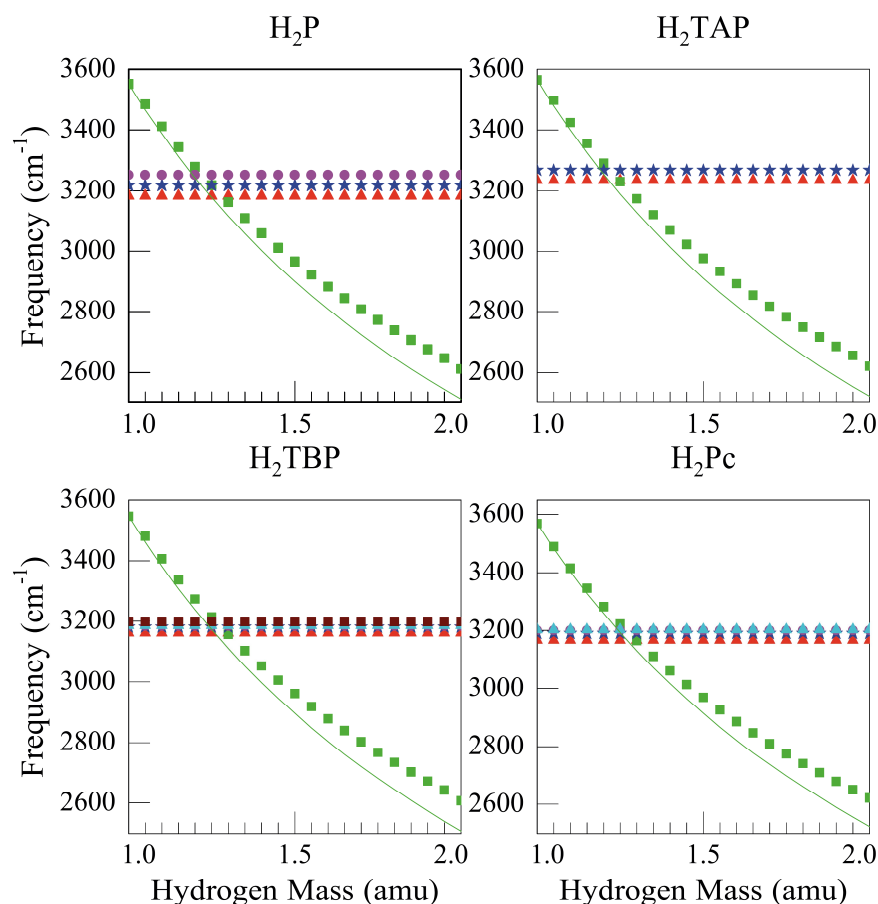


Figure IV.3: As for Figure IV.2 except for the IR-active B_{1u} symmetry normal modes.

The frequencies of the N-H stretching modes of P, TAP, TBP and Pc are collected in the upper section of Table IV.3 for the light and heavy isotopomers. The ISR (v_H/v_D) values calculated from these frequencies are listed for the two symmetries involved. From the values provided in Table IV.3 it is clear that they span a small range from 1.364, for the A_g mode of phthalocyanine (Pc), to 1.360 for the B_{1u} mode of porphyrin (P). It is evident that for the A_g and B_{1u} symmetries presented in Figure IV.2 and Figure IV.3 respectively that the N-H stretching mode passes directly through the C-H stretching modes in all four molecules without any interaction amongst these high frequency modes. An examination of the C-H stretching modes reveals that the change in their frequencies, after being crossed by the N-H modes, is extremely small. In all cases except TBP where it is 0.04 cm^{-1} , these changes are in the third decimal place. With this small magnitude, these shifts are less than the uncertainty of the method and are not considered significant.

An analysis of the internal modes reveals the small deviation of the calculated ISR values (1.36) from $\sqrt{2}$ arises from the involvement of the pyrrole ring deformation which accompanies the N-H stretching motion for kinematic reasons. No other internal motions are involved in these nearly pure NH(D) modes. See the upper panels of Table IV.4 and Table IV.5 for details of the % internal N-H stretch modes of the smaller tetrapyrroles, TAP and porphyrin respectively.

Table IV.3: H/D isotope shifts for the 6 internal N-H modes of the four tetrapyrrole molecules studied. All frequencies are unscaled DFT results given in wavenumber units. The isotope shift ratios (ISR) are calculated as ratio $\nu_{\text{H}}/\nu_{\text{D}}$ i.e., the hydrogen frequency divided by the deuterium value. ISR values significantly less than one are highlighted in bold as they are indicative of strongly avoided-crossings.

Motion	Molecule	ν_{H2}	ν_{D2}	Shift	$\nu_{\text{H}}/\nu_{\text{D}}$	ν_{H2}	ν_{D2}	Shift	$\nu_{\text{H}}/\nu_{\text{D}}$
N-H Stretch		B_{1u}				A_g			
	P	3552.34	2611.88	940.46	1.3601	3593.47	2638.31	955.16	1.3620
	TAP	3565.39	2621.13	944.25	1.3602	3629.13	2661.83	967.30	1.3634
	TBP	3546.71	2606.78	939.93	1.3606	3583.25	2630.36	952.89	1.3623
	Pc	3569.08	2621.36	947.73	1.3615	3625.17	2657.21	967.96	1.3643
N-H OP Bend		B_{3u}				B_{2g}			
	P	739.89	541.8	198.09	1.3656	631.22	473.78	157.44	1.3323
		651.38	657.91	-6.53	0.9901	NC	NC		
	TAP	760.83	547.66	213.17	1.3892	641.4	479.74	161.66	1.3370
		656.65	664.47	-7.82	0.9882	NC	NC		
	TBP	766.76	560.41	206.35	1.3682	711.65	520.08	191.57	1.3683
		713.22	720.33	-7.11	0.9901	689.24	695.66	-6.42	0.9908
		684.58	684.84	-0.26	0.9996	637.72	638.56	-0.84	0.9987
	Pc	778.36	566.31	212.05	1.3744	680.33	495.23	185.1	1.3738
		740.49	746.78	-6.29	0.9916	657.47	659.1	-1.63	0.9975
704.03		704.28	-0.25	0.9996	505.86	511.42	-5.56	0.9891	
N-H IP Bend		B_{2u}				B_{3g}			
	P	1003.52	882.82	120.7	1.1367	1264.1	1184.6	79.5	1.0671
		967.16	967.43	-0.27	0.9997	1213.11	1214.33	-1.22	0.9990
	TAP	970.33	851.43	118.9	1.1396	1250.89	1240.82	10.07	1.008*
		957.24	957.49	-0.25	0.9997	1216.82	1202.66	14.16	1.012*
	TBP	1067.7	989.03	78.67	1.0795	1253.59	1181.6	71.99	1.0609
		1038.52	1038.81	-0.29	0.9997	1217.56	1218.7	-1.14	0.9991
	Pc	1068.39	981.15	87.24	1.0889	1223.56	1191.4	32.16	1.0270
1029.31		1029.37	-0.06	0.9999	1211.42	1211.42	0	1.0000	

*No curve crossings occur between these two modes in TAP. The values chosen for inclusion were selected on the basis of the similarities of their motion with the three other tetrapyrrole molecules.

Table IV.4: Contributions of the N-H internal modes to the normal modes involving crossings, or avoided-crossings of TAP. Avoided crossings are easily identified when the ISR values are less than 1. Instances with particularly strong coupling, producing large avoided-crossings, are highlighted in bold type.

H₂TAP				D₂TAP			
Sym.	Mode#	Frequency	% Int.Mode	Mode#	Frequency	% Int.Mode	v_H/v_D
A_g	96	3629.132	68% N-H Stretch	88	2661.833	61.6% N-D Stretch	1.3634
B_{1u}	95	3565.385	68% N-H Stretch	87	2621.135	62.4% N-D Stretch	1.3602
B_{2g}	23	641.4	54.8% N-H OPB	22	479.7375	68.4% N-D OPB	1.3370
B_{3u}	36	760.8292	52.8% N-H OPB	24	547.6603	72% N-D OPB	1.3892
	24	656.6503	22.4% N-H OPB	25	664.4674	7.6% N-D OPB	0.9882
B_{2u}	67	1266.18	21.2% N-H IPB	66	1242.04	7.6% N-D IPB	1.0194
	63	1198.73	18.8% N-H IPB	62	1116.18	18% N-D IPB	1.0740
	52	970.3289	19.2% N-H IPB	46	851.4276	24% N-D IPB	1.1396
	51	957.2362	4% N-H IPB	52	957.4918	0% N-D IPB	0.9997
	38	776.51	10.8% N-H IPB	33	726.39	23.2% N-D IPB	1.0690
	33	748.85	2% N-H IPB	36	754	9.6% N-D IPB	0.9932
B_{3g}	62	1164.357	20.4% N-H IPB	61	1108.938	17.2% N-D IPB	1.0500
	65	1250.89	15.6% N-H IPB	65	1240.82	6% N-D IPB	1.0081
	64	1216.82	11.2% N-H IPB	65	1202.66	4.8% N-D IPB	1.0118
	49	950.62	26.4% N-H IPB	45	849.92	16.8% N-D IPB	1.1185
	39	778.95	14% N-H IPB	29	711.09	30% N-D IPB	1.0954

Table IV.5: Contributions of the N-H internal modes to the normal modes involving crossings, or avoided-crossings of porphyrin. Avoided crossings are identified as the $ISR < 1$.

Sym	H ₂ P			D ₂ P			v_H/v_D
	Mode	Frequency	% Int.Mode	Mode	Frequency	% Int.Mode	
A _g	108	3593.47	77.8% N-H Stretch	96	2638.31	61.2% N-D Stretch	1.3620
B _{1u}	107	3552.34	77.8% N-H Stretch	95	2611.88	61.4% N-D Stretch	1.3601
B _{2g}	23	631.22	50.8 % N-H OPB	22	473.78	65.2 % N-D OPB	1.3323
B _{3u}	35	739.89	32% N-H OPB	24	541.81	70.4% N-D OPB	1.3656
	24	651.38	21.2% N-H OPB	25	657.91	8.4% N-D OPB	0.9901
B _{2u}	71	1260.59	26 % N-H IPB	65	1120.28	16.4 % N-D IPB	1.1252
	67	1179.31	7.6 % N-H IPB	69	1195.31	8 % N-D IPB	0.9866
	57	1003.52	14.8 % N-H IPB	50	882.81	27.2 % N-D IPB	1.1367
	53	967.16	1.6 % N-H IPB	55	967.44	0 % N-D IPB	0.9997
	41	796.36	8 % N-H IPB	38	759.71	18 % N-D IPB	1.0482
B _{3g}	72	1264.10	26.4 % N-H IPB	68	1184.59	10.8 % N-D IPB	1.0671
	69	1213.11	4 % N-H IPB	72	1214.33	0 % N-D IPB	0.9990
	43	800.34	8.8 % N-H IPB	36	752.31	24.4 % N-D IPB	1.0638
	56	992.92	16.8 % N-H IPB	49	881.53	20.0 % N-D IPB	1.1264

IV.3.II: Out-of-Plane (B_{3u} & B_{2g}) Bending Modes

IV.3.IV.a: B_{3u} N-H Bending Modes

The mass dependences of the out-of-plane B_{3u} N-H bending (OPB) modes of P, TAP, TBP and Pc are shown in the four panels of Figure IV.4. In the frequency range 800 - 550 cm⁻¹ shown in the plot, all four molecules have the same number of normal modes and the mass dependence is clearly not simple in any of them. Most conspicuous is the pronounced avoided crossing which occurs between two modes in the central-section of the P and TAP plots. In both cases a normal mode which starts out strongly mass dependent, and is an N-H out-of-plane bending motion, becomes mass independent and evolves into a mode that involves large amplitude C-H OPBs. This is clearly not a correct mode attribution from the light to heavy isotopomers so to help analyse the complex behaviour exhibited, the theoretical mass dependence given by Equation IV.1 is overlaid as a solid trace in Figure IV.4. This was calculated from the lowest frequency D₂ mode because the N-H OPB

motion is manifested more strongly in the heavier isotopomers of these molecules than in the lighter ones (corresponding to a less congested spectral region for B_{3u} modes), in contrast with the previous case of A_g and B_{1u} modes. The internal mode analysis provided in Table IV.4 for TAP shows the contribution in D_2 TAP as 72% while it is only 53% in H_2 TAP. Table IV.5 reveals a similar pattern for the B_{3u} mode of porphyrin.

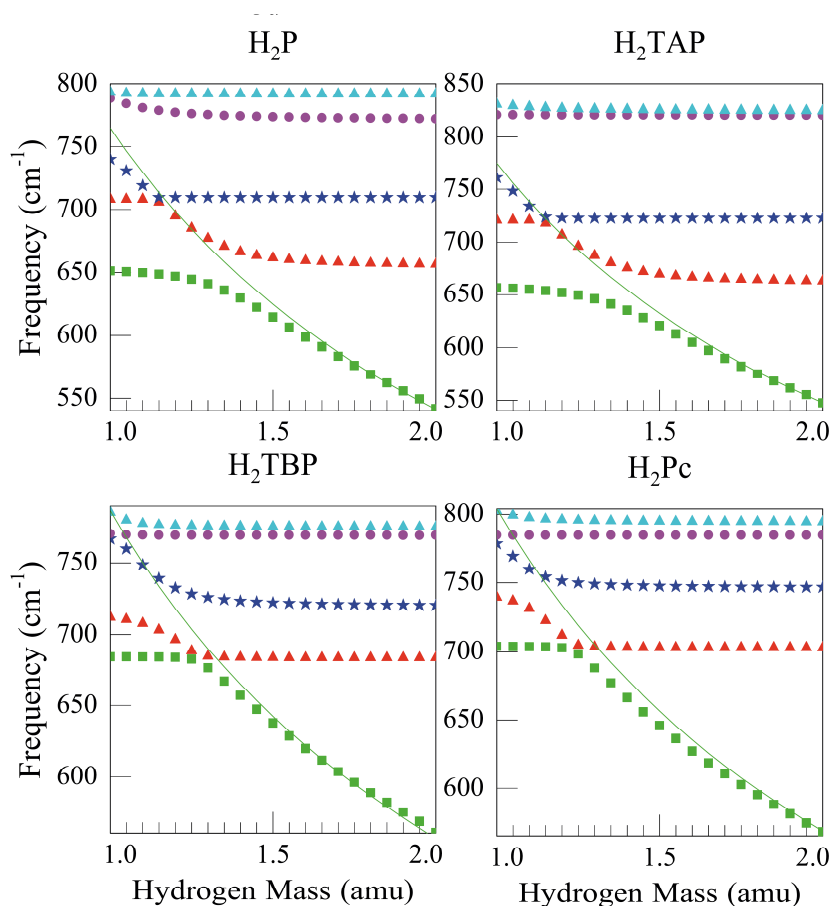


Figure IV.4: Mass dependence of the IR-active B_{3u} symmetry normal modes for the out-of-plane bending vibrations. In contrast to the high frequency modes, strong coupling occurs between the N-H OP bending modes and especially the C-H OP bending modes. This is indicated by the large avoided crossing that is clearly evident in the top two panels where P and TAP results are shown. A strong correlation exists between the N-H OP bending modes of the light and heavy isotopomers as indicated by the theoretical dependence of the frequency on the square root of mass. However, the frequency of the C-H OP bending mode “crossed” by the N-H mode increases in the deuterated molecule leading to a reversed isotope shift ratio ($ISR < 1$).

From the match shown for P in the upper left panel of Figure IV.4, between the calculated data and the $(m_H^{-1/2})$ dependence, it is clear that the frequency of the “pure” N-H OP mode decreases from 739.9 cm^{-1} in H_2P to 541.8 cm^{-1} in D_2P . The resulting v_H/v_D ratio is 1.366,

quite close to the expected value of $\sqrt{2}$. This mode crosses a pure C-H OPB with a frequency of 709.5 cm^{-1} , which is H-atom mass-independent and is thereby not affected by the N-H isotopic substitution. In contrast, it produces an avoided crossing with another C-H OP bending mode which has an initial value of 651.4 cm^{-1} in H_2P but increases to 657.9 cm^{-1} in D_2P . A clear consequence of the avoided crossing is that this mode shifts up in frequency by 6.53 cm^{-1} and produces a $v_{\text{H}}/v_{\text{D}}$ ratio considerably less than unity - the value is 0.9901. As indicated in Table IV.3, similar behaviour is exhibited by this mode in all four molecules. The most extreme situation is found for TAP which has an ISR value of 0.9882.

Vector diagrams for the atomic motions involved in the modes of TAP which exhibits the most pronounced reversed ISR effect are shown in Figure IV.5. From the motions presented, the association of the 760.8 cm^{-1} mode with the 547.7 cm^{-1} mode is unquestionable. Thus as illustrated, the vector diagrams for the N-H OP bending motions of H_2TAP and D_2TAP are indistinguishable for these two modes. However, a consequence of these mode assignments is that the mode at 656.7 cm^{-1} must be correlated with that at 664.5 cm^{-1} - an upward shift of 7.82 cm^{-1} in D_2TAP . This correlation is supported by the very similar C-H OP bending motions illustrated for both isotopomers on the bottom of Figure IV.5. However, on closer scrutiny of these two diagrams it can be seen that the direction of the N-H bending motion with respect to the molecule is reversed in the N-D mode. This change in the motion of the light and heavy isotopomers is found to be a characteristic of all the modes exhibiting the large reverse ISR which involve strongly avoided mode crossings. This behaviour is in fact the physical explanation of the reverse ISR. Reverse ISRs are observed to be larger in cases with more pronounced avoided crossings, i.e., with stronger coupling, W , between the modes. The reversal of the directions of the H-atom motions in the light and heavy species can be seen as a direct consequence of perturbation theory in first order. In the simplified case of two coupled modes, one mode, v_{H} , involving large H motion and the other, v_{N} , involving little H motion as is the case for when the $\text{H} \rightarrow \text{D}$ progression is very flat except in the region of the crossing, the result of perturbation theory will give new modes v'_{N} with

$$|v'_{\text{N}}\rangle = |v_{\text{N}}\rangle + W/(E_{\text{nN}} - E_{\text{nH}})|v_{\text{H}}\rangle \quad \text{Eq. IV.2}$$

The reason for the reversed directions can be understood as follows. Since the sign of the matrix element W ($\langle v_{\text{H}} | W | v'_{\text{N}} \rangle$) does not change from H to D, but it does change for the energy term, i.e., $(E_{\text{nN}} - E_{\text{nH}}) < 0$ for H, whereas $(E_{\text{nN}} - E_{\text{nH}}) > 0$ for D, this means that the

motion of $H(|m_H\rangle)$ appears with opposite signs in the description of $|v_N\rangle$ in the hydrogenated and the deuterated species, i.e., reversal of directions. This “reversal” is larger and more obvious when the coupling W strength is greater.

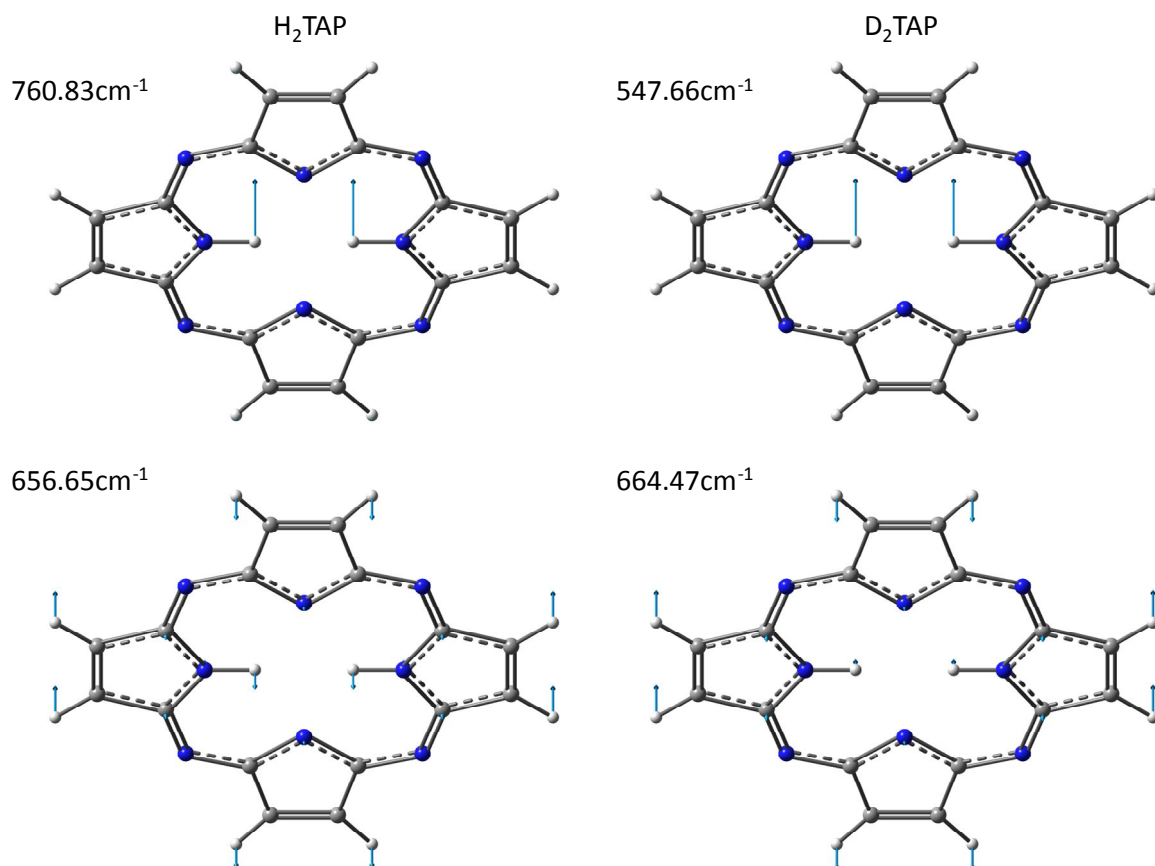


Figure IV.5: Vector diagrams showing the very similar atomic motions involved in the pure N-H OP bending motion of TAP for the normal and deuterated molecules – top left and right respectively. In the bottom the motions in the C-H mode involved in the avoided crossing with the N-H OPB are shown. The mode correlations of the two isotopomers are clearly correct, but on closer scrutiny it is evident that the direction of the small N-H motion, which this mode possesses, is reversed in the H and D molecules. This behaviour is exhibited in all the modes involved in the avoided crossings.

IV.3.IV.b: B_{2g} N-H Bending Modes

The H/D isotope dependences of the Raman-active B_{2g} N-H OP bending modes of porphyrin and TAP are, as shown in the upper panels of Figure IV.6, relatively straightforward exhibiting a continuous mode evolution from the hydrogen to the deuterium isotopomer. As indicated in Table IV.3, they also exhibit an ISR of 1.33 and

follow the simple mass dependence shown by the smooth curve in Figure IV.6. In contrast, TBP and Pc are both complicated by the existence of an additional mode which is crossed by the N-H B_{2g} OP bending mode at different locations. Again the mass dependence curve is very instructive in identifying the correct mode evolution. As listed in Table IV.3, the 711.7 cm^{-1} mode of H_2TBP correlates with the 520.1 cm^{-1} mode of D_2TBP , giving an ISR value of 1.37 – a similar value is present for phthalocyanine. However, the curve-avoidance which is now present produces ISR values significantly less than 1 in both cases. Table IV.3 lists these as 0.991 and 0.989 for TBP and Pc respectively.

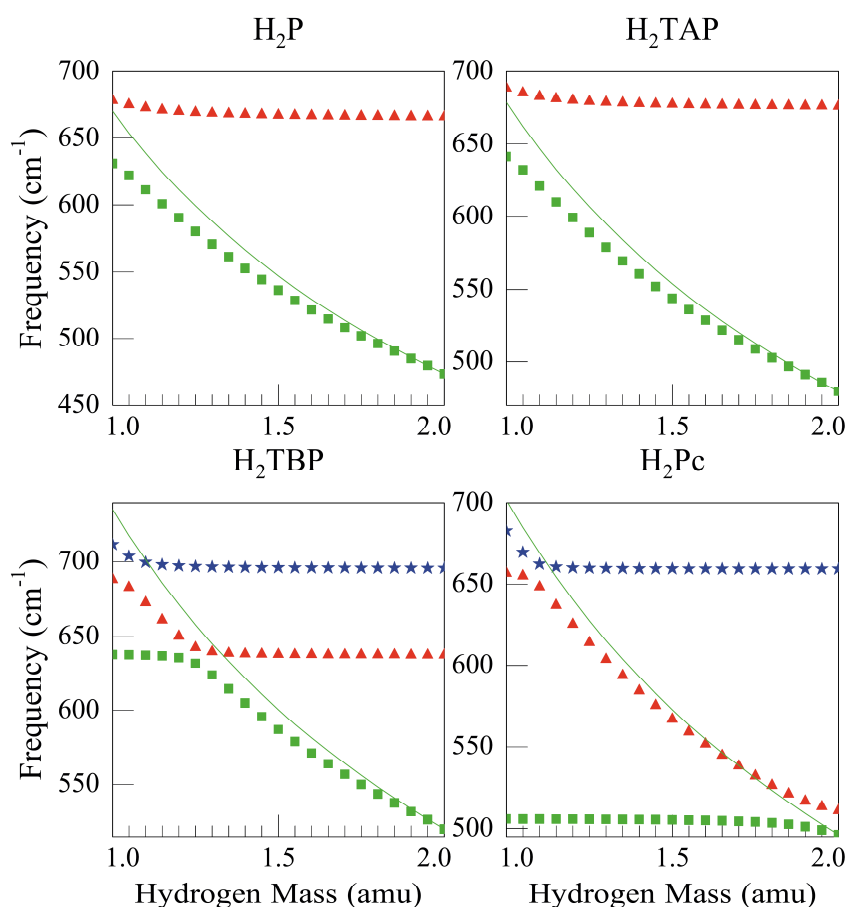


Figure IV.6: As for Figure IV.4 except for the Raman-active B_{2g} symmetry OP N-H bending modes. Particularly simple behaviour is exhibited in the smaller molecules P and TAP as indicated by the close agreement with the solid theoretical curve showing the calculated mass dependence.

IV.3.III: In-Plane (B_{2u} & B_{3g}) Bending Modes

A summary of the isotope dependences of the N-H IP bending modes is provided in Figure IV.7 and Figure IV.8. The mass dependences of these modes are quite similar for all four

molecules and evidently are not simple. It is clear that these IPB modes do not show a mass dependence that is as strong as $(m_H^{-1/2})$, shown by the smooth line. Instead, several modes appear to have a weak, near-linear dependence on mass. The slope of the $(m_H^{-1/2})$ law is never approached, whatever the isotopomer. This effect is due to an extreme dilution of NH IP motions in many modes of the same symmetry. Modes exhibiting the highest absolute slope at $m_H = 1$ or 2 correspond in fact to the modes involving the highest % of NH or ND IP motion respectively. This can be checked in Tables IV.4 and IV.5 where the B_{2u} and B_{3g} modes exhibiting the highest % are reported for TAP and P respectively.

IV.3.IV.a: B_{2u} N-H Bending Modes

Some mode crossings do occur also for this N-H motion and because of the similarity of the behaviour in the mid-frequency region for all four molecules; we have chosen the modes in this region for inclusion in Table IV.3.

The IR-active B_{2u} modes of porphyrin and TAP are quite similar, showing a diluted effect upon isotopic substitution of the inner hydrogens. As listed in Table IV.3, the mode at 1003.5 cm^{-1} in H_2P , involving the N-H in-plane bend drops to 882.8 cm^{-1} in D_2P . This shift corresponds to a v_H/v_D ratio of only 1.137 – a value much less than $\sqrt{2}$. This mode shows a weak avoided crossing with the one at 967.2 cm^{-1} – which is a pyrrole ring stretching mode. This avoided crossing has the effect of increasing the frequency of the pyrrole ring stretching mode in D_2P by a small amount to 967.4 cm^{-1} and generating a v_H/v_D ratio of 0.9997. While the 0.27 cm^{-1} shift in frequency for the pyrrole mode is small, similar values are exhibited by all the tetrapyrroles except Pc where it is yet smaller 0.06 cm^{-1} . The significance of these ISR values is hard to ascertain because while it is consistently less than 1, it is very close to it. It is worth noting however, that for the pure C-H stretching A_g and B_{1u} modes crossed over by the N-H(D) mode (see Figure IV.2 and Figure IV.3), the ISR values are much closer to 1. In the present IP bending B_{2u} mode, vector diagrams indicate that there is some N-H character in the pyrrole ring stretch, so the small ISR values are deemed significant.

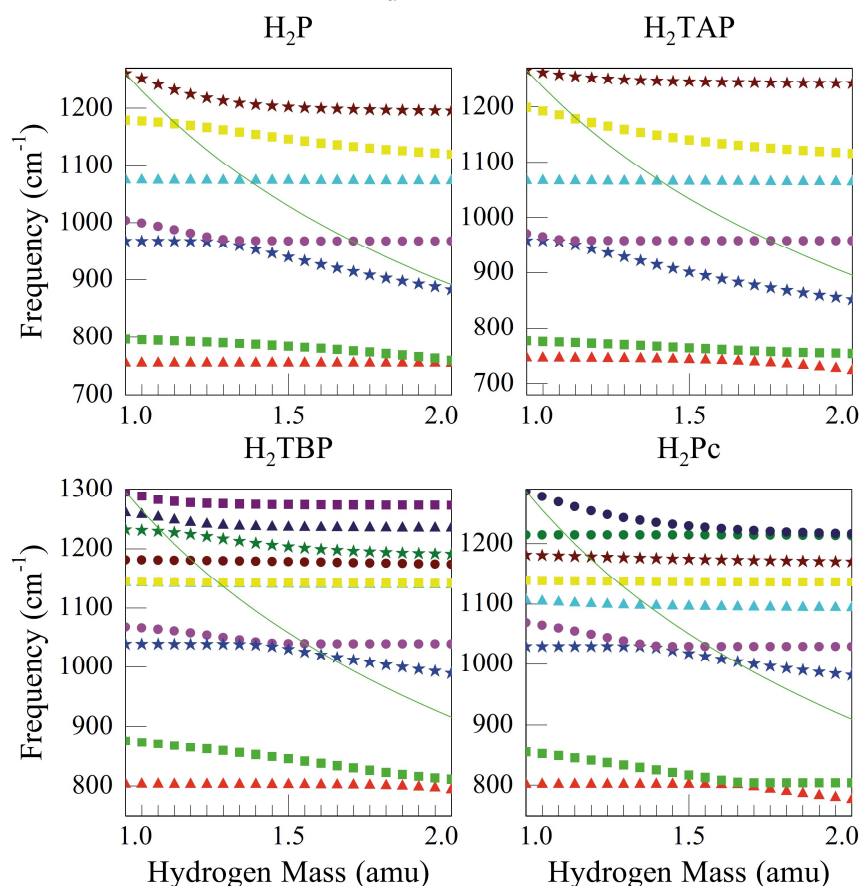


Figure IV.7: Mass dependence of the IR-active B_{2u} symmetry for the in-plane N-H bending modes. Particularly evident is the large number of modes and the fact that they nearly all show a dependence on mass. This reveals immediately that the N-H bending vibration is diluted over many modes, none of which can show the expected mass dependence of a pure mode which is indicated by the smooth curve.

While not included in the global ISR summary provided in Table IV.3, it is evident in Figure IV.7 that mode crossings do occur in the lower frequency range but the crossing regions vary from molecule to molecule. Thus direct crossings are exhibited by P and Pc while avoided crossings are present in TAP and TBP. Information on the avoided crossing in the former is provided in Table IV.4, where the 776.5 cm^{-1} mode of H_2TAP decreases to 726.4 cm^{-1} for D_2TAP with a small ISR value of 1.069. However, this then produces a frequency increase in the interacting mode at 748.9 cm^{-1} which moves up to 754.0 cm^{-1} in D_2TAP and has an ISR considerably less than 1 with a value of 0.9932. Porphyrin does not exhibit this behaviour, so a corresponding value is not given in Table IV.5.

In the higher frequency region only P and TBP exhibit avoided crossings and detailed information on the behaviour of porphyrin is presented in Table IV.5. It is evident there that

a reverse ISR is present with an upward frequency shift of 16 cm^{-1} producing an ISR value of 0.9866. Thus the highest frequency N-H IP bending mode at 1260.6 cm^{-1} correlates with the 1120.3 cm^{-1} mode of D_2P yielding a diminished ISR of 1.125. A consequence of this attribution is that the H_2P mode at 1179.3 cm^{-1} must be associated with the 1195.3 cm^{-1} mode of D_2P . This mode was previously highlighted by Li *et al*⁶ but their correlation involved modes with a much larger frequency gap. The value they proposed was an upward shift of 108 cm^{-1} .

IV.3.IV.b: B_{3g} IP N-H Bending Modes

The Raman-active B_{3g} modes presented in Figure IV.8 exhibit similar behaviour to the IR-active B_{2u} modes, but the mass dependence is even more diluted. This dilution effect is extreme in the case of the larger molecules TBP and Pc where every mode, except one at 1040 cm^{-1} shows a slight mass-dependence. As a result, most of the modes are parallel which mitigates against curve crossings. In contrast, the behaviour in P and TAP is more well-defined with two modes at around 810 and 1020 cm^{-1} clearly mass independent while the remainder all show a weak mass dependence.

Taking porphyrin as an example, the most “pure” N-H IPB mode (listed in Table IV.5 as 26.4%) has a frequency of 1264.1 cm^{-1} , a value which decreases to 1184.6 cm^{-1} as the mass is increased from 1 to 2 amu. This correlation produces a $v_{\text{H}}/v_{\text{D}}$ ratio of 1.067 (as quoted in Table IV.3) and the aforementioned mode exhibits an avoided crossing with that at 1213.1 cm^{-1} containing C-H IPBs. It thereby generates a small increase in the frequency in the heavy isotopomer. This increase is listed in Table IV.3 as 1.22 cm^{-1} and when compared with TBP, consistent ISR values of 0.999 are obtained. No curve crossings occur between these two modes in TAP. The TAP values chosen for inclusion in Table IV.3 were selected on the basis of the similarities of their motion with the three other tetrapyrrole molecules.

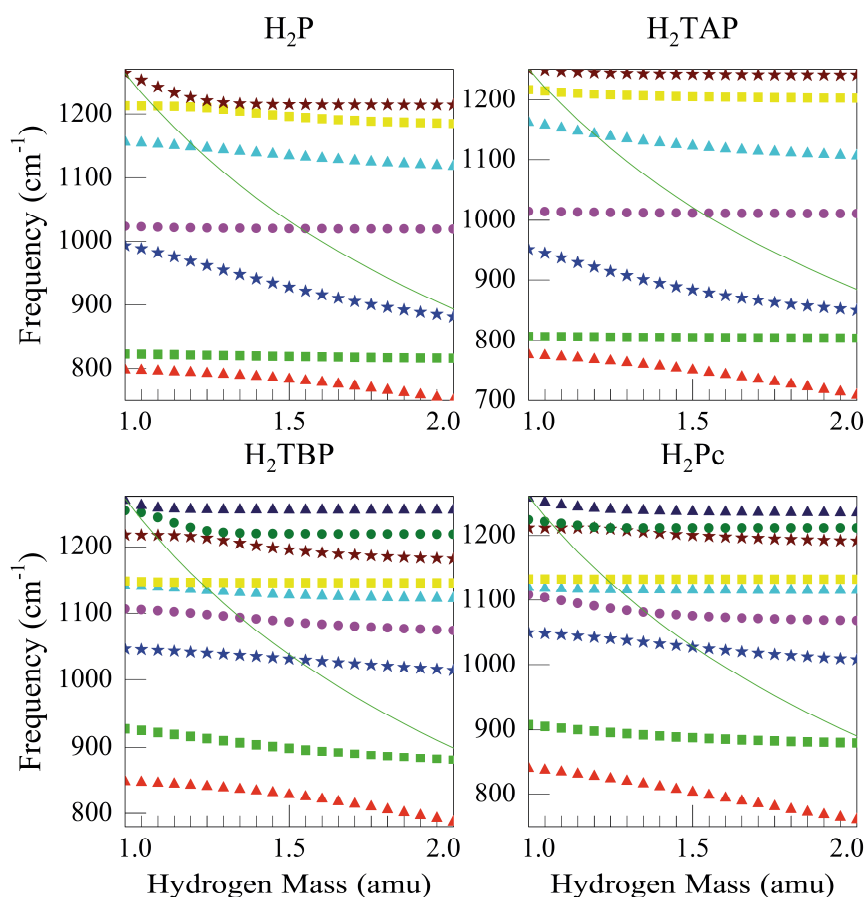


Figure IV.8: As for Figure IV.7 except for the Raman-active B_{3g} symmetry IP N-H bending modes.

IV.4: Discussion

IV.4.I: Comparison with Other Calculations

In the detailed theoretical study carried out by Li & Zgierski⁶ on establishing a force field for free-base porphyrin, upward frequency shifts were proposed upon deuteration for the B_{1g} and B_{2u} IP bending modes. However, the previous study focussed only on the N-H stretching and in-plane bending modes. Because of the use of a different axis system in the current and previous works, Li *et al*⁶ B_{1g} symmetry corresponds to this work's B_{3g} mode, while the B_{2u} modes are the same in both. These workers proposed (Scheme I, Ref. ⁶) a large increase in the frequency of two modes upon H/D isotopic substitution, both of which involved in-plane bending. Specifically they proposed that the B_{1g} N-H IP bending mode crosses with a pyrrole half ring stretch mode. This had the effect of shifting the frequency of the pyrrole mode up by 56 cm^{-1} , from 976 cm^{-1} in H_2P to 1032 cm^{-1} in D_2P . The other

mode which showed this effect was a B_{2u} mode, in which the asymmetric N-H IP bending vibrations and the pyrrole ring stretch cross. This causes the pyrrole stretch to shift up in energy by 108 cm^{-1} , from 986 cm^{-1} to 1094 cm^{-1} . It is not evident why the OP bending modes were not analysed for this effect in the earlier study⁶, but it may have been due to their interest in the role of the N-H stretch and IP bending vibrations in the tautomerism of free-base porphyrin.

As indicated in the upper left panels in Figure IV.7 and Figure IV.8, reverse isotope shifts of this magnitude are not exhibited by porphyrin in the B_{3g} and B_{2u} IP bending modes respectively. It is immediately clear that there are significant differences between Li's results⁶ and the findings of the present DFT method¹⁰. The earlier work identified only two instances of this increased frequency, both of which are much larger than what is observed in this study. This may arise for a number of reasons. Their calculations were carried out with the GF matrix method and a valence force field. While their method was parameterised to give a good match with experimental data it is likely the valence force field is not capable of accounting for all the interactions present in molecules of this size. Complete sets of force constants are of course available from quantum chemical calculations and the use of high level DFT calculations are currently the most powerful for predicting the ground state vibrational frequencies of large polyatomic molecules. Based on the favourable findings from earlier DFT results on ZnPc and H₂Pc in matrix-IR spectra⁵ it is likely that the present results are a more accurate reflection of the extent of the up-shifted frequencies.

Li *et al.*⁶ identified the NH(D) IPB B_{2u} modes at $1223\text{ (}825\text{)}\text{ cm}^{-1}$, corresponding to $1261\text{ (}883\text{)}\text{ cm}^{-1}$ in our calculations: these modes exhibits the highest % of NH(D) IPB motion (Table IV.5). The mode which involves also non-negligible NH bendings is identified at 986 cm^{-1} (ν_{44a}) in the previous work and corresponds to the mode at 1003 cm^{-1} in the present work (14.8% N-H IPB in Table IV.5). This mode is found to correlate with the mode at 883 cm^{-1} in the deuterated species, i.e. the mode involving the highest % N-D IPB motion. The curves of Figure IV.7 and Figure IV.8 show clearly the correlations between H and D species, as summarized in Table IV.5. In the discussed case, they show that modes at 1261 and 1003 cm^{-1} in the H species correlate with modes at 1120 and 883 cm^{-1} , with a decrease of the N-“H” IPB % in the highest frequency mode and an increase of the N-“H” IPB % in the lowest frequency one, explaining the earlier result. (Note that the B_{2u} mode at 1094 cm^{-1} mentioned by Li *et al.*⁶ in the correlations for the D species corresponds

to a mode at 1076 cm^{-1} in our calculation, a mode which does not involve N-D IPB motion). Because of a strong mixing of various atomic motions in B_{1g} and B_{2u} modes in the frequency range of interest, a slightly different description of normal modes can have important consequences in their assignments, as proved by this last discussion.

IV.4.II: Comparison with Experiments

The results of the current calculations can be compared with experimental isotope substitution work, but because the mass-related shifts are quite small in the congested $1500 - 500\text{ cm}^{-1}$ spectral range, high resolution methods yielding narrow line transitions are required for analysis. The matrix-isolation technique is particularly well suited for this work. Currently however, only a very limited number of tetrapyrroles have been examined in this way. One that has been mentioned already is the earlier work on the phthalocyanines⁵ from which the current investigation has emerged. The other is the earlier study of Radziszewski *et al*¹³ who used matrix-IR spectroscopy to look at deuteration effects in free-base porphine. In order to compare the present theoretical results on porphine with the experimental matrix work¹⁴, the simulated DFT IR absorption spectra of H_2P and D_2P are shown scaled by a factor of 0.98 in Figure IV.9 on the same spectral range as shown in Figure 12 of the Radziszewski *et al*¹³ paper. The agreement between the two studies is very good which testifies to the strength of the current DFT method in predicting not only the IR absorption frequencies of the tetrapyrroles but also their intensities.

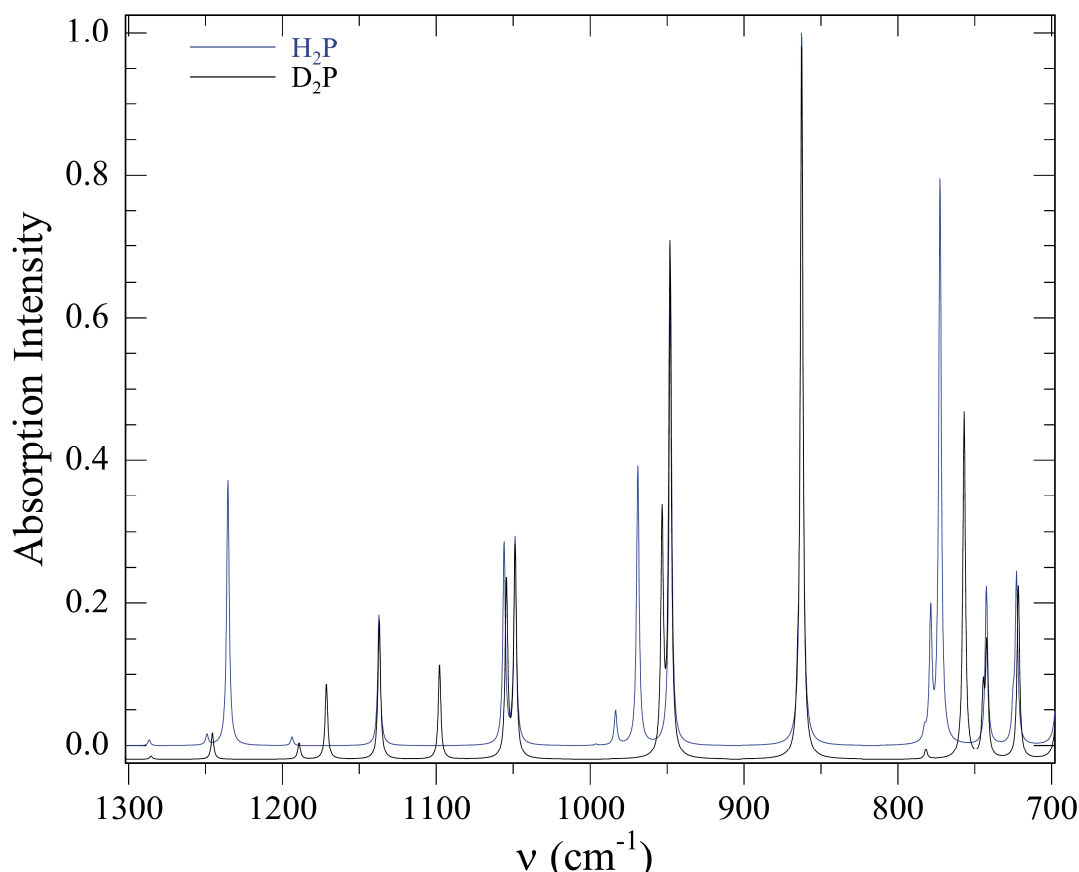


Figure IV.9: Low resolution ($\text{fwhm} = 4 \text{ cm}^{-1}$) plots of the IR absorption spectra generated by the DFT/B3LYP method for the vibrational modes of H_2P and D_2P . The spectral range and format has been selected for direct comparison with the matrix-IR absorption data published by Radziszewski *et al*¹⁵. The predicted values are scaled by a factor of 0.98 throughout.

In agreement with Radziszewski *et al*¹³ the mode of H_2P which they observed at 731 cm^{-1} and attributed to OP bend, is predicted at 739.9 cm^{-1} (scaled $\times 0.98$, 725.1 cm^{-1}) in the present calculations. However, their comment that this motion will be distributed over several fundamental modes of D_2P is not borne out by our calculations. As Figure IV.10 shows (and listed in Table IV.3), the N-D OP bend is well defined – it is located at 541.8 cm^{-1} (scaled $\times 0.98$, 530.9 cm^{-1}) in a sparse region of the IR spectrum. Moreover, it is actually much stronger than the corresponding H_2P OPB so it should be easily identified. However, Radziszewski *et al*¹³ did not present any spectra for this lower frequency region. The reason it is not diluted over several modes is evident in Figure IV.4. As indicated in that plot, its mass dependence is limited to just two modes both of which exhibit the simple root of mass dependence. This simple behaviour is entirely attributable to the small number

(10) of B_{3u} symmetry modes listed in Table IV.1 for the out-of plane bend of free-base porphyrin. Essentially identical behaviour is predicted for TAP, while Figure IV.4 predicts the OPB will only be slightly more complex because of the crossing of a single, lower frequency mode in TBP and Pc.

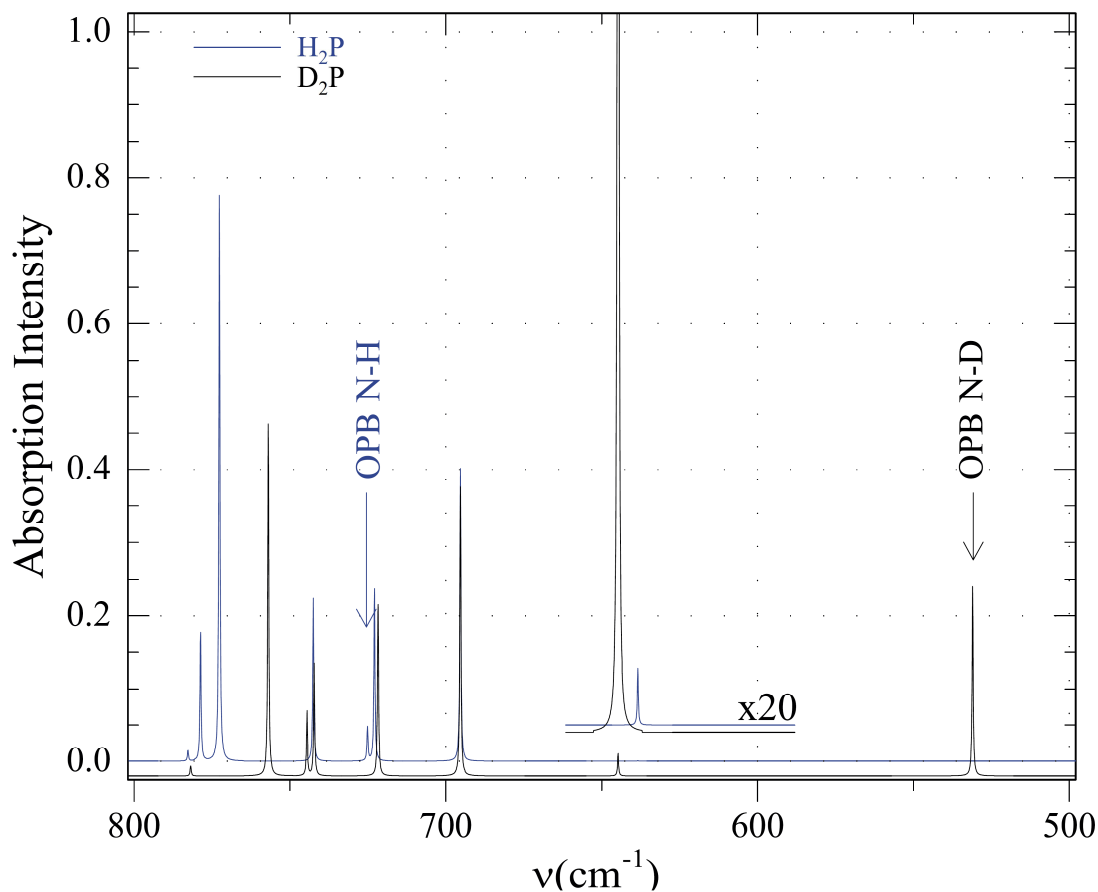


Figure IV.10: High resolution ($\text{fwhm} = 0.2 \text{ cm}^{-1}$) plots of the IR absorption spectra generated by the DFT/B3LYP method for H₂P and D₂P. The spectral range presented is the region where the large isotope shift on the OP bend is predicted. This range was not presented in the matrix-IR absorption data published by Radziszewski *et al.*¹³

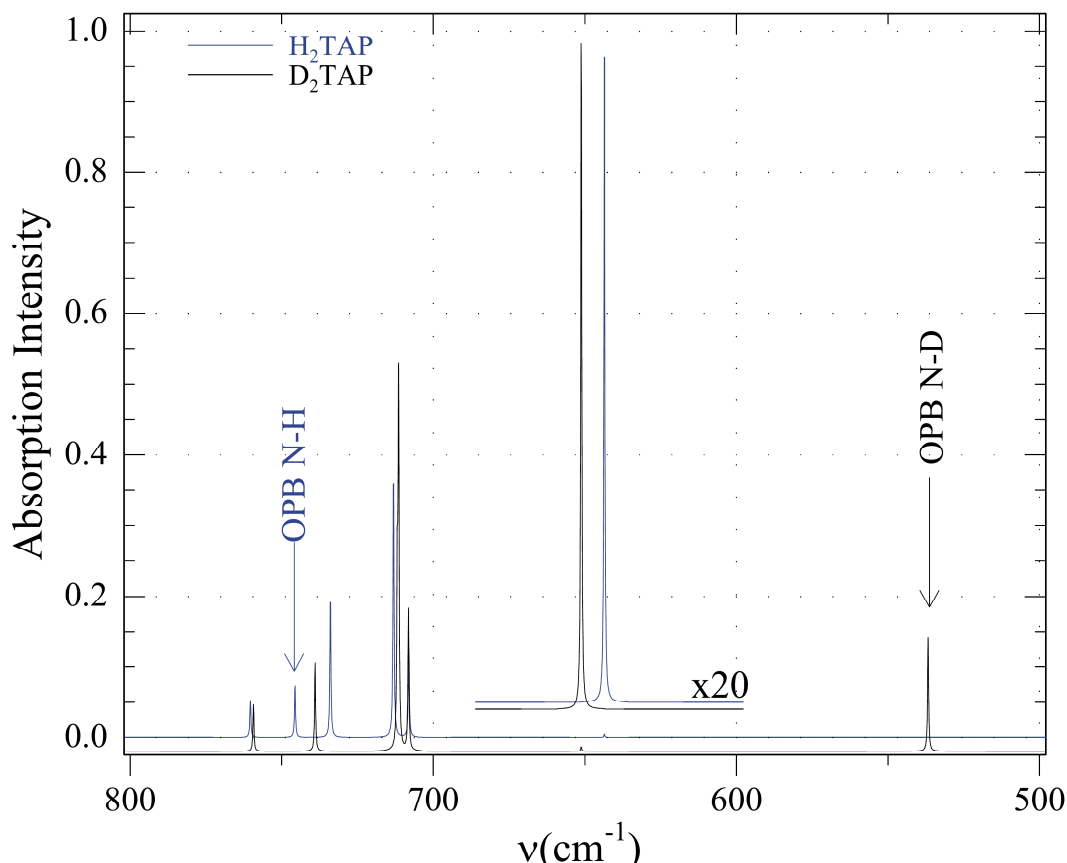


Figure IV.11: High resolution (fwhm = 0.2 cm^{-1}) plots of the IR absorption spectra generated by the DFT/B3LYP method for H_2TAP and D_2TAP . The spectra range and format has been selected for examination of the region where the large isotope shift on the OP bend is predicted to occur.

A key aspect of the current work is the upward shift in the frequencies of specific modes (highlighted in Table IV.3) in the heavier isotopomer upon H/D substitution. As indicated in that table, the most pronounced instance of this effect in free-base porphine is expected in the OP bending mode where the 651.4 cm^{-1} mode shifts up to 657.9 cm^{-1} . This region is also highlighted in Figure IV.10 on an expanded intensity scale. Unfortunately this region is not presented in the paper by Radziszewski *et al*¹⁵ (perhaps for experimental reasons). However, this effect will not be immediately evident in the recorded spectra, because while the D_2P mode at 657.9 cm^{-1} has acceptable intensity (4.3 km/mol), that of the related H_2P mode at 651.34 cm^{-1} is very weak (0.08 km/mol). In the experimental spectrum of the heavier isotope this ISR effect will present an “unknown” peak in the spectrum not easily connected with H_2P . However, using the matrix-isolation technique which has high sensitivity, it should be possible to observe the ISR effect in porphine as already done in phthalocyanine⁵.

IV.5: Conclusions

The results of the present DFT calculations of H/D substitution on the free-base tetrapyrroles can be summarised as follows. For the high frequency, N-H bond stretching modes are very well localized and crossings occur with the C-H stretching modes. As these internal modes involve such different motions and are very localised, no inter-mode coupling occurs, yielding the expected H_2/D_2 ISR ratios.

Contrary to usual expectations, the lower frequency N-H OP bending motions are not distributed over several modes as they are not numerous. As a result, these modes involve well defined out-of-plane bending motions in both the N-H to N-D bonds. For the smaller tetrapyrroles (P and TAP) no crossings occur for the B_{2g} symmetry Raman-active modes. In the larger molecules crossings occur but the B_{2g} modes of Pc and TBP still involve localised N-H motions as illustrated by the similarity with the simple mass dependence curves. Due to a single mode crossing which occurs in both Pc and TBP, frequency increases do occur in the heavier isotopomer but because of the involvement of only two modes, instances of reversed ISR can be easily identified in the mass dependent calculations.

The IR-active B_{3u} OP bending modes are slightly more numerous than their Raman counterparts and exhibit more complex behaviour. For all four molecules the N-H OP bending mode is crossed by two modes. Clear differences exist between crossings of these two modes. One is very weakly coupled with the N-H OP bend and passes directly through while the other mode is strongly coupled and produces a large avoided crossing. A consequence of the strong coupling in the latter case is that the frequency in the heavier isotopomer increases significantly yielding reversed ISR values. In all these situations the vector diagrams of the motions reveal a reversal of the N-H and N-D motions between the light and heavy isotopomer. Based on predictions made in the present work the instance of an ISR which has already been identified in matrix-IR work on the phthalocyanines, it would appear that TAP is the ideal system to make a definitive study of this effect.

The OPB modes provide simple examples of the effect of avoided crossing. In situations where no effect on the crossing mode without coupling (showing simple crossing) to be compared with reversed ISR values obtained in case of large avoided crossing (crossing between modes involving same atomic motions) leading to a mixture of these motions strongly depending on small molecular effects such as the mass of H.

More complicated behaviour is observed for the N-H IP bending modes than the OP bending modes just described due to the larger number of modes with B_{2u} and B_{3g} symmetries. As a result, the N-H motions are dispersed over many normal modes. Accordingly, the decrease in the NH frequencies is much less than the $m_H^{-1/2}$ mass dependence due to the dilution of this motion over several modes. No IPB mode can be identified as “the” NH or ND IPB mode, percentages of NH(D) motion are always below 30%. Another consequence of this is that most of the modes are nearly parallel which reduces the extent of modes crossings. Crossings appear in congested spectral region where a mode exists involving no NH(D) motion. This is the case in the region of 1000 cm^{-1} in all molecules. In all instances the crossing is direct and the modes are clearly not strongly coupled. For the B_{3g} modes couplings occur for some molecules in the high frequency (1200 cm^{-1}) range but produce only weak avoided crossings. The best examples of this are present in porphyrin and TBP. This coupling does not occur in TAP and only weakly in Pc.

IV.6: References

1. Braun, J.; Limbach, H.-H.; Williams, P. G.; Morimoto, H.; Wemmer, D. E., Observation of Kinetic Tritium Isotope Effects by Dynamic NMR. The Tautomerism of Porphyrin. *Journal of the American Chemical Society* **1996**, *118* (30), 7231-7232.
2. Baker, J.; Kozlowski, P. M.; Jarzecki, A. A.; Pulay, P., The inner-hydrogen migration in free base porphyrin. *Theoretica Chimica Acta* **1997**, *97* (1-4), 59-66.
3. Krumbiegel, P., Book review. *Isotopes in Environmental and Health Studies* **2006**, *42* (3), 325-325.
4. Herzberg, G., *Molecular Spectra and Molecular Structure: Infrared and Raman of Polyatomic Molecules*. Krieger Pub Co., 1991.
5. Murray, C.; Dozova, N.; McCaffrey, J. G.; FitzGerald, S.; Shafizadeh, N.; Crepin, C., Infra-red and Raman spectroscopy of free-base and zinc phthalocyanines isolated in matrices. *Physical Chemistry Chemical Physics* **2010**, *12* (35), 10406-10422.

6. Li, X. Y.; Zgierski, M. Z., Porphine force field: in-plane normal modes of free-base porphine; comparison with metalloporphines and structural implications. *The Journal of Physical Chemistry* **1991**, *95* (11), 4268-4287.
7. Wilson, E. B., Jr.; Decius, J. C.; Cross, P. C., *Molecular Vibrations*. McGraw-Hill Book Co.: 1955; p 388 pp.
8. Liu, Z.; Zhang, X.; Zhang, Y.; Jiang, J., Theoretical investigation of the molecular, electronic structures and vibrational spectra of a series of first transition metal phthalocyanines. *Spectrochimica Acta Part A: Molecular and Biomolecular Spectroscopy* **2007**, *67* (5), 1232-1246.
9. Zhang, X.; Zhang, Y.; Jiang, J., Isotope effect in the infrared spectra of free-base phthalocyanine and its N,N-dideuterio-derivative: density functional calculations. *Vibrational Spectroscopy* **2003**, *33* (1-2), 153-161.
10. Henchy, C.; Murray, C.; Crépin, C.; McCaffrey, J. G., A DFT study of reversed isotope shifts in H/D substitution of free-base porphyrin and related free-base tetrapyrroles. *Canadian Journal of Chemistry* **2012**, *90* (12), 1078-1091.
11. Gardner, A. M.; Wright, T. G., Consistent assignment of the vibrations of monosubstituted benzenes. *The Journal of chemical physics* **2011**, *135* (11), -.
12. Groner, P., Normal Coordinate analysis. In *Handbook of Vibrational Spectroscopy*, Chalmers, J. M. G., P. R., Ed. Wiley, NY: 2002; Vol. 3, p 1992.
13. Radziszewski, J. G.; Waluk, J.; Michl, J., Site-population conserving and site-population altering photo-orientation of matrix-isolated free-base porphine by double proton transfer: IR dichroism and vibrational symmetry assignments. *Chemical Physics* **1989**, *136* (2), 165-180.
14. Radziszewski, J. G.; Waluk, J.; Nepras, M.; Michl, J., Fourier transform fluorescence and phosphorescence of porphine in rare gas matrixes. *The Journal of Physical Chemistry* **1991**, *95* (5), 1963-1969.
15. Radziszewski, J. G.; Nepras, M.; Balaji, V.; Waluk, J.; Vogel, E.; Michl, J., Polarized Infrared Spectra of Photooriented Matrix-Isolated Free-Base Porphyrin Isotopomers. *The Journal of Physical Chemistry* **1995**, *99* (39), 14254-14260.

Chapter V: Visible Spectroscopy of GaPcCl Isolated in Inert Gas Matrices

V.1: Introduction

This chapter presents the visible absorption and luminescence spectroscopy of GaPcCl isolated in inert gas hosts, focusing on the region of the Q band. Emission spectra recorded with pulsed laser excitation will be presented in each host matrix and the vibronic bands will be assigned with the help of high level DFT calculations. An analysis of the vibronic structure in emission is performed by comparing it to the ground state Raman results presented in Chapter III. Excitation spectra were recorded by monitoring specific emission bands and scanning with the dye laser. A strong similarity was observed between the absorption, emission and excitation spectra. This allows for a vibrational assignment of the bands present in absorption/excitation. Fluorescence lifetimes were also measured in the matrix and compared to lifetime values predicted by TD-DFT calculations. Due to the well documented non-linear optical properties of aluminium phthalocyanine chloride^{1,2}, GaPcCl was investigated to see if it exhibits amplified emission (AE) in the solid state at cryogenic temperatures as well as the conditions required for samples to exhibit this effect.

V.2: Experimental

Matrix-isolation experiments were performed in the Low Temperature Laboratory at Maynooth University of the National University of Ireland, using the apparatus described in Chapter II. Matrix samples were prepared in a variety of hosts which included the molecular gas N₂ and the rare gases Ar, Kr and Xe. Various deposition conditions were used in the preparation of samples, the specifics of which led to different spectral properties of a given sample. The three parameters which could be altered were (1) the temperature of the oven, (2) the flow rate of the host gas and (3) the temperature of the matrix window during deposition. The first two parameters controlled the concentration of the sample and the third parameter was associated with properties such as the number of sites present in the sample, the extent of aggregation and the optical quality of the sample. In addition to this, selected samples were also annealed to investigate the stabilities of the sites in each matrix. Solution phase absorption spectra of GaPcCl in ethanol were recorded

with a Perkin-Elmer Lambda 35, UV-Vis Spectrometer. Raman experiments were carried out in the Focus Institute in DIT, the specifics of which are provided in Chapter II.

V.3: Results

The results section of this chapter introduces the luminescence spectroscopy of GaPcCl isolated in various inert gas hosts. The main spectroscopic results will be presented for each individual host, which involve the following;

Sample preparation techniques

Absorption spectroscopy

Emission spectroscopy and emission lifetimes

Excitation spectroscopy

Amplified emission

After the aforementioned topics have been presented for each matrix host, a comparison of each host be provided. This highlights some of the effects each host has on the spectroscopy of the molecule. A more detailed analysis of the main trends observed are presented in the Section V.4, with the exception of the amplified emission results, which is discussed in greater detail in Chapter VI.

V.3.I: Argon

V.3.I.a: Sample Optimization

GaPcCl isolated in solid Ar was prepared by co-depositing hot phthalocyanine vapour with the host gas onto a cryogenically cooled CaF₂ window. In order to obtain the best samples for spectroscopic studies, a number of different deposition conditions were examined and will be presented below. GaPcCl concentrations were controlled by changing the oven temperature and gas flow. Sample composition, i.e. the formation of aggregates, number of sites and the resolution of absorption bands were controlled by changing the window temperature. The effect of the different deposition conditions were monitored using absorption spectroscopy in the region of the Q band.

Figure V.1 presents a concentration study of GaPcCl/Ar. The blue trace shows a sample prepared with an oven temperature of 324 °C. The spectrum contains two regions of interest; from ~700 to 550 nm which corresponds to the Q (S_1) \leftarrow G (S_0) transition^{3,4} and the vibronic bands associated with this transition, and the region from ~400 to 300 nm which arises from the B (S_2) \leftarrow G (S_0) transition^{3,4}. The red trace shows the spectrum recorded for a sample prepared with a higher oven temperature of 357 °C. This spectrum is saturated in the region of the band origin of the Q band, but the vibronic structure extending up to 603 nm is more resolved. The weaker bands located further to the blue (up to 550 nm) are beyond the expected region of fundamental vibronic bands of GaPcCl. This has been demonstrated in Chapter III, where no fundamental vibrational modes exist between 1600 and 3000 cm^{-1} . Instead the bands between 600 – 550 nm in Figure V.1 may be caused by combination modes. These are not evident in the low oven temperature sample due to their weak intensity.

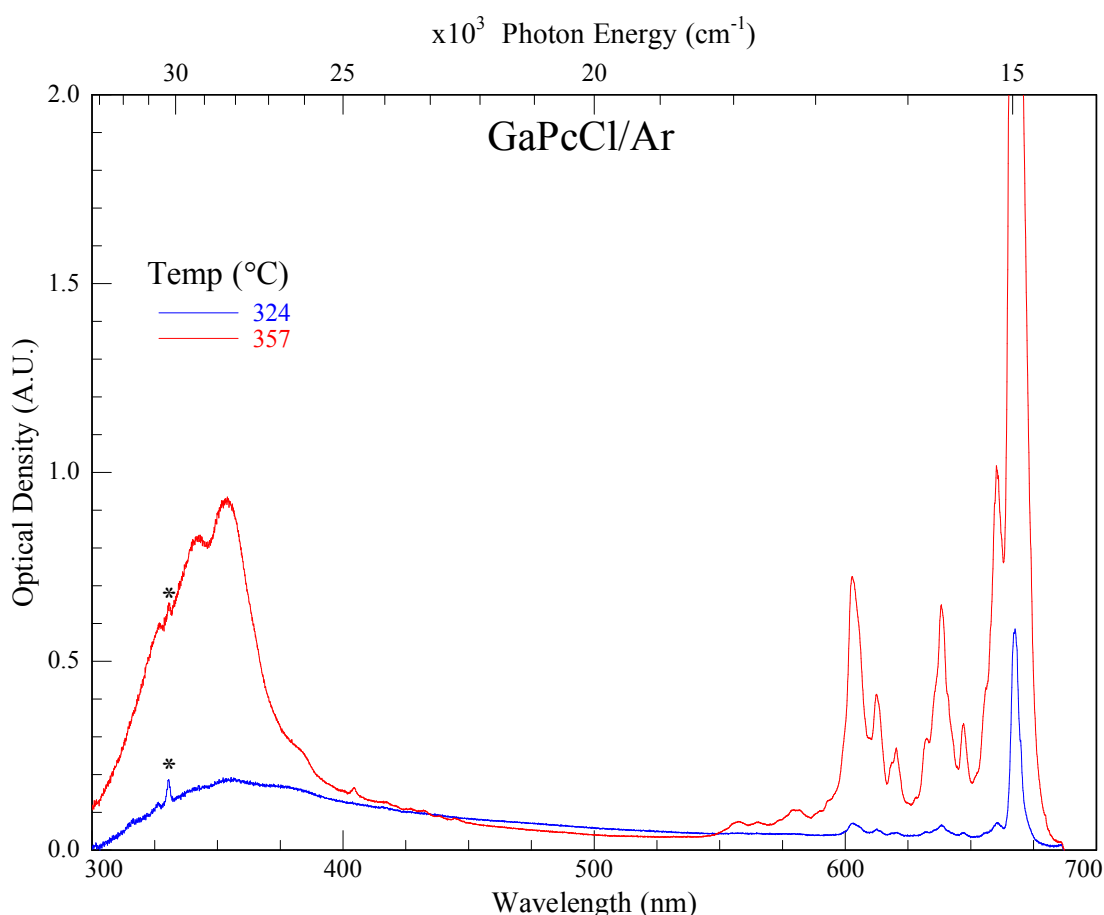


Figure V.1: The effect of the oven temperature on the absorption spectrum of GaPcCl isolated in solid Ar which was prepared with a window temperature of 10 K. The absorption spectrum of the sample made with an oven temperature of 10.2 mV (324 °C) is shown by the blue trace and the sample formed with an oven temperature of 11.4 mV (357

°C) is shown by the red trace. The sharp peak located on the B band at 330.6 (highlighted by the asterisks) was present in the earlier samples prepared. This peak corresponds to small amounts of pyrene impurities. This material was studied on the matrix-isolation rig prior to GaPcCl. Later samples do not show the same band, indicating the impurity was removed after several samples were prepared.

A series of bands to the red of the B band are located between 400 and 450 nm, whose origin is unknown. They are too far to the red to belong to pyrene (see figure caption) and too far to the blue to be vibronic bands of the $Q \leftarrow G$ transition of GaPcCl. These bands may in fact be weak electronic transitions of GaPcCl that are distinct from the Q and B bands. This will be discussed in more detail after the TD-DFT results have been presented in Section V.4.I.

The two spectra presented in Figure V.1 show a striking difference in the relative absorption strengths. The sample prepared with the low oven temperature deposition (blue trace) has a maximum optical density of 0.604 at 670.3 nm, whereas the high temperature sample (red trace) is saturated at this wavelength in absorption. The vibronic bands extending up to 603 nm are not saturated in either sample and can be used to get an estimate of the optical density of the high temperature sample. The low temperature sample has an OD of 0.084 for the band at 603 nm, whereas the high temperature sample has an OD of 0.740. This represents an 8.8-fold increase in intensity of the high temperature sample. Assuming the same ratio exists on the 0-0 band, the optical density of the high oven temperature sample works out to be 5.52. The effect of concentration on samples has ramifications in the spectral properties of the emission and excitation spectra, which will be presented in a later section. Specifically, high concentration samples exhibited amplified emission, whereas lower concentrations were restricted to fluorescence.

Figure V.2 presents absorption spectra of GaPcCl/Ar samples prepared with the optical window held at the specified temperatures during deposition. Only the region of the Q band has been shown for clarity. The sample prepared at 22 K (black trace) shows the best resolution on the 0-0 transition and the accompanying vibronic bands. It appears that there are multiple sites present in this matrix due to the splitting observed on the vibronic bands. This sample also appears to contain some aggregate species which is manifested as a broad band that is red-shifted with respect to the band origin. The sample prepared at 18 K (red trace) shows similar structure to the 22 K sample, with the 0-0 transition located at 670 nm

and vibronic bands extending up to 603 nm. The resolution on the 0-0 band as well as the vibronic bands is slightly less in this sample and there is an indication of several sites being present due to the structure on the vibronic bands. A smaller amount of aggregate species is present in this sample but a weak aggregate band can be clearly seen at 673.9 nm. The blue trace was prepared with a window temperature of 10 K, which is typically the minimum temperature achievable with the cryogenic apparatus. The band origin (0-0 transition) is identifiable at around 670 nm, as indicated by the dashed line, but is much less resolved than in the spectra recorded for the higher temperature samples. The vibronic bands are barely resolved and are quite noisy. It is difficult to tell from absorption if there are many sites present in this matrix, but it does not appear that many aggregates have formed.

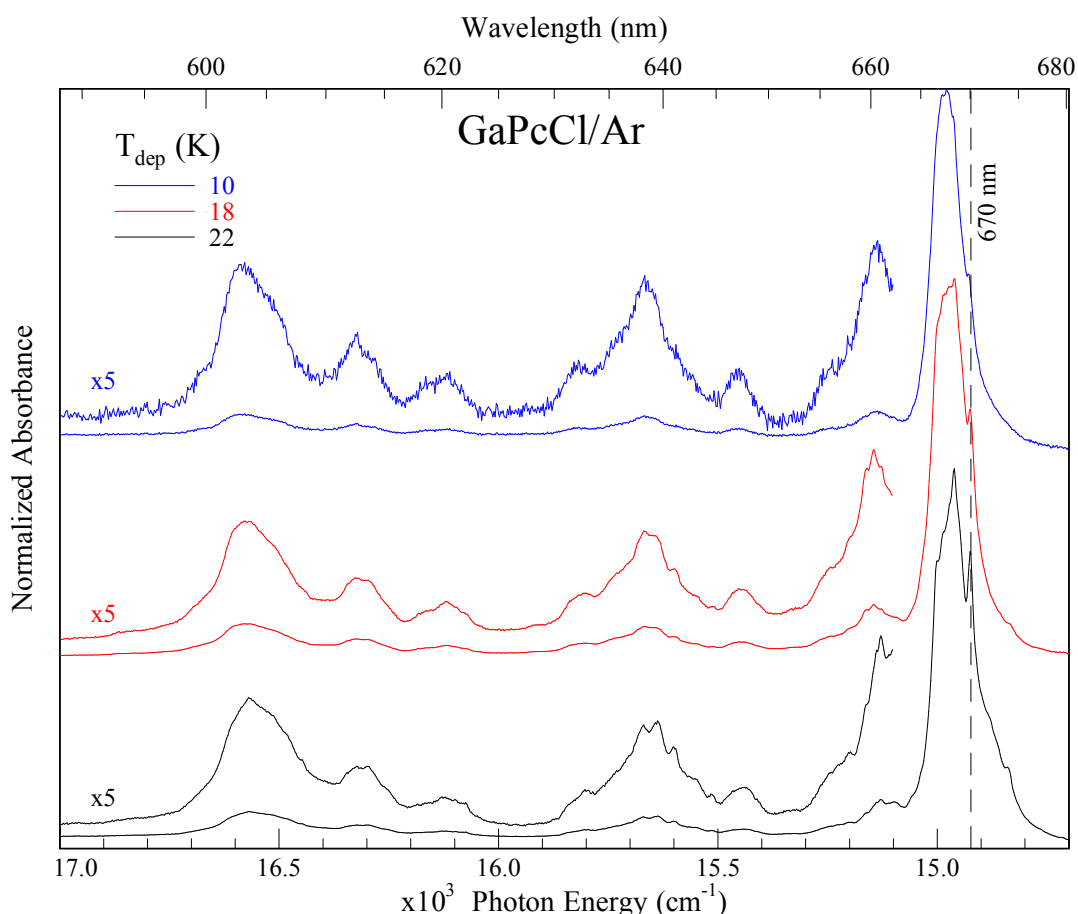


Figure V.2: The absorption spectra of GaPcCl isolated in solid Ar prepared with different temperatures of the CaF₂ window. The blue trace was prepared with a window temperature of 10 K, the red trace with temperature of 18 K and the black trace with a temperature of 22 K. All samples were prepared with oven temperatures below 330 °C to prevent saturation of the strongest absorption band at 668.4 nm.

The temperature of the CaF₂ window clearly changes the composition of the sample. An increasing resolution of the 0-0 band is evident as the window temperature increases. This is highlighted with the dashed line in Figure V.2, which best matches the 0-0 band of the 22 K sample. A sharpening on the vibronic bands with increasing temperature can also be observed, which indicates a matrix containing better resolved sites. The improved resolution of high temperature depositions means that the 22 K data will be analysed in the most detail in the upcoming sections. Aggregation becomes more of an issue at higher temperatures where the matrix is softer and clustering can occur more easily. The properties of these sites of isolation will be investigated in more detail later by studying the emission and excitation spectroscopy of these matrices.

V.3.I.b: Absorption

The absorption spectrum of a GaPcCl/Ar sample deposited at 22 K is presented in Figure V.3 in the region of the Q band prepared with an oven temperature of 340 °C. As demonstrated earlier, these deposition conditions yielded the best resolution on the 0-0 transition and the vibronic bands. The band origin of this spectrum is located at 670.0 nm (14925 cm⁻¹), with vibronic bands extending up to 603.6 nm (16567 cm⁻¹). This highest energy resolved vibronic band is located 1642 cm⁻¹ above the 0-0 transition, which is in the same energy region of the highest frequency fundamental vibrational modes (with the exception of the C-H stretching modes) observed in the ground state DFT calculations (see Table III.A4). This sample appears to contain more than one site, as indicated by the pairs of peaks evident through the spectrum. These features were not apparent in every matrix sample prepared, particularly samples made with lower window temperatures. A partially resolved peak from an aggregate species is evident at 673.9 nm, to the red of the 0-0 band. Because this peak is not present in the absorption spectra of all GaPcCl/Ar samples, it must originate from a species that is dependent on the sample deposition conditions, and therefore cannot be from the well-isolated molecule. A list of the absorption bands and their shift from the band origin are presented in Table V.1.

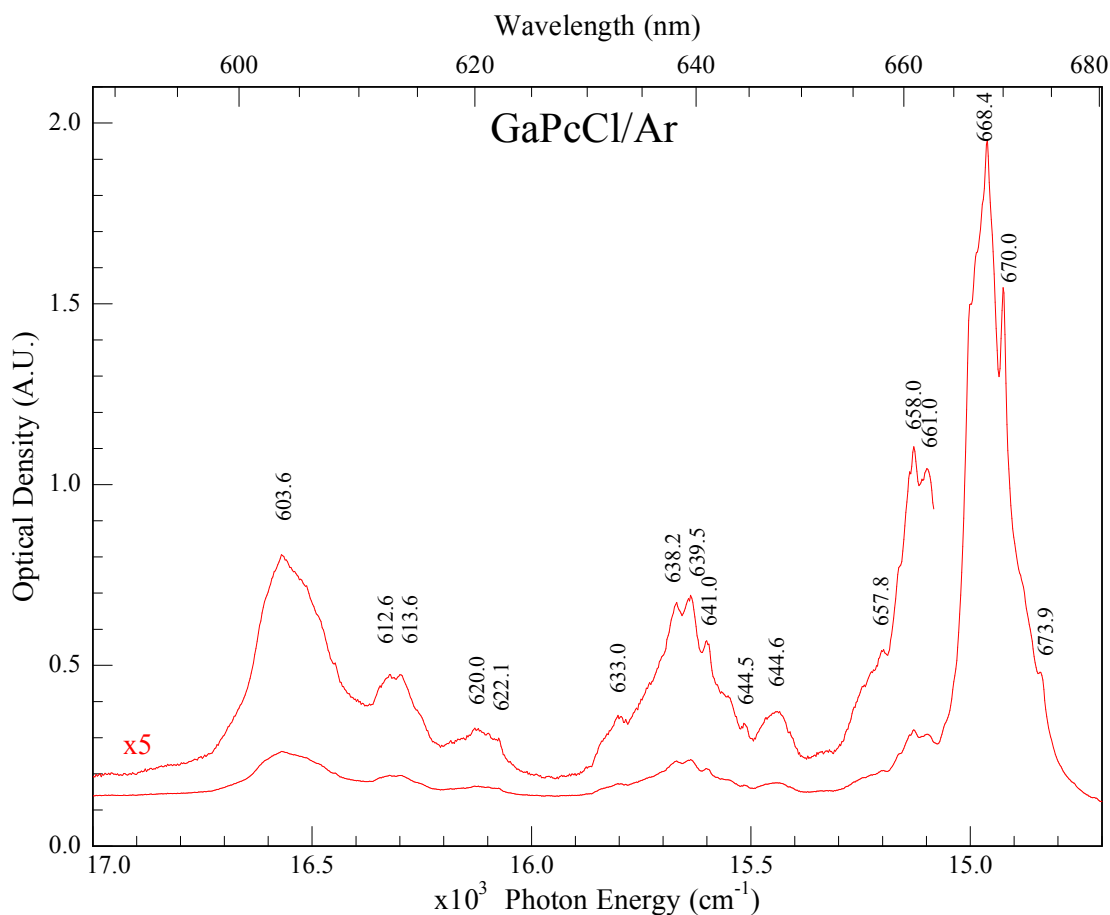


Figure V.3: Absorption spectrum in the region of the Q band of GaPcCl isolated in solid Ar at cryogenic temperatures. The above sample was prepared with a window temperature of 22 K and an oven temperature of 340 °C. The vibronic bands have been identified and labelled, with their values given in nm. The equivalent energy values are given in Table V.1.

Table V.1: Absorption bands of GaPcCl isolated in a solid Ar matrix taken from Figure V.3. The bands have been shown in wavelength, energy and as their shift from the band origin (0-0).

Wavelength (nm)	Energy (cm ⁻¹)	Shift from 0-0 (cm ⁻¹)
673.9	14839	-86
670.0	14925	0
668.4	14961	36
661.0	15129	203
658.0	15198	272
657.8	15202	277
657.8	15202	277
644.6	15513	588
644.5	15516	591
641.0	15601	675
639.5	15637	712
638.2	15669	744
633.0	15798	872
622.1	16075	1149
620.0	16129	1204
613.6	16297	1372
612.6	16324	1398
603.6	16567	1642

V.3.I.c: Emission

Fluorescence spectra of GaPcCl isolated in solid Ar were recorded with laser excitation using the apparatus described in Chapter II. The spectrum shown by the red trace in Figure V.4 was recorded by exciting into the 0-0 band in absorption ($\lambda_{\text{ex}} = 670.3$ nm) and gives the simplest fluorescence spectrum. It exhibits a set of sharp emission bands (linewidth ~ 10 cm⁻¹) extending up to 747 nm. These bands correspond to the excited vibrational levels in the ground electronic state. Due to this excitation being into the 0-0 transition in absorption, the 0-0 band is not visible in this emission spectrum. However, this region has been recorded with $\lambda_{\text{ex}} = 662.7$ nm, and yields peaks 0 – 4. The peaks labelled 0 to 23 are presented in Table V.2. An indication of the presence of emission from aggregate species is evident due to the broad red shoulder on some of the intense emission bands. Emission from a dominant site is observed with this excitation wavelength and allows for a detailed analysis of the vibronic bands in emission to be performed. This analysis will be carried out in Section V.4.III.

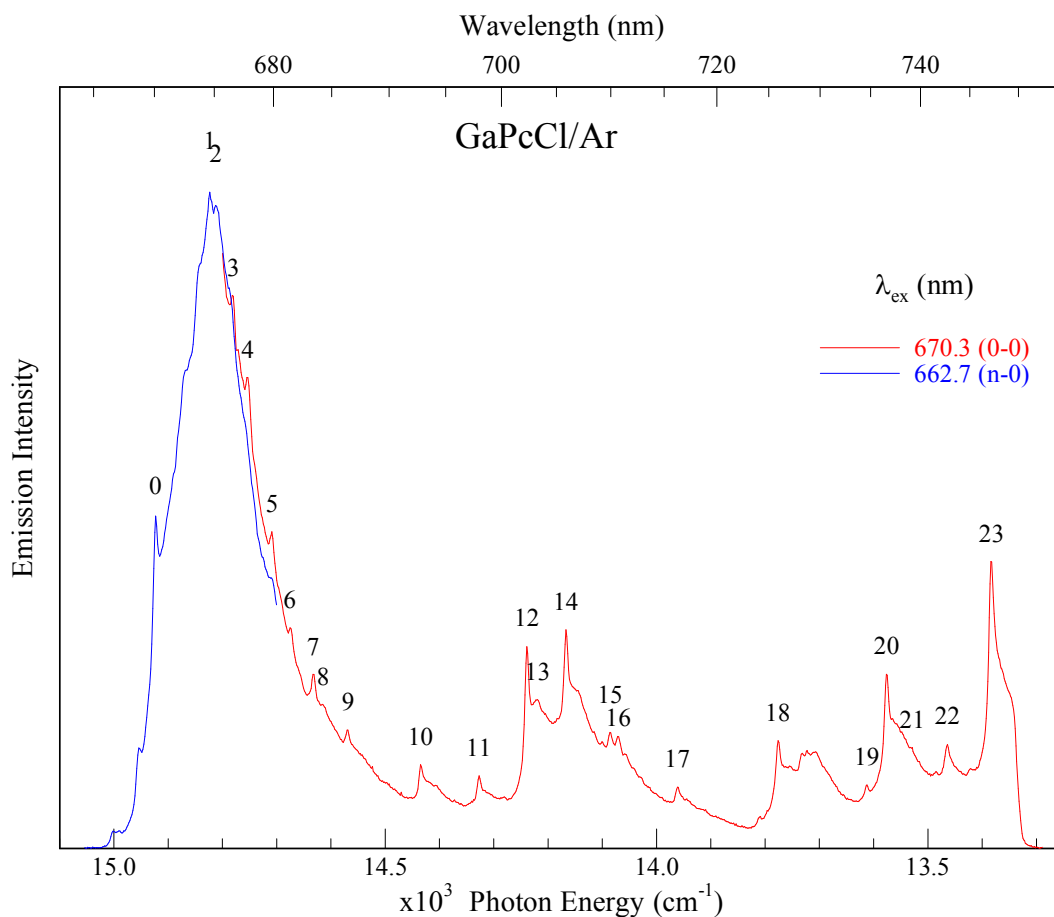


Figure V.4: Emission spectrum of GaPcCl/Ar recorded by exciting into the 0-0 band in absorption ($\lambda_{\text{ex}} = 670.3$ nm, red trace). The region of the 0-0 transition in emission was recorded at 662.7 nm (blue trace). The vibronic bands have been labelled, with the wavelength values of the peaks given in Table V.2. Peaks have been labelled on the basis of their resolution.

Table V.2: Positions of the emission bands of GaPcCl isolated in solid Argon. The values are taken from the red site, obtained by exciting into the 0-0 band in absorption. The labelling system is presented in Figure V.4.

Peak #	Wavelength (nm)	Energy (cm ⁻¹)	Shift from 0-0 (cm ⁻¹)
0	670.112	14922.9	0.0
1	674.619	14823.2	99.7
2	675.110	14812.4	110.5
3	676.597	14779.9	143.0
4	677.825	14753.1	169.8
5	679.871	14708.7	214.2
6	681.424	14675.2	247.7
7	683.386	14633.0	289.9
8	684.284	14613.8	309.1
9	686.407	14568.6	354.3
10	692.769	14434.8	488.0
11	697.980	14327.1	595.8
12	702.291	14239.1	683.8
13	703.267	14219.4	703.5
14	705.867	14167.0	755.9
15	709.927	14086.0	836.9
16	710.738	14069.9	853.0
17	716.254	13961.5	961.3
18	725.894	13776.1	1146.8
19	734.633	13612.2	1310.6
20	736.574	13576.4	1346.5
21	739.162	13528.8	1394.0
22	742.719	13464.0	1458.8
23	747.246	13382.5	1540.4

A series of fluorescence spectra recorded with specified excitation wavelengths in the vicinity of the band origin are presented in Figure V.5. The red trace was recorded by exciting into the 0-0 transition in absorption ($\lambda_{\text{ex}} = 670.3$ nm) and shows the same data presented in Figure V.4. The effects of exciting to the blue of the 0-0 band is shown by the blue trace ($\lambda_{\text{ex}} = 668.9$ nm) of Figure V.5. The emission spectrum changes considerably compared to the red trace. A series of emission bands arise with energies that are blue shifted with respect to the bands observed in Figure V.4, the most intense of which have been labelled 'B'. These peaks correspond to the vibronic bands in emission from a 'blue' site. A series of bands (labelled 'R') are also present in this spectrum, whose energies exactly match those observed in the red trace. This is emission from the dominant 'red site' which was not directly excited by the laser. The vibronic bands from both sites emit,

causing a ‘doubling’ of the emission spectrum. The shift, which is constant throughout the entire emission spectrum, is 26 cm^{-1} .

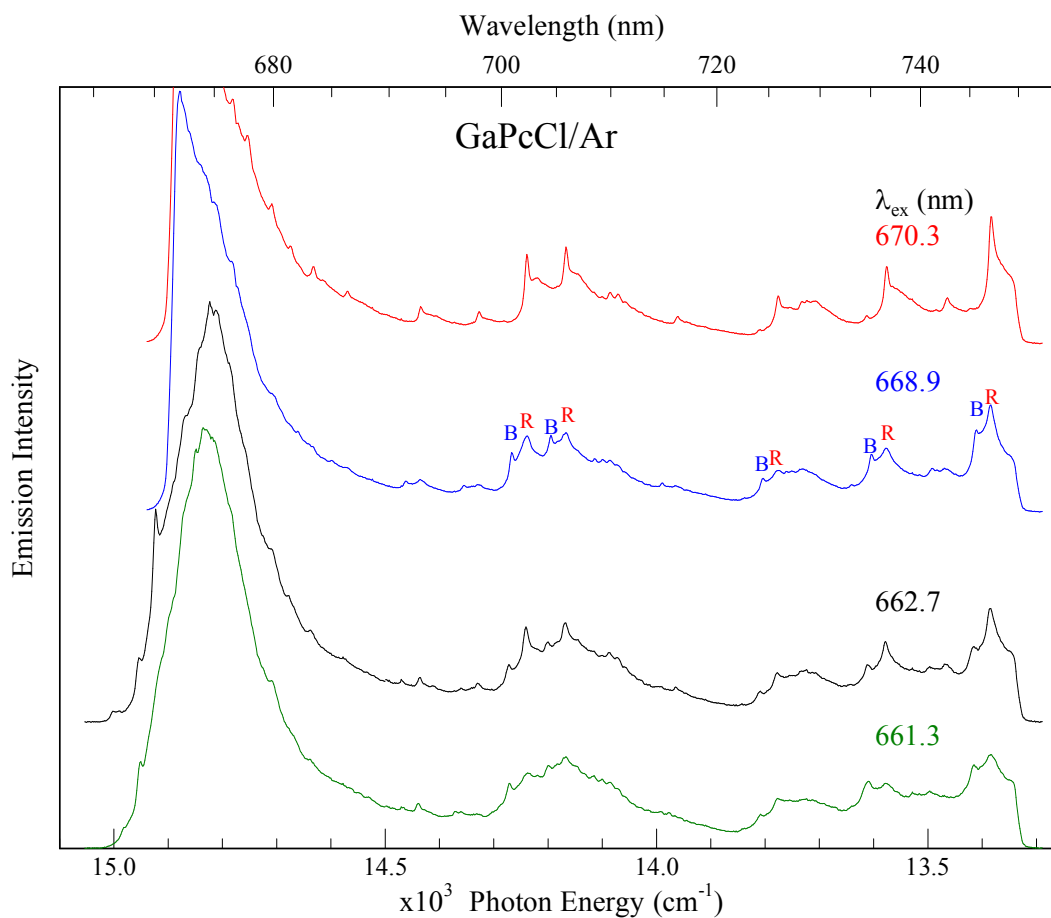


Figure V.5: Fluorescence spectra of GaPcCl/Ar recorded with a range of different excitation wavelengths.

Excitations with wavelengths even further to the blue from the 0-0 transition are shown by the black and green traces, where $\lambda_{\text{ex}} = 662.7$ and 661.3 nm respectively. Exciting in this region allows for the 0-0 band in emission to be observed. The location of the 0-0 band in emission is also dependent on the excitation wavelength as each site has a unique band origin. The band origin of the red-most site has been identified as 670.19 nm. It can also be seen that the site splitting of bands (i.e. emission from a blue and a red site) which was observed in the blue trace is also present with these excitation wavelengths. The energy difference between the emission bands of the red and blue sites does not match the difference observed in the blue trace. This indicates that there are more than two sites, and this rich site structure of GaPcCl/Ar will be investigated in more detail later using 2D excitation-emission spectra. Due to the relative simplicity of the fluorescence spectrum

recorded by exciting into the 0-0 band, these results will be presented and discussed in the greatest detail, unless otherwise stated.

The emission decay times of the excited electronic state of GaPcCl/Ar were measured using the apparatus and methods described in Chapter II, namely pulsed dye laser excitation and ICCD detection. Decay curves of a number emission bands are shown on a semi-log plot in Figure V.6. The decay profiles of the shorter wavelength emission bands closer to the 0-0 transition are shown in the left panel, and those of longer wavelength emission bands in the right panel. This time profile of the excitation laser pulse is also shown for comparison in each panel. A wavelength dependence on the emission decay time is evident, due to the decay profiles of the various emission bands not matching up exactly. The longer wavelength emission bands appear to have the shortest decay times, with the shorter wavelength emission bands being more long lived.

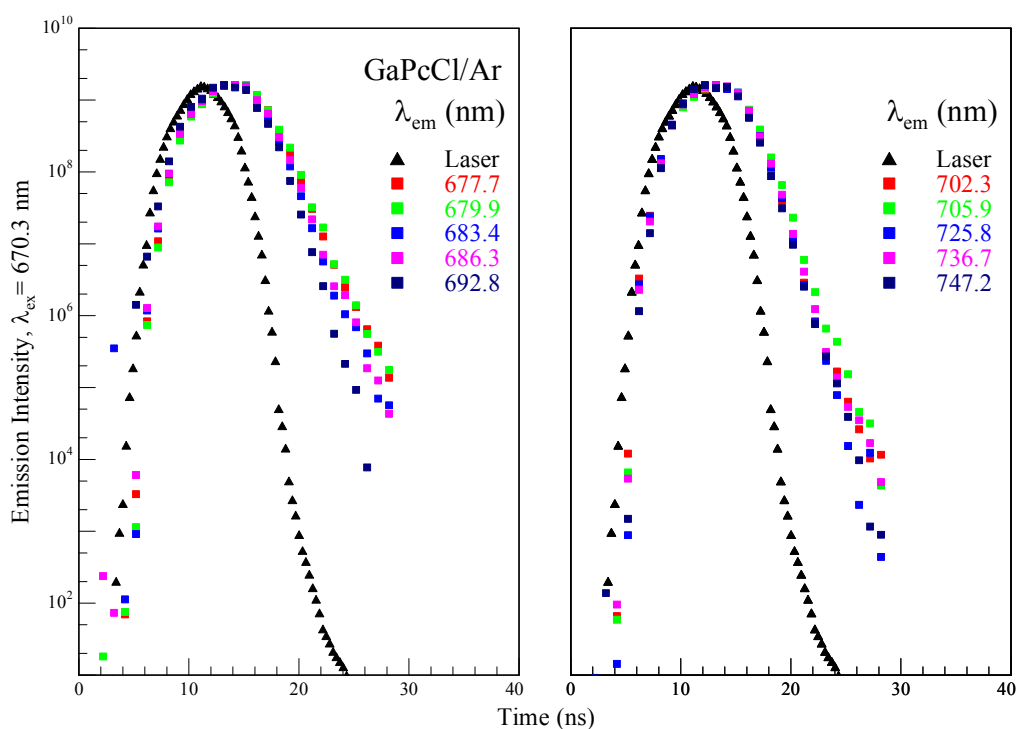


Figure V.6: Emission decay curves of GaPcCl/Ar recorded for a number of different emission bands. The profile of the laser decay is shown for comparison.

The temperature dependence on the emission lifetime was examined by recording time-resolved spectra with different CaF₂ window temperatures. Time-resolved scans were recorded at intervals of 1 K from 10 – 15 K for the sample of GaPcCl/Ar. The results of

this study are presented in Figure V.7, in which the emission band at 747.2 nm was monitored. The decay profiles recorded at each temperature appear almost identical, with slight differences within the margin of error of the experimental setup. This demonstrates that this emission decay time is not sensitive to changes in temperature, which is an indication that the fluorescence lifetime is being measured.

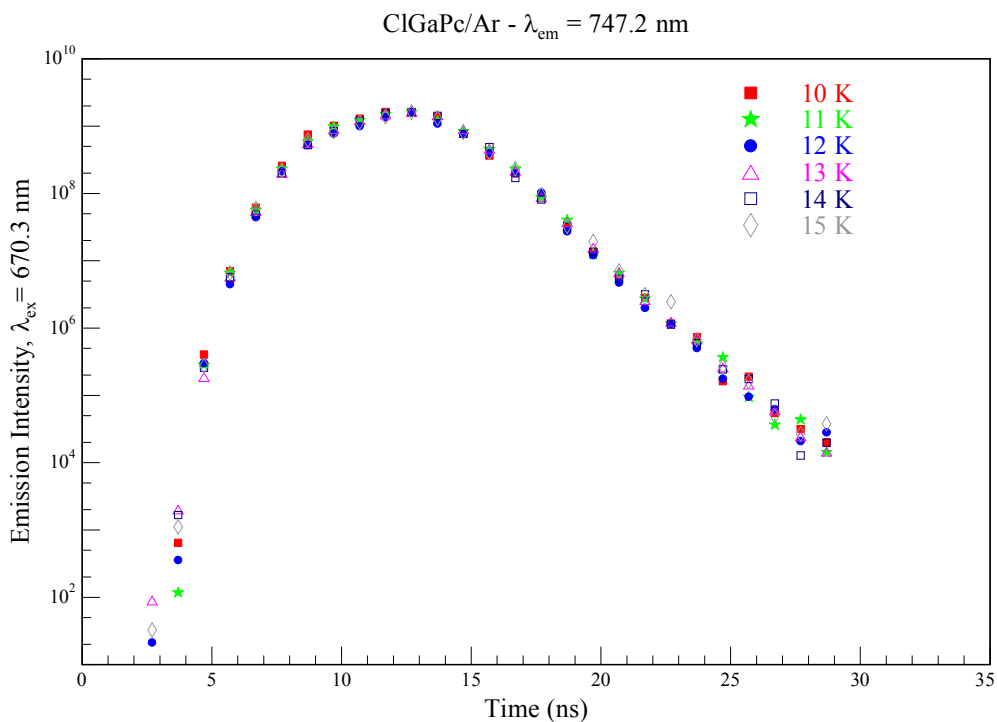


Figure V.7: Emission decay curves of GaPcCl/Ar recorded at the specified sample temperatures.

Figure V.8 shows a single exponential fit overlaid with the emission data in order to determine the excited state lifetime. The emission band at 736.7 nm has been chosen as it is sufficiently far from the band origin to give a more representative value for the lifetime than a short wavelength emission band. The lifetime has been measured as 2.3 ns in Ar. This value is in the expected range for a fully allowed electronic transition. The residuals shown by the top panel of Figure V.8 indicate an imperfect fit of the single exponential function with the experimental data. This means there may be some slight deviation in the actual lifetime compared to what has been measured, but due to the short timescales of the phenomena being measured, the difference is within the range of the error of measurement.

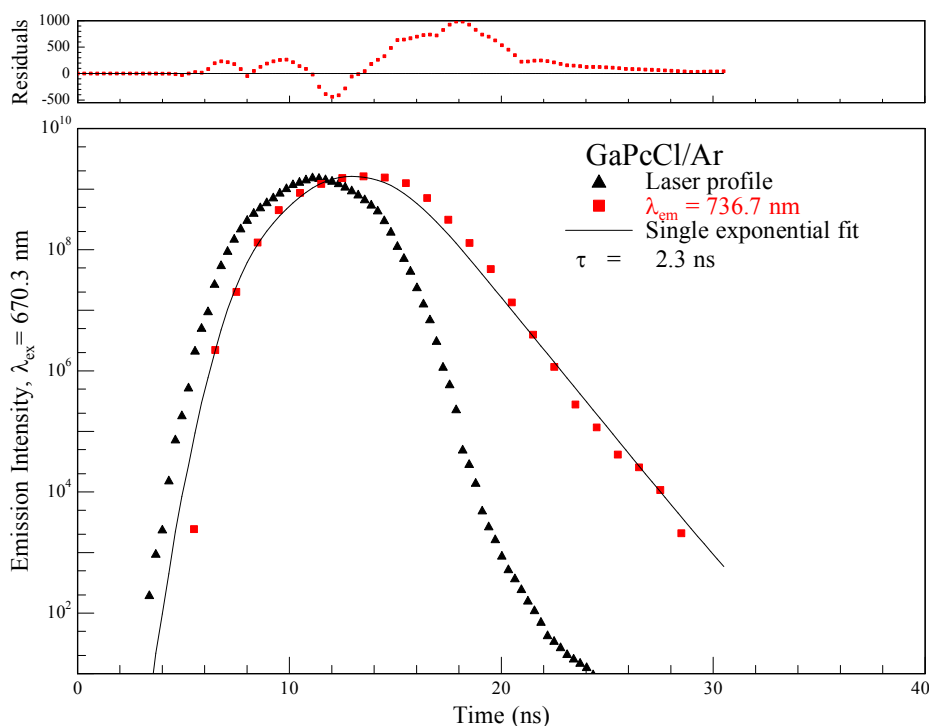


Figure V.8: Semi-log plot of the emission decay curve of GaPcCl extracted from time-resolved emission spectra recorded at 10 K in solid Ar. The shape of the excitation pulse of the laser is also shown. The emission band monitored was located at 736.7 nm and its lifetime was measured at 2.3 ns.

V.3.1.d: Excitation

Excitation spectra were recorded in one of two ways; both of which have been described in detail in Chapter II. Lamp scans recorded with the PMT were primarily used for long range excitation spectra, whereas laser scans recorded with the iCCD were limited by the tuning range of the dye. The advantage of the latter is considerable, as the excitation spectra of all emission wavelengths are recorded simultaneously at high resolution ($\sim 1 \text{ cm}^{-1}$). From here on, all excitation spectra presented will have been recorded by scanning the dye laser and monitoring emission with the iCCD, unless otherwise stated. Excitation spectra of GaPcCl/Ar recorded for a series of different emission bands are shown in Figure V.9.

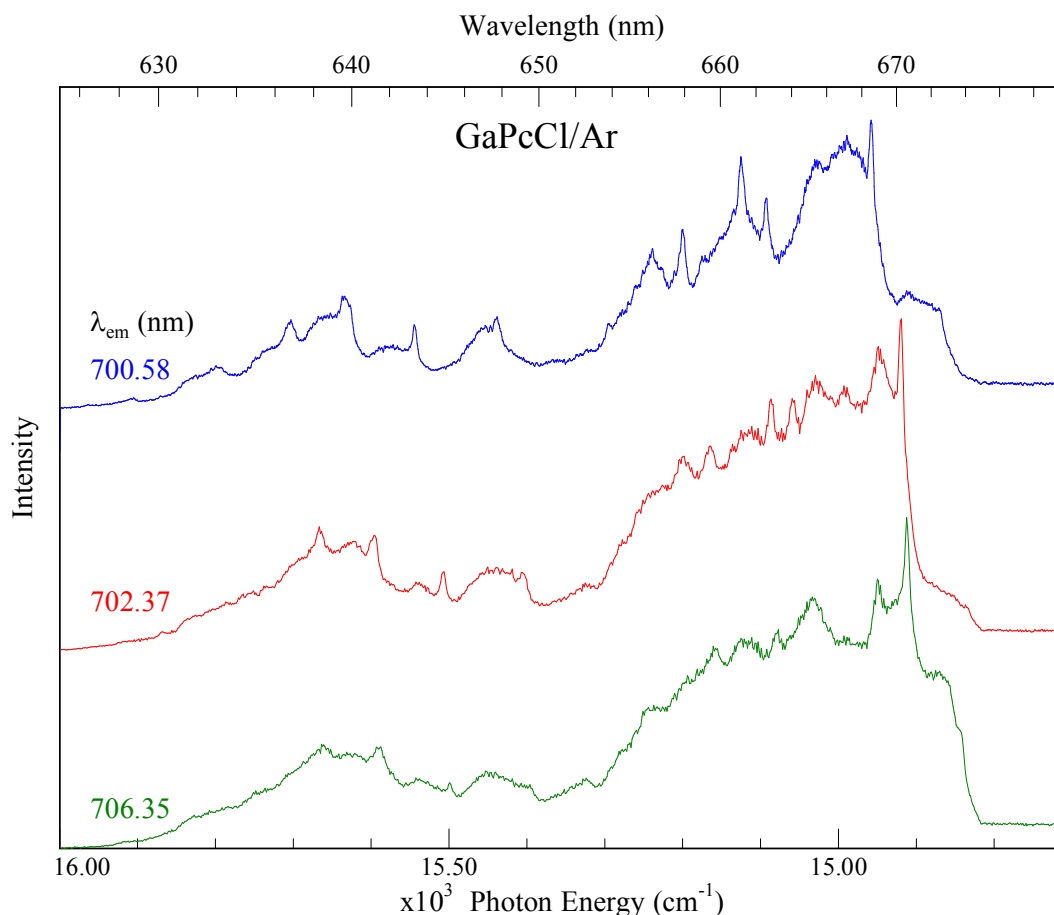


Figure V.9: Laser excitation spectra of GaPcCl recorded in Ar. The emission bands monitored were located at 700.58, 702.37 and 706.35 nm. The shifting of the spectra with respect to the excitation wavelength is an indication of multiple sites.

An example of a 2D-EE plot from which these spectra were extracted is shown in Figure V.A6. Bands start to inhabit the spectrum from about 670 nm up to 625 nm. The spectra show some nice structure and narrow linewidths. The 0-0 band of the excitation spectrum is very sharp, with the bands at higher energies becoming slightly broader. A migration of the band origin in excitation is evident; an effect of monitoring emission bands from different sites in the sample. The same vibronic bands appear in all three spectra shown in Figure V.9, albeit with their energies shifted. When the excitation spectra are plotted as the shift from the 0-0 transition (as shown in Figure V.A1), the energies of the vibronic bands are almost identical. The main difference between the blue curve from the other two is the feature immediately to the blue of the 0-0 band (~ 667 nm). The blue trace shows a very broad emission band whereas the red and green traces show fairly narrow bands in the corresponding regions. The resolution on the excitation scans recorded for the 700.58 nm

emission band (blue trace) is superior to the other two spectra, due to it being the dominant site in the matrix and thus carrying the greatest intensity in emission (and hence excitation). The broad wings to the red of the narrow 0-0 lines probably arise due to aggregate species in the sample, similar to what is observed in absorption.

V.3.1.e: Amplified Emission

In samples with an optical density greater than 2, excitation into selected absorption bands exhibited a significant increase in the intensity of one of the emission bands with only a modest increase of laser power. The fluorescence spectra presented in Figure V.5 were recorded using only the oscillator of the dye laser, whereas spectra in the upcoming section were recorded with the pre-amplifier. An example of the amplification of one of the emission bands of GaPcCl in the Ar matrix is presented in Figure V.10, where the band at 747.16 nm exhibits the effect. The main area of the plot shows the normalized fluorescence spectrum (red trace) produced with excitation into the 0-0 band using the oscillator. When the dye laser power is increased, by using the pre-amplifier, the vibronic band at 1540 cm^{-1} from the band origin, exhibits a huge increase in intensity as shown by the black trace. Such behaviour is an indication that this process being observed might be amplified emission (AE). The inset spectrum shows the bands in fluorescence and amplified emission, both of which have been normalized. As well as the increase in intensity, there is also an obvious narrowing of the linewidth of the AE band; the linewidth of the fluorescence band is 10 cm^{-1} compared to 4 cm^{-1} for the AE band. The full extent of the narrowing of the AE band is limited by the resolution of the 1200 groove/mm grating (0.04 nm) of the monochromator. A red shoulder on both the fluorescence and amplified emission band is apparent, which will be discussed in more detail in Chapter VI.

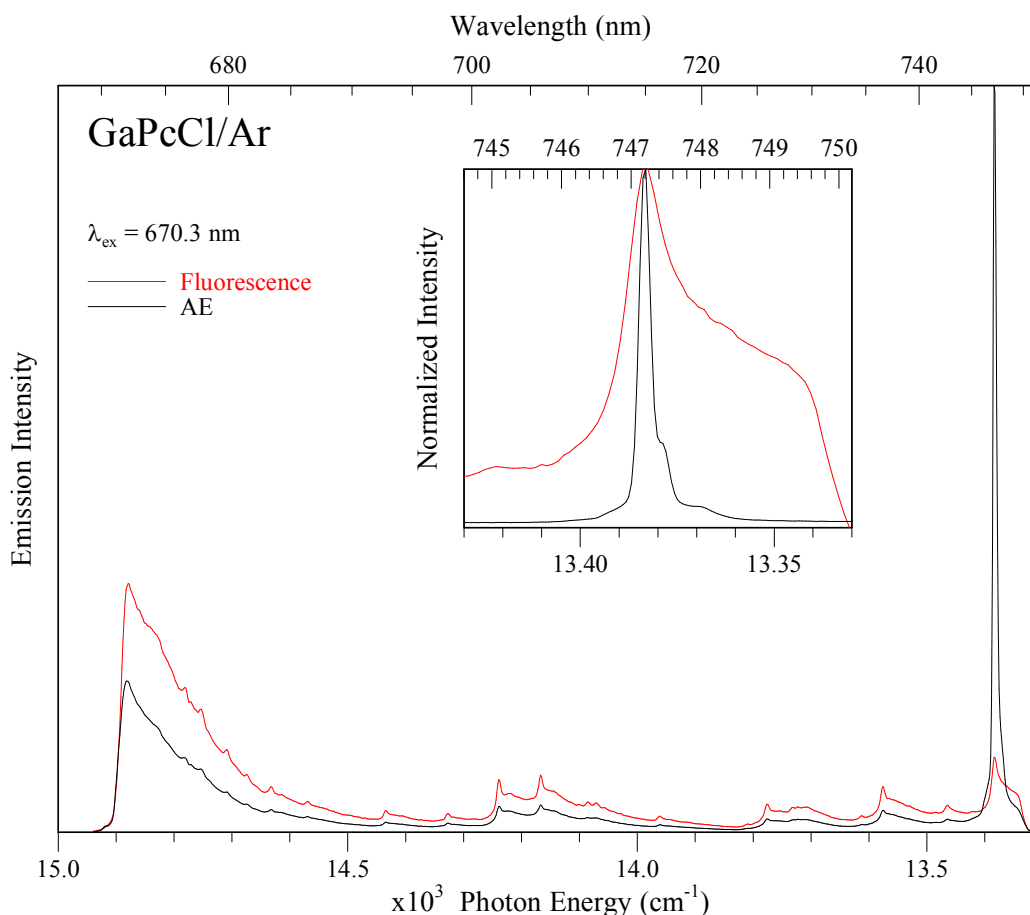


Figure V.10: Emission spectra of GaPcCl recorded in an Ar matrix at 10 K with an excitation wavelength of 670.3 nm. The red trace presents the normal emission (fluorescence) produced with lower laser power (10 $\mu\text{J}/\text{pulse}$). The black trace shows the significant increase in the intensity of the 747.16 nm emission with the use of approximately 100 $\mu\text{J}/\text{pulse}$. The inset on the right shows details of the lineshape changes on the 747.16 nm band under both low and high pulse energies.

The band at 747.16 nm was not the only one to exhibit the effect; by changing the excitation wavelength, the position of the amplified band also changes, as demonstrated in Figure V.11. As the excitation wavelength moved to the blue so did the AE band. With certain excitation wavelengths, such as 668.6 and 666.4 nm, several bands were amplified at once. Two such emission spectra are shown by the blue and black traces of Figure V.11 respectively. The origin of the duplicate AE bands is from the presence of multiple sites in the matrix, similar to what was observed in fluorescence. In cases where multiple AE bands were observed in a single spectrum, the splitting between the bands was identical to those observed in the corresponding fluorescence spectra (some of which are shown in Figure V.5). This is another strong indication that many sites exist in this matrix that are

sufficiently occupied to exhibit the effect, and will be discussed in more detail in Chapter VI. The green trace of Figure V.11 shows the vibronic bands (in fluorescence) of GaPcCl from a pair of sites, located at 13610 (734.8) and 13570 cm^{-1} (736.9 nm), which are comparable in intensity. These two peaks are fluorescence bands of a common vibronic level from different sites. The next common vibronic level of these two sites shows a significant intensity difference. The band from the blue site at 13420 cm^{-1} (745.2 nm) has a similar intensity to the two fluorescence bands mentioned previously. The corresponding vibronic band from the red site at 13380 cm^{-1} (747.4 nm) has gained significant intensity, meaning this site has evidently reached the threshold value required to exhibit AE with an excitation wavelength of 657.8 nm.

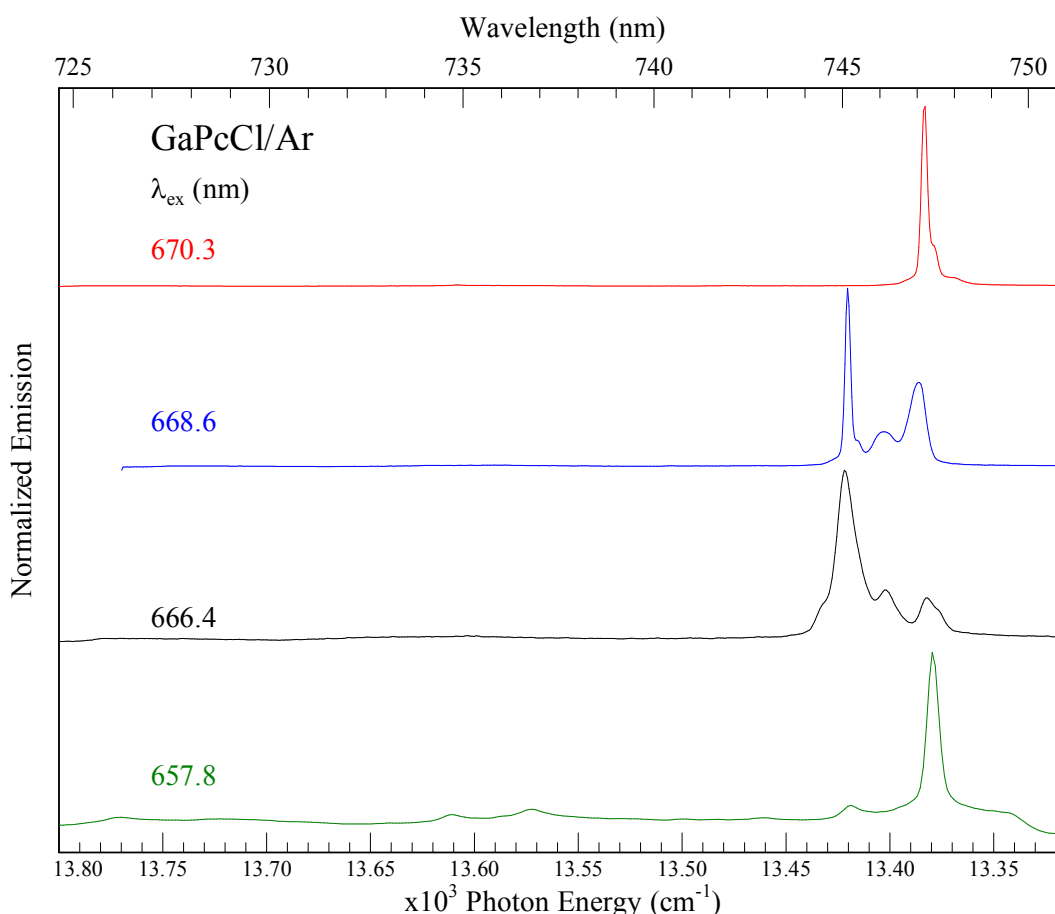


Figure V.11: Amplified emission bands of GaPcCl/Ar recorded with various excitation wavelengths. Changing λ_{ex} excites into different/multiple sites and shows evidence for the complex site structure of the sample.

Figure V.12 presents the decay curve of the emission band at 747.16 nm shown in Figure V.10 as well as a nearby fluorescence band which does not exhibit an increase in emission

intensity. The fluorescence band (black squares) is comparable to the decay curve shown in Figure V.8, whereas the AE decay curve (blue stars) is similar to the laser profile. The emission band at 747.16 nm was presented after being recorded with both the low and high power laser excitation intensities (Figure V.10). When emission was recorded with the oscillator (low laser power), regular fluorescence was observed and the decay time of the band at 747.16 nm matched that of the results shown in Figure V.6. When the pre-amplifier was used to record emission, the fluorescence band at 747.16 nm exhibited AE and the decay time shortened significantly, resembling that of the laser pulse, as demonstrated in Figure V.12. Also shown in this figure is the decay curve of a normal fluorescence band ($\lambda_{em} = 736.66$ nm) taken from the same time-resolved emission spectrum. From the spectral and temporal behaviour observed on this band, it is concluded that the 747.16 nm emission is being amplified when the excitation laser intensity exceeds a certain value. It corresponds to reaching a threshold value in the population inversion between $v' = 0$ of the excited (Q) electronic state and $v'' = 1$ of a specific vibrational mode in the ground electronic state. For the mode involved, spontaneous emission is amplified by stimulated emission once the threshold value is exceeded.

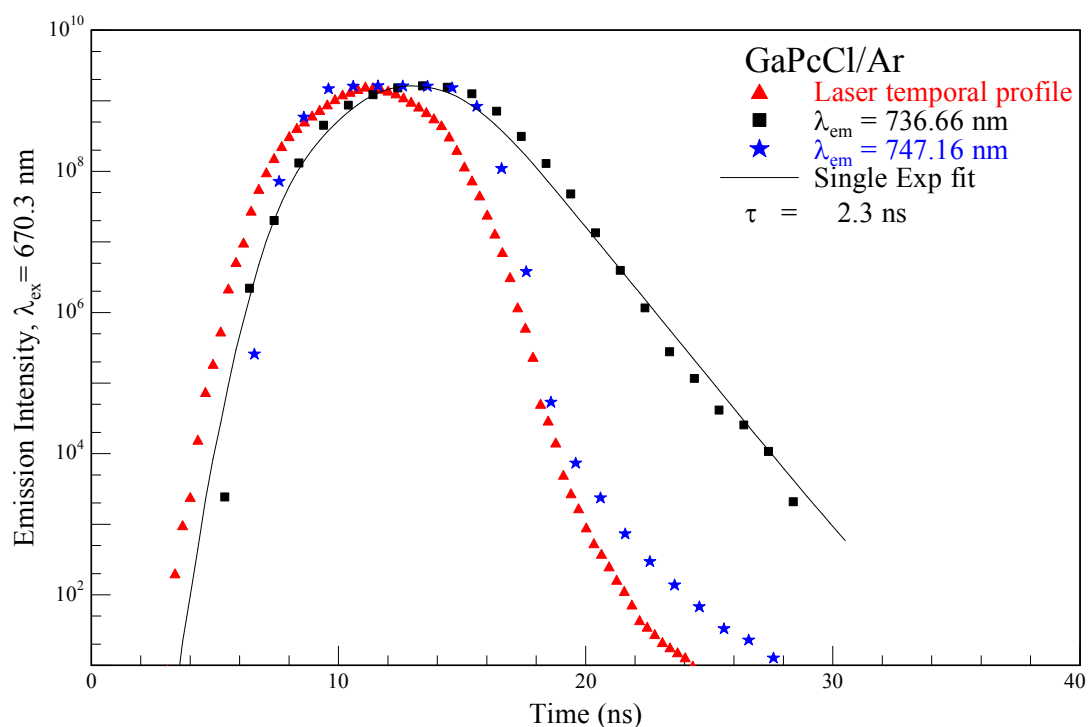


Figure V.12: The emission decay profile of GaPcCl isolated in an Ar matrix. The black squares represent the decay of a normal fluorescence band and resemble the decay in Ar observed in Figure V.8. The blue stars come from monitoring the decay of the amplified emission band at 747.16 nm. The fact that this band has a similar decay time to the laser

temporal profile (red triangles) is further proof that the process is being caused by amplified emission.

A series of excitation spectra were recorded of the AE band from various sites and are shown in Figure V.13, along with the excitation scan of a fluorescence band. The excitation spectrum of the fluorescence band at 702.37 nm is shown as the pink trace in Figure V.13. The fluorescence band in question is a separate vibronic band to the one which exhibits AE, coming from the same site as the spectrum shown by the red trace, and contains several fairly well resolved peaks. A comparison of this spectrum with excitation spectra from other sites is shown in Figure V.9. This spectrum appears quite noisy when compared to the excitation spectra of some of the AE bands. This is due to the huge increase in intensity of emission in these spectra, which completely drowns out electronic noise from the CCD detector. There also appears to be a narrowing of the excitation bands in the AE spectra, similar to what is observed in emission, but not as dramatic.

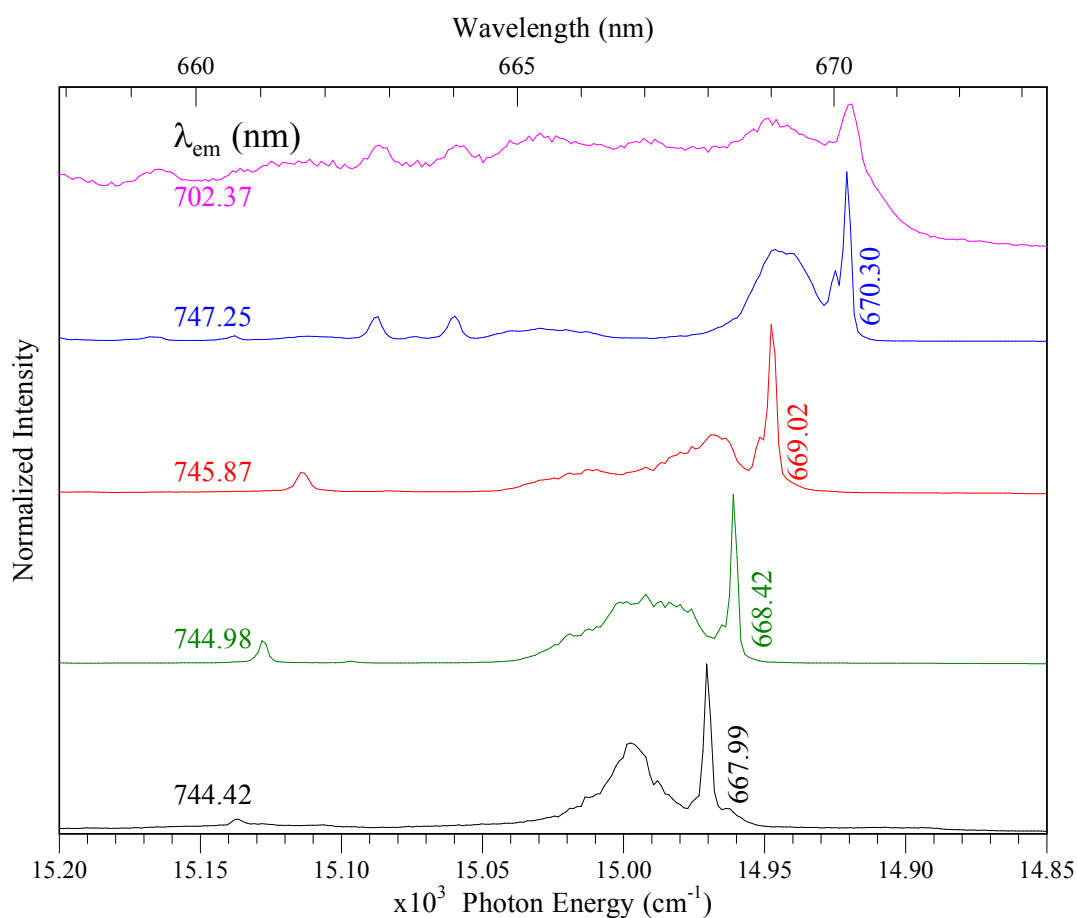


Figure V.13: A selection of excitation scans of the site specific AE bands of GaPcCl/Ar involving the vibronic mode at 1540 cm^{-1} . Also shown for comparison is an excitation

spectrum of a fluorescence band (pink trace). The vertical labels identify the wavelength positions of the maxima of the most intense band in each spectrum.

The sharp resolved lines on the excitation spectra at 670.30, 669.02, 668.42 and 667.99 nm in Figure V.13 correspond to the zero phonon lines (ZPL's). These ZPL's are shifted from the 0-0 transition by 7, 31, 44 and 54 cm^{-1} respectively. The shifting of the ZPL with respect to the emission wavelength being monitored corresponds to a progression of the $Q \leftarrow S_0$ transition in excitation. Each AE excitation spectrum shows a very sharp and identifiable ZPL (coming from different sites), with a much weaker phonon side band (PSB) to the blue. Overlap between the ZPL of a 'blue site' with the PSB of a 'red site' means that excitation into the ZPL of the blue site can simultaneously excite the PSB of the overlapping red site. This has been shown earlier in the fluorescence data (Figure V.5), where excitation to the blue of the 0-0 transition caused emission from the site being directly excited into, as well as emission from the dominant red site. A similar effect is demonstrated in Figure V.11 for the amplified emission bands. A lineshape analysis on the AE bands in both emission and excitation will be performed using the Wp distribution function (Equation II.14) in Chapter VI to extract the characteristics of the ZPLs and PSBs.

The Ar matrix samples contained many sites of isolation, several of which, as demonstrated in Figure V.11 exhibit stimulated emission. The red trace, obtained with excitation into the 0-0 band, shows the simplest AE spectrum, where a single feature dominates; a sharp band centred on 747.2 nm corresponding to AE from a specific vibronic band. A weak shoulder on the red side of the intense band may indicate aggregate species being present or the possibility of phonon structure. Exciting to the blue of the 0-0 transition yields more than one AE band (each coming from the same vibronic band of GaPcCl within different sites), as observed in the blue, black and green traces of Figure V.11. These spectra demonstrate the rich site structure present in the Ar matrix and will be discussed in further detail in Chapter VI.

V.3.II: Krypton

V.3.II.a: Sample Optimization

While the sample deposition conditions were optimized well for Ar matrices, the same conditions were not necessarily ideal for preparing good samples in other matrices. As such, the same procedure outlined for Ar of varying the deposition conditions was

performed for krypton samples. The spectra shown in Figure V.14 illustrate the effect of varying the oven temperature on deposition. The blue trace represents the lower oven temperature (321 °C) in which the spectrum is moderately absorbing with the Q and B bands clearly evident, but the vibronic transitions of the Q band are quite weak. The red trace shows a spectrum recorded for a sample prepared with a higher oven temperature (360 °C). This sample shows saturation of the band origin, but has an excellent signal-to-noise ratio on the higher energy vibronic bands in the Q. Some additional structure appears to be forming on the Q band. The bands to the red of the B band between 400 – 450 nm observed in Ar persist in this matrix. This indicates that either a common impurity inhabits both the Ar or Kr matrices or that these bands are part of the GaPcCl electronic absorption spectrum. The bands are probably too far from the origin of the Q band ($\sim 8000 - 9500 \text{ cm}^{-1}$) to be considered vibronic bands, combination bands or overtones, but are distinct weakly allowed electronic transitions.

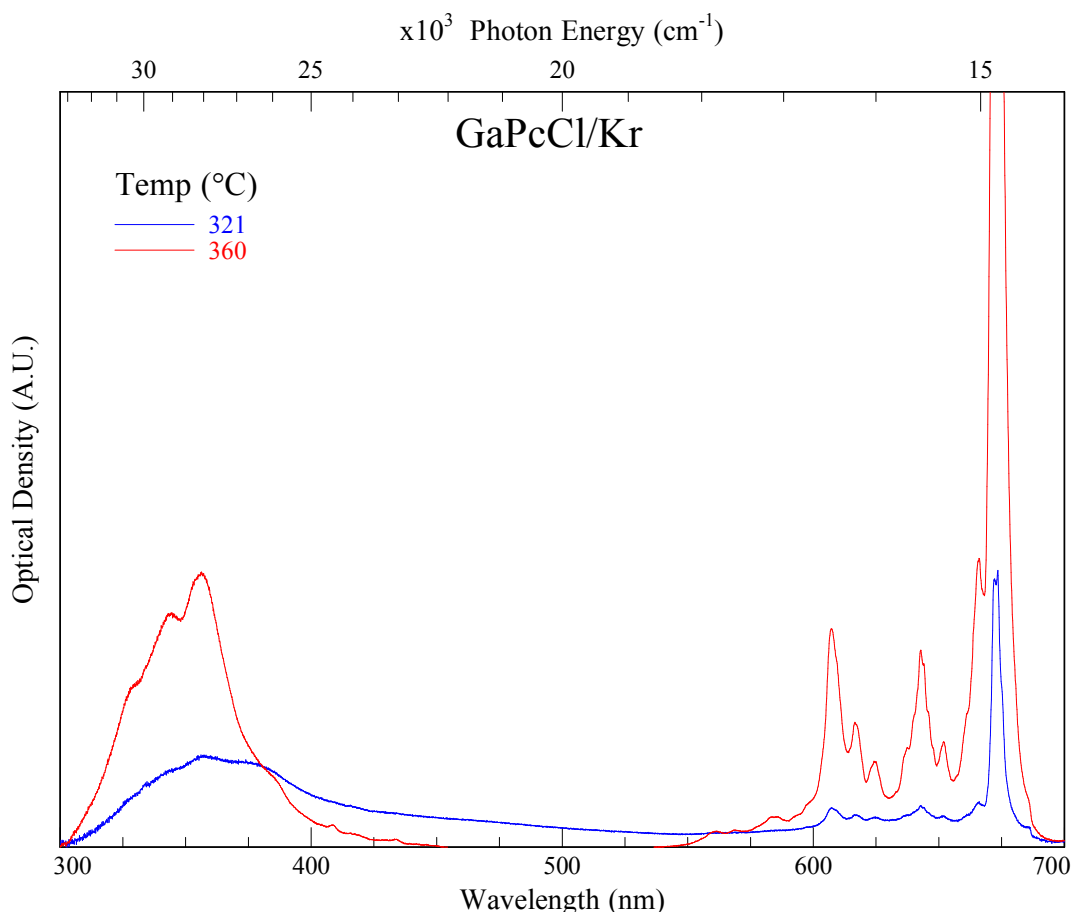


Figure V.14: The absorption of GaPcCl isolated in solid Kr prepared with a window temperature of 10 K. The blue trace was prepared with an oven temperature of 10.1 mV (321 °C) and the red trace with an oven temperature of 11.5 mV (360 °C). The pyrene

impurity is not present in either spectrum, indicating it is no longer present in the matrix rig.

In a similar manner to Ar, the optical density of the band origin of the high concentration sample in Kr can be estimated by measuring the relative increase in one of the vibronic bands which is not saturated and extrapolating the intensity of the band maximum. This will allow for a determination of the optical density required to produce amplified emission in highly absorbing samples. The intensity of the vibronic band at 607.3 nm is 0.103 for the weakly absorbing sample and 0.577 for the strongly absorbing sample. This represents a 5.6-fold increase in intensity. If this relative intensity difference holds true for the band origin at 673.6 nm, then with the low intensity curve having an OD of 0.733, the saturated peak should have an OD of 4.11. This was one of the few GaPcCl/Kr samples that exhibited AE, indicating that a high optical density is required for the process in this matrix.

A study was also performed to examine the effect of the window temperature on the sample composition, the results of which are presented in Figure V.15. The sample prepared at 10 K (blue curve) shows some unresolved structure. A shoulder to the red of the band maximum may be the unresolved 0-0 transition. The vibronic bands are not highly resolved at this deposition temperature either. The 22 K deposition (red curve) shows much more resolved structure throughout the spectrum. The region of the 0-0 band shows three well resolved bands and the 0-0 transition is clearly identifiable at 675.3 nm. The other two sharp bands in this region, located at 673.6 and 671.8 nm, may be the band origins of two other sites in the matrix. The vibronic bands in the 22 K sample are also much more resolved than in the sample prepared at 10 K. There appears to be a doubling of the peaks, indicative of multiple sites being present in the matrix. This is similar to the high temperature deposition in Ar. The formation of sites in the Kr matrix does not appear as extensive in absorption as that observed in Ar. The reduction of the number of sites in Kr may be a property of the host, or may be due to a higher host to guest ratio than what was used in the preparation of Ar matrices.

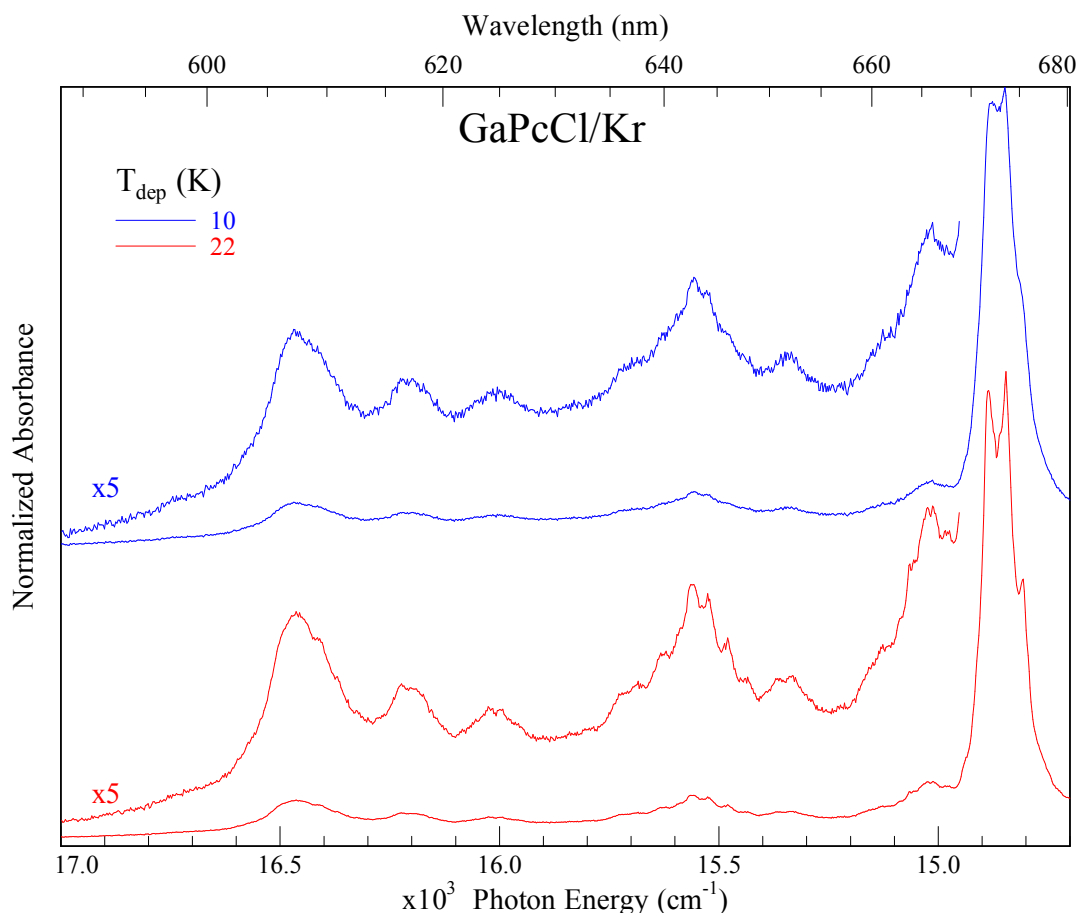


Figure V.15: The absorption of GaPcCl isolated in solid Kr, prepared with different temperatures of the CaF₂ window. The blue trace was prepared with a window temperature of 10 K, the red trace with a window temperature of 22 K. All samples were prepared with an oven temperature < 330 °C to prevent saturation of the strongest absorption band at 673.6 nm.

V.3.II.b: Absorption

Details of the absorption spectrum recorded in the region of the $Q \leftarrow G$ electronic transition of GaPcCl/Kr is presented in Figure V.16. The band origin of this transition is located at 675.3 nm (14808 cm⁻¹), which is red-shifted compared to Ar. This is due to a stronger interaction between the host and the guest species, caused by the larger polarizability of the Kr atoms compared to those of Ar. The vibronic bands extend up to 607.3 nm (16466 cm⁻¹), which is about 1658 cm⁻¹ above the band origin. A doubling-up of some of the peaks indicates that there is more than one highly occupied site of isolation in this host. An indication of a small amount of aggregates being present in the sample is demonstrated by the weak peak, to the red of the 0-0 band, located at 680.6 nm. The vibronic bands located in the absorption spectrum are collected in Table V.3.

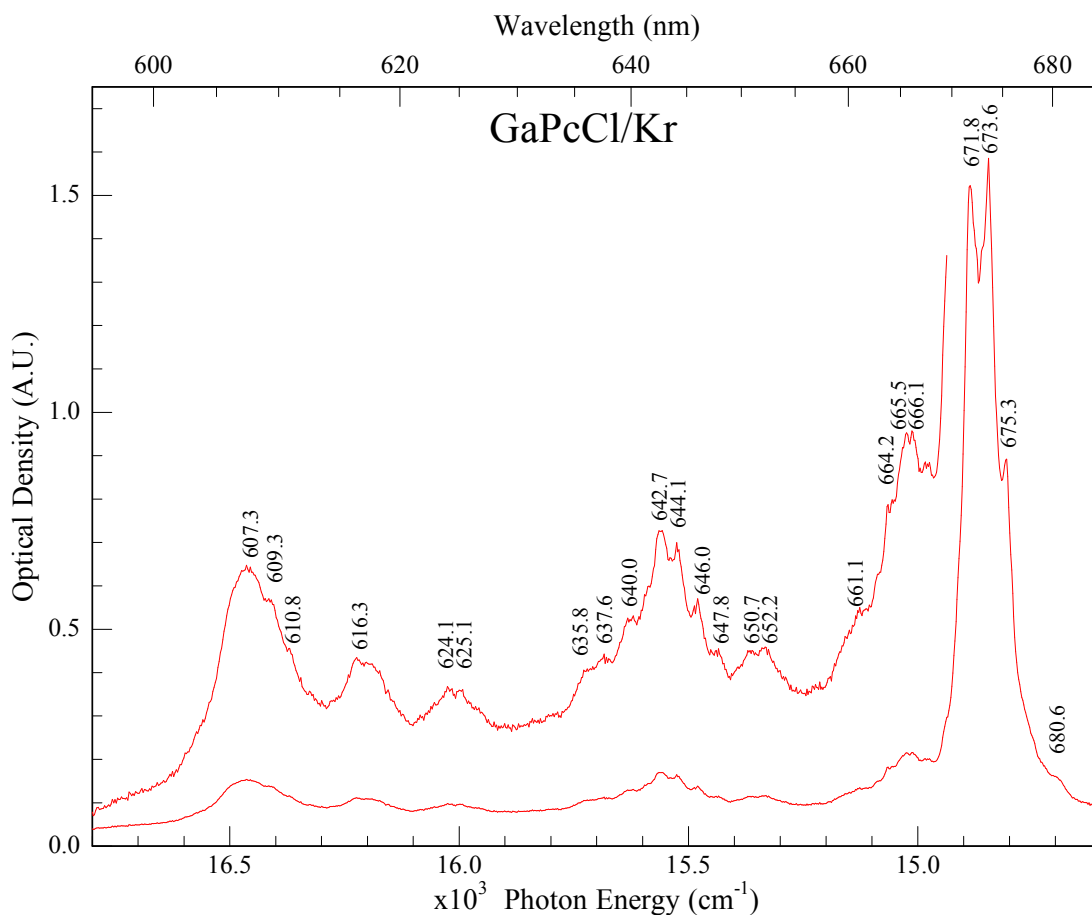


Figure V.16: Absorption spectrum in the region of the $Q \leftarrow G$ electronic transition of GaPcCl isolated in solid Kr at cryogenic temperatures. The above sample was prepared with a window temperature of 22 K and an oven temperature of 340 °C. The strongest vibronic bands have been identified and labelled, with their wavelength values given in nm. The converted energy values (and their shift from the 0-0 band) are given in Table V.3.

Table V.3: Absorption bands of GaPcCl isolated in a solid Kr matrix taken from Figure V.16. The bands have been shown in wavelength, energy and as their shift from the band origin (0-0).

Wavelength (nm)	Energy (cm ⁻¹)	Shift from 0-0 (cm ⁻¹)
680.6	14693	-115
675.3	14808	0
673.6	14846	37
671.8	14885	77
666.1	15013	205
665.5	15026	218
664.2	15056	247
661.1	15126	318
652.2	15333	524
650.7	15368	560
647.8	15437	629
646.0	15480	672
644.1	15526	717
642.7	15559	751
640.0	15625	817
637.6	15684	876
635.8	15728	920
625.1	15997	1189
624.1	16023	1215
616.3	16226	1418
610.8	16372	1564
609.3	16412	1604
607.3	16466	1658

V.3.II.c: Emission

The emission spectrum of GaPcCl/Kr recorded with excitation at 675.3 nm, into the 0-0 band in absorption, is presented in Figure V.17. This excitation wavelength yields the simplest fluorescence with a single set of emission bands extending up to approximately 760 nm. The linewidths of these bands are slightly broader than those observed in Ar, but are still reasonably narrow at 13 cm⁻¹. The 0-0 transition in emission cannot be observed at this excitation wavelength, but has been obtained with excitation ($\lambda_{\text{ex}} = 662.8$ nm), into a vibronic band to the blue of the band origin. In addition to the 0-0 transition at 675.6 nm, it shows the vibronic bands labelled 0 – 3 in Figure V.17. Emission from aggregate species does not appear in this sample. Only emission bands from a single site are observed which makes identification and analysis of the vibronic bands in this spectrum more

straightforward. The energies of the vibronic modes are collected in Table V.4. A vibrational analysis of the vibronic bands in emission will be performed in Section V.4.III.

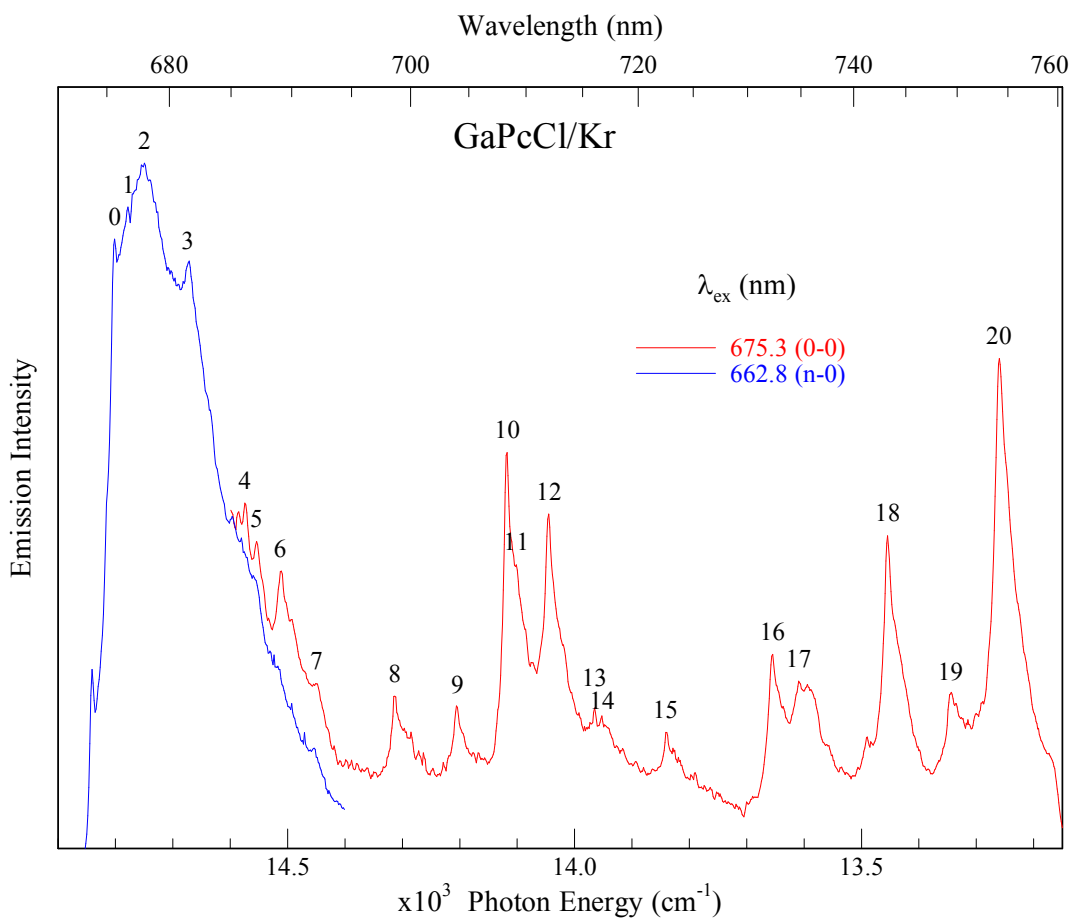


Figure V.17: Emission spectrum of GaPcCl/Kr recorded by exciting into the 0-0 band in absorption (675.3 nm). The region around the 0-0 transition was obtained with $\lambda_{\text{ex}} = 662.8$ nm. The peaks have been labelled, with their values given in Table V.4.

Table V.4: Positions of the emission bands of GaPcCl isolated in solid Kr. The values are taken from the red site, and the labels of each of the modes are shown in Figure V.17.

Peak #	Wavelength (nm)	Energy (cm ⁻¹)	Shift from 0-0 (cm ⁻¹)
0	675.614	14801.4	0.0
1	676.679	14778.1	23.3
2	677.989	14749.5	51.8
3	681.506	14673.4	128.0
4	686.120	14574.7	226.6
5	687.096	14554.0	247.4
6	689.050	14512.7	288.6
7	692.061	14449.6	351.8
8	698.652	14313.3	488.1
9	704.024	14204.1	597.3
10	708.337	14117.6	683.8
11	709.150	14101.4	700.0
12	711.999	14045.0	756.4
13	716.068	13965.2	836.2
14	716.719	13952.5	848.9
15	722.497	13840.9	960.5
16	732.344	13654.8	1146.6
17	734.785	13609.4	1191.9
18	743.249	13454.4	1346.9
19	749.353	13344.9	1456.5
20	754.154	13259.9	1541.5

Emission spectra of GaPcCl/Kr were recorded with several different excitation wavelengths identified from the absorption spectrum, a selection of which are presented in Figure V.18. The red trace ($\lambda_{\text{ex}} = 675.3$ nm) is excitation into the band origin and shows the data already presented in Figure V.17. Excitations to the blue of the 0-0 band are shown by the blue, black and green traces, with excitation wavelengths of 673.6, 666.2 and 662.8 nm respectively. These excitations yield the same set of emission bands observed with excitation into the 0-0 band, albeit with a lower intensity and a set of duplicate bands to the blue of each emission band. The reason for the duplication is due to multiple sites being present in this matrix; similar to the effect that was observed in Ar matrices. The black and green curves in Figure V.18 had excitations sufficiently far from the band origin in absorption that the 0-0 transition in emission could be observed. The 0-0 band of GaPcCl in emission for the dominant red site has been measured as 675.6 nm in Kr matrices.

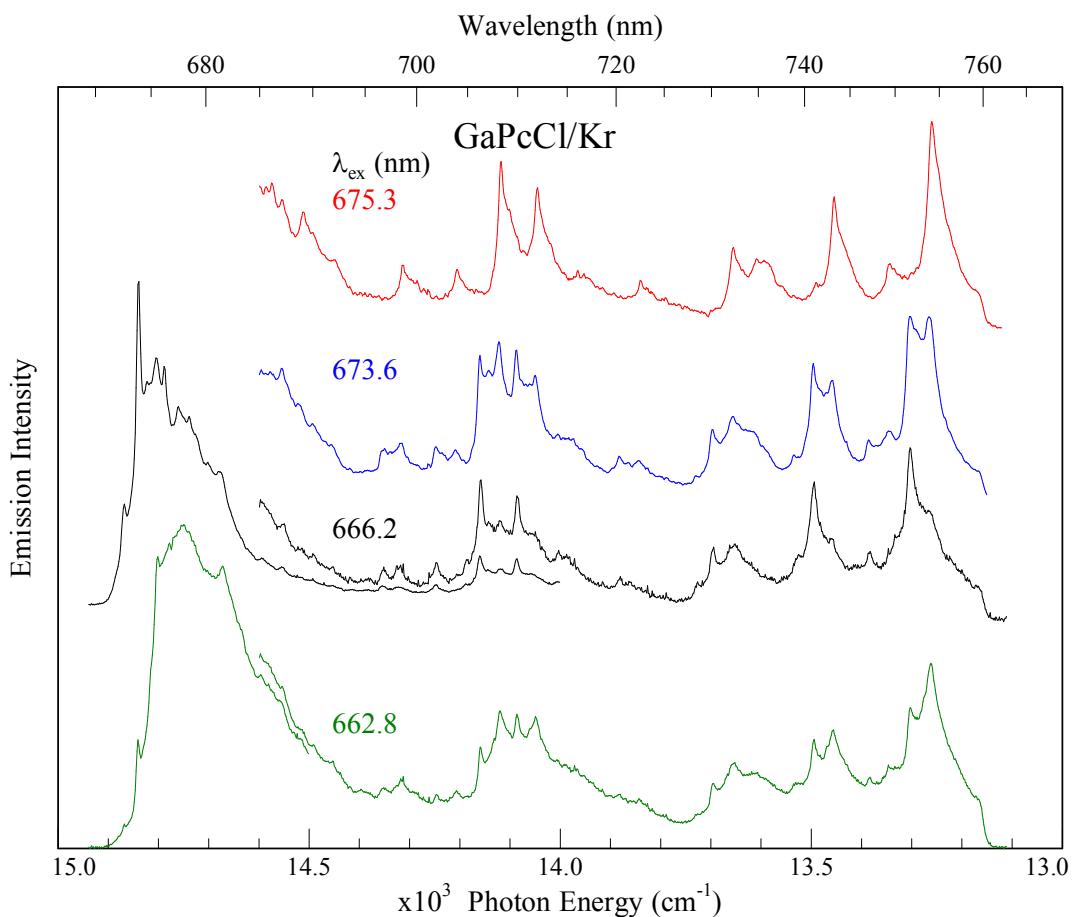


Figure V.18: Fluorescence spectra of GaPcCl/Kr recorded with the specified excitation wavelengths.

The emission decay curves of GaPcCl in Kr were recorded for a range of emission bands which are plotted in Figure V.19. The rise time of each emission band is almost identical, but the decay times are different. The emission band centred on 673.98 nm has the shortest decay time of those shown in Figure V.19, whereas the band at 739.16 nm has the longest. A wavelength dependence on the emission decay time is evident, with the shorter wavelength emission bands exhibiting shorter decay times than those at longer wavelengths. This is in contrast to the GaPcCl/Ar system, where the opposite trend was observed (i.e. short wavelength emission bands had longer decay times and vice versa).

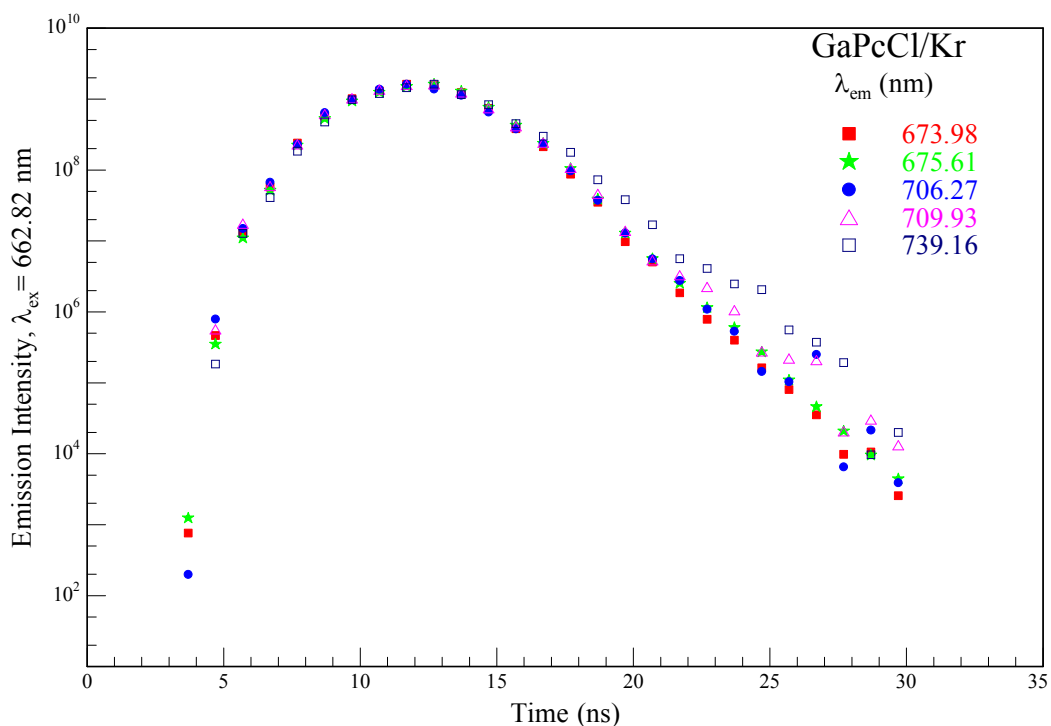


Figure V.19: A series of emission decay curves of GaPcCl/Kr recorded for specified emission wavelengths.

The thermal stability of the emission lifetime of GaPcCl/Kr was examined by recording time-resolved spectra at several wavelengths, as shown by Figure V.20. No significant changes in the decay times are observed, even at temperatures above 20 K. The slight variations in the curves are well within the expected range of the experimental error.

The excited state lifetime of GaPcCl/Kr was measured by recording time resolved emission and plotting the decay curve against a single exponential fit. To be consistent, the same vibronic band used to determine the lifetime in Ar matrices was also chosen for Kr – the band at 743.2 nm. This plot is shown in Figure V.21. The value measured for this system was 2.4 ns, which is a reasonable decay time for a fully allowed electronic transition. The decay time is slightly longer than that observed in an Ar matrix, which is not what one would expect to happen based on earlier studies⁵. These measurements were confirmed in several Kr samples made under different deposition conditions.

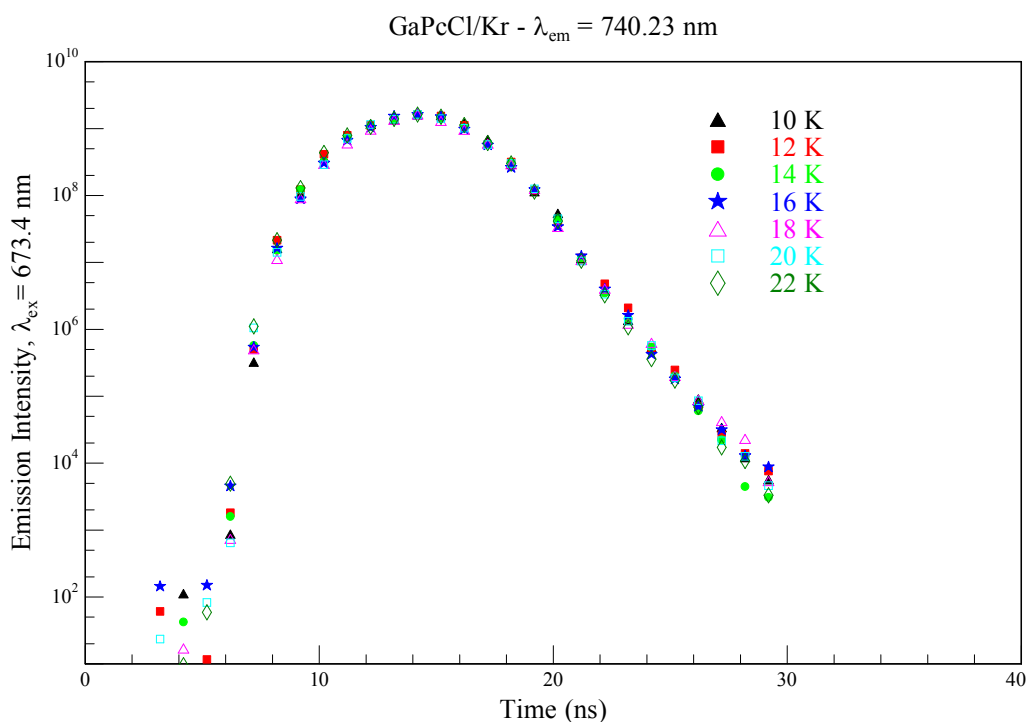


Figure V.20: Emission decay curves of GaPcCl/Kr recorded at the specified sample temperatures.

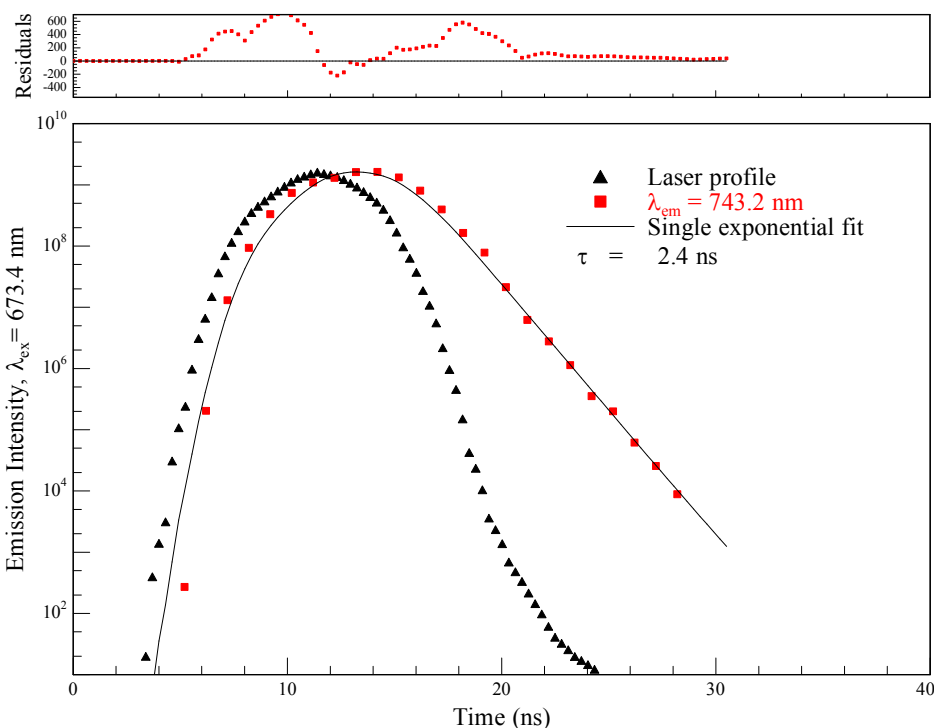


Figure V.21: Semi-log plot of the emission decay curve of GaPcCl extracted from a time-resolved emission spectrum recorded at 10 K in a Kr matrix. The shape of the excitation pulse of the laser is also shown. The emission was recorded with 673.4 nm excitation and the lifetime extracted from the fit was 2.4 ns.

V.3.II.d: Excitation

Excitation scans recorded for three distinct emission bands of GaPcCl/Kr are presented in Figure V.22, revealing bands from 675 nm up to 630 nm. Each spectrum contains a sharp band corresponding to the 0-0 transition in excitation, and slightly broader bands to the blue. The location of the band origin in excitation is dependent on the emission wavelength monitored. This further consolidates the idea that more than one site is occupied in this host solid.

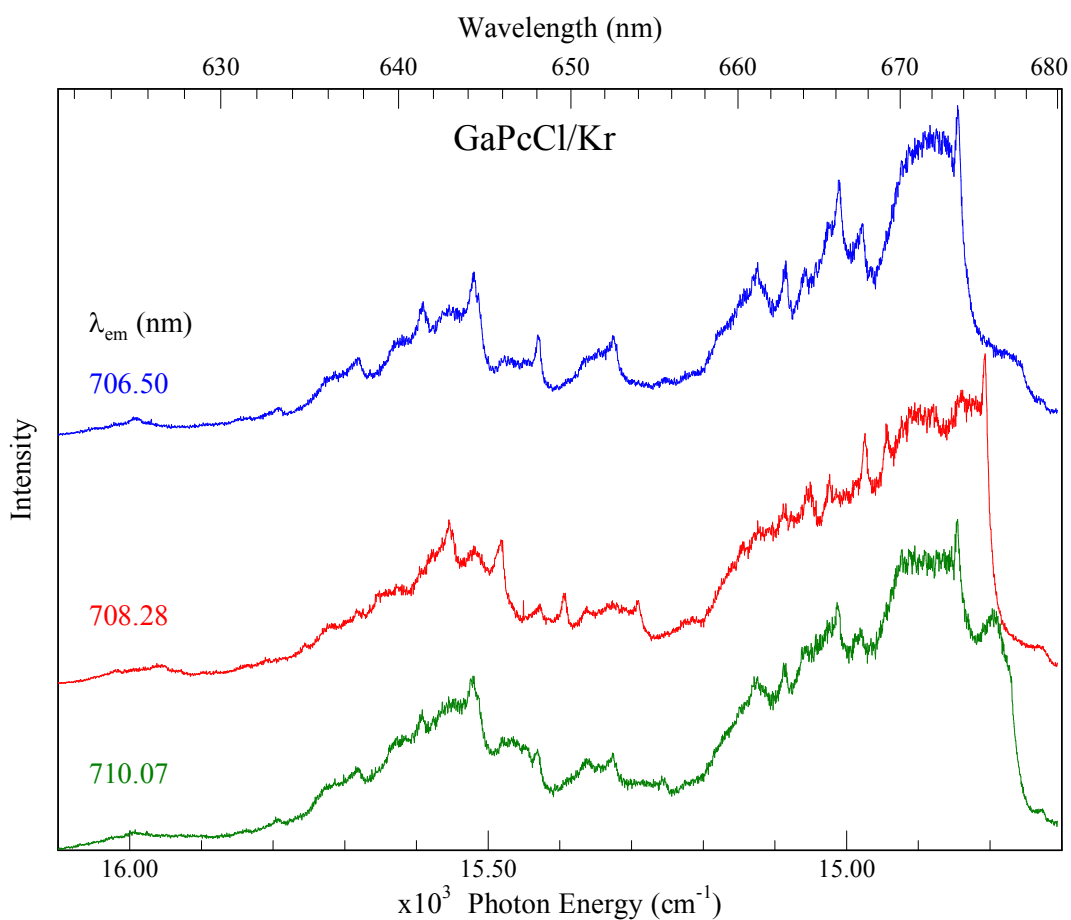


Figure V.22: Excitation spectra of GaPcCl recorded in Kr. The emission bands monitored were located at 706.50, 708.28 and 710.07 nm.

The excitation spectrum obtained by monitoring at 706.50 (blue trace) and 710.07 nm (green trace) in Figure V.22 share the same 0-0 band and vibronic bands up to 630 nm. This means that these two emission bands being monitored originate from the same site. As was the case with the emission spectra, the Kr system seems to resemble Ar closely. A clear migration of the 0-0 band in excitation is observed by monitoring different sites in

emission. The spectrum recorded by monitoring at 708.28 nm (red trace) has its 0-0 band located to the red of the other two spectra, indicating it originates from a site to the red of the previous one being monitored. There is a shift of about 40 cm^{-1} between the two sites. The associated vibronic bands are all shifted by the same amount.

Some aggregates are present in this sample, which have manifested as a broad band to the red of the 0-0 band in the green trace ($\lambda_{\text{em}} = 675.94\text{ nm}$), and a shoulder in the blue trace of Figure V.22. This is consistent with the absorption results where a weak band to the red of the band origin was observed.

V.3.II.e: Amplified Emission

Amplified emission was observed in GaPcCl/Kr samples where the optical density of the Q band was sufficiently high (typically greater than 2.5). Figure V.23 shows the normalized fluorescence spectrum (red trace) and an ‘amplified emission’ spectrum (black trace). Both spectra were recorded with 675.4 nm laser excitation, with the only variable being the laser power – fluorescence was recorded with a power of $\sim 10\text{ }\mu\text{J/pulse}$ and amplified emission was recorded at about 10 times that power. The most striking feature of Figure V.23 is the gain in intensity of the emission band at 754.1 nm. The inset spectrum shows this band in fluorescence (red trace) and after amplification (black trace). The band width is significantly narrowed when it is exhibiting stimulated emission, and is limited only by the resolution of the monochromator. An evident asymmetry on the curve suggests that there may be more than one species exhibiting this effect, but which remains unresolved under the current conditions.

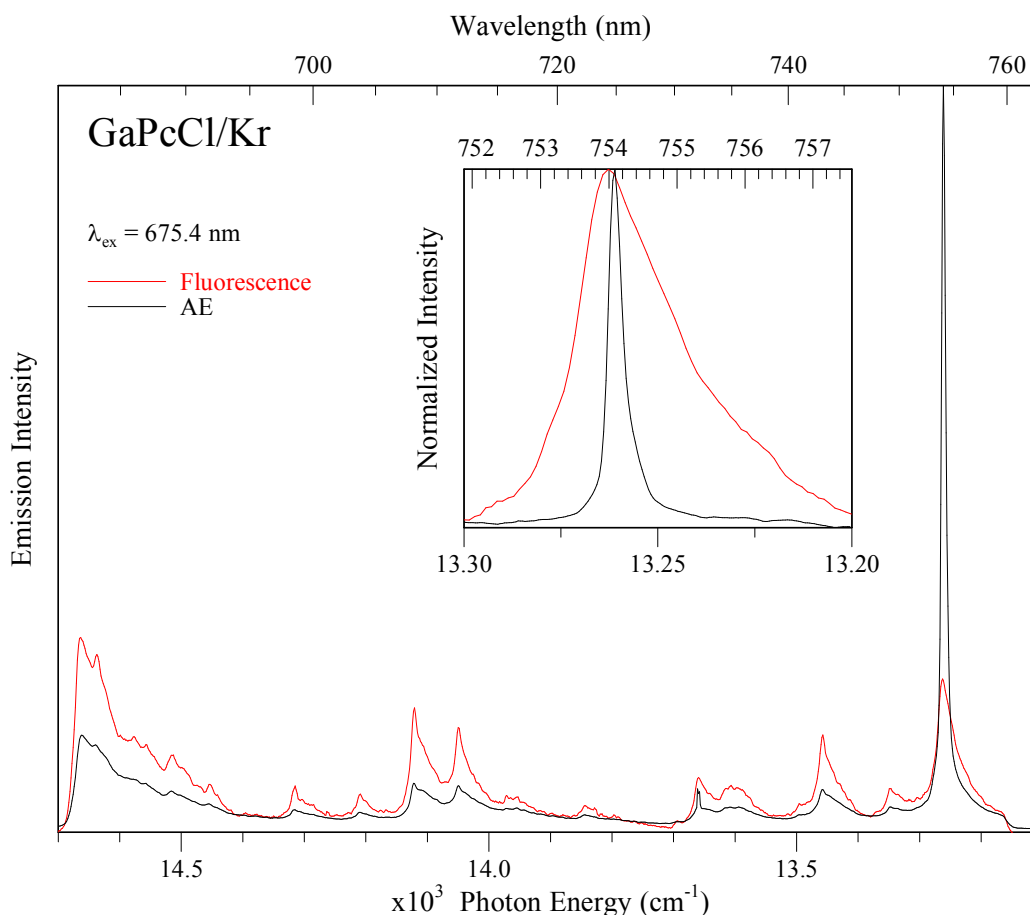


Figure V.23: Emission of GaPcCl isolated in Kr excited with 675.4 nm pulsed laser radiation with low power (red trace) and high power (black trace). The band at 754.1 nm is clearly amplified by increasing the laser power. Furthermore, the linewidth of the amplified band is narrowed considerably compared to the corresponding fluorescence band as shown in the inset of the figure. The asymmetry of the fluorescence band is probably due to unresolved weaker sites very close in energy to the intense band.

V.3.III: Xenon

V.3.III.a: Sample Optimization

Samples of GaPcCl isolated in solid Xe were optimized in the same manner as for Ar and Kr. The first effect examined was varying the oven temperature, the results of which are presented in Figure V.24. The sample prepared with the lower oven temperature (321 °C) is shown by the blue trace. The Q and B bands can be clearly observed in the spectrum, albeit with an oddly shaped baseline. The vibronic bands are not very well resolved, especially compared to the low temperature samples presented in Figure V.1 and Figure V.14 for Ar and Kr respectively. The top of the Q band does exhibit some very well resolved structure that will be shown in more detail in Section V.3.III.b. The sample

prepared with the higher oven temperature (363 °C) is shown by the red trace. This sample is saturated in the region of the 0-0 transition of the Q band, but the vibronic bands extending up to 612.9 nm are highly resolved compared to the low temperature sample. There is a slight narrowing of the B band, but the triplet of bands observed in the Kr matrix is not obvious here.

The weak bands from around 410 to 450 nm are also present in this matrix and are red-shifted with respect to their positions in the Ar and Kr matrices. This confirms that they originate from a source that is trapped in the matrix, and not from a thin film of material present on the surface of one of the CaF₂ windows. An interesting observation is that they appear more intense in Xe matrices than in any other host.

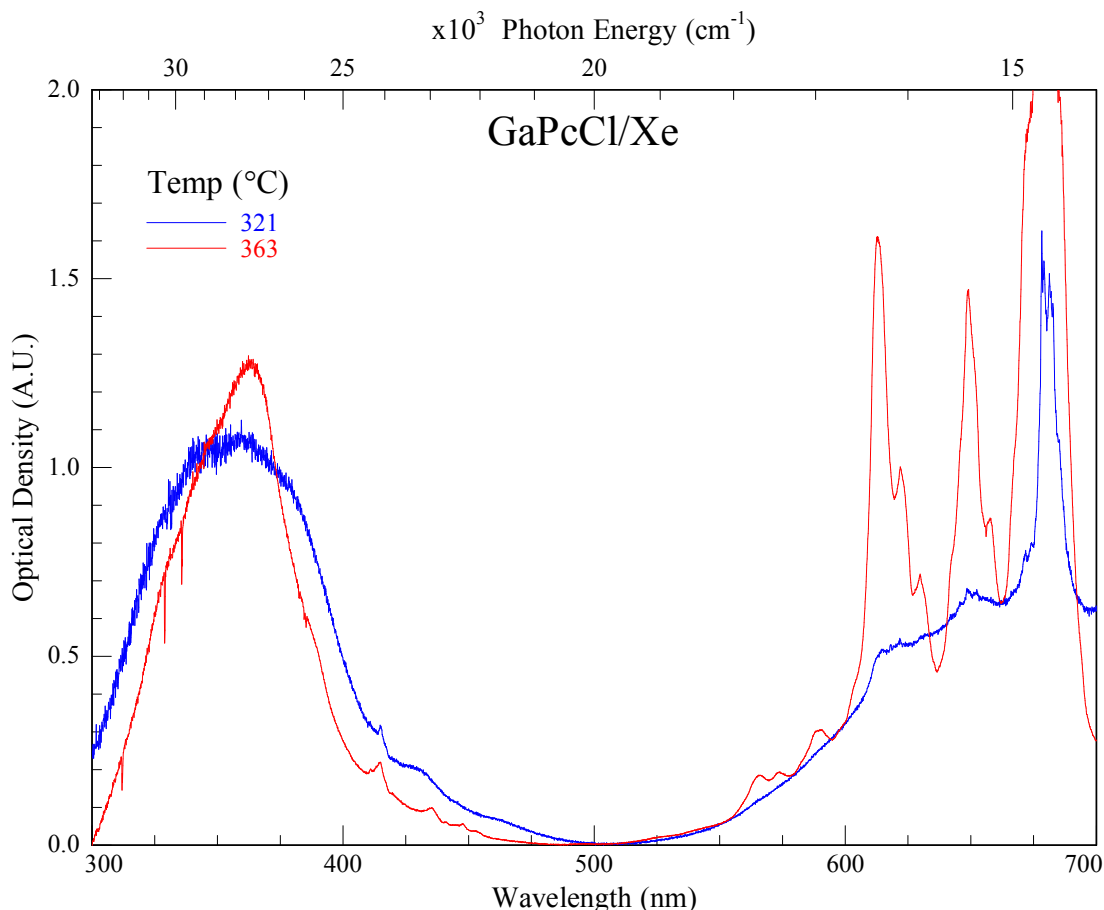


Figure V.24: Absorption spectra of GaPcCl isolated in solid Xe deposited with a window temperature of 10 K. The blue trace was prepared with an oven temperature of 10.1 mV (321 °C) and the red trace with an oven temperature of 11.6 mV (363 °C).

The effect of the window temperature on the sample composition was also studied for Xe matrices. The results of this effect are shown in Figure V.25, where samples deposited with three different window temperatures are shown. The blue trace was a sample deposited at 10 K. This sample shows resolved structure around the 0-0 transition of the Q band, but the vibronic bands beyond 665 nm are not very well resolved. There is an indication of sites in this sample owing to the number of closely spaced bands centred around 680 nm. It also appears that aggregates have formed in this sample due to the broad area under the curve, and a wing lying to the red of the band origin.

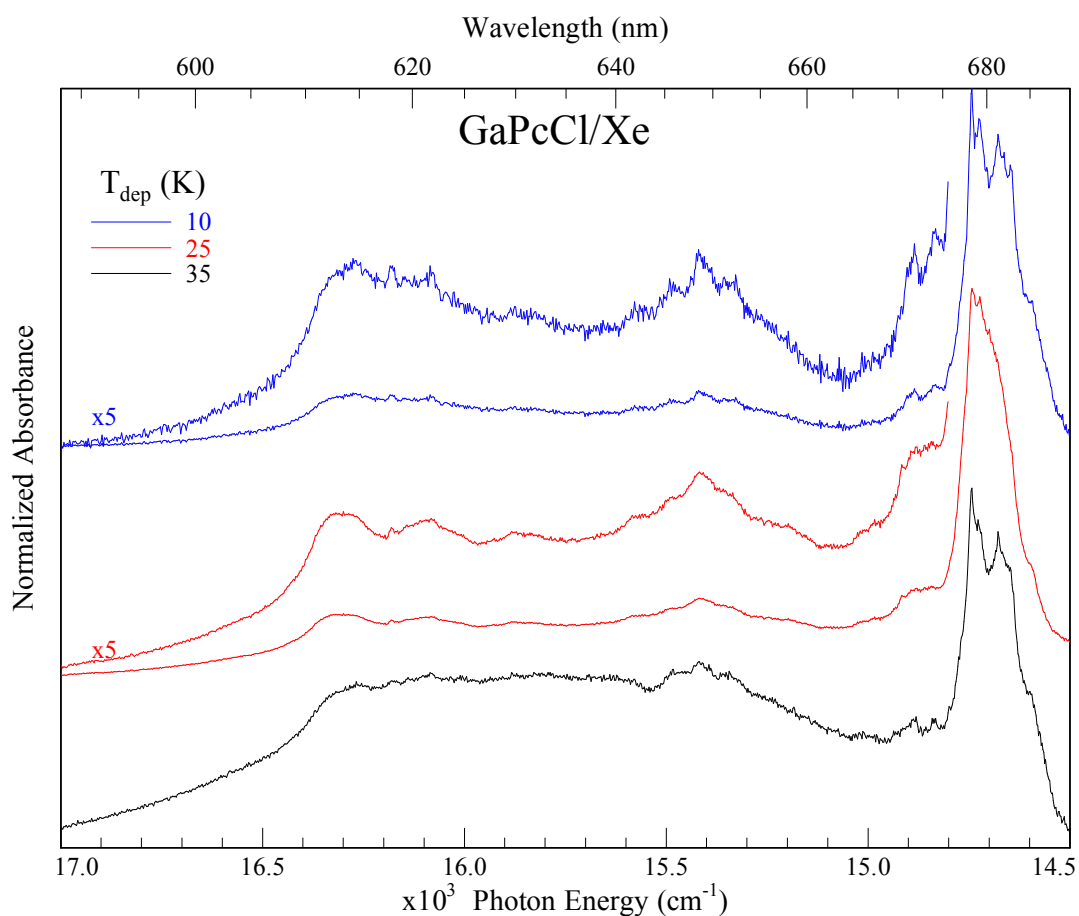


Figure V.25: The absorption of GaPcCl isolated in solid Xe prepared with different temperatures of the CaF₂ window. The blue trace was prepared with the window temperature held at 10 K, the red trace at 25 K and the black trace at 35 K. All samples were prepared with an oven temperature < 330°C in order to prevent saturation of the strongest absorption band at 677.9 nm.

The sample prepared with a window temperature of 25 K (red trace) looks quite different in the region of the band origin in that resolved structure is lost and the 0-0 band is difficult to identify. The vibronic bands appear more resolved, but are not as narrow as those

observed in either Ar or Kr. There also appears to be some aggregates present in this sample, albeit less than in the 10 K sample. The sample made at 35 K (black trace) is different to the two other samples. The region of the 0-0 transition of the Q band closely resembles the 10 K sample, although there appears to be fewer bands in the 35 K sample. This suggests not as many sites are occupied in the 35 K sample. The vibronic structure beyond 665 nm is very broad and individual vibronic bands cannot be identified. This may be due to the presence of aggregates, which clearly exist due to the presence of a fairly strong wing to the red of the 0-0 transition.

The differences observed with the various sample deposition conditions made Xe matrices the most inconsistent and difficult to control. The highly scattering nature of this solid always tends to produce samples with complex baselines. This often affects the resolution of the weaker bands in the spectrum, particularly the vibronic bands beyond 665 nm.

V.3.III.b: Absorption

In spite of the difficulties associated with obtaining well resolved absorption spectra of GaPcCl isolated in solid Xe, an attempt to locate and identify the band origin and the vibronic bands was made by using two samples with very different concentrations. A low concentration sample was used to identify the band origin and is shown by the blue trace in Figure V.26. This has been identified at 682.7 nm. A higher concentration sample was used to identify the vibronic bands which extend up to 612.9 nm. The location of two bands belonging to aggregate species have also been identified and labelled. The location of the band origin and vibronic bands of GaPcCl/Xe are compiled in Table V.5.

The region of the 0-0 band in the low concentration sample exhibits excellent resolution, with several well defined bands occupying the region between 678 and 685 nm. Some of these bands may arise due to the presence of sites in the matrix, as they were not observed in the absorption spectra of Ar and Kr (at most 3 resolved bands were observed in the region of the 0-0 transition in these matrices). The poor resolution and intensity on the vibronic bands for this sample is unfortunate, as the corresponding high concentration spectrum does not show the same degree of resolution. The region around the 0-0 band is saturated in this spectrum, so no direct comparison of the bands can be performed. The vibronic bands extending up to 612.9 nm are quite broad however, and certainly appear much less resolved than the 0-0 bands in the low concentration sample. This means the site structure of the high concentration sample is lost. The broadness of the vibronic bands may

be due to the presence of aggregates in the matrix, so some useful information about the makeup of the sample (apart from the peak positions) is still obtained.

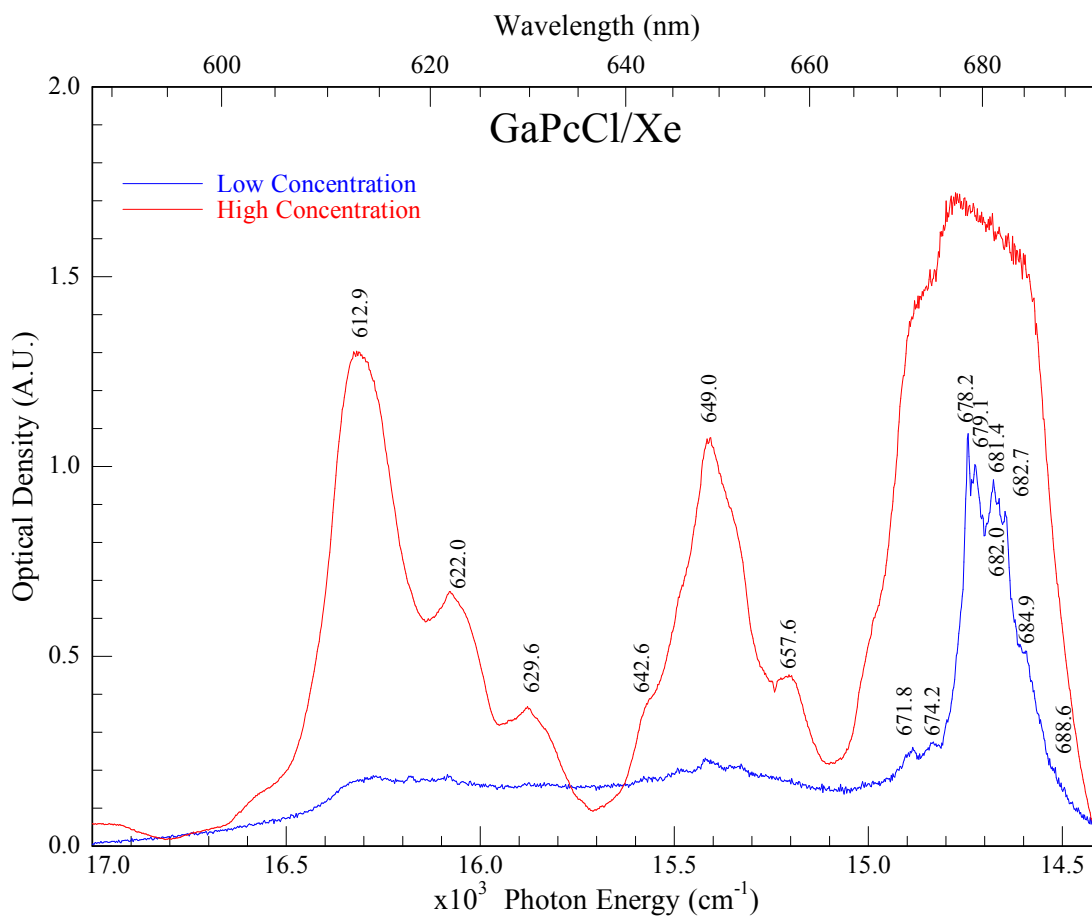


Figure V.26: Absorption spectrum in the region of the Q band of GaPcCl isolated in solid Xe at cryogenic temperatures. The blue trace was prepared with a window temperature of 10 K and an oven temperature of 320 °C. The red trace was prepared with a window temperature of 20 K and an oven temperature of 363 °C. The vibronic bands have been labelled, with their values quoted in nm. The corresponding wavenumber values are given in Table V.5.

Table V.5: Absorption bands of GaPcCl isolated in a solid Xe matrix taken from Figure V.26. The bands have been shown in wavelength, energy and as their shift from the band origin (0-0).

Wavelength (nm)	Energy (cm ⁻¹)	Shift from 0-0 (cm ⁻¹)
688.6	14522	-126
684.9	14601	-47
682.7	14648	0
682.0	14663	15
681.4	14676	28
679.1	14725	78
678.2	14745	97
674.2	14832	185
671.8	14885	238
657.6	15207	559
649.0	15408	761
642.6	15562	914
629.6	15883	1235
622.0	16077	1429
612.9	16316	1668

V.3.III.c: Emission

The emission spectrum of GaPcCl/Xe produced with excitation into the region of the band origin (0-0 band), where many sites are located in absorption, is presented in Figure V.27. Excitation at 683.1 nm yields the simplest fluorescence with the fewest emission bands. This spectrum shows a similar structure to that observed in the Ar and Kr matrices, however, the linewidths of the emission bands in Xe are broader (25 cm⁻¹) than those observed in Ar and Kr. This may be due to an abundance of sites being present, located close together in energy, or because of the presence of aggregates in the sample. This reflects what was observed in the absorption spectra of Xe samples, where many sites were present. The region around the 0-0 band in emission was obtained with $\lambda_{\text{ex}} = 652.6$, and allows for the low energy vibronic bands (0 – 2) to be observed. A list of the emission bands of the red-most site of GaPcCl/Xe (labelled 0 – 13 in Figure V.27) are presented in Table V.6. These will be compared to ground state Raman results and analysed in Section V.4.III.

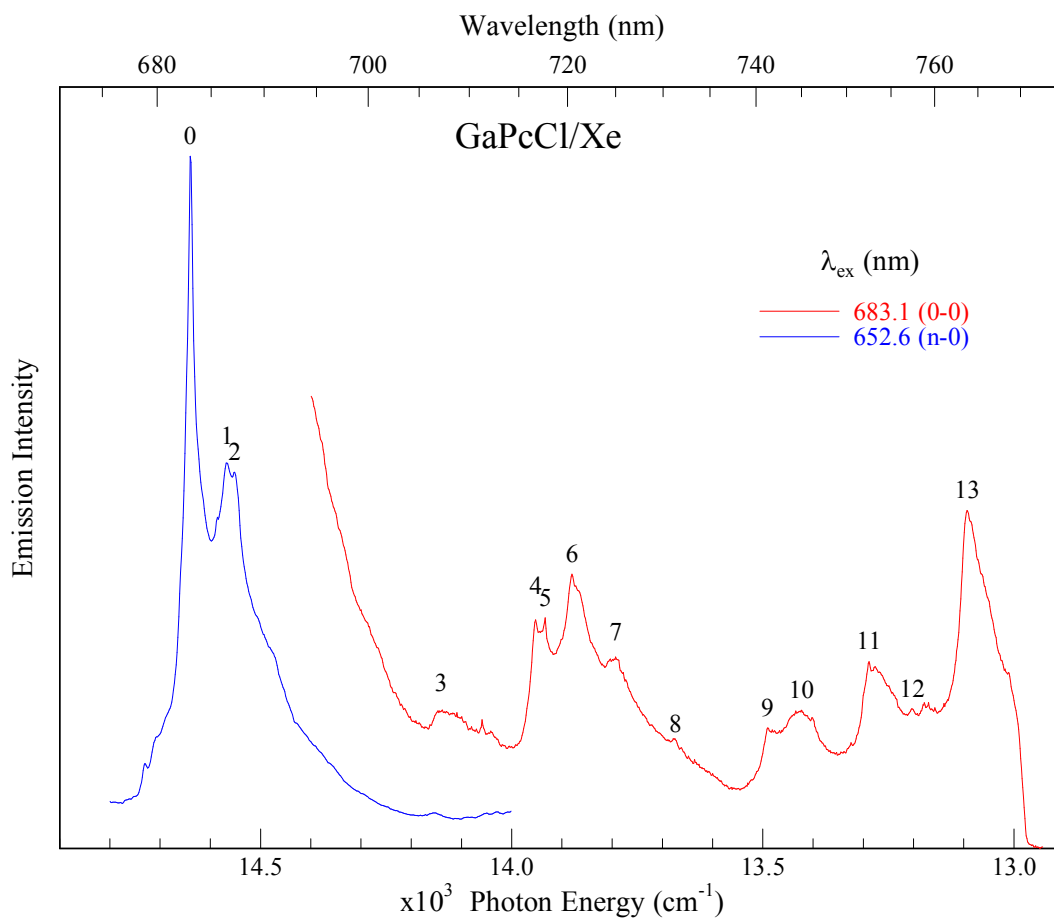


Figure V.27: Emission spectrum of GaPcCl/Xe recorded by exciting into the 0-0 band in absorption (683.1 nm). The region of the 0-0 transition was obtained with an excitation wavelength of 652.6 nm. The peaks have been labelled, with their values given in Table V.6.

Table V.6: Energies of the emission bands of GaPcCl isolated in solid Xe. The values are taken from the red site. The labelling used for the peak numbers is shown in Figure V.27.

Peak #	Wavelength (nm)	Energy (cm ⁻¹)	Shift from 0-0 (cm ⁻¹)
0	683.059	14640.0	0.0
1	686.489	14566.9	73.2
2	687.224	14551.3	88.7
3	707.213	14140.0	500.0
4	716.728	13952.3	687.7
5	717.702	13933.4	706.7
6	720.464	13880.0	760.1
7	725.008	13793.0	847.1
8	731.330	13673.7	966.3
9	741.286	13490.1	1150.0
10	745.006	13422.7	1217.3
11	752.520	13288.7	1351.4
12	757.445	13202.3	1437.8
13	763.739	13093.5	1546.6

A variety of fluorescence spectra recorded with selected excitation wavelengths are shown in Figure V.28. The excitation wavelengths chosen do not coincide with the maxima of the absorption bands because this tended to yield fairly broad fluorescence bands, probably due to the high number of sites in Xe matrices. The spectrum shown by the red trace was recorded by exciting at 683.1 nm, which has already been shown in Figure V.27. Excitation to the blue of the 0-0 band shows the site structure more clearly, as demonstrated by the blue trace ($\lambda_{\text{ex}} = 675.0$ nm) of Figure V.28. The vibronic bands in emission are more resolved and the site splitting can be clearly seen throughout the entire range of the spectrum. The locations of the most resolved vibronic bands from the ‘red’ and ‘blue’ sites have been marked with R and B respectively. The set of duplicate bands are shifted compared to those in the red trace, which suggests more than two sites occupy this matrix.

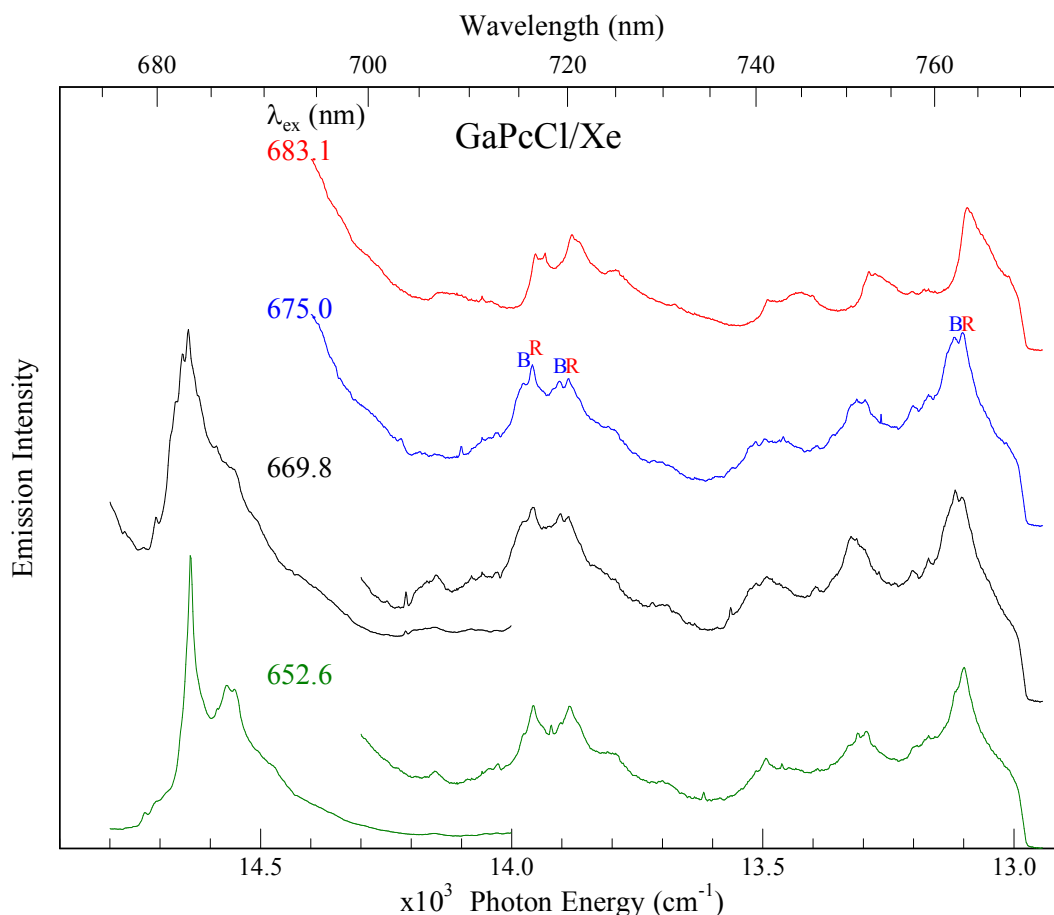


Figure V.28: Fluorescence spectra of GaPcCl/Xe recorded with a range of different excitation energies.

Excitations even further to the blue of the 0-0 band are shown by the black and green traces of Figure V.28, where $\lambda_{\text{ex}} = 669.8$ and 652.6 nm respectively. Using wavelengths to the blue of the band origin in absorption allows for the band origin in emission to be identified. This has been assigned as 683.1 nm. The region around the 0-0 transition in emission shows some sharp features that are not present throughout the rest of the spectrum. This may be due to the significantly greater intensity of the emission bands in this region having a vast improvement on the signal to noise ratio. Site splitting is also observed with these two excitation wavelengths, although it is not as pronounced as in the blue curve.

Decay curves recorded for a number of emission bands of GaPcCl/Xe are presented in Figure V.29. The decay time does not vary significantly with respect to the emission wavelength. The rise time is almost identical for all emission bands and the decay profiles are all similar and within the margin of error of the experimental measurement. This

suggests that little or no wavelength dependence exists on the emission decay time of GaPcCl/Xe. This result is in contrast to the Ar and Kr matrices where a slight wavelength dependence on the decay time was observed.

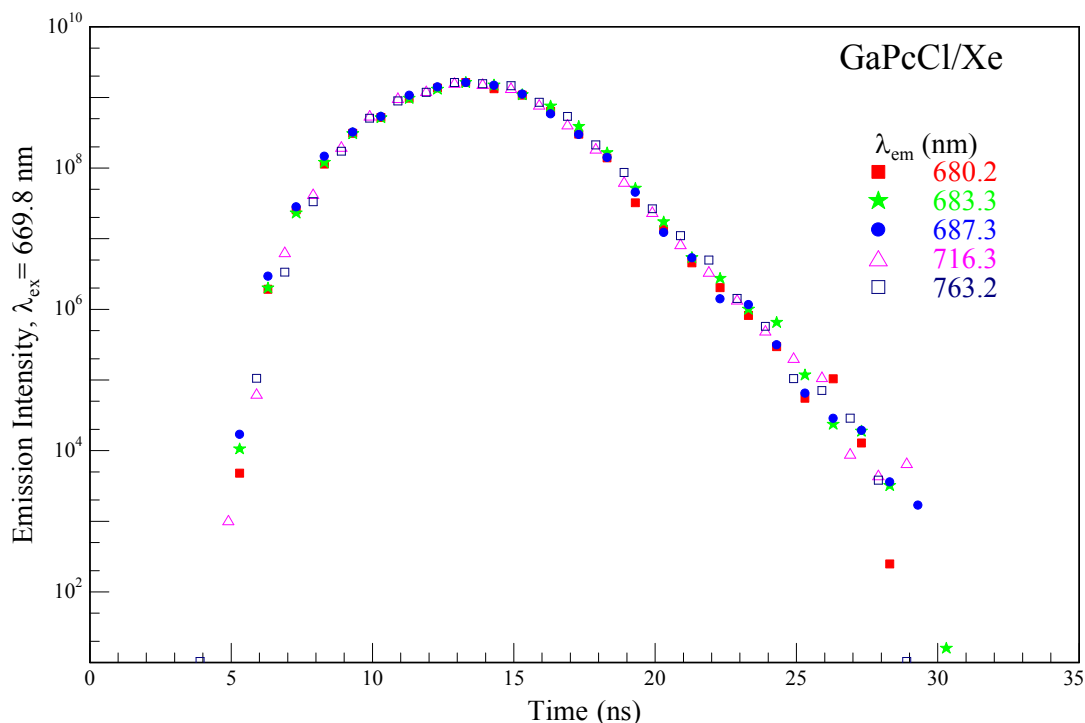


Figure V.29: Decay curves of GaPcCl/Xe recorded for various emission bands in the fluorescence spectrum. The laser profile is shown for comparison.

The excited state lifetime of GaPcCl/Xe was measured by recording time-resolved emission, and plotting the decay curve against a single exponential fit. The emission decay plot of the vibronic band at 752.5 nm is shown in Figure V.30. This emission band is the same vibronic band used to determine the lifetimes in Ar and Kr matrices. The value measured for this system was 2.3 ns, which is a reasonable decay time for a fully allowed electronic transition. The decay time is identical to that observed in an Ar matrix (2.3 ns), but shorter than that in a Kr matrix (2.4 ns). These results will be discussed in greater detail in a later Section V.4.I.

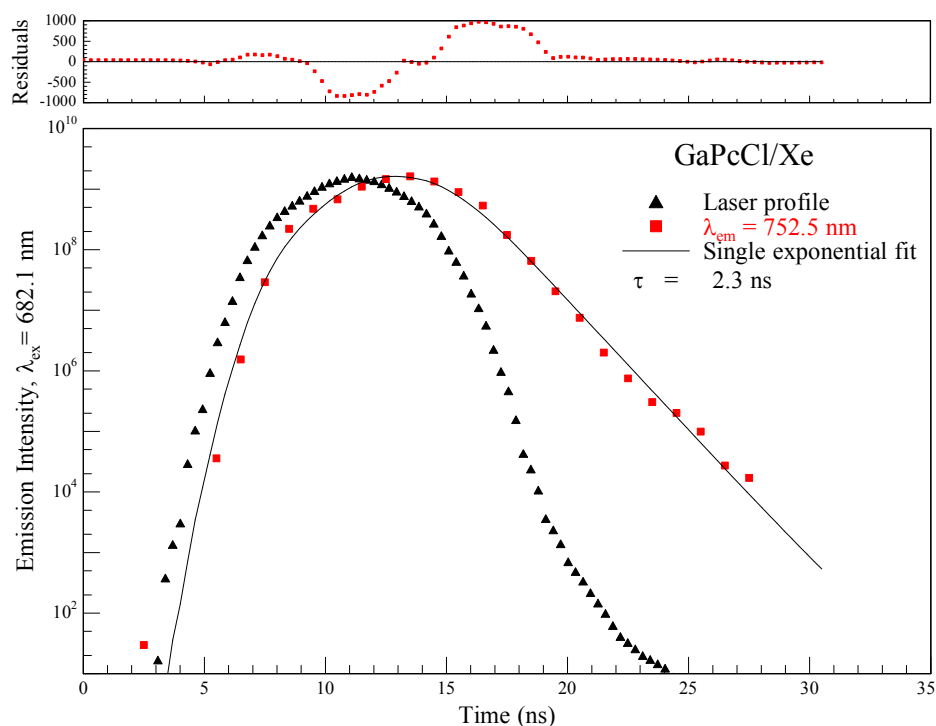


Figure V.30: Semi-log plot of the emission decay curve of GaPcCl extracted from time-resolved emission spectra recorded at 10 K in solid Xe. The shape of the excitation pulse of the laser is also shown. The emission was recorded with 682.1 nm excitation and the lifetime was measured at 2.3 ns.

V.3.III.d: Excitation

Excitation spectra of GaPcCl/Xe were recorded in the same manner described for Ar and Kr. A number of different emission bands were monitored and their excitation spectra are presented in Figure V.31. The spectra show fairly narrow excitation bands from 683 to 645 nm. The spectra are quite noisy and some of the weaker bands are probably lost because of this. The 0-0 band in excitation is not as strong or as resolved as in the other matrices; it is not the most intense band in Xe, unlike Ar and Kr, although it does appear narrower than the other excitation bands. A shift of the 0-0 band is evident with the various emission wavelengths, indicating each emission band being monitored comes from a different site of isolation. This is unsurprising given the site structure observed for Xe in both absorption and emission spectra.

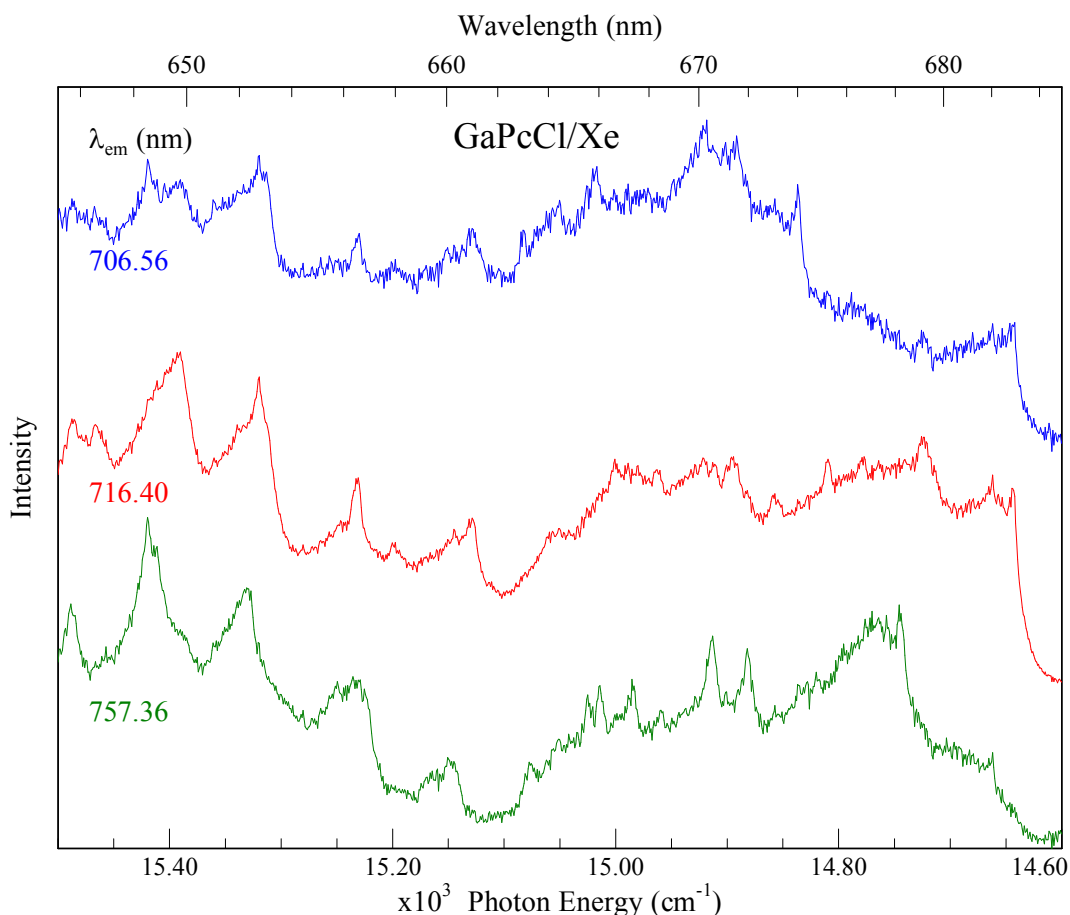


Figure V.31: Excitation spectra of GaPcCl recorded in Xe. The emission bands monitored were located at 706.56, 716.40 and 757.36 nm.

V.3.III.e: Amplified Emission

Amplified emission was observed in Xe matrices, although samples capable of exhibiting the effect were difficult to prepare reproducibly. The best sample that exhibited the effect in a Xe matrix was prepared with a high oven temperature, gas flow and window temperature. Figure V.32 shows fluorescence (red trace) and AE spectra (black trace) overlaid. Both spectra were recorded with excitation at 675 nm. Unlike most of the other data which has and will be presented in this chapter, the data presented in Figure V.32 was not obtained by exciting into the red most site. It was observed that excitation at 675 nm gave the most resolved AE spectrum. The emission band at 763.2 nm is amplified in the black trace compared to its fluorescence counterpart. This vibronic band lies 1547 cm^{-1} above the band origin. The inset spectrum is a good demonstration of how strong the amplified vibronic band at 763.2 nm is compared to a regular fluorescence band. Two fluorescence bands are located close together in energy originating from separate sites,

only one of which exhibits AE with excitation at 675 nm. By increasing the laser power only the AE band from the ‘red’ site gets amplified, with the ‘blue’ emission band showing regular fluorescence. By changing the excitation wavelength, the blue site can be preferentially excited, with the vibronic band at 1547 cm^{-1} exhibiting AE and the corresponding band from the red site exhibiting normal fluorescence. These results will be discussed in Chapter VI in relation to the sites in GaPcCl/Xe matrices. The spectral narrowing normally associated with AE is more difficult to appreciate in the current spectrum as there are two fluorescence bands located close together. Linewidth narrowing does occur in Xe however, as shown in Figure V.31, although perhaps not to the same extent as in the other matrices.

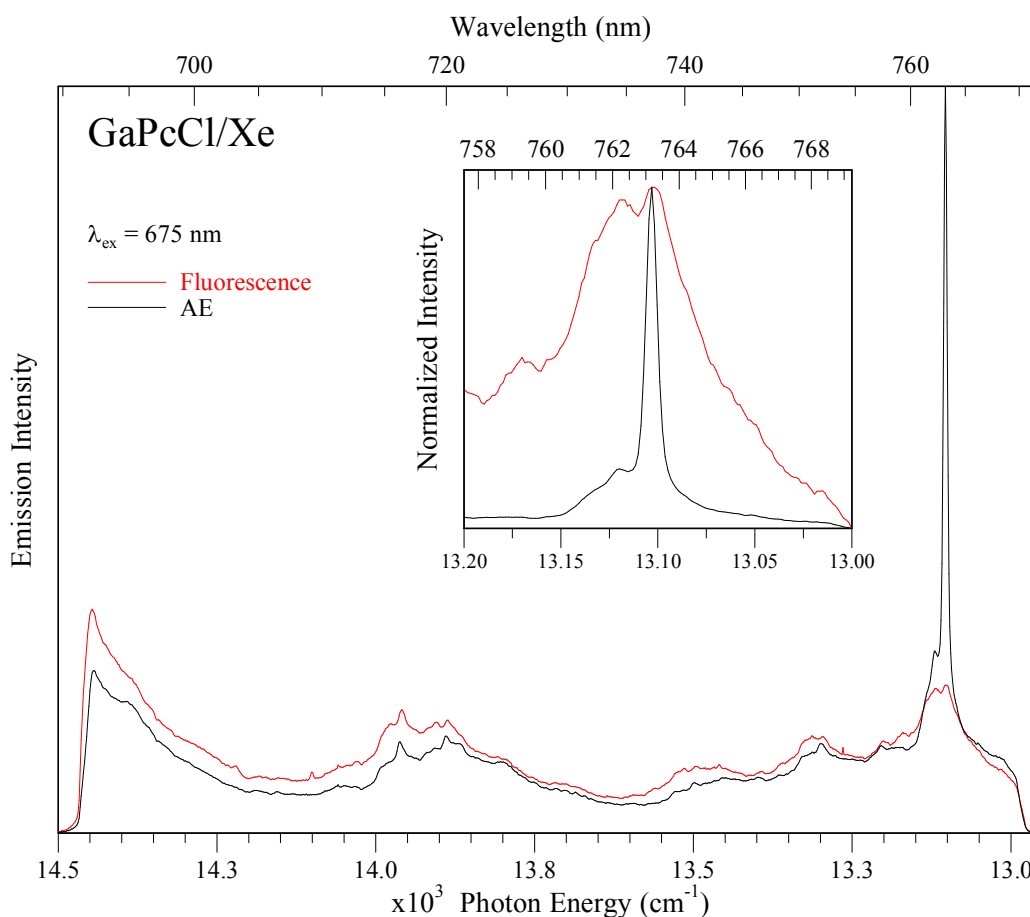


Figure V.32: Emission of GaPcCl isolated in Xe excited with 675 nm pulsed laser radiation with low power (red trace) and high power (black trace). The band at 763.2 nm is amplified by increasing the laser power. The changing linewidth of the band is shown on the inset spectrum.

Higher laser powers were required to induce stimulated emission in Xe matrices than in Ar and Kr, and the relative intensity of the AE bands to the fluorescence bands was much lower than in the other matrices, as indicated in Figure V.32. There are two possible reasons for this difficulty; the heavy atom effect⁶ of the matrix may partially quench emission or the optical density may be ‘diluted’ by the presence of many sites or highly scattering samples. The heavy atom effect may be ruled out because this would shorten the emission lifetime compared to the lifetimes recorded in Ar and Kr. Certainly the region of the band origin in absorption spectra, pointed to an abundance of sites in the Xe matrix. Even though there are sufficient GaPcCl molecules located in the matrix, they are separated into many different sites, meaning the optical density of a given species is not large enough to exhibit the same degree of amplification as in the other matrices. This may also help to explain the difficulty associated with getting samples to exhibit the effect in the first place in this matrix.

V.3.IV: Nitrogen

V.3.IV.a: Sample Optimization

Samples of GaPcCl in solid nitrogen were optimized following the method described previously for the other matrices. The first variable to be examined was the effect of the oven temperature. Figure V.33 shows two samples of GaPcCl/N₂ prepared with an oven temperature of 320 °C (blue trace) and 357 °C (red trace). Similar to other matrices, the Q and B bands can be clearly seen in both spectra. The location of the 0-0 transition of the Q band in N₂ has been identified at 667.6 nm. This band is saturated in the high temperature sample, but the intensities of the weaker vibronic bands and the B band are improved greatly compared with than the low temperature sample.

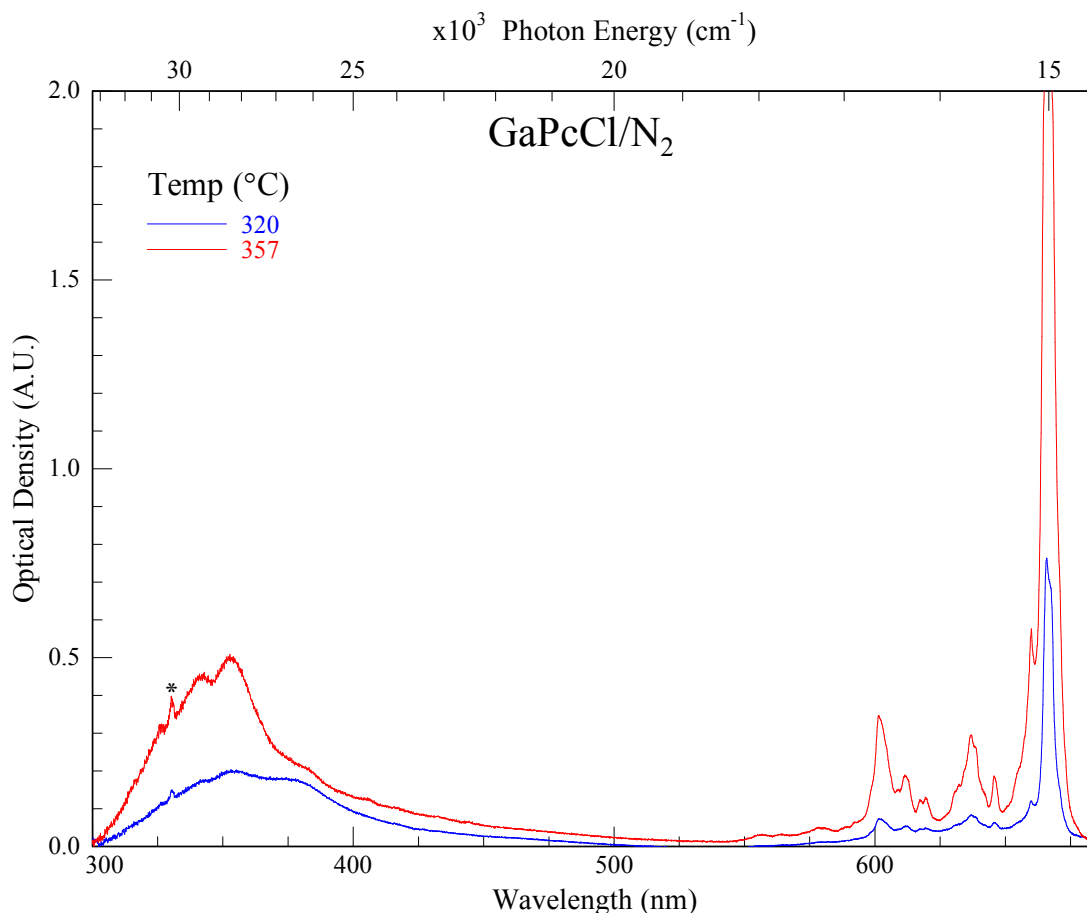


Figure V.33: Absorption of GaPcCl isolated in solid N₂ prepared with a window temperature of 10 K. The blue trace was prepared with an oven temperature of 10.1 mV (320 °C) and the red trace with an oven temperature of 11.4 mV (357 °C). The pyrene band (highlighted by an asterisks) observed in Ar is also present in this matrix.

The optical density of the Q band in the saturated absorption spectrum can be estimated by extrapolating a value based on the ratio between the vibronic bands in both absorptions. The band at 603 nm has an OD of 0.071 in the low concentration sample. This is increased to 0.345 in the high concentration sample; representing a 4.86-fold increase. Assuming the same ratio exists for the main absorption band at 665.9, and knowing the OD of the low concentration sample is 0.762, the OD of the high concentration sample is calculated to be 3.703. It was noted that all samples in N₂ that were saturated in absorption exhibited amplified emission with pulsed laser excitation. These results will be shown in a Section V.3.IV.e. A series of bands extend beyond 603 nm up to around 550 nm, which may be due to overtones or combination bands, as described for the rare gas samples. The weak absorption bands which have been observed in the other matrices between 400 – 450 nm are also present in the N₂ matrix.

The other variable examined was that of the window temperature on the sample composition. Figure V.34 presents samples prepared with the window held at 10 K (blue trace) and 15 K (red trace). Unfortunately, all of the higher temperature samples attempted ended up in saturation. Both samples look quite similar in absorption. The resolution on the 0-0 band is better on the 15 K sample, but is not as well resolved as any of the band origins observed in the rare gas matrices. Vibronic bands extend up to 601.5 nm and show similar structure in both samples. There is a very slight improvement in resolution of these bands in the 15 K sample. Small amounts of aggregates are present in both samples, indicated by the shoulder to the red of the 0-0 transition. Thus, the window temperature does not appear to affect the number of sites present in a given sample, at least in absorption.

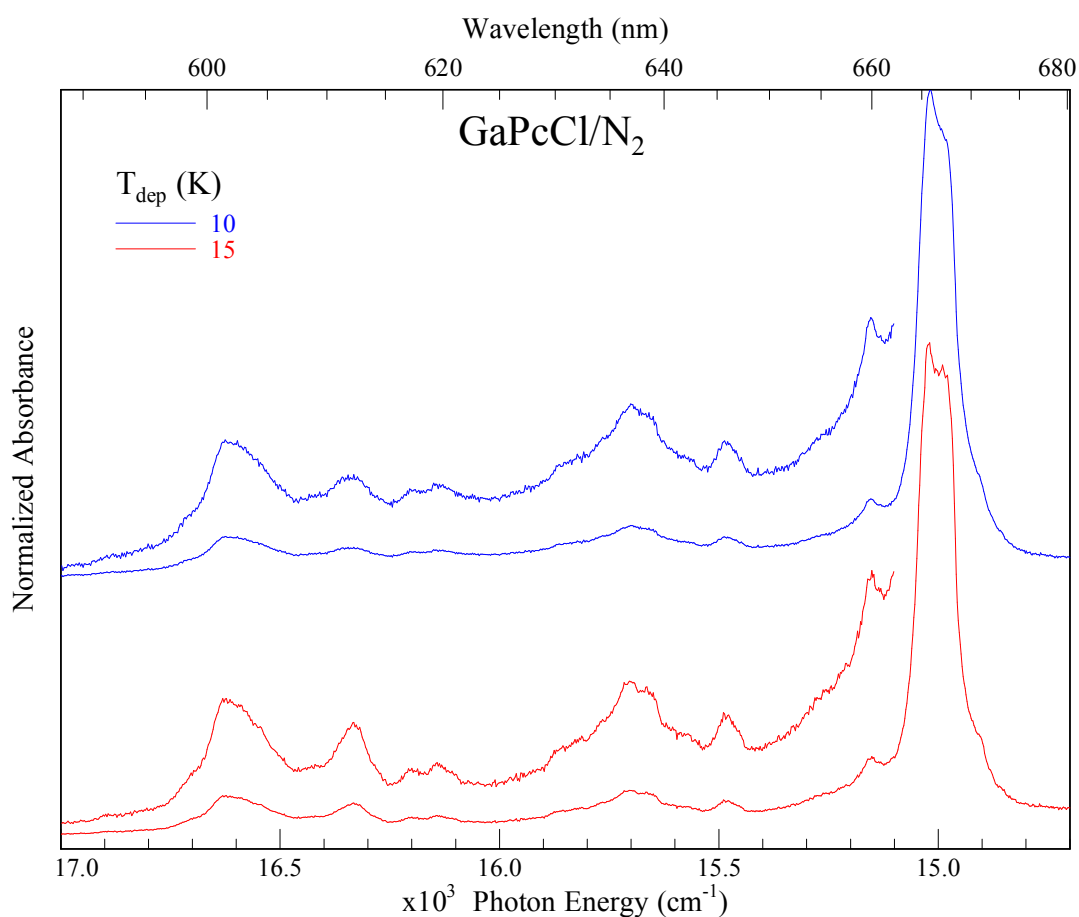


Figure V.34: Absorption spectra of GaPcCl isolated in solid N₂ prepared with different temperatures of the CaF₂ window. The blue trace was prepared with a window temperature of 10 K and the red trace at 15 K. Both samples were prepared with an oven temperature < 330°C to prevent saturation of the strongest absorption band at 667.1 nm.

V.3.IV.b: Absorption

The most resolved absorption spectrum recorded for GaPcCl in solid nitrogen is shown in Figure V.35. The band origin of the Q transition has been identified and is located at 667.6 nm. This is blue shifted compared to the rare gas matrix values reported earlier. Vibronic bands extend up to 601.5 nm, about 1669 cm^{-1} above the band origin. The splitting on the vibronic bands is not evident in this matrix, possibly indicating the existence of only a single dominant site in absorption, or a very small shift between sites. A small amount of aggregation is manifested as a weak shoulder to the red of the band origin at 670.8 nm. The location of the vibronic bands in absorption and their shift from the band origin are collected in Table V.7.

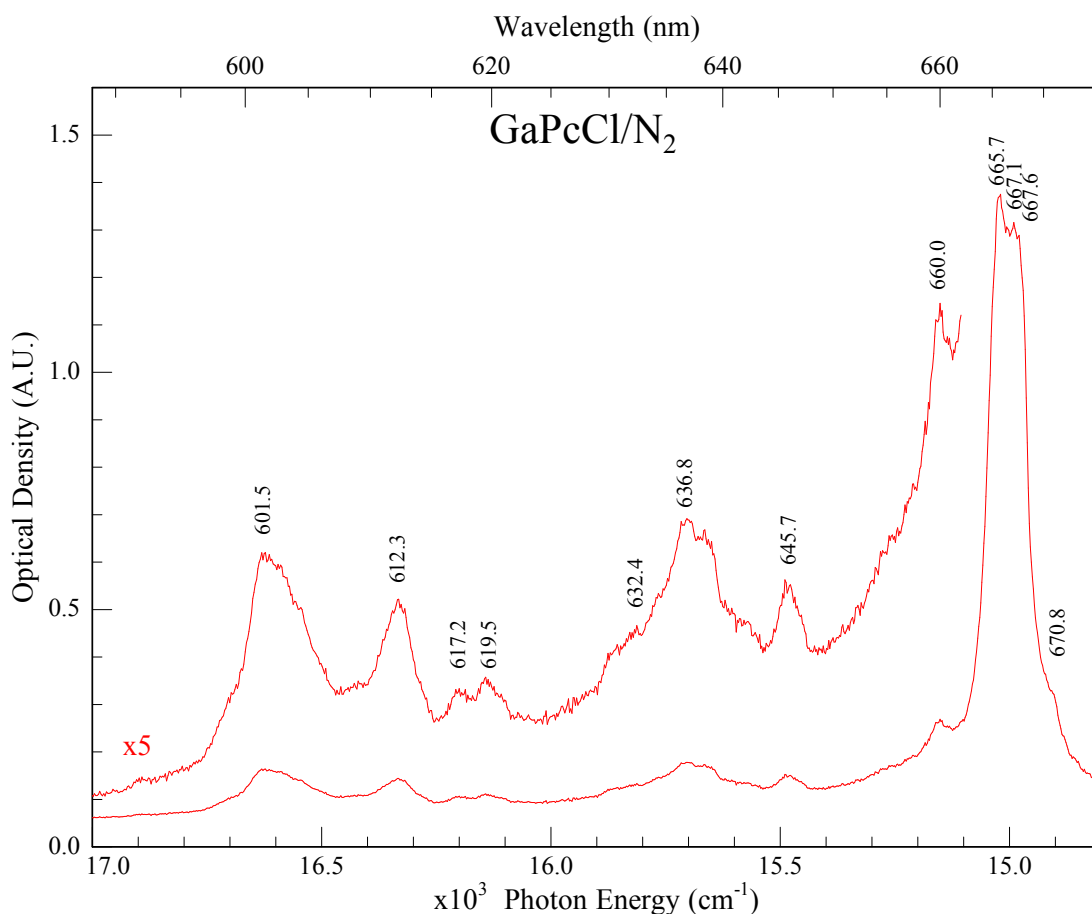


Figure V.35: Absorption spectrum in the region of the Q band of GaPcCl isolated in solid N₂ at cryogenic temperatures. The above sample was prepared with a window temperature of 15 K and an oven temperature of 320 °C. The vibronic bands have been labelled, with their values given in nm. The corresponding wavenumber values are given in Table V.7.

Table V.7: Absorption bands of GaPcCl isolated in a solid N₂ matrix taken from Figure V.35. The bands have been shown in wavelength, energy and as their shift from the band origin (0-0).

Wavelength (nm)	Energy (cm ⁻¹)	Shift from 0-0 (cm ⁻¹)
670.8	14908	-71
667.6	14979	0
667.1	14990	11
665.7	15022	43
660.0	15152	172
645.7	15487	508
636.8	15704	724
632.4	15813	834
619.5	16142	1163
617.2	16202	1223
612.3	16332	1353
601.5	16625	1646

V.3.IV.c: Emission

Figure V.36 shows the fluorescence spectrum of GaPcCl/N₂ recorded by exciting into the 0-0 band in absorption with pulsed laser excitation. This spectrum shows a similar and possibly simpler structure to that observed in the rare gas matrices. Emission bands extend up to 745 nm and are quite broad (linewidth = 18 cm⁻¹) compared to Ar and Kr. Only a single set of emission bands are evident, although the broadness of the bands may indicate multiple unresolved sites are present. The 0-0 transition in emission has also been shown ($\lambda_{\text{ex}} = 652.3$ nm) in order to obtain the positions of all of the vibronic bands in emission. The values of the 0-0 transition and the vibronic bands in emission are presented in Table V.8. These bands will be analysed in greater detail in Section V.4.III.

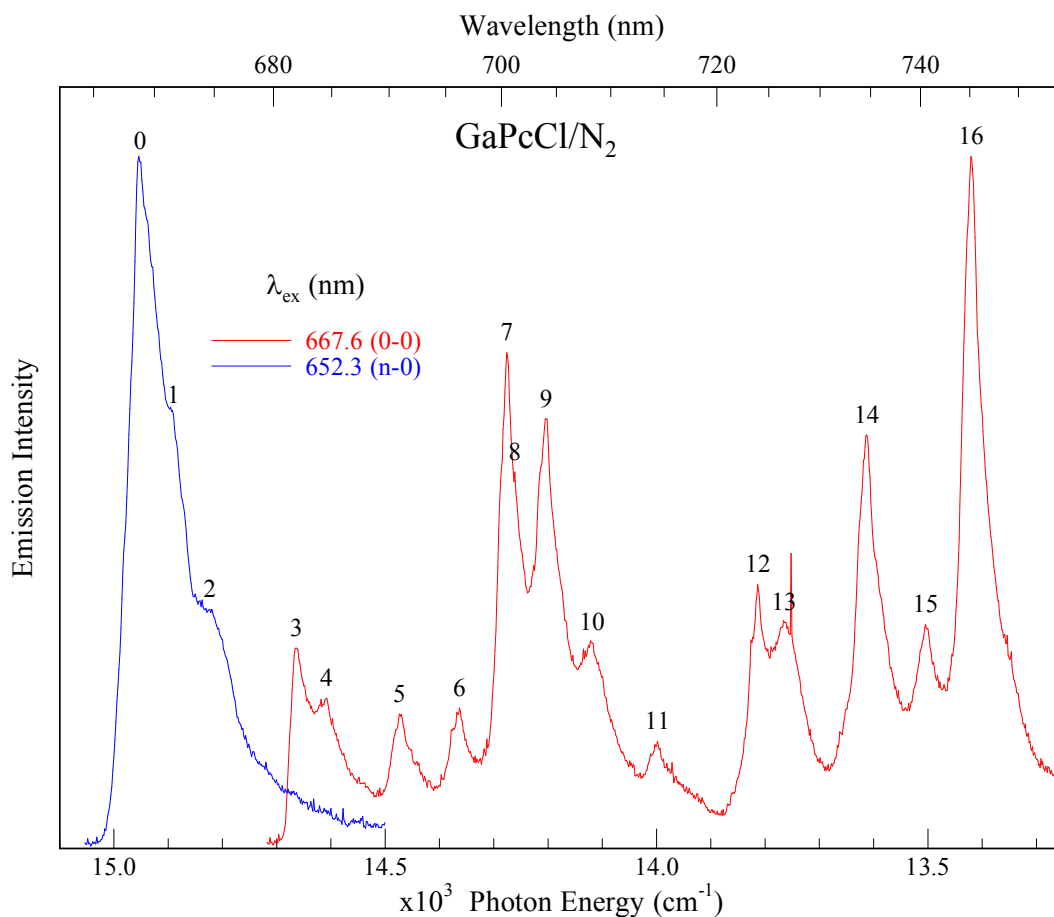


Figure V.36: Emission spectrum (red trace) of GaPcCl/N₂ recorded by exciting into the 0-0 band in absorption (667.6 nm). The region showing the 0-0 transition in emission (blue trace) was recorded with a excitation at 652.3 nm. The peaks have been labelled, with their values shown in Table V.8.

Table V.8: Energies of the emission bands of GaPcCl isolated in solid N₂. The values are taken from the red site, obtained by exciting into the 0-0 band in absorption. The labelling of the peak #'s is the same as that in Figure V.36.

Peak #	Wavelength (nm)	Energy (cm ⁻¹)	Shift from 0-0 (cm ⁻¹)
0	668.800	14952.2	0.0
1	671.588	14890.1	62.1
2	674.619	14823.2	129.0
3	681.929	14664.3	287.9
4	684.571	14607.7	344.5
5	690.904	14473.8	478.4
6	696.227	14363.1	589.0
7	700.472	14276.1	676.1
8	701.206	14261.1	691.0
9	704.057	14203.4	748.8
10	708.285	14118.6	833.5
11	714.370	13998.3	953.8
12	723.924	13813.6	1138.6
13	726.513	13764.4	1187.8
14	734.601	13612.8	1339.3
15	740.508	13504.2	1447.9
16	745.126	13420.6	1531.6

A selection of fluorescence spectra, recorded with various excitation wavelengths matching some of the strongest absorption bands, is shown in Figure V.37. The red trace was recorded by exciting at 667.6 nm and presents the same data shown in Figure V.36. Excitation into the blue of the 0-0 band tended to have the effect of resolving the site structure in other matrices, so this was attempted in N₂ in order to elucidate more information on the existence of sites. The blue trace in Figure V.37 was generated by exciting with 667.1 nm laser light. This spectrum is almost identical to the red trace. The duplication of emission bands observed in the rare gas matrices does not occur in N₂, but the blue shoulders persist at this excitation wavelength.

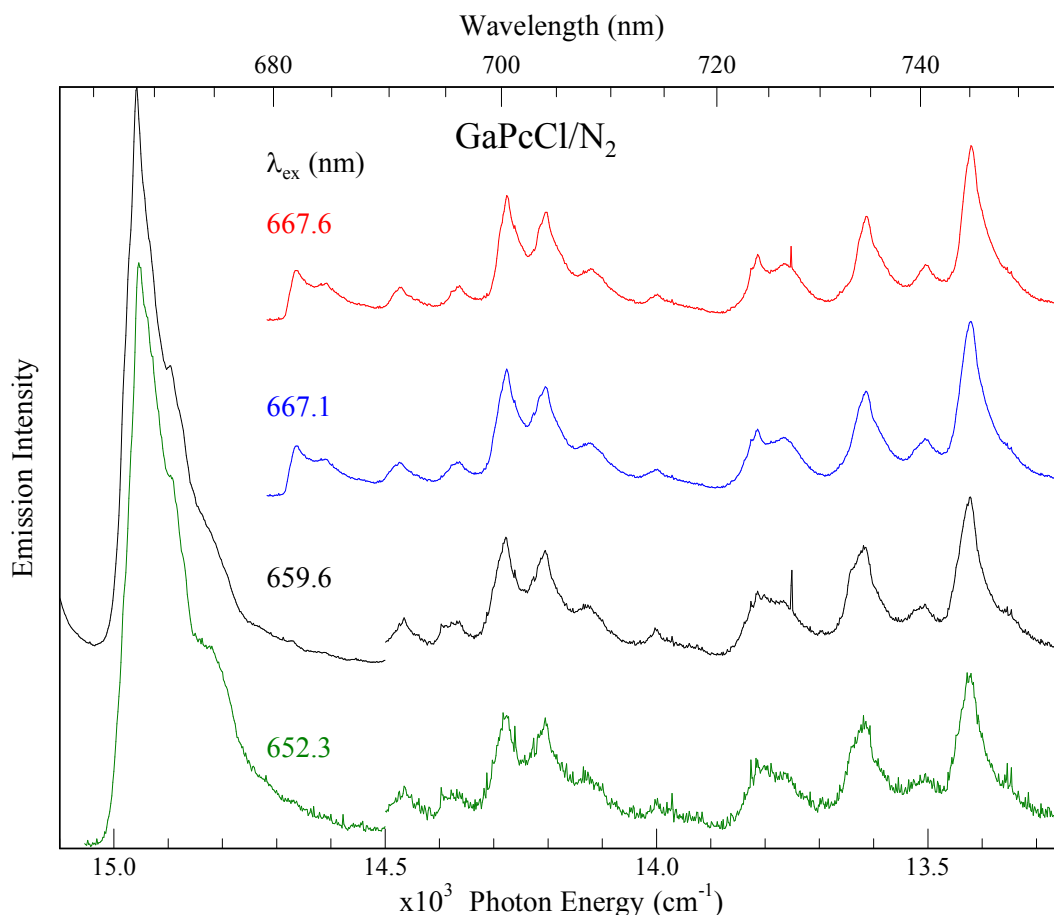


Figure V.37: Fluorescence spectra of GaPcCl/N₂ produced with the specified excitation wavelengths.

Two more excitation wavelengths were used to produce emission spectra; 659.6 and 652.3 nm. These are shown by the black and green traces on Figure V.37 respectively. These spectra are noisier than the two shown above, owing to the weaker intensity of the absorption bands being excited into. The black and green traces were obtained with excitation energies far enough away from the 0-0 band in absorption that the 0-0 band in emission could be observed instead of being drowned out by scattered laser light. The 0-0 transition in emission has far more intensity than the other vibronic bands in emission. This transition is located at 668.8 nm, and allows for the energies of the vibronic bands to be displayed as their shift from this position.

The decay curves of a number of GaPcCl/N₂ emission bands are shown in Figure V.38. This plot shows the decay curve of the excitation laser pulse as well as the emission decay profiles. The rise time of each emission band is almost identical, but this is not the case with the decay profile, where some bands are more long lived than others. This indicates a

wavelength dependence on the emission lifetime, similar to what was observed in Ar and Kr matrices. The shorter wavelength emission bands appear to be more long-lived than the long wavelength counterparts, with the exception of the band at 700.3 nm.

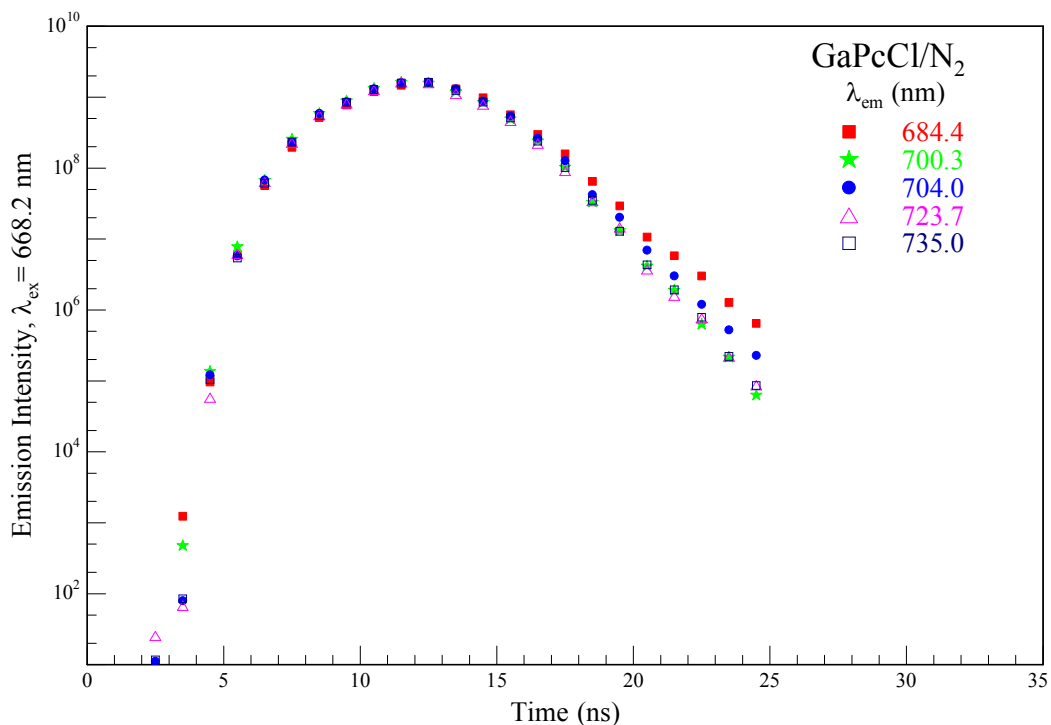


Figure V.38: Emission decay profile of GaPcCl/N₂ recorded for some of the main emission bands. The laser profile is also shown for comparative purposes.

A series of lifetime measurements were performed at various temperatures in N₂ in order to probe whether or not the 10 K emission decay curves are representative of the true fluorescence lifetime. The results of this study are shown in Figure V.39. Emission spectra were recorded with 666.1 nm excitation between 10 K and 22 K at 2 K intervals. A kinetic slice was taken through the emission band at 702.4 nm at each temperature. The remaining emission decays were then overlaid on the same scale to see if they matched up with the 10 K data and the fit. With the exception of the 22 K decay curve, there is no significant shortening of the decay time with increasing temperature, indicating that the true fluorescence lifetime has been measured below 20 K. This was repeated by monitoring other emission bands and using various excitation wavelengths and found to be a consistent result.

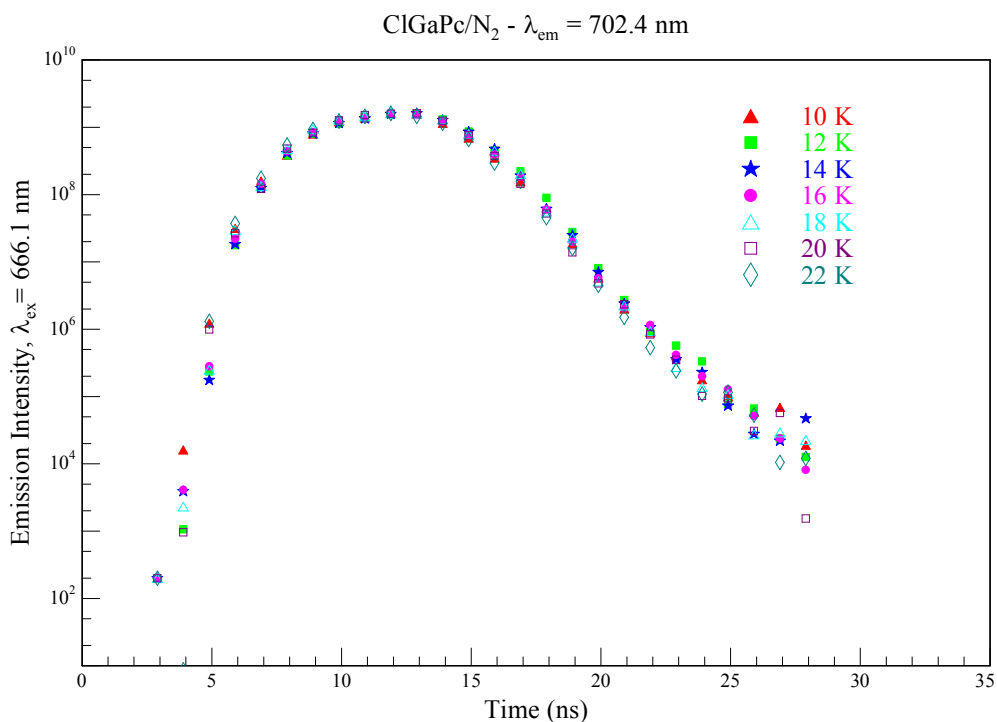


Figure V.39: Emission lifetime of GaPcCl isolated in an N₂ matrix recorded at various temperatures between 10 and 22 K. The emission band monitored was located at 702.4 nm and was excited by 666.1 nm pulsed laser excitation. The stability of the measurement indicates that the true fluorescence lifetime has been detected.

The emission decay curve of GaPcCl/N₂ was measured as described earlier, with the decay plot shown in Figure V.40. Time resolved emission was recorded by exciting at 665.7 nm and a kinetic slice was taken through the emission band at 734.6 nm. This is the same vibronic band that was monitored for the lifetime measurements in the rare gas matrices. A single exponential fit was overlaid on the emission profile to determine the fluorescence lifetime in solid N₂, which was measured to be 2.6 ns, a similar value to what has been measured in the rare gas matrices. The decay time is very slightly longer than that observed in an Ar, Kr and Xe matrices (2.3 2.4 and 2.3 ns respectively). These results will be discussed in greater detail in a Section V.4.I.

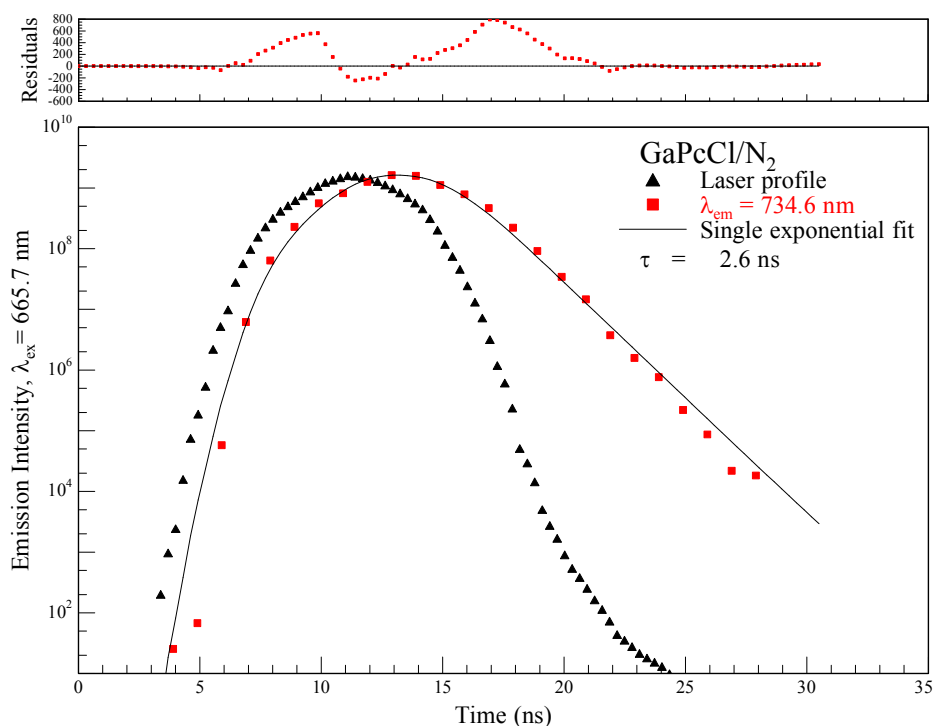


Figure V.40: Semi-log plot of the emission decay curve of GaPcCl extracted from time-resolved emission spectra recorded at 10 K in N_2 . The shape of the excitation pulse of the laser is also shown. The emission was recorded with 665.70 nm excitation and the lifetime was measured at 2.6 ns.

V.3.IV.d: Excitation

Excitation spectra of GaPcCl/ N_2 were recorded by monitoring a range of different emission bands, the results of which are presented in Figure V.41. The spectra show two general structures; one which is fairly similar to the rare gas matrices (red trace) and the other which consists of a series of doublets throughout the entire range of the spectrum. Each spectrum contains a narrow band around 669 nm corresponding to the band origin in excitation, with broader excitation bands extending up to 625 nm. Monitoring the emission band at 713.98 nm is shown by the red trace. This shows a somewhat similar structure to the excitation spectra recorded in the rare gas matrices, although the bands are not as well resolved.

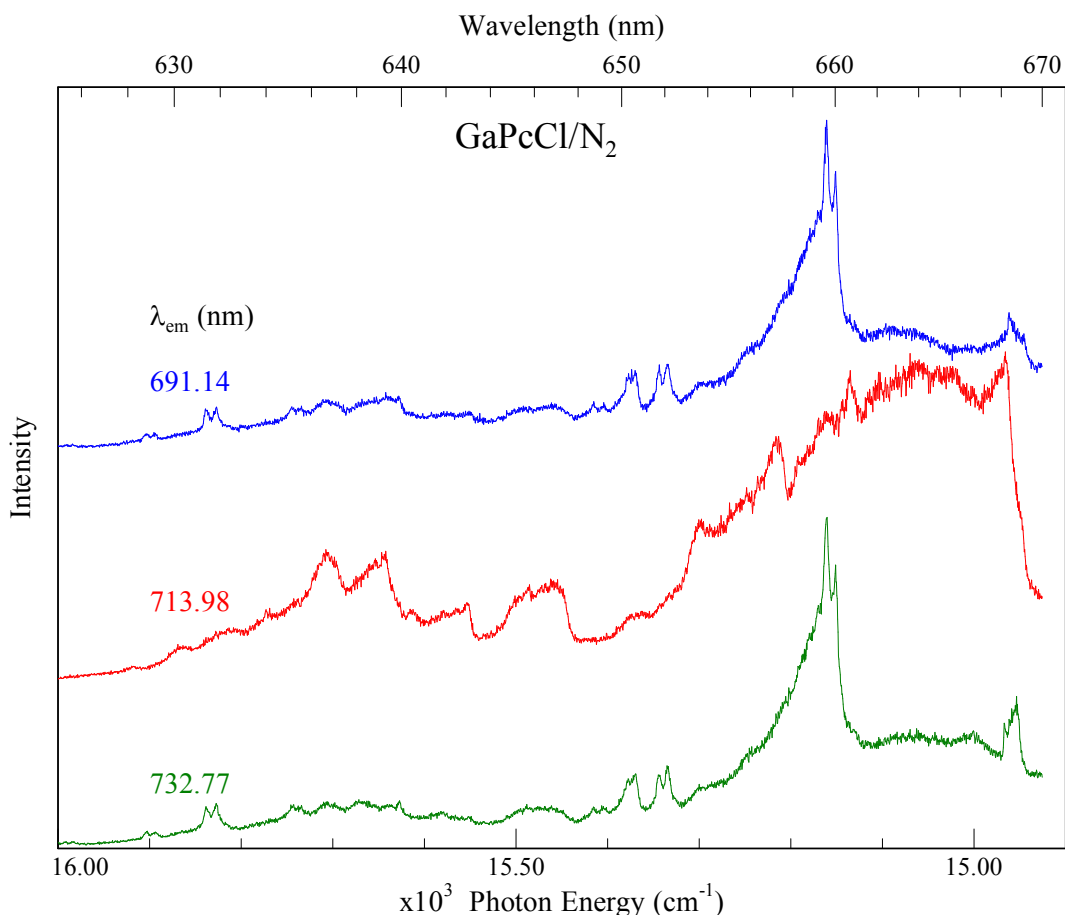


Figure V.41: Excitation spectra of GaPcCl recorded in N₂. The emission bands monitored were located at 691.14, 713.98 and 732.77 nm.

The excitation spectrum recorded by monitoring the emission band at 691.14 nm (blue trace) has its 0-0 transition red-shifted in excitation by 2.7 cm⁻¹ compared to the red trace. This typically indicates that the excitation spectra of two different sites have been recorded, however this may not be quite the same situation in this case. In the rare gas matrices, the excitation spectra originating from different sites were similar in structure, with the vibronic bands exhibiting a constant shift with respect to one another (i.e. if the 0-0 band in excitation was red shifted by 10 cm⁻¹ from the 0-0 transition of a second site, so too would each of the vibronic bands). The different structure observed throughout the spectrum in N₂ indicates that a different species is being observed. Some of the vibronic bands in this spectrum are split into doublets, which may be due to Davydov splitting⁷. The splitting between the doublets is typically 10 cm⁻¹. Davydov splitting has previously been identified in the Raman spectra of GaPcCl by Aroca⁷. The presence of Davydov splitting may indicate another species exists in the matrix (e.g. a dimer).

The green trace ($\lambda_{\text{em}} = 732.77$ nm) shows remarkable similarity to the blue trace. Almost all of the bands in these two spectra match up exactly, and the presumed Davydov splitting is also evident (with the splitting ~ 10 cm^{-1}). The only exception is in the region of the 0-0 transition, where a fairly broad structure is observed to the red of this wavelength in the green trace. A weaker equivalent of this is present in the blue trace also.

V.3.IV.e: Amplified Emission

N_2 was the easiest matrix in which to observe amplified emission, with many samples made under various deposition conditions capable of exhibiting stimulated emission. Figure V.42 shows the fluorescence (red trace) and AE (black trace) spectra overlaid. The intensity of the AE band, shown by the black trace, dwarfs that of the rest of the fluorescence bands present in the spectrum. The inset spectrum shows the normalized vibronic band at 744.9 nm under conditions that yield fluorescence and AE. The band is significantly narrowed when the laser power has been increased to produce AE. Unlike the other matrices there is little indication of another site close by that can exhibit the effect. Nevertheless, a series of excitation energies were investigated to see if they could produce AE, with all experiments yielding a single AE band. The band at 744.9 nm shifted by a single pixel number on the CCD; a shift of 0.04 nm. The close energy of the sites in solid nitrogen may explain why AE is so easy to observe in this matrix. Because the OD and the laser power are the only two variables governing AE, when the sites are so close in energy, the OD will be very large. All of the other matrices had sites split by several wavenumbers and this ‘dilutes’ the OD of a given site, reducing their capacities to exhibit AE.

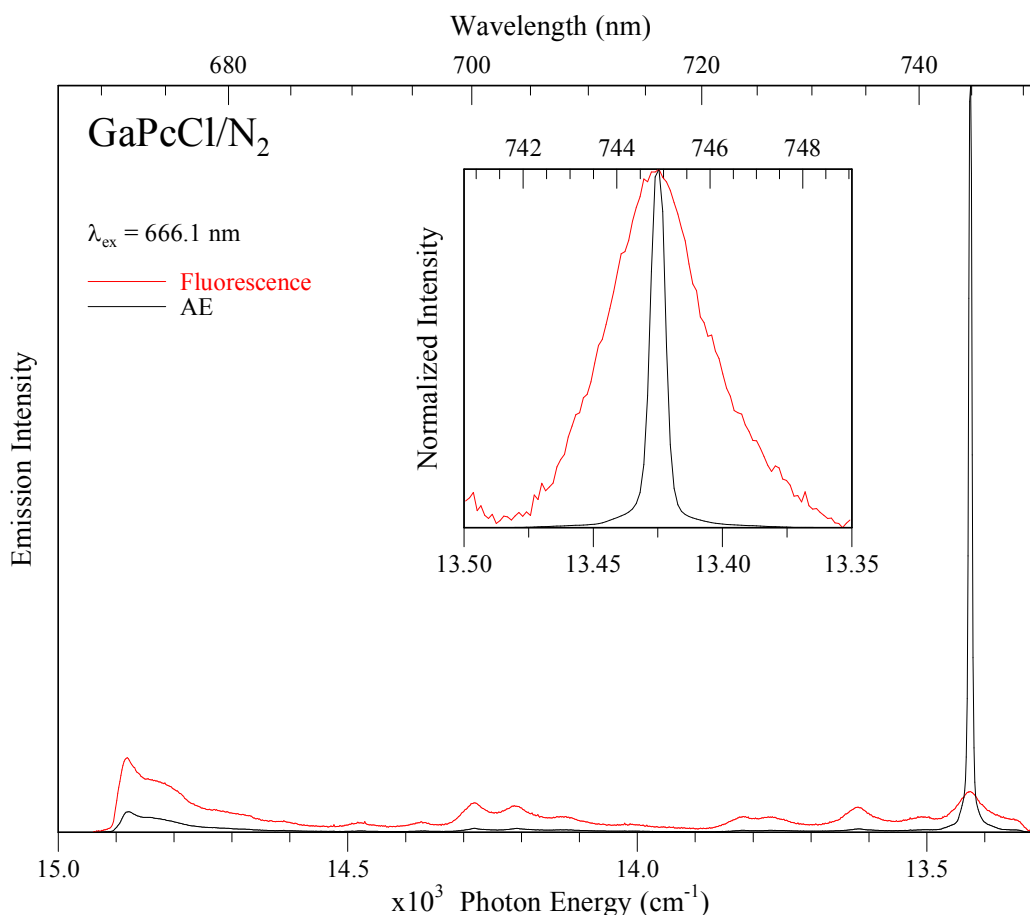


Figure V.42: Emission of GaPcCl isolated in N₂ excited with 666.1 nm pulsed laser radiation with low power (red trace) and high power (black trace). The band at 744.9 nm is significantly amplified by increasing the laser power. Furthermore, the linewidth of the amplified band is narrowed considerably compared to the corresponding fluorescence band as shown in the inset of the figure.

V.3.V: Matrix Comparison

V.3.V.a: Absorption

Figure V.43 shows a comparison of the room temperature solution phase absorption spectrum of GaPcCl and a spectrum recorded in solid Ar at 10 K. The solution phase absorption spectrum of GaPcCl dissolved in EtOH show two main features – an intense band at 676.1 nm (14791 cm⁻¹) corresponding to the fully allowed Q (S₁) ← G (S₀) electronic transition and a weaker band at 352.4 nm (28409 cm⁻¹) which corresponds to the B (S₂) band. The region of the solution phase spectrum between 700 and 600 nm contains three features in ethanol. The red-most feature, centred on 676.1 nm, is clearly the origin of the Q band due to its position and intensity. A second, weaker band, located at 645.4 nm

(15494 cm^{-1}) is not fully resolved but clearly present as a shoulder in the spectrum. Another weak but better resolved band located at 609.8 nm (16399 cm^{-1}) hints at more vibronic transitions in absorption.

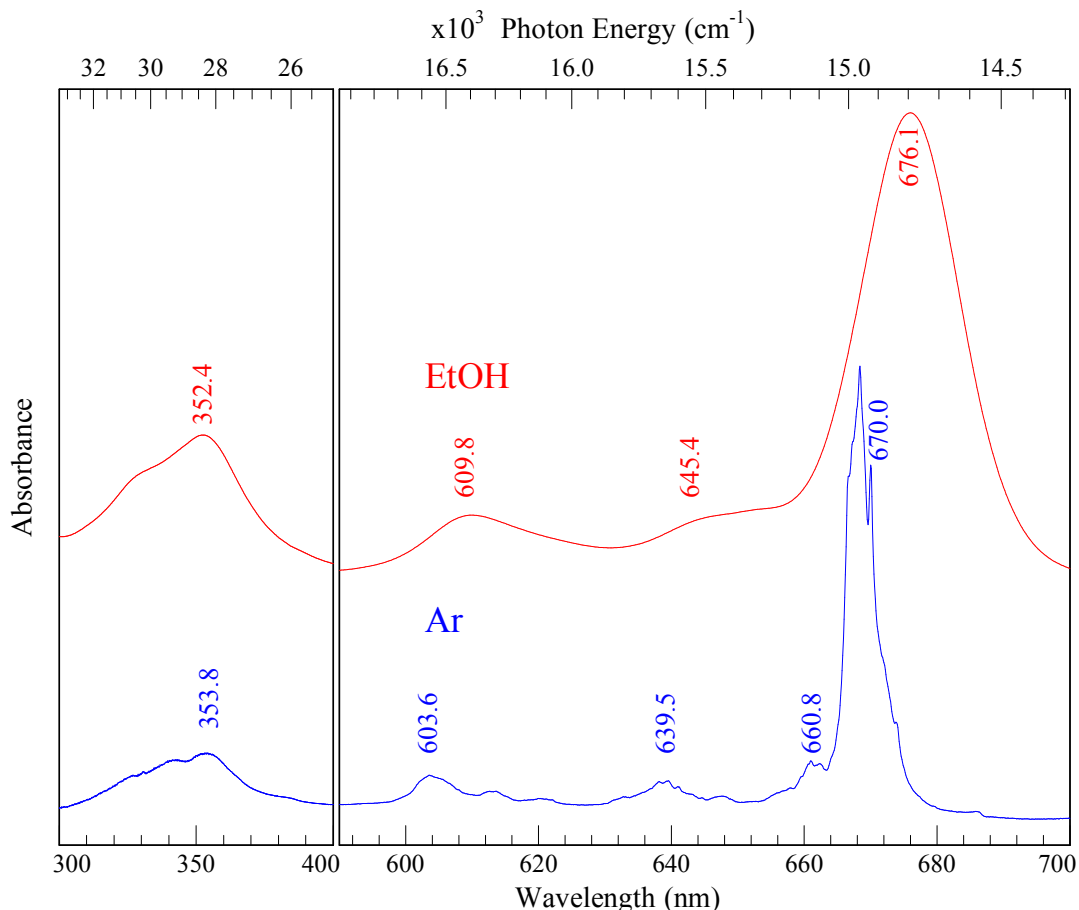


Figure V.43: The absorption spectra of GaPcCl recorded in ethanol at room temperature (red trace) and in solid Ar at 10 K (blue trace). The main peaks in the solution phase have been labelled (in nm) as well as the corresponding peaks in the matrix spectrum.

The main absorption bands in solid Ar match the two main bands observed in solution; the strong Q band at 670.0 nm and the weaker B band at 353.8 nm in solution. The most obvious difference between the matrix and solution phase spectra is the band width; the bands are much narrower in the matrix absorption spectra due to much weaker interactions between the host and the guest material. This effect is also observed to the blue of the main absorption band where the matrix spectrum shows several resolved vibronic bands. In contrast, the structure of the B band is remarkably similar in both spectra. The B band does not become more resolved in the matrix, and no vibronic structure can be observed.

Bursa *et al.*⁸ described the solution phase absorption spectrum of a substituted GaPcCl molecule (2,3-tetrakis(4-benzyloxyphenoxyphthalocyanato)gallium(III)). The structure of the spectrum is remarkably similar to the results presented here for the unsubstituted molecule. Bursa correctly identified the location of the band origin of the Q band and noted the presence of the two weaker bands to the blue of the 0-0 band. However, the band at 645.4 nm was identified as an aggregate species by Bursa. From the matrix data recorded, the assignments of the bands by Bursa appear to be incorrect. Thus the band to the blue of the 0-0 transition at 664.4 nm is unlikely to originate from an aggregate species, as the matrix spectrum presented in Figure V.43 shows that vibronic bands are located in the region of the unresolved solution peak. The intensity of the matrix band is comparable to that of the solution phase band. The solution phase band at 609.8 nm is located 703 cm⁻¹ from the band origin, comparable to the value of the vibronic band at 712 cm⁻¹ in Ar. The solution phase band at 609.8 nm also agrees well with vibronic bands in the matrix spectrum. The shift from the 0-0 band is 1608 cm⁻¹, and probably corresponds to the vibronic band in Ar located at 1642 cm⁻¹. It is unclear if Bursa has assigned the equivalent bands in their results as vibronic transitions or as a separate Q band (possibly from another species).

The Q band absorption spectrum of GaPcCl recorded in four different inert host matrices - N₂, Ar, Kr and Xe - are shown in Figure V.44. The spectra are dominated by an intense band located between 665 and 680 nm corresponding to the fully allowed Q (S₁) ← G (S₀) transition. The band origins (0-0) of the Q ← G electronic transitions in absorption are 14959, 14916, 14806 and 14680 cm⁻¹ in N₂, Ar, Kr and Xe respectively. Several weaker vibronic bands are also present ranging from 680 – 600 nm (about 2000 cm⁻¹ above the band origin). Vibronic bands are expected to arise up to 1600 cm⁻¹ beyond the band origin based on the vibrational study performed in Chapter III, but bands at higher energies may arise due to combination modes or overtones. The vibronic bands beyond 1600 cm⁻¹ are also much weaker than the bands up to 1600 cm⁻¹ which is another good indication that they are not fundamental modes. The fact that they appear in both the solution phase and the matrix spectra rules out the possibility of hot bands, as the temperature in matrix samples is too low for thermally occupied vibrational levels to exist. The B (S₂) band is located around 350 nm in each host (region not shown in Figure V.44), but carries less intensity than the Q band. N₂ has the highest absorption energy for the 0-0 transition of the Q band. The equivalent bands in Ar, Kr and Xe are red-shifted with respect to N₂ by 54,

171 and 331 cm^{-1} respectively, as matrix interactions between the host and the guest species get stronger. Table V.9 lists the location of the main resolved absorption bands of GaPcCl in various hosts, as well as their shifts from the band origin. Well resolved structure is observed around the 0-0 band in some of the matrices, possibly an indication of sites being present. Furthermore, most matrices show a very weak shoulder to the red of the 0-0 band which is probably originating from the presence of a small amount of aggregates within the sample; a common occurrence under low temperature depositions.

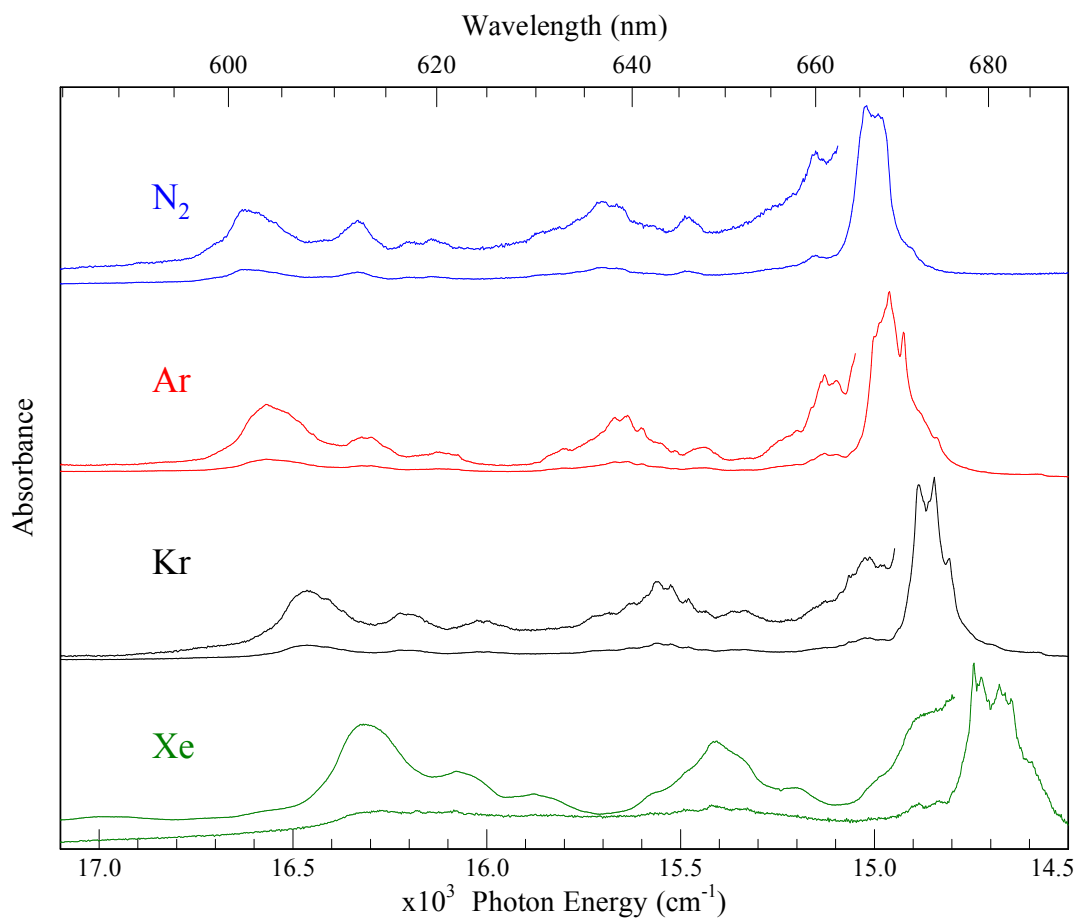


Figure V.44: Absorption spectra in the region of the Q band of GaPcCl isolated in solid matrices of N₂, Ar, Kr and Xe, recorded at 10 K.

Table V.9: Absorption energies of the Q band and its vibronic transitions of GaPcCl recorded cryogenic matrices of N₂, Ar, Kr and Xe. All energies are reported in wavenumbers (cm⁻¹). The right hand side column for each system includes the shift (in cm⁻¹) from the band origin of the electronic transition. The values highlighted in italics are believed to be from overtones or combination bands.

N ₂		Ar		Kr		Xe	
Energy	Shift	Energy	Shift	Energy	Shift	Energy	Shift
-	-	-	-	-	-	14522	-126
14908	-83	14839	-86	14693	-115	14601	-47
14979	0	14925	0	14808	0	14648	0
14990	11	-	-	-	-	14663	15
15022	43	14961	36	14846	37	14676	28
-	-	-	-	14885	77	14725	78
-	-	-	-	-	-	14745	97
15152	172	-	-	-	-	14832	185
-	-	15129	203	15013	205	-	-
-	-	-	-	15026	218	-	-
-	-	15198	272	15056	247	14885	238
-	-	15202	277	15126	318	-	-
15487	508	-	-	15333	524	-	-
-	-	15513	588	15368	560	15207	559
-	-	15516	591	-	-	-	-
-	-	-	-	15437	629	-	-
-	-	15601	675	15480	672	-	-
15704	724	15637	712	15526	717	-	-
-	-	15669	744	15559	751	15408	761
15813	834	-	-	15625	817	-	-
-	-	15798	872	15684	876	-	-
-	-	-	-	15728	920	15562	914
16142	1163	16075	1149	15997	1189	-	-
16202	1223	16129	1204	16023	1215	15883	1235
16332	1353	16297	1372	-	-	-	-
-	-	16324	1398	-	-	-	-
-	-	-	-	16226	1418	16077	1429
-	-	-	-	16372	1564	-	-
-	-	-	-	16412	1604	-	-
16625	1646	16567	1642	16466	1658	16316	1668
<i>17268</i>	<i>2289</i>	<i>17238</i>	<i>2322</i>	<i>17112</i>	<i>2306</i>	<i>16981</i>	<i>2301</i>
<i>17727</i>	<i>2748</i>	<i>17683</i>	<i>2767</i>	<i>17587</i>	<i>2781</i>	<i>17425</i>	<i>2745</i>
<i>17976</i>	<i>3000</i>	<i>17940</i>	<i>3024</i>	<i>17819</i>	<i>3013</i>	<i>17687</i>	<i>3007</i>

Basova⁹ recorded the absorption spectrum of GaPcCl in thin solid films and observed the Q band at 13333 cm⁻¹ with a shoulder at 14925 cm⁻¹. The width of the absorption band in the thin films is much broader than that recorded in inert gas matrices due to the high degree of aggregation and absence of isolated molecules owing to the method by which

these samples are produced. Linsen and co-workers¹⁰ have determined the band origin lies at 15374.5 cm^{-1} in superfluid helium droplets. Del Cano *et al.*¹¹ have measured the absorption spectra of mixed films of GaPcCl and bis(neopentyl)-3,4,9,10-perylenebis(dicarboximide), and have reported the origin of the Q band at 13698.6 cm^{-1} . This result was verified by growing neat thin films of GaPcCl¹². To the best of the author's knowledge, the gas phase position of the Q_{0-0} band origin of the $Q \leftarrow G$ transition has never been recorded.

V.3.V.b: Emission

Emission spectra recorded by exciting into the 0-0 band in absorption for the four matrices used in this study are shown together in Figure V.45. Fluorescence bands were observed up to around 740 – 760 nm depending on the host matrix. Emission spectra recorded in N_2 (blue trace) yielded fluorescence with the fewest emission bands, although these bands are quite broad, especially when compared to emission in Ar (red trace). This is perhaps indicative of there being several unresolved sites occupied by GaPcCl in N_2 . These sites must be very close in energy, as they were not resolvable with laser excitation, which typically excites into a single site selectively. The fluorescence from the Ar matrix is more resolved than in N_2 , with a hint of there being some site structure present. The shoulders to the red of the narrow emission bands are not resolved with excitation into the 0-0 band, and their broadness suggests that they are emission from an aggregate species. The vibronic bands in emission are red-shifted in the rare gas matrices with respect to N_2 . Emission spectra from the Kr matrix closely resemble those from Ar, with quite sharp bands and a red wing coming off each emission band. Xe matrices always yielded the broadest emission bands, probably due to the presence of sites located close together in energy.

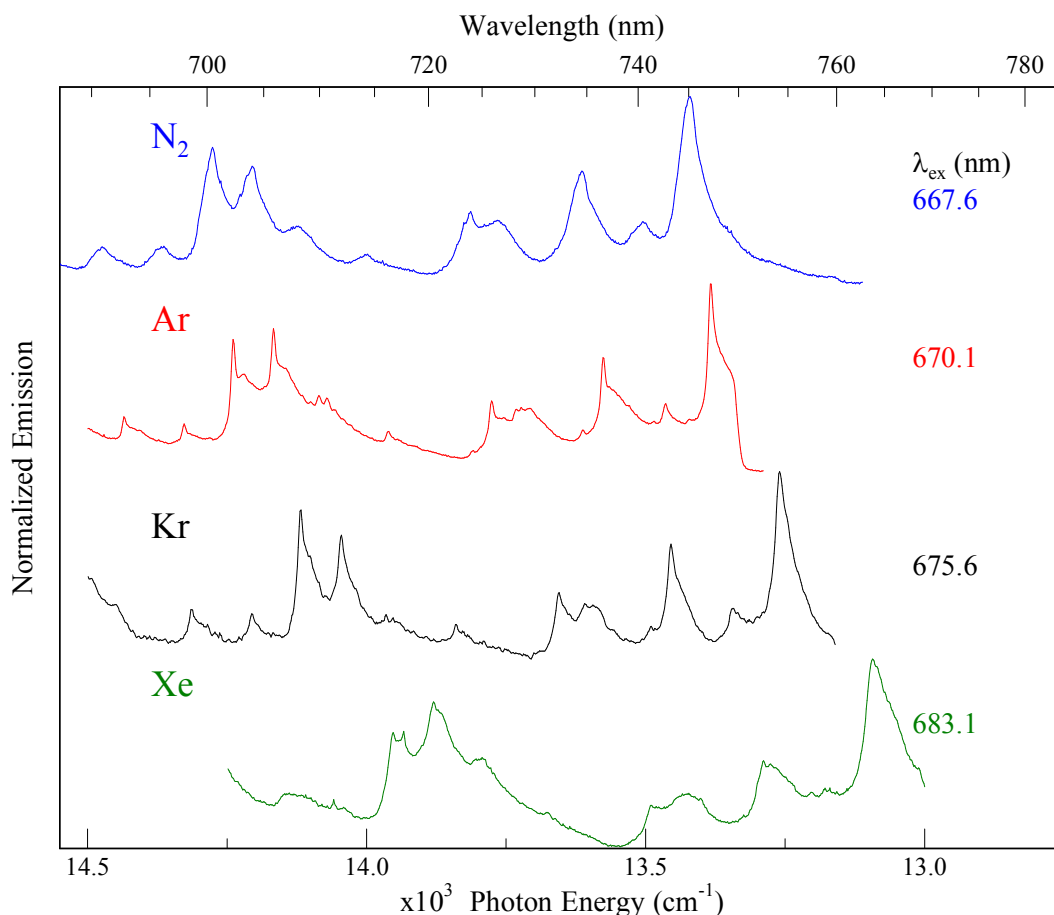


Figure V.45: Fluorescence spectra of GaPcCl isolated in solid matrices of N₂, Ar, Kr and Xe at 10 K. These spectra were recorded by exciting into 0-0 transition of the Q band – namely 667.6, 670.1, 675.6 and 683.1 nm for N₂, Ar, Kr and Xe respectively.

The vibronic structure of GaPcCl observed in each matrix appears, as shown in Figure V.45, to be quite similar. To analyse this further the emission spectra recorded in each matrix are plotted in Figure V.46 as the shift from the 0-0 transition. The plot has been split into two regions; the region close to the 0-0 band from -100 – 250 cm⁻¹ and the region from 250 – 1700 cm⁻¹. An almost identical set of signature peaks are evident in all matrices, albeit with different relative intensities. The existence of a blue site can be clearly seen in Ar and Kr at about -20 cm⁻¹ from the band origin of the dominant site. This also manifests itself throughout the rest of the emission spectrum, where a doubling of the peaks is observed. A list of the vibronic frequencies (in cm⁻¹) of GaPcCl in each matrix is compiled in Table V.12. Where multiple sites are present in the matrix, the frequency of the red site has been selected. It is also evident in Figure V.46 that the 0-0 transition dominates the emission intensity. This is consistent with the results of measurements made

for ZnPc in which the 0-0 transition was found to carry most of the Franck-Condon intensity¹³.

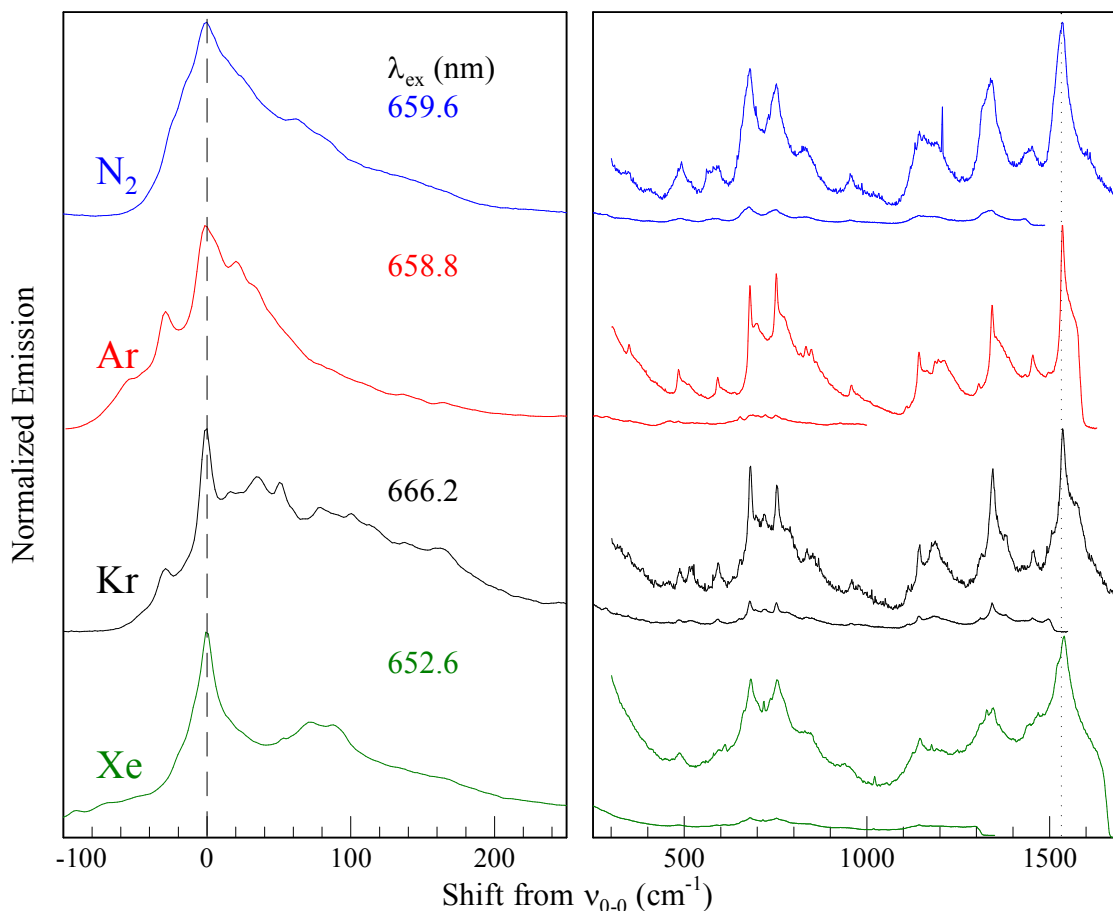


Figure V.46: Emission spectra of GaPcCl isolated in solid matrices of N₂, Ar, Kr and Xe at 10 K plotted as the shift from ν_{0-0} . In samples where multiple sites were observed the spectra are shifted from the band origin of the red site. Spectra were recorded by exciting into the blue of the 0-0 band in absorption in order to see the band origin in emission. The excitation wavelengths were 659.6, 658.8, 666.2 and 652.6 nm for N₂, Ar, Kr and Xe respectively. The dashed line highlights the location of the 0-0 transition in each spectrum. The dotted line highlights the vibronic band located at ~ 1540 cm⁻¹ (in Ar).

A slight change in the emission spectra is observed in most matrices when the laser excitation frequency is tuned to the blue of the 0-0 transition (Figure V.46) of the Q band compared with direct excitation of the first excited state (Figure V.45). This change occurs because a different site is being preferentially excited depending on the laser wavelength. Slight differences in terms of frequency shift and shape of the vibronic bands are evident. Generally, 2 – 3 main families of sites are present in each matrix, with the exception of N₂, where it appears that a single site dominates, but is in fact an indeterminate number of

unresolved sites. The sites in N₂ are clearly different to those in the rare gas matrices as they cannot be resolved by changing the excitation wavelength of the laser. Instead, a single broad emission band is observed with all excitation wavelengths. Certain Ar samples also showed a continuum of sites which were not observed in any of the other matrices. In order to determine the location of the band origin in emission it was necessary to excite to the blue of the 0-0 band in absorption. A by-product of a higher energy excitation is that sites other than the main site will be excited. Emission from one of these sites can be reabsorbed by a red site and re-emitted from there. This will then result in a 'doubling' of the bands in the emission spectrum, with one set of bands arising from excitation into the desired site, and another set arising from a site to the red. The vibronic bands present in emission in each matrix are highly consistent, with only the weakest bands not showing up in emission in each host. The frequencies of the vibronic modes change very little in the different hosts (when considered as the shift from the 0-0 transition), with frequencies typically differing by less than 10 cm⁻¹ between matrices, as shown in Table V.12.

A summary of the emission decay curves recorded for GaPcCl isolated in different inert gas solids (N₂, Ar, Kr and Xe) is given in Figure V.47. The same vibronic band was monitored in each host, located approximately 1345 cm⁻¹ from the 0-0 transition in emission. This band was chosen because it has a long wavelength, and therefore is more representative of the true decay time. Furthermore, this band is not prone to exhibiting AE, so it will not be shortened by this effect. The fluorescence decay curves were measured with time-gated iCCD detection and the lifetimes extracted by single exponential fits. Fluorescence lifetimes were measured to be 2.6, 2.3, 2.4 and 2.3 ns in N₂, Ar, Kr and Xe respectively. The recorded lifetimes are all in the nanosecond range, as expected for fully allowed electronic transitions. These results closely resemble the results obtained by Murray⁵ for ZnPc, which were typically around 3 ns. The slight shortening of the fluorescence lifetime of GaPcCl may be due to the internal heavy atom effect caused by the gallium atom and/or chlorine counter ion.

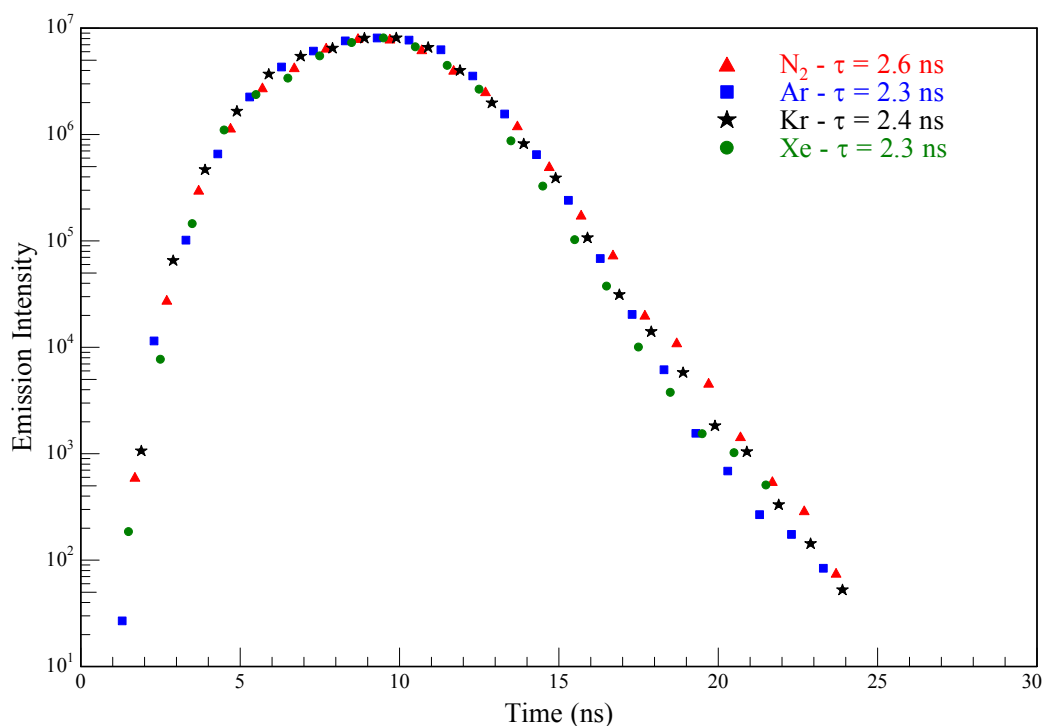


Figure V.47: Semi-log plots of the emission decay curves extracted from time-resolved emission spectra recorded at 10 K for GaPcCl isolated in a variety of low temperature matrices. The emission wavelength being monitored in each matrix coincided with a common vibronic band located $\sim 1345 \text{ cm}^{-1}$ from the band origin. The shape of the excitation pulse of the laser is also shown.

V.3.V.c: Excitation

The excitation spectra recorded of GaPcCl isolated in different matrices are shown in Figure V.48. The spectra are presented as the shift from the band origin (ν_{0-0}) up to 900 cm^{-1} . Obtaining data beyond 1000 cm^{-1} from the band origin was limited by the tuning range of the dye used, which has been specified in Chapter II. Well resolved vibronic structure is evident in all matrices up to 750 cm^{-1} , with the exception of N_2 , which has quite broad excitation bands. The frequencies (in cm^{-1}) of the vibronic bands observed in excitation are presented in Table V.10.

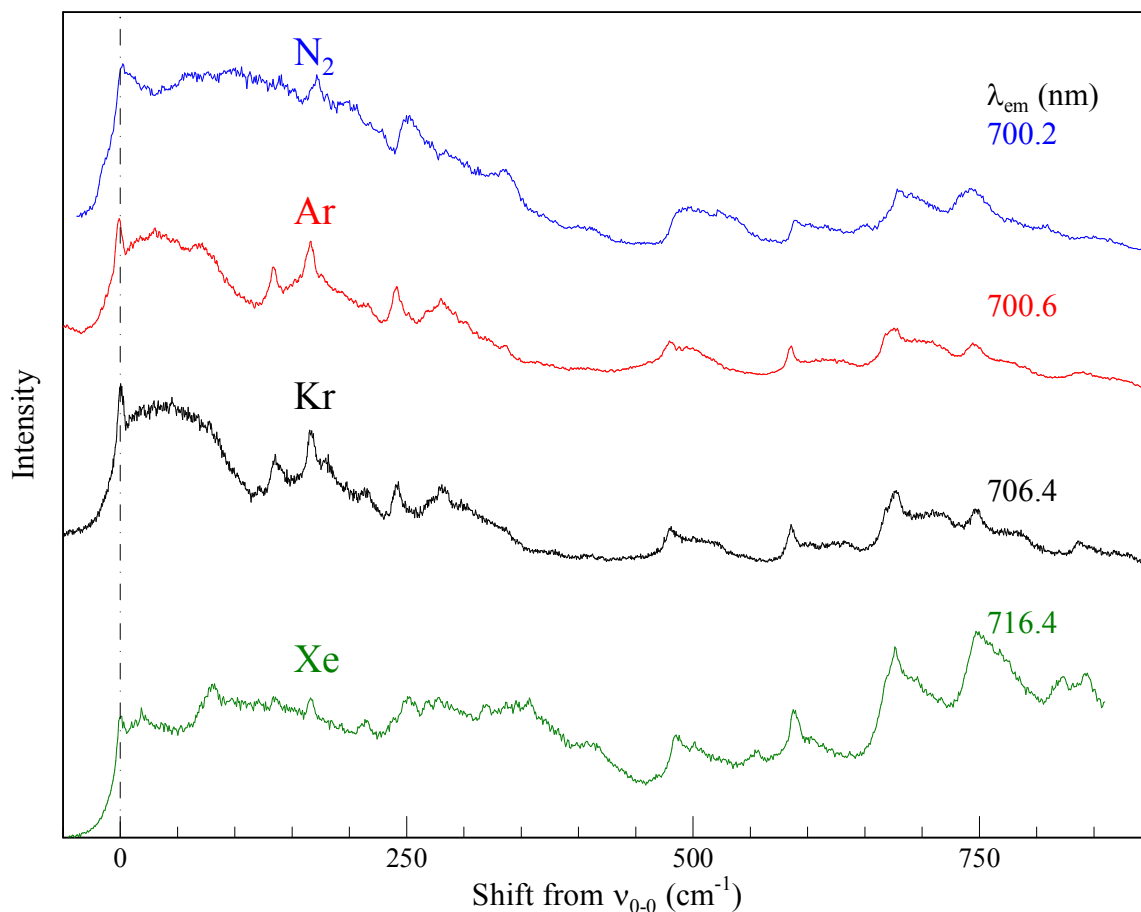


Figure V.48: Excitation spectra of GaPcCl recorded in N₂, Ar, Kr and Xe. The emission bands monitored were located at 734.6, 700.6, 706.4 and 716.4 nm for N₂, Ar, Kr and Xe respectively and were scanned with the dye laser.

The excitation spectra recorded in Ar and Kr are quite similar. A well-defined 0-0 transition in excitation is evident in both matrices and the vibronic bands match up excellently over the entire range of the spectra. The data presented in Table V.10 show these bands agree to within 2 cm⁻¹ in most instances. N₂ shows broader bands than those observed in Ar and Kr, but appear in the same regions as observed for the other matrices. Xe has weaker intensity around the 0-0 band compared to the other three host materials studied, but the excitation bands are comparable to those measured in Ar and Kr. The results presented in Table V.10 show how the three rare gas matrices (Ar, Kr and Xe) are much more similar than the molecular matrix (N₂) when it comes to the excitation spectra. The reason for the excitation spectra in N₂ being so different than the other matrices is unexpected, but may be related to the fact that the sites cannot be resolved in emission.

Table V.10: Energies (in cm^{-1}) of the observed bands in the excitation spectra of GaPcCl isolated in various matrices. The values are given as shifts from the band origins (taken from Figure V.48) and indicate the vibronic bands in excitation.

N₂	Ar	Kr	Xe
21	30	-	18
-	73	-	80
-	110	-	121
-	138	138	134
172	168	167	168
-	-	216	214
252	245	244	252
-	280	278	279
-	-	317	322
335	-	338	358
-	402	408	408
-	486	483	484
524	519	519	-
-	-	555	556
589	587	585	590
-	619	620	-
650	675	675	676
-	703	713	-
741	747	747	748
809	-	772	822
-	-	877	842

V.3.V.e: Time Dependent DFT Calculations

The absorption spectrum of GaPcCl was predicted using time dependent DFT (TD-DFT) calculations. The structure of the molecule used was the optimized structure from Chapter III. The same basis set (6-311++g(2d,2p)) and functional (B3LYP) were used and the first 50 singlet excited states were calculated. A list of the transition energies and oscillator strengths calculated for this system are presented in Table V.A1. The molecular orbitals associated with the Q←G and B←G transitions have been shown in Figure V.A4 and Figure V.A5 respectively.

The predicted absorption spectrum from TD-DFT is shown in Figure V.49, as well as the absorption recorded in Ar. Time dependent DFT results show the same general structure in absorption as those measured experimentally, with the Q and B bands clearly dominating the spectrum. The Q and B bands are located at 621.95 and 338.94 nm respectively, both of which are blue-shifted with respect to the experimental results. The calculated spectrum

does not account for the vibronic structure of the excited state, but this will be analysed in Section V.4.III using the Raman scattering spectra presented for GaPcCl in Chapter III.

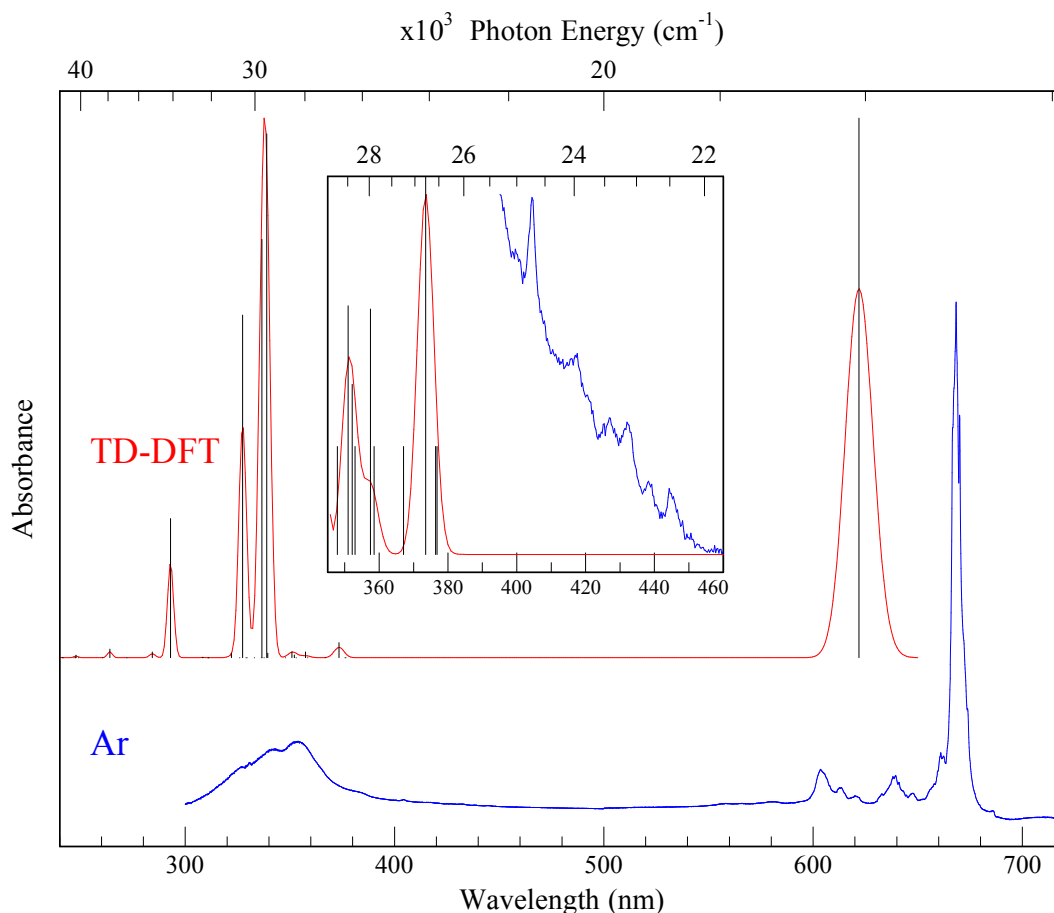


Figure V.49: The absorption spectra of GaPcCl predicted by time dependent DFT calculations (red trace) and experimental results in solid Ar at 10 K (blue trace). A linewidth of 200 cm^{-1} was used in the generation of the TD-DFT spectrum. A stick spectrum showing the wavelengths of the electronic transitions are shown by the black lines. An extended view of the region of weak intensity between the Q and B bands is shown in the inset, as well as in Figure V.A2.

V.4: Discussion

V.4.I: TD-DFT

Time dependent DFT predicts the $Q \leftarrow G$ electronic transition to be located at 16078 cm^{-1} and the $B \leftarrow G$ transition at 29504 cm^{-1} . These values are comparable to the values measured in solid N_2 of 14979 s and 28409 cm^{-1} for the Q and B bands respectively. Both predicted transitions are blue-shifted with respect to the N_2 results by 1088 and 1095 cm^{-1} for the Q and B transitions respectively. This represents a 7% and 4% difference between

the theoretical and experimental findings. This is perhaps unsurprising, as the theoretical approach does not consider any external species (such matrix host atoms) interacting with the molecule, which can perturb the energy gap between the ground and excited electronic states. The closest experimental approach for determining the accuracy of the calculation would be measuring the gas phase absorption energy, but as far as the author is aware, no such data exists. A similar oscillator strength is predicted for the Q and B bands, where $f = 0.3915$ and 0.3802 respectively. The difference in intensity of the two bands measured experimentally is clearly much greater. A similar result was observed with a TD-DFT calculation on ZnPc. Because TD-DFT does not account for additional external interactions (such as host matrix atoms), it indicates that there is something erroneous in the way that it calculates the excited states of molecules.

The TD-DFT calculation shows several weak transitions just to the red of the B band, the strongest of which arises at 373.52 nm with an oscillator strength of $f = 0.011$. Similarly, weak bands are present in the experimental matrix absorption spectra of GaPcCl in Figure V.1, Figure V.14, Figure V.24 and Figure V.33 for Ar, Kr, Xe and N₂ matrices respectively. These bands were tentatively assigned as weak electronic transitions of the GaPcCl molecule, and the TD-DFT results give more credibility to this assignment. These weak bands in each host, as well as the calculated transitions are shown in Figure V.A2. A similar structure is observed in each matrix, and the bands appear to be experiencing a matrix shift, similar to the Q band. The weak bands situated between the Q and B bands have also been predicted by TD-DFT for AlPcCl, H₂TAP, ZnTAP and the entire group II M-TAPs (shown in Figure V.A3), as well as in ZnPc. This may indicate that there are weak bands present in the absorption spectra of the phthalocyanines which have not been documented before. The matrix absorption spectra presented in the results section showed some weak absorption bands in the 400 – 450 nm region of the spectrum. It may be the case that these weak bands are the experimental evidence of the bands predicted by TD-DFT. It is clear that these bands originate from a species isolated in the matrix because they shift location depending on the host gas as shown in Figure V.A2. While these potential electronic transitions have been noted, they have not been analysed in significant detail and warrant further study, particularly as they have not been widely mentioned in the literature.

The excited state lifetime can also be obtained from the extinction coefficient measured in absorption. Due to solubility problems with the GaPcCl/EtOH system, the accuracy of the

molar concentrations was put into doubt, particularly at higher concentrations. This in turn will affect the molar extinction coefficient recorded. Nevertheless, a molar extinction coefficient for GaPcCl/EtOH was calculated from absorption data to be $\epsilon \sim 7.2 \times 10^9$ m/M at 676.07 nm. The oscillator strength can then be calculated by the following equation:

$$f = \frac{2303\epsilon_0^2 m_e c}{e^2} B_{12} \quad \text{Eq. V.1}$$

where ϵ_0 is the vacuum permittivity, c is the speed of light and m_e and e are the mass and charge of an electron respectively. B_{12} is the Einstein coefficient. By substituting the relative physical constants, Equation V.1 simplifies to:

$$f = 4.32 \times 10^{-9} \int \epsilon dv \quad \text{Eq. V.2}$$

where $\int \epsilon dv$ is the integral of the extinction coefficient over the range of the absorption band. Substituting in the value for the extinction coefficient calculated from the absorption data gives an oscillator strength, $f = 0.313$. The fluorescent lifetime (τ) of a transition may then be calculated from the oscillator strength (f) and transition wavelength (λ) using the Strickler and Berg¹⁴ equation,

$$\tau_0 = \frac{\lambda^2 \epsilon_0 m_e c}{2\pi e^2 f} \quad \text{Eq. V.3}$$

where the constants are the same as in Equation. V.1. Applying Equation V.3 with λ and f values for the lowest energy Q transitions determined from the absorption data in ethanol (676.07 nm and 0.313) and TD-DFT (621.95 nm and 0.3915), the lifetimes calculated for GaPcCl are 2.16 ns and 14.8 ns respectively. The difference of the TD-DFT calculated lifetime may be reduced by applying a field correction to the predicted oscillator strength, f , to approximate the apparent oscillator strength f'' given as:

$$f'' = \frac{(s(n^2-1)+1)^2}{f} \quad \text{Eq. V.4}$$

Where n is the index of refraction of the host material and s is a shape factor for the cavity related to the depolarization factor¹⁵. Taking into account the experimentally measured matrix shifts from the 0-0 transitions measured in N₂, Δ , the value for λ becomes:

$$\lambda = \lambda_{TD-DFT} + \Delta \quad \text{Eq. V.5}$$

Substituting in the values calculated for f'' and λ into Equation. V.3 allows for the lifetimes of GaPcCl in different matrix hosts to be predicted. The results of these calculations are displayed in Table V.11.

Table V.11: Theoretically predicted ($\tau_{\text{TD-DFT}}$) and experimental (τ_{Exp}) lifetimes of GaPcCl trapped in different media. All values are reported in ns.

	n	$\tau_{\text{TD-DFT}}$	τ_{Exp}
Vacuum	1	14.8	-
N ₂	1.22	2.25	2.6
Ar	1.29	2.23	2.3
Kr	1.428	2.18	2.4
Xe	1.49	2.17	2.3
EtOH	1.36	2.16	-

When the field correction is applied to the TD-DFT results, the fluorescence lifetime becomes comparable to the values measured experimentally in the matrix. The expected trend of a shortening of the fluorescence lifetime in the heavier hosts also becomes apparent. This expected trend was not observed experimentally however, with Kr showing a longer lifetime than Ar, and Xe having an identical lifetime to Ar. The reason the predicted lifetimes do not match the experimental results may be due to the margin of error associated with the lifetime measurements, typically around 0.1 ns. Because of the short timescales being measured, a small error will appear exaggerated, and this may be the source of the skewed lifetimes in the different matrices. The lifetimes measured in the rare gases all lie within the margin of error, and could be considered to be identical, but a more accurate measurement is required to make a definitive assessment of this idea.

V.4.II: Comparison of the Absorption, Emission and Excitation Spectra

Figure V.50 provides a comparison of the absorption, excitation and emission spectra recorded for GaPcCl in Ar. An enhanced region of this plot is shown in Figure V.A7, where the correlation between the 0-0 transition and the vibronic bands in absorption and excitation is evident. The apparent weak intensity of the 0-0 emission band (shown on the inset of Figure V.50) is an artefact due to strong re-absorption arising from the overlap between absorption and emission bands for this fully allowed electronic transition. A mirror symmetry exists between the absorption (excitation) and emission spectra in Figure V.50. While the emission spectrum is better resolved than the absorption and excitation, the vibronic structure is similar. The vibronic bands above 16000 cm^{-1} were not recorded

in excitation due to the limitations of the dye laser. The broad absorption bands make it difficult to accurately compare with the sharp vibronic bands in emission. The similarity between the absorption, emission and excitation spectra is best illustrated in Ar data but is also present in the other matrices. The frequencies found for the vibronic modes in emission and excitation are listed for a variety of matrices in Table V.12 and Table V.10 respectively.

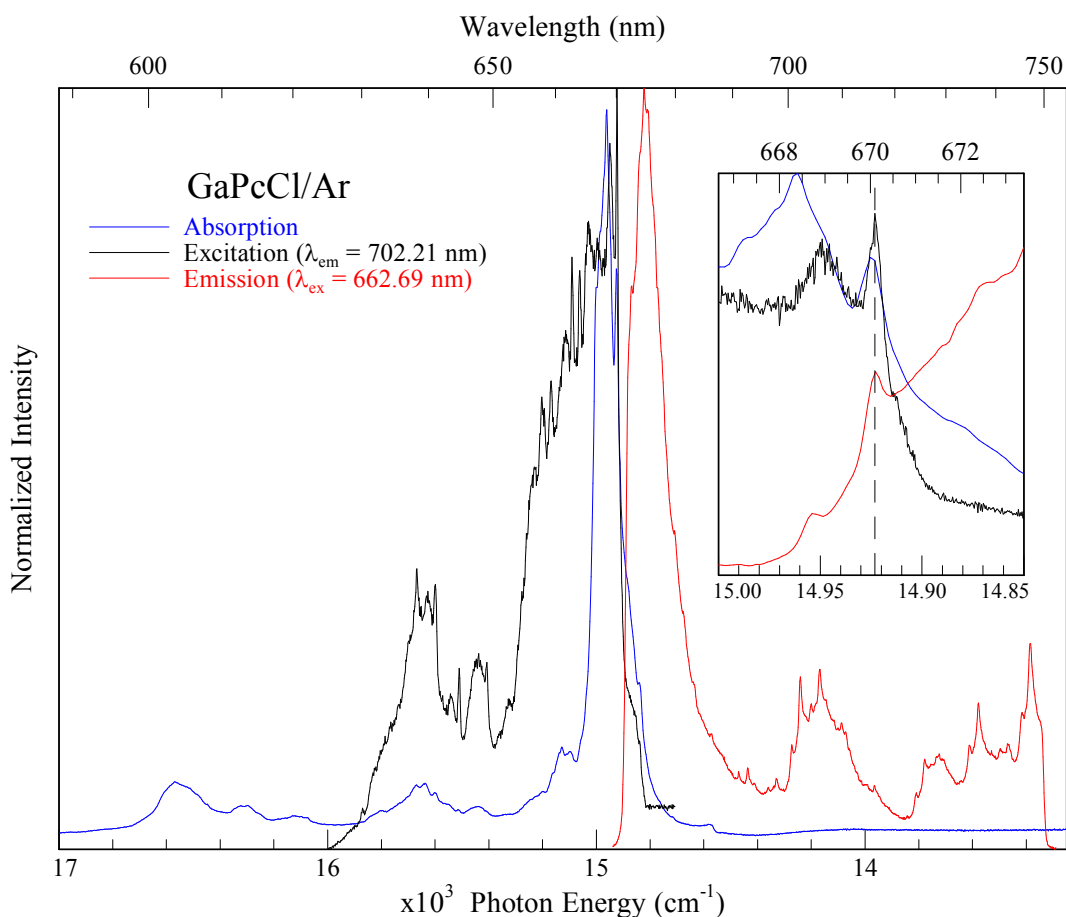


Figure V.50: A comparison of the absorption (blue trace), excitation (black trace) and emission (red trace) of GaPcCl in Ar. Very close agreement exists between the excitation and reversed emission indicating very strong mirror symmetry of the two spectra. The spectrum shown on the inset shows the overlap between the 0-0 bands in absorption, emission and excitation and is highlighted by the dashed line.

The same selection rules exist for vibronic coupling for an electronic transition in both absorption and emission. The similarities in the vibronic intensity distributions in emission and excitation indicate that the molecular geometry in this molecule is not greatly changed when in the first excited electronic state compared to the ground state. Another important observation has been highlighted by the dashed line at 670.1 nm; the positions of the 0-0

band in absorption, emission and excitation are all very close together, to within 1 cm^{-1} , which is less than the experimental error in the current setup.

V.4.III: Vibronic Structure in Emission

The normal Raman scattering spectrum of GaPcCl recorded in KBr discs with CW 660 nm excitation is shown by the red trace in Figure V.51. The vibrational frequencies measured for the Raman active modes of GaPcCl have been presented and analysed in Chapter III. What is evident from Figure V.51 is the strong similarity between the visible emission in Ar (blue trace) and the recorded Raman spectrum. The good agreement between the Raman and fluorescence frequencies was expected because of the similar selection rules, but the observed intensities in Raman and fluorescence spectra are also very similar. This is consistent with the fact that all the vibronic transitions observed in fluorescence are transitions from $v'=0$ to $v_n''=1$ for different vibrational modes. Thus it appears that no overtones or progressions are observed in emission. This allows for the vibrational structure of the excited electronic state of GaPcCl to be analysed in the same manner as the ground state Raman by using high level DFT calculations.

The correlation between the Raman modes and the vibronic bands is shown in Table V.12. The normal vibrational modes associated with the vibronic bands in emission spectrum are compiled in Table V.13 and all involve a distortion of the macrocycle, either directly such as a breathing mode, or indirectly from a distortion of the isoindole units for example. Almost all of the strong vibronic bands are in-plane modes of A_1 or B_2 symmetry. Weaker B_1 and E modes are also evident in the spectrum, but tend to occur below 300 cm^{-1} . In all matrices the strongest vibronic band in emission was a B_2 mode, located around 1540 cm^{-1} in Ar (1552 cm^{-1} for scaled DFT), and corresponds to the strongest band in the Raman spectrum (both experimental and predicted). This mode involves an asymmetric stretch of the $C_\alpha-N_m-C_\alpha$ bonds of the inner macrocycle. This mode will be discussed in more detail in Chapter VI in relation to amplified emission.

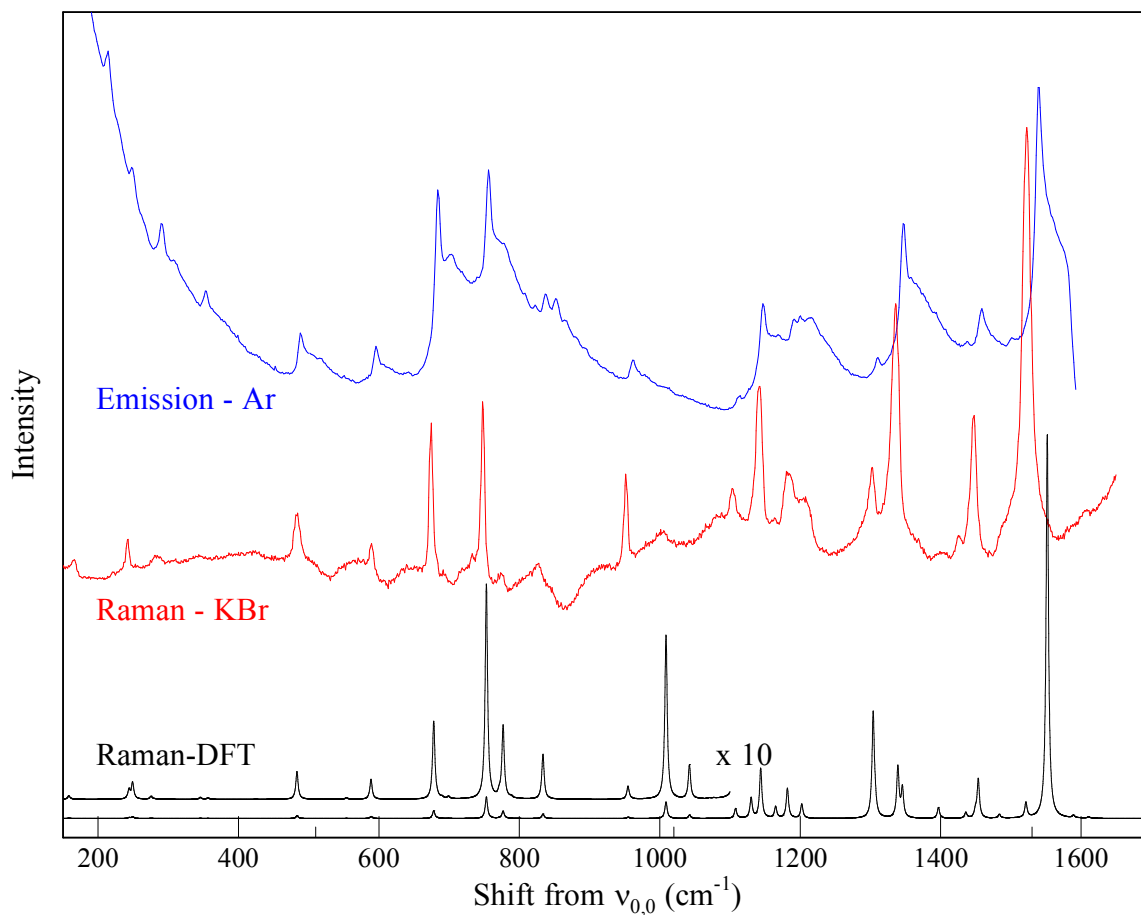


Figure V.51: Raman shifts of GaPcCl recorded in KBr (red trace) with a 660 nm CW laser excitation and predicted by DFT calculations (black trace) which have been scaled by a factor of 0.98. Emission recorded in Ar has been compared as the shift from the 0-0 transition.

Table V.12: Frequencies (in cm^{-1}) of the vibronic bands of GaPcCl present in emission for different matrices. The measured frequencies compare very well to ground state Raman energies. The symmetries come from the DFT results of the Raman vibrational modes presented in Chapter III. The same scaling factors used in Chapter III have been applied to DFT results here.

Emission				KBr	DFT	DFT	Sym
N ₂	Ar	Kr	Xe	Raman	x 0.98	Raw	
-	-	23	-	-	20	21	B ₂
62	-	52	73	-	51	52	B ₁
-	100	-	89	-	89	91	E
-	111	-	-	-	114	116	B ₁
129	143	128	-	-	129	132	B ₂
-	170	-	-	165	158	162	B ₂
-	214	227	-	221	215	220	B ₁
-	248	247	-	237	244	249	B ₁
288	290	289	-	285	275	281	A ₁
-	309	-	-	-	303	309	E
344	354	352	-	347	345	352	A ₁
478	488	488	500	484	483	493	B ₁
589	596	597	-	590	589	601	A ₁
676	684	684	688	674	678	692	A ₁
691	704	700	707	701	699	713	B ₂
749	756	756	760	748	753	768	B ₂
834	837	836	-	827	834	851	A ₁
-	853	849	847	-	879	897	E
954	961	960	966	951	955	974	B ₁
1139	1147	1147	1150	1140	1144	1167	B ₂
1188	-	1192	1217	1181	1182	1206	B ₂
-	1311	-	-	1302	1307	11334	B ₁
1339	1347	1347	1351	1335	1339	1366	A ₁
-	1394	-	-	1335	1346	1373	B ₂
1448	1459	1457	1438	1447	1454	1483	B ₂
1532	1540	1541	1547	1523	1552	1584	B ₂

Table V.13: Normal mode descriptions of the main vibronic bands in emission of GaPcCl. Mode descriptions have been derived from the vector diagrams of the vibrational modes from DFT calculations presented in Figure V.51. Correlations between the DFT frequencies and the experimental Raman and matrix emission bands can be seen in Table V.12.

DFT x 0.98	DFT Raw	Sym	Mode description
20	21	B ₂	Isoindole OOP twist
51	52	B ₁	Isoindole OOP twist
89	91	E	Isoindole OOP twist
114	116	B ₁	Isoindole IP twist
129	132	B ₂	Isoindole OOP twist
158	162	B ₂	Macrocycle breathing, Isoindole rocking
215	220	B ₁	Macrocycle OOP twist
244	249	B ₁	Macrocycle OOP twist
275	281	A ₁	Isoindole OOP twist, N-Ga-N bend
345	352	A ₁	N-Ga-N OPB, C _α -N _m -C _α OPB
483	493	B ₁	Macrocycle breathing
589	601	A ₁	Macrocycle breathing
678	692	A ₁	Macrocycle breathing
699	713	B ₂	Macrocycle OOP deformation, C-H OPB
753	768	B ₂	Macrocycle In-Plane Twisting
834	851	A ₁	Macrocycle breathing
879	897	E	C-H OPB
955	974	B ₁	Macrocycle breathing, Isoindole rocking
1144	1167	B ₂	C-H IPB
1182	1206	B ₂	C-H IPB, isoindole breathing
1339	1366	A ₁	Isoindole Breathing
1346	1373	B ₂	Isoindole Breathing
1454	1483	B ₂	C-H IPB
1552	1584	B ₂	C _α -N _m stretch

V.4.IV: Site Structure in Emission

The emission spectroscopy of GaPcCl produced with laser excitation can shed light on the site structure of the various matrices, as the narrow linewidth of the dye laser can selectively excite into an individual site. A good indication of the presence of multiple sites in the matrix is when the emission bands shift with respect to the laser excitation wavelength. A series of emission spectra of GaPcCl recorded with different excitation wavelengths in each matrix host are presented in Figure V.52 and Figure V.53. The left hand panel of Figure V.52 presents emission spectra of GaPcCl/Ar recorded with several excitation wavelengths between 670.3 and 661.3 nm. The red trace shows excitation at 670.3 nm, which is very close to the 0-0 band in absorption. This spectrum shows a single set of sharp emission bands extending up to 747 nm. The broad red shoulders on these

peaks most likely originate from emission from an aggregate species. Due to the single set of sharp bands, it is apparent that a single site dominates at this wavelength.

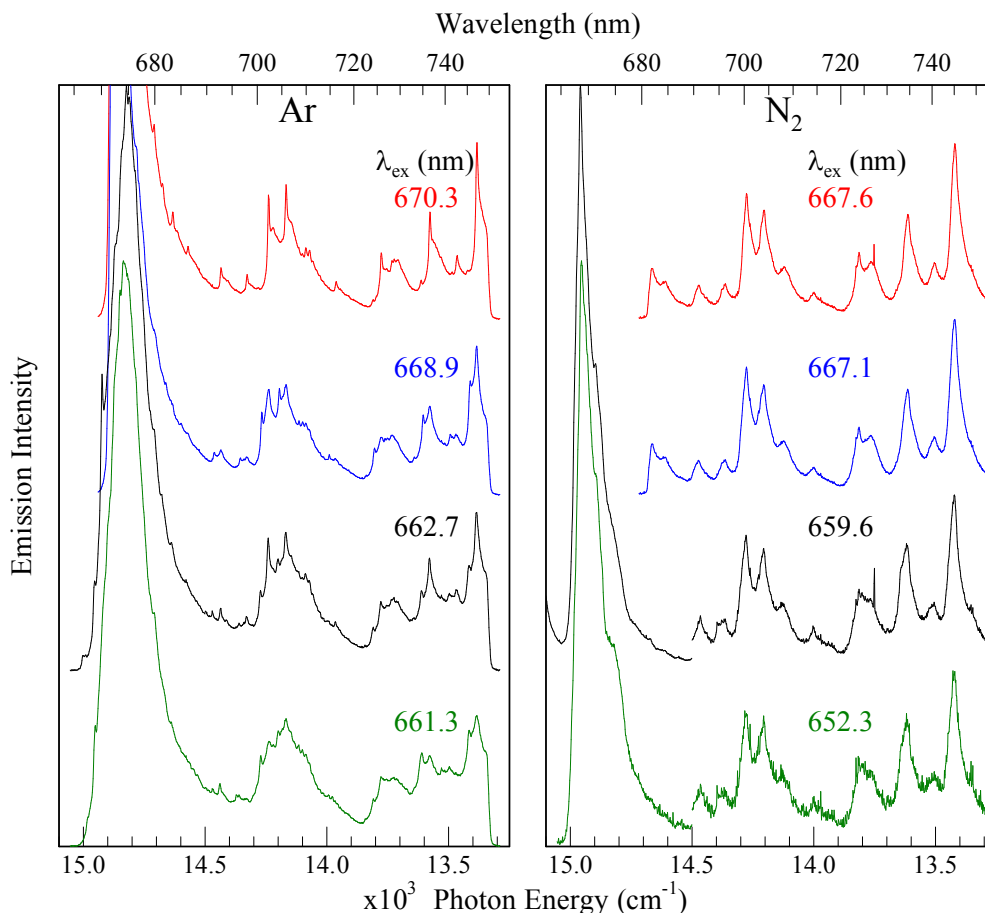


Figure V.52: The fluorescence of GaPcCl trapped in solid Ar (left panel) and N₂ (right panel) produced with a number of different excitation wavelengths. Ar matrices show a range of sites in emission whereas N₂ produces similar structure in emission regardless of excitation wavelength.

The blue trace shows excitation at 668.9 nm, which is slightly to the blue of the 0-0 transition. The same vibronic bands observed with excitation at 670.3 nm are present in the spectrum, as well as a duplicate set of bands to the blue. This indicates a second site has been excited. The splitting between the two sites is 26 cm⁻¹. The red shoulders present in the red trace are no longer as pronounced with the $\lambda_{\text{ex}} = 668.9$ nm, indicating this wavelength cannot excite the aggregate species. The black trace shows excitation even further to the blue, at 662.7 nm. This spectrum also shows signs of emission emerging from two sites, this time split by 32 cm⁻¹. The red bands are at identical wavelengths to those observed with excitation into the 0-0 band, with the blue bands originating from a

site to the blue of the red-most site in the matrix. The green trace presents the emission spectrum recorded with an excitation wavelength of 661.3 nm. A similar result is observed as with the other two excitations shown to the blue of the 0-0 transition. A set of emission bands emanating from the red site are evident as well as a duplicate set of bands from a blue site. The site splitting in this case was measured at 30 cm^{-1} . The fact that the splitting between the red and blue sites varies with respect to the excitation wavelength indicates that numerous sites exist in the matrix. This will be investigated in greater detail in a later chapter by employing 2D excitation-emission spectra in the region of the amplified emission bands.

The right hand panel of Figure V.52 presents emission spectra of GaPcCl/N₂ recorded with several excitation wavelengths between 667.6 and 652.3 nm. The red trace shows excitation at 667.6 nm, which is into the 0-0 band in absorption. Emission bands extend up to 745 nm, which correspond to the vibronic bands of the ground electronic state. A subtle asymmetry is observed on the emission bands, with a slight shoulder appearing to the red of the band maximum. This is indicative of emission from an aggregate species, similar to what was observed with excitation into the 0-0 band in Ar. The blue trace shows excitation at 667.1 nm, which into the 0-0 transition of a blue site absorption. This spectrum is almost indistinguishable from the red trace. The black trace was obtained with excitation at 659.6 nm, which is to the blue of the 0-0 transition. This spectrum is made up of the same emission bands observed in the previous two spectra, but the band shapes are slightly different. Shoulders to the blue of the band maxima are observed instead of to the red. This is indicative of the presence of another site of isolation in the matrix. Some bands almost show splitting into two distinct bands, as was observed in Ar, but are not resolved. A similar phenomenon is observed with the green trace ($\lambda_{\text{ex}} = 652.3 \text{ nm}$). The spectrum is noisier than any of the previous spectra shown, but clearly resembles the black trace most closely. The emission bands all have a blue shoulder, the sign of a second site of isolation. Unfortunately, even so far to the blue from the 0-0 band, the two sites cannot be resolved. Because the sites in N₂ are located too close together to be resolved with fluorescence they will be examined by looking for AE from the two sites in Chapter VI.

The emission bands in Ar matrices are considerably narrower (10 cm^{-1}) than those observed in N₂ (18 cm^{-1}). This is most likely due to the sites present in the respective matrices, with Ar containing many sites located sufficiently far apart to be resolved, and N₂ containing sites very close together in energy. Changing the excitation wavelength allows

emission from different sites to be observed in Ar matrices. In contrast, changing the excitation wavelength in N₂ matrices exhibits negligible changes on the emission spectra.

The emission data recorded with a range of different excitation wavelengths for GaPcCl/Kr are shown on the left panel of Figure V.53. The red trace was obtained by exciting close to the 0-0 band in absorption ($\lambda_{\text{ex}} = 675.6$ nm). A single set of sharp emission bands are observed up to 754 nm. Emission from an aggregate species is observed, which has manifested itself as red wings on the strong emission bands.

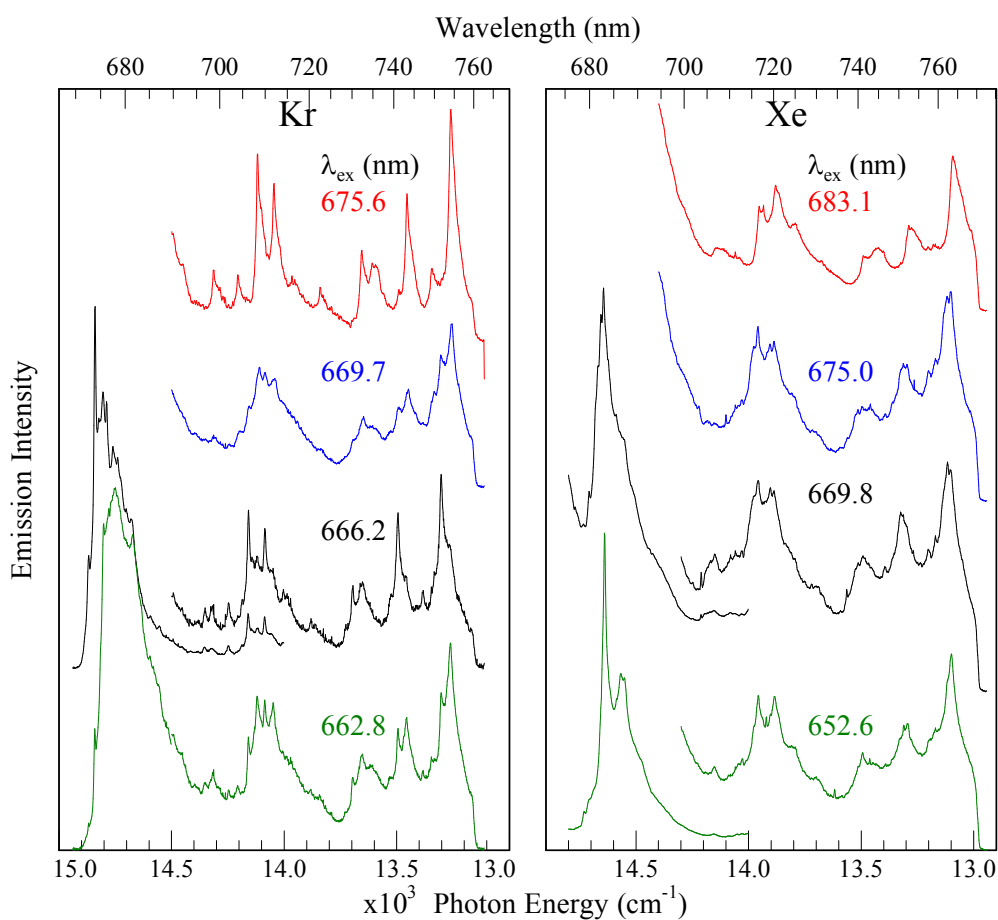


Figure V.53: The fluorescence of GaPcCl trapped in solid Kr (left panel) and Xe (right panel) recorded with a number of different excitation wavelengths.

The blue trace shows excitation to the blue of the 0-0 band, where $\lambda_{\text{ex}} = 669.7$ nm. A duplication of the emission bands is noted, with intense emission from the red site (identical to the emission bands shown by the red trace) and weaker emission bands located to the blue. The splitting between these two bands is rather large, approximately 50

cm^{-1} . The splitting is larger than anything observed in the Ar matrix. The black trace shows the excitation at 666.2 nm, where emission from the blue site dominates and emission from the red site appears weaker. This is due to an overlap between the excitation wavelength with a strong absorption band of the blue site and a weak absorption band of the red site. A number of weaker emission bands are also observed, which indicate more sites occupy the region between the red and blue sites. The green trace shows excitation at 662.8 nm; further to the blue of the 0-0 transition in absorption. The same splitting pattern is observed in this spectrum, with the red and blue sites separated by 50 cm^{-1} . The presence of weak shoulders to the blue of the emission bands of the red site indicate that there may be more sites present in this matrix that remain unresolved in fluorescence. This will be explored further by examining the sites capable of exhibiting amplified emission in a Chapter VI.

Emission spectra of GaPcCl/Xe recorded with a series of different excitation wavelengths are presented in the right panel of Figure V.53. The red trace shows excitation in the region of the 0-0 band in absorption, at 683.1 nm. The spectrum contains emission bands up to 763 nm, many of which show a red shoulder reminiscent to emission from aggregates in the other hosts. The emission bands in Xe are broader than in the other matrices owing to the number of sites within the host. The blue trace shows an excitation to the blue of the 0-0 band ($\lambda_{\text{ex}} = 675 \text{ nm}$). This excitation yields two sets of emission bands; one from a blue site which has been excited directly, and one from a red site, which was excited due to overlap between the emission from blue site and absorption of the red site. The emission bands from the two sites are split by 16.7 cm^{-1} . The black trace shows an excitation at 669.8 nm. A similar spectrum to the blue trace is observed, with emission bands originating from a pair of closely situated sites dominating the spectrum. The splitting between these two sites is 12.4 cm^{-1} . The green trace presents the emission spectrum of GaPcCl generated by exciting at 652.6 nm. This spectrum does not show two sets of resolved bands, but a single set of bands each with a blue wing. This indicates that two sites are again excited at this wavelength, but are very close together in energy. This is a trend which appears to be common in the Xe matrix regardless of the excitation energy. The largest splitting observed between the site furthest to the red and furthest to the blue was measured at 24.6 cm^{-1} . This is around half of the value measured for the largest splitting in Kr, and significantly smaller than in Ar also. Only N_2 , with negligible site splitting is smaller. The movement of the location of the emission bands in Xe with respect to the excitation wavelength suggests that the matrix contains many sites.

Emission spectroscopy has been used to probe the site occupancy of each matrix host. Ar and Xe appear to be filled with many sites. Kr matrices also contain several sites, but two of these sites dominate the emission spectra. N₂ forms at least two sites of isolation, but they are located so close in energy that they cannot be resolved with the current experimental setup. In order to further investigate the site structure of the matrices, emission from strongly absorbing samples capable of exhibiting AE will be analysed in Chapter VI.

V.5: Conclusions

The electronic spectroscopy of GaPcCl was studied in four inert gas hosts – namely N₂, Ar, Kr and Xe – at cryogenic temperatures as well as in an ethanol solution at room temperature. The origins of the Q bands were identified in absorption for each host and the main vibronic bands in absorption were also documented. The 0-0 transition shifts depending on the host environment, with the lighter matrix hosts having a higher energy band origin than the heavier hosts. The band origins of the Q ← G electronic transitions in absorption are 14959, 14916, 14806 and 14680 cm⁻¹ in N₂, Ar, Kr and Xe respectively. Vibronic bands extend up to ~1650 cm⁻¹ in each host, with weaker combination bands extending up to around 3000 cm⁻¹ (as shown in Table V.9). The B band was located around 352 – 354 nm in each host matrix. A series of weak transitions to the red of the B band were observed between 400 – 450 nm which may be weak electronic transitions of GaPcCl. This assignment is supported by TD-DFT calculations, which also predicts a number of weak transitions located slightly to the red of the B bands.

Emission was recorded in each of the matrix hosts and fluorescence bands were observed up to 740 – 760 nm depending on the host. Tuning the excitation wavelength allowed for selective excitation of individual sites which manifests as a constant energy shift on the location of the fluorescence bands. In many cases emission from the site being excited as well as emission from a dominant red site (obtained with excitation into the 0-0 band) was observed on the same spectrum. This is due to good overlap between the ZPL of a blue site being directly excited into and the PSB of a site located to the red of this. The decay profiles of the emission bands were investigated and a wavelength dependence on the decay time was noted in Ar, Kr and N₂. Short wavelength emission bands in Ar and N₂ matrices exhibited the longest decay times, whereas longer wavelength emission bands

showed the shortest decay times. The opposite effect was observed in Kr matrices. No such wavelength dependence was seen in Xe matrices. The fluorescence lifetimes of a common vibronic band was measured in each host and found to be between 2.3 – 2.6 ns; an appropriate timescale for such a strongly absorbing dye molecule.

The vibronic bands in absorption, emission and excitation were found to be very similar, indicating the structures of the ground and excited electronic states do not differ significantly. A vibrational analysis of the emission bands could thus be performed by making a comparison with the vibronic bands observed in emission with the ground state Raman bands owing to the similar set of selection rules that govern both sets of transitions. The strongest emission bands coincide with Raman active modes of A_1 or B_2 symmetry, usually involving in-plane motion of the macrocycle. Weaker B_2 and E modes are also evident in both the emission and Raman spectra.

Excitation spectra tend to show a fairly sharp 0-0 band corresponding to the ZPL. Vibronic bands in excitation were recorded up to $\sim 1000\text{ cm}^{-1}$ beyond the band origin. This region was limited by the tuning range of the dye used (as shown in Chapter II). Good overlap between the ZPL of a blue site and the PSB of a red site allowed for more than one set of emission bands to occupy a given spectrum and allowed for the observation that there were many sites present in the rare gas matrices.

Amplified emission was a feature consistently observed for samples with large optical densities (> 2.5). This phenomenon was observed in each of the hosts used in the current study and was often noted to have occurred from many sites in a given sample. A single vibronic band, located $\sim 1540\text{ cm}^{-1}$ from the band origin (in Ar), was determined to be responsible for the effect. The AE bands are shorter lived than their fluorescence counterparts and show spectral narrowing of their linewidths – both characteristics determined by the excitation laser. The narrow linewidths will be taken advantage of in the upcoming Chapter, which will analyse the site structure in each matrix by looking at the high resolution emission and excitation spectra in the region of the AE bands.

The choice of host material can have a significant effect on the spectroscopy of GaPcCl, affecting properties such as the band origin of the electronic transition, the linewidth of emission bands, the number of sites present and how easily it can exhibit stimulated emission. Ar and Kr matrices tend to give the simplest fluorescence spectra with sharp bands and clear site structure evident. N_2 and Ar matrices were excellent host materials for

observing amplified emission and this was also used to study the sites present in these matrices. It was more difficult to prepare samples of GaPcCl in Kr and Xe that were capable of exhibiting AE, but it was achieved nonetheless.

V.6: References

1. Wei, T.-H.; Huang, T.-H.; Lin, M.-S., Signs of nonlinear refraction in chloroaluminum phthalocyanine solution. *Applied Physics Letters* **1998**, *72* (20), 2505-2507.
2. Sorokin, P. P.; Lankard, J. R., Stimulated emission observed from an organic dye, chloro-aluminum phthalocyanine. *IBM Journal of Research and Development* **1966**, *10* (2), 162-163.
3. Gouterman, M.; Wagniere, G.; Snyder, L. C., Spectra of porphyrins. II. Four-orbital model. *Journal of Molecular Spectroscopy* **1963**, *11* (2), 108-27.
4. Bajema, L.; Gouterman, M.; Meyer, B., Spectra of porphyrins: XI. Absorption and fluorescence spectra of matrix isolated phthalocyanines. *Journal of Molecular Spectroscopy* **1968**, *27* (1-4), 225-235.
5. Murray, C.; Dozova, N.; McCaffrey, J. G.; Shafizadeh, N.; Chin, W.; Broquier, M.; Crepin, C., Visible luminescence spectroscopy of free-base and zinc phthalocyanines isolated in cryogenic matrices. *Physical Chemistry Chemical Physics* **2011**, *13* (39), 17543-17554.
6. Verhoeven, J. W., Glossary of terms used in photochemistry (IUPAC Recommendations 1996). In *Pure and Applied Chemistry*, 1996; Vol. 68, p 2223.
7. Aroca, R.; Jennings, C.; Loutfy, R. O.; Hor, A.-M., Raman spectra of thin solid films—VI. Davydov splitting. *Spectrochimica Acta Part A: Molecular Spectroscopy* **1987**, *43* (6), 725-730.
8. Bursa, B.; Wróbel, D.; Biadasz, A.; Kędzierski, K.; Lewandowska, K.; Graja, A.; Szybowicz, M.; Durmuş, M., Indium–chlorine and gallium–chlorine tetrasubstituted phthalocyanines in a bulk system, Langmuir monolayers and Langmuir–Blodgett

nanolayers – Spectroscopic investigations. *Spectrochimica Acta Part A: Molecular and Biomolecular Spectroscopy* **2014**, *128*, 489-496.

9. Basova, T. V.; Kiselev, V. G.; Latteyer, F.; Peisert, H.; Chassé, T., Molecular organization in the thin films of gallium(III) phthalocyanine chloride and its μ -(oxo)dimer: Optical spectroscopy and XPS study. *Applied Surface Science* **2014**, *322*, 242-248.

10. Linsen, P.; Jie, Z.; Wei, K., Electronic polarization spectroscopy of metal phthalocyanine chloride compounds in superfluid helium droplets. *Journal of Chemical Physics* **2007**, *127* (17), 174308.

11. Caño, T. D.; de Saja, J. A.; Aroca, R., Emission enhancement in chlorogallium phthalocyanine-N,N'-bis(neopentyl)-3,4,9,10-perylenebis(dicarboximide) mixed films. *Thin Solid Films* **2003**, *425* (1-2), 292-296.

12. Del Cano, T.; Parra, V.; Rodriguez-Mendez, M. L.; Aroca, R. F.; De Saja, J. A., Characterization of evaporated trivalent and tetravalent phthalocyanines thin films: different degree of organization. *Applied Surface Science* **2005**, *246* (4), 327-333.

13. Leng, W.; Myers Kelley, A., Resonance Hyper-Raman Spectra of Zinc Phthalocyanine. *The Journal of Physical Chemistry A* **2008**, *112* (26), 5925-5929.

14. Strickler, S. J.; Berg, R. A., Relationship between Absorption Intensity and Fluorescence Lifetime of Molecules. *The Journal of chemical physics* **1962**, *37* (4), 814-822.

15. Shibuya, T., A dielectric model for the solvent effect on the intensity of light absorption. *Journal of Chemical Physics*. **1983**, *78* (8), 5175-82.

V.7: Appendix

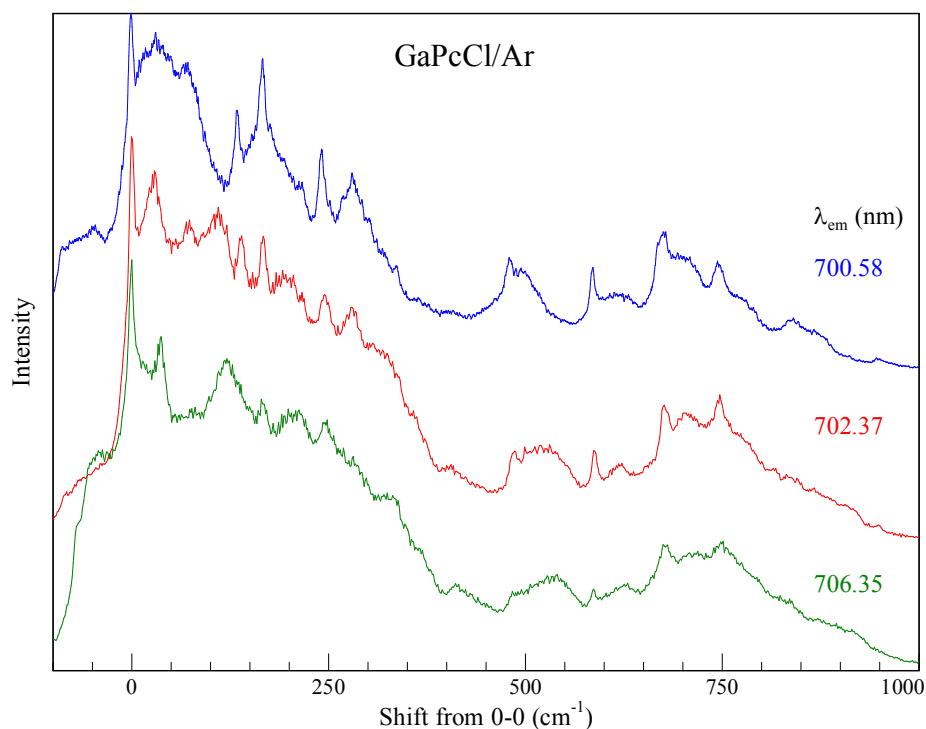


Figure V.A1: Laser excitation spectra of GaPcCl recorded in Ar plotted as the shift from the 0-0 band in excitation. The emission bands monitored were located at 700.58, 702.37 and 706.35 nm and correspond to slices through vibronic bands from different sites.

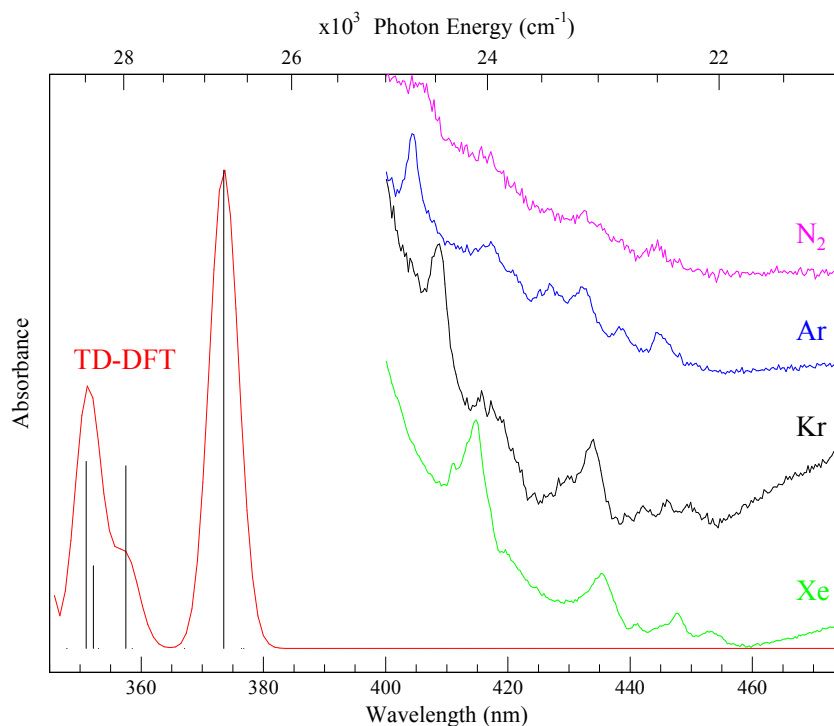


Figure V.A2: Absorption spectra of GaPcCl isolated in inert gas matrices in the region between the Q and B bands. The predictions made by TD-DFT calculations are also shown for comparison.

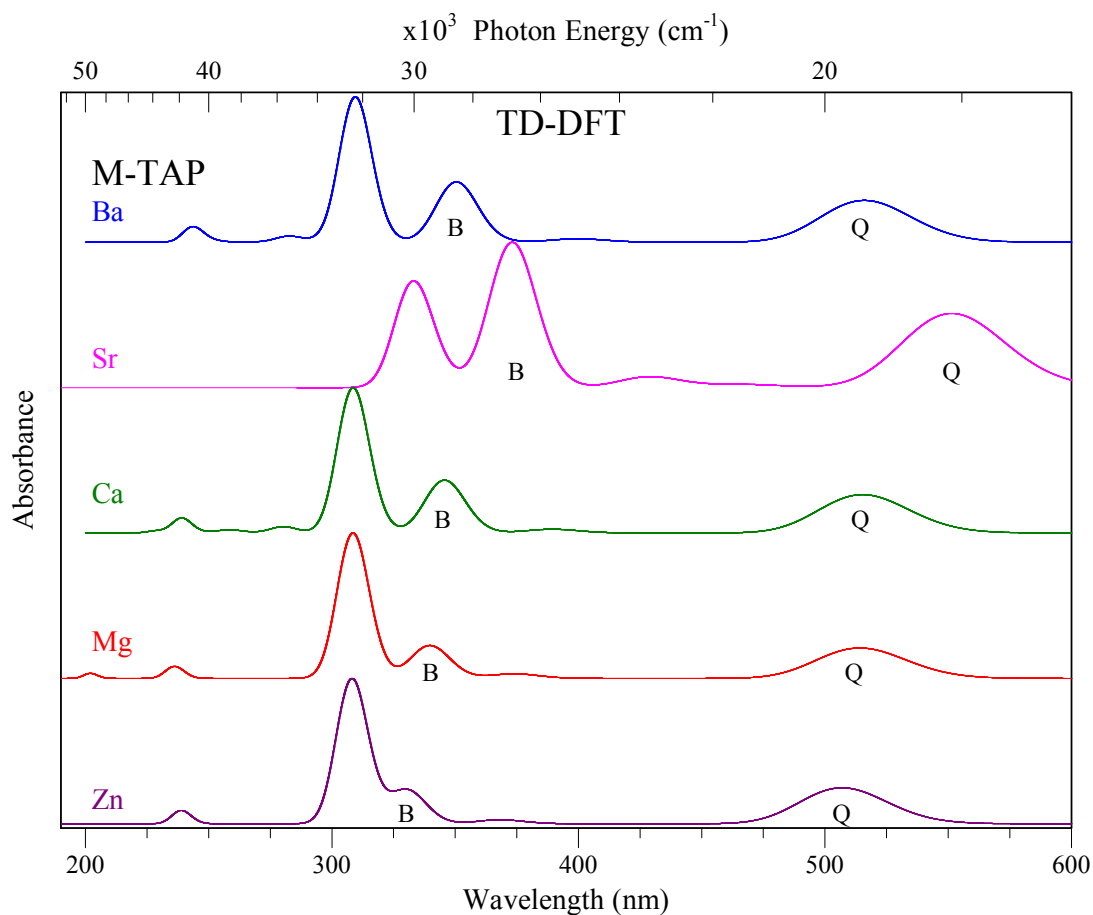


Figure V.A3: Electronic absorption spectra of selected M-TAPs predicted by TD-DFT calculations. In all instances, the Q and B bands have the greatest intensity. Weaker bands located between these well-known transitions are evident in each spectrum.

Table V.A1: Time Dependent DFT results for the first 50 singlet excited states of GaPcCl. The MO contributions of the Q and B bands are shown in Figure V.A4 and Figure V.A5 respectively.

Excited state	Sym	Energy (eV)	Wavelength (nm)	Oscillator strength
1	Singlet-E	1.9935	621.95	f=0.3915
2	Singlet-E	1.9935	621.95	f=0.3915
3	Singlet-E	3.2905	376.8	f=0.0000
4	Singlet-E	3.2938	376.42	f=0.0000
5	Singlet-E	3.3193	373.52	f=0.0110
6	Singlet-E	3.3193	373.52	f=0.0110
7	Singlet-E	3.3775	367.09	f=0.0000
8	Singlet-B2	3.458	358.54	f=0.0000
9	Singlet-E	3.4681	357.5	f=0.0042
10	Singlet-B1	3.5122	353.01	f=0.0000
11	Singlet-E	3.5206	352.17	f=0.0019
12	Singlet-E	3.5206	352.17	f=0.0019
13	Singlet-E	3.5323	351.01	f=0.0043
14	Singlet-E	3.5323	351.01	f=0.0043
15	Singlet-E	3.5644	347.84	f=0.0000
16	Singlet-E	3.6525	339.45	f=0.0033
17	Singlet-E	3.658	338.94	f=0.3802
18	Singlet-E	3.658	338.94	f=0.3802
19	Singlet-A2	3.6719	337.66	f=0.0000
20	Singlet-E	3.6829	336.64	f=0.3036
21	Singlet-E	3.6829	336.64	f=0.3036
22	Singlet-E	3.6832	336.62	f=0.0000
23	Singlet-E	3.7229	333.03	f=0.0000
24	Singlet-E	3.7627	329.51	f=0.0000
25	Singlet-E	3.7676	329.08	f=0.0000
26	Singlet-E	3.7865	327.44	f=0.2486
27	Singlet-E	3.7865	327.44	f=0.2486
28	Singlet-E	3.8025	326.06	f=0.0000
29	Singlet-E	3.8498	322.05	f=0.0033
30	Singlet-E	3.9838	311.22	f=0.0000
31	Singlet-E	3.9876	310.93	f=0.0000
32	Singlet-E	4.0194	308.46	f=0.0000
33	Singlet-E	4.023	308.19	f=0.0004
34	Singlet-E	4.2318	292.98	f=0.1009
35	Singlet-E	4.2318	292.98	f=0.1009
36	Singlet-E	4.3613	284.29	f=0.0042
37	Singlet-E	4.3613	284.29	f=0.0042
38	Singlet-A2	4.5562	272.12	f=0.0000
39	Singlet-E	4.697	263.97	f=0.0062
40	Singlet-E	4.697	263.97	f=0.0062
41	Singlet-E	4.7571	260.63	f=0.0000
42	Singlet-E	4.7571	260.63	f=0.0000
43	Singlet-B1	4.9778	249.07	f=0.0000
44	Singlet-E	5.0033	247.81	f=0.0018
45	Singlet-E	5.0033	247.81	f=0.0018
46	Singlet-A1	5.0132	247.31	f=0.0001
47	Singlet-A2	5.0226	246.85	f=0.0000
48	Singlet-B2	5.1299	241.69	f=0.0000
49	Singlet-A2	5.141	241.17	f=0.0000
50	Singlet-E	5.1621	240.18	f=0.0005

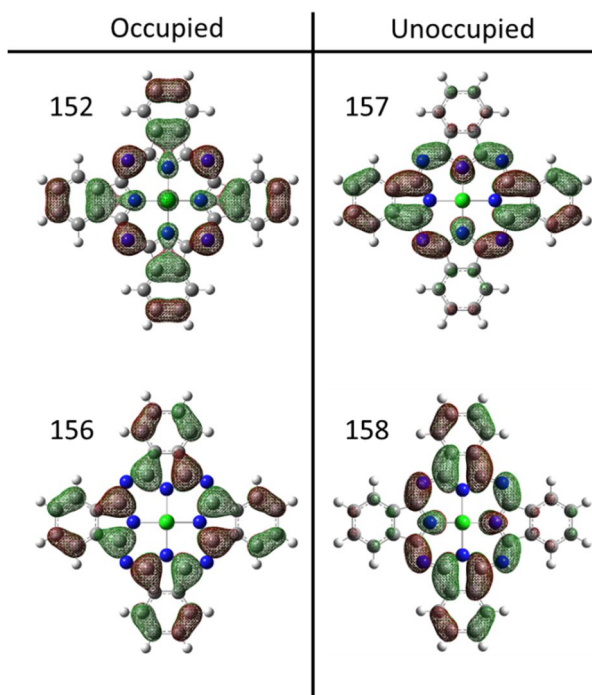


Figure V.A4: Molecular orbitals involved with the $Q \leftarrow G$ electronic transition predicted by TD-DFT calculations. TD-DFT predicts the transition energy to be 621.95 nm. The MO # of each orbital is given.

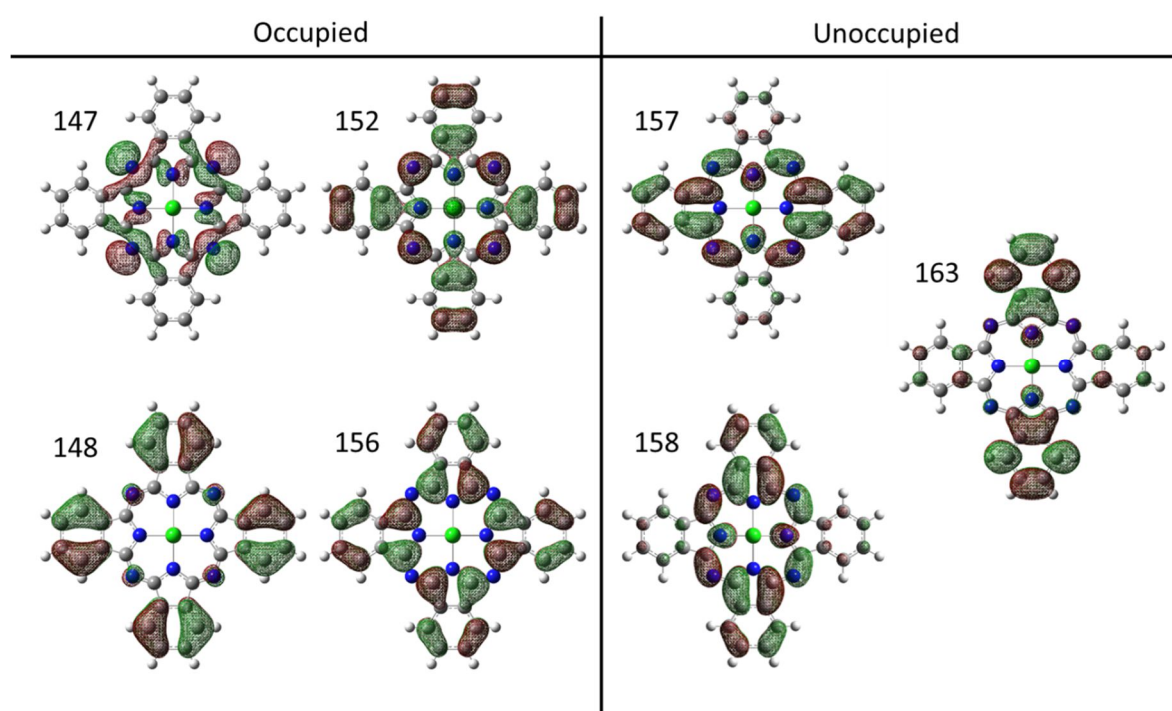


Figure V.A5: Molecular orbitals involved with the $B \leftarrow G$ electronic transition predicted by TD-DFT calculations. TD-DFT predicts the transition energy to be 338.94 nm. The MO # of each orbital is given.

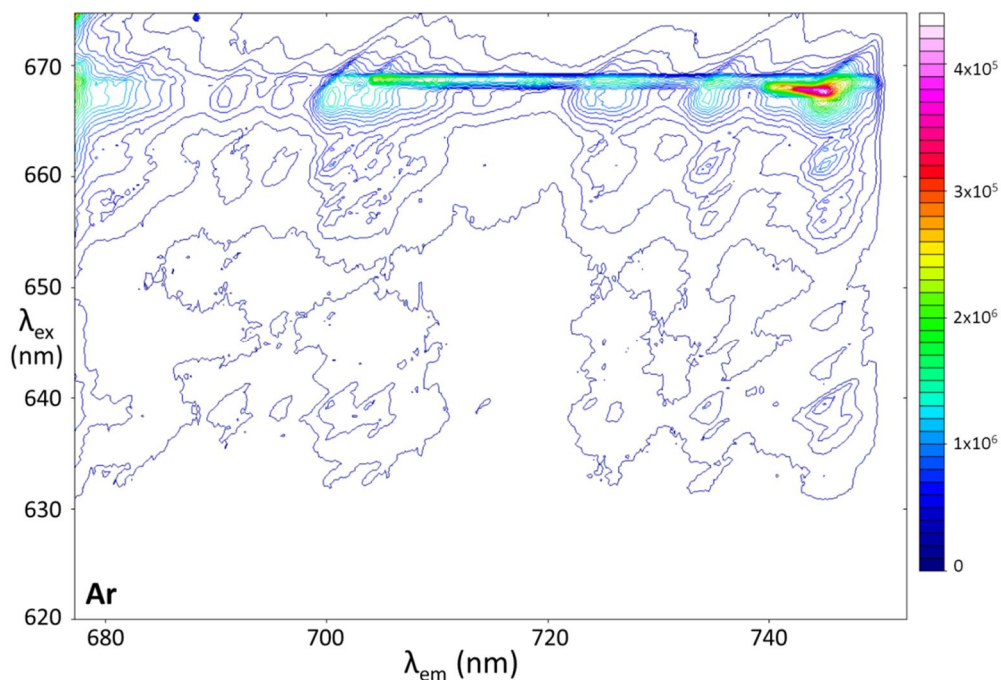


Figure V.A6: Example of a 2D Excitation-Emission scan of GaPcCl/Ar. Emission and excitation ‘slices’ were extracted from files such as this for presentation in the present chapter.

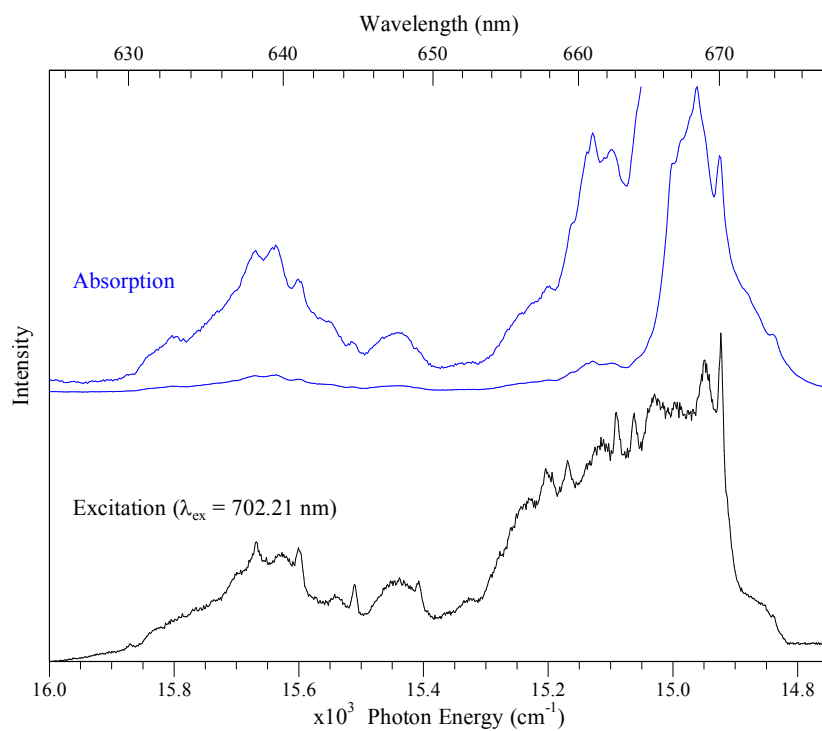


Figure V.A7: Comparison of the absorption and excitation spectra of GaPcCl/Ar.

Chapter VI: Amplified Emission of GaPcCl Isolated in Inert Gas Matrices

VI.1: Introduction

This chapter develops the results presented in Chapter V for GaPcCl isolated in inert gas matrices, where the molecule was shown to exhibit amplified emission (AE). The vibrational mode responsible for AE is identified using DFT calculations, by comparing the amplified band to the vibronic bands observed in emission spectra presented in Chapter V. The site splitting of each matrix host is probed by employing 2D excitation-emission (2D-EE) plots in the region of the AE bands. Emission and excitation ‘slices’ of the 2D-EE plots are extracted to highlight the main spectral features within a given matrix sample. A comparison of the different matrix hosts is provided by concentrating on the emission spectra. The results of annealing the matrix are also presented, with an emphasis given to the Ar system, where the most significant effects were observed. The phonon structure of GaPcCl/Ar is investigated with the so-called Wp lineshape function.

VI.2: Experimental

Matrix-isolation experiments were conducted in the Low Temperature Laboratory at Maynooth University, using the apparatus described in Chapter II. Matrix samples were prepared in a variety of hosts which included the molecular gas N₂ and the rare gases Ar, Kr and Xe. From the absorption data presented in Chapter V, it was determined that the minimum optical density (OD) a sample required in order to exhibit AE was in excess of 2.5. All data presented in this chapter was recorded using a pulsed dye laser for excitation and the time-gated iCCD Camera for detection. Unless otherwise stated, the high resolution 1200 grooves/mm grating installed in the SP-500i monochromator was used for the recording of spectra.

VI.3: Results

The phenomenon of amplified emission was, as indicated in Chapter V, observed for GaPcCl isolated in each of the matrices examined in the present study. A summary of the AE spectra recorded in the four inert gas hosts is shown in Figure VI.1. A vibronic band, located in the range of 1532 – 1547 cm^{-1} (depending on the host) from the 0-0 in emission is observed to exhibit amplified emission. Table VI.1 gives the location of this vibronic band in each host, as well as the recorded Raman and predicted DFT Raman values. For ease of discussion, the frequency of this mode in Ar (1540 cm^{-1}) will be used from this point onwards when referring to the AE vibrational mode. The left panel of Figure VI.1 demonstrates the striking enhancement in the intensity of the vibronic band at 1540 cm^{-1} when it undergoes AE compared to fluorescence. In Ar samples the emission band at 747.16 nm achieves a 20-fold increase in intensity with the increased laser excitation energy. In contrast, the emission band at 736.66 nm is only 1.1 times more intense with the increased laser energy. A similar phenomenon is observed in the other matrices, although the extent of the intensity change is variable and is highly dependent on the laser intensity, sample concentrations and site occupancies.

Table VI.1: Vibrational frequencies of the vibronic band of GaPcCl in emission associated with AE for each host material. The values reported in the matrices have been extracted from the red-most site. The KBr and DFT Raman results are shown for comparison.

Host Material	Frequency (cm^{-1})
Ar	1540
Kr	1541
Xe	1547
N ₂	1532
Raman (KBr)	1523
Raman (DFT x 0.98)	1552

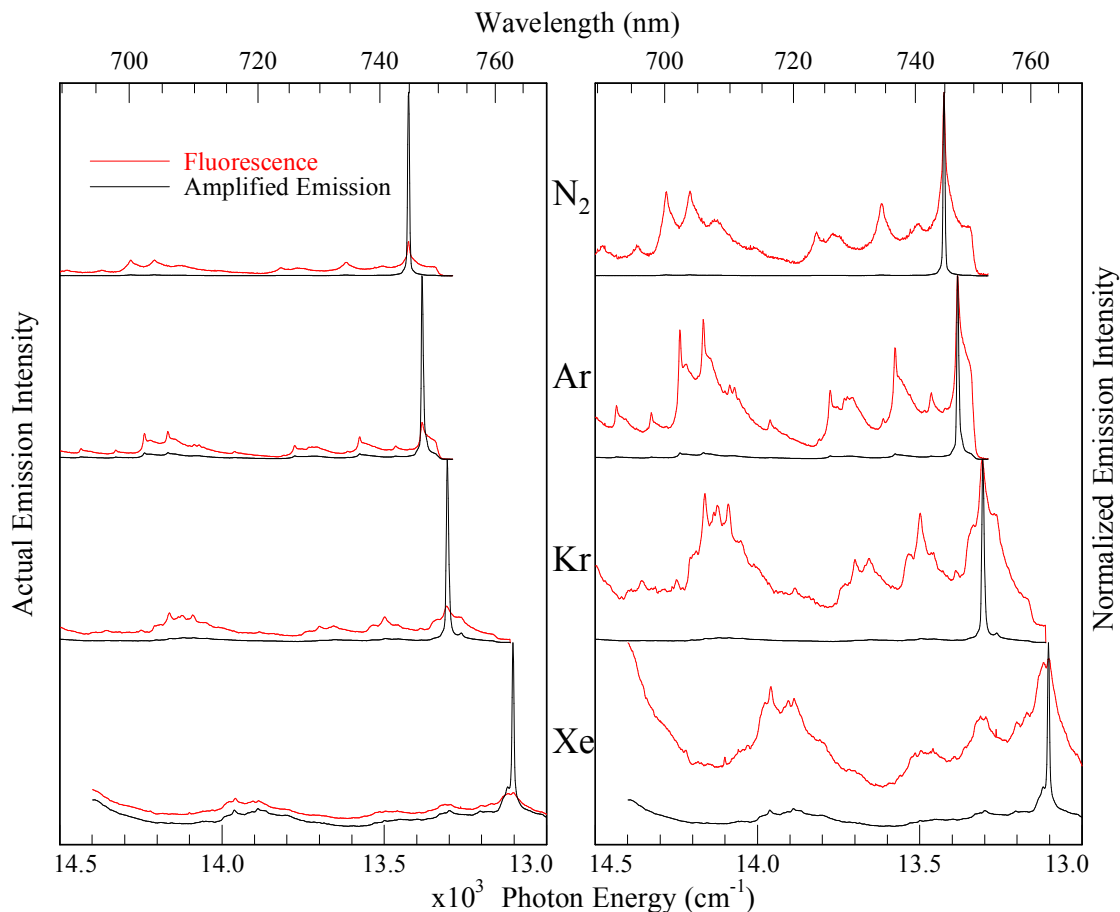


Figure VI.1: Fluorescence (red trace) and amplified emission (black trace) of GaPcCl recorded in N₂, Ar, Kr and Xe at 10 K. The left panes show the increased intensity of the vibronic band at ~ 1540 cm⁻¹ in the AE spectrum compared to the fluorescence. The right panel shows the normalized plots and clearly demonstrates the narrowness of the AE bands compared to those of the fluorescence bands.

The right hand side panel of Figure VI.1 shows normalized plots of spectra exhibiting fluorescence and amplified emission recorded in each matrix. These spectra clearly demonstrate the narrow linewidths of the AE bands compared to those of the fluorescence bands. This characteristic will be exploited in the present chapter to gain additional information on the features present in the host solids. Although the actual wavelength position of the AE band shifts depending on its environment, it is always the same vibronic transition that is responsible for the effect – the vibrational mode around 1540 cm⁻¹. Figure VI.2 shows the amplified emission of GaPcCl recorded in the various matrices plotted as their shift from the band origin. When plotted in this manner it is clear that the same vibrational mode is associated with amplified emission in each matrix. In a similar manner to Figure V.44, the emission bands shown in Figure VI.2 (dashed lines) in each matrix also

show excellent agreement, exactly what is expected given the results presented in Table V.12. Due to the same vibrational mode being responsible for AE in every matrix, it is possible to use this phenomenon to analyse the different sites occupied in each host. This will be presented ahead in Section V.4.VI, where 2D-EE plots will be used to characterise the site splitting.

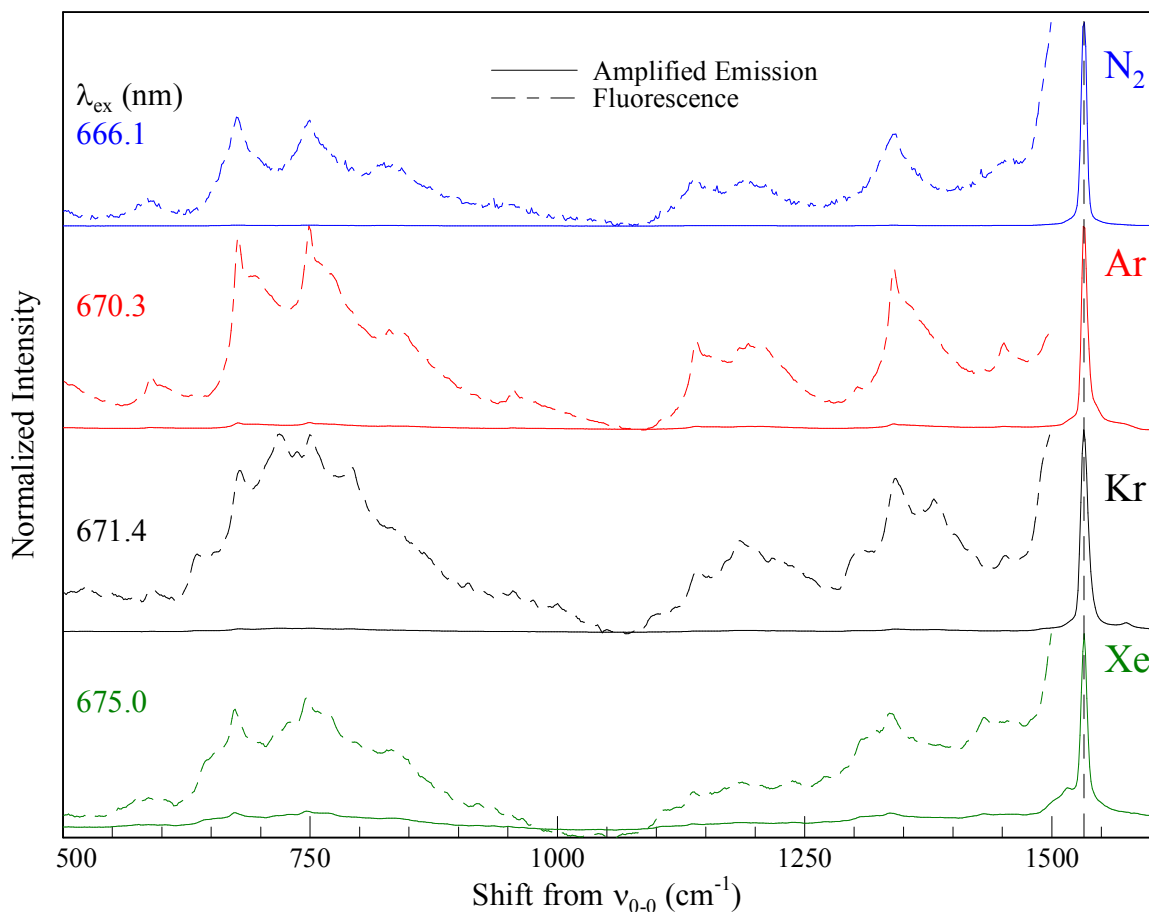


Figure VI.2: Amplified emission of GaPcCl (solid trace) recorded in N₂, Ar, Kr and Xe at 10 K plotted as their shift from the band origin (ν_{0-0}). The normalized emission (dashed trace) from the same scan is also presented to show that there is also good agreement for the vibronic bands in each matrix. The dashed vertical line highlights the location of 1540 cm⁻¹ on the scale.

The dependence of the intensity of the amplified emission was investigated by varying the laser energy and monitoring the effect it had on the intensity of a fluorescence band and the AE band, the results of which are shown in Figure VI.3. This was achieved by keeping the wavelength of the dye laser constant and changing its energy. As described in Chapter V, the dye laser was operated under two conditions; the first used only the oscillator, which

has a typical output of ~ 10 $\mu\text{J}/\text{pulse}$, while in the second the pre-amplifier was used which has an energy of ~ 100 $\mu\text{J}/\text{pulse}$. Generally only fluorescence was observed with the oscillator. The energy of the pre-amplifier beam hitting the matrix window was reduced by placing neutral density filters in the path of the beam. The intensity of the laser beam was measured at the sample window prior to an emission spectrum being recorded. The data shown in Figure VI.3 is for the dominant site in emission at 747.2 nm for GaPcCl/Ar, produced with excitation at 670.3 nm. The band exhibiting amplification at 747.2 nm is represented by the red triangles. For comparison, normal fluorescence from a nearby vibronic band at 736.7 nm is also shown in Figure VI.3, which is not amplified with the increase in laser pulse energy.

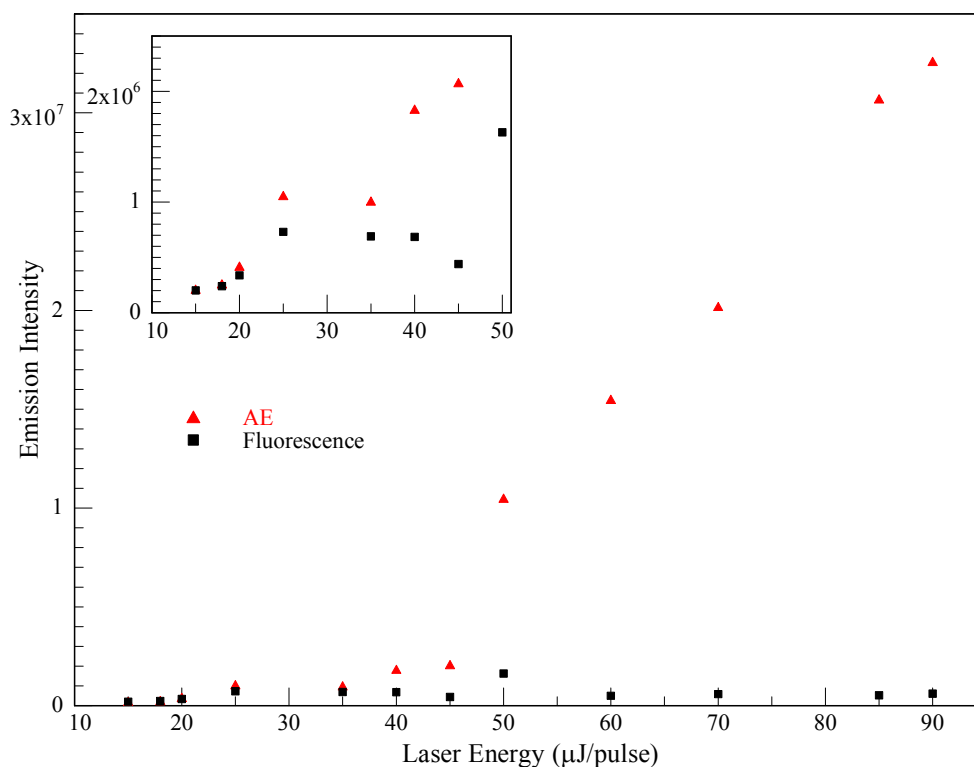


Figure VI.3: The dependence of the amplified emission intensity of GaPcCl in Ar with respect to the excitation laser energy. The red triangles show how the intensity of band at 747.2 nm increases dramatically as the laser energy increases from 10 $\mu\text{J}/\text{pulse}$ to 100 $\mu\text{J}/\text{pulse}$. The black squares show how a regular fluorescence band at 736.7 nm is not significantly affected by the increasing the laser intensity. The inset shows up to laser energies of around 50 $\mu\text{J}/\text{pulse}$. On this scale it can be seen that only a small difference manifests between the intensity of the fluorescence and the AE bands when low laser energies are used.

At lower excitation laser energies ($< 20 \mu\text{J/pulse}$) the intensity of the two bands being monitored is almost identical on the scale shown. As the intensity increases up to around $45 \mu\text{J/pulse}$ it is evident that there is a slightly higher intensity associated with the AE band. When the energy of the laser is increased above $50 \mu\text{J/pulse}$ the intensity of the band at 747.2 nm is greatly enhanced compared to the band at 736.7 nm . At this energy stimulated emission has been 'switched on', having reached a certain threshold value. As the laser energy is increased even further, the AE band gains more and more intensity until the iCCD becomes saturated at laser energies above $90 \mu\text{J/pulse}$.

Excitation scans of the AE vibronic band of GaPcCl were recorded in the same manner as the excitation spectra of the fluorescence bands shown in Chapter V. The excitation spectra of the dominant site in each matrix are presented in Figure VI.4 as their shift from the band origin. The excitation spectra recorded of the AE bands are far more resolved than those recorded of the same fluorescence bands. Spectra recorded in Ar and Kr each contain a sharp band corresponding to the zero phonon line (ZPL) of GaPcCl which has been identified with the dashed line in Figure VI.4. Ar shows the most resolved ZPL, which can be easily identified for a number of different sites. This will be discussed in more detail in Section VI.4.II. The ZPL is noticeably weaker in Kr, and is difficult to identify in Xe and N_2 . A weaker PSB band is present to the blue of the ZPL in Ar, but cannot be identified in the other matrices. A much broader band is evident in Ar and Kr hosts up to around 50 cm^{-1} , and out to 100 cm^{-1} in N_2 and Xe. These features are too broad to be considered vibronic bands, so may originate from a different species in the matrix, possibly an aggregate.

Vibronic bands in excitation are observed in each matrix from 100 cm^{-1} and are quite similar up to 750 cm^{-1} . The most resolved bands are observed in Ar, which is due to the massive intensity of the AE bands. These bands also have the narrowest linewidths of any recorded in the rare gas matrices in the current study. The positions of the bands in Kr and Xe are in good agreement with Ar. GaPcCl/ N_2 shows different excitation spectra for the AE bands with broad, unstructured profiles extending up to 750 cm^{-1} . While the positions of the broad vibronic bands in N_2 roughly match those observed in the rare gas matrices, they are not sufficiently resolved to make a proper comparison. The positions of the vibronic bands in excitation are given in Table VI.2. The high resolution excitation spectra recorded for the AE bands of GaPcCl allow for highly accurate positions of the vibronic bands to be extracted, as their absolute shift from the ZPL can be easily determined. As

such, the values in Table VI.2 are given to more significant figures than the corresponding numbers in Table V.10.

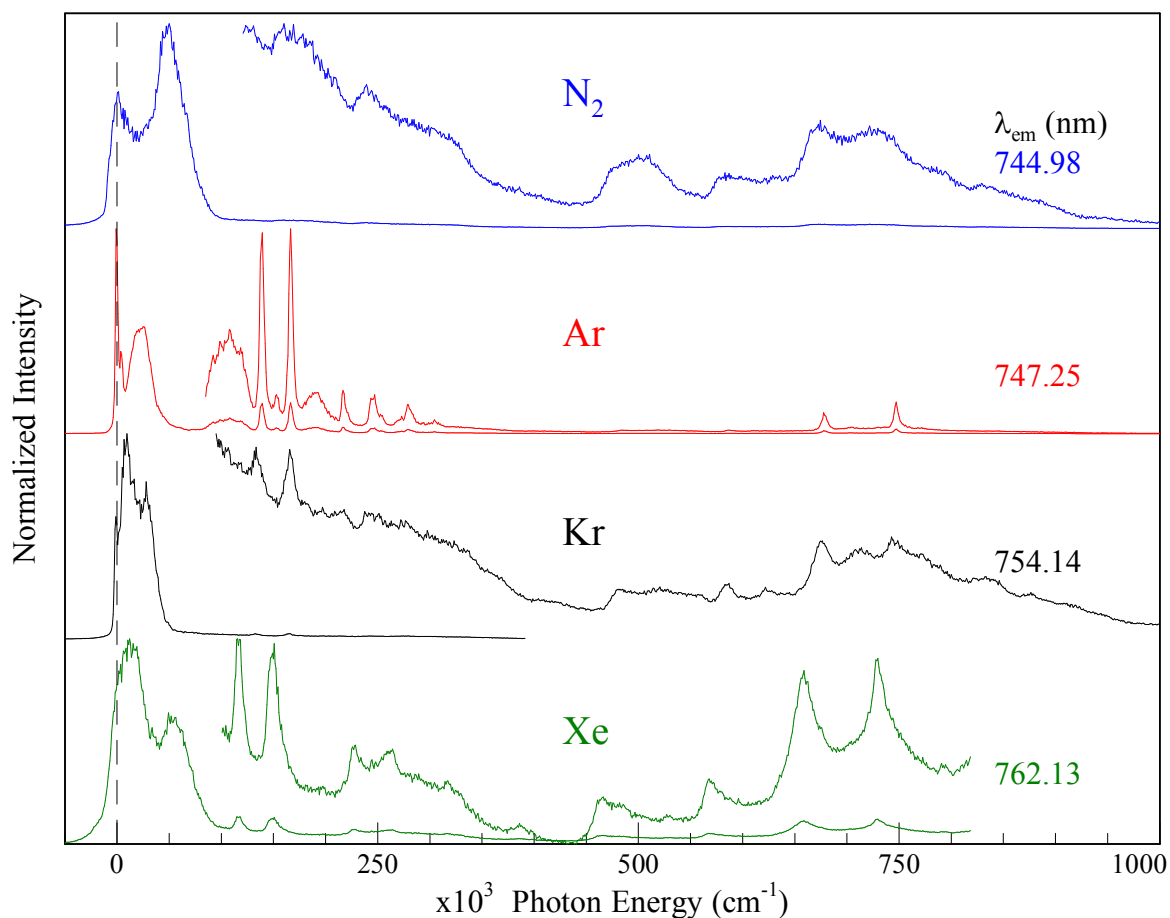


Figure VI.4: Excitation spectra of the amplified emission band of GaPcCl isolated in various matrices. The dashed vertical line represents the location of the ZPL in each host.

The vibronic bands in excitation are consistent for all sites in the matrix. To demonstrate this, a series of excitation spectra of GaPcCl/Ar are shown in Figure VI.A5 as their shift from ν_{0-0} in excitation. It is evident from this plot that the vibronic bands are common to all of the excitation spectra extracted at the given emission wavelengths. The main difference between spectra shown in this figure is the broad band below 50 cm^{-1} , which will be discussed in detail in Section VI.4.II.a. While only the Ar results have been presented, the same argument is valid for the excitation spectra recorded in the other matrices in the current work.

Table VI.2: Vibronic bands in observed in the excitation spectra recorded for the AE band of GaPcCl in various hosts. All values are given in cm^{-1} and have been taken as their shift from the 0-0 band in excitation.

N₂	Ar	Kr	Xe
-	4.45	6.13	6.91
-	-	17.55	17.27
26.97	26.76	28.99	31.99
48.62	-	49.26	47.60
-	109.43	-	114.77
158.71	140.21	133.57	149.02
-	167.48	165.77	-
-	191	198.11	195
-	217.73	218.85	-
237.01	246.19	238.74	225.12
-	279.39	277.21	262.56
-	305.01	-	315.49
-	-	-	384.21
498.87	-	482.49	464.58
-	-	-	525.43
583.65	586.73	587.91	566.26
-	-	623.05	-
673.28	678.65	676.55	658.00
725.39	-	714.99	728.01
791.75	748.05	743.94	790.03

From the data presented in Figure VI.4 it is clear that the sharpest ZPL and vibronic bands in excitation occur in the Ar matrix. A lineshape analysis of the emission and excitation spectra of the site furthest to the red of GaPcCl/Ar is presented in Figure VI.5. The regions where these emission/excitation spectra were extracted are shown in the 2D-EE plot shown in Figure VI.A2. This site was chosen because it is known from Chapter V to yield the simplest emission spectrum. Furthermore, being the most red site enables only a single site to be excited, which allows for the true structure of the bands in emission and excitation to be recorded.

Both spectra show a sharp and intense band which corresponds to the ZPL, as well as some weaker bands. A Wp line fit was performed on both the excitation and emission bandshapes. The position of the band origin ($\nu_{0,0}$), or ZPL in this case, was located at 14918 and 13384 cm^{-1} in excitation and emission respectively. The gap between the ZPL and PSB, $\hbar\omega$, was measured to be 4.4 and 3.9 cm^{-1} in excitation and emission respectively. Both spectra were recorded at 9.8 K and had a linewidth (fwhm) of 1.3 cm^{-1} . The electron-

phonon coupling strength, S , was found to be 0.2 following the fitting procedure outlined in Section II.10. When these parameters were substituted into the Wp function given by Equation II.14, the band profiles shown by the black traces in Figure VI.5 are generated.

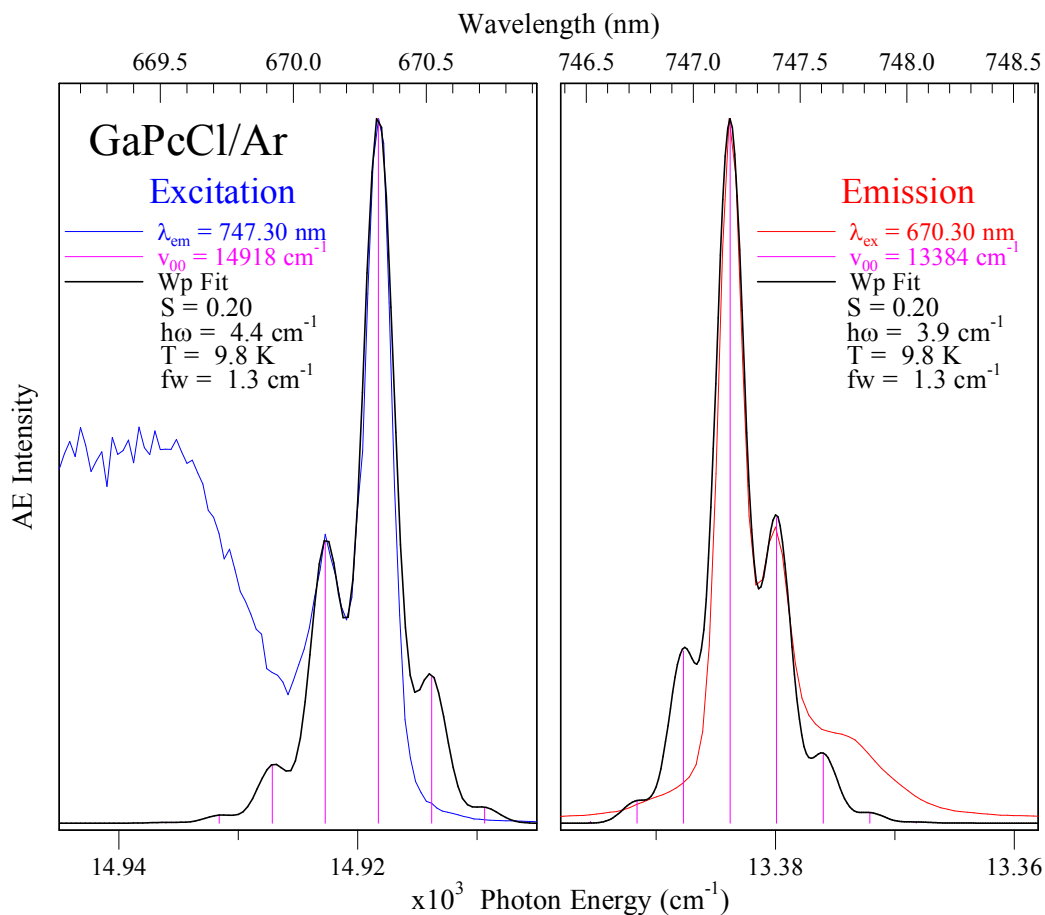


Figure VI.5: A comparison of the emission and excitation spectra recorded from the red-most site of GaPcCl/Ar. The locations through which these slices were taken from are shown in Figure VI.A2. The zero phonon line and phonon side band are clearly visible in both excitation (left panel) and emission (right panel). The Wp fit was performed within the single-configurational-coordinate model described in Chapter II using Equation II.14.

The left panel of Figure VI.5 shows the excitation spectrum in the region of the ZPL, which is located at 670.32 nm (14918 cm^{-1}). A weaker band to the blue at 670.12 nm (14923 cm^{-1}) corresponds to the first PSB. The Wp fit matches these bands very closely. A broad unstructured band even further to the blue, centred on 669.2 nm, does not exhibit any resolved ZPL or PSB (or the vibronic bands from Figure VI.4), suggesting the existence of a different species such as an aggregate. This proposal will be discussed in more detail in Section VI.4.I. The Wp fit predicts a weak phonon side band in this region, but if it exists,

it is obscured by the broad feature. The fit also predicts a fairly intense band to the red of the ZPL, but only a weak band is observed in the experimental spectrum. This is a hot band and is the region of the fit with the greatest discrepancy between the calculated and measured intensities. The difference in intensity of this hot band may be due to the threshold conditions associated with AE, i.e. the density of thermally excited molecules may be insufficient to reach the threshold value for stimulated emission to occur.

The emission recorded by exciting into the ZPL of the most red site is shown in the right hand panel of Figure VI.5. With the exception of the broad excitation feature at 669.2 nm, mirror symmetry is apparent between the excitation and emission spectra. The ZPL in emission is located at 747.2 nm (13384 cm^{-1}), with the PSB located at 747.4 nm (13380 cm^{-1}). As was the case in excitation, the Wp fit matches the experimental ZPL and PSB excellently. Two weaker phonon bands further to the red are also predicted by the Wp function, and evidence of this is present from the partly resolved shoulder centred on 747.7 nm and the wing extending up to 748 nm in the experimental spectrum. This region is obstructed in the excitation spectrum by the broad band. The fact that this broad band does not show up in emission is evidence that it originates from a different species in the matrix. The weak band to the blue of the ZPL in emission ($\sim 746.8\text{ nm}$) represents a hot band which arises at temperatures as low as 9.8 K due to the low frequency of the coupling mode ($\sim 3.9\text{ cm}^{-1}$). While the intensity of the hot band in emission is not as strong as that predicted by the Wp fit, it is stronger than that observed in the excitation spectrum. This may be due to the slightly larger coupling frequency in the excited state ($\sim 4.4\text{ cm}^{-1}$).

Because the excitation and emission spectra shown in Figure VI.5 were extracted from the extreme red portion of the 2D-EE scans (see Figure VI.A2), they represent the simplest profiles for the AE bands. Accordingly, they are considered the intrinsic profile of a single type of site, one in which the monomer GaPcCl is isolated. From the good agreement with the Wp fits, it is concluded that the spectral structure exhibited arises from very weak electron-phonon coupling.

VI.4: Discussion

VI.4.I: Amplified Emission

In spite of the fact that several studies^{1,2,3} have already been performed on the electronic spectroscopy of GaPcCl, the current work is the first known instance of this molecule demonstrating amplified emission. This is a surprising situation since aluminium phthalocyanine chloride (AlPcCl) has been known to exhibit amplified emission for a long time⁴. In fact it was the first example of an operational dye laser. The mechanism for the process of AE in this system can be described by the 3-level energy level diagram shown in Figure VI.6. Level 1 in the diagram is the ground state (S_0 ($v'' = 0$)), which is highly populated at the cryogenic temperatures used in matrix-isolation experiments. Level 2 (S_1 ($v' = 0$)) is only populated following laser irradiation, and must be sufficiently long lived for a population inversion to take place with respect to Level 3. This level is a specific vibrational mode of the ground electronic state (S_0 ($v_n'' = 1$)). It is the vibrational mode observed at 1523 cm^{-1} in the Raman spectrum and at 1540 cm^{-1} in emission of GaPcCl/Ar. This mode is of B_2 symmetry and corresponds to the normal mode #144 from the DFT vibrational analysis.

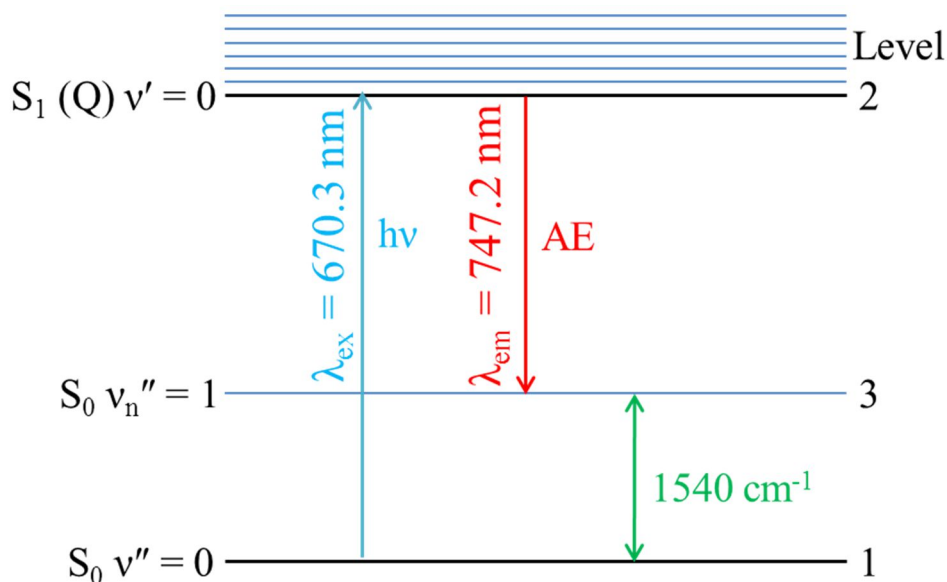


Figure VI.6: Energy level diagram depicting the process of amplified emission in GaPcCl/Ar. A 3 level system is involved; Level 1: The electronic ground state (S_0) where $v'' = 0$, Level 2: The first excited electronic state (S_1 (Q)) where $v' = 0$, and Level 3: An excited vibrational level corresponding to mode #144 at 1540 cm^{-1} in S_0 .

In order to produce stimulated emission, Level 2 must be populated with great efficiency. This was achieved by pumping the GaPcCl molecule with nanosecond pulsed dye laser excitation. A set of experiments by Huang *et al.*⁵ did not result in any AE when exciting free-base, Mg, AlCl, Zn, and Cu phthalocyanines isolated in Shpol'skii matrices with continuous wave (CW) laser excitation. Studies by Dozova⁶, Crepin⁷ and Arabei^{8,9} showed that pulsed laser excitation was capable of producing AE in the structurally related systems free-base and zinc phthalocyanine, free-base tetraazaporphyrin and free-base tetrabenzoporphyrin. Another important factor in achieving AE is exciting into an electronic transition with a large extinction coefficient. This has been (tentatively) measured as $\epsilon \sim 7.2 \times 10^9$ m/M at 676.07 nm for GaPcCl in EtOH, although, for solubility reasons the actual value is expected to be somewhat larger. Level 3 at 1540 cm^{-1} corresponds to a non-thermally populated level so that the population inversion between the (2) \rightarrow (3) transition is easily obtained. To maintain the population inversion during the course of the 6 ns laser pump pulse, the vibrational Level 3 must rapidly relax to the vibrationless level ($\nu'' = 0$) of the ground state. Fluorescence lifetimes of GaPcCl were measured as 2.6, 2.3, 2.4 and 2.3 ns in N₂, Ar, Kr and Xe matrices respectively, indicating that Level 3 must decay much more rapidly than this. The vector diagram representing the vibrational mode #144 is shown in Figure VI.7, and involves an out-of-phase asymmetric stretching of the C _{α} -N_m-C _{α} bonds of the inner ring macrocycle. This mode is now well known to be associated with the process of stimulated emission as it has been observed in several related porphyrin and phthalocyanine systems^{8,6,9}. Thus it is expected that this excited vibrational mode can relax very quickly to the vibrationless ground state.

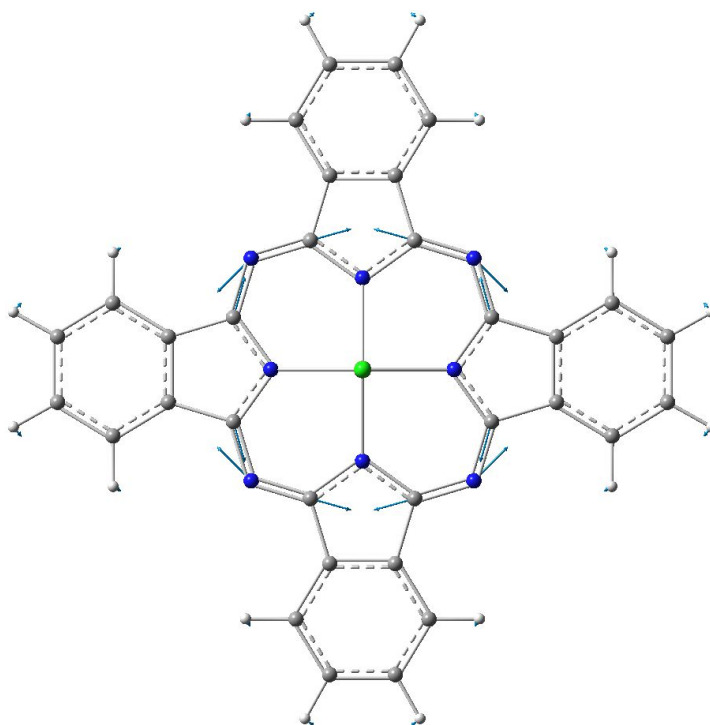


Figure VI.7: Vector diagram showing the atomic motions of vibrational mode #144 of GaPcCl at 1540 cm^{-1} associated with amplified emission which has been calculated by DFT with the B3LYP/6-311++g(2d,2p) functional and basis set. As depicted, the mode involves mostly an out of phase stretching of the bridging $C_{\alpha}\text{-N}_m\text{-C}_{\alpha}$ bonds, coupled with small amounts of ‘in-plane’ C-H bends on the aryl groups. The direction of motion of the atoms is depicted with the blue arrows and the extent of the motion is given by the length of the arrows.

VI.4.II: Site Splitting of Amplified Emission

It was observed from the emission data presented in Chapter V that GaPcCl can occupy a number of different sites depending on the matrix host it is trapped in. Several sites within a given sample can exhibit AE, with the vibronic band at $\sim 1540\text{ cm}^{-1}$ being the mode involved in all cases. This will be demonstrated in Sections VI.4.II.a through VI.4.II.d. The spectral features of each matrix will be analysed using the AE bands originating from different sites. This method is preferable to using regular fluorescence data owing to the exceptionally narrow line widths of the AE bands and the very large signal-to-noise ratios compared to those of the fluorescence bands. 2D emission-excitation (2D-EE) plots of GaPcCl in each host gas give a complete overview of the emission data that is not always obvious from individual emission or excitation spectra. In order to relate these plots to the more conventional spectra, emission and excitation ‘slices’ of these 2D-EE plots will be

presented to show how the spectra change with respect to the wavelengths (λ_{ex} and λ_{em}) monitored.

VI.4.II.a: Argon

The 2D-EE plot recorded in the spectral region of the AE bands of GaPcCl/Ar is shown in Figure VI.8. This plot presents emission on the x-axis and excitation on the y-axis. Emission intensities are plotted as coloured contour lines, whose scale is shown to the right hand side of the main plot area. A series of dashed lines are shown on the plot with labels Mn and Xn (where $n = 1, 2, 3...$ etc.), which represent emission and excitation ‘slices’ respectively of the 2D-EE plot. For example, the line M1 denotes the emission spectrum obtained with an excitation wavelength equal to the position of M1 ($\lambda_{\text{ex}} = 670.3$ nm). The same is true for the excitation spectra, where the emission wavelengths being monitored match the position of the Xn lines. A more detailed account of how the emission and excitation spectra are extracted from 2D-EE plots is given in Chapter II and accompanied by a plot showing an emission and excitation spectrum in Figure II.16. The same method will be used for each matrix host.

The structure of the 2D-EE plot of GaPcCl/Ar shows a white background (low intensity) with contours of different colours (higher intensity) in the upper centre of the plot. The contour lines represented by pink, red, yellow and green correspond to the strongest amplified emission. Turquoise and blues represent weaker AE which is seen predominantly at $\lambda_{\text{ex}} < 665$ nm, which correspond to the higher energy vibronic bands in excitation. The highest intensity regions are shown by the red/pink contours and there are three such regions in this plot. The first region (highlighted as region ‘I’ on Figure VI.8) has its strongest emission centred at 747.2 nm, with $\lambda_{\text{ex}} = 670.3$ nm, and shall be referred to as the ‘red site’. The other intense region exhibits the strongest emission intensity at ~ 745.1 nm, with $\lambda_{\text{ex}} = 668.6$ nm, and shall be referred to as the ‘blue site’ (highlighted as region ‘III’ on Figure VI.8). An area of moderate intensity exists between the red and blue sites and has been labelled as region II.

An expanded view of regions I - III of this 2D-EE plot are presented in Figure VI.A1 - Figure VI.A4, which provide more details of three main features in the plot. These three regions show the features of the most abundantly occupied sites. In Figure VI.A1, the location of the strong ZPLs and weaker resolved PSBs are represented by the diagonal

features. The Wp fit shown in Figure VI.5 is applicable to all of the excitation bands present. In contrast, the spectral band shape of the broad ex/em feature at 669.5/747.2 nm has completely different properties. Accordingly it is attributed to a different species, possibly an aggregate, as indicated in Figure VI.A1. Immediately to the blue (in excitation) of each ZPL lies its corresponding PSB, although this is not evident on the scale shown in Figure VI.8. A series of weaker AE bands are located between the red and blue sites in what appears to be a continuum of sites in the matrix (highlighted as region ‘II’ on Figure VI.8, and shown in detail in Figure VI.A3). The ZPLs of the weaker sites can be clearly seen as the region of intense emission between the intersections of M1-X4 and M2-X1. The PSBs of the weaker sites are difficult to observe in the contour plot, even on the scale presented in Figure VI.A3, due to their low intensity.

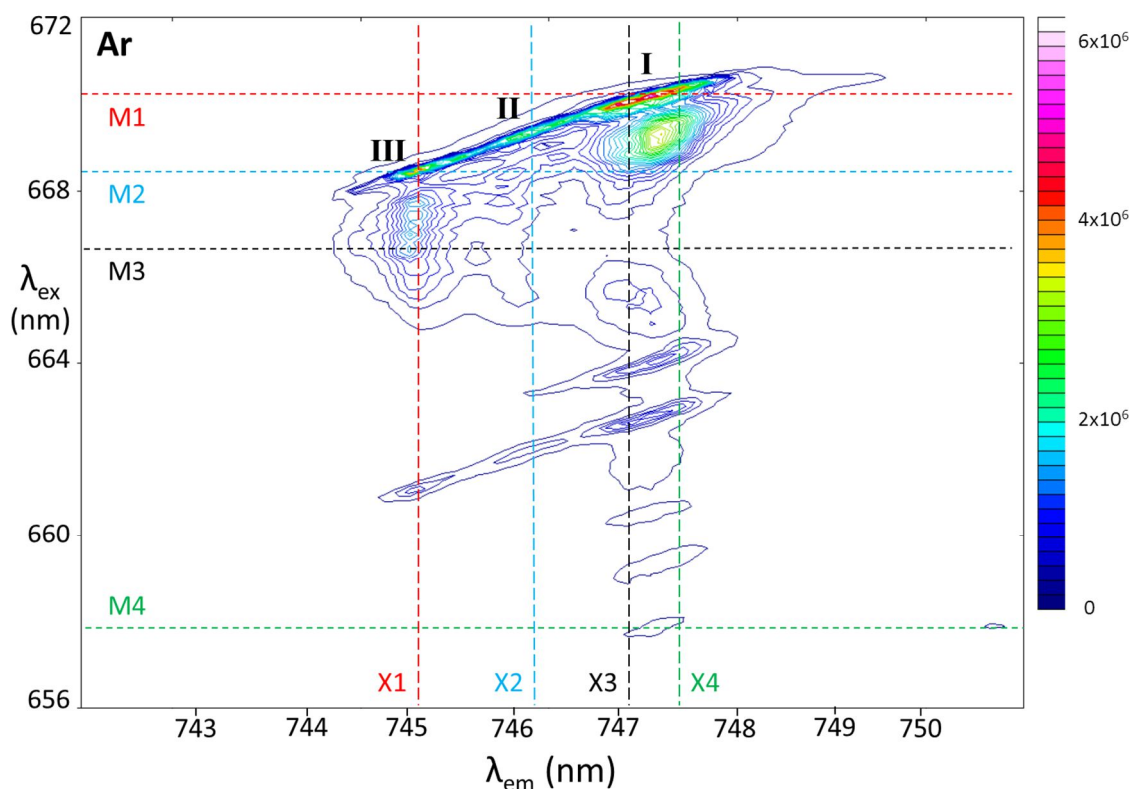


Figure VI.8: 2D excitation-emission plot of GaPcCl trapped in solid Ar recorded in the region of the amplified emission bands. A number of sites are clearly present. A selection of emission slices (M1 – M4) have been extracted from this spectrum and are shown in Figure VI.9. A selection of excitation spectra (X1 – X4) have also been taken from the spectrum and are shown in Figure VI.10. All slices will be shown in linear energy (cm^{-1}) for analysis.

Selected emission spectra from the 2D-EE spectrum of GaPcCl/Ar have been extracted and are presented in Figure VI.9. The ‘slices’ were chosen based on the intensity of the AE bands for different sites. These spectra show how the amplified emission bands change drastically with different excitation wavelengths. The red trace corresponds to M1 ($\lambda_{\text{ex}} = 670.3$ nm) and cuts through the AE band of the dominant red site at 747.2 nm in Figure VI.8. Similar to the fluorescence data presented in Chapter V, excitation into the 0-0 band in absorption yields the simplest emission. This excitation wavelength is only capable of exciting the lowest energy sites and a single strong AE band is observed. A weaker shoulder to the red of the intense band at 747.2 nm is, according to the Wp fits done, due to emission from the PSB. A very weak band even further to the red ($\lambda_{\text{em}} = 748.05$ nm) is observed, which is most likely emission of a second PSB.

The blue trace (M2) corresponds to $\lambda_{\text{ex}} = 668.6$ nm on Figure VI.8, which cuts through the maximum of the AE band from the blue-most site at 745.1 nm. The PSB of this site ($\lambda_{\text{em}} = 745.4$ nm) can be seen as a weak band to the red of the intense emission band. This slice also cuts through the feature to the blue of the dominant red site (in excitation), which manifests as a broad emission band centred at 747 nm. Another broad emission band is observed at 746.1 nm. The broadness of the band (at 746.1 nm) may indicate that this is emission from more than a single site, similar to why the fluorescence bands in N_2 and Xe were so broad. Alternatively, this could be emission from an aggregate species.

Two broad emission features are evident in Figure VI.8, whose excitation maxima are located to the blue of the ZPLs of the dominant red and blue sites (regions I and III). The emission and excitation slices taken through the maxima of these bands are shown in Figure VI.A6. The excitation spectra show that the ZPL dominates the intensity, but that the broad features are also emitting strongly. The lineshapes of the ZPL and the broad feature are different, with the broad feature perhaps showing some unresolved structure. The linewidths of both ZPLs in excitation are 1.3 cm^{-1} whereas the broad bands have linewidths of 22.9 and 23.2 cm^{-1} for the blue and red features respectively. The emission spectra shown in Figure VI.A6 also highlight the difference between the lineshape of the ZPL and the two broad features; the ZPL has a linewidth of 1.3 cm^{-1} and the broad bands have linewidths of 11.9 and 8.7 cm^{-1} for the blue and red sites respectively. This difference is also demonstrated by the bands at 745 nm in traces M2 (which shows the ZPL) and M3 (which shows the broad feature) in Figure VI.9. The very different spectral characteristics

indicate that these features do not originate from the well isolated molecule, but may instead be due to the presence of aggregates in the matrix. Even though this is not a definitive assignment, these features will be referred to as aggregates in future for ease of discussion. These bands were present in all samples of GaPcCl/Ar, although changing the deposition conditions caused a variation in the relative intensities of emission from the ‘aggregate’ and monomer species. The spectrum shown in Figure VI.8 was prepared with a high oven temperature with the sample window held at 10 K, and is representative of the relative intensities of these features in most Ar samples.

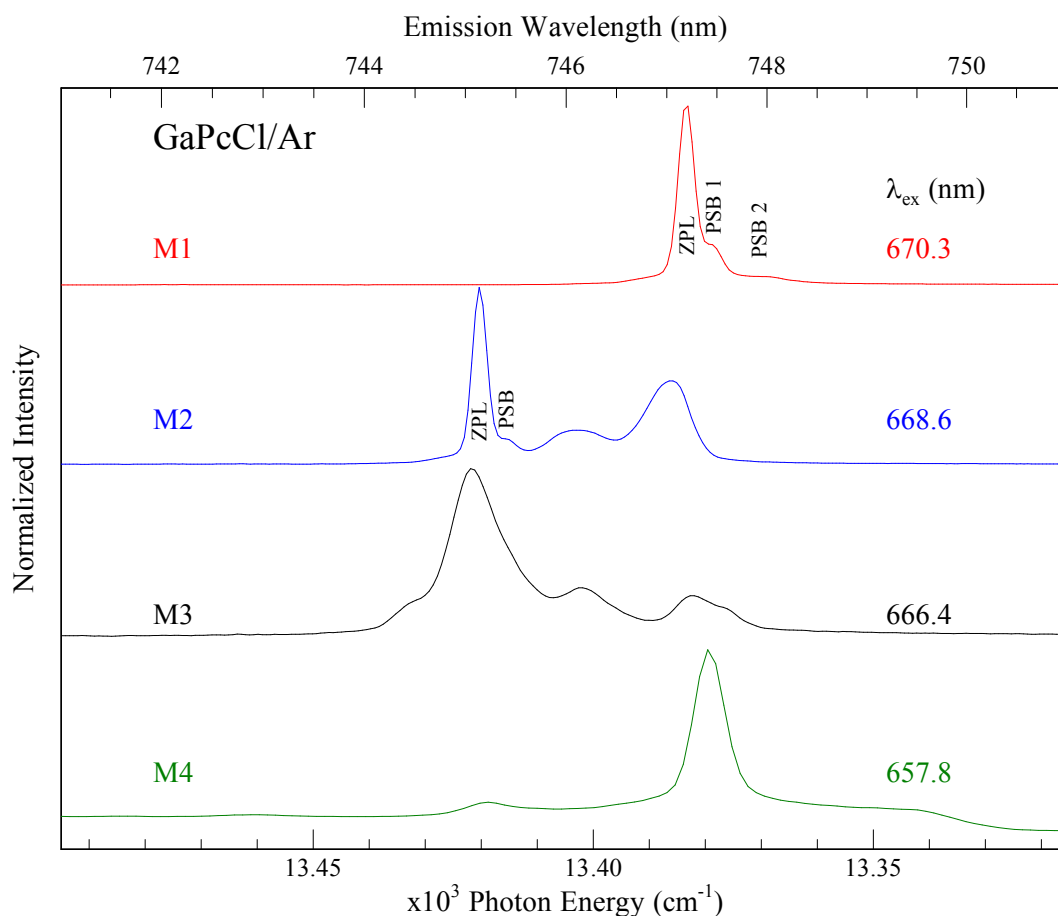


Figure VI.9: A series of emission spectra of GaPcCl/Ar recorded with different excitation wavelengths. The position on the 2D-EE plot that each spectrum is extracted from is shown in Figure VI.8.

At excitation wavelengths shorter than 664 nm amplified emission has all but stopped, except for the vibronic bands of the dominant sites. The same trend for the region around the ZPLs is observed here, with some strong emission around 747.2 nm, moderate

emission around 745.1 nm and weaker emission between these two regions. This trend arises because the same vibronic structure in excitation is common to all of the sites (i.e. the shift of a given vibronic band from the ZPL will be identical for every site, as demonstrated in Figure VI.A5). Further vibronic structure can be observed at excitation wavelengths to the blue of 660 nm for the dominant red site only.

The black trace (M3) corresponds to $\lambda_{\text{ex}} = 666.4$ nm on Figure VI.8 and cuts through the AE bands of both the red and blue sites. All of the AE bands observed with excitation at M3 are much broader than the bands observed with excitations at M1 and M2. This is due to the fact that M3 does not intersect with the narrow ZPLs of these sites, but rather the broader aggregate species exhibiting AE in this region. At least 5 emission bands are present and exhibit different degrees of resolution depending on the excitation wavelength. The final excitation wavelength shown in Figure VI.9 corresponds to M4 ($\lambda_{\text{ex}} = 657.8$ nm) on Figure VI.8. At this wavelength, AE is only exhibited by the most red site, and with a diminished intensity, as fluorescence from the vibronic band at 1540 cm^{-1} of the blue site is clearly visible on the same scale. The band which is exhibiting AE corresponds to one of the vibronic bands in excitation which is shown by X4 in Figure VI.10.

A series of excitation spectra extracted by taking slices at the emission wavelengths specified in Figure VI.8, are presented in Figure VI.10. Slice X1 (red trace), taken at the emission wavelength 745.06 nm, coincides with the maximum of the emission from the blue site observed in Figure VI.9. The excitation spectrum shows a very sharp band at 668.0 nm which corresponds to the zero phonon line (ZPL) for this site. The phonon side band (PSB) to the blue of the ZPL is difficult to identify due to its overlap with the broad bands centred at 666.6 nm. This broad band corresponds to the feature which has been tentatively assigned as an aggregate species. A weak shoulder to the red of the ZPL may be a hot band which is thermally populated at 10 K. This is possibly due to the small splitting ($\sim 4.4\text{ cm}^{-1}$) between the ZPL and the PSB. A weak vibronic band is evident at 660.6 nm, representing a vibronic mode with a frequency of 167.5 cm^{-1} , as listed in Table VI.2.

The blue trace (X2) was obtained by monitoring the emission band located at 746.20 nm. This corresponds to a site (Region II) which exhibits amplified emission, but not as strongly as the blue or red sites described earlier. The spectrum is dominated by a sharp ZPL located at 668.45 nm, with a broad ($\sim 90\text{ cm}^{-1}$) band, possibly originating from another aggregate species. The PSB is located in between the ZPL and the emission band from the

aggregate. A vibronic band in excitation is also observed around 661 nm, with a much weaker band also arising at 663.3 nm. All of the bands are red-shifted compared to their counterparts shown by X1, which is expected as the excitation spectrum is centred on an emission band from a site to the red of X1.

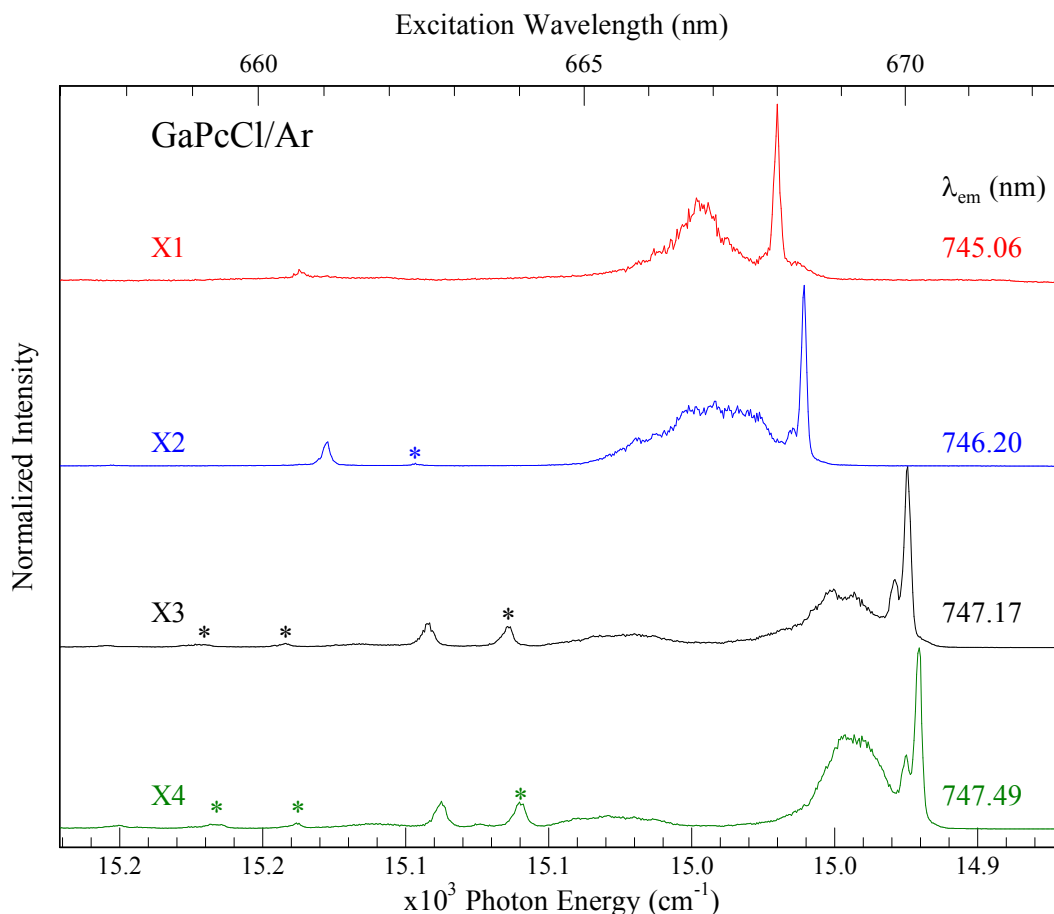


Figure VI.10: A series of excitation spectra of GaPcCl/Ar recorded by monitoring various emission wavelengths. The relationship between the emission wavelength, X_n , and the 2D-EE spectrum is shown in Figure VI.8.

The excitation spectrum extracted at X3 (black trace) shows a similar structure to that of X2, with an intense ZPL (670.14 nm), a resolved PSB and several vibronic bands further to the blue. The broad band from the aggregate species is present, but appears to have a different structure to its counterparts in the other excitation spectra. From the 2D-EE contour plot shown in Figure VI.8, it looks like X3 cuts through two broad bands, which may be two distinct species. The bands in this spectrum are all red-shifted with respect to the bands from X1 and X2. The presence of the ‘extra’ bands in the spectrum (highlighted

by asterisks) is due to how highly occupied each site is, with the vibronic bands of X3 exhibiting greater intensity than those of X1 and X2. X2 is moderately occupied, and can exhibit AE with only a few excitation wavelengths to the blue of the ZPL. A similar result is obtained for the blue site (X1), although this site is well occupied. The site shown by X3 is very highly occupied as all of the vibronic bands in excitation observed in Figure VI.10 exhibit AE.

The spectrum shown by the green trace is a slice taken through X4. Because it is located in the extreme red, this was the only site which produced amplified emission with excitation at M1. The excitation spectrum is similar to that obtained with X3, exhibiting a sharp ZPL and PSB which dominate the spectrum, with much broader excitation bands located to the blue of the PSB exhibiting some weaker amplification. These broad excitation bands originate from the aggregate species. Pairs of vibronic bands extending up to 658 nm are also evident.

The 2D-EE plot, as well as the corresponding emission and excitation spectra, show that GaPcCl/Ar exists in many sites of isolation. A continuum of weaker sites exist between the three most abundantly occupied ones (shown in Figure VI.A2 - Figure VI.A4), whose AE bands are located at 745.06, 747.17 and 747.49 nm. The splitting between the AE bands of the red site at 747.49 nm and the sites whose AE bands are located at 747.17 and 745.06 nm are 6 and 44 cm^{-1} respectively. As well as a number of monomer species which exhibit narrow ZPLs in excitation, other species also exist in Ar matrices. These 'aggregate' species also emit strongly in the AE region, although both emission and excitation bands from this species are much broader than those of the isolated molecule. Slice M3 in Figure VI.9 cuts directly through the maximum of the blue aggregate feature, and demonstrates the pronounced broadening of this species in emission, especially when compared to the narrow ZPL from the blue site shown by slice M2. The excitation slice X1 passes directly through the ZPL of a blue monomer species as well as the maximum of the blue aggregate feature. This demonstrates the broadening exhibited in excitation for the aggregate compared to the highly isolated monomer.

The fact that the continuum of sites exists and can exhibit AE indicates that Ar forms very stable sites of isolation and is sufficiently robust to withstand high powered laser irradiation over long time periods. Due to the high number of monomer sites, and possibly other species (aggregates) in the Ar matrix, a complex picture has emerged whereby a

single excitation wavelength can result in emission from an array of different sites/species. This rich spectroscopy of GaPcCl/Ar is reminiscent of earlier AE work⁶ done on H₂Pc/N₂ and ZnPc/N₂.

VI.4.II.b: Krypton

The 2D-EE plot of GaPcCl/Kr is presented in Figure VI.11. This plot was generated in the same manner as for GaPcCl/Ar, and is laid out the same way. The features present in this plot are similar to those observed in Ar. The two broad red/pink regions in the plot correspond to the most intense amplified emission in this matrix. The maxima of these bands are located at 751.6 and 754.1 nm in emission. This suggests that two highly occupied features (probably aggregates) dominate in this matrix, with some less well occupied sites also present. The splitting between the two dominant features is 44 cm⁻¹.

Sharp features which correspond to ZPLs are located to the red (in excitation) of the dominant features, which are labelled more clearly in the expanded regions of the 2D-EE plot shown in Figure VI.A7 and Figure VI.A9. The fact that the ZPLs do not dominate the intensity may mean that Kr matrices do not preferentially form sites where GaPcCl molecules get isolated as the monomeric species, but rather tend to arrange into larger sites where aggregation can occur. While the ZPLs are not as intense as those observed in Ar, and do not have the same phonon structure, they do appear in the correct location.

In Ar matrices a ‘diagonal’ region showing intense ZPLs (and PSBs) of a continuum of sites was clearly identifiable on the 2D-EE plots. A region of lower intensity connects the two main bands in Kr, which is similar to Ar, where the continuum of sites was observed between the dominant sites. While the region between the red and blue sites does not show intense AE in Kr matrices (unlike in Ar) as shown in Figure VI.A8, this may be merely a concentration issue. If the sites do not contain a large enough number density of molecules, then the process of stimulated emission will not reach its threshold value and AE will not occur. Vibronic bands are observed to the blue of the ZPLs in excitation, and extend as far as 666 nm for the blue site.

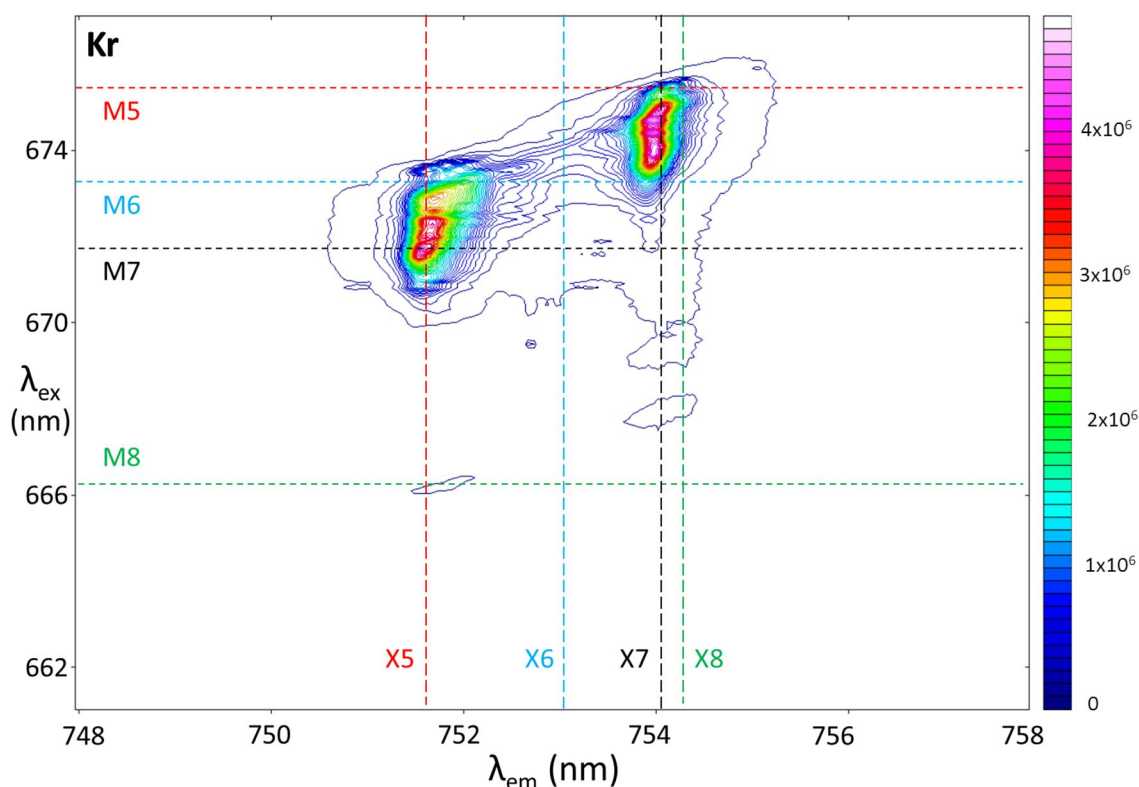


Figure VI.11: 2D-EE plot of GaPcCl trapped in solid Kr recorded in the region of the amplified emission band. A number of sites are clearly present. A series of emission slices (M5 – M8) have been extracted from this spectrum and are shown in Figure VI.12. A selection of excitation spectra (X5 – X8) have also been taken from the spectrum and are shown in Figure VI.13.

The series of emission spectra extracted from Figure VI.11 at wavelengths represented by the dashed lines M5 – M8, are presented in Figure VI.12. Slice M5 ($\lambda_{\text{ex}} = 675.5$ nm), shown by the red trace, cuts through the amplified emission band of the red-most site. This excitation wavelength was chosen as it should yield the simplest emission spectrum with the fewest possible features. This is indeed the case as the spectrum is dominated by the narrow AE band at 754.2 nm. The equivalent ‘slice’ in Ar (i.e. through the site furthest to the red) exhibited phonon structure to the red of the main emission band, as well as a hot band to the blue. While the band at 754.2 nm in Kr may be the ZPL of the red site, the spectrum does not show any indications of a resolved PSB being present. As suggested above, the Kr matrix appears to contain less of the isolated monomer than Ar matrices owing to the much weaker intensity on the ZPLs.

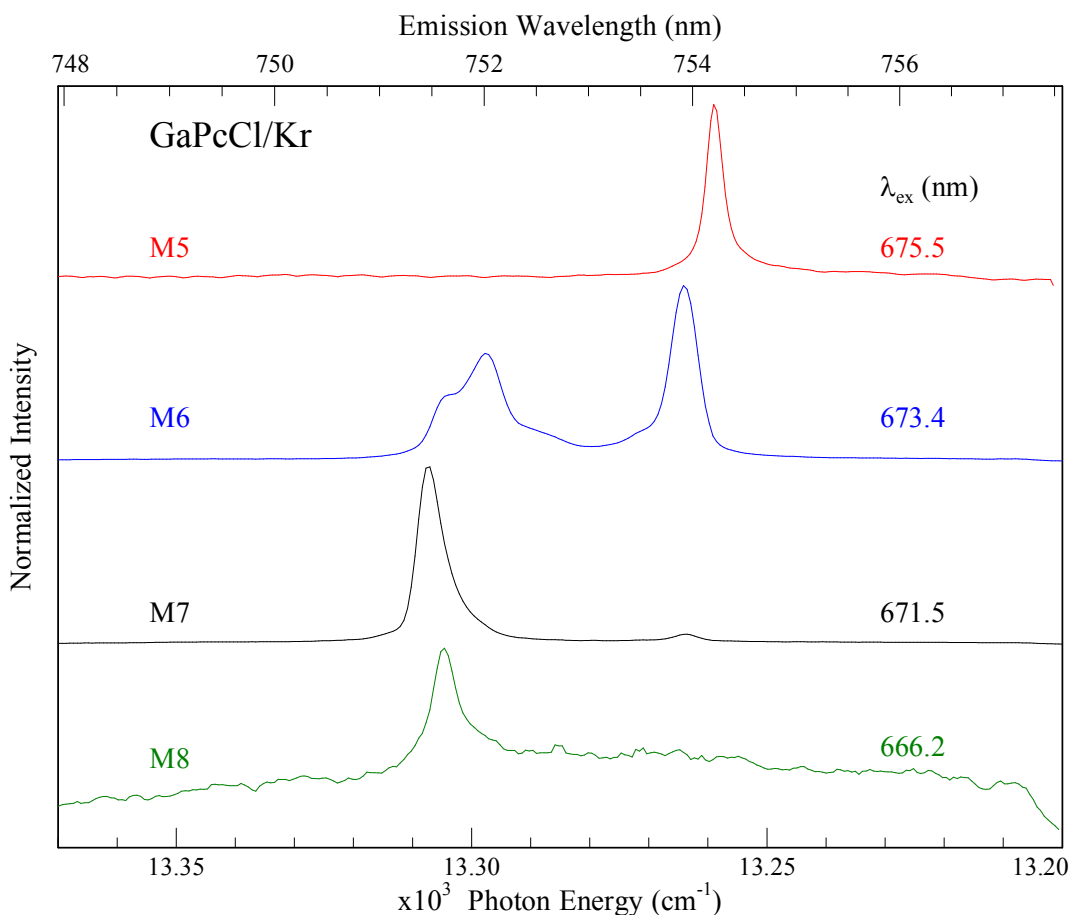


Figure VI.12: A series of emission spectra of GaPcCl/Kr recorded with different excitation wavelengths. The relationship between the excitation wavelength, M_n , and the 2D-EE spectrum is shown in Figure VI.11.

The blue trace presents slice M6, where $\lambda_{\text{ex}} = 673.4$ nm, and contains three peaks and two unresolved features. The intense narrow band at 754.1 nm corresponds to AE from the red site, and a weak shoulder to the blue is evident on this band. A triplet of partially resolved bands is located between 751 and 753 nm. The most intense of these bands is centred on 752.0 nm. A shoulder to the red of this band is not fully resolved. A shoulder to the blue shows better resolution and is centred on 751.7 nm. Each of these bands represents AE from a different site in the matrix. They are located too close together to be fully resolved under current conditions, but do point to a variety of sites being present in this matrix, similar to Ar.

The black trace shows the spectrum corresponding to M7 ($\lambda_{\text{ex}} = 671.5$ nm) on Figure VI.11. This spectrum cuts through the amplified emission band of the blue site, located at

751.6 nm. The red site no longer exhibits AE strongly at this wavelength, showing only weak intensity in Figure VI.12. This can be explained by the excitation wavelength moving too far to the blue to overlap with any of the strong absorption bands of the red site, but now coinciding with strong absorption bands of the blue site.

Slice M8 is shown by the green trace in Figure VI.12, representing an excitation at 666.2 nm. This is much farther to the blue than the other slices shown earlier and is not in the region of the band origin of the AE bands. Instead, this slice cuts through one of the vibronic bands of the blue site, where fluorescence is observed. The intensity of the bands are much weaker than those of M5 – M7, and electronic noise is evident on the baseline. Emission from the blue site is clearly visible. The corresponding emission from the red site is located at 668/754 nm in the 2D-EE plot shown in Figure VI.11, manifesting as a broad, weak band.

The excitation spectra extracted from Figure VI.11 are presented by the lines X5 – X8 in Figure VI.13. Spectrum X5 was obtained by monitoring the emission band at 751.70 nm, and is shown by the red trace. This slice cuts through the AE band of the blue site. Two main features dominate the spectrum; a strong, broad band centred on 672 nm, and a weaker, narrow band at 673.5 nm. The narrow band may be the ZPL from a weak site, but due to its low intensity, it is clearly not the dominant species in this excitation spectrum. The broader band to the blue shows the greatest intensity and corresponds to emission from the dominant blue feature. Due to the broadness of this excitation band, it is likely that it originates from the suspected aggregate species and not a well isolated monomer.

The blue trace shows the slice X6, which is located at 753.00 nm, between the intense blue and red features. It is known from the emission slice M6 that there is a site present here that shows weak amplified emission. This is found to be the case by the peak centred around 674 nm. A shoulder to the blue of this is observed centred on 673.2 nm. This would suggest two features are present.

The black trace shows the spectrum X7, which corresponds to an excitation spectrum through the AE band of the dominant red feature (754.14 nm). This spectrum is similar to the spectrum shown by X5 in that it shows a weak, but narrow line (possibly a ZPL) and a broader band consisting of at least two features which may arise from the aggregate species. All of these bands are red-shifted compared to X5, as expected for the red site,

with the ZPL located at 675.2 nm and the aggregate band centred on 674.3 nm. The aggregate feature appears to be showing signs of resolution into two separate bands, but this is not certain due to the noise on the top of the band. A series of weaker bands to the blue are also present, correspond to the vibronic bands at 133.97 and 165.77 cm^{-1} given in Table VI.2.

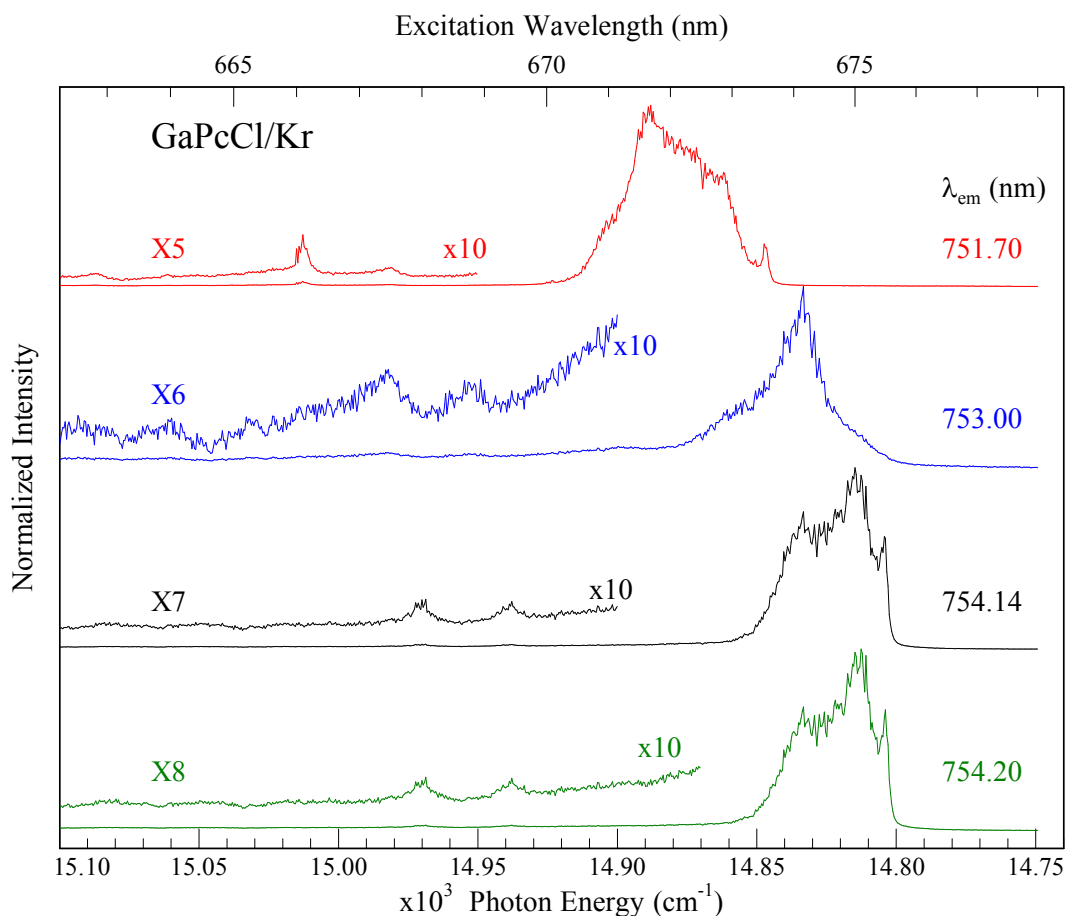


Figure VI.13: A series of excitation spectra of GaPcCl/Kr recorded by monitoring various emission wavelengths. The relationship between the emission wavelength, X_n , and the 2D-EE spectrum is shown in Figure VI.11.

The green trace in Figure VI.13 shows slice X8, which was taken through the feature furthest to the red capable of exhibiting intense AE. This slice should yield the simplest excitation spectrum, yet it appears substantially the same as X7. The ZPL, centred on 675.5 nm is evident, but lacks a resolved PSB which was evident on the equivalent excitation spectra recorded in Ar. Unfortunately, the broad feature is also present in this spectrum, which may be obscuring additional structures to the blue of the ZPL. This probably means

that the true lineshape of the monomer species cannot be determined in Kr. A solution to this would be to attempt a lower concentration sample to reduce the amount of aggregates present, but this would also inhibit the samples ability to exhibit AE.

The 2D-EE spectrum of GaPcCl/Kr, as well as slices through this spectrum, shows that this matrix contains two dominant structures reminiscent of the aggregate species present in the Ar matrix spectrum shown in Figure VI.8. The sharp ZPLs are not as evident in Kr, yet they are present (as highlighted in Figure VI.A7 and Figure VI.A9). Two main features exist in the matrix, with their AE bands located at 751.6 nm and 754.1 nm. Several sites exist between these blue and red features, but are less concentrated within the matrix, meaning the intensity of AE from these sites is weaker than that of the two major features. Some sites are so close together that their bands overlap, even given the narrow linewidths of the AE band, and this is demonstrated in the emission spectrum shown by M6 in Figure VI.12. Excitation slices through the main features of Figure VI.11 indicate that ZPLs from highly isolated molecules are indeed present in the regions of the dominant red and blue sites, but carry much less intensity than the emission from the so-called aggregate species. This is in contrast to the Ar matrices, where the ZPLs from many sites were clearly observed, and were of greater intensity than the broad aggregate species. This suggests that Ar preferentially traps individual GaPcCl molecules in sites, with small amounts of aggregates also forming, whereas Kr matrices tend to form aggregates more easily than sites in which the molecule is in its monomeric form.

VI.4.II.c: Xenon

The 2D-EE plot recorded for AE of GaPcCl/Xe is presented in Figure VI.14. The plot was generated in the same manner as the Ar and Kr matrices shown earlier. This system shows two main emission features; an intense blue band at 762.1 nm and an even more intense red band at 763.2 nm, both located in excitation between 683 and 680 nm. The splitting between the two emission features is 19 cm^{-1} . The region in the 2D-EE spectrum of GaPcCl/Ar that showed well-defined ZPLs does not manifest itself in this system, indicating that Xe matrices are less effective at trapping the GaPcCl molecule as the isolated molecule. This suggests that the two dominant features in Xe matrices may be the so-called aggregate species described in the Ar and Kr matrices. Both features are broad in both emission and excitation. The region between the red and blue sites also shows strong

emission intensity, and most likely corresponds to another site that is not as highly occupied in the matrix.

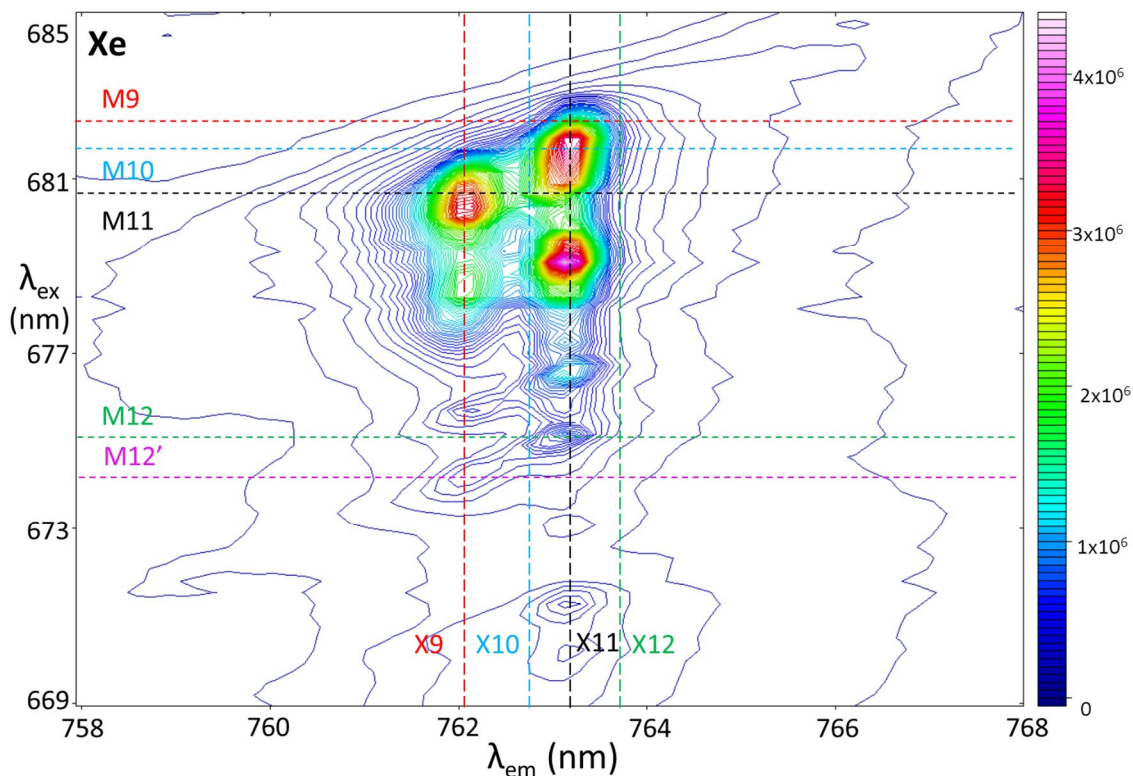


Figure VI.14: 2D Excitation-emission plot of GaPcCl trapped in solid Xe recorded in the region of the amplified emission band. Two major sites are evident in this host. A selection of emission slices (M9 – M12) have been extracted from this spectrum and are shown in Figure VI.15. A selection of excitation spectra (X9 – X12) have also been taken from the spectrum and are shown in Figure VI.16. The data presented for Xe was recorded with the 600 grooves/mm grating.

A second pair of excitation bands are evident between 680 and 677 nm, whose emission maxima do not exactly match those of the red and blue sites described above, indicates additional features being present in Xe. The excitation bands located to the blue of 677 nm correspond to the vibronic transitions of the dominant sites, especially the red one and are presented in Figure VI.16.

A number of emission spectra corresponding to the slices M9 – M12 on Figure VI.14 are presented in Figure VI.15. The red trace is the emission spectrum represented by M9, which is excitation into the red fringe of the AE band from the red site. The spectrum

contains one main feature; an emission band at 763.7 nm. A shoulder to the red of the absorption maximum possibly corresponds to emission from an aggregate species, or perhaps some unresolved phonon structure.

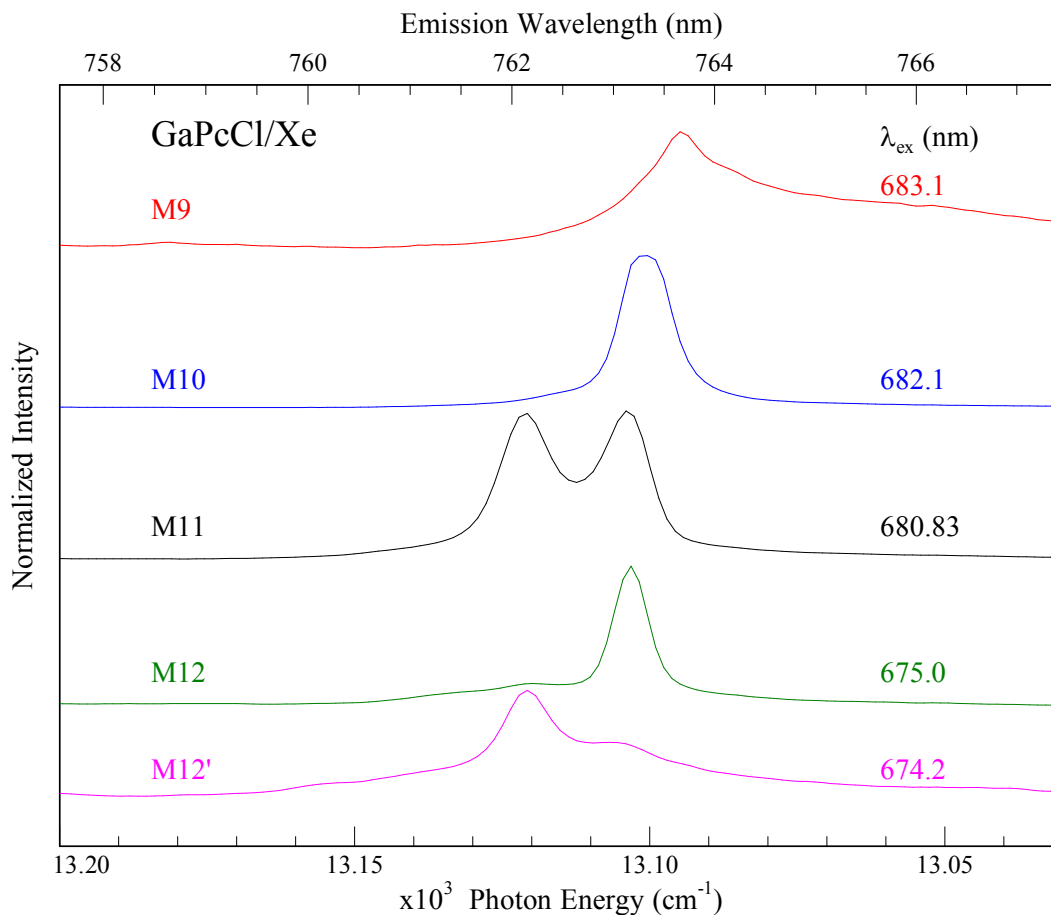


Figure VI.15: A series of emission spectra of GaPcCl/Xe recorded with different excitation wavelengths. The relationship between the excitation wavelength, M_n , and the 2D spectrum is shown in Figure VI.14. The data presented was recorded with the 600 grooves/mm grating, and is of lower resolution than those presented in the other systems.

M10, shown by the blue trace, represents an excitation at 682.1 nm, which passes through the intense region of the AE band of the red site. The spectrum is dominated by the intense band at 763.2 nm, although there is a very weak blue wing on the band which is emission from another, weaker site. The band is not sufficiently resolved with the 600 grooves/mm grating to identify its energy accurately. The blue site is not excited at this wavelength, or at least not sufficiently for its emission to be evident on the same scale as the band at 763.2 nm.

Site splitting is more clearly observed in the emission produced with the excitation at M11 ($\lambda_{\text{ex}} = 680.83$ nm), which excites into the intense region of the blue site. This wavelength also excites into a region of the red site where it is capable of exhibiting AE. A region of moderate intensity lies between the red and blue sites, which may originate from a distinct site that remains unresolved. The maximum of the red band in this spectrum is blue shifted slightly compared to the band shown by M10, perhaps indicating a unique site or it being part of a continuum of sites. The shifting of the emission bands with respect to the excitation wavelength is the same trend observed in Ar and Kr which represented a large number of sites being present in the matrix. Based on the results of the absorption and emission spectra for GaPcCl/Xe shown in earlier sections, it is highly likely that this host also contains a large number of sites.

M12, shown by the green trace in Figure VI.15, presents the result of excitation into the wing of the bluest of the intense amplified emission bands and into one of the vibronic bands of the red site ($\lambda_{\text{ex}} = 675$ nm). There is one intense band located at 763.2 nm in the spectrum and a broader and weaker band to the blue. The intense band is AE from the red site, albeit with diminished intensity compared to excitations further to the red. This is due to most of the strong absorption bands being located close to the 0-0 transition, with only a few bands strongly absorbing to the blue of the 0-0. The blue site does not show AE from the corresponding vibronic band to the one excited by M12 for the red site due to it having a lower concentration in the matrix than the red site. A complementary slice, M12' ($\lambda_{\text{ex}} = 674.2$ nm), shows emission from the corresponding vibronic band from the blue site as that shown by M12 for the red site. Because the red site is more highly occupied, it can still be seen to be exhibiting AE at M12', but it is not nearly as intense as that shown in M12.

A series of excitation spectra were extracted from Figure VI.14 by monitoring the emission bands labelled X9 – X12 and are presented in Figure VI.16. The spectrum obtained from monitoring at X9 ($\lambda_{\text{em}} = 762.21$ nm) is shown by the red trace of Figure VI.16. This slice is centred on the most intense emission wavelength from the AE band of the blue site. The spectrum is dominated by two broad bands centred at 680.3 and 678.5 nm, with a pair of weaker and narrower bands located to the blue (corresponding to the vibronic bands at 114.77 and 149.02 cm^{-1} from Table VI.2). The intense bands correspond to AE from the two aggregate features, and the weaker vibronic bands originate from the same species. There does not appear to be a sharp ZPL present in this spectrum, unlike the Ar excitation

spectra, where the ZPL dominates the intensity in excitation or Kr, where the ZPL is weak but present.

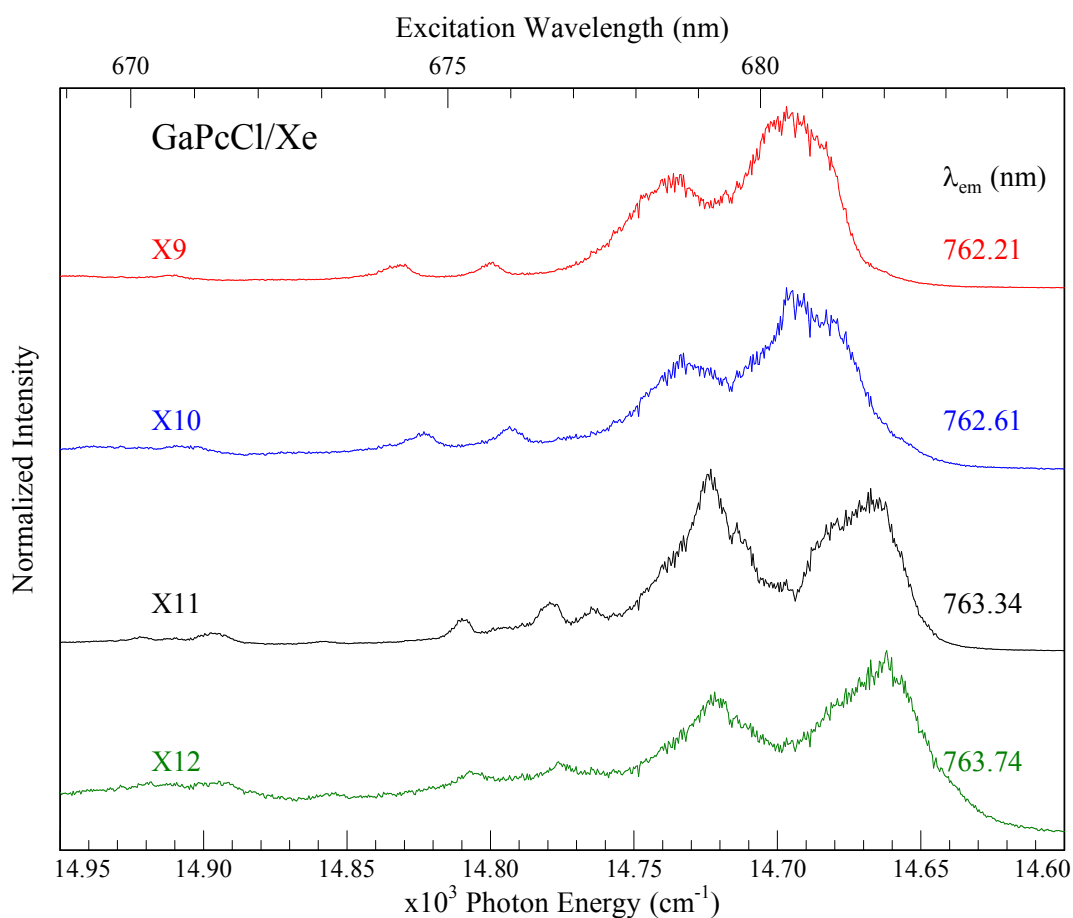


Figure VI.16: A series of excitation spectra of GaPcCl/Xe recorded by monitoring various emission wavelengths. The relationship between the emission wavelength, X_n , and the 2D spectrum is shown in Figure VI.14. The data presented were recorded with the 600 grooves/mm grating.

The blue trace shows the excitation spectrum represented by X10 in Figure VI.14, which monitored the blue wing of the emission band at 762.61 nm. This wavelength intersects the region between the red and blue sites. The spectrum is also dominated by two broad bands, each of which appears to be split into two. The maxima of these bands shift with the maxima of the excitation spectra from X9 and X11, as expected for different sites. While there may be a distinct site present, it is more likely that this spectrum is the result of the overlap of bands from a red and a blue site. Weaker vibronic bands are also present in this spectrum. Consistent with X9, the ZPL cannot be identified in X10.

The spectrum generated by extracting X11 from the 2D-EE plot is shown by the black trace in Figure VI.16. This slice cuts directly through the most intense region of the amplified emission band of the red feature. The spectrum shows comparable structure to that of X9 and X10, but the relative intensities of the two intense bands (centred on 681.6 and 679.2 nm) are reversed and the shapes of the broad bands are different. A narrowing of the intense blue band is observed, as well as the resolution of a new band, located at 679.6 nm. Several weaker and narrower bands are observed to the blue of the two intense bands, most of which were observed in the other excitation spectra. All of the bands are red-shifted with respect to the other sites, as expected for the red site. As was the case with the other excitation spectra in Xe, no sharp ZPLs were observed. The splitting of the excitation bands at 679.2 and 679.6 nm may be indicative of two species being simultaneously excited, similar to what was observed with X10.

The excitation spectrum shown by X12 (green trace) was extracted by monitoring emission at 763.74 nm, at the very red fringe of the AE band from the red feature. This emission wavelength should give the best opportunity to observe the simplest band structure of GaPcCl/Xe because only a single site is excited. Even under these ‘ideal’ conditions, no ZPL is evident in the spectrum. It may be due to the spectrum being recorded with the 600 grooves/mm grating, or it could be intrinsic to the system that no ZPLs can be observed. The spectrum itself looks similar to the other excitation spectra recorded in Xe, with two intense broad bands ($\lambda_{\text{ex}} = 679.3$ and 682.0 nm) to the red and several weaker vibronic bands located to the blue.

The site splitting present in Xe is similar to that of Kr, with two main sites and several weaker ones. A continuum of sites is evident, as changing the excitation wavelengths causes a shifting of the emission bands. Not many of these sites were strongly occupied and very few could exhibit AE. The sites all absorb at wavelengths very close in energy and were difficult to resolve. The lack of sites capable of exhibiting AE between the red and blue features does not mean that they are not present in the matrix; their concentration may be so low that their emission intensity is too weak to be observed compared to the AE from the red and blue features. This result was shown by X10, where the excitation spectrum in this region shows a pair of bands whose splitting matches the excitation bands of X9 and X11, the blue and red sites respectively. As it was difficult to prepare samples of GaPcCl/Xe capable of exhibiting AE, no samples with better resolution were obtained. The

absence of clearly defined ZPLs (and PSBs) indicates that Xe matrices tend to form aggregates of GaPcCl preferentially to trapping single molecules in a given site. This follows the trend set by the other rare gas systems, where Ar tends to trap GaPcCl in highly isolated sites with a moderate amount of aggregates, and Kr contains a lot of aggregate species and less of the monomeric form of the molecule. An interesting experiment would be to prepare a sample of GaPcCl trapped in a solid Ne matrix to examine if this host preferentially forms the monomeric species ahead of aggregates, in line with what was observed with the heavier gases. Unfortunately, due to the low temperatures (~4 K) required to form Ne matrices, this proposed experiment cannot be attempted on the apparatus used in the current work.

This tendency for the heavier gases (Kr and Xe) to form aggregates does not agree with earlier studies on matrix isolated porphyrins, where contrasting behaviour was observed. The previous studies^{6,8,9} were performed on planar molecules, whereas the GaPcCl molecule is known to be non-planar¹⁰, having a protruding Cl atom. This may have an influence on the ability of the heavier rare gas matrices to form highly symmetric sites of isolation. Furthermore, the structures of aggregates of planar and non-planar phthalocyanines are different. Planar phthalocyanines have π - π stacking interactions¹¹, but this arrangement is blocked by the Cl counter-ion in GaPcCl. Instead, an interaction between the Cl atom of one molecule and the C _{α} atom of another can occur in the metal phthalocyanine chlorides. Alternatively, the halogen atom can bridge between two metal atoms of neighbouring GaPcCl molecules¹².

VI.4.II.d: Nitrogen

The 2D-EE plot of the amplified emission region of GaPcCl/N₂ is shown in Figure VI.17. Only one region of intense emission is present in the plot consisting the band at 745 nm. The rich site splitting that was present in the rare gas matrices does not appear to be manifested in N₂. Where the rare gas matrices contained two strongly occupied sites of isolation which could exhibit AE (as well as several weaker sites), N₂ lacks this structure entirely. Two regions in the AE band are evident in excitation; a narrow band around 668 nm (perhaps corresponding to the ZPL in excitation) and a broader region around 665 nm (which is probably the aggregate species). A region of moderate intensity exists between these two maxima, with the intensity dropping off dramatically as the excitation wavelengths move further into the blue.

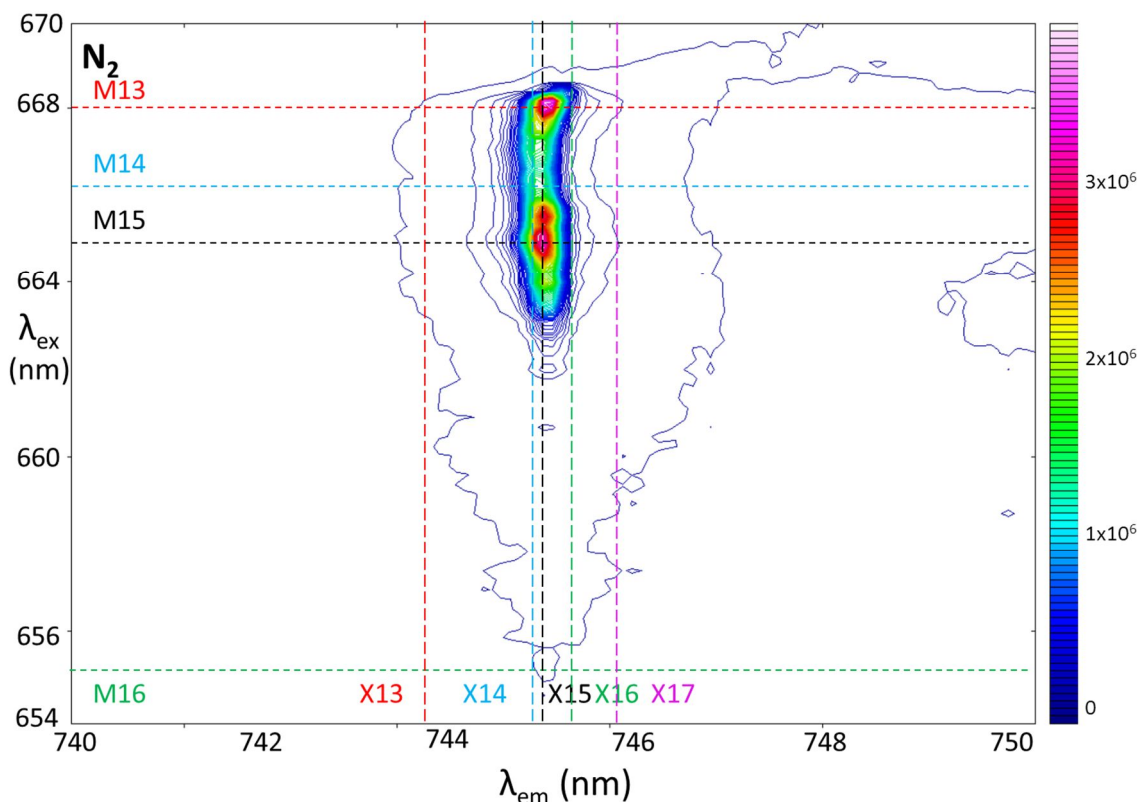


Figure VI.17: 2D Excitation-emission plot of GaPcCl trapped in solid N_2 recorded in the region of the amplified emission band. A number of sites are clearly present. A selection of emission slices (M13 – M16) have been extracted from this spectrum and are shown in Figure VI.18. A selection of excitation spectra (X13 – X17) have also been taken from the spectrum and are shown in Figure VI.19.

A series of emission spectra were extracted from Figure VI.17 labelled M13 – M16 which are shown in Figure VI.18. The emission spectrum represented by M13 is shown by the red trace and is produced with excitation into the narrower of the intense excitation regions. A single peak dominates the emission spectrum at 745.09 nm, indicative of a single site exhibiting AE with this excitation wavelength. The blue trace shows M14, which passes through the region between the two most intense AE regions on Figure VI.17. A single emission band centred on 745.06 nm is observed in this spectrum, similar to M13. No asymmetry is observed on the curve at this excitation wavelength, indicating only a single site has been excited. A very slight shift between the maxima of M13 and M14 is noted, which works out to be 0.75 cm^{-1} .

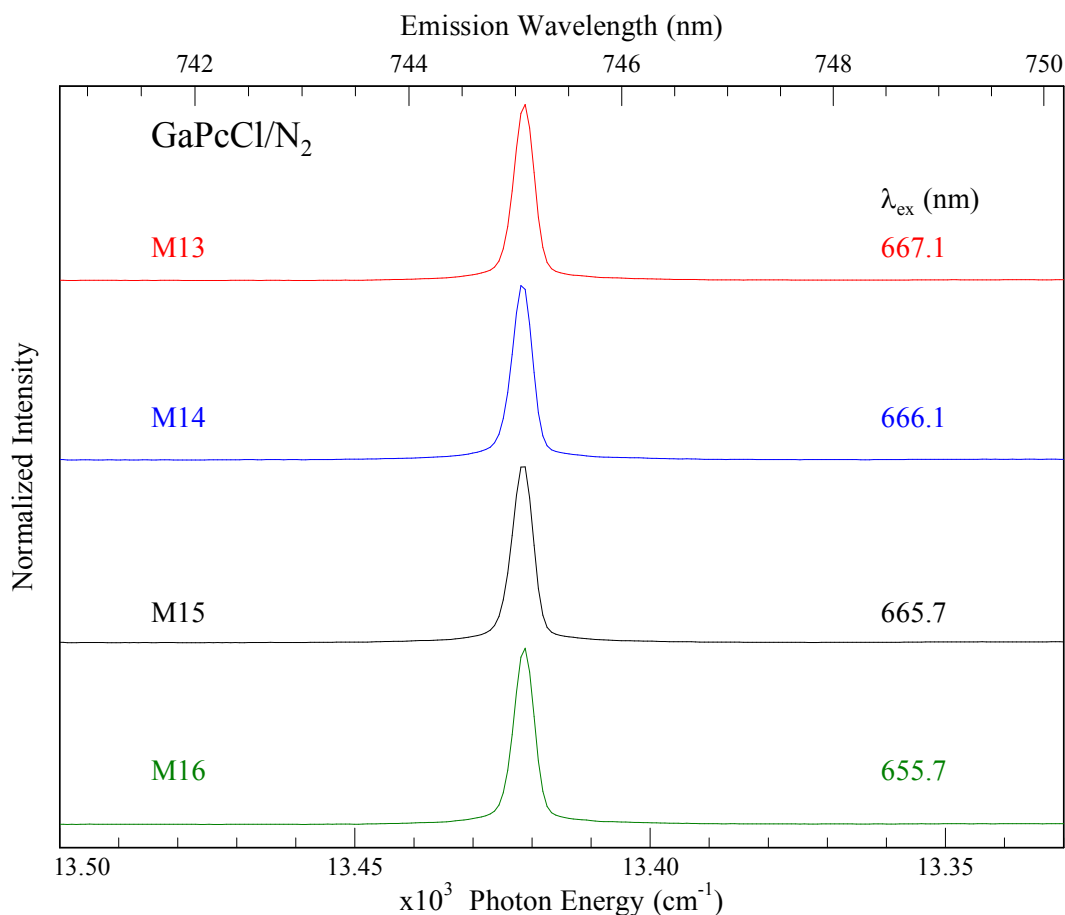


Figure VI.18: A series of emission spectra of GaPcCl/N₂ recorded with different excitation wavelengths. The relationship between the excitation wavelength, Mn , and the 2D spectrum is shown in Figure VI.17.

The spectrum obtained by extracting M15 is shown by the black trace. This spectrum is very similar to that shown by M14, with a symmetric band indicating a single site excitation and an identical position of the band maximum. The green trace shows the emission spectrum represented by M16, which is located to the blue of the amplified emission region. An almost identical emission profile to M13 is observed. The only difference between the two spectra is the intensity of the band (the maximum of M13 is about 10 times that of M16), although this is not apparent in Figure VI.18, as the intensities of the bands have all been normalized.

Figure VI.19 shows a series of excitation spectra generated by taking slices through various emission wavelengths from Figure VI.17. X13 is a slice taken on the blue edge of the AE band ($\lambda_{em} = 743.53$ nm), and is shown by the red trace. The spectrum contains one

strong band around 667.8 nm and a pair of broad unresolved bands to the blue of this region. A hint of some structure on the strong band is evident, but due to the low intensity, may be noise. A weak side band located to the red of the main excitation band is observed, but cannot be definitively assigned.

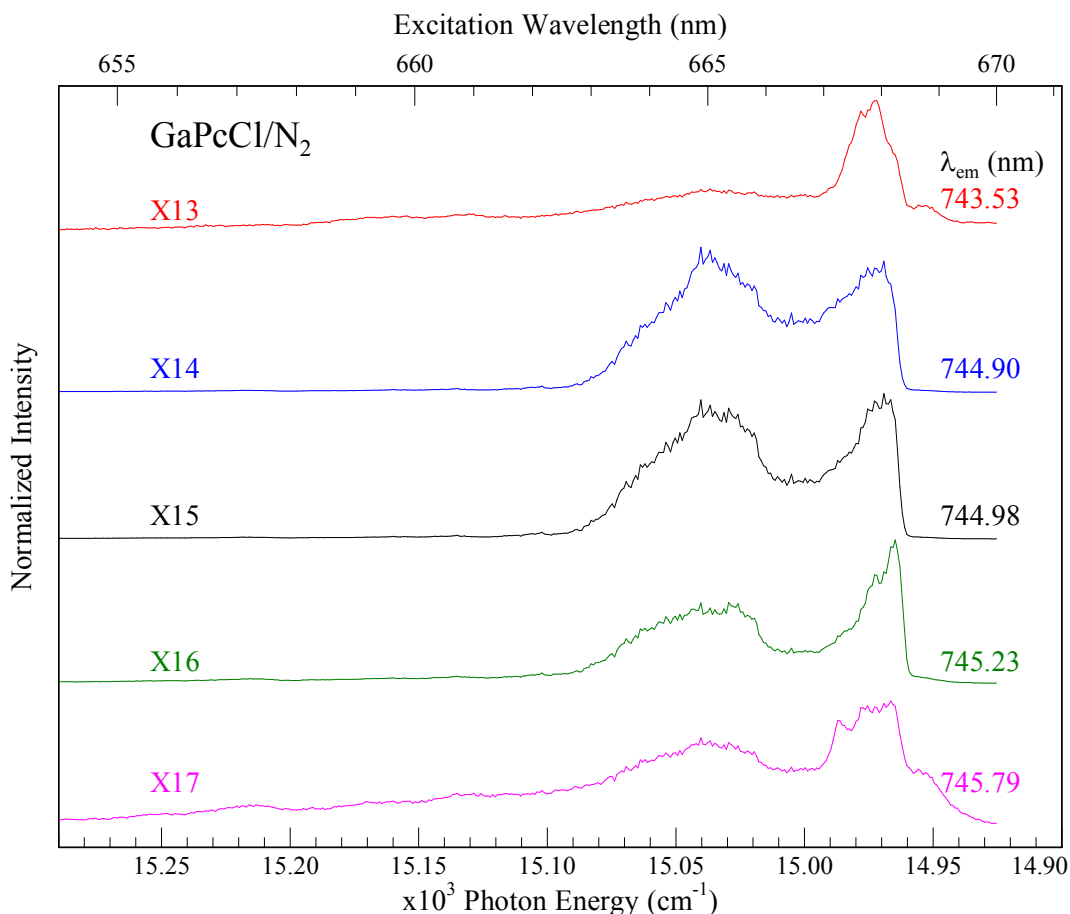


Figure VI.19: A series of excitation spectra of GaPcCl/N₂ recorded by monitoring various emission wavelengths. The relationship between the emission wavelength, X_n, and the 2D spectrum is shown in Figure VI.17.

The slices through X14 and X15 ($\lambda_{em} = 744.90$ and 744.98 nm respectively) are shown by the blue and black traces. These spectra show excitation spectra of the most intense region of the AE band. These excitation spectra were extracted for emission wavelengths separated by ~ 1 cm⁻¹, which is similar to the splitting observed for the two sites showing AE. The two excitation spectra are very similar, showing two regions of strong intensity (667.99 and 665.02 nm). These bands correspond to the two regions of high intensity in Figure VI.17 and are the only regions to show amplified emission in this matrix. The

feature at 667.99 nm shows a sharp rise in intensity on the red side of the band, which may be indicative of it being a ZPL. The broadness of the band is not what one would expect to see for a ZPL, however. A possible reason for the broadness of this may be due to the presence of multiple sites. Certainly the fluorescence spectra pointed to there being several sites located very close in energy, and this may also be manifested in excitation. While a ZPL is not distinct, it may be the case that a series of ZPLs from numerous sites are present but unresolved, which causes the broadening of the band. The other excitation band in X14 is centred on 665.02 nm and probably originates from an aggregate species based on its broadness. No weak bands to the blue are observed in either X13 or X14, indicating that the vibronic bands in excitation do not exhibit AE. The weak red band suggested to be a hot band in X13 does not manifest itself in either X14 or X15. Slice X16 (green trace) was taken at the most red region of the intense AE ($\lambda_{em} = 745.23$ nm). This spectrum appears the most narrow in the region where the ZPL is expected to occur, a set of three partly resolved bands is observed. These bands are centred at 668.2, 667.9 and 667.4 nm. The broad band which has been assigned as the aggregate species is present at ~665 nm. Otherwise the spectrum is very similar to X14 and X15.

Slice X17 (pink trace) is taken at the extreme red edge of the AE band ($\lambda_{em} = 745.79$ nm). This spectrum is similar to X13 in terms of its intensity, but more similar to X14 and X15 in relation to its structure. The spectrum shows the two strong bands related to the amplified emission, but also shows the weaker bands to the blue and the aggregate band to the red which were observed in X13. There also appears to be additional, partly resolved features in this spectrum around 667.1 nm, which may be similar to the three bands observed in X16.

The number of sites present in GaPcCl/N₂ matrices is difficult to elucidate, even using high resolution 2D-EE scans with laser excitation. The narrow line widths of the amplified emission bands were not sufficient to resolve individual sites, with the possible exception of the spectrum shown by X16. Based on the emission and AE spectra it is probable that there are several major sites of isolation in N₂ matrices, with a splitting of only 0.75 cm⁻¹. This is too small to be resolved under the current experimental conditions. This result was consistent over a range of different deposition conditions and did not show any changes upon annealing the matrix. The lack of any fully resolved ZPLs in excitation is quite similar to what was observed in Xe matrices. The difference in N₂, however, is that there is

evidence of several ZPLs located very close together in energy in the excitation spectra. These ZPLs are all located between 667.2 and 668.2 nm, which is a range of about 22 cm^{-1} . This evidence of phonon structure in excitation is not backed up in the emission data. The site splitting in N_2 is not entirely analogous to that in the rare gases, as there are no well-defined red and blue sites in N_2 matrices.

A study on the structurally related molecules H_2Pc and ZnPc by Dozova *et al.*⁶ showed that nitrogen matrices trapped these molecules in a large number of sites, similar to what was observed with GaPcCl/Ar in this study. The complete reversal of site splitting in N_2 was a surprise but may be explained by structural factors; H_2Pc and ZnPc are both planar molecules, whereas GaPcCl is non-planar owing to the Cl^- counter ion. This may have an effect on the type of sites the N_2 matrix can form.

VI.4.II.e: Matrix Summary

Figure VI.20 provides a comparison of the 2D-EE plots in the AE region of GaPcCl in the four matrices used in the present study. The plot shown in the top left of Figure VI.20 shows GaPcCl trapped in solid Ar. This matrix shows the richest spectroscopy of any of the hosts used in the current study. Two major sites of isolation dominate in this matrix, with the vibronic bands associated with AE located at 745.1 nm (blue site) and 747.2 nm (red site). The red and blue features are split by 38 cm^{-1} . The region between the red and blue sites is filled with sites of lower concentration, forming a continuum of amplified emission bands. The top diagonal band of high intensity corresponds to the ZPLs from the continuum of sites. Immediately to the blue of this narrow band lies a pair of features which have been assigned as aggregate species due to their relative broadness in comparison to the ZPLs. At shorter excitation wavelengths ($\lambda_{\text{ex}} = 664 - 656\text{ nm}$) vibronic structure is clearly evident for the red site.

The top right plot of Figure VI.20 shows the Kr data, which looks quite similar to the Ar data in that two main regions are evident. The main difference between the two systems is the diminished intensity of the narrow ZPL region in the Kr data. In Kr, two main emission bands dominate; one coming from a blue site at 751.6 nm and the other from a red site at 754.1 nm. The two main features are split by 44 cm^{-1} . The sites located between the red and blue sites do not exhibit AE as strongly as the corresponding bands in Ar, indicating these sites are not as strongly occupied in the Kr matrix. This is a property that is

consistent throughout the matrix, as the excitation spectra show AE can be exhibited with many bands to the blue of the 0-0 in emission in Ar, whereas Kr is primarily excited in the region very close to the 0-0. This is probably due to GaPcCl/Kr samples often having a lower ODs compared to the Ar samples prepared.

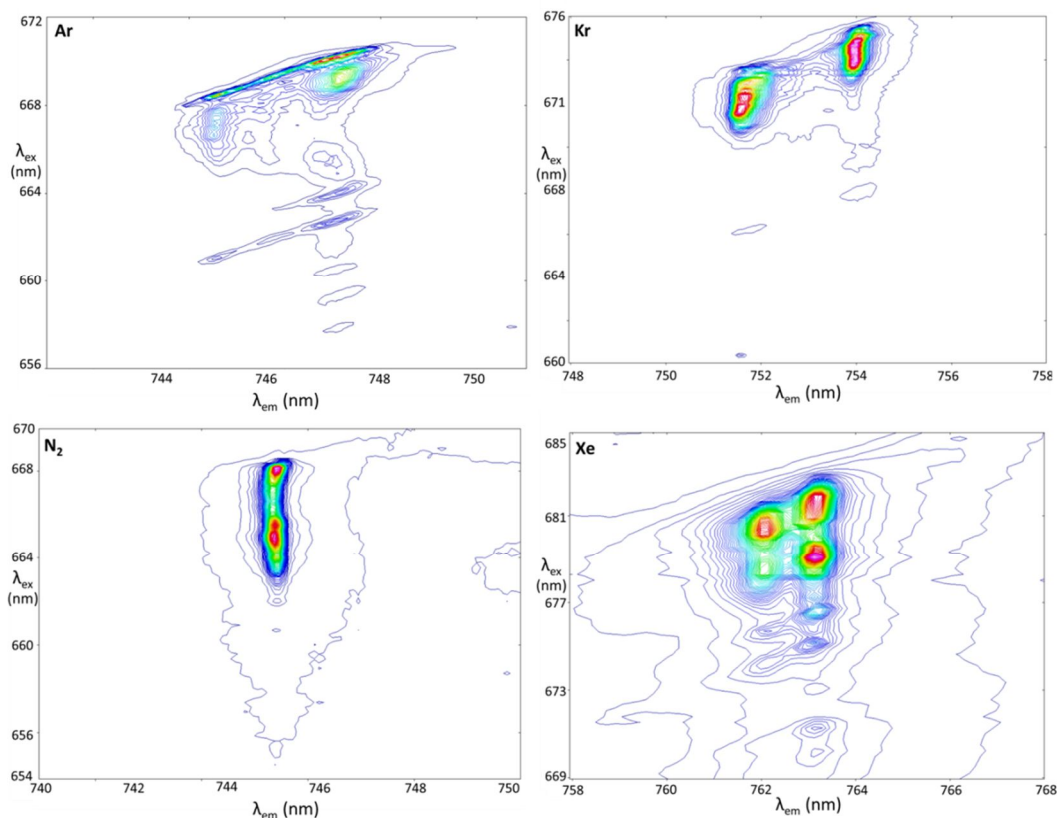


Figure VI.20: 2D-EE spectra of GaPcCl isolated in various inert gas hosts. The region shown in each matrix is centred on the vibronic band(s) at 1540 cm^{-1} above the band origin(s) which is responsible for amplified emission.

The bottom right panel shows the results obtained in the Xe matrix. The spectrum looks almost like a compressed version of the Kr data, having two regions of high intensity (originating from AE from the vibronic band at 1547 cm^{-1}), a blue site at 762.1 nm and a red site at 763.2 nm , corresponding to a splitting of 19 cm^{-1} . The splitting between the two sites in Xe is about half of that of the two main sites in Ar and Kr. The Xe plot also lacks the ZPL region that was observed in Ar and Kr, a possible indication that aggregate formation is predominant in this host. The presence of other sites was also observed in Xe, but these sites were difficult to resolve, partly due to how close in energy they are situated. Vibronic bands are evident from $677\text{ to }669\text{ nm}$, reminiscent of Ar.

The bottom left panel of Figure VI.20 presents the 2D-EE plot of GaPcCl isolated in N₂. At first glance this appears to be the simplest of all the matrices, with only a single amplified emission band, located at 744.9 nm. However, by taking a closer look at the emission and excitation slices through this spectrum (Figure VI.18 and Figure VI.19 respectively) it was determined that there were at least two sites of isolation, split by only 0.75 cm⁻¹. The SP-500i monochromator, with the 1200 grooves/mm grating, can achieve a resolution of 0.04 nm, so these sites were not fully resolved. This is consistent with the results in emission (Figure V.26), where only a single set of bands in the fluorescence spectra was observed, but there is evidence for multiple sites being present in the form of shoulders appearing on the emission bands with certain excitation wavelengths. A vast difference of the site splitting observed on the AE band between the molecular matrix, N₂, and the rare gas matrices Ar, Kr and Xe is clearly present. An earlier study performed by Dozova⁶ on H₂Pc and ZnPc show that N₂ matrices isolate these molecules in many sites spread over a wide wavelength range in emission, similar to what happens with GaPcCl in Ar matrices.

A series of emission slices taken through the 2D-EE plots have been plotted side-by-side in Figure VI.21 and Figure VI.22. These plots aim to highlight the differences in the site splitting of the matrices. Figure VI.21 presents amplified emission bands obtained with various excitation wavelengths of GaPcCl trapped in solid N₂ (left panel) and Ar (right panel). The emission wavelengths are taken from M13 – M16 for N₂ and M1 – M4 for Ar. This plot is complementary to Figure V.52, which shows the sites in fluorescence from N₂ and Ar. The N₂ AE spectra show two sites of isolation capable of exhibiting AE, separated by only 0.75 cm⁻¹. Each emission ‘slice’ through the 2D spectrum shows only a single band, indicating that only one site is excited at any given time, or if both are excited together their bands are overlapping and unresolved. Amplified emission in the Ar matrix is the complete opposite, with many sites of isolation all exhibiting AE, and being spread far enough apart for each site to be fully resolved. The splitting of the two most intense AE bands is 38 cm⁻¹, which allows several bands to be resolved in between. Excitations can excite either a single site (M1 for example), or many sites whose absorption bands overlap (M2 and M3). Many sites can therefore be observed on a single spectrum.

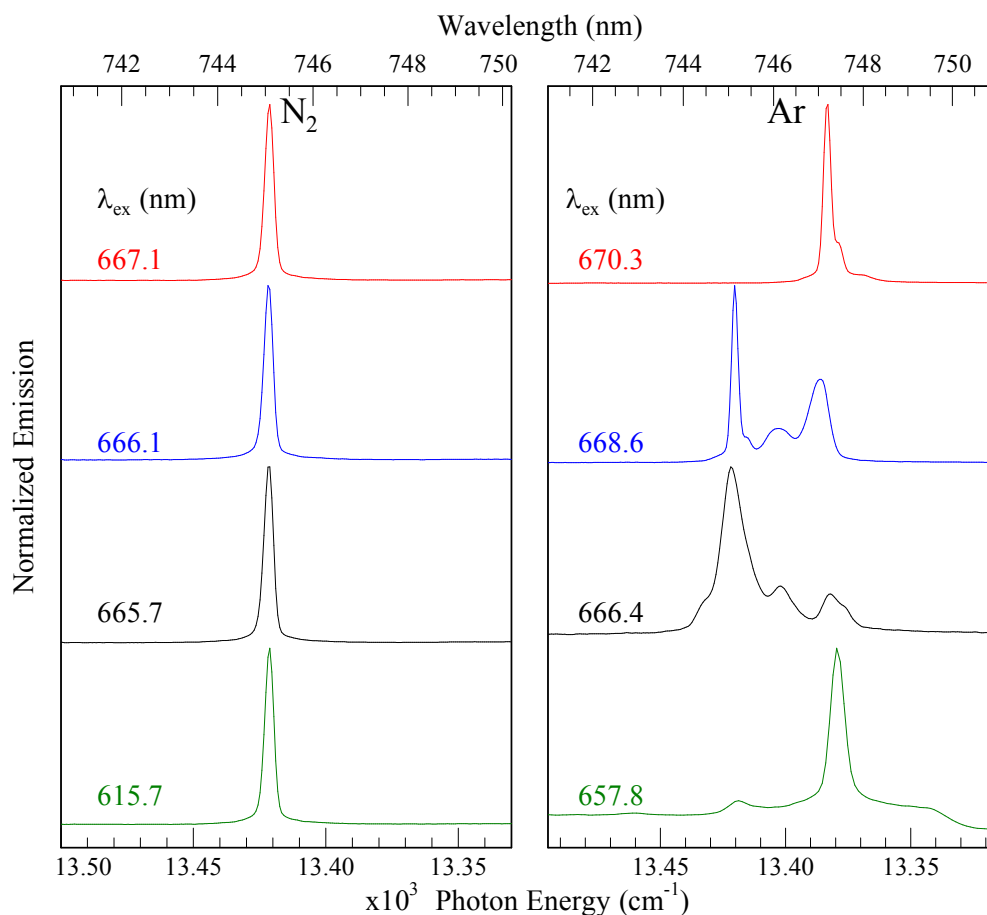


Figure VI.21: Emission slices of GaPcCl in N₂ (left panel) and Ar (right panel) recorded at the specified excitation wavelengths. The regions shown are located around the amplified emission bands in each matrix.

The AE spectra of Kr (left panel) and Xe (right panel) are shown in Figure VI.22 where some interesting observations can be made. The Kr data resembles the Ar system most closely, with two sites dominating in the matrix, split by 44 cm⁻¹. Several sites are observed to occupy the region between the two main sites. Excitation with different wavelengths can produce AE from either a single site (black trace) or from numerous sites (red and blue traces). This can be achieved by selecting a wavelength that overlaps with a strong absorption band of only one of the sites, or with many sites.

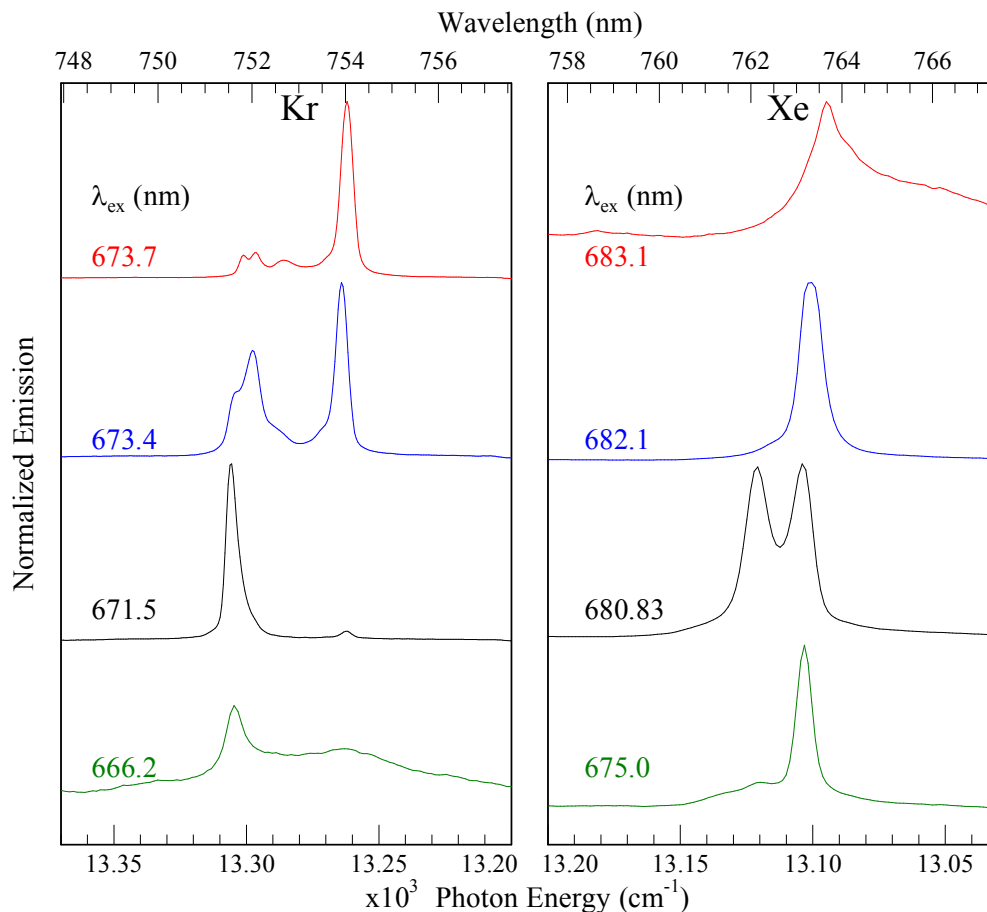


Figure VI.22: Emission slices of GaPcCl in Kr (left panel) and Xe (right panel) recorded at the specified excitation wavelengths. The regions shown are located around the amplified emission bands in each matrix. The Xe data were recorded with the 600 grooves/mm grating while the Kr was recorded with the 1200 grooves/mm grating.

Xe is similar to Ar and Kr, but does not contain quite as rich a site splitting as either. The two main sites in Xe are split by only 18 cm^{-1} , and no sites can be observed occupying the region between the two AE bands of these sites. The splitting is such that the two bands cannot be fully resolved under the current experimental conditions. Some sites are observed to the blue of these main sites, but can only weakly exhibit AE, and cannot be fully resolved either. Nevertheless, some resolution can be achieved on the red site by selectively exciting into one of its absorption bands that does not coincide with an absorption band of the blue site ($\lambda_{\text{ex}} = 682.1 \text{ nm}$). The Xe sample is similar to Ar and Kr in some ways, but unique in others. The shape of the Xe atom is the same as the other noble gases, but its van der Waals radius¹³, and hence lattice parameter is larger, at 6.1 \AA compared to 5.3 and 5.6 \AA for Ar and Kr respectively. This increased atomic radius will

have an effect on the size of the trapping sites that it can form and this may explain the different site splitting in this matrix.

An analysis of the excitation spectra of the AE bands in each matrix showed that the choice of host can have a dramatic effect on the features present in a sample. Ar matrices tend to exhibit sharp ZPLs for all of its sites in excitation, as well as a defined PSB. The excitation structures to the blue of the PSB have been assigned as aggregate species based on their broadness and lack of structure. Kr matrices also exhibit a sharp ZPL for some emission bands, but not all of them. The corresponding PSBs were not easily detected. The broad feature which was assigned as an aggregate in Ar is clearly present in Kr matrices and dominates the excitation spectrum. This indicates that Kr allows a greater degree of aggregation than Ar. Xe matrices do not exhibit any well-defined ZPLs in excitation, indicating the monomer species is not easily isolated in this but instead show only the broad excitation band which was dominant in Kr and present in Ar. This suggests that the larger host materials allow for aggregation to occur more easily than the smaller ones. A study of this effect in a Ne matrix would be useful to see if this trend is maintained. The N₂ matrix was different in excitation to the rare gas matrices. While no resolved ZPLs were observed, evidence for partly resolved features indicate that several sites are present located very close in energy. While the sites in the rare gas matrices were spread out over an emission range of 40 – 50 cm⁻¹, all of the sites in N₂ appear to be located to within 2 cm⁻¹ of one another. The broad aggregate feature was also present to the blue of the ‘ZPLs’ in excitation, indicating that aggregates are easily formed in all hosts.

The source of the aggregates makes for an interesting discussion. The AE of the planar phthalocyanines H₂Pc and ZnPc⁶, as well as the structurally related molecules H₂TBP⁹ and H₂TAP⁸ have all been studied in inert gas matrices. None of these studies reported the existence of phonon structure, which has been observed for GaPcCl in the rare gases. Furthermore, these molecules appear to preferentially form the isolated monomer, whereas GaPcCl can form high amounts of both the monomer and aggregate species in the matrix. The predominant force of attraction for the planar molecules will be π - π stacking, due to the conjugation of the macrocycles. This is clearly not a strong enough force to cause the preferential formation of aggregates in the matrix based on the previous studies mentioned above. The GaPcCl molecule cannot undergo π - π stacking interactions because it is non planar due to the presence of the Cl atom. However, this atom gives the molecule a strong

electric dipole moment. The magnitude of the dipole moment has been calculated in the current work to be 3.6163 Debye from the DFT results. A depiction of the charge of the molecule is given in Figure VI.23. The dark atoms in this diagram have close to a neutral charge. The bright red atoms (i.e. the pyrrole nitrogens and the chlorine) are negatively charged and the bright green Ga atom is positively charged. The direction of the dipole moment is shown by the blue arrow. Interactions between the negatively charged Cl atom and positively charged Ga atom of neighbouring molecules will produce a strong electrostatic attraction which may be the reason aggregates form so easily in the matrix. A complementary calculation on ZnPc shows it to have no permanent dipole moment, indicating that the only forces of attraction between neighbouring molecules will be the weaker π - π stacking.

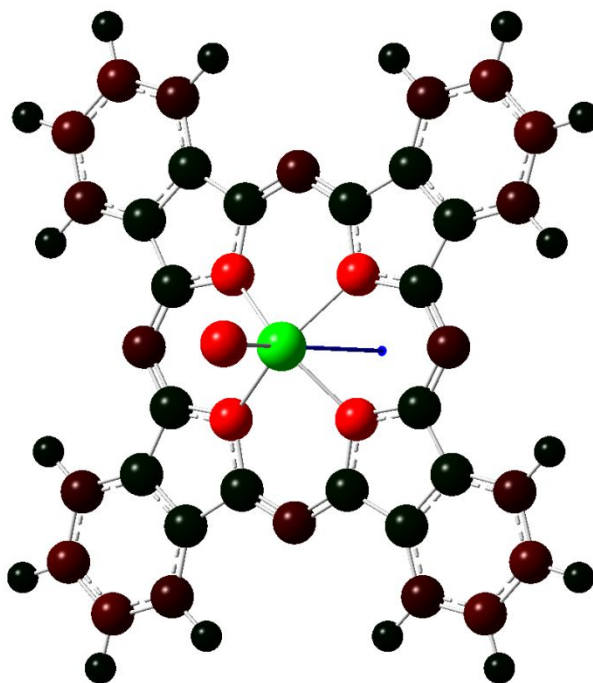


Figure VI.23: Depiction of the electric dipole moment of GaPcCl predicted by DFT calculations. The brighter atoms have a greater electrostatic charge than the darker atoms. The blue arrow shows the direction and magnitude in which the dipole moment ($\mu = 3.6163$ D) is orientated.

VI.4.III: Temperature Effects

An investigation into the thermal stability of the AE bands of GaPcCl/Ar is presented in Figure VI.24. The left panel shows the intensity of a set of fluorescence bands and the right panel shows the AE bands at a range of different temperatures between 12 K and 24 K. As

the temperature increases the structure and the intensity of the fluorescence bands remain fairly constant. The AE bands, in contrast, change quite clearly with respect to temperature. At 12 K (black trace) three resolved bands are present in the spectrum, originating from three distinct sites of varying intensities. At 16 K (green trace) the blue band appears fairly stable, the middle band is clearly showing less intensity than at lower temperatures and the red band is also beginning to show a drop in intensity. When the temperature has reached 20 K (pink trace) the blue band has also started to lose some of its intensity. The middle band has disappeared completely, indicating AE has been ‘switched off’ for this site. The red site is still diminishing in intensity. By 24 K (purple trace) the intensity of both remaining bands has dropped further, but the red band is probably close to being switched off. No temperatures higher than 24 K were attempted due to approaching the melting point of the host material. A curious effect is observed upon cooling the sample back down to 10 K (grey trace); the intensities of the red and blue sites have interchanged, perhaps indicating that the red aggregate feature is more thermally stable than the blue monomer feature.

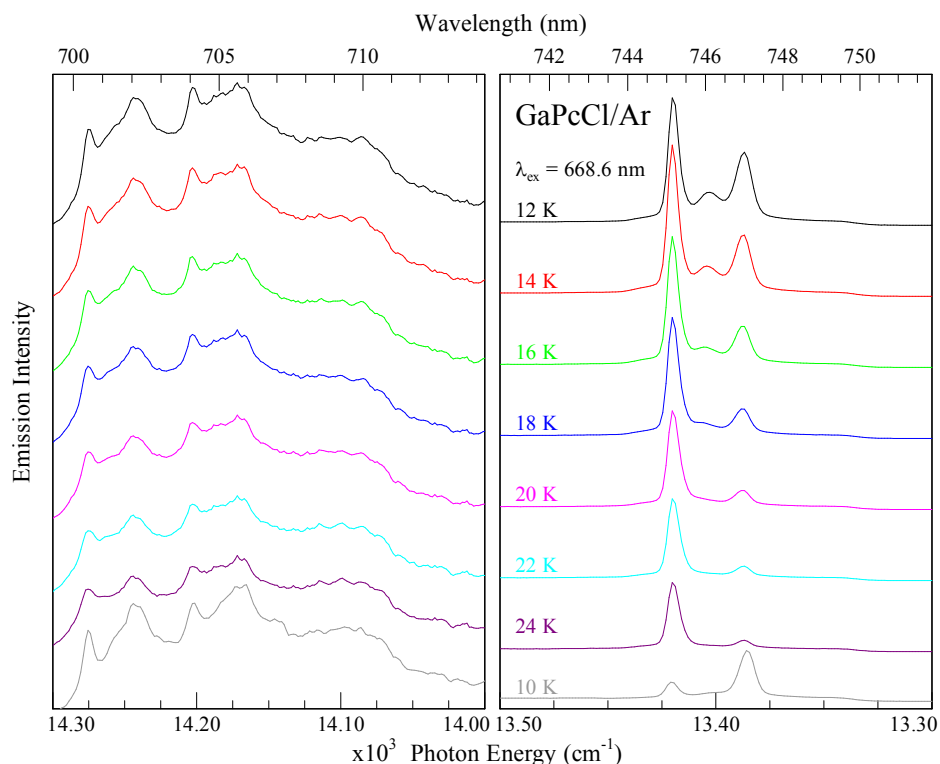


Figure VI.24: The effect of sample temperature on the intensity of fluorescence (left panel) and amplified emission (right panel) of GaPcCl/Ar obtained with excitation at 668.6 nm. The 10 K spectrum (grey trace) was recorded after the sample was cooled back down.

Nitrogen matrices, which show two AE bands (split by 0.75 cm^{-1}) exhibited a curious affect upon annealing; the red AE band moved to the blue as the temperature increased from 10 K to 24 K, as shown in Figure VI.25. It returned to its original position when the temperature was cooled back down to 10 K. The location of the AE band moves from 745.06 to 744.66 nm. This represents a shift of 7.2 cm^{-1} , much larger than the site splitting observed in the matrix at 10 K. The left panel of Figure VI.25 indicates that the same process is occurring with the fluorescence bands also. The intensity of the AE band was diminished by 4.3 % upon heating, in contrast to what was observed for Ar in Figure VI.24, where the intensity of the bands was reduced considerably. The origin of this effect may be that the N_2 matrix is becoming softer at higher temperatures leading to a small change packing structure¹⁴ around the GaPcCl molecule, and then returns to its original state when the temperature is cooled back to 10 K. Unfortunately, even with the migration of the AE band with increasing temperature, only one peak is observed throughout the entire process, so the full extent of the N_2 temperature site splitting cannot be elucidated in this manner.

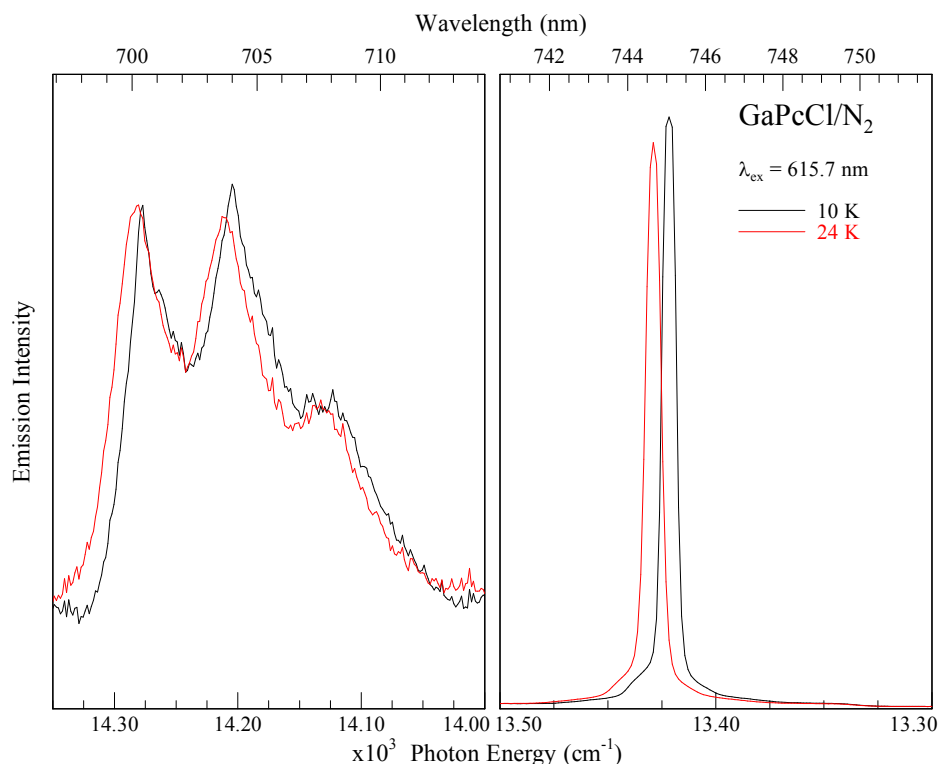


Figure VI.25: Temperature effects on the fluorescence (left panel) and AE (right panel) spectra of GaPcCl/ N_2 . As the temperature of the sample window is increased from 10 K to 24 K, the location of the emission bands move to the blue. The spectra recorded at the intermittent temperatures have not been shown for clarity. The reverse process was observed on cooling the window back to 10 K.

A similar set of temperature dependence experiments have been performed in Kr and are shown in Figure VI.26. The results show some similarities to N₂, and some similarities to Ar. The emission bands exhibit a blue shift as the temperature increases, just as was observed in N₂. The other effect being observed is the change in the relative intensities of the red and blue features. At 10 K (black trace) the intensity of the red feature is greater than that of the blue. The blue feature is also quite broad, indicating it is part of the aggregate species.

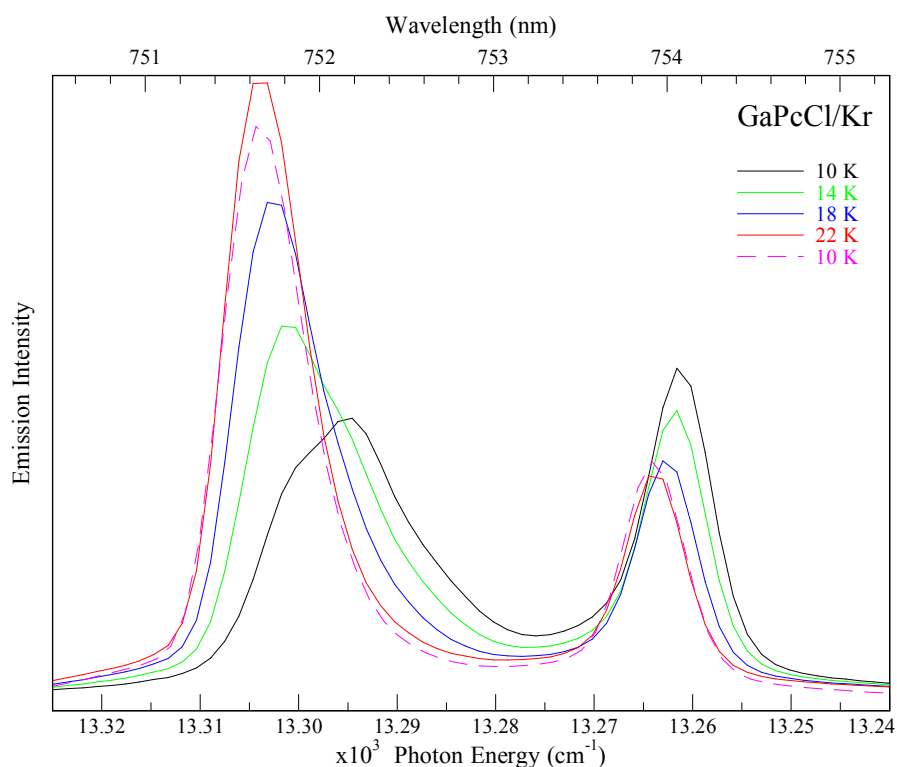


Figure VI.26: Emission spectra AE bands of GaPcCl/Kr recorded at the specified temperatures. The solid lines represent spectra recorded at the specified temperatures during the annealing process. The dashed pink line represents a spectrum recorded when the sample was cooled back down to 10 K.

At 12 K (green trace) the intensity of the red feature has diminished slightly and has shifted slightly to the blue. The blue feature shows an asymmetry on the band, possibly the partial resolution of another site. Its intensity has increased and position has shifted to the blue. At 18 K (blue trace) the red feature continues the pattern of losing some of its intensity and getting shifted further to the blue. The blue feature has now lost its asymmetry and the band width appears narrower than in the lower temperature spectra. The intensity of the band is significantly greater at 18 K than at 10 K. At 22 K (red trace) the trend continues

for both features. The growing intensity of the blue feature coupled to the diminishing intensity of the red feature may indicate that the two species are connected, with the red site transferring its intensity to the more thermally stable blue site. The positions of the maxima of the red site are 13262 and 13264 cm^{-1} at 10 and 22 K respectively, which coincides with a shift of 2 cm^{-1} . The corresponding locations for the blue sites are 13295 and 13305 cm^{-1} at 10 and 22 K respectively, which is a shift of 10 cm^{-1} . The two features present at 22 K are present when the temperature is returned to 10 K. The intense blue band at 13262 cm^{-1} does not return to the unresolved structure observed in the black trace of Figure VI.26, and its position does not shift. This means that the most stable site has been formed during the annealing process. The red feature remains the same when the temperature is brought back to 10 K. This result indicates that there are two highly stable species in the matrix that are related to one another. The two broad bands observed in the 2D-EE plot in Figure VI.11 are probably aggregates, and the gap between the features may be due to Davydov splitting. This is similar to the Ar system, where the red and blue aggregate features show temperature dependence.

Annealing of an Ar sample exhibiting a continuum of sites also led to an interesting result. Figure VI.27 shows a 2D-EE plot of the AE observed in an Ar sample before and after annealing. The deposited sample shows a continuous region of colour, all of which corresponds to different sites exhibiting amplified emission. There are two major sites either side of this continuum which carry most of the AE intensity; namely 745.1 nm and 747.2 nm. A broad feature below the red site shows moderate intensity, and was earlier (tentatively) assigned as an aggregate species. Following annealing to 24 K the 2D-EE scan was performed again under identical conditions. The interesting result is that, while much of the intensity is lost, almost all of the intensity has transformed into the red aggregate species, with a small amount of intensity remaining in the red and blue sites and almost nothing remaining of the continuum of sites (or at least not enough to reach the threshold for amplified emission). The initial scan shows that all three sites are highly occupied, and two have almost equal abundancies; the blue site (745 nm) has about 87 % the intensity of the red site (747 nm). The middle site is obviously weaker, but still carries a significant intensity of about 60 % of the red site.

Following annealing of the sample, there is a shift in the relative intensities of these bands; the blue band is now only about 27 % as intense as the red band, and the middle band is

even lower at 13 %. It appears that amplification has in fact switched off for this site, as the number density has fallen below the threshold for stimulated emission – in fact this appears to be the case for all of the AE bands associated with the continuum of sites observed in the deposited sample. The dramatic change in the structure of the sites after an annealing process indicates that there is one predominantly stable site – the red site – and a number of less stable sites that are only occupied on deposition. The heating process transforms the arrangement of the matrix, and appears to promote aggregation.

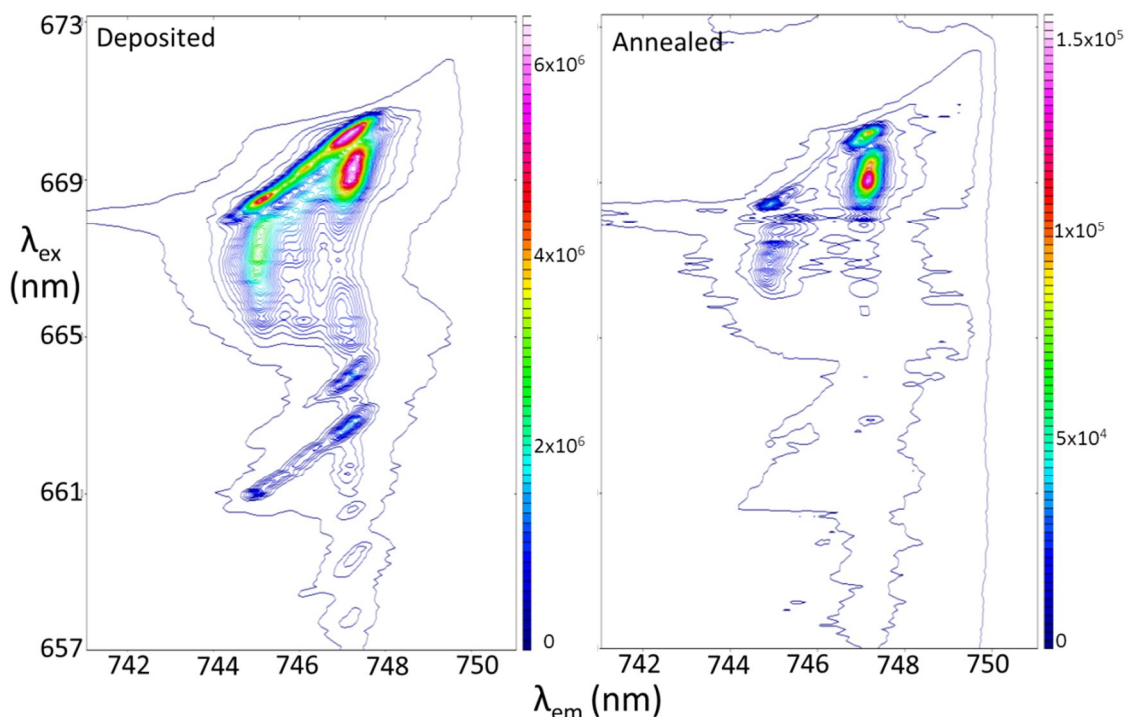


Figure VI.27: 2D Excitation-emission plots of GaPcCl in Ar recorded at 10 K. The plot on the left has been recorded after deposition and the plot on the right after annealing to 24 K. These spectra were recorded with the 600 grooves/mm grating installed in the monochromator.

A series of emission slices with excitation wavelengths M1 – M4 are presented in Figure VI.28 for the deposited and annealed samples of GaPcCl/Ar. The effect of annealing clearly has a significant effect on the sites in the matrix which can be seen from the differences in the AE bands present with the various excitation wavelengths. The red traces show excitation into the 0-0 band in absorption. This has been shown in earlier figures to exhibit emission from a single site at 747 nm and is no different in Figure VI.28. Emission from the shoulder to the red of the AE band (possibly from the PSB of another site) in the

deposited spectrum is not evident in the annealed sample. This may indicate that these weaker sites have been rearranged to that of the dominant red site, or have formed aggregates.

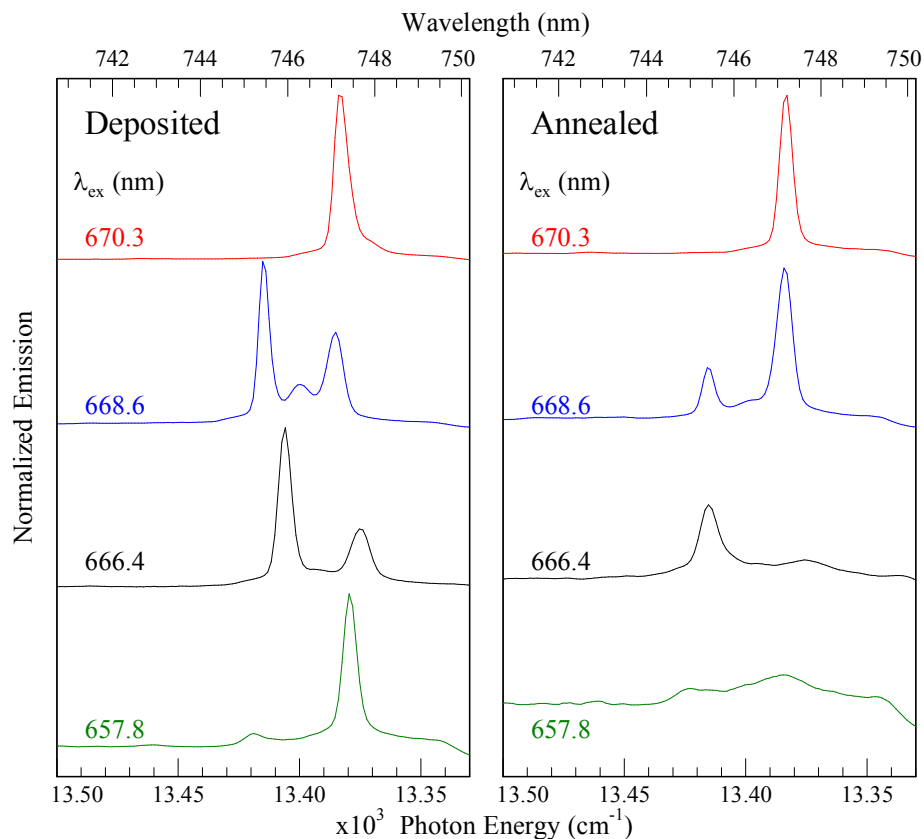


Figure VI.28: Emission slices extracted from the 2D-EE plots presented in Figure VI.27, which show GaPcCl/Ar before and after annealing. The emission wavelengths match those of M1 – M4. These spectra were recorded with the 600 grooves/mm grating installed in the monochromator.

The blue traces show excitation at 668.6 nm (M2) and display the most dramatic effect of annealing. A reversal of the intensities of the AE bands from the red aggregate and blue site (located at 747.06 and 745.47 nm respectively) occurs after annealing. This indicates a significant restructuring of the sites in the matrix upon a heating and cooling cycle of the sample window. The intensity of the aggregate emission is weaker than that of the blue site in the deposited sample. Most of the emission intensity is either lost or has shifted to the aggregate species after annealing. This restructuring is also evident in the 2D-EE plot, where the AE band of the blue site changes from being one of the most intense bands in the deposited sample to being just above the fluorescence intensity in the annealed sample.

The AE band of the site located at 746.28 nm loses much of its intensity upon annealing. This may be due to the matrix softening at high temperatures and allowing the GaPcCl molecules to diffuse and, due to the large dipole moment on the molecule, preferentially form aggregates in the more thermally stable red feature. The black traces ($\lambda_{\text{ex}} = 666.4$ nm) also show an interesting effect on the emission before and after annealing. AE from the red site appears to have switched off completely after annealing. The AE band at 745.95 nm on the deposited sample has shifted to 745.39 nm after annealing (a shift of 10.2 cm^{-1}), and also carries much less intensity.

The green traces ($\lambda_{\text{ex}} = 657.8$ nm) indicate that AE has been completely switched off in the annealed sample at this excitation wavelength. As the intensity of the emission has been shown to decrease after annealing, it is unsurprising that excitations into the vibronic bands no longer yield AE. The two bands present in the deposited sample are still evident, but are broader and much weaker. This is a good indication that normal fluorescence is again being observed.

VI.4.IV: Matrix Influences on the Amplified Emission of GaPcCl

VI.4.IV.a: Argon

Emission of GaPcCl recorded in Ar was notable for its sharp bands and a well-defined 0-0 transition. Excitation into the 0-0 in absorption gave the simplest fluorescence with a single set of emission bands, as shown in Figure V.5. Excitation into the blue produced a 'doubling' of the observed emission bands. Emission from the 0-0 of the 'blue' site can be reabsorbed by the red site causing a second set of emission bands to appear in the spectrum. The location of the of the 'blue' emission bands changes with respect to the excitation wavelength, indicating multiple sites are present in the matrix. High concentration samples also showed amplified emission on the vibronic band measured to be 1540 cm^{-1} above the band origin (747.2 nm from the red site). Due to the absorption and emission spectra showing evidence of many sites of isolation, high concentration samples could also exhibit amplified emission from a large number of well occupied sites. Figure VI.8 and the Figure VI.9 demonstrate the different sites in Ar that can exhibit AE. The three major sites responsible for AE emit at 745.1, 746.1 and 747.2 nm. Several more AE bands were observed in this matrix, but they were all weaker than the three mentioned above. The fact that so many bands exhibit the property indicates a high density of

molecules occupying many different sites and a very efficient method for exciting into Level 2 of the energy level diagram shown in Figure VI.6.

The excitation spectra recorded in Ar exhibited the most resolved features in any matrix for both the regular fluorescence bands and the AE bands. The spectra shown in Figure V.9 and Figure V.12 show the shifting of the location of the 0-0 in excitation of a number of fluorescence bands and AE bands respectively. These shifts are due to the presence of many sites in the matrix. In all instances there is a well-defined sharp peak corresponding to the zero phonon line. The phonon side band was evident for the most abundantly occupied sites. The very weak phonon coupling ($S = 0.2$) is responsible for the complicated emission spectra recorded with excitations to the blue of the 0-0, as discussed in Chapter V. Vibronic bands extended up to 1000 cm^{-1} in excitation, some of which were capable of exhibiting AE.

A pair of strong features is evident in the 2D-EE spectrum which manifest as broad bands in both emission and excitation. The locations of the maxima of the red and blue features, which have been assigned as aggregate bands, are located at $\lambda_{\text{em}} = 747.22$ and 745.11 nm respectively. These are located very close to the emission wavelengths of ZPLs of the dominant red and blue sites, but do not match up exactly indicating that they are a distinct species. The relative intensity of these aggregate bands changes with respect to the intense ZPLs depending on the deposition conditions used in the preparation of a given sample. The ZPL of the red site was typically the most intense band in the spectrum regardless of deposition conditions. The aggregate species were found to be more stable than the monomers upon annealing.

VI.4.IV.b: Krypton

The spectroscopy of GaPcCl recorded in Kr is in part, similar to that in Ar. The 0-0 transition in absorption becomes more clearly defined with higher temperature depositions, as does the resolution of the vibronic bands and this can be seen in Figure V.14. The 0-0 was identified at 675.6 nm , red shifted with respect to both N_2 and Ar. Higher temperature ovens and larger gas flows again yielded more concentrated samples, but where N_2 and Ar matrices typically showed AE once the sample was saturated in absorption, this was not the case for Kr. While AE was observed in Kr, it was more difficult to produce samples capable of exhibiting the effect in this host than in Ar or N_2 . In samples where AE was

observed, the presence of two strong AE bands was also reported; 751.6 and 754.1 nm. Both AE bands involved the vibronic mode at 1540 cm^{-1} , and therefore originated from two distinct sites. A number of weaker AE bands are present in the spectrum also, but with much lower intensity than the main AE bands.

The 2D-EE plot presented in Figure VI.11 shows two major features that are quite broad in both emission and excitation, similar to the aggregate species reported in Ar. This suggests that aggregate formation may be more common in Kr matrices than in Ar matrices. A series of emission slices through the 2D plot were presented in Figure VI.12, and show a number of intense AE bands. Depending on the excitation wavelength, several bands can exhibit AE at once, and in some cases the bands are located too close together to be fully resolved. This indicates a continuum of sites is present in Kr, similar to what was observed in Ar.

Excitation spectra in Kr show similar features to those observed in Ar. A selection of excitation spectra presented in Figure VI.13 show only weak ZPLs compared to their intense counterparts in Ar. The phonon structure observed in Ar is not present in Kr, possibly due to the low intensity of the ZPLs. The 2D-EE plot shows two regions of very sharp lines (less intense than in Ar, but in the same location) which indicates that a continuum of sites exists in Kr. The broad bands which were attributed to aggregate species in Ar dominate the excitation spectra in Kr. This is consistent with the earlier observation that the 2D-EE plot contains two main sites which are quite broad in both emission and excitation.

VI.4.IV.c: Xenon

Emission from Xe was comparable to both the N_2 system and Ar and Kr systems. The broad fluorescence bands are reminiscent of the N_2 samples, while the doubling of the spectrum due to the presence of sites is more like Ar and Kr. The spectra presented in Figure V.44 show how Xe has similarities to all of the matrix hosts used in the current work. The broadness of the fluorescence in Xe may be intrinsic due to its light scattering properties. Figure V.26 shows how the fluorescence changes with respect to the excitation wavelength. Two main sites seem to dominate the spectra and this is verified by looking at the amplified emission. Figure VI.14 and right panel of Figure VI.15 show two AE bands (762.1 and 763.2 nm), consistent with the fluorescence data. While it is probable that more

than two sites are present in this host, only the aforementioned AE bands show any degree of resolution.

Excitation spectra in Xe are less resolved than in Ar or Kr, but do show similar structures up to 1000 cm^{-1} . The 0-0 band in excitation is much weaker than in any of the other matrices and is not even the most intense peak on the spectrum. The excitation spectra of the AE bands are far more resolved and have very similar vibronic structure to the AE excitation spectra recorded in Ar and Kr. The ZPL is not evident in Xe, unlike the lighter rare gas matrices, which indicates the monomer species is not present in Xe matrices. The aggregate species observed in Ar and Kr dominates the AE region in both emission and excitation.

VI.4.IV.d: Nitrogen

N_2 matrices were easily able to exhibit amplified emission with pulsed laser excitation. The emission spectra recorded in N_2 tended to be quite broad with the hint that there may be several sites present very close together in energy. Despite several attempts, these sites could not be resolved. Figure V.35 shows the emission spectra of GaPcCl trapped in N_2 excited by a number of different wavelengths. In all instances, the band positions appear at the same energy and there is little difference in their shapes either. In spite of this, it is likely that a number of sites are the cause for the broadness of the fluorescence bands. The more concentrated samples were also capable of exhibiting amplified emission. Only a single band was observed at 744.9 nm, 1532 cm^{-1} above the band origin. Due to the narrowness of AE bands, these would be the perfect candidate to elucidate the site splitting in this matrix, but alas only two bands could be distinguished (745.06 and 744.98 nm) as shown in Figure VI.17 and Figure VI.18.

Excitation spectra mirror what was observed in emission in the sense that the bands were generally quite broad. There is a sharp peak corresponding to the 0-0 in excitation and several broader bands extending to about 1000 cm^{-1} beyond this. The spectra shown in Figure V.39 show the excitation spectra in N_2 monitoring a host of different emission peaks. A very small, but noticeable shift ($< 5\text{ cm}^{-1}$) in the position of the 0-0 is evident which indicates the presence of multiple sites. The small energy difference between the sites may be the reason they cannot be resolved, as the splitting in other matrices can be as large as 50 cm^{-1} . Excitation spectra of the AE band show two broader structures which are

believed to the aggregate species observed in the rare gas matrices. Vibronic bands extend up to 1000 cm^{-1} , similar to what was observed for the excitation of the fluorescence bands. The resolution of the vibronic bands of N_2 in excitation is poor in comparison to the rare gas matrices and could not be improved despite forming several samples with various different deposition conditions.

VI.5.V: Phonon structure of GaPcCl/Ar

The high resolution emission and excitation spectra of GaPcCl/Ar contained well resolved ZPLs and PSBs. A Wp line fit was performed on the most red site in order to gain insights into the phonon structure of this system, the results of which are shown in Figure VI.5. The line fit matches the ZPL and first PSB in both emission and excitation. It also correctly predicts additional weaker PSBs to the red of the ZPL in emission, although the position of this band is slightly off what is observed experimentally. The fit also predicts additional PSBs to the blue of the ZPL in excitation, but these are obstructed by the so-called aggregate species which has been observed in all matrices. The ZPL and PSB are observed in excitation for each site present in the continuum of sites, as shown most clearly in Figure VI.A1 and Figure VI.A5. Due to the abundance of features in this host material, the same cannot be said in emission, because excitation wavelengths to the blue of 670.3 nm tend to produce AE from multiple sites as well as from the aggregate species. Even though this is a problem, the intense blue site (region III in Figure VI.8) does show this phonon structure, as well as emission from additional sites, as shown by trace M2 in Figure VI.9.

The aspect of the Wp fit which does not match the experimental data very well are the intensities of the hot bands. These bands are predicted to have a comparable intensity to the first phonon side band, but are present only as very weak shoulders in the experimental spectra. While this may indicate a deficiency of the model to correctly describe the behaviour of AE, it may instead be an experimental issue surrounding the threshold conditions of the non-linear optical process for the hot bands. Recording spectra at higher temperatures should result in some enhancement of the intensity of the hot bands, but these experiments have not been performed with the higher resolution 1200 grooves/mm grating. High temperature scans recorded with the 600 grooves/mm grating were inconclusive as to the effect of the temperature on the intensity of the hot bands, owing to the ZPL and PSB not being resolved in these scans.

The phonon structure observed for GaPcCl/Ar supports two of the assignments made in this matrix; a large amount of the isolated monomer is trapped in this host, spread out among a continuum of sites (shown by Figure VI.A1), and that the excitation features to the blue of the ZPLs in the 2D-EE plot shown in Figure VI.8 do not correspond to emission from the isolated monomer. Instead, due to their broadness and lack of resolved sites, these have been assigned as aggregates.

The same phonon structure observed in Ar was not as evident in any of the other host materials used in the current work. Kr showed the presence of a ZPL in excitation, but this narrow band was less intense than the broad band from the aggregate species and there was no evidence for PSBs. This would indicate that Kr is less effective than Ar at trapping GaPcCl as a monomer. Xe matrices contained no traces of any phonon structure, which suggests the trend that the heavier matrices promote the aggregation of GaPcCl. These observations suggest an interesting follow-up study to investigating the lineshapes and possible phonon structure of GaPcCl trapped in Ne matrices. The AE band of GaPcCl in N₂ matrices exhibits some different effects. In AE it appears that very few sites are present, and no phonon structure is observed. In excitation, however, a sharp rise in intensity on the band centred at ~668 nm is perhaps indicative of a ZPL, as shown in Figure VI.19. This band is unresolved, probably due to the high number of sites which are evident in N₂ matrices. No resolved phonon structures were observed in this matrix.

VI.5: Conclusions

The observation of amplified emission in all matrices indicates GaPcCl is a robust dye molecule which can be isolated in stable sites in a range of different environments. A threshold dependence on the AEs process was evident as low concentration samples did not exhibit this phenomenon, whereas slightly higher concentration samples could produce an array of AE bands, each originating from a different site. The vibronic band associated with this phenomenon was identified with input from DFT calculations and this also confirmed that the multiple AE bands in a sample were originating from different sites of isolation, and not from different vibronic bands. The vibrational mode responsible for the effect involved an asymmetric stretch of the bridging C_α-N_m-C_α bonds, and coincides with the strongest Raman-active mode observed experimentally and predicted by DFT.

2D-EE plots were used in conjunction with amplified emission to extract information about the sites present in each matrix. It was observed that N₂ produces the seemingly simplest matrices with only a single band evident under the highest possible resolution of the experiment. Kr and Xe matrices were more complicated, showing several stable sites of isolation. Ar was the most complicated matrix, trapping molecules in numerous different sites causing what looks like a continuum of emission and amplified emission bands. Annealing of the sample showed a preference for the red-most site to be occupied, indicating it is the most stable. A reversal of the trend of site occupancies was observed for GaPcCl compared to H₂Pc and ZnPc⁶. Where the planar phthalocyanines showed many sites in N₂ matrices, the non-planar GaPcCl appears to have much simpler site splitting in this host. The opposite was observed in the rare gas matrices, where GaPcCl contains several highly occupied sites compared to H₂Pc and ZnPc, which contain fewer sites. The energy gap of the dominant red and blue ‘aggregate’ features was largest in Kr (44 cm⁻¹) and Ar (38 cm⁻¹), while that in Xe was only 19 cm⁻¹. The splitting’s in N₂ were too small to be resolved under current experimental conditions.

Ar tended to form matrices capable of trapping the molecule in its monomeric form (as demonstrated by the *Wp* lineshape analysis of the simplest emission and excitation bands in Figure VI.5), but these samples always contained significant amounts of aggregate species. The heavier rare gases, Kr and Xe, were very poor at trapping the molecule in its monomeric form, but were efficient at producing samples containing large amounts of the aggregate species. The presence of aggregates was also observed in N₂ matrices. This trend is inconsistent with other porphyrin systems studied in the matrix⁶, where the heavier matrices were excellent at trapping the guest species in highly isolated sites as a monomer. The difference between GaPcCl and the other porphyrin systems which have been studied in the matrix is that it is a non-planar molecule due to the presence of the Cl⁻ ion. This atom prevents π - π stacking of GaPcCl dimer, which occurs in the planar phthalocyanines¹¹, and would suggest that the planar Pcs should be more efficient at forming aggregates. However, the Cl atom gives the GaPcCl molecule a large electric dipole moment (calculated at 3.6163 Debye from DFT calculations in the current work), and this allows for strong Coulombic interactions to occur, promoting aggregation.

The current work on GaPcCl has yielded new insights into the different features that can form when non-planar phthalocyanines are isolated in inert gas hosts. This is the first

known instance of a phthalocyanine molecule exhibiting phonon structure when isolated in solid Ar, and has allowed for the GaPcCl monomer to be identified in Ar and Kr. Its position in N₂ is also expected to be located around 745 nm in excitation based on these results. The narrowness of the ZPL of the monomer has given credibility to the assignment of the broad emission/excitation features being aggregate species. The calculation of a strong electric dipole moment for GaPcCl also gives a mechanism for how aggregates may form more easily than for the planar phthalocyanines. This work also opens the questions as to whether phonon structures and aggregation occurs in the other non-planar phthalocyanines. The first obvious candidate for a follow-up study would be the well-known AlPcCl molecule.

VI.6: References

1. Basova, T. V.; Kiselev, V. G.; Latteyer, F.; Peisert, H.; Chassé, T., Molecular organization in the thin films of gallium(III) phthalocyanine chloride and its μ -(oxo)dimer: Optical spectroscopy and XPS study. *Applied Surface Science* **2014**, 322, 242-248.
2. Mathew, S.; Sudarsanakumar, C.; Menon, C. S., Optical, electrical and structural characterization of gallium phthalocyanine chloride thin films. *Optoelectronics Advanced Materials, Rapid Communications* **2007**, 1 (11), 614-619.
3. Pyatosin, V. E.; Tsvirko, M. P., Triplet-triplet absorption spectra of phthalocyanine and its metal complexes. *Zhurnal Prikladnoi Spektroskopi* **1980**, 33 (2), 320-5.
4. Sorokin, P. P.; Lankard, J. R., Stimulated emission observed from an organic dye, chloroaluminum phthalocyanine. *I.B.M. Journal of Research and Development* **1966**, 10 (2), 162-3.
5. Huang, T. H.; Rieckhoff, K. E.; Voigt, E. M., Shpol'skii effect and vibronic spectra of the phthalocyanines. *The Journal of chemical physics* **1982**, 77 (7), 3424-3441.
6. Dozova, N.; Murray, C.; McCaffrey, J. G.; Shafizadeh, N.; Crepin, C., Amplified emission of phthalocyanine isolated in cryogenic matrices. *Physical Chemistry Chemical Physics* **2008**, 10 (16), 2167-2174.

7. Crépin, C.; Shafizadeh, N.; Chin, W.; Galaup, J.-P.; McCaffrey, J. G.; Arabei, S. M., Unveiled optical properties of tetrapyrrolic pigments in cryogenic environments. *Low Temperature Physics* **2010**, *36* (5), 451-457.
8. Arabei, S.; McCaffrey, J. G.; Galaup, J.-P.; Shafizadeh, N.; Crepin, C., Stimulated emission in cryogenic samples doped with free-base tetraazaporphine. *Physical Chemistry Chemical Physics* **2015**, Ahead of Print.
9. Arabei, S. M.; Galaup, J. P.; McCaffrey, J. G.; Shafizadeh, N.; Crépin, C., Electronic spectroscopy, stimulated emission, and persistent spectral hole burning of cryogenic nitrogen matrices doped with tetrabenzoporphin. *Low Temperature Physics* **2012**, *38* (8), 727-731.
10. Wynne, K., *Journal of Inorganic Chemistry* **1984**, *23*, 4658.
11. Naito, Y.; Matsumoto, T.; Sugiura, K.; Sakata, Y.; Kawai, T., Observation of zinc phthalocyanine one-dimensional π -stacking structures. *Hyomen Kagaku* **2000**, *21* (8), 496-501.
12. Linsky, J. P.; Paul, T. R.; Nohr, R. S.; Kenney, M. E., Studies of a series of haloaluminum,-gallium, and-indium phthalocyanines. *Inorganic Chemistry* **1980**, *19* (10), 3131-3135.
13. Bondi, A., van der Waals Volumes and Radii. *The Journal of Physical Chemistry* **1964**, *68* (3), 441-451.
14. Legay, F.; Legay-Sommaire, N., Cooperative two-phonon absorption in solid α -nitrogen in the 4600–4700 cm^{-1} region. *Chemical Physics* **1996**, *206* (3), 363-373.

VI.7: Appendix

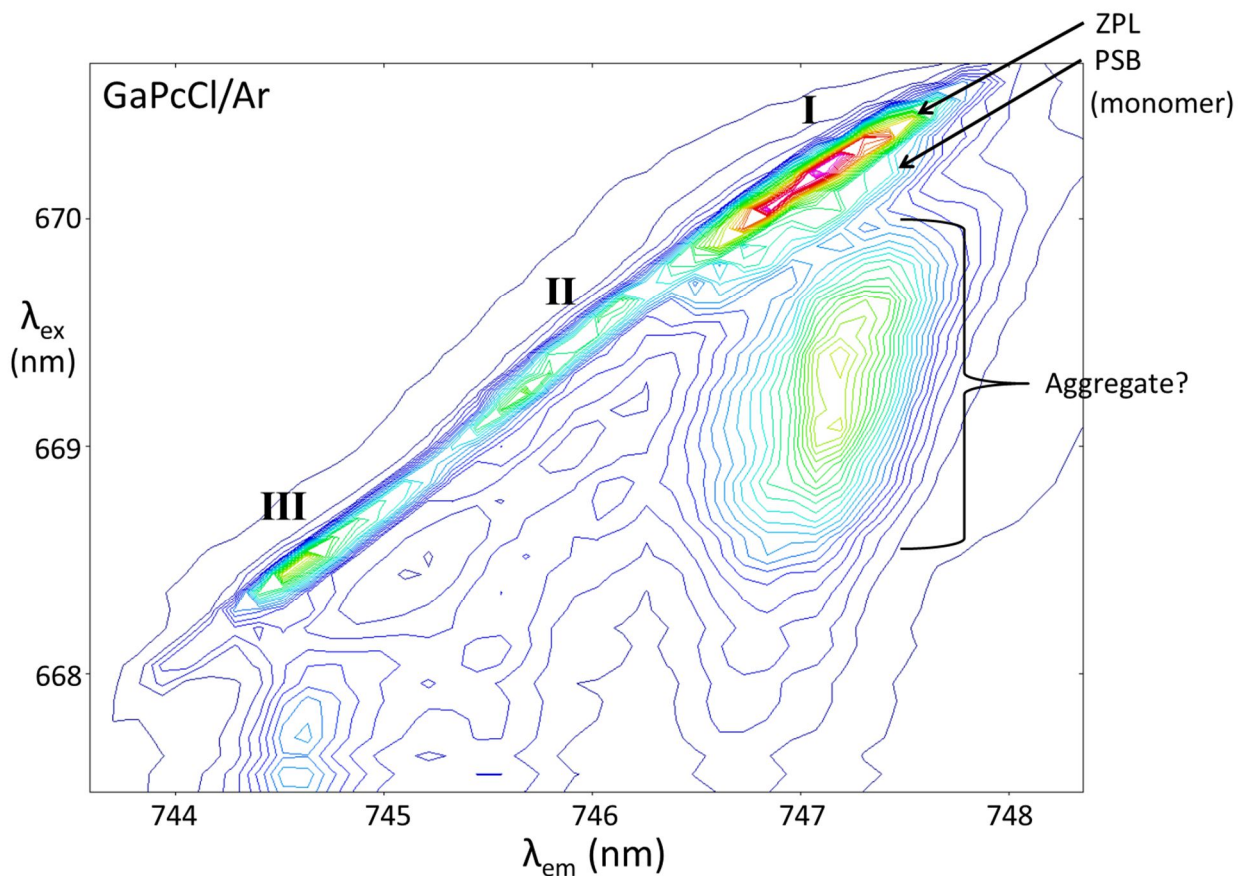


Figure VI.A1: An expanded view of the 2D-EE plot of GaPcCl/Ar in the three regions of the AE bands. The regions corresponding to the ZPLs and PSBs of the isolated species are labelled. The region which has tentatively been assigned as an aggregate species has also been labelled.

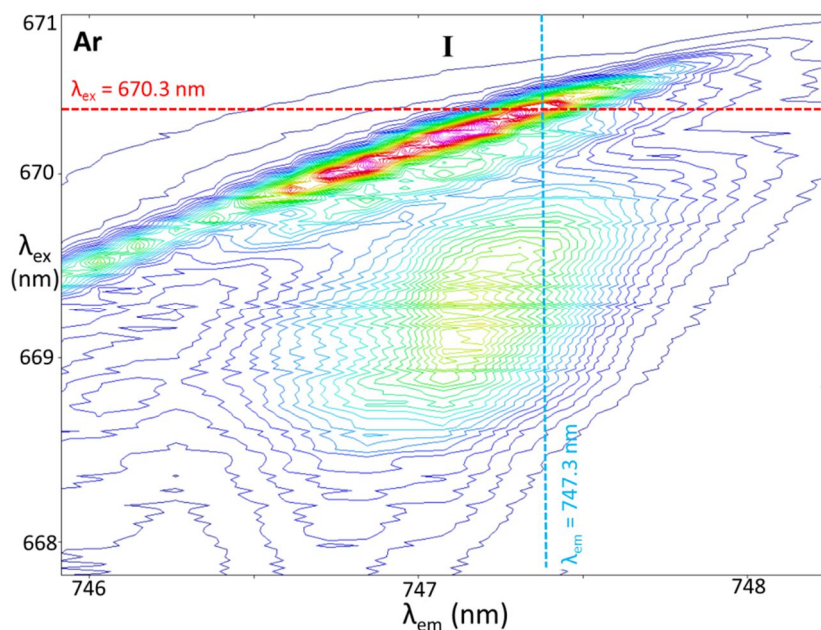


Figure VI.A2: Expanded view of region I (the red features) from the 2D-EE plot of GaPcCl/Ar shown in Figure VI.8. Here the region corresponding to the ZPLs are represented with the red contour lines. The region immediately to the blue in excitation of the ZPLs are the PSBs, which carry much less intensity. Even further to the blue is a broad feature which has been tentatively assigned as an aggregate. The red and blue dashed lines show the wavelengths of the emission and excitation spectra that were extracted to perform the Wp fit function on.

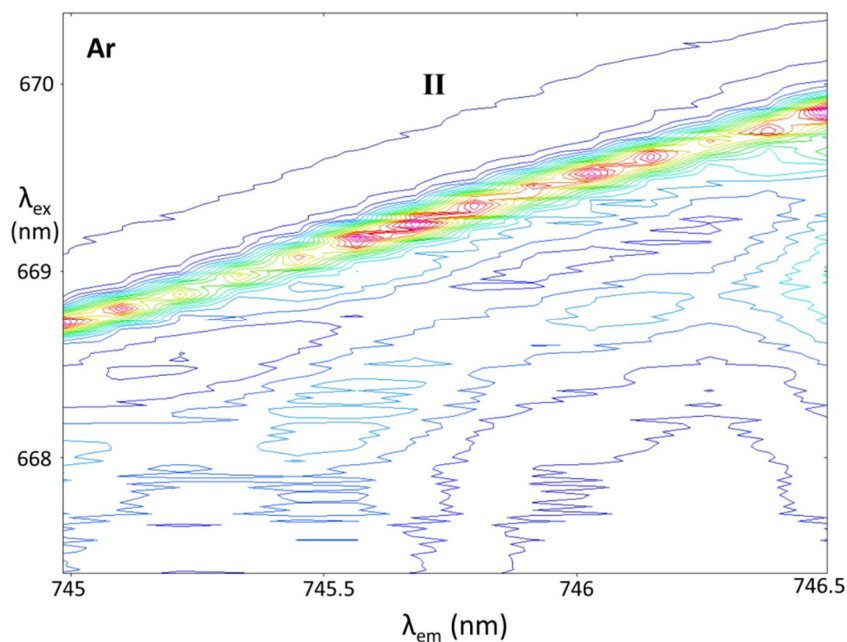


Figure VI.A3: Expanded view of region II (between the red and blue features) from the 2D-EE plot of GaPcCl/Ar shown in Figure VI.8. Here the region corresponding to the

ZPLs are represented with the red/orange contour lines. The PSBs are more difficult to identify in this region. There is no evidence of the broad feature which is present in both the red and blue regions.

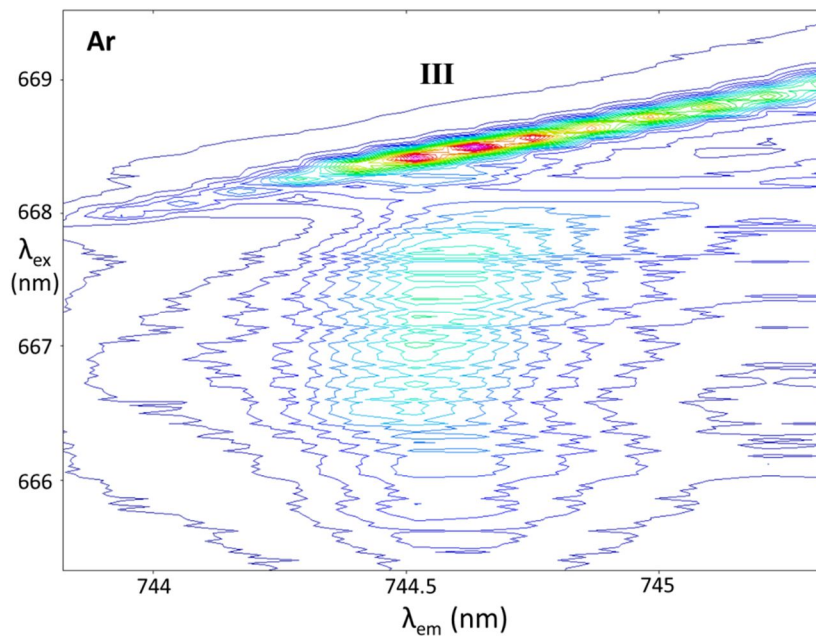


Figure VI.A4: Expanded view of region III (the blue features) from the 2D-EE plot of GaPcCl/Ar shown in Figure VI.8. Here the region corresponding to the ZPLs are represented with the red contour lines. The PSBs are difficult to identify on this scale. A broad feature located to the blue of the ZPLs has been tentatively assigned as an aggregate.

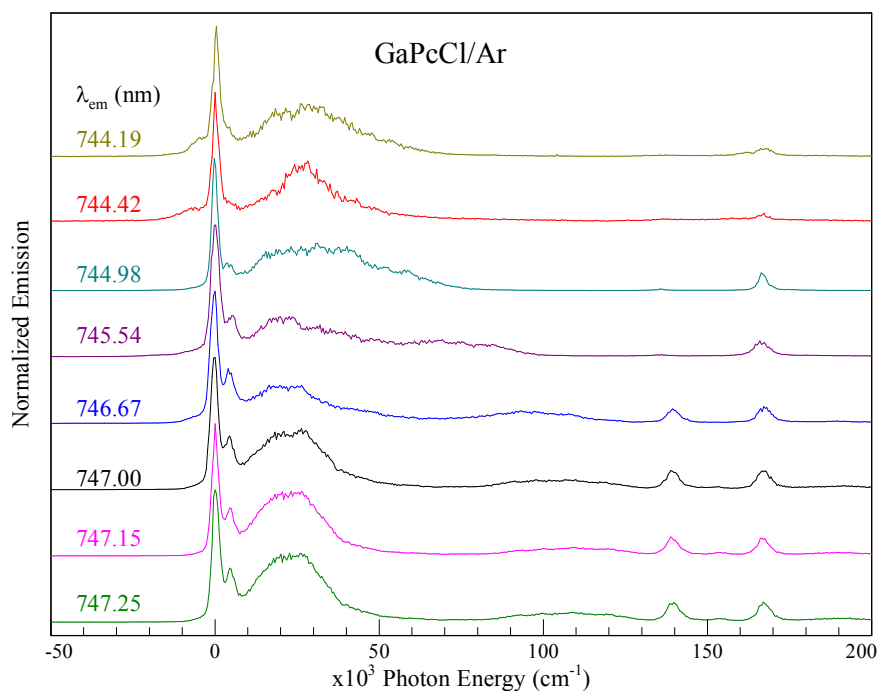


Figure VI.A5: A selection of excitation spectra of GaPcCl/Ar extracted from a 2D-EE plot at different emission wavelengths. Each spectrum is shown as its shift from the 0-0 band to demonstrate that the vibronic structure is common to all sites.

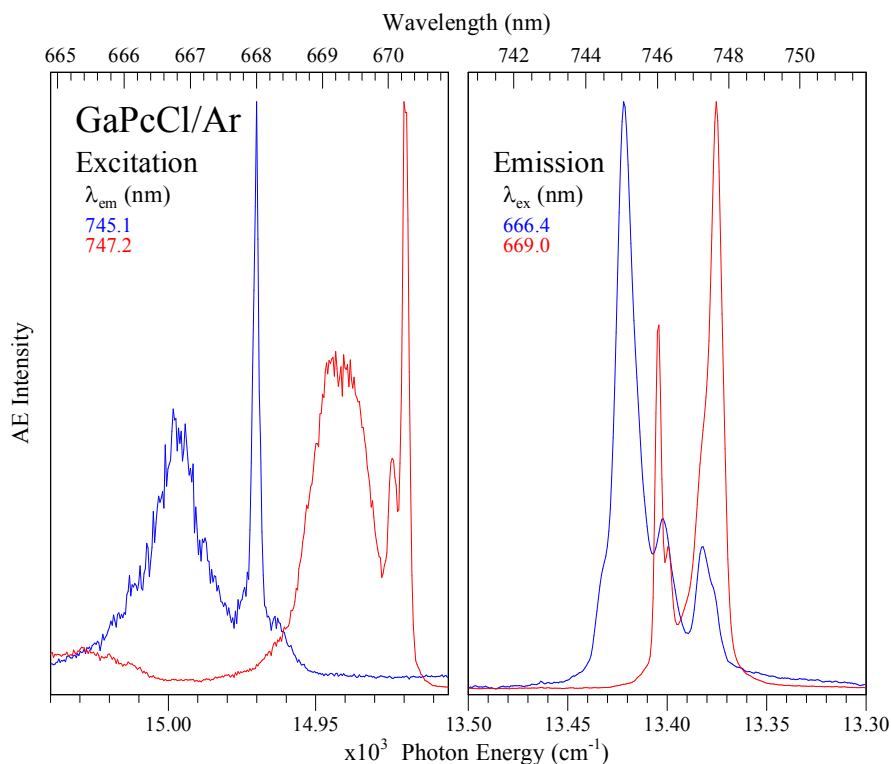


Figure VI.A6: Emission and excitation slices extracted through the maxima of the broad red and blue features in Figure VI.8. The broadness of the bands, especially when compared to the ZPLs of the monomer species, indicate that these features are aggregates.

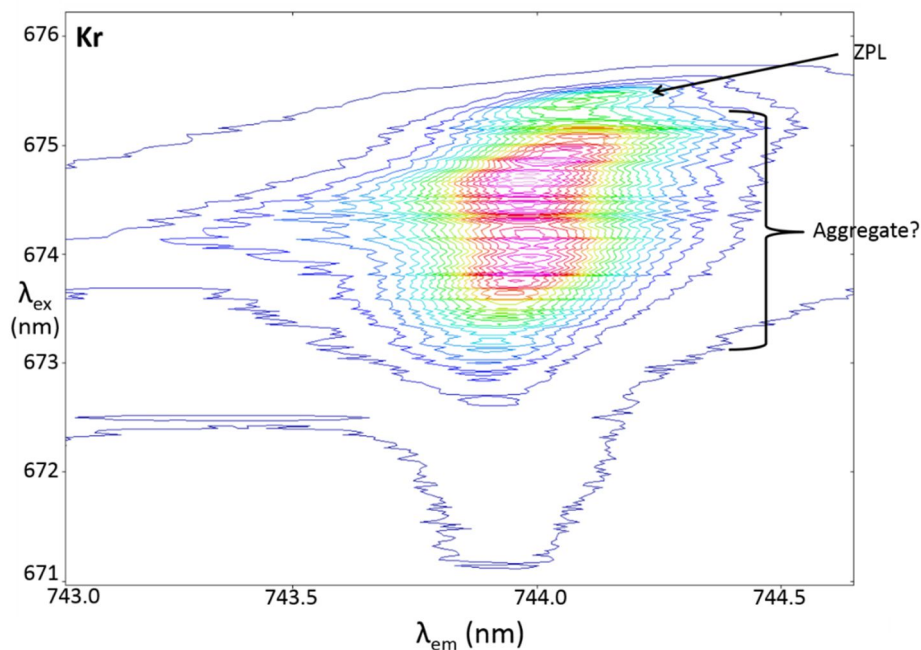


Figure VI.A7: Expanded region of the red features from the 2D-EE plot of GaPcCl/Kr shown in Figure VI.11. The region represented by the red contour lines corresponds to the aggregate species identified in the Ar matrix. The ZPLs from the most red sites are located to the red of this feature, but carry significantly less intensity. This is contrasting behaviour to Ar, where the ZPLs carried the most intensity.

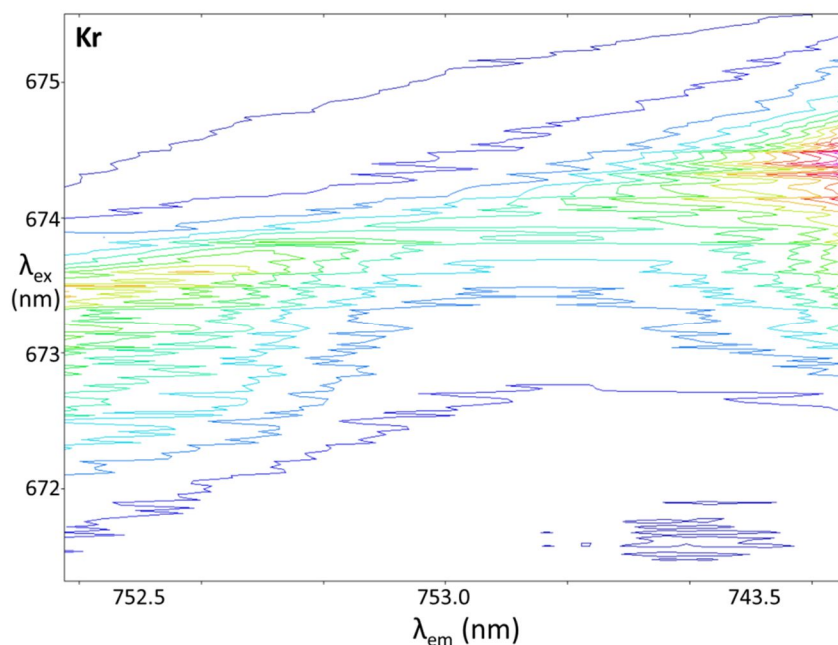


Figure VI.A8: Expansion of the region between the red and blue features from the 2D-EE plot of GaPcCl/Kr shown in Figure VI.11. The corresponding area in the Ar spectrum showed a series of ZPLs which are not evident here.

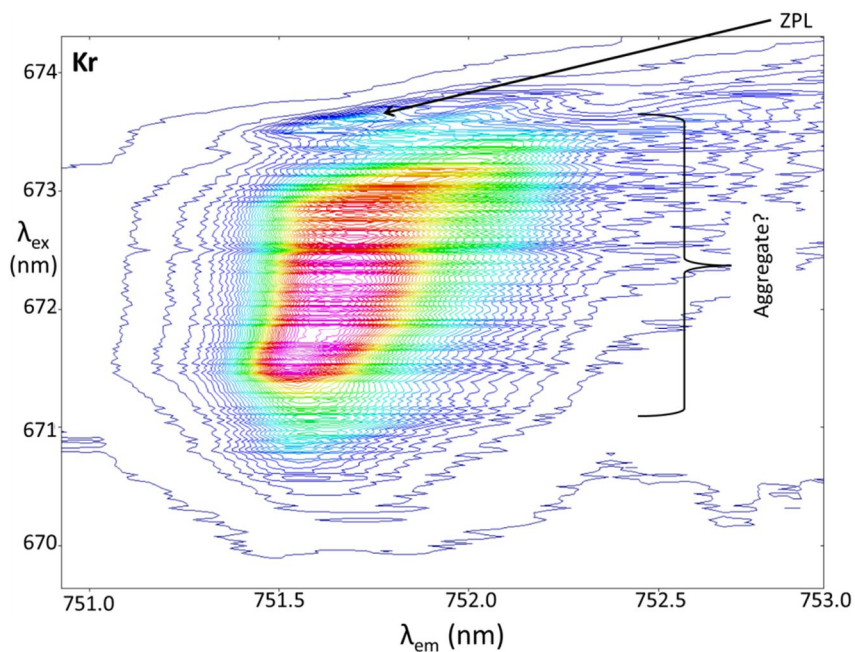


Figure VI.A9: Expanded region of the blue features from the 2D-EE plot of GaPcCl/Kr shown in Figure VI.11. The region represented by the red contour lines corresponds to the aggregate species identified in the Ar matrix. The ZPLs from the monomer species are located to the red (in excitation) of this feature, but carry significantly less intensity. This is contrasting behaviour to Ar, where the ZPLs carried the most intensity.

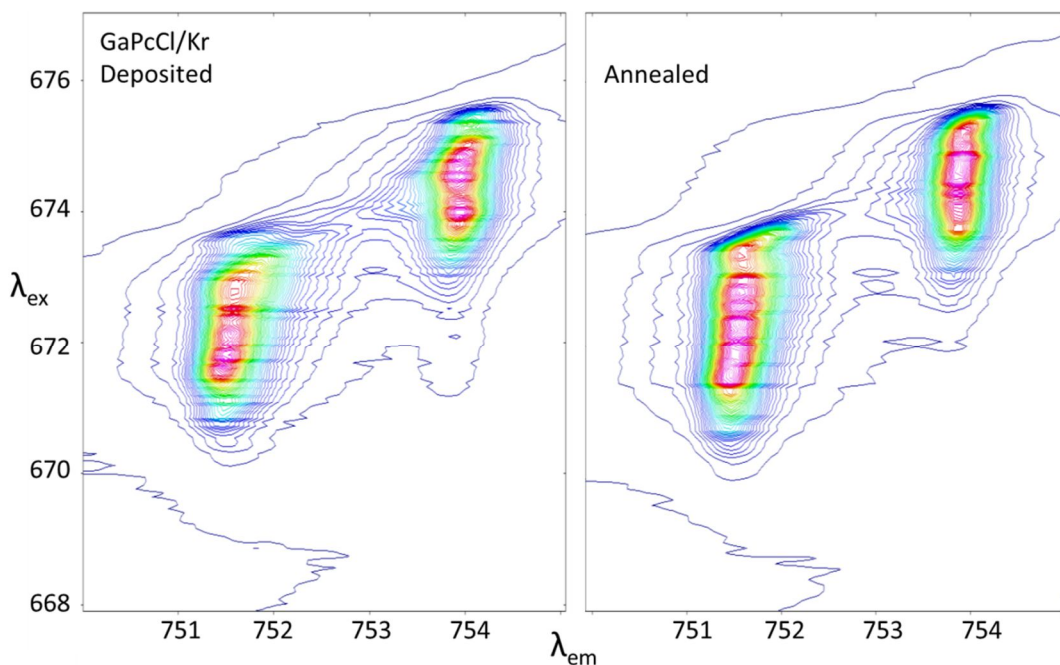


Figure VI.A10: 2D-EE plots of GaPcCl in Kr recorded at 10 K. The plot on the left has been recorded after deposition and the plot on the right after annealing to 22 K. Both spectra were recorded with the 600 grooves/mm grating installed in the monochromator.

Chapter VII: Conclusions

The aim of this work was to conduct a combined experimental and theoretical study on some of the structural and spectroscopic properties of metal phthalocyanines (M-Pcs) and metal tetraazaporphyrins (M-TAPs). Experimental work consisted primarily of matrix-isolation spectroscopy of M-Pcs and M-PcCl_s. Quantum chemical calculations were extensively employed to assist with the analysis of complicated experimental results and as a standalone method for investigating other phenomena. Density functional theory (DFT) was the preferred theoretical method in this work, as it has a proven track record for accurately describing the ground state properties of small to medium sized molecules. DFT was used to examine the structure of a number of metal phthalocyanine and metal tetraazaporphyrin species. The effect of isotopic substitution of the inner hydrogens on free-base porphine and related tetrapyrroles was also studied using DFT calculations. Infrared spectroscopy experiments were conducted on MgPc, AlPcCl and GaPcCl isolated in inert gas matrices. Raman scattering experiments and DFT calculations were also run on these molecules, allowing for a comprehensive vibrational analysis to be performed. The visible luminescence spectra of matrix-isolated GaPcCl were recorded in a number of different inert gas hosts. The effect of the host on the absorption, emission and excitation spectroscopy was thereby analysed. Amplified emission from GaPcCl was observed in highly concentrated matrix samples, and this was used to probe the features present in each matrix host.

VII.1: Symmetry of the M-Pcs and M-TAPs

A theoretical approach was used to determine the effect of a metal occupying the central cavity in TAP and Pc using DFT methods. The free-base (metal-free) TAPs and Pcs are expected to be planar with D_{2h} symmetry¹. Incorporating a metal into the inner cavity changes the symmetry based on the fact that it will bind to all four of the pyrrole nitrogens. A series of DFT calculations was performed on the M-TAPs and M-Pcs where M = Mg, Ca, Sr, Ba, Zn, Cd, Hg, AlCl, GaCl, Al⁺ or Ga⁺. Each molecule was given an initial D_{4h} symmetry (except for the M-PcCl_s/M-TAPCl_s) and the structure was then optimized using DFT methods. Where available, the structures predicted by DFT agreed excellently with crystal structures. Two structures emerged from the calculations depending on the size of the metal atom – planar with D_{4h} symmetry or non-planar with C_{4v} symmetry. The extent

to which the metal lies above the plane of the ring was entirely dependent on its size, with larger metal atoms sitting higher above the plane. A doming was observed on the rest of the porphyrin for the non-planar molecules, the severity of which was also related to the size of the metal atom.

Calculations performed on AlPcCl and GaPcCl showed these molecules to be non-planar with the metal atom slightly above the the N₄ plane. The porphyrin ring also exhibited the doming effect observed when large metal atoms inhabited the cavity. A complementary calculation on the related AlPc⁺ and GaPc⁺ molecules showed them to be planar with D_{4h} symmetry, indicating that the presence of a counter-ion pulls the metal from the macrocycle cavity and distorts the planarity of the porphyrin ring. The extent of doming observed on the M-PcCl/M-TAPCl was significantly smaller than the M-Pcs/M-TAPs. The macrocycles of AlPcCl and GaPcCl are distorted from being planar by only 2.8 and 3.9 ° respectively. This may explain why these molecules are so strongly absorbing in the visible, as they have not lost any of their conjugation – a requirement for aromaticity.

The symmetry of these molecules has a significant effect on their vibrational spectra. The structural difference between a D_{4h} and a C_{4v} M-TAP/M-Pc does not appear great; both symmetries will have the same number of atoms and hence the same number of vibrational modes (3N-6). The D_{4h} point group contains the ‘*i*’ symmetry element, denoting a centre of inversion exists in the molecule. This implies that the ‘rule of mutual exclusion’ applies, where IR active modes are not Raman active and *vice versa*. This rule does not apply to the C_{4v} point group, so IR active modes can also be Raman active. This effect was observed by investigating the vibrational spectra of the C_{4v} molecule CaTAP and the D_{4h} molecule MgTAP, where some modes of CaTAP show well defined peaks in both its IR and Raman spectra, whereas the equivalent mode of MgTAP will appear in only one spectrum. This symmetry effect was also observed in the experimental IR and Raman spectra of MgPc and AlPcCl.

VII.2: Vibrational Analysis of Matrix-Isolated MgPc, AlPcCl and GaPcCl

The infrared spectra of MgPc, AlPcCl and GaPcCl have been recorded in solid Ar and N₂ matrices at cryogenic temperatures. Highly resolved vibrational bands were observed in the 400 cm⁻¹ to 1700 cm⁻¹ region for each molecule. Spectra recorded in inert gas matrices were compared to those recorded in KBr discs. A substantial improvement in the resolution

and the linewidths of bands was observed in the matrix owing to molecules being highly isolated and weakly interacting with the host material. The IR spectra were analysed with the input of high level DFT calculations, which agreed excellently with experimental results when a scaling factor was applied to the predicted vibrational frequencies. The DFT calculations allowed for the symmetries and motions of each vibrational mode to be described and it was found that the IR spectra of MgPc (AlPcCl, GaPcCl) consist of mostly A_{2u} (A_1) and E_u (E) modes, pertaining to out-of-plane and in-plane distortions of the porphyrin ring and outer hydrogens.

The Raman scattering spectra of MgPc, AlPcCl and GaPcCl were recorded in room temperature KBr discs using two excitation sources; a 532 and a 660 nm CW laser. Deviations in the positions of the high frequency vibrational bands with respect to the laser excitation wavelength indicate a slight calibration issue with the spectrometer system. Intensities of several bands differed significantly depending on the excitation source, which is an indication of resonance Raman effects. A broad fluorescence background was also observed with the 660 nm excitation – a wavelength where these molecules tend to have their strongest absorption bands^{2,3}. Scaled DFT Raman frequencies compared well with the experimental spectra, although not as well as with the IR results. The intensities of the modes below 1000 cm^{-1} were underestimated, but the frequencies were predicted to a reasonable accuracy. An analysis of the Raman spectra shows that the Raman active modes which carry the most intensity are all in-plane vibrations, usually involving distortion of either the macrocycle or the isoindole units.

VII.3: Reverse ISR of Free-base Porphyrin and Related Tetrapyrroles

The effect of isotopic substitution of the inner hydrogens on the free-base tetrapyrroles showed some intriguing effects. Contrary to expectations, not all of the vibrational modes associated with the N-H(D) bond showed an isotopic shift ratio (ISR) value of greater than 1. The high frequency, N-H stretching modes show the expected trend. This is because they are highly localized and crossings can occur with the C-H stretching modes as the mass of the hydrogen increases. This is due to the fact that there is no inter-mode-coupling in these modes and thus the expected ISR ratios are observed for these modes.

The lower frequency N-H OP bends involve well defined out-of-plane bending motions in both the N-H and N-D bonds. No crossings occur for the B_{2g} symmetry Raman-active

modes for the smaller tetrapyrroles (P and TAP), but crossings do occur for the B_{2g} modes of Pc and TBP as they still involve localised N-H motions, as can be shown with simple mass dependence curves. Due to a single mode crossing which occurs in both Pc and TBP, frequency increases do occur in the heavier isotopomer but because of the involvement of only two modes, instances of reversed ISR can be easily identified in the mass dependent calculations.

The IR-active B_{3u} OP bending modes are slightly more numerous than their Raman counterparts and exhibit more complex behaviour. The N-H OP bending mode is crossed by two modes for all four molecules. One of these modes is weakly coupled with the N-H OP bend and passes directly through the N-H OP bending mode, while the other mode is strongly coupled and produces a large avoided crossing. The strong coupling of the two modes causes an increase in the frequency of the heavier isotopomer, and this produces a reversed ISR value. In all these situations the vector diagrams of the motions reveal a reversal of the N-H and N-D motions between the light and heavy isotopomer. The OPB modes provide the simplest examples of the effect the reverse ISR effect, where coupling of modes is necessary for an avoided crossing to exist.

The N-H IP bending modes show more complex behaviour than their OPB counterparts due to the large number of modes with B_{2u} and B_{3g} symmetries. This results in the N-H(D) IP bending modes to be dispersed over many vibrational modes. The change in the N-H frequencies is less than the predicted $m_H^{-1/2}$ mass dependence due to the dilution of this motion over several modes. No IPB mode can be assigned as the true NH(D) IPB mode as the contribution of NH(D) motion in these modes is always below 30%. These modes are located in a congested spectral region (around 1000 – 1200 cm^{-1}) where crossings occur with modes containing no NH(D) motion. These crossings all involve modes that are not strongly coupled. Some B_{3g} modes experience coupling in the high frequency (1200 cm^{-1}) range but produce only weak avoided crossings. The best examples of this are present in porphyrin and TBP. This coupling does not occur in TAP and only weakly in Pc.

VII.4: Visible Spectroscopy of Matrix-Isolated GaPcCl

The UV/Vis absorption of GaPcCl was studied in the inert gas hosts N_2 , Ar, Kr and Xe at cryogenic temperatures. The locations of the Q and B bands were measured around 670 and 350 nm respectively. The location of these bands shifted towards the red as the mass of the host gas increased and the interaction between the host and guest species got stronger.

TD-DFT calculations were performed to determine the electronic transitions of GaPcCl and were found to be consistently blue-shifted from their experimental counterparts. Weak transitions were observed experimentally in the 400 – 450 nm region which were also found in the TD-DFT calculations. A comparison of matrix absorption spectra with solution phase results show that the solid state produces much sharper bands with vibronic structure extending up to around 600 nm. The solution phase spectrum shows three broad features in the region of the Q band. These three bands correspond to the band origin and two of the strongest vibronic bands, which were identified in the higher resolution matrix absorption spectra.

Emission spectra of GaPcCl were recorded by exciting into the strong absorption bands. Sharp fluorescence peaks were typically observed up to 760 nm. A measurement of the shift from the 0-0 shows vibronic bands in emission extending up to about 1600 cm^{-1} from the band origin, and was consistent for all matrix hosts. Shifts in the positions of the vibronic bands with respect to the excitation wavelength were indicative of there being more than one site present in the matrix. The simplest fluorescence spectra were recorded by exciting into the dominant red site, where only a single site produced emission. The vibronic bands in emission were compared with ground state Raman results and a good agreement was found. This agreement is due to the similar set of selection rules that govern both sets of transitions, and allowed for a vibrational analysis of the first excited electronic state to be performed. Mirror symmetry between the absorption and emission bands was observed, indicating the structures of the ground and excited electronic states do not differ significantly. The emission lifetime of GaPcCl was measured in each matrix host and found to be consistently between 2.3 – 2.6 ns; a timescale expected for a strongly absorbing dye molecule.

Excitation spectra were also recorded and showed some good structure up to 1000 cm^{-1} from the 0-0 in excitation. Similar vibronic bands in excitation were found in all of the hosts used in the current work, with varying levels of resolution. Good agreement between the 0-0 and vibronic bands in absorption and excitation further reinforced the idea that the ground and excited states have a very similar structure. Site structure was also observed in excitation, as the 0-0 in excitation shifted depending on which emission wavelength was being monitored.

VII.5: Amplified Emission of Matrix-Isolated GaPcCl

In high concentration samples of matrix-isolated GaPcCl a single vibronic band in emission showed a significant gain in intensity when excited with a high powered pulsed dye laser. This phenomenon was observed in all four host gases and was attributed to being amplified emission (AE). This was proven to be the correct assignment by identifying three key properties of AE. Firstly was the aforementioned enhancement of the emission intensity of a single vibronic band, along with a significant narrowing of the bandwidth of the peak compared to that of the normal fluorescence. The second piece of evidence for this being AE was the lifetime of this enhanced band, which closely resembled the decay profile of the laser pulse more so than the fluorescence decay profile. Finally, a threshold dependence on this process was observed by varying the intensity of the laser pulses. The threshold dependence argument is also consolidated by the fact that the lower concentration samples did not exhibit AE under any circumstances. A comparison of the emission and Raman/DFT spectra allowed for identification of the vibronic band associated with AE. The most intense Raman active mode is responsible for the effect; a B_2 mode at 1540 cm^{-1} (for GaPcCl/Ar) corresponding to an asymmetric stretch of the C_α - N_m - C_α bonds. A similar vibrational mode has been identified to be responsible for AE in the structurally related molecules H_2Pc , $ZnPc^4$, H_2TBP^5 and H_2TAP^6 .

In most samples of matrix-isolated GaPcCl, it was possible to excite more than one AE band with a single excitation wavelength. This was indicative of there being several sites present in these samples, consistent with observations from the fluorescence data. A Wp fit was performed on the high resolution emission and excitation AE spectra of the most red site of GaPcCl/Ar (which gives the simplest emission/excitation spectra) in order to understand the nature of the electronic transition. A sharp ZPL was observed, along with a moderately intense PSB. A second PSB was evident in emission, but was obscured in excitation by a different species which was tentatively assigned as an aggregate due to its broadness. The Wp fit also predicts fairly intense hot bands to arise, but these were not observed experimentally. This may be a threshold issue associated with AE, as the Wp fit is generally used to describe fluorescence.

2D excitation-emission (2D-EE) spectra recorded in the region of the AE bands were used to investigate the sites in each matrix due to the highly selective nature of AE, coupled with the narrow bandwidths it produces. A continuum of sites was observed in Ar matrices,

each with a well-resolved ZPL and PSB. These sharp lines were attributed to being the isolated monomer from different sites. Two major features to the blue of the ZPLs in excitation also exhibit AE strongly. These features, separated by 38 cm^{-1} , have been tentatively assigned as aggregates due to their broadness, especially when compared to the narrow ZPLs. Kr and Xe matrices showed some similarities to the Ar matrix, although they did not appear as extreme with the number of sites present, and the phonon structure is not as clear in either matrix. The ZPLs from isolated monomers of GaPcCl may have been evident in Kr, but they were not the dominant species in this host. Instead, Kr matrices showed two main features which exhibit AE (split by 44 cm^{-1}), and a host of sites which exhibited weaker emission located between these two sites. These features were most likely the aggregate species observed in Ar. Xe matrices also had this structure, although the splitting between the two major features was only 19 cm^{-1} . No ZPLs were observed in Xe, indicating very little isolated monomer was present in this host, and certainly not enough to reach the threshold value required to exhibit AE. N_2 matrices showed sites located very close together in energy; too close together to be resolvable under the current experimental conditions. The rich abundance of features in the atomic matrices and apparent lack of sites in N_2 was incongruous with previous matrix studies on porphyrin and phthalocyanine molecules. The reversal of site structure between the atomic and molecular matrices was likely due to the non-planar structure of GaPcCl compared to the planar structure of the species used in the earlier studies. The presence of large amounts of aggregates in the matrix in the current study was also inconsistent with previous work. The most likely explanation for the formation of the aggregate species (particularly in the heavier hosts) was due to the permanent dipole moment of GaPcCl. This strong attractive force (at short distances) allowed for neighbouring molecules to form dipole-dipole interactions, and these 'aggregate' species were responsible for the broad AE bands observed in the 2D-EE spectra.

The current experimental and theoretical work has given some novel insights into the spectroscopy of matrix-isolated phthalocyanines. The Q and B bands are the most well-known absorption bands of the porphyrins and phthalocyanines. A set of weaker bands have been identified immediately to the red of the B band in the absorption spectra of GaPcCl isolated in inert gas hosts, and these weak transitions have also been predicted by TD-DFT calculations. To the best of the author's knowledge, these bands have not been

described for other porphyrin/phthalocyanine systems, and may warrant further research. While the observation of AE for GaPcCl is perhaps unsurprising given the historical significance of the closely related AlPcCl molecule⁷, this phenomenon has allowed for the identification of several features in the matrix which could not have been observed with normal fluorescence. Resolved phonon structure has been observed in both emission and excitation for the continuum of sites in Ar, as well as for the most abundantly occupied sites in Kr. This is the first time such an effect has been described for a phthalocyanine molecule in the matrix, and its origin may be related to the non-planar structure of GaPcCl. While the sharp ZPL was related to the isolated monomer, a broad feature, assigned as an aggregate, dominates in the heavier matrices. This arises due to the strong dipole moment of the GaPcCl molecule. These interesting behaviours and properties of GaPcCl not only advance the literature work on the phthalocyanines, but give rise to new questions and the potential for future studies.

VII.6: References

1. Xin, Z.; Ai-Min, R.; Ji-Kang, F.; Xiao-Juan, L., Theoretical studies on the one- and two-photon absorption of tetrabenzoporphyrins and phthalocyanines. *Canadian Journal of Chemistry* **2004**, *82* (1), 19-26.
2. Basova, T. V.; Kiselev, V. G.; Latteyer, F.; Peisert, H.; Chassé, T., Molecular organization in the thin films of gallium(III) phthalocyanine chloride and its μ -(oxo)dimer: Optical spectroscopy and XPS study. *Applied Surface Science* **2014**, *322*, 242-248.
3. Linsen, P.; Jie, Z.; Wei, K., Electronic polarization spectroscopy of metal phthalocyanine chloride compounds in superfluid helium droplets. *Journal of Chemical Physics* **2007**, *127* (17), 174308.
4. Dozova, N.; Murray, C.; McCaffrey, J. G.; Shafizadeh, N.; Crepin, C., Amplified emission of phthalocyanine isolated in cryogenic matrices. *Physical Chemistry Chemical Physics* **2008**, *10* (16), 2167-2174.
5. Arabei, S. M.; Galaup, J. P.; McCaffrey, J. G.; Shafizadeh, N.; Crépin, C., Electronic spectroscopy, stimulated emission, and persistent spectral hole burning of

cryogenic nitrogen matrices doped with tetrabenzoporphin. *Low Temperature Physics* **2012**, 38 (8), 727-731.

6. Arabei, S.; McCaffrey, J. G.; Galaup, J.-P.; Shafizadeh, N.; Crepin, C., Stimulated emission in cryogenic samples doped with free-base tetraazaporphine. *Physical Chemistry Chemical Physics* **2015**, Ahead of Print.

7. Sorokin, P. P.; Lankard, J. R., Stimulated emission observed from an organic dye, chloro-aluminum phthalocyanine. *IBM Journal of Research and Development* **1966**, 10 (2), 162-163.